Planar Reflection of Gaseous Detonations

Thesis by

Jason Scott Damazo

In Partial Fulfillment of the Requirements

for the Degree of

Doctor of Philosophy

California Institute of Technology

Pasadena, California

2013

(Defended May 31, 2013)

Acknowledgements

Prof. Joe Shepherd is an **incredible** advisor. His breadth and depth of knowledge are staggering. I hope I grow up to be half as clever and kind as Joe. He trusted me—most of the time, more than I trusted myself (and probably more than I deserved). This caused me to be a better researcher than I merited. I cannot thank him enough for the incredible experience I've had at Caltech.

From the time I was a nervous master's student in Prof. Beverley McKeon's Ae101 class, I've looked up to and respected Beverley. She has an intellect worthy of great admiration, and also happens to be a dynamite ultimate frisbee player. Beverley also read my thesis to an amazing level of detail, for which I am very grateful. Prof. Guillaume Blanquart, who insists I drop the honorific and simply call him Guillaume, is always generous with his time. He provided many thoughtful insights into combustion, and is as friendly a face as I could hope to find; even if he never did accept my crème brûlée duel. My final committee member was Prof. Dan Meiron. Dan gave a fresh take on my thesis and I greatly appreciate his time and contributions.

The great faculty, students, and staff at Caltech make it a very special place. Bahram and the Aero Shop have both come to my rescue with last-minute help and greatly contributed to my degree completion. Prof. Shepherd's Explosion Dynamics Laboratory has had an amazing group of students in my time. My very first day in the lab, Sally Bane gave up her desk for me, showed me around, and made me feel at home. Phil Boettcher gave me a crash course in designing experiments and, through example, showed me how to get things done. Sally and Phil are both fantastic lab partners, colleagues, and friends. Visiting Belarus with them was a once-in-a-lifetime

experience that I'll never forget.

I spent more time with Jim Karnesky than any other member of the EDL. I'm lucky to have had so much time with someone so capable. And outside the lab... well, did you know about Los Angeles's secret stairways? I didn't, but that's the type of surprising fun you have when you spend time with Jim and his girlfriend Flora. I owe much to Jack Ziegler for patiently explaining computational fluid dynamics; his beautiful images never fail to amaze. I've had the great pleasure of working with two undergraduates, Kliulai Chow-Yee and Jeff Odell.[1] Kliulai didn't shy away from the dirtiest of jobs, and was always eager to work. Jeff is incredibly capable and was able to accomplish anything I asked. Both Kliulai and Jeff greatly contributed to the work presented herein and were fun, intelligent people to work with besides.

Nick Parziale and I endeavored together to take pictures of things traveling very quickly. I learned a lot from him, but it's his genuine affability that I'll remember, and miss, the most. Joe Jewell showed me how to install the heat-flux gauges and can always be counted on for a joke; he and I earned a lot of time-and-a-half working late. Visiting Manchester with Nick and Joe was phenomenal, and that experience included probably the best joke I will ever witness. Neal Bitter has, without a doubt, the highest product of intelligence times running speed of anyone I know. I fondly remember discussing research with him after gasping my way across the half-marathon finish line; Neal had, of course, been done for over 30 minutes. Stephanie Coronel grew from an eager summer student to senior combustion graduate student in what seemed to be the blink of an eye. Through jokes and unlimited chai lattes, Rémy Mével made sure my spirits were high as I wrote my thesis. Drinking coffee with Stephanie and Rémy in the Pasadena spring is one of my favorite memories of Caltech.

Lindsey: You make my life fun, and fix my typos. Thanks for being my sky. I love you.

[1] Kliulai was extensively involved in the driven-thin experiments and Jeff helped to design the splitter plate and focused schlieren visualization systems.

Abstract

Pipes containing flammable gaseous mixtures may be subjected to internal detonation. When the detonation normally impinges on a closed end, a reflected shock wave is created to bring the flow back to rest. This study built on the work of Karnesky (2010) and examined deformation of thin-walled stainless steel tubes subjected to internal reflected gaseous detonations. A ripple pattern was observed in the tube wall for certain fill pressures, and a criterion was developed that predicted when the ripple pattern would form. A two-dimensional finite element analysis was performed using Johnson-Cook material properties; the pressure loading created by reflected gaseous detonations was accounted for with a previously developed pressure model. The residual plastic strain between experiments and computations was in good agreement.

During the examination of detonation-driven deformation, discrepancies were discovered in our understanding of reflected gaseous detonation behavior. Previous models did not accurately describe the nature of the reflected shock wave, which motivated further experiments in a detonation tube with optical access. Pressure sensors and schlieren images were used to examine reflected shock behavior, and it was determined that the discrepancies were related to the reaction zone thickness extant behind the detonation front. During these experiments reflected shock bifurcation did not appear to occur, but the unfocused visualization system made certainty impossible. This prompted construction of a focused schlieren system that investigated possible shock wave–boundary layer interaction, and heat-flux gauges analyzed the boundary layer behind the detonation front. Using these data with an analytical boundary layer solution, it was determined that the strong thermal boundary layer present behind the detonation front inhibits the development of reflected shock wave bifurcation.

Contents

List of Figures

List of Tables

Nomenclature

Greek symbols

α	Aperture angle in schlieren systems
δ	Boundary layer thickness
η, ζ, τ	Transformed coordinate system for boundary layer analysis
Γ	Fundamental derivative
γ	Ratio of specific heats, $\gamma = c_p/c_v$
κ	Shear correction factor
λ_b	Tube bending length
λ_r	Ripple wavelength
μ	Dynamic viscosity
ν	Poisson's ratio
Ψ	Compressible stream function
ρ	Fluid density
ρ_t	Specimen tube density
σ	Material stress
ε	Material strain

ε_p Plastic strain

Roman characters

$\dot{m}$ Mass flux per unit area

$\dot{q}$ Heat flux

$\overline{I}$ Image intensity averaged across the span-wise direction

a Wave acceleration

A, B, n, c Johnson-Cook material parameters

b Size of schlieren source

C Chapman-Rubesin parameter

c Fluid sound-speed

C_f Skin friction coefficient

c_p Specific heat at constant pressure

D Detonation tube diameter

d_{1o} Distance between collimating mirror and camera focus

d_{kc} Distance between schlieren knife-edge and camera

d_{o2} Distance between camera focus and focusing mirror

E_1 Elastic modulus

E_2 Plastic modulus

Ec Eckert number

f, g Non-dimensional quantities used in the laminar boundary layer solution

f_1 Focal length of the schlieren collimating lens

f_2	Focal length of the schlieren focusing lens
f_{xs}	Natural frequency for elastic oscillation
G	Shear modulus
h	Fluid enthalpy
h_t	Tube thickness
h_{t0}	Initial tube thickness
k	Thermal conductivity
L	Detonation tube length
l_{ind}	Detonation induction length
M	Image magnification in schlieren system
M_{rs}	Mach number of reflected shock
p	Fluid pressure
Pr	Prandtl number
r	Tube radius
r'	Change in tube radius, $r' = r - r_0$
r_0	Initial tube radius
Re	Reynolds number
Re_x	Reynolds number per unit distance
s	Fluid entropy
St	Stanton number
T	Fluid temperature

t	Time
t_{exp}	Image exposure time
t_{ta}	Wave time of arrival
U	Wave speed in the lab-fixed frame
u	Fluid velocity in the lab-fixed frame
U_{det}	Measured detonation speed
U_{rsi}	Idealized reflected shock speed
U_{rsr}	Reacting reflected shock speed
U_{rs}	Measured reflected shock speed
U_b	Dilatational speed in a bar
U_{CJ}	Theoretical Chapman-Jouguet detonation speed
U_{gf}	Flexural wave speed
U_p	Dilatational speed in a plate
v	Fluid specific volume, $v = \rho^{-1}$
W	Wave speed in the shock-fixed frame
w	Fluid velocity in the shock-fixed frame
X	Wave location
x	Axial coordinate of detonation tube
x_{end}	Distance from reflecting end-wall, $x_{end} = L - x$
y	Transverse coordinate of detonation tube
CJ	Chapman-Jouguet

GDT GALCIT detonation tube

TZ Taylor-Zel'dovich expansion

ZND Zel'dovich, von Neumann, and Döring

Subscripts

0 Conditions calculated at the time of detonation reflection

1 Experimental fill conditions

2 Post-detonation conditions

3 Post-TZ expansion conditions

eq Properties calculated assuming chemical equilibrium

θ Solid conditions in the hoop direction

R Conditions relating to the reflected shock wave, or the region between the reflected shock and the reflecting end-wall

y Yield point

Chapter 1

Introduction

Gaseous detonations are self-sustaining shock waves propagating in a combustible mixture, coupled to and sustained by exothermic chemical reactions (Fickett and Davis, 1979). These supersonic combustion events produce substantial increases in mixture pressure and temperature. Detonations also induce a velocity in the fluid through which they propagate. When a detonation impinges upon a wall, the moving fluid is impulsively stagnated by a reflected shock wave that travels away from the wall back into the detonated gas (Shepherd et al., 1991). Hence in regions near a reflecting wall, the pressure and temperature will be increased twice in quick succession—first by the detonation and second by the reflected shock—thereby making regions near surfaces of reflection particularly important when examining how detonations effect destruction.

The forces produced by detonations have prompted research into the safety hazards of accidental detonation as well as the possibilities of harnessing this energy to produce useful work. Shepherd (2009) describes the danger of accidental detonations in nuclear and chemical processing industries where flammable gases can accumulate, ignite, and undergo deflagration-to-detonation transition (DDT) (Oran and Gamezo, 2006). Research into the elastic response (Beltman and Shepherd, 2002), plastic response (Karnesky et al., 2013), and rupture (T.Chao and Shepherd, 2004) of metal tubes to internal detonation has been performed in the Explosion Dynamics Laboratory at Caltech; the work described in Karnesky et al. (2013) will be discussed in detail in section 1.3 because it motivated the research described in chapters 4 and

5. Other research into the gaseous detonation phenomenon revolves around the possibility of harnessing detonations to convert chemical energy to useful work. The detonation thermodynamic cycle has been proposed as an alternative to the Brayton cycle in jet engines (Braun et al., 2010). Implementations such as pulse detonation engines (Kailasanath, 2000, Roy et al., 2004) and rotating detonation engines (Schwer and Kailasanath, 2011, Lu et al., 2011) are proposed concepts that, if successfully designed, may offer theoretical increases to engine efficiency.

The present work is focused on gaining fundamental understanding of detonation behavior so that the hazards and prospects of gaseous detonation may be better realized. Experiments combined with computations and theory are used to gain understanding into how detonations and reflected shock waves affect and, through energy transfer to the wall, are affected by surrounding structures. We begin in this chapter by introducing gaseous detonation waves. Of particular relevance to the current work is the reflected shock wave created when a detonation normally impinges upon an end-wall. In section 1.2 a one-dimensional model for the behavior of the reflected shock is introduced. This model is used to predict the detonation-induced material deformation presented in chapter 2; in chapter 2 we conclude the research of Karnesky (2010) of studying detonation-driven plastic deformation of thin-walled steel tubes by extending the investigation to specimen tubes made of 304L stainless steel, a better characterized material than the mild steel used by Karnesky. When we compare the pressures predicted by the one-dimensional model for the reflected shock to experimental traces obtained from an array of pressure gauges spaced near the reflecting end-wall, we observe that this model does not properly account for all of the relevant gasdynamics of detonation reflection. This results in inaccuracies in the predicted reflected shock speed and strength. These discrepancies motivate the second aspect of the present work, which is concerned with understanding the gasdynamics of detonation reflection. Chapter 3 introduces the experimental facility used to study reflected detonation waves and describes the measurement techniques used in our investigation. Chapter 4 addresses the possible shortcomings of the reflected shock model by investigating normally reflected detonations using high-speed

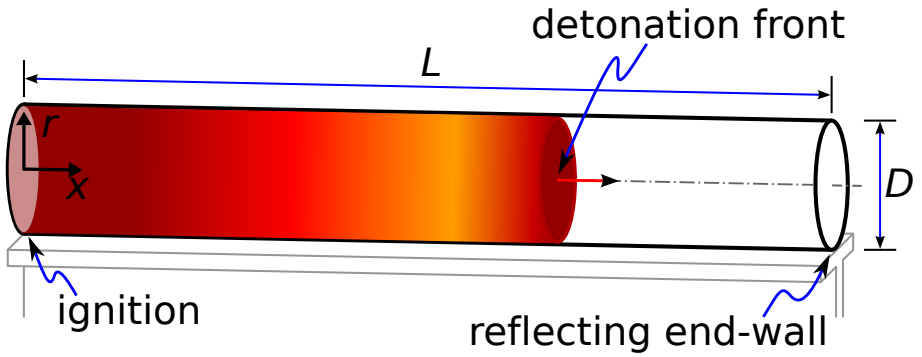

Figure 1.1: Illustration of the detonation domain used in experiments, computations, and analysis. Detonations are initiated at $x = 0$ and propagate towards the reflecting end-wall at $x = L$.

schlieren photography and an array of pressure sensors. The possibility of the reflected shock wave interacting with the boundary layer created by the incident detonation prompted research into the thermal and viscous boundary layers in the induced flow; this forms the third and final aspect of the present investigation. Chapter 5 examines these boundary layers through data obtained using heat-flux gauges, and examines shock wave–boundary layer interaction as it pertains to reflected detonations.

1.1 Gaseous Detonations in Tubes

We will be confining our discussion to detonations propagating in tubes. This restriction implies that the detonations have a primary Cartesian direction of propagation. The coordinate system and general physical domain shown in figure 1.1 will be assumed throughout this document. Here we see detonations are initiated at the ignition end where $x = 0$ and propagate towards the closed end at $x = L$ along the primary axis of the tube.

Detonations are inherently three-dimensional (Fickett and Davis, 1979, Lee, 2008). Examples of this are shown in images such as those presented by Austin (2003) and included in figure 1.2. The main features of the multi-dimensional detonation structure are shown in figure 1.2(b). The lead shock is divided by triple points that separate a cellular front from a transverse shock. The cellular front propagates along

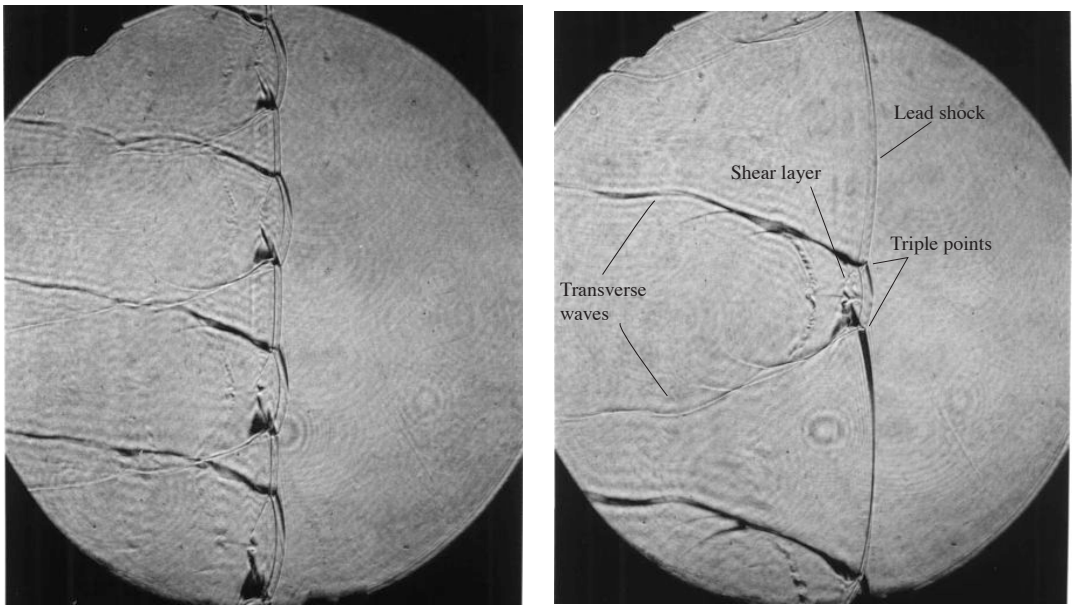

(a) (b)

Figure 1.2: Schlieren images of detonation waves propagating left-to-right as described by Austin (2003), figures used with permission. The field of view is approximately 146 mm. The initial mixture is stoichiometric hydrogen-oxygen at initial pressure 20 kPa with (a) 80% and (b) 85% argon dilution.

the principal axis of the tube, while the transverse waves travel in a direction that is essentially orthogonal to the direction of travel of the detonation. Shear layers demarcate flow that only passed through a lead shock, and flow that passed through a lead shock and much weaker transverse waves. The size of the cellular structure is an important measure of the instability of a detonation (Strehlow, 1969a,b). However, when the cell size, λ, is much smaller than the tube diameter, D, it is acceptable to approximate detonations as one-dimensional waves. We will discuss two methods, the Chapman-Jouguet (CJ) theory and the ZND theory (named after its discoverers Zel'dovich, von Neumann, and Döring), used to approximate detonations as one-dimensional waves. The difference between the methods is that CJ theory circumvents the internal structure of the detonation and instead considers possible solutions to the one-dimensional conservation relations to determine how detonation waves behave. Conversely, ZND theory considers the structure of the detonation, which allows for the reaction zone to have finite thickness.

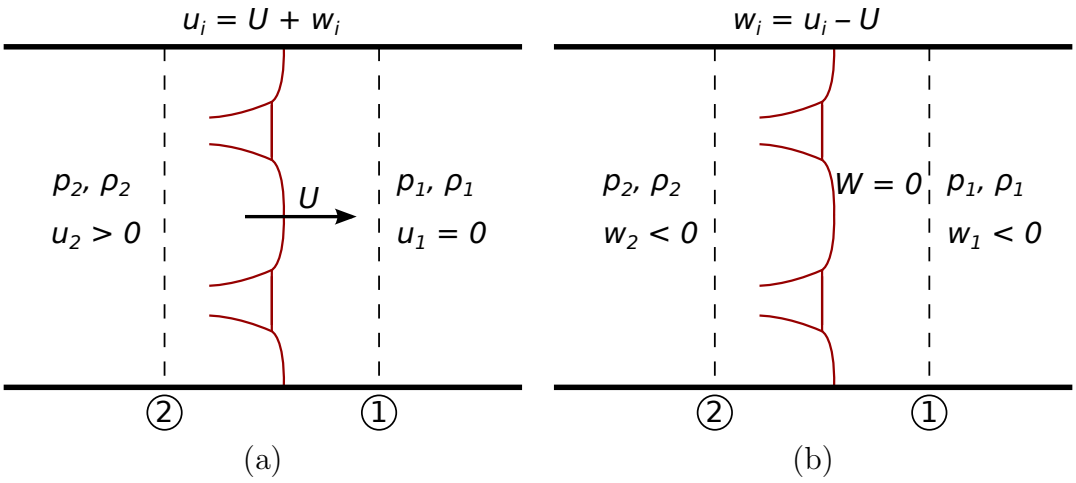

Figure 1.3: (a) Lab-fixed and (b) wave-fixed frames of reference used in the conservation equations. State 1 is ahead of the disturbance and is assumed to be at pressure p_1 and density ρ_1 with zero velocity in the lab-fixed frame. State 2 is behind the disturbance at an unknown state. The wave is propagating with speed U.

1.1.1 Chapman-Jouguet Theory

Chapman (1899) and Jouguet (1905) independently developed a theory to predict the speed of detonation and post-detonation properties. The Chapman-Jouguet theory is discussed in every textbook on detonations. We will introduce the theory in a manner similar to Thompson (1972) by considering the conservation of mass, momentum, and energy across a generic one-dimensional disturbance moving with speed U into a quiescent fluid at conditions denoted with subscript 1. This is shown in figure 1.3(a) in the laboratory-fixed frame, and figure 1.3(b) in the wave-fixed frame. Note that wave velocities are denoted by U, fluid velocities in the lab-fixed frame are denoted by u, and fluid velocities in the wave-fixed frame are denoted by $w = u - U$. The fluid state after the disturbance is denoted with subscript 2. We approach the problem assuming state 1 is known, and we wish to determine the wave velocity U and fluid conditions at state 2.

The conservation of mass, momentum, and energy relationships for a control volume moving with velocity $\mathbf{u}_V$ containing a Newtonian fluid with density ρ, pressure p, specific internal energy e, and velocity $\mathbf{u}$ with applied body force $\mathbf{G}$, viscous tensor

τ, and heat-flux $\mathbf{q}$ are:

$$\int_{\partial V} \rho\left(\mathbf{u}-\mathbf{u}_V\right)\cdot\hat{\mathbf{n}}\; dA = \frac{d}{dt}\int_V \rho\; dV \tag{1.1}$$

$$\int_{\partial V} \left[\rho\mathbf{u}\left(\mathbf{u}-\mathbf{u}_V\right)-pI\right]\cdot\hat{\mathbf{n}}\; dA = \int_V \rho\mathbf{G}\; dV - \frac{d}{dt}\int_V \rho\mathbf{u}\; dV + \int_{\partial V}\tau\cdot\hat{\mathbf{n}}\; dA \tag{1.2}$$

$$\int_{\partial V}\left[\rho\left(e+\frac{1}{2}u^2\right)\left(\mathbf{u}-\mathbf{u}_V\right)-p\mathbf{u}\right]\cdot\hat{\mathbf{n}}\; dA = \int_V \rho\mathbf{G}\cdot\mathbf{u}\; dV - \frac{d}{dt}\int_V \rho\left(e+\frac{1}{2}u^2\right) dV + \int_{\partial V}\left(\tau\cdot\mathbf{u}-\mathbf{q}\right)\cdot\hat{\mathbf{n}}\; dA. \tag{1.3}$$

We define the control volume as moving at the velocity of the detonation, that is $\mathbf{u}_V = U\hat{\mathbf{x}}$. For a thin control volume, the storage terms are negligible. Further, the small surface area implies that any flux terms to the side-walls are minimal. Lastly, we assume constant properties on either side of the disturbance resulting in zero heat-flux into the control volume. With these assumptions, the right-hand sides of equations (1.1)–(1.3) equate to zero and, after rearranging terms and assuming one-dimensional flow, our shock jump relations become

$$\rho_1 w_1 = \rho_2 w_2 \tag{1.4}$$

$$p_1 + \rho_1 w_1^2 = p_2 + \rho_2 w_2^2 \tag{1.5}$$

$$h_1 + \frac{1}{2}w_1^2 = h_2 + \frac{1}{2}w_2^2 \tag{1.6}$$

where $h = e + p/\rho$ is the specific enthalpy. If we substitute $w_1 = -U$ and $w_2 = u_2 - U$, then the conservation of mass and momentum relationships result in the equation for the Rayleigh line:

$$p_2 - p_1 = -\left(v_2 - v_1\right)\rho_1^2 U^2 = -\left(v_2 - v_1\right)\dot{m}^2 \tag{1.7}$$

where $v = 1/\rho$ is the specific volume and $\dot{m} = \rho\,|w|$ is the mass flux per unit area across the wave. The Rayleigh line represents the thermodynamic path that satisfies the conservation of mass and momentum. Combining the equations for conservation of mass, momentum, and energy produces the equation for the Rankine-Hugoniot curve:

$$h_2 - h_1 = \frac{1}{2}\,(p_2 - p_1)\,(v_1 + v_2)\,. \tag{1.8}$$

Given an equation of state of the form

$$h_2 = h_2(p_2, v_2) \tag{1.9}$$

we have three equations for four unknowns (p_2, v_2, h_2, and U).

Solutions to the Rayleigh and Rankine-Hugoniot lines for an ideal gas are plotted in figure 1.4 for three different detonation speeds. We observe that for $U < U_{CJ}$, the Rayleigh line does not intercept the product Hugoniot, implying these solutions are not physical. For $U > U_{CJ}$, two post-detonation thermodynamic states satisfy the conservation relations. Chapman-Jouguet theory closes equations (1.7)–(1.9) by postulating that the detonation speed is such that the Rayleigh line is tangent to the product Hugoniot as shown with $U = U_{CJ}$. In addition to being convenient by limiting the products to a single thermodynamic state, the CJ condition implies the shock-fixed post-detonation velocity equals the product sound-speed

$$w_2 = c_2 \tag{1.10}$$

$$\Rightarrow\ u_2 = U_{CJ} - c_2 \tag{1.11}$$

where c is the sound-speed in the fluid computed on the basis of chemical equilibrium. This is the only steady-state physical possibility, because if $w_2 < c_2$ (as would occur at state 2_{OD}), then an expansion fan would develop behind the detonation front to decelerate the detonation until the post-detonation velocity was sonic, at which

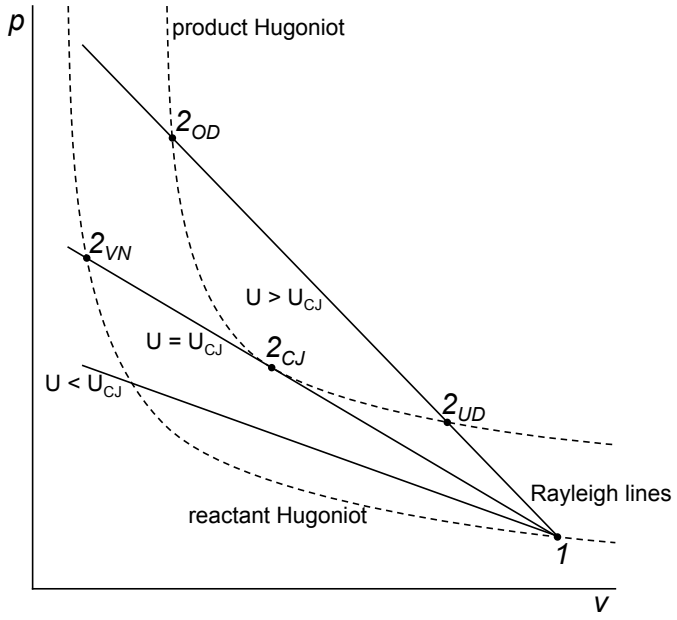

Figure 1.4: Possible solutions to the Rayleigh and Rankine-Hugoniot equations.

point no further deceleration would be possible; this is called an over-driven detonation. Further, in the absence of a converging-diverging nozzle, no mechanism exists to accelerate the fluid velocity to values larger than the sound speed c_2, implying the under-driven detonation state 2_{UD} is unachievable. Becker (1922) and Scorah (1935) also show that the entropy is at a minimum for CJ detonations, providing further justification for the steady CJ state. Hence the Chapman-Jouguet point is the only physical steady one-dimensional detonation speed. Using the computational chemistry capabilities of Cantera (Goodwin, 2003) with the Shock and Detonation Toolbox (Browne et al., 2008), we are able to predict theoretical detonation speeds and post-detonation conditions. A few representative values are given in table 1.1. As discussed by Fickett and Davis (1979) and shown in section 4.3, this simple theory predicts the detonation speed remarkably well, frequently to within a few percent when the detonation cell size is much smaller than the tube diameter.

1.1.2 ZND Theory

The Chapman-Jouget theory bypasses the details of what occurs inside the detonation. Zel'dovich (1940), Neumann and Taub (1942), and Döring (1943) independently developed a model that examines the one-dimensional structure of detonation waves and allows for a reaction zone of finite thickness. The ZND model assumes a shock wave processes the reactants to bring them from the initial state 1 up to the von Neumann state (point 2_{VN} in figure 1.4) before any chemical reaction occurs. Chemical time scales are much longer than the time the gas spends inside the shock, making this chemically frozen flow assumption reasonable. Once the gas is at the von Neumann point, chemical reaction occurs to gradually bring the gas to the final equilibrium state 2_{CJ}.

By allowing for a finite reaction zone thickness, this model provides further insight into the one-dimensional detonation structure. Using the Shock and Detonation Toolbox, we can predict the detonation properties through the ZND profile, as has been done in figure 1.5. The induction length, l_{ind}, is the characteristic reaction zone length defined to be the distance behind the shock of maximum thermicity (see Fickett and Davis, 1979). l_{ind} is included with other detonation properties in table 1.1.

Table 1.1: Detonation properties computed with the thermodynamic software Cantera and the Shock and Detonation Toolbox. Representative mixtures are those used in experiments in later sections. Parameters are defined in the text and the nomenclature section.

p_1 (kPa)	Mixture	U_{CJ} (m/s)	p_2 (MPa)	ρ_2 (kg/m^3)	u_2 (m/s)	$\gamma_{2,eq}$	l_{ind} (μm)	$p_R\,(t_{\text{ref}})$ (MPa)
25	H_2-O_2	2759	0.443	0.221	1259	1.12	178	1.086
50	H_2-O_2	2796	0.908	0.442	1275	1.13	83	2.229
50	C_2H_4-O_2	2339	1.602	1.143	1067	1.13	41	3.986
200	C_2H_4-O_2	2406	6.803	4.594	1104	1.14	11	17.054

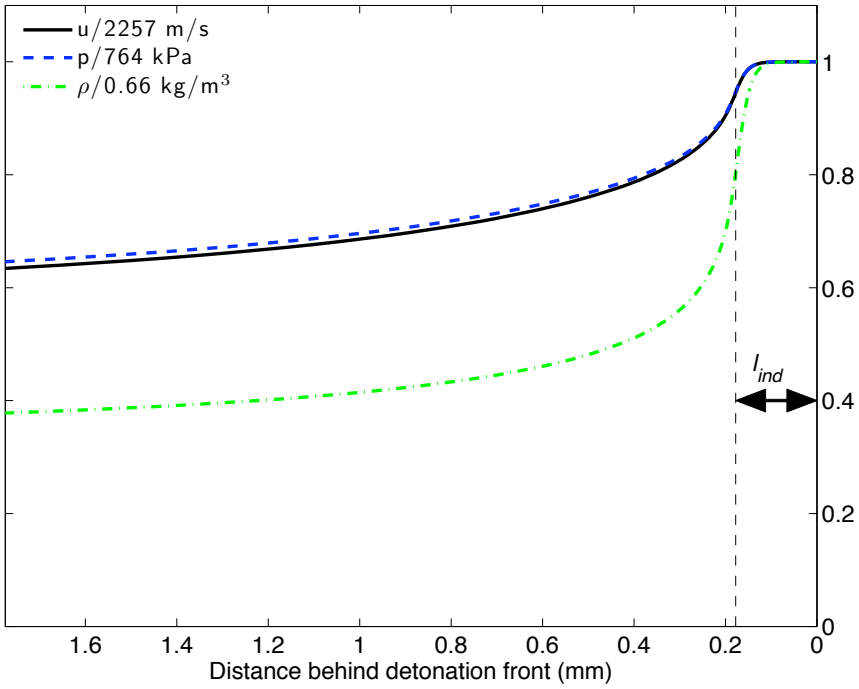

Figure 1.5: Computed detonation profile for a detonation in stoichiometric hydrogen-oxygen at initial pressure 25 kPa. Note that the x-axis is right-to-left to correspond to the detonation propagating to the right.

1.1.3 Taylor-Zel'dovich Expansion Wave

It has been shown above that the fluid velocity behind the detonation, u_2, is not zero. For a detonation propagating in a tube, there exists the boundary condition that the flow must be stationary at the ignition end, $x = 0$. This condition is satisfied with an expansion wave as shown in figure 1.6. This wave is referred to as the Taylor-Zel'dovich, or TZ, wave due to their analyses in Taylor (1950) and Zel'dovich and Kompaneets (1960) which we will summarize here. Assuming the flow behind the detonation is homentropic and chemically frozen with no dissipative effects, we can derive the one-dimensional flow conditions as described in Thompson (1972) and Nettleton (1987) using the method of characteristics and assuming the gas behind the detonation front can be treated as calorically perfect.

The inviscid one dimensional equations for conservation of mass and momentum

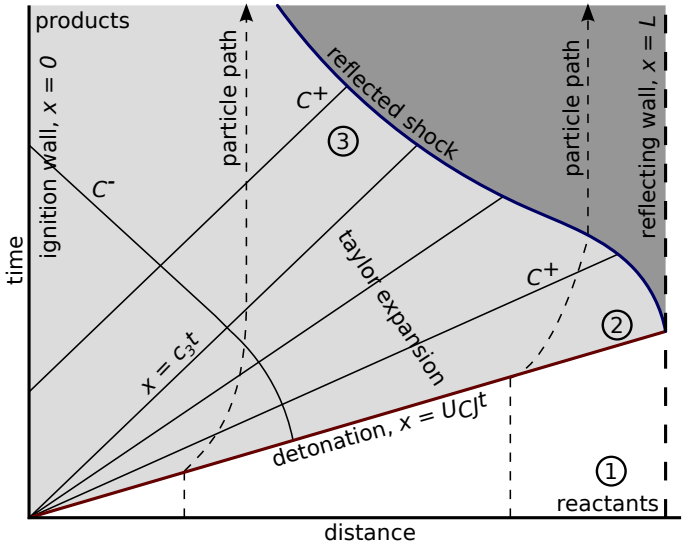

Figure 1.6: Space-time diagram of a detonation and attached Taylor-Zel'dovich expansion wave. The detonation reflects off the wall located at $x = L$ and the reflected shock wave passes through the expansion.

for one-dimensional flow without body forces are

$$\frac{\partial \rho}{\partial t} + u\frac{\partial \rho}{\partial x} + \rho\frac{\partial u}{\partial x} = 0 \tag{1.12}$$

$$\frac{\partial u}{\partial t} + u\frac{\partial u}{\partial x} + \frac{1}{\rho}\frac{\partial p}{\partial x} = 0. \tag{1.13}$$

The homentropic assumption implies that there is only one independent thermodynamic variable. Selecting p as our independent variable, we write $\rho = \rho(p)$, and

$$d\rho = \left.\frac{\partial \rho}{\partial p}\right|_s dp = \frac{1}{c^2}dp \tag{1.14}$$

implying equation (1.12) becomes

$$\frac{1}{c^2}\frac{\partial p}{\partial t} + \frac{u}{c^2}\frac{\partial p}{\partial x} + \rho\frac{\partial u}{\partial x} = 0. \tag{1.15}$$

Combining equations (1.13) and (1.15) places the equations into characteristic form:

$$\left(\frac{\partial u}{\partial t} \pm \frac{1}{\rho c}\frac{\partial p}{\partial t}\right) + (u \pm c)\left(\frac{\partial u}{\partial x} \pm \frac{1}{\rho c}\frac{\partial p}{\partial x}\right) = 0. \tag{1.16}$$

It now becomes useful to define the homentropic thermodynamic property $F = F(p)$ where

$$F \equiv \int_{p_0}^{p} \frac{dp}{\rho c} \tag{1.17}$$

$$\Rightarrow \quad \frac{\partial F}{\partial t} = \frac{dF}{dp}\frac{\partial p}{\partial t} = \frac{1}{\rho c}\frac{\partial p}{\partial t} \tag{1.18}$$

$$\frac{\partial F}{\partial x} = \frac{1}{\rho c}\frac{\partial p}{\partial x} \tag{1.19}$$

which transforms equation (1.16) into

$$\left[\frac{\partial}{\partial t} + (u \pm c)\frac{\partial}{\partial x}\right](u \pm F) = 0 \tag{1.20}$$

or

$$\frac{D^{\pm}}{Dt}(u \pm F) = 0 \tag{1.21}$$

with

$$\frac{D^{\pm}}{Dt} \equiv \frac{\partial}{\partial t} + (u \pm c)\frac{\partial}{\partial x}. \tag{1.22}$$

Using the fundamental derivative Γ, where

$$\Gamma = 1 + \rho c \left.\frac{\partial c}{\partial p}\right|_s \tag{1.23}$$

we have

$$F = \int_{p_0}^{p} \frac{dp}{\rho c} = \int_{c_0}^{c} \frac{dc}{\Gamma - 1}. \tag{1.24}$$

For a calorically perfect gas

$$\Gamma = \frac{\gamma_{2,eq} + 1}{2} \tag{1.25}$$

where $\gamma_{2,eq}$ is the ratio of specific heats behind the detonation front computed on the basis of chemical equilibrium (as described in Radulescu and Hanson, 2005). This implies

$$F = \frac{2}{\gamma_{2,eq} - 1}\left(c - c_0\right) \tag{1.26}$$

and since we only ever consider the derivative of F, we can drop the constant. This leaves

$$F = \frac{2}{\gamma_{2,eq} - 1}c. \tag{1.27}$$

Therefore we have shown that the quantities

$$J^{\pm} \equiv u \pm \frac{2}{\gamma_{2,eq} - 1}c \tag{1.28}$$

are constant along the characteristic lines with slopes

$$C^{\pm}: \quad \frac{dx}{dt} = u \pm c. \tag{1.29}$$

Several of these characteristics are plotted in figure 1.6. Examining the C^- characteristics for the detonation case and noting that $u = 0$ at the ignition end, we observe

$$J^- = u_2 - \frac{2c_2}{\gamma_{2,eq} - 1} = -\frac{2c_3}{\gamma_{2,eq} - 1} \tag{1.30}$$

$$\Rightarrow \; c_3 = c_2 - \left(U_{CJ} + c_2\right)\frac{\gamma_{2,eq} - 1}{2} \tag{1.31}$$

$$= \frac{\gamma_{2,eq} + 1}{2}c_2 - \frac{\gamma_{2,eq} - 1}{2}U_{CJ} \tag{1.32}$$

where we have applied the Chapman-Jouguet relation from equation (1.11). Hence all of the equilibrium thermodynamic properties may be calculated. The self-similarity inherent to the C^+ characteristic lines allows us to deduce the profile for the fluid

velocity and sound speed inside the TZ expansion as shown in equations (1.33) and (1.34). Other thermodynamic quantities may be derived using the isentropic relations as shown in equations (1.35) and (1.36), and thus we have the full solution for the flow field behind the detonation:

$$u(x,t) = \begin{cases} 0 & U_{CJ} < x/t \\ \dfrac{2c_3}{\gamma_{2,eq}+1}\left(\dfrac{x}{c_3 t} - 1\right) & c_3 < x/t \leq U_{CJ} \\ 0 & 0 \leq x/t \leq c_3 \end{cases} \tag{1.33}$$

$$c(x,t) = \begin{cases} c_1 & U_{CJ} < x/t \\ c_3\left[1 + \dfrac{\gamma_{2,eq}-1}{\gamma_{2,eq}+1}\left(\dfrac{x}{c_3 t} - 1\right)\right] & c_3 < x/t \leq U_{CJ} \\ c_3 & 0 \leq x/t \leq c_3 \end{cases} \tag{1.34}$$

$$p(x,t) = \begin{cases} p_1 & U_{CJ} < x/t \\ p_2\left[1 - \dfrac{\gamma_{2,eq}-1}{\gamma_{2,eq}+1}\left(\dfrac{U_{CJ}}{c_2} - \dfrac{x}{c_2 t}\right)\right]^{\frac{2\gamma_{2,eq}}{\gamma_{2,eq}-1}} & c_3 < x/t \leq U_{CJ} \\ p_3 & 0 \leq x/t \leq c_3 \end{cases} \tag{1.35}$$

$$\rho(x,t) = \begin{cases} \rho_1 & U_{CJ} < x/t \\ \rho_2\left[1 - \dfrac{\gamma_{2,eq}-1}{\gamma_{2,eq}+1}\left(\dfrac{U_{CJ}}{c_2} - \dfrac{x}{c_2 t}\right)\right]^{\frac{2}{\gamma_{2,eq}-1}} & c_3 < x/t \leq U_{CJ} \\ \rho_3 & 0 \leq x/t \leq c_3 \end{cases} \tag{1.36}$$

where

$$p_3 = p_2\left[\frac{\gamma_{2,eq}+1}{2} - \frac{U_{CJ}}{c_2}\left(\frac{\gamma_{2,eq}-1}{2}\right)\right]^{\frac{2\gamma_{2,eq}}{\gamma_{2,eq}-1}} \tag{1.37}$$

$$\rho_3 = \rho_2\left[\frac{\gamma_{2,eq}+1}{2} - \frac{U_{CJ}}{c_2}\left(\frac{\gamma_{2,eq}-1}{2}\right)\right]^{\frac{2}{\gamma_{2,eq}-1}}. \tag{1.38}$$

Graphs of these quantities for a representative detonation are included in figure 1.7.

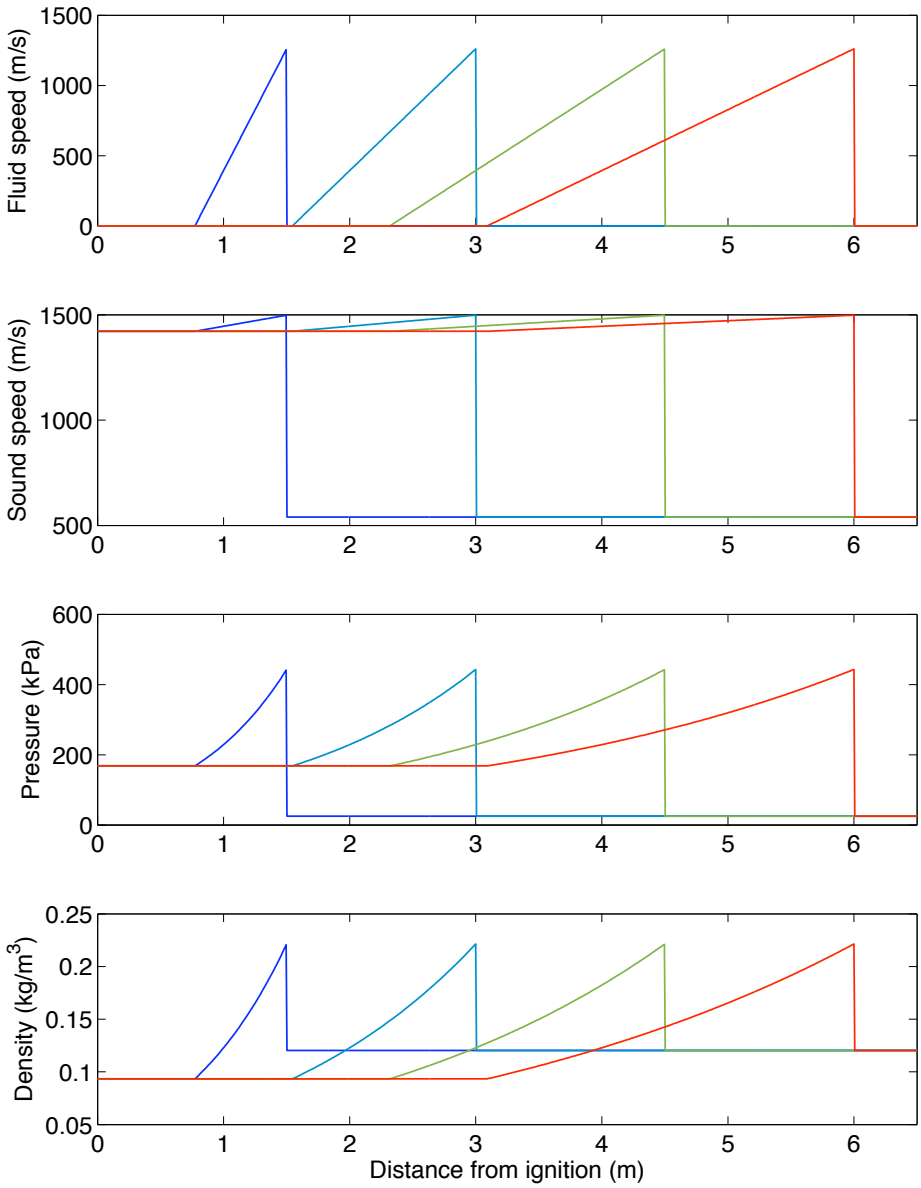

Figure 1.7: Computed fluid parameters through the Taylor-Zel'dovich expansion for a stoichiometric hydrogen-oxygen detonation with fill pressure 25 kPa at four times after detonation initiation when the detonation has propagated 1.5, 3, 4.5, and 6 m.

1.2 Reflected Shock Waves

When the detonation wave reaches the reflecting end-wall at $x = L$, a reflected shock wave is created to bring the moving gas behind the detonation back to rest, as portrayed in figure 1.6. As the shock propagates through the unsteady TZ expansion, its speed and strength fluctuate. Eventually the reflected wave will decay, but for times soon after reflection the gas between the reflected shock and the reflecting end-wall has pressure $p_R > p_2$. This increase in pressure above that found behind the detonation causes the region near wave reflection to be of considerable interest to safety analysis.

1.2.1 Initial Shock Strength

The initial speed and strength of the reflected shock wave may be approximated by assuming chemically frozen flow and using the conservation equations with the no-flow condition at the end-wall to predict the shock conditions at the moment of reflection. Using a known incident wave speed and upstream state, the reflected wave properties may be determined by applying the normal shock jump conditions. The approximate flow conditions before and after the moment of wave reflection are shown in figure 1.8. The reflected shock speed at the moment of reflection, $U_{R0} \equiv U_R(t_{\text{ref}})$, is chosen such that $u_R = 0$ to satisfy the no-flow condition at the wall where t_{ref} is the time of detonation reflection. Thus at $t = t_{\text{ref}}$ in the shock-fixed frame the flow velocities are given by

$$w_2 = U_R + u_2 \tag{1.39}$$

$$w_R = U_R. \tag{1.40}$$

Following Stanyukovich (1960), we can derive an approximate solution for the limit of a strong detonation. In this limit

$$v_2 \approx \frac{\gamma_{2,eq} v_1}{\gamma_{2,eq} + 1} \tag{1.41}$$

and thus the Rayleigh line may be written as

$$u_2^2 = \frac{p_2 v_1}{\gamma_{2,eq} + 1}. \tag{1.42}$$

The Rayleigh line for the reflected shock at the time of reflection is given by

$$u_2^2 = (p_{R0} - p_2)(v_2 - v_R) \tag{1.43}$$

where p_{R0} is the pressure at the reflecting end-wall at the moment of detonation reflection. The Hugoniot is then

$$\frac{v_{R0}}{v_2} = \frac{(\gamma+1)\,p_{R0} + (\gamma-1)\,p_2}{(\gamma-1)\,p_{R0} + (\gamma+1)\,p_2} \tag{1.44}$$

and we can eliminate the specific volumes to get a quadratic relationship for p_{R0}/p_2:

$$0 = 2\gamma \left(\frac{p_{R0}}{p_2}\right)^2 - (5\gamma+1)\left(\frac{p_{R0}}{p_2}\right) + (\gamma+1) \tag{1.45}$$

$$\therefore \quad \frac{p_{R0}}{p_2} = \frac{5\gamma + 1 + \sqrt{17\gamma^2 + 2\gamma + 1}}{4\gamma} \tag{1.46}$$

where we have eliminated the other solution to the quadratic as unphysical for $1 < \gamma \leq 5/3$. Thus we have

$$2.48 \leq \frac{p_{R0}}{p_2} < 2.62 \tag{1.47}$$

for the approximation of chemically frozen flow using the strong detonation limit.

A more accurate approximation for the pressure ratio is obtained by applying the same theory but using the computational chemistry capabilities of Cantera to bypass the strong detonation assumption and calculate the reflected shock speed directly as described by Browne et al. (2008). This results in

$$\frac{p_{R0}}{p_2} \approx 2.4 \tag{1.48}$$

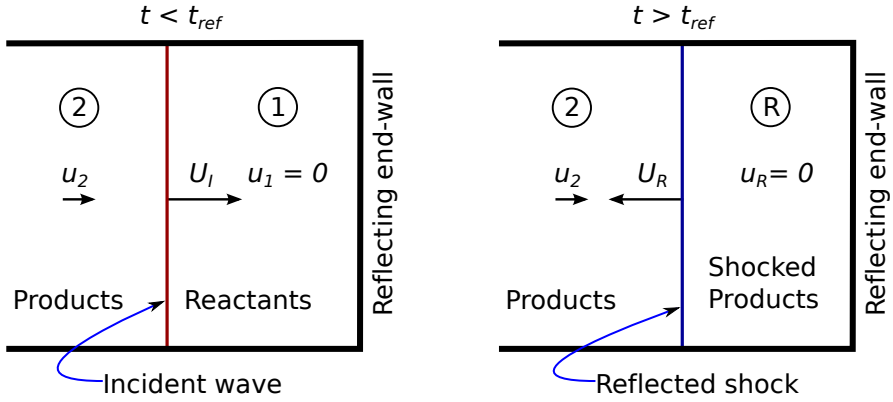

(a) (b)

Figure 1.8: Flow conditions (a) before and (b) after wave reflection.

with exact values depending on the specific detonation conditions. Once the pressure ratio p_{R0}/p_2 at the time of reflection is known, the instantaneous shock speed may be determined using the shock jump conditions:

$$U_{R0} = -u_2 + c_2\sqrt{1 + \frac{\gamma_{2,eq}+1}{2\gamma_{2,eq}}\left[\frac{p_{R0}}{p_2} - 1\right]} \tag{1.49}$$

This speed is only a valid approximation for times soon after reflection because, as the fluid velocity decays through the TZ wave, the shock will accelerate. Then, as the pressure behind the shock decays, the shock will decelerate until it is completely through the TZ expansion, at which point viscosity will cause the shock to continue to decelerate until it reaches the ignition wall at $x = 0$.[1] In addition to neglecting the TZ wave, this theoretical reflected shock speed omits the structure of the detonation wave and treats it as a planar discontinuity, bringing the gas from state 1 to the Chapman-Jouguet state 2.

[1] At which point a second reflected shock will propagate from $x = 0$ towards $x = L$. This sequence of reflected shocks propagating back and forth through the tube will continue until viscosity dissipates all motion in the tube. The fluid velocity and pressure behind each subsequent reflected shock will be smaller than previous shocks, and thus these continued reflections are outside the scope of the present investigation, since our primary interest is in understanding the high pressure and flow fields associated with detonations.

1.2.2 Reflected Shock Model

In order to do safety analysis, it is necessary to have a model for the reflected shock after it has left the reflecting end-wall, so that the pressure exerted on the tube wall may be determined. This could be done with computational fluid dynamics, but research in our laboratory (Karnesky, 2010, Karnesky et al., 2013) has led to the development of a simple one-dimensional model for the speed and strength of this reflected shock wave that is valid until the shock has left the TZ expansion. In this section we will introduce this model for the reflected shock, and describe experimental evidence collected by Karnesky et al. (2013) that both supports one aspect of the model while calling into question another. It is the failings of this model for predictions regarding the reflected shock that motivates much of the work described in chapters 4 and 5.

The pressure model developed by Beltman and Shepherd (2002) is a semi-empirical model wherein it is assumed that no spatial gradient exists in fluid velocity or thermodynamic properties between the reflected shock and the reflecting end-wall. With this assumption, it is only necessary to determine the pressure at the end-wall as a function of time to calculate the speed and strength of the reflected shock. This is done by calculating the initial pressure ratio at the time of reflection as described in equation (1.48) and determining the final pressure, p_3, as done in equation (1.37). An exponential decay in pressure is then assumed with a time constant, τ, fit to experimental data:

$$p_R(t) = (p_{R0} - p_3) \exp\left[-\frac{t - t_{\text{ref}}}{\tau}\right] + p_3. \tag{1.50}$$

The speed of the shock is then given by

$$U_R(t) = -u\left(X_R^-(t), t\right) + c\left(X_R^-(t), t\right)\sqrt{1 + \frac{\gamma_{2,eq} + 1}{2\gamma_{2,eq}}\left[\frac{p_R(t)}{p\left(X_R^-(t), t\right)} - 1\right]} \tag{1.51}$$

where $X_R(t)$ is the location of the reflected shock at time t and the velocity, sound

speed, and pressure are computed with equations (1.33)–(1.35). This model completely specifies the pressure associated with the incident detonation and reflected shock.

1.2.3 Reflected Shock Model Validation

The experimental setup described in Karnesky et al. (2013) and discussed in chapter 2 was used to validate this reflected shock model. The resulting pressure traces are shown in figure 1.9, where data from two experiments are plotted to illustrate the repeatability of the experimental measurements. In this figure the left-hand axis shows the gauge location relative to the reflecting end-wall, while the right-hand axis shows the pressure for each gauge. The detonation arrived first at the gauge located 133 mm from the end-wall, as noted by the increase in pressure at time $t = -0.06$ ms. The detonation then propagated towards the end-wall, as revealed by the increase in pressure in each subsequent gauge. At $t = 0$ the detonation impinged upon the end-wall, and the reflected shock propagated back towards the point of ignition, which produced a second increase in pressure in each gauge. The locations of the gauges were chosen to correspond to the regions of maximum deformation, as discussed in chapter 2.

There are two metrics that determine the accuracy of this model. The first is the predicted arrival time of the reflected shock wave, and the second is the accuracy of the predicted time-resolved pressures. As observed in figure 1.9, the predicted arrival time of the reflected shock is accurate to within the rise-time of the pressure signals; the mean error in arrival time for these gauges was 2.3 μs.[2] This indicates that, for the region measured, the average speed of the reflected shock is well predicted by this model. The second metric of fidelity for the reflected shock model is the predicted time-resolved pressures; here the model over-predicts the pressure by up to 20%.

In spite of the over-predicted peak pressure, the ability of this model to predict the arrival time of the reflected shock implies that it may be useful in finite element

[2]The pressure signals exhibit a rise-time of several microseconds, and thus the arrival time is defined here to be the time at which the signal has reached 95% of its peak value.

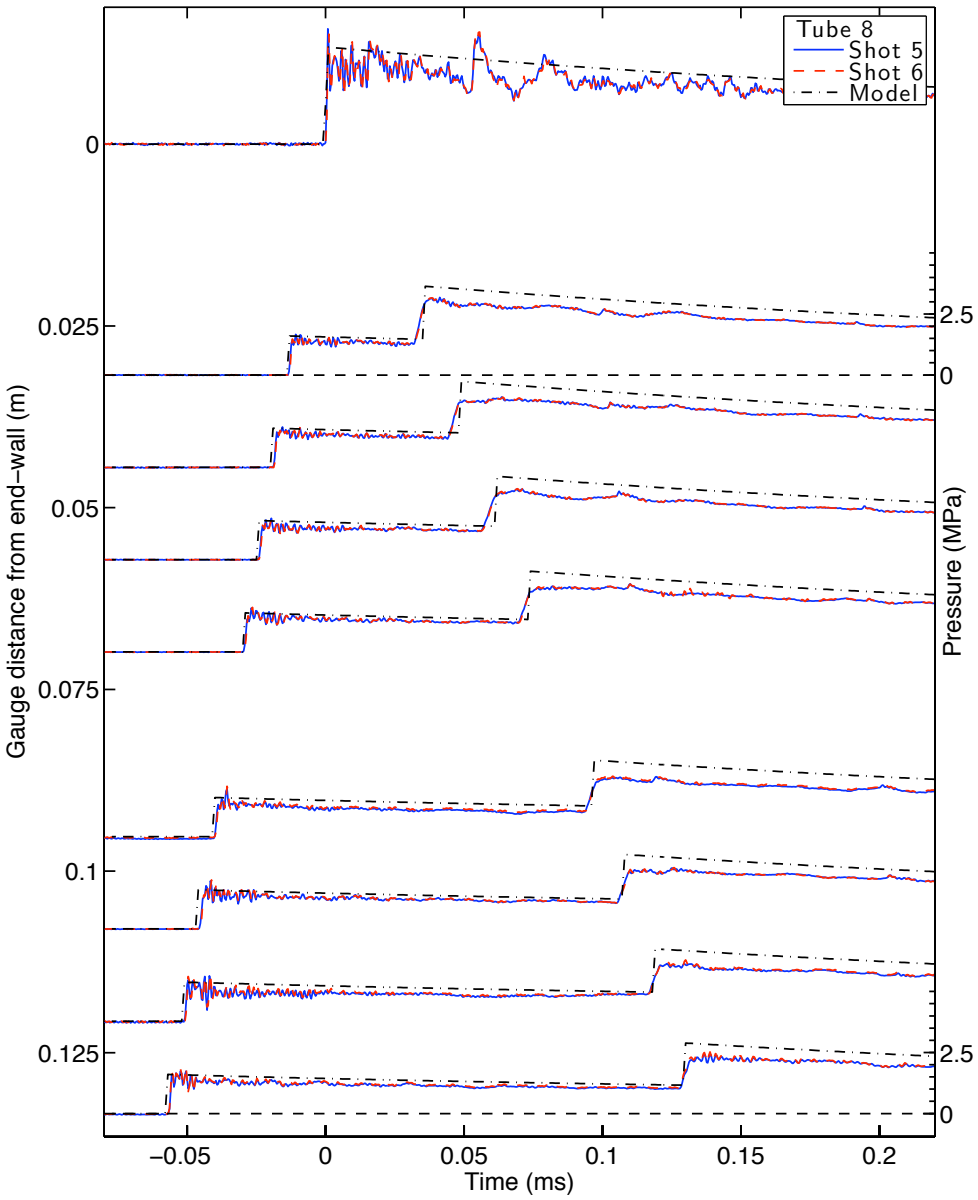

Figure 1.9: Pressure-time traces for an incident detonation and reflected shock wave. The left-hand axis gives the gauge location in meters from the location of detonation reflection and the right-hand axis shows the pressure. The initial mixture was stoichiometric ethylene-oxygen at fill pressure $p_1 = 50$ kPa. Data from two subsequent detonations are shown to illustrate experiment repeatability.

analyses to predict detonation-driven material deformation as described in chapter 2. However, the discrepancy in predicted wall pressure suggests that the fluid dynamics of detonation reflection are not as simple as this reflected shock model describes. To address this discrepancy, data were gathered from an array of pressure sensors and simultaneous schlieren imaging using the GALCIT detonation tube described in chapter 3. Results from these data are presented in chapter 4, and led to a better understanding of the fluid dynamics of detonation reflection.

1.3 Fluid-Structure Interaction

Detonations produce pressures and temperatures that are significantly larger than present in the pre-combustion gases. The pressure and temperature are further increased if the detonation undergoes normal reflection as described in section 1.2. These pressures will cause the containment vessel to undergo deformation. Predicting the degree of deformation is necessary to enable us to properly assess the safety hazards of accidental detonation in pressure vessels. Despite the importance of this prediction ability, relatively little investigation on detonation-driven deformation has been conducted outside our laboratory. Mirzaei et al. (2006) performed analytical and numerical modeling of the elastic response of tubes to internal detonation loading, building on the work of Beltman and Shepherd (2002). Kuznetsov et al. (2010) computes deformation for a few cases directly related to nuclear safety, but in the case examined the strains are less than 0.12%–well below the plastic limit.

Other areas of research interest have similarities to detonation-induced strains. Multiple investigators have researched damage to steel plates from underwater explosions (as reviewed in Rajendran and Narasimhan, 2006). Underwater explosions have a similar impulsive loading profile as gaseous detonations in tubes, and many of the same considerations–such as strain-rate effects–are present in both cases. However, the details necessary to accurately predict damage can be quite different. For example, the majority of damage in underwater explosions comes from reloading, rather than the primary pressure pulse (Keil, 1956). Other discrepancies include the strain-

rates, which are typically between 1 and 100 s^{-1} for underwater explosions (Keil, 1961), whereas detonation loadings can be in excess of 1000 s^{-1}. Also, the precise pressure loading profile can be quite different than experienced in gaseous detonations. Still, it is worth noting that plastic deformation from underwater explosions may be accurately predicted (Nurick and Martin, 1989a,b).

Although there has been little directly relevant research outside the Explosion Dynamics Laboratory, there has been extensive research performed in our lab on detonation-driven deformation. Multiple regimes have been investigated that result in varying degrees of deformation. Depending on the pressure, deformation will be purely elastic (as described by Beltman and Shepherd (2002) and Karnesky (2010)), a combination of elastic and plastic (Karnesky et al., 2013), or will result in tube rupture (T.Chao and Shepherd, 2004). Experiments in thin-walled C1010 mild steel tubes are described by Karnesky (2010). These experiments used the same experimental setup presented in chapter 2, but with a different tube material. An example of these results as presented in Karnesky et al. (2013) is included in figure 1.10.

Although figure 1.10 shows that good agreement between finite element modeling of the tube and experimental results was obtained, in practice the constitutive relation for mild steel proved to be difficult to specify in the high strain-rate regime present in detonation loadings. The agreement between experiments and computations shown in figure 1.10 was only possible by using a custom multilinear strain-hardening model with Cowper-Symonds rate hardening governing the stress-strain location of one of the yield points. Thus these plastic deformation experiments were repeated using 304L stainless steel tubes of identical geometry. A detailed material model combined with the previously described wall pressure loading may be used with finite element software to determine the material deformation of reflected detonation loading. The results for stainless steel tubes are presented in chapter 2, and the general theory outlined by Shepherd (2009) is included here.

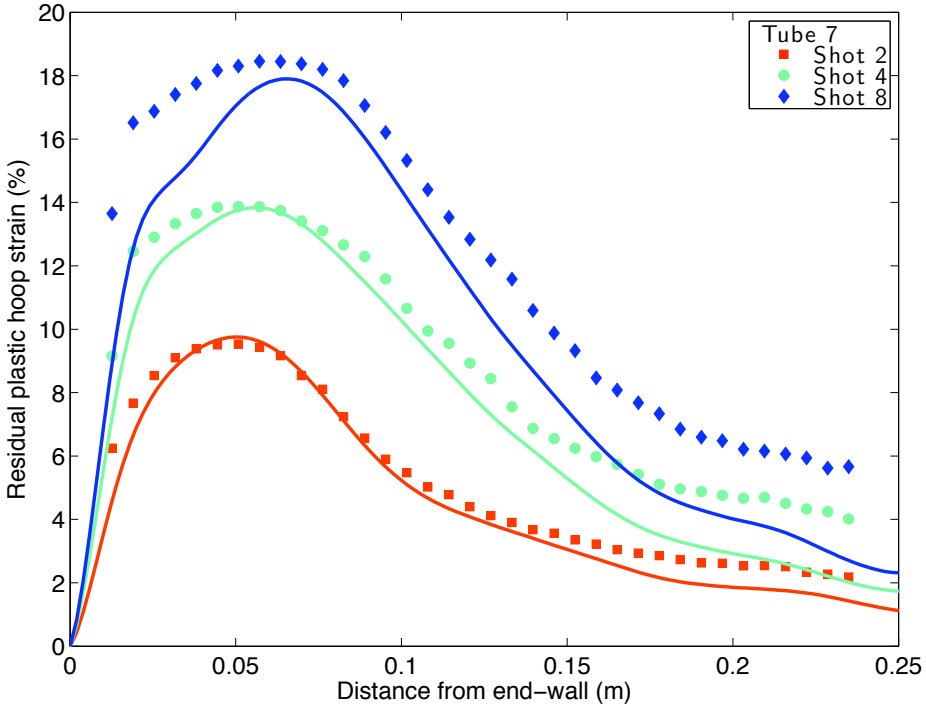

Figure 1.10: Experimental and computed detonation-driven deformation of a thin-walled mild steel tube subjected to three subsequent detonation/reflected shock loadings in a stoichiometric ethylene-oxygen mixture at fill pressure $p_1 = 300$ kPa. Data by Karnesky (2010) and presented in Karnesky et al. (2013), used with permission.

1.3.1 Detonation-Driven Deformation

Detonations excite structural waves in the containment tube; these waves travel at three characteristic speeds that are determined by solving the dispersion relationship (Tang, 1965). The flexural wave group speed may be determined analytically if shear and rotary inertia are neglected (Simkins, 1987), resulting in the approximation

$$U_{gf} \approx \left[\frac{E_1^2 h_t^2}{3\rho_t^2 r^2 \left(1-\nu^2\right)} \right]^{1/4} \tag{1.52}$$

where E_1 is the elastic modulus of the tube material, h_t is its thickness, ρ_t is the tube density, r is the radius, and ν is Poisson's ratio. This is the velocity at which resonances are observed in detonation experiments (Beltman and Shepherd, 2002) and is therefore the most important solid wave speed in detonation loading. Careful experimentation can also reveal longitudinal waves that propagate between the dilatational speed in a bar, given by

$$U_b = \sqrt{\frac{E_1}{\rho_t}}, \tag{1.53}$$

and the dilatational speed in a plate,

$$U_p = \sqrt{\frac{E_1}{\rho_t \left(1 - \nu^2\right)}}. \tag{1.54}$$

In stainless steel (the tube material in chapter 2), both of these longitudinal speeds are greater than the CJ detonation speed, implying that these waves will propagate faster than the detonation. There is also a shear wave propagating at

$$U_\gamma = \sqrt{\frac{\kappa G}{\rho_t}} \tag{1.55}$$

where κ is the shear correction factor and G is the shear modulus, but the shear wave is not observed in the experiments presented herein and will not be discussed further. Values for the flexural and dilational wave speeds corresponding to 304L stainless steel tubes with the geometry described in chapter 2 and material properties given in table 1.3 are included in table 1.2.

Table 1.2: Wave speeds in 304L stainless steel specimen tubes described in chapter 2. A CJ detonation speed is included for comparison; this speed corresponds to a detonation in stoichiometric ethylene-oxygen at a fill pressure of 200 kPa.

U_{gf} (m/s)	U_b (m/s)	U_p (m/s)	U_{CJ} (m/s)
602	5032	5274	2406

For material strains below the yield point, the internal circumferential–or hoop–stress is given by Hooke's Law:

$$\sigma_\theta = E_1 \varepsilon_\theta \quad \text{for } \varepsilon_\theta < \varepsilon_y \tag{1.56}$$

where E_1 is the elastic modulus, $\varepsilon_\theta = \log r/r_0$ is the hoop strain, and $\varepsilon_y = \sigma_y/E_1$ is the yield strain. For deformations in excess of ε_y, plastic deformation occurs that permanently increases the yield stress as tracked by

$$\frac{d\sigma_y}{dt} = \frac{d\sigma_y}{d\sigma}\frac{\partial\sigma}{\partial\varepsilon}\frac{\partial\varepsilon}{\partial t} \tag{1.57}$$

where

$$\frac{d\sigma_y}{d\sigma} = \begin{cases} 1 & \sigma \geq \sigma_y \\ 0 & \sigma < \sigma_y. \end{cases} \tag{1.58}$$

In general, the yield stress for a given material is a function of the strain history, strain-rate, and temperature. The Johnson-Cook model is used to determine the strain-rate dependent yield stress for 304L stainless steel and is described next.

1.3.2 Johnson-Cook Material Model

Measured strain-rates in reflected detonation experiments have been shown to be in excess of 1000 s^{-1} (Karnesky et al., 2013). The yield stress for stainless steel can vary by a factor of nearly 2 over this strain-rate regime, and thus it is essential to properly account for strain-rate hardening when modeling the deformation caused by reflected detonation loading. The Johnson-Cook model (Johnson and Cook, 1983) was chosen to determine the yield strain for the 304L stainless steel used in experiments described in chapter 2. In these experiments, the strain level is sufficiently low such that the temperature increase does not induce a thermal softening of the material, and the process of phase transformation for 304L stainless is not encountered (Zaera et al., 2012). Hence the flow stress is adequately defined by the temperature-independent

Table 1.3: Material properties for the Johnson-Cook model for 304L SS tubes used in the finite element simulations (Lee et al., 2006).

A (MPa)	310
B (MPa)	1000
n	0.65
c	0.07
$\dot{\varepsilon}_{p,0}$ (s^{-1})	1.00
E_1 (GPa)	200
ρ_t (kg/m^3)	7900
ν	0.3

form of the Johnson-Cook model, shown in equation (1.59), which was used in all stainless steel finite element computations:

$$\sigma_y = \left(A + B\overline{\varepsilon}_p^n\right)\left[1 + c\log\frac{\dot{\overline{\varepsilon}}_p}{\dot{\varepsilon}_{p,0}}\right] \tag{1.59}$$

where A, B, n, and c are the parameters fit to deformation data, $\overline{\varepsilon}_p$ is the von Mises equivalent plastic strain, and $\dot{\overline{\varepsilon}}_p/\dot{\varepsilon}_{p,0}$ is the von Mises equivalent plastic strain-rate normalized by the plastic strain-rate used in the experiment performed to determine the fit parameters. The 304L stainless steel of which the tubes described in chapter 2 were made was not independently characterized. Instead, the Johnson-Cook material parameters for 304L stainless steel as determined in impact experiments performed by Lee et al. (2006) are given in table 1.3, and the yield stress is plotted in figure 1.11 for various strain-rates.

1.4 Viscous Effects on Detonation Waves

Viscous effects are usually neglected when considering gaseous detonation waves because viscosity does not impact detonation propagation, except in small-diameter tubes where heat and momentum losses in the reaction zone become significant and serve to slow the detonation (Fay, 1959, Camargo et al., 2010). Behind the reaction

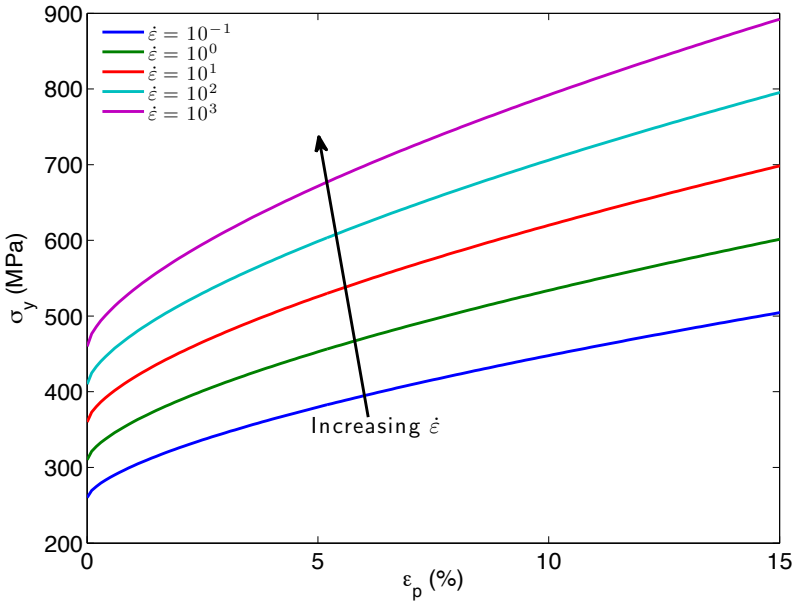

Figure 1.11: Yield stress-plastic strain trends for 304L stainless steel as determined by the Johnson-Cook constitutive relationship for increasing strain-rates.

zone the Reynolds number per unit distance, Re_x, is large. For example

$$Re_x \equiv \frac{\rho u}{\mu} = 2.6 \cdot 10^6 \text{ m}^{-1} \tag{1.60}$$

for a detonation in stoichiometric hydrogen-oxygen at fill pressure 25 kPa with properties calculated using the GRI30 high temperature mechanism (Smith et al., 1999) in Cantera. Thus the boundary layer behind the detonation is typically much smaller than the tube diameter, and therefore does not substantially affect net fluid motion. However, one potential macroscopic effect the boundary layer behind the detonation may have on the flow field is if it interacts with the reflected shock wave through reflected shock bifurcation (Mark, 1958, Taylor and Hornung, 1981, Gamezo et al., 2001). This possibility is discussed in detail in chapter 5.

Laminar boundary layer growth through the expansion wave behind blast (Liu and Mirels, 1980) and detonation (Liu et al., 1983) waves has been examined numerically. Alternatively, if we assume steady free-stream flow (thereby neglecting the TZ expansion behind the detonation), we may derive a similarity solution for

the laminar boundary layer growth behind a shock wave traveling at constant speed (Schlichting, 1979). This is a reasonable approximation of a detonation when the expansion fan width is much longer than any relevant physical dimensions (as is the case for the GALCIT detonation tube described in chapter 3). This analysis, along with the implications as they apply to gaseous detonation experiments, is included in chapter 5.

Using the Reynolds number given in equation (1.60), and the transition Reynolds number of $Re_{tr} = 0.6 \cdot 10^6$ as compiled by Chabai and Emrich (1958) from a collection of shock tube experiments, we predict turbulent transition 231 mm behind the detonation. Tanaki et al. (2009) suggest a transition Reynolds number between $0.6 \cdot 10^6 < Re_{tr} < 3 \cdot 10^6$ which implies a maximum transition distance of 1154 mm for this specific detonation. Therefore, we investigated the possibility of a turbulent boundary layer behind the detonation. This was done by measuring the heat-flux to the side-wall of the detonation tube. The heat-flux changes based on the thickness and nature (laminar or turbulent) of the boundary layer. The similarity solution of the laminar temperature profile and a turbulent skin friction coefficient were used as benchmarks for analyzing experimental heat-flux data gathered in the GALCIT detonation tube.

We have assumed in this analysis that a detonation can be approximated as a shock with the relevant shocked conditions. However, unlike shock waves, detonations are intrinsically three-dimensional. The reaction zone and transverse waves behind the detonation complicate boundary growth and transition. Thus it should be noted that both laminar and turbulent models are highly idealized, and are therefore unlikely to incorporate the physical processes required to quantitatively model the momentum and thermal boundary layers behind the detonation for all cases.

Chapter 2

Detonation-Driven Deformation of Stainless Steel Tubes

2.1 Introduction

Section 1.3 detailed how accidental internal explosions effect destruction and how the pressure profile caused by detonations distinguishes them from other high strain-rate impulsive loadings. In order to develop the capability of predicting the damage–defined here as the degree of plastic deformation–caused to thin-walled metal tubes by internal gaseous detonation loading, it was necessary to measure the detonation-induced damage of a test specimen whose constituent behavior is well-characterized. To accomplish this goal, detonation experiments and finite element computations were performed to study detonation-driven plastic deformation of thin-walled 304L stainless steel tubes.[1]

This research builds on similar experiments performed in C1010 mild steel tubes by Karnesky (2010). In that study, mild steel was chosen due to its applicability to industry. However, it proved problematic to find a suitable standard material model for C1010 mild steel capable of describing the detonation-induced deformation over the range of plastic strain and plastic strain-rates characteristic of detonation loadings. Thus in the present study detonation experiments were performed in tubes constructed of 304L stainless steel, which is better characterized than C1010 mild steel.

[1] This chapter is based in part on Karnesky et al. (2013).

In the previous study, it was observed that strain-rate hardening (such as described in Rusinek and Klepaczko, 2001) has a dominating effect on the degree of plastic deformation in steel tubes subject to internal detonation. Hence the Johnson-Cook model is used to allow for strain-rate hardening in the finite element analysis. Good agreement was achieved between residual plastic strain measurements and computed results using established Johnson-Cook parameters. Both the stainless steel results discussed herein and the earlier mild steel results are published in Karnesky et al. (2013).

2.2 Driven-Thin Experimental Setup

An experimental facility was constructed to study the plastic deformation of thin-walled metal tubes caused by normally reflected gaseous detonation waves. This facility is termed the driven-thin detonation tube to differentiate it from the GALCIT detonation tube described in chapter 3; it is identical to the driven-thin assembly described in Karnesky (2010). Figure 2.1 illustrates the general construction of the driven-thin detonation tube. It is composed of two component tubes–the driver tube and a specimen tube–joined in the center by a gland seal to form one long tube. This long tube is mounted on a track and coupled to an inertial mass. The driver tube did not undergo plastic deformation and was used in all experiments. The specimen tubes were interchangeable, and we will be discussing data from three specimen tubes: tubes 9, 10, and 11.[2] Combustion was initiated inside the driver tube at the end marked "ignition" in figure 2.1. The detonation impinged on the end-wall marked "reflection" inside the specimen tube. As discussed in section 1.2, the location of detonation reflection experiences the largest pressures, and thus the largest deformation was expected in the region near the reflecting end-wall.

The driver tube, located on the left in figures 2.1 and 2.2, is the same tube used in previous DDT studies, such as those described in Liang et al. (2006) and Pintgen and Shepherd (2006b). It is made of 316L stainless steel of 12.7 mm wall thickness

[2]Tubes 1 through 8 were discussed by Karnesky (2010).

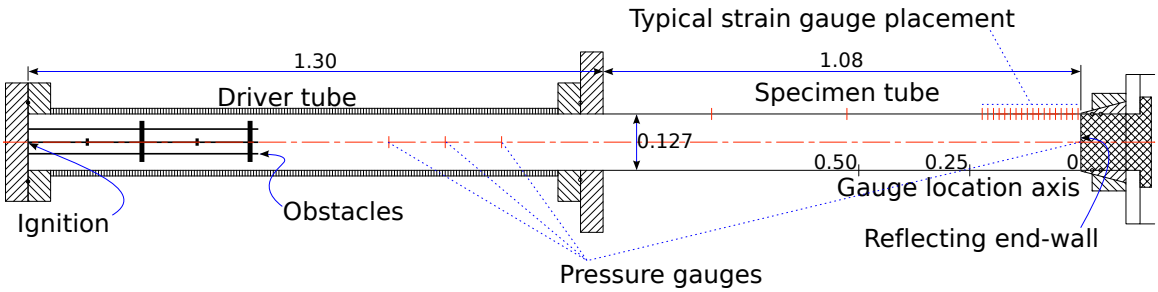

Figure 2.1: Driven-thin detonation tube schematic, dimensions in meters.

and 127 mm internal diameter (which equals the internal diameter of the specimen tubes). The purpose of the driver tube was to contain the unsteady detonation start-up process of flame initiation, turbulence generation, and DDT so that these unpredictable pressure loadings would not effect strain in the specimen tube.

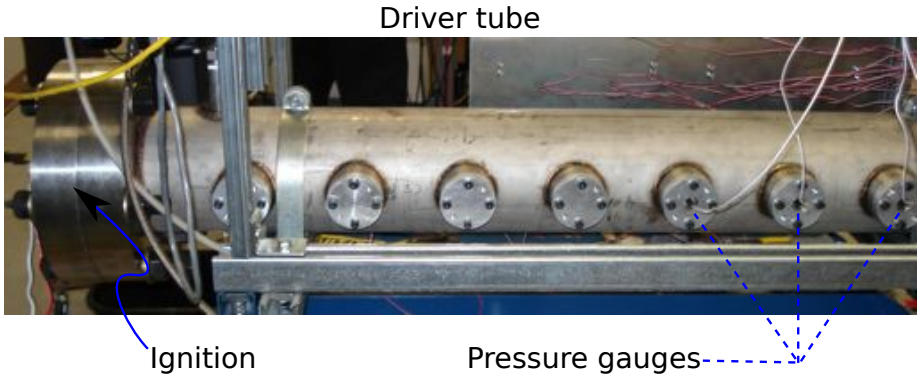

Figure 2.2: Photograph of the driver portion of the driven-thin detonation tube.

Prior to each experiment, the driven-thin detonation tube was evacuated to an initial pressure below 50 mTorr. It was then filled using the method of partial pressures with a stoichiometric ethylene-oxygen mixture to the target fill pressure of either 50, 200, or 300 kPa. A circulation pump was used to mix the gas for a period of 5 minutes. Ignition was achieved by applying 10 V at a current of 9.5 A to a Bosch 0-250-202-051 glow plug. After a flame was initiated, DDT was facilitated through the turbulence generated by four paddle-shaped obstacles with a blockage ratio of 37% evenly spaced in the 508 mm nearest the point of ignition as shown in figure 2.1, alternating in the 90° pattern shown in figure 2.3. The pressure was measured in the driver tube using

three PCB 113A24 piezoelectric pressure gauges amplified by a PCB 482A22 signal conditioner located 813, 940, and 1069 mm from the ignition wall (1559, 1432, and 1305 mm, respectively, from the reflecting wall); this allowed us to determine whether DDT occurred before the combustion wave entered the specimen tube. By examining the wave speeds between the three driver tube pressure gauges, and comparing this measured speed to the Chapman-Jouguet theoretical detonation speed, it was determined that detonation was achieved prior to the wave reaching the first pressure gauge–and thus prior to it entering the test specimen–in every experiment performed.

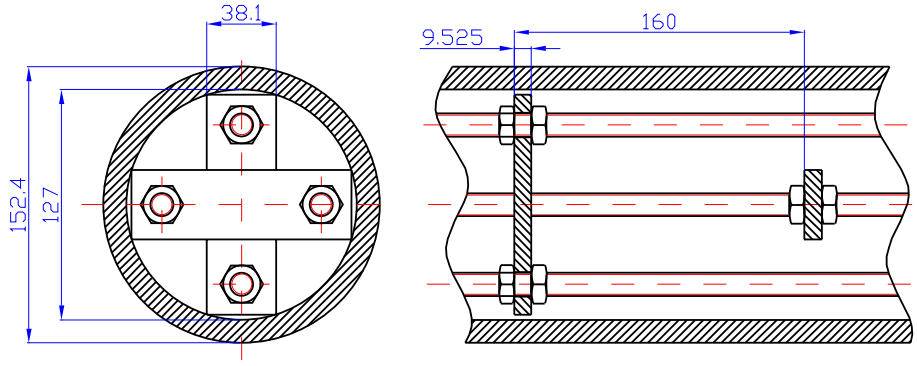

Figure 2.3: Obstacle placement and orientation in driven-thin detonation tube, dimensions in millimeters. Figure by Karnesky (2010), used with permission.

The driver and specimen tubes were sealed in the center by a flange with two internal gland seals. This flange mated with a face-seal onto the open end of the driver tube, and the thin specimen tubes slipped into the gland seals as seen in figure 2.4. This arrangement allowed the detonation to propagate unaffected from the driver tube into the specimen tube. After the detonation entered the specimen tube it continued to propagate until it impinged upon a solid aluminum plug located in the reflecting end-wall of the specimen tube. A PCB 113B23 pressure transducer amplified by a PCB 482A22 signal conditioner was mounted flush with the surface of the plug to measure the pressure at the reflecting end-wall.

Previous research performed in the Explosion Dynamics Laboratory investigating plastic deformation of thin-walled mild steel tubes in an alternate experimental setup

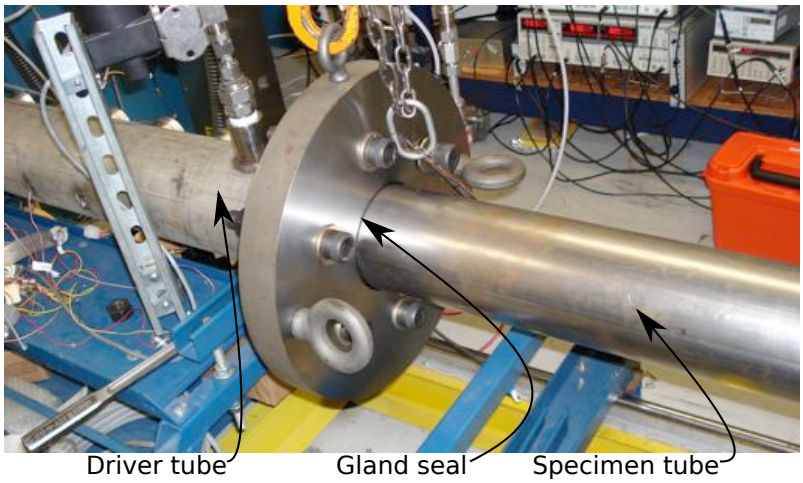

Figure 2.4: Photograph of the flange used to couple the driver tube to the specimen tube.

(Pintgen and Shepherd, 2006a) emphasized the importance of a robust module to firmly grip the specimen tube on the reflecting end so as to ensure a well-defined boundary condition that does not apply pre-stresses. In order to achieve this, a collet was constructed to clamp down on the reflecting end of the specimen tube. The collet was cut by wire-EDM out of tool steel and hardened. At 100 mm in length, the collet was designed such that its end point, when tightened, matched the face of the reflecting surface of the aluminum plug located inside the tube, as seen in figure 2.5.

A ring with an internal taper forced the collet closed and was bolted to a plate using eight 9/16"-18 bolts with minimum preloads of 68 N·m, resulting in a clamping force in excess of 125 kN.[3] The collet assembly was fastened to a 2700 kg steel mass to absorb the recoil of the reflecting detonation. Figure 2.6 shows the reflecting end of the specimen tube before and after the collet ring was secured. The collet and driver tube were held together with chains to prevent the force of the detonation pulling the test specimen and driver tubes apart.

Specimen tubes were manufactured out of 304L stainless steel sheets of 1.5 mm thickness that were rolled and flash-control welded to make tubes with 127 mm inner

[3]Clamping force calculated from $F_{clamp} = n_{bolt} \cdot T_{bolt} / (c_{fric} \cdot D_{bolt}) = 127$ kN, where $n_{bolt} = 8$ is the number of bolts, $T_{bolt} = 68$ N·m is the applied torque, $c_{fric} = 0.3$ is the assumed friction constant, and $D_{bolt} = 9/16$ in $= 14.3$ mm is the nominal bolt diameter.

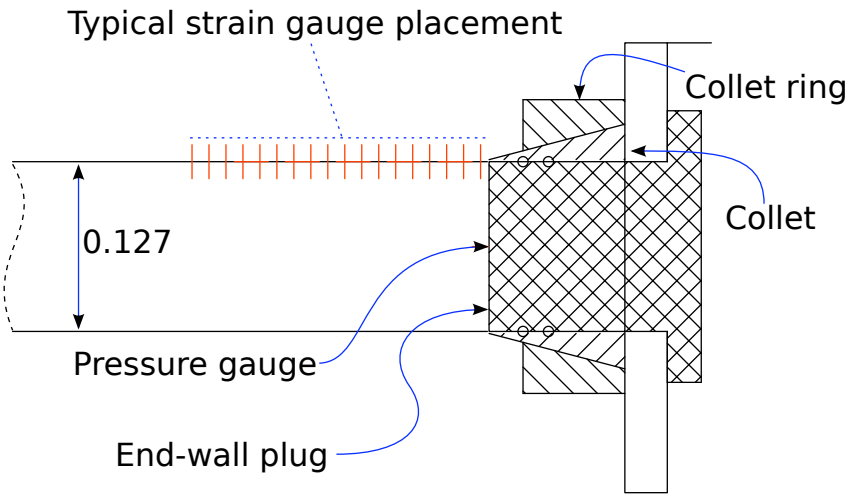

Figure 2.5: Schematic of the driven-thin detonation tube reflecting end-wall. Dimensions are in meters.

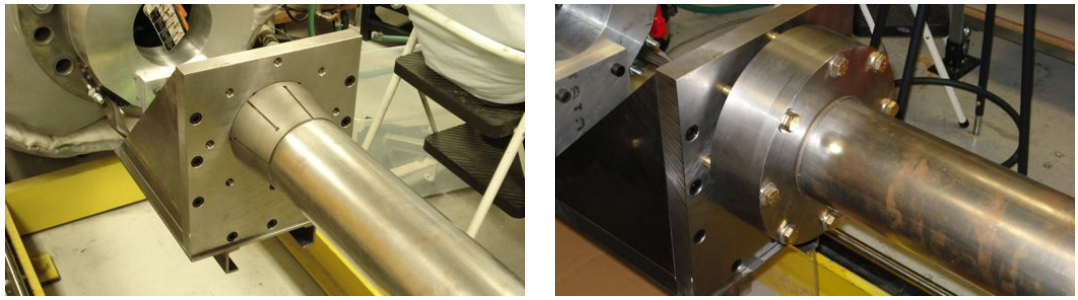

(a) (b)

Figure 2.6: Photographs of the reflecting end of the specimen tube (a) before and (b) after the collet ring had been secured.

diameter, 1.5 mm wall thickness, and 1.2 m length. The specimen tubes were instrumented with Vishay strain gauges connected in a quarter bridge configuration and amplified with Vishay 2310 signal conditioners. The model number and placement of strain gauges varied between specimen tubes to better accommodate the increased deformation in the 300 kPa fill pressure experiments, but were always concentrated near the reflecting end where the maximum deformation was observed. Strain gauges were oriented to measure either circumferential strain (also known as "hoop" strain) or longitudinal strain. The largest strain component in all experiments was the circumferential strain, and thus the majority of gauges were in this orientation. Most

tubes experienced multiple detonations that produced plastic deformation. In these cases, the strain gauges were checked between experiments. For some experimental conditions, the gauges in high strain locations would break. Times at which failure occurs are clearly seen on the strain plots by the data spiking or going to zero, depending on the failure mode incurred. In these cases, or when the strain gauge did not return to within 1% of the initial resistance of 350 Ω, the gauges would be replaced between experiments without removing the specimen tube from the experimental fixture, in order to avoid errors caused by differing tube placement. Strain gauge placement, orientation, and type for tubes 9, 10, and 11 are shown in tables 2.1, 2.2, and 2.3, respectively.

Table 2.1: Strain and pressure gauge placement for driven-thin tube 9.

Gauge Number	Type	Orientation	Model	Distance From Reflection (mm)
1	Strain	Longitudinal	C2A-06-125LT-350	781
2	Strain	Hoop	C2A-06-125LT-350	781
3	Strain	Longitudinal	C2A-06-125LT-350	578
4	Strain	Hoop	C2A-06-125LT-350	578
5	Strain	Longitudinal	C2A-06-125LT-350	375
6	Strain	Hoop	C2A-06-125LT-350	375
7	Strain	Hoop	EP-08-125AC-350	171
8	Strain	Hoop	EP-08-125AC-350	146
9	Strain	Hoop	EP-08-125AC-350	121
10	Strain	Hoop	EP-08-125AC-350	108
11	Strain	Hoop	EP-08-125AC-350	95
12	Strain	Hoop	EP-08-125AC-350	83
13	Strain	Hoop	EP-08-125AC-350	70
14	Strain	Longitudinal	EP-08-125AC-350	57
15	Strain	Hoop	EP-08-125AC-350	57
16	Strain	Hoop	EP-08-125AC-350	44
17	Strain	Hoop	EP-08-125AC-350	32
18	Strain	Longitudinal	EP-08-125AC-350	19
19	Strain	Hoop	EP-08-125AC-350	19
20	Strain	Hoop	EP-08-125AC-350	6
21	Pressure	N/A	PCB 113A24	1559
22	Pressure	N/A	PCB 113A24	1432
23	Pressure	N/A	PCB 113A24	1305
24	Pressure	N/A	PCB 113B24	0

Table 2.2: Strain and pressure gauge placement for driven-thin tube 10.

Gauge Number	Type	Orientation	Model	Distance From Reflection (mm)
1	Strain	Longitudinal	C2A-06-125LT-350	768
2	Strain	Hoop	C2A-06-125LT-350	768
3	Strain	Longitudinal	C2A-06-125LT-350	565
4	Strain	Hoop	C2A-06-125LT-350	565
5	Strain	Longitudinal	C2A-06-125LT-350	362
6	Strain	Hoop	C2A-06-125LT-350	362
7	Strain	Hoop	EP-08-125AC-350	159
8	Strain	Hoop	EP-08-125AC-350	133
9	Strain	Hoop	EP-08-125AC-350	108
10	Strain	Longitudinal	EP-08-125AC-350	83
11	Strain	Hoop	EP-08-125AC-350	83
12	Strain	Hoop	EP-08-125AC-350	70
13	Strain	Longitudinal	EP-08-125AC-350	57
14	Strain	Hoop	EP-08-125AC-350	57
15	Strain	Hoop	EP-08-125AC-350	44
16	Strain	Longitudinal	EP-08-125AC-350	32
17	Strain	Hoop	EP-08-125AC-350	32
18	Strain	Hoop	EP-08-125AC-350	19
19	Strain	Longitudinal	EP-08-125AC-350	6
20	Strain	Hoop	EP-08-125AC-350	6
21	Pressure	N/A	PCB 113A24	1559
22	Pressure	N/A	PCB 113A24	1432
23	Pressure	N/A	PCB 113A24	1305
24	Pressure	N/A	PCB 113B24	0

Before applying strain gauges, the surface of the specimen tube was prepared following the procedures described by Vishay (2005b). To secure the strain gauges, one of two types of adhesives was used. Strain gauges of model C2A-06-125LT-350 used M-Bond 200, a cyanoacrylate adhesive typical of strain gauge affixation, and were installed per Vishay (2005a). When the gauge location or fill pressure led us to expect strains in excess of 3%–the nominal maximum measurable strain for C2A-06-125LT-350 gauges–model EP-08-125AC-350 strain gauges were employed that have a nominal range up to 20%. However, in practice we were not able to measure strains of this magnitude due to failure of the adhesive. To allow for strains approaching this magnitude, M-Bond A-12 epoxy was used in place of the M-Bond 200. To speed the

Table 2.3: Strain and pressure gauge placement for driven-thin tube 11.

Gauge Number	Type	Orientation	Model	Distance From Reflection (mm)
1	Strain	Longitudinal	C2A-06-125LT-350	565
2	Strain	Hoop	C2A-06-125LT-350	565
3	Strain	Longitudinal	C2A-06-125LT-350	362
4	Strain	Hoop	C2A-06-125LT-350	362
5	Strain	Hoop	EP-08-125AC-350	159
6	Strain	Hoop	EP-08-125AC-350	133
7	Strain	Longitudinal	EP-08-125AC-350	108
8	Strain	Hoop	EP-08-125AC-350	108
9	Strain	Hoop	EP-08-125AC-350	95
10	Strain	Longitudinal	EP-08-125AC-350	83
11	Strain	Hoop	EP-08-125AC-350	83
12	Strain	Hoop	EP-08-125AC-350	70
13	Strain	Longitudinal	EP-08-125AC-350	57
14	Strain	Hoop	EP-08-125AC-350	57
15	Strain	Hoop	EP-08-125AC-350	44
16	Strain	Longitudinal	EP-08-125AC-350	32
17	Strain	Hoop	EP-08-125AC-350	32
18	Strain	Hoop	EP-08-125AC-350	19
19	Strain	Longitudinal	EP-08-125AC-350	6
20	Strain	Hoop	EP-08-125AC-350	6
21	Pressure	N/A	PCB 113A24	1559
22	Pressure	N/A	PCB 113A24	1432
23	Pressure	N/A	PCB 113A24	1305
24	Pressure	N/A	PCB 113B24	0

curing of this epoxy, heaters were used to hold the tube wall temperature at 75°C for a period of 2 hours as described by Vishay (2007). An example of epoxied strain gauges is shown in figure 2.7.

Strain and pressure data were recorded during the detonation event via three National Instruments PXI-6133 S Series 8 channel, 14-bit multifunction DAQ cards housed in an NI PXI-1042 chassis. After each detonation that resulted in plastic deformation, the post shot diameter and thickness were measured using an outside micrometer and a Checkline TI-007 ultrasonic wall-thickness gauge. These measured values were then transformed to residual plastic hoop and thickness strains using the known undeformed values.

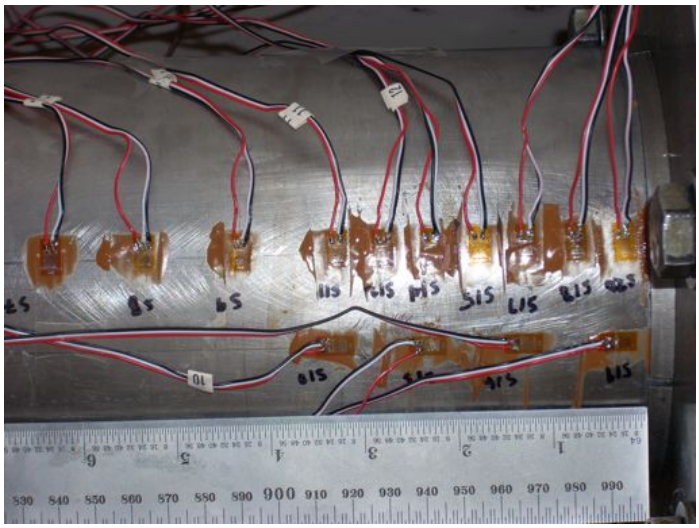

Figure 2.7: EP-08-125AC-350 strain gauges applied to driven-thin detonation tube using M-Bond A-12 epoxy.

2.3 Data

The pressure created by gaseous detonation inside a tube will cause deformation of the tube wall. For a fixed flammable mixture and fixed initial temperature, the incurred damage regime will only be a function of the fill pressure. As the fill pressure increases, the test specimen will undergo strains that fall into one of four deformation regimes: (1) purely elastic deformation, (2) plastic deformation upon detonation reflection, (3) plastic deformation from the incident detonation (and further deformation upon detonation reflection), or, if the fill pressure is further increased, (4) tube rupture. Experiments in the driven-thin tube with 50 kPa fill pressure fall into the purely elastic regime. Tubes with a fill pressure of 200 kPa experienced very little plastic deformation behind the incident detonation and essentially fall into the second strain regime. Increasing the fill pressure to 300 kPa produced sizable plastic deformation from both the incident detonation and the reflected shock, placing these experiments in the third strain regime. If we further increased the fill pressure, or if we repeated the plastic deformation experiments a suitable number of times in the same tube, we would eventually reach the fourth regime of tube rupture. However, this was avoided in the present experiments since the experimental facility was not designed to contain

the ensuing blast wave.

In each experiment, the driven-thin detonation tube assembly was filled with stoichiometric ethylene-oxygen to an initial pressure of 50, 200, or 300 kPa as explicated in table 2.4. The fill pressure was chosen based on the desired deformation regime. Plastic deformation was observed in each case except those with initial pressure of 50 kPa. Repeated detonations in the same specimen tubes were performed with initial pressures of 200 and 300 kPa to investigate strain ratcheting. The initial conditions for each experiment are shown in table 2.4. Note that each experiment that resulted in plastic deformation was preceded by an experiment that only produced an elastic response. The purpose of this was to create a database of elastic deformation and to test the strain gauges before performing an experiment that resulted in permanent deformation. In a few instances, such as tube 9 test numbers 9 and 10, experiments were repeated if there was an anomaly in the elastic strain results.

Table 2.4: Overview of initial conditions used in driven-thin detonation experiments. In all cases, the mixture used was stoichiometric ethylene-oxygen.

	Fill Pressure (kPa)	Test Numbers	Deformation Regime
Tube 9	50	1, 2, 4, 6, 8, 10	Purely elastic
	200	3, 5, 7, 9, 11	Plastic on reflection
Tube 10	50	1	Purely elastic
	300	2	Plastic on incident
Tube 11	50	1, 3, 4	Purely elastic
	300	2, 5	Plastic on incident

2.3.1 Results From Tube 9

The goal of the experiments performed in tube 9 was to investigate the strain resulting from repeated detonations of initial pressure 200 kPa. This fill pressure was such that the plastic strain resulting from the incident detonation was negligible, and thus the permanent deformation was almost completely attributable to the reflected shock. Tube 9 was tested with 11 detonations; six were “elastic shots” with a fill pressure of 50 kPa, and five were “plastic shots” with a fill pressure of 200 kPa. Details for each

Table 2.5: Description of driven-thin detonation experiments performed in tube 9.

Shot Number	Fill Pressure (kPa)	Comments
1	50	Strain gauge 1 did not record for any experiment in tube 9 (or experiments in subsequent tubes). The related data acquisition channel seemed to function properly to test signals and the gauge was replaced multiple times. It was later deemed to be a problem with the data acquisition channel and no data were recorded with this gauge.
2	50	
3	200	
4	50	
5	200	Strain gauges 17 and 19 broke.
6	50	
7	200	
8	50	
9	200	Strain gauge 13 broke.
10	50	Strain gauge 13 exhibited odd behavior.
11	200	Strain gauges 13 and 17 broke.

experiment are given table 2.5. The most relevant results are reported here, but all data are included in appendix A.

A complete description of strain gauge type and location is given in table 2.1, and gauge locations are also shown on relevant plots. Figure 2.8(a), for example, shows hoop and longitudinal strain measurements taken during the second elastic experiment in tube 9 for strain gauges placed 578, 375, and 57 mm from the location of detonation reflection. Through examining the strain signals in figure 2.8(a), each gauge reveals two definitive times that show changes in strain behavior and thus indicate wave arrivals. The first time (at $t_1 = -0.26$ ms for the marked location; note that $t = 0$ is when the detonation impinges upon the reflection wall) shows a slight increase in longitudinal strain and a corresponding, but barely visible, dip in hoop strain caused by the Poisson effect. This corresponds to the arrival of the longitudinal wave in the tube wall as discussed in section 1.3.1, and indicates that the tube is slightly lengthening as the upstream deformation pulls the tube towards

the location of ignition. This longitudinal wave is the only event of consequence that precedes the arrival of the detonation. The second change in strain behavior (at $t_2 = -0.02$ ms for the marked gauge) portrays a substantial increase in hoop strain followed by an oscillation with frequency $f_{xs} = 12.7$ kHz (as determined by the fast Fourier transformation (Brigham, 1974) shown in figure 2.9); this strain behavior change corresponds to the arrival of the detonation and resulting flexural oscillation of the tube wall. The longitudinal measurement undergoes a related decrease in strain brought about by Poisson coupling. When the reflected shock wave arrives, the increased internal pressure causes a third change in strain behavior; however, the reflected shock is not strong enough to produce a significant change in the strain signals when the fill pressure is 50 kPa.

The strains shown in figure 2.8(a) are purely elastic because the initial pressure of 50 kPa did not result in pressures large enough to cause plastic deformation. Figure 2.8(b) shows the strains obtained from the first detonation in tube 9 of fill pressure 200 kPa. The same general wave systems observed in figure 2.8(a) and explained above are still present, but the ensuing strain magnitudes are increased due to the increased internal pressure. We also observed strains resulting from the arrival of the reflected shock wave (at $t_3 = 0.06$ ms for the marked gauge). As previously discussed, the largest pressures are associated with the reflected wave near the location of detonation reflection, and thus strains of the greatest magnitude are near the reflecting end-wall.

Data from five subsequent experiments with initial pressure 200 kPa are shown in figure 2.10. The repeated tests show the substantial effect of strain-hardening. The plastic strain increment on the first plastic shot of a test series is always higher than that of the second and subsequent shots. This is particularly pronounced for strain gauges at 19, 32, and 44 mm from the point of detonation reflection. This is caused by the increase in yield strain as the specimen tube undergoes permanent deformation. The strain is smaller in the immediate vicinity of detonation reflection (as seen in the strain gauge located 6 mm from the end-wall) due to the boundary condition preventing material deformation.

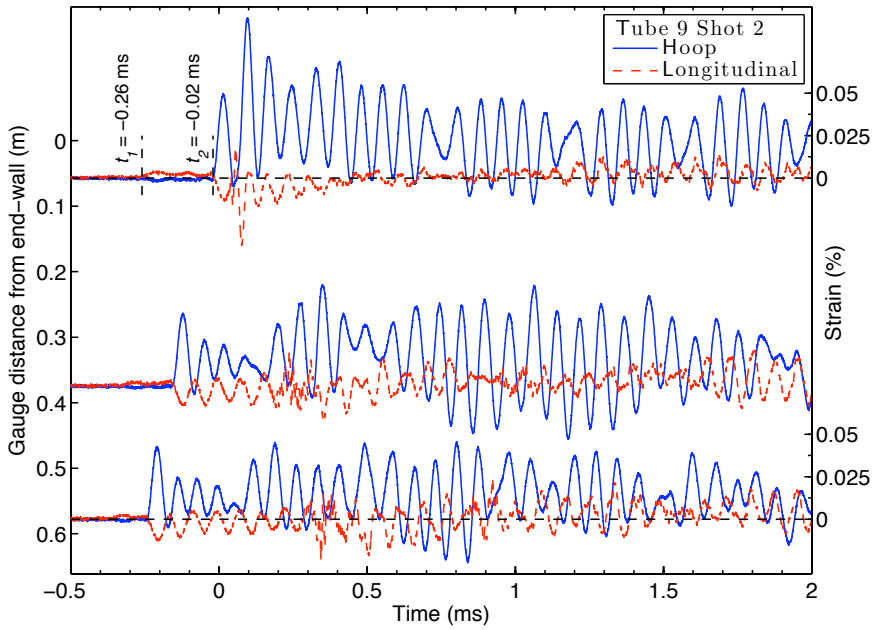

(a)

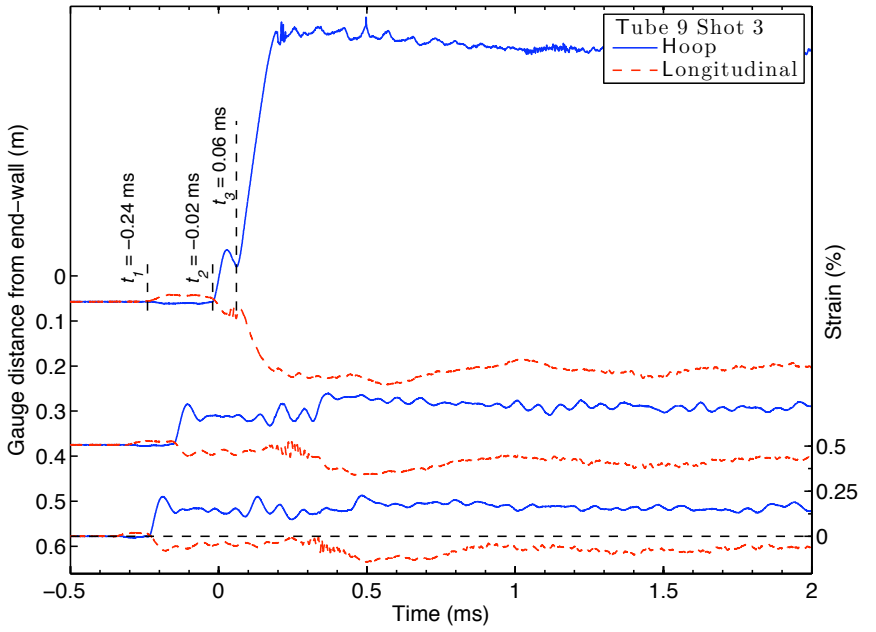

(b)

Figure 2.8: Time-resolved hoop and longitudinal elastic strain measurements caused by detonations of stoichiometric ethylene-oxygen taken in tube 9 during shot numbers (a) 2 with a fill pressure of 50 kPa and (b) 3 with a fill pressure of 200 kPa.

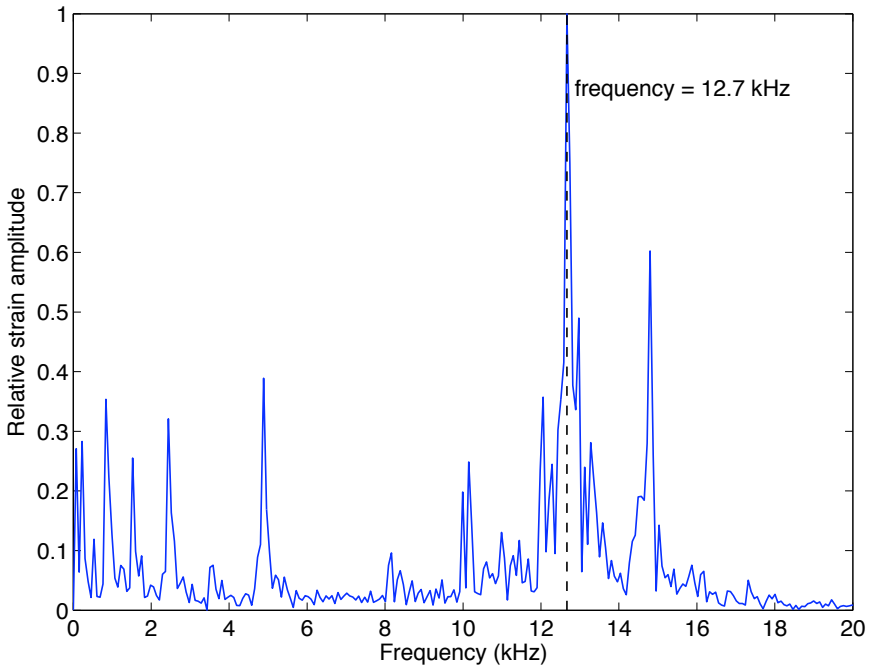

Figure 2.9: Fast Fourier transform of elastic oscillation data in driven-thin tube 9, shot 2.

After every plastic experiment, the outer diameter and tube wall thickness were measured. The wall thickness did not change enough in tube 9 for the thickness measurements to be useful. The outer diameter data are plotted in figure 2.11. It is striking to note that the tube surface exhibits a rippled appearance. This periodic deformation had a peak-to-peak spacing of 68 mm $\pm$ 2 mm as determined by a photograph of the tube wall atop a 1 mm grid. This ripple pattern is also observed in the photograph of tube 9 shown in figure 2.12. An identical ripple pattern was reported by Karnesky (2010) for detonations of initial pressure 200 kPa in mild steel tubes. The origin of this phenomenon is explained in section 2.4.1.

Experiments after the first detonation to result in plastic strain will differ in three main aspects from previous experiments. First, assuming the plastic instability is not reached, the tube material will be stronger and thus decreased strains are expected for identical loading conditions. This was observed and is discussed above. Second, the plastic strain serves to increase the internal volume, and thus more moles of combustible gas are present in later experiments for an identical fill pressure. Third, the

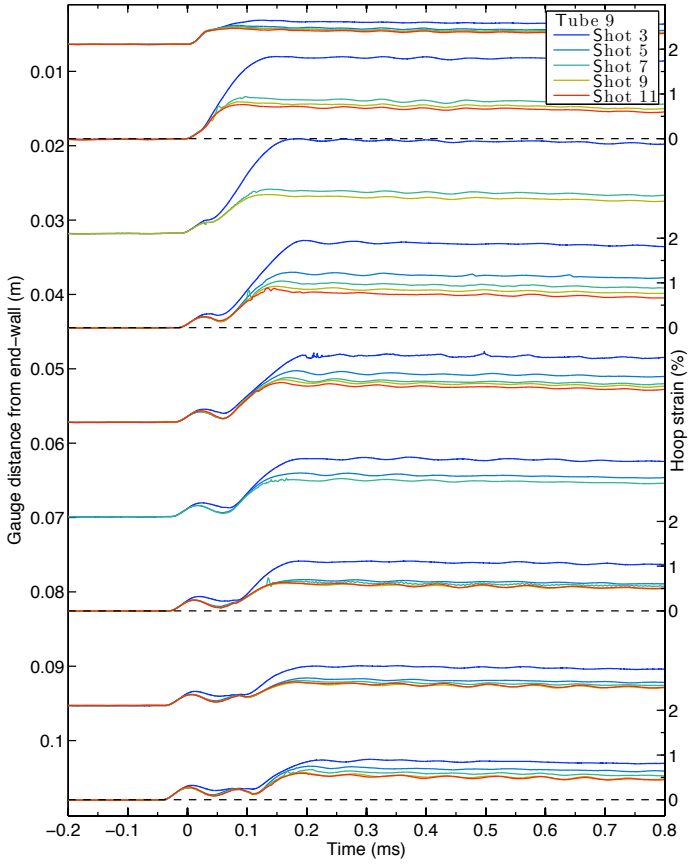

(a)

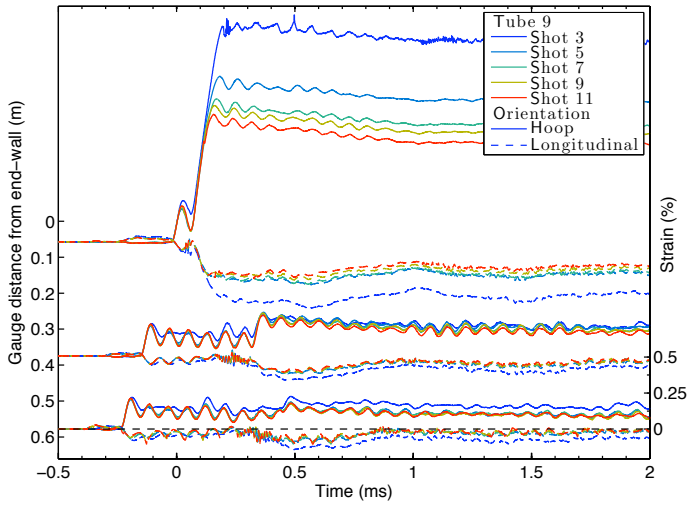

(b)

Figure 2.10: Time-resolved strains in tube 9 during five subsequent detonations with a fill pressure of 200 kPa. We see (a) hoop strain traces for gauges located near the reflecting end, and (b) colocated hoop (solid lines) and longitudinal (dashed lines) strain traces.

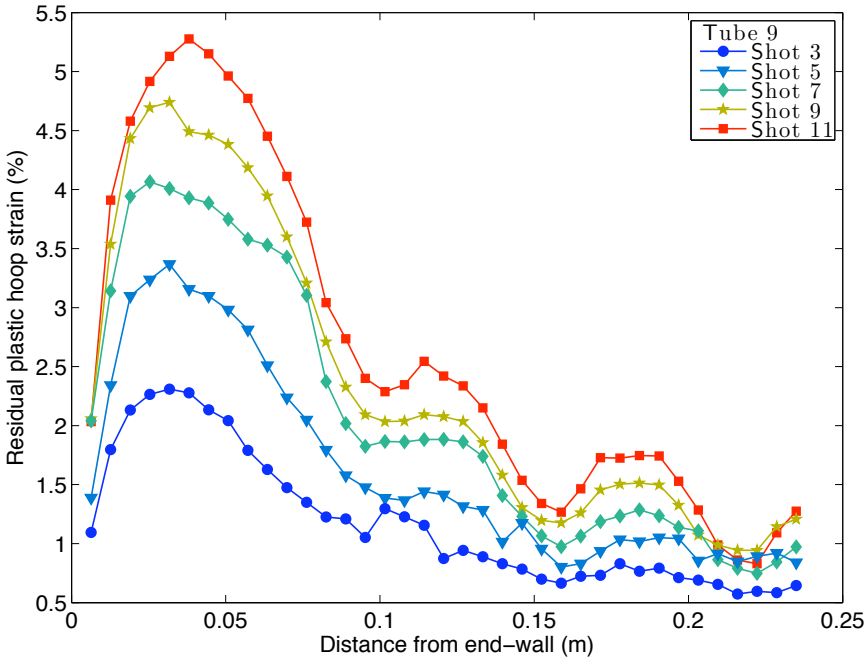

Figure 2.11: Residual plastic hoop strain of driven-thin specimen tube 9 after each of five successive detonations at fill pressure 200 kPa.

area change will cause the detonation and shock waves to diffract; this will result in two-dimensional wave propagation. The area change was relatively minor for experiments in tube 9 (the maximum area increase was 4.7% after the first experiment resulting in plastic strain and 10.8% after the fifth experiment resulting in plastic strain), but was more substantial in later tubes when the fill pressure was increased. For these reasons we only sought to obtain quantitative agreement with the first experiment to result in plastic strain.

2.3.2 Results From Tube 10

The experiments performed in specimen tube 10 investigated the third strain regime where substantial plastic deformation is caused by both the incident detonation and the reflected shock. This was accomplished by detonations in stoichiometric ethylene-oxygen with a 300 kPa fill pressure. A description of each experiment is included in table 2.6, and measurement gauge locations are given in table 2.2. The intent was to investigate the effect of strain ratcheting, but only a single plastic shot was performed

Figure 2.12: Photograph of driven-thin specimen tube 9 after five plastic experiments at fill pressure 200 kPa. We observe that the tube surface has become rippled by the detonation loadings.

in tube 10 due to strain gauge failure. After every detonation experiment, strain gauges that did not return to within 1% of their original resistance (350 Ω) were replaced. For the 200 kPa fill pressure experiments in tube 9, this resulted in only a few gauges being replaced after each experiment to result in plastic deformation. In tube 10, however, no strain gauge returned to the original resistance and most gauges failed during the experiment; the primary mode of failure for the catastrophic failure case was the gauge adhesive debonding from the tube. As seen in figure 2.13, the large deformations proved too severe for strain gauge survival, and thus the experiments were repeated in tube 11. Figure 2.14 shows specimen tube 10 after the single shot to result in plastic deformation, and the residual plastic hoop and thickness strains are plotted in figure 2.15 with the data from tube 11 to illustrate experiment repeatability; the entire set of collected data is included in appendix A.

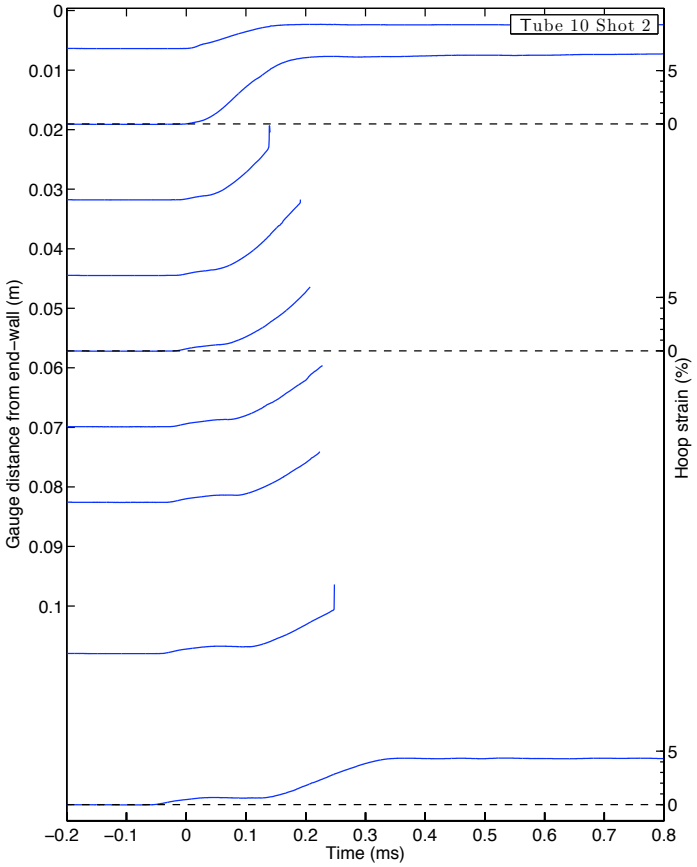

(a)

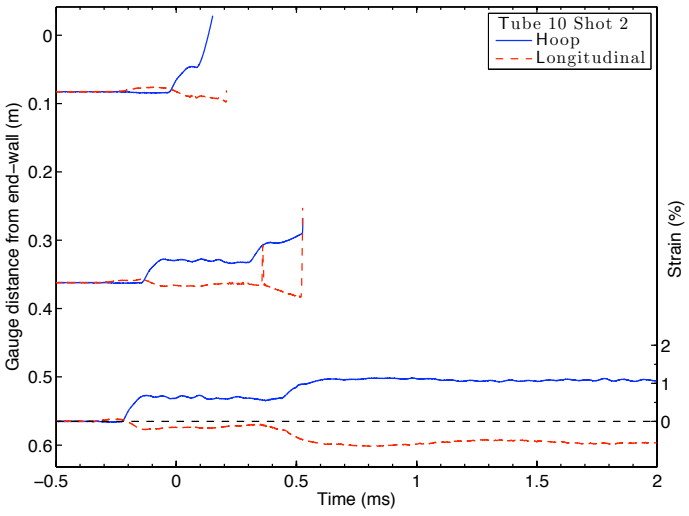

(b)

Figure 2.13: Time-resolved plastic hoop strain data for tube 10 during a detonation of fill pressure 300 kPa. Times where data spike or cease represent gauge failure. We see (a) hoop strain traces for gauges located near the reflecting end, and (b) colocated hoop (solid lines) and longitudinal (dashed lines) strain traces.

Table 2.6: Description of driven-thin detonation experiments performed in tube 10.

Shot Number	Fill Pressure (kPa)	Comments
1	50	Data acquisition channel 1 was deemed to be broken and no data were recorded for strain gauge 1.
2	300	Strain gauges 5, 9–17, and 19 broke.

Figure 2.14: Photograph of driven-thin specimen tube 10 after one plastic experiment at fill pressure 300 kPa.

2.3.3 Results From Tube 11

Like tube 10, the goal of experiments performed in tube 11 was to gather strain ratcheting data for detonations with a fill pressure of 300 kPa. The surface of the tube was roughened with grade 20 sandpaper and a file applied in a cross-hatch pattern prior to strain gauge application in an attempt to improve strain gauge survivability. However, gauge survivability was even worse than tube 10, and thus the post-shot outer diameter measurements will be our primary method of comparison to the computational results for the case of 300 kPa fill pressure. Two plastic shots were

performed in tube 11, but because the point of plastic instability was approached in the second test and because the experimental facility was not set up to contain blast waves resulting from tube rupture, no further plastic experiments were conducted. A description of each test is given in table 2.7, and measurement gauge locations are included in table 2.7. Appendix A contains all recorded data.

Table 2.7: Description of driven-thin detonation experiments performed in tube 11.

Shot Number	Fill Pressure (kPa)	Comments
1	50	
2	300	Strain gauges 2 and 4–19 broke.
3	50	No further time-resolved strain data were recorded for tube 11 due to extreme strain gauge failure.
4	50	
5	300	

The residual plastic hoop and thickness strains are plotted in figures 2.15(a) and (b). Unlike tube 9, detonations in tubes 10 and 11 did not produce a noticeably rippled tube surface (see, for example, the photo of tube 10 shown in figure 2.14). The reason for this is explained in section 2.4.1.

2.4 Modeling

The primary goal of the previously presented experiments was to provide high-precision data to compare to computational models. With the data in hand, two separate modeling techniques were employed to understand detonation-induced deformation. The first technique is a single degree of freedom model that explains the periodic deformation mode observed in tube 9. The second technique is a two-dimensional finite element analysis that gives quantitatively correct strain predictions using the Johnson-Cook material model with standard parameters for 304L stainless steel.

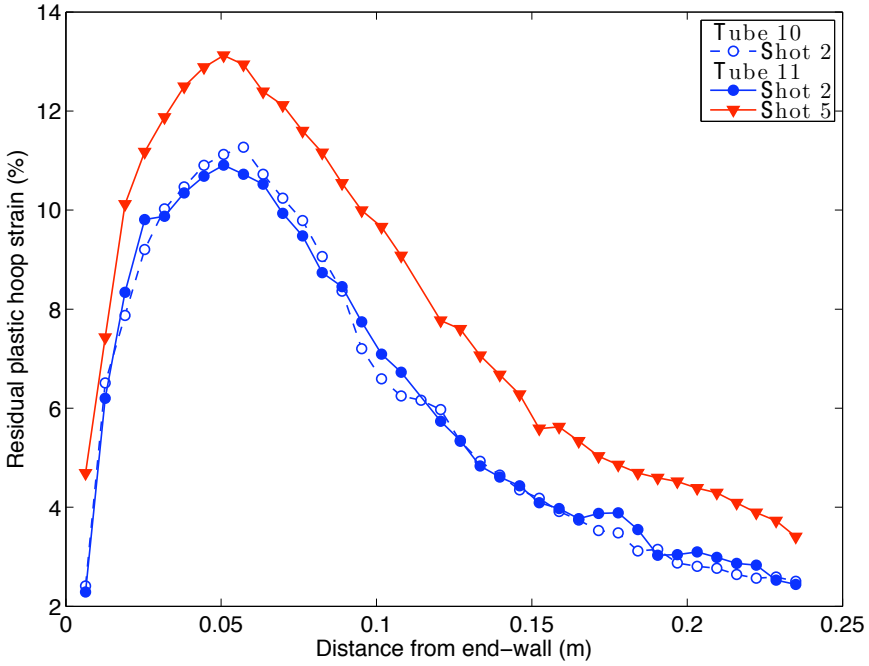

(a)

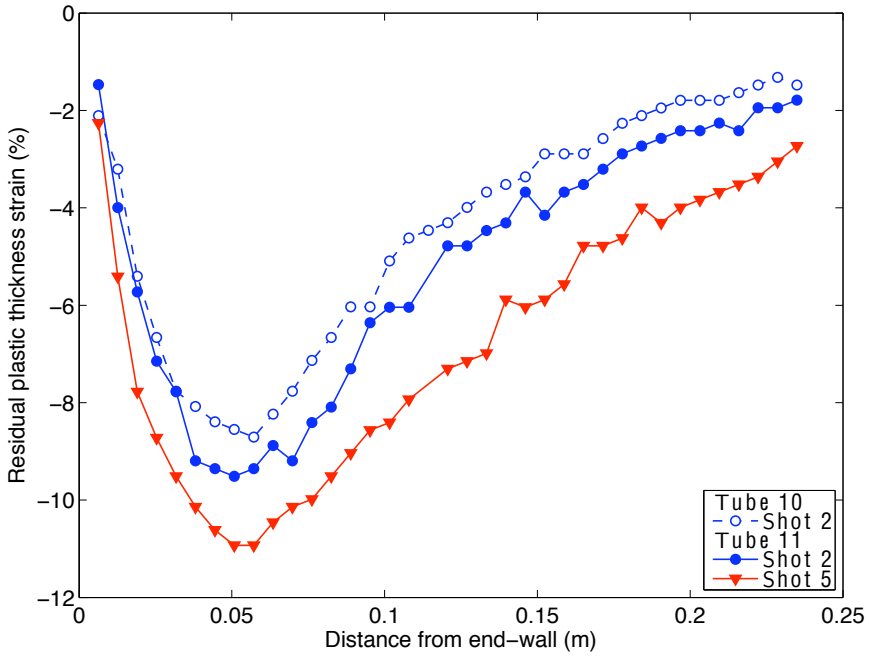

(b)

Figure 2.15: Residual plastic (a) hoop and (b) thickness strain of driven-thin specimen tubes 10 and 11 after each detonation with fill pressure 300 kPa.

2.4.1 Single Degree of Freedom Model

Fundamental understanding of the dynamics of the tube wall may be gained by considering a one-dimensional oscillator subject to time-dependent loading. This approximates the specimen tube as infinitely long and immune to two-dimensional effects. These approximations are reasonable for locations more than five bending lengths from the boundaries, where the bending length is defined as

$$\lambda_b \equiv \left[\frac{r_0^2 h_{t0}^2}{3\left(1-\nu^2\right)}\right]^{1/4} \tag{2.1}$$

where r_0 is the initial undeformed tube radius, h_{t0} is the undeformed tube thickness, and ν is the Poisson ratio (Young and Budynas, 2002). The details of the single degree of freedom model are derived by Karnesky et al. (2013). The core of the model is in the dynamic oscillator equation

$$\frac{d^2 r'}{dt^2} = \frac{\Delta p(t)}{\rho_t h_{t0}} - \frac{\sigma_\theta}{\rho_t r_0} \tag{2.2}$$

where the hoop stress, σ_θ, is related to the hoop strain, ε_θ, where

$$\varepsilon_\theta = \log\frac{r}{r_0} \approx \frac{r-r_0}{r_0} = \frac{r'}{r_0} \tag{2.3}$$

by the plane stress relation

$$\sigma_\theta = E_1 \varepsilon_\theta \qquad \text{for } \varepsilon_\theta < \varepsilon_y \tag{2.4}$$

in the elastic regime. In the plastic regime, a linear strain-hardening curve is applied such that

$$\sigma_\theta = \sigma_y + E_2\left(\varepsilon_\theta - \varepsilon_y\right) \qquad \text{for } \varepsilon_\theta \geq \varepsilon_y \tag{2.5}$$

Table 2.8: Geometric and material properties used in the single degree of freedom model for 304L SS tubes.

r_0 (mm)	63.5
h_{t0} (mm)	1.5
ρ_t (kg/m^3)	7900
ν	0.3
E_1 (GPa)	200
E_2 (GPa)	1
$\varepsilon_{y,0}$ (%)	0.3

and the yield stress is tracked by the additional equation

$$\frac{d\sigma_y}{dt} = \frac{d\sigma_y}{d\sigma_\theta}\frac{\partial\sigma_\theta}{\partial\varepsilon_\theta}\frac{\partial\varepsilon_\theta}{\partial t} \tag{2.6}$$

where

$$\frac{d\sigma_y}{d\sigma_\theta} = \begin{cases} 0 & \sigma_\theta < \sigma_y \\ 1 & \sigma_\theta \geq \sigma_y. \end{cases} \tag{2.7}$$

Thus, from equations (2.2) and (2.4), the natural frequency for elastic oscillation of the tube cross-section is

$$f_{xs} = \frac{1}{2\pi r_0}\sqrt{\frac{E_1}{\rho_t}} = 12.6 \text{ kHz} \tag{2.8}$$

using the material properties for 304L stainless steel given in table 2.8. This corresponds closely to the measured elastic oscillation frequency of 12.7 kHz as determined by a fast Fourier transform of the elastic data plotted in figure 2.9. Although 12.7 kHz is the most prevalent frequency, other frequency peaks exist that represent higher degree of freedom vibrational modes.

Equation 2.2 may be applied to the plastic regime with an elasto-plastic model with linear strain-hardening as detailed in appendix B; a yield strain of 0.3% was chosen to account for strain-rate hardening. This differential equation was solved in Matlab using the Runge-Kutta solver `ode45` over a range of axial locations. The

internal pressure loading, $p(t)$, was computed from the pressure model described in section 1.2.2. The results are plotted in figures 2.16(a), 2.16(b), and 2.16(c) for fill pressures of 50, 200, and 300 kPa, respectively, corresponding to the experimental conditions performed in the specimen tubes. In each graph the detonation arrives at time t_2 and the reflected shock arrives at time t_3, corresponding with the notation used in figure 2.8. An inset is included in the time-resolved stress plots showing the bilinear stress-strain behavior.

Much of the same strain behavior is observed here as was seen in the previous experimental strain-time plots. The detonation arrives at t_2 and deforms the tube to a peak value that is a function of the fill pressure. Elastic oscillation then sets in, and the strain peaks decay with each oscillation period as the pressure behind the detonation decays through the Taylor-Zel'dovich expansion. The reflected shock then arrives at t_3; this raises the pressure a second time and increases the strains to their maximum observed values. After the reflected shock the pressure again decays, and this is observed by a second decrease in peak strains. There is no damping in the single degree of freedom model, and thus the oscillations in stress and strain continue unabated. The residual strain can be taken to be the average strain value after the pressure has decayed behind the reflected shock.

In each curve shown in figure 2.16, the measurement location was chosen such that the reflected shock wave arrived halfway between the third peak and the third trough of oscillation. If we vary the time of arrival of the reflected shock (which corresponds to varying the gauge distance from the reflecting end-wall), the residual strain changes. There are two reasons why this occurs. First, the reflected shock pressure is a monotonically decreasing function with respect to time, and smaller deformations are expected for later times when the pressure is diminished. Second, there is the possibility of interference between the reflected shock and the elastic oscillation induced by the incident detonation. This interference is illustrated in figure 2.17. In figure 2.17(a) the reflected shock arrives at $t_3 = 0.135$ ms, which corresponds to a trough in oscillation, whereas in figure 2.17(b) the reflected shock arrives at $t_3 = 0.161$ ms, which corresponds to a peak in oscillation. At first glance, we

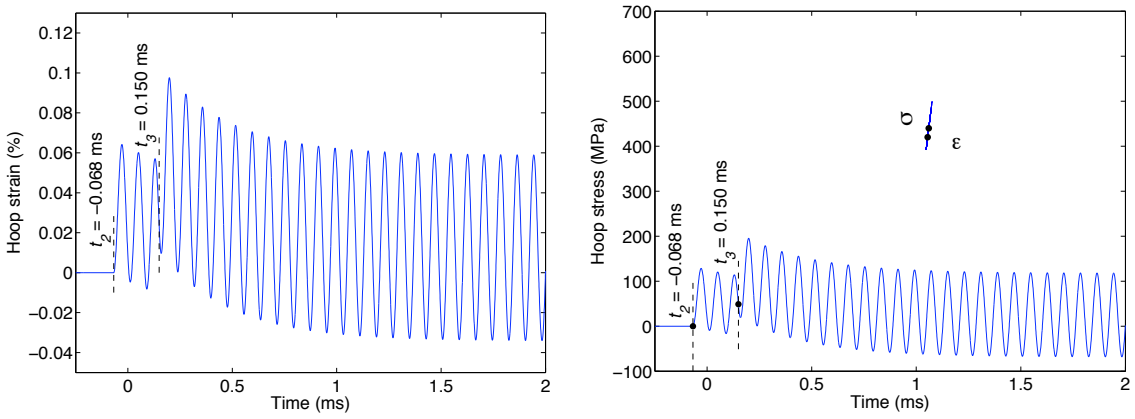

(a)

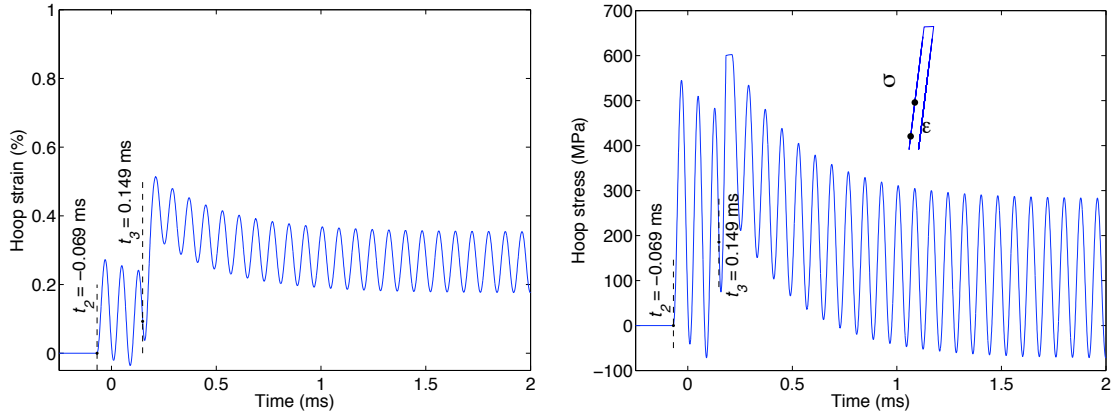

(b)

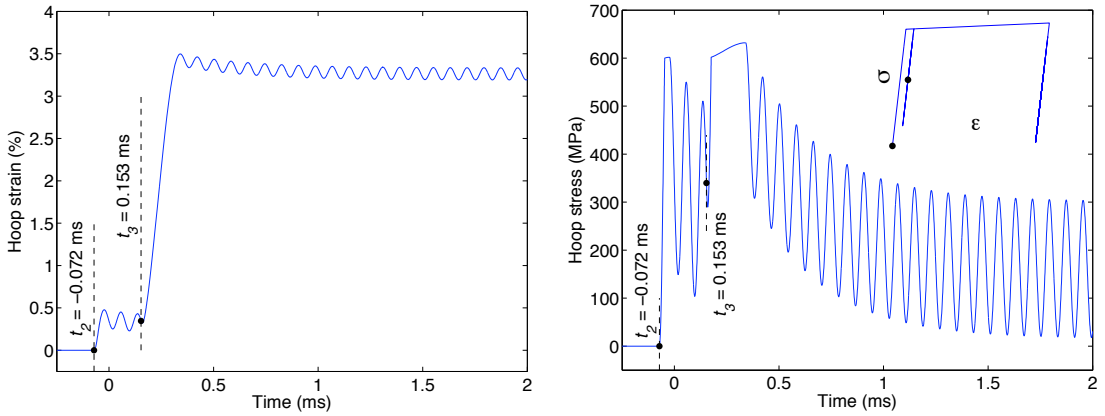

(c)

Figure 2.16: Time-resolved strain and stress results as predicted by the single degree of freedom model for detonations of initial pressure (a) 50 kPa, (b) 200 kPa, and (c) 300 kPa. Note the inset in the time-resolved stress plots showing a stress-strain plot for each case with the points corresponding to detonation and reflected shock arrival.

would expect the final strain to be larger for the case shown in figure 2.17(b) because the strain when the reflected shock arrives is larger, and the earlier time implies that the internal pressure is greater. However, we see that the opposite is true. Even though the pressure is larger in figure 2.17(b), the resulting strain is less than observed in figure 2.17(a). This is due to interference between the elastic oscillation induced by the incident detonation and the reflected shock wave. In figure 2.17(a) the pressure and stress terms of equation (2.2) are in alignment when the reflected shock arrives, resulting in large accelerations and correspondingly large residual strains. This contrasts with the case shown in figure 2.17(b), where the pressure and stress terms are in opposition.

Figure 2.18 shows the residual plastic strain predicted by the single degree of freedom model as a function of distance from the reflecting end-wall for a detonation of fill pressure 200 kPa. We immediately see that the interference described above results in a ripple pattern very similar to that observed in the experiment. Recall that these strains are found by modeling the tube wall as a simple oscillator with a linear elasto-plastic material model that does not incorporate strain-rate hardening. For these reasons, the strain predictions are meant to be estimates that highlight the physical effects dominating detonation-induced deformation. In particular, in the region near the reflecting end-wall the strain predictions are not physical. The single degree of freedom model, by definition, does not incorporate the multi-dimensional effects introduced by boundary conditions. Obtaining quantitatively accurate strain predictions requires a more sophisticated investigation, such as described in section 2.4.2.

We can confirm that this interference is the origin of the ripple pattern by predicting the ripple wavelength. The ripple wavelength is a function of the time between the detonation and reflected shock arrival, Δt. This time can be calculated by using the known Chapman-Jouguet detonation speed, U_{CJ}, and an average shock speed, $\overline{U}_R$; an average speed is necessary because the speed of the shock changes through the Taylor-Zel'dovich expansion. The time between wave arrivals at a given x_0 location

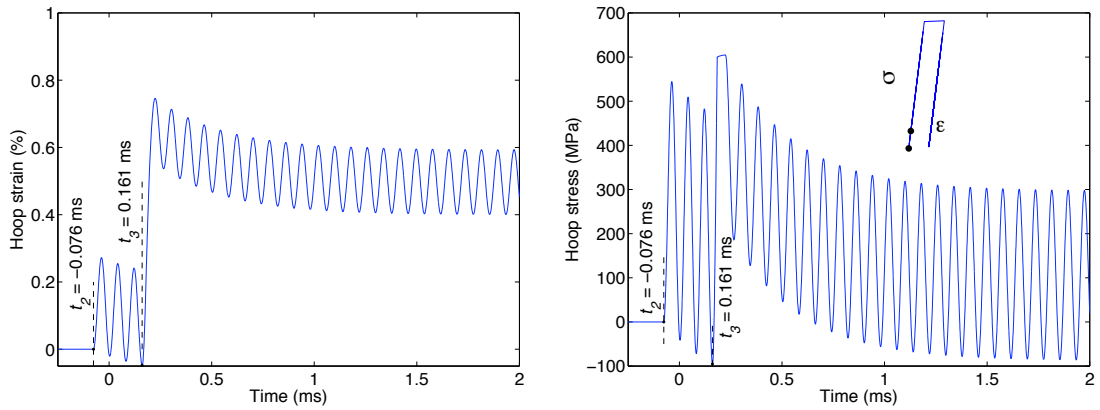

(a)

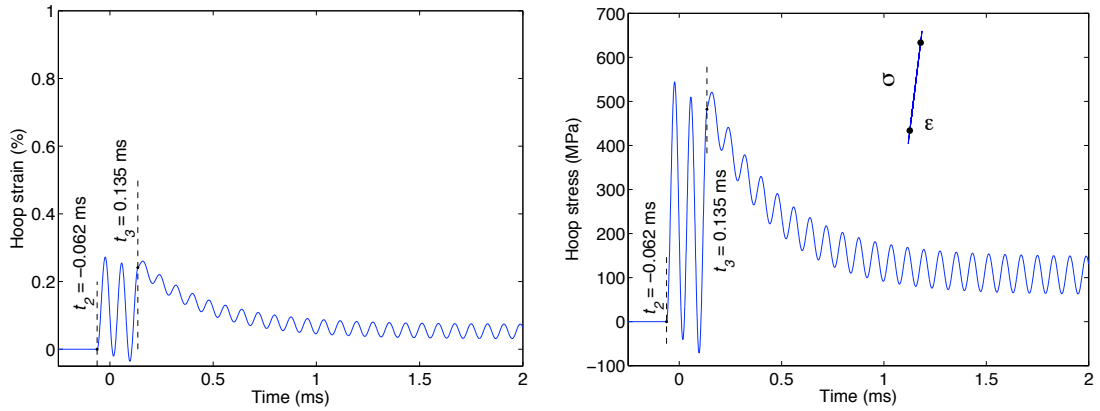

(b)

Figure 2.17: Time-resolved strain and stress results as predicted by the single degree of freedom model for detonations of initial pressure 200 kPa, when the shock arrives (a) at a trough in the elastic oscillation, resulting in constructive interference and (b) at a peak, resulting in destructive interference.

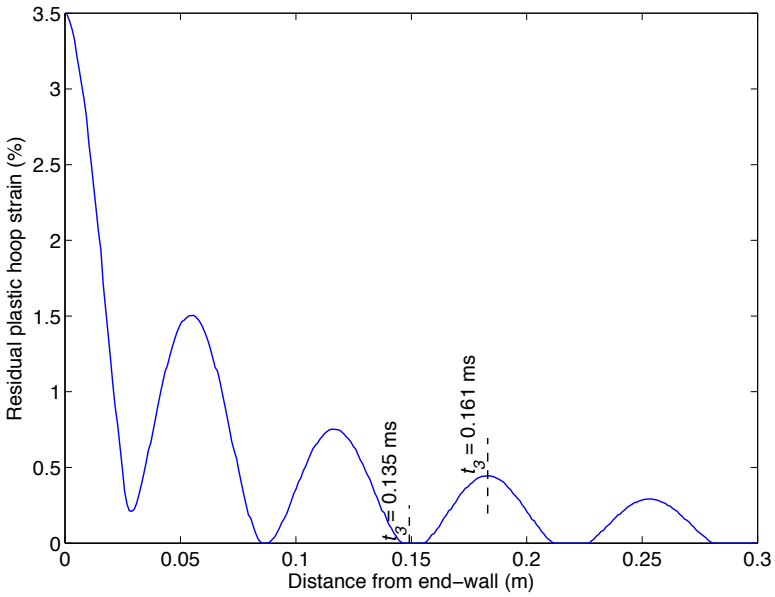

Figure 2.18: Spatially-resolved residual plastic strains as predicted by the single degree of freedom model for an internal detonation of ethylene-oxygen and fill pressure of 200 kPa.

is then given by

$$\Delta t = \frac{x_0}{U_{CJ}} + \frac{x_0}{\overline{U}_R} = \frac{\overline{U}_R + U_{CJ}}{\overline{U}_R U_{CJ}} \cdot x_0 \tag{2.9}$$

and the time difference required for the waves to arrive exactly one period out of phase is $1/f_{xs}$ where f_{xs} is the frequency of the cross-sectional oscillation given by equation (2.8). Thus for two different locations to be one period out of phase implies the difference in time between wave arrivals is

$$\Delta t_2 - \Delta t_1 = \frac{1}{f_{xs}}. \tag{2.10}$$

We can then determine the ripple wavelength to be

$$\lambda_r = x_2 - x_1 = \frac{1}{f_{xs}} \left(\frac{\overline{U}_R U_{CJ}}{\overline{U}_R + U_{CJ}} \right). \tag{2.11}$$

Evaluating this expression with oscillation frequency and speeds appropriate for the

200 kPa fill pressure condition[4] predicts a ripple wavelength of 69.5 mm–essentially identical to the experimentally measured peak-to-peak spacing of 68 mm ± 2 mm.

We are now equipped to determine why the ripple pattern is most visible after detonations of fill pressure 200 kPa. Examining equation (2.2), we note that for the 200 kPa fill pressure case, the magnitude of the hoop stress term evaluated at a peak in oscillation and the pressure behind the reflected shock are of the same order:

$$\left.\frac{h_t}{r}\sigma_\theta\left(t_3\right)\right|_{200\ \text{kPa}} = 11.6\ \text{MPa} \tag{2.12}$$

$$\Delta p_R|_{200\ \text{kPa}} = 12.2\ \text{MPa} \tag{2.13}$$

where p_R is computed per equation (1.48). This implies that the acceleration, which is proportional to the difference of the terms given in equations (2.12) and (2.13), will be approximately zero for this special case. Thus, even though the pressure is increased by the reflected shock, the strain will not be significantly increased because the pressure is balanced by the internal stress in the tube wall. In the suppositional case of the stress and pressure terms exactly balancing, the tube wall will be momentarily stilled; this is close to the case shown in figure 2.17(b). Conversely, if the reflected shock arrives at a trough in oscillation, the internal hoop stress will be nearly zero and the pressure term will be unopposed, producing the large strains seen in figure 2.17(a). However, if we increase the fill pressure to 300 kPa, the stress and pressure terms at an oscillation peak are

$$\left.\frac{h_t}{r}\sigma_\theta\left(t_3\right)\right|_{300\ \text{kPa}} = 12.1\ \text{MPa} \tag{2.14}$$

$$\Delta p_R|_{300\ \text{kPa}} = 18.3\ \text{MPa} \tag{2.15}$$

and we observe that the pressure term dominates the acceleration. Hence the impact of the interference between the elastic oscillation and the reflected shock wave is minimal when the fill pressure is increased, and the ripple pattern is not observed.

[4] A stoichiometric ethylene-oxygen detonation of fill pressure 200 kPa in the stainless steel specimen tubes has $f_{xs} = 12.6$ kHz, $U_{CJ} = 2400$ m/s, and $\overline{U}_R = 1380$ m/s.

2.4.2 Finite Element Analysis

Obtaining quantitatively accurate strain predictions requires expanding the geometry to allow for two-dimensional effects and incorporating a material model that includes strain-rate hardening. This was accomplished using the finite element solver LS-DYNA V970 (Livermore Software, 2005). Figure 2.19 shows the two-dimensional mesh used to represent the specimen tube. The tube was modeled using two-dimensional axisymmetric Galerkin volume-weighted shell elements with selective-reduced integration over a 2 x 2 Gaussian quadrature. Six nodes were used through the thickness and 4000 through the tube length. The computational model did not take into account the compound nature of the driven-thin detonation tube (which was composed of a thick-walled driver tube and thin-walled driven tube) and instead approximated the entire span as a single tube 2 m in length. This was done because our primary goal was to analyze the deformation of the specimen tube. The detonation propagates from left to right in figure 2.19. The boundary conditions used were as follows: the left-hand end was confined in the radial direction and the right-hand end was clamped to symbolize the collet used in the experiment.

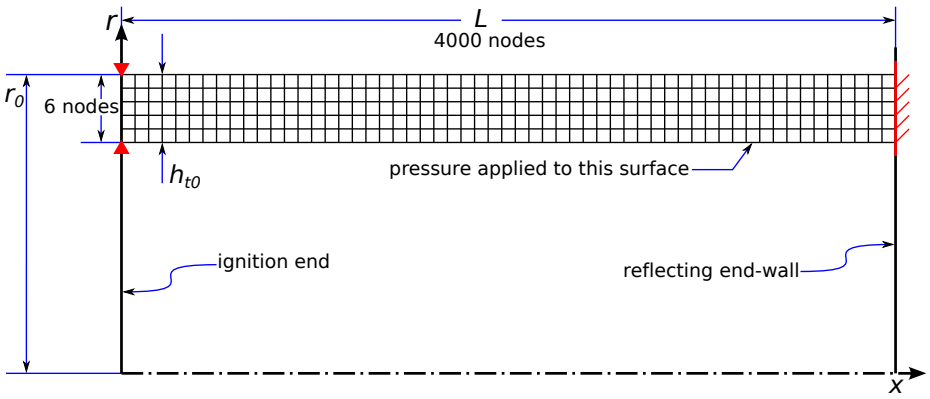

Figure 2.19: Mesh used for finite element computations in LS-DYNA.

The Johnson-Cook material model introduced in section 1.3.2 was used with the pressure model which was decoupled from the material deformation as discussed in section 1.2.2 to model the plastic response of stainless steel tubes to internal detonation loadings with fill pressure of either 200 or 300 kPa. Figure 2.20 shows the

computed LS-DYNA results corresponding to a fill pressure of 200 kPa plotted with the outer diameter measurements taken after the first plastic deformation in tube 9. Examining figure 2.20, we see that the computed deformed tube wall shape and average residual plastic strains are in good agreement with experimental values. The calculated ripple pattern, however, is out of phase, and this leads to over-predicting the peak strain by 11%. The two marked locations where the residual plastic strain is accurately predicted ($x_{end} = 0.121$ m) and poorly predicted ($x_{end} = 0.146$ m) are discussed below.

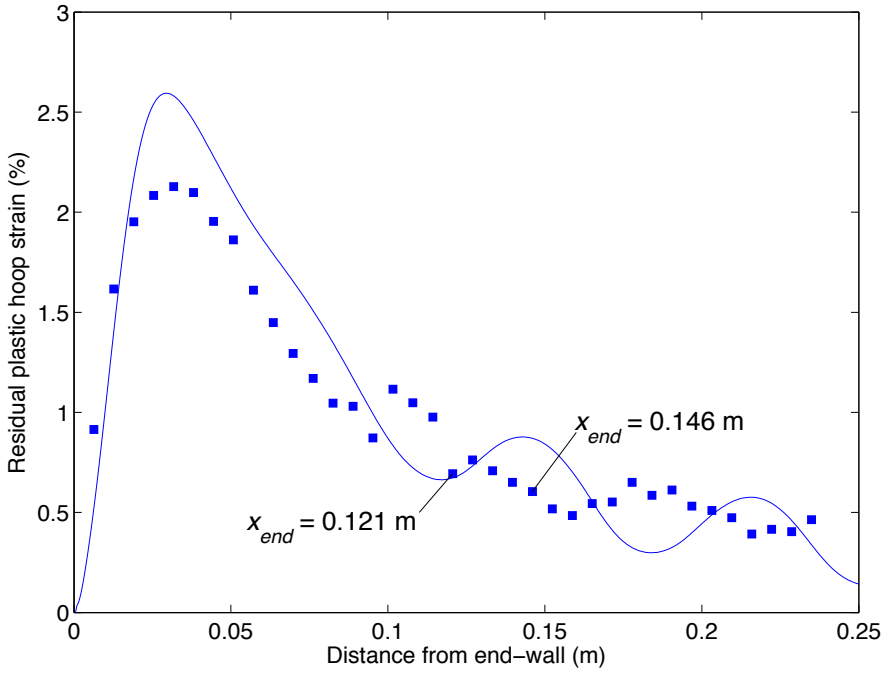

Figure 2.20: Comparison of measured and computed residual plastic deformation after the first detonation of 200 kPa ethylene-oxygen in specimen tube 9.

Figure 2.21 compares the computed and measured time-resolved strain traces resulting from a detonation with fill pressure 200 kPa for gauge locations near the reflecting end-wall. Time-resolved strains from the two marked locations in figure 2.20 are shown in figure 2.22. In examining the time-resolved strains, we observe that the peak strains from the incident detonation are well predicted for all locations. The computation only begins to show substantial discrepancies in the predicted peak strain for times following the arrival of the reflected shock wave. The source of this

discrepancy is two-fold. First, we observe that the elastic peak-to-peak oscillation has a smaller amplitude in the experiment than the computation for some gauge locations. In previous simulations of the elastic response of tube walls due to detonation waves, such as those by Karnesky (2010), it was shown that the elastic oscillation can be accurately computed if factors such as circumferential wall thickness variation are included. It is possible that such a complicating factor is influencing the elastic strain predictions. Second, it was shown in section 2.4.1 that small differences in wave arrival time relative to the phase of elastic oscillation can produce substantial differences in the resulting plastic strain for the 200 kPa fill pressure case. This is depicted in figure 2.22, where computed and measured strain-time traces are plotted for the two locations marked in figure 2.20. In figure 2.22(a), we observe that the computed and experimental traces are in good agreement, both in arrival time of the reflected wave and in the resulting residual plastic strain. In figure 2.22(b), however, the modeled material response caused by the reflected shock wave occurs nearly half of a natural period before the measured response. This results in a completely different excitation of the cross-sectional vibration and a considerably larger computed final residual plastic strain. This illustrates the sensitive nature of the strain calculations to minor differences in reflected shock arrival time. Thus, we conclude that differences in the computed residual plastic strain originate from small differences in the elastic oscillation, particularly due to misalignment in the phase of the elastic oscillation when the reflected shock arrives.

Figure 2.23 shows the LS-DYNA computation of residual plastic strain from a detonation with fill pressure 300 kPa, compared to the experimental measurements taken after the first plastic experiment in tube 11. Here we see that the computations are in excellent agreement with the experimental measurements. The difference in peak strain is only 0.44%, and the maximum difference is 4% and occurs at the location furthest from the reflecting end-wall, where strains are at a minimum. This agreement is achieved by properly modeling both the detonation pressure loading and the material properties of the tube. The reduction in error in the 300 kPa case over the 200 kPa case is due to the reduced effect that the elastic oscillation has on the

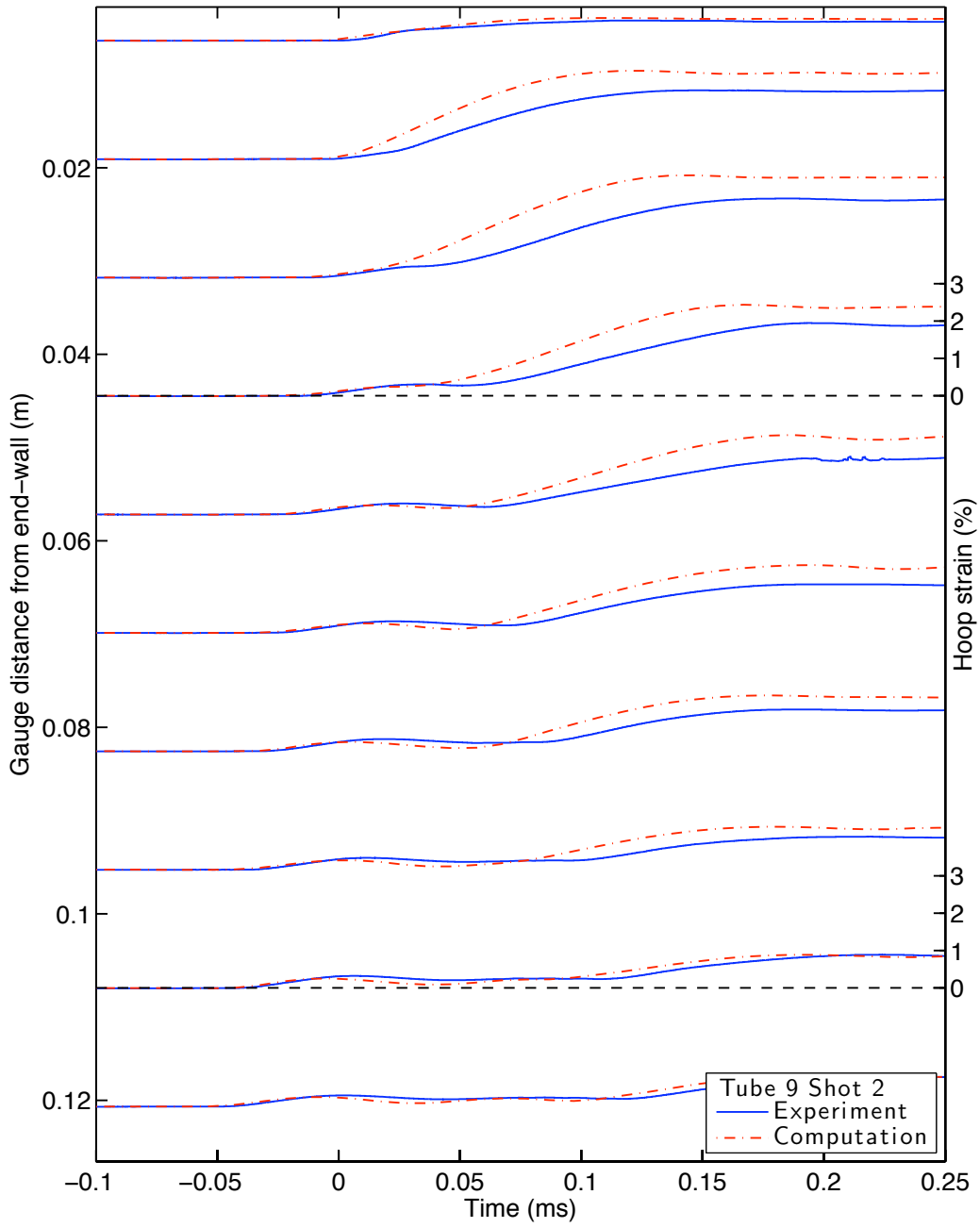

Figure 2.21: Comparison of measured and computed time-resolved strain during the first detonation of 200 kPa ethylene-oxygen in specimen tube 9 shows the strains resulting from the incident detonation are well predicted for all gauge locations.

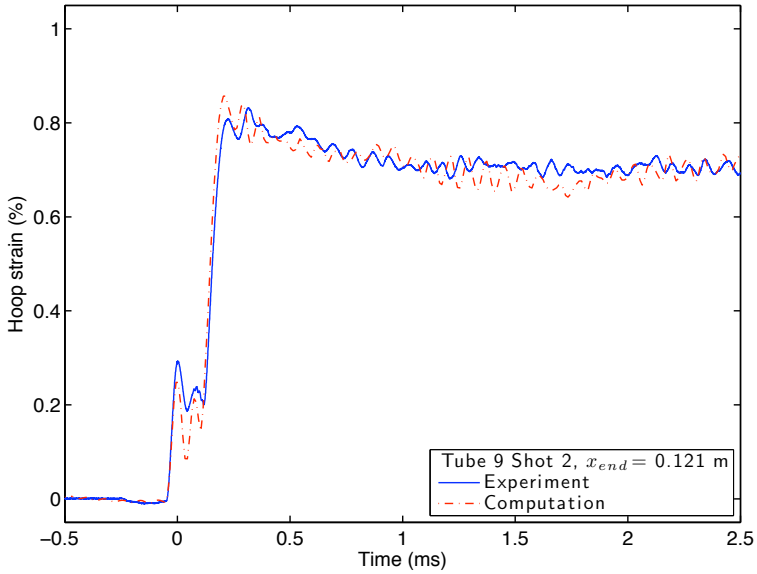

(a)

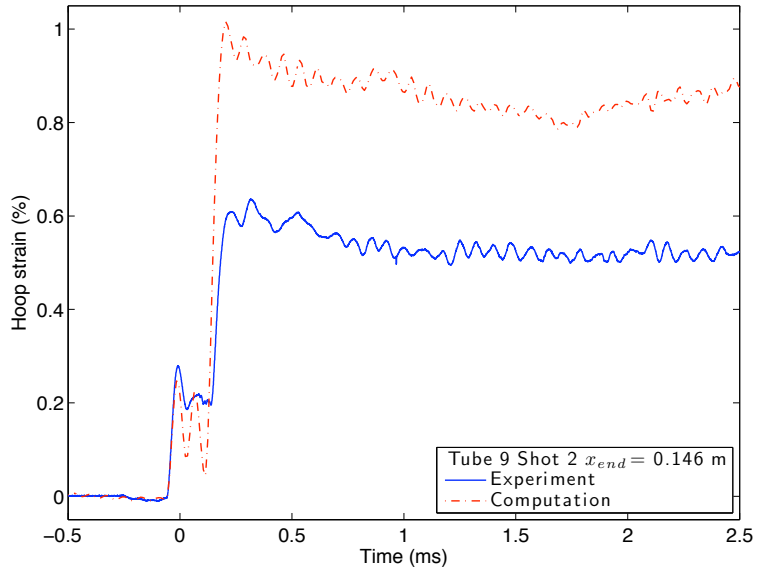

(b)

Figure 2.22: Comparison of measured and computed time-resolved strain during the first detonation of 200 kPa in specimen tube 9. (a) Good agreement in the residual plastic strain is obtained when the reflected shock arrives at the same phase of oscillation in both the experiment and computation. (b) Sizable differences occur when the elastic oscillation is out of phase.

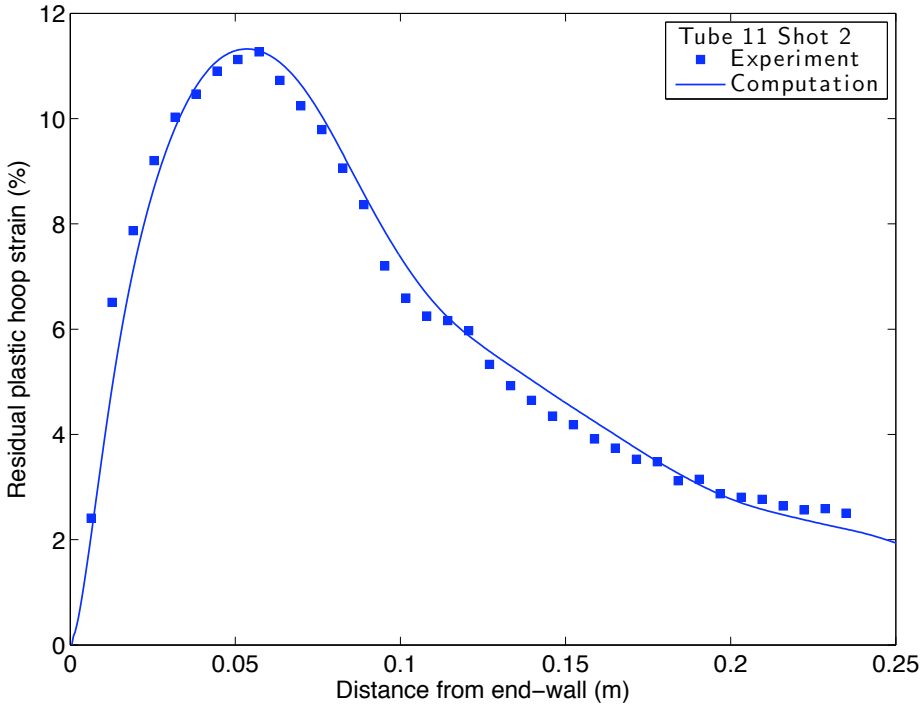

Figure 2.23: Comparison of measured and computed residual plastic deformation after the first detonation of 300 kPa ethylene-oxygen in specimen tube 11.

residual plastic strain, which makes the deformation less sensitive to small errors in wave arrival.

2.5 Conclusion

Experimentation was conducted to characterize the detonation-driven deformation of thin-walled 304L stainless steel tubes. Strain measurements were taken during and after the experiment to measure the material response to detonations of stoichiometric ethylene-oxygen at fill pressures of 50, 200, and 300 kPa. However, the deformations resulting from the 300 kPa case were too large for a useful number of strain gauges to survive, and thus all comparisons for this case used the post-experiment strain measurements. The same ripple pattern observed by Karnesky (2010) in mild steel specimen tubes was extant in the stainless steel tubes, and ripple wavelength measurements agree with the theory that the ripple pattern is caused by interference between the elastic oscillation induced by the incident detonation with the arrival of

the reflected shock wave.

The tube wall was modeled as a single degree of freedom oscillator to understand the relevant physical effects present in detonation-driven tube deformation, including the origin of the ripple pattern. Using this model, it was shown that this pattern dominates residual plastic deformation for intermediate fill pressures around 200 kPa for this particular geometry. If the fill pressure is increased, the elastic oscillation that is responsible for the ripple pattern is overshadowed by the large internal pressures created by detonation reflection.

Quantitatively accurate strain measurements were obtained using a two-dimensional LS-DYNA finite element simulation with standard Johnson-Cook material properties and the same pressure model developed in earlier work. The best agreement was obtained for fill pressures of 300 kPa when the elastic oscillation effects were not important. Examining strain-time plots revealed that the peak deformation caused by the incident detonation is well predicted at all measurement locations, and the errors observed in the 200 kPa fill pressure case were due to miscalculating the elastic oscillation and the arrival time of the reflected shock relative to the phase of the elastic oscillation. This work built on the research of Karnesky (2010), who was unable to find a standard material model capable of appropriately describing the detonation-driven deformation of C1010 mild steel tubes. Success was possible using 304L stainless steel, thanks to this material being better characterized by models such as Johnson-Cook at the strains and strain-rates typical of detonation loading.

Chapter 3

GALCIT Detonation Tube Experimental Setup

3.1 Introduction

The reflected detonation experiments performed in the driven-thin detonation tube described in section 1.2.2 revealed a misconception in our understanding of how reflected detonations behave. As shown in section 2.4.2, the error in shock wave arrival time was not serious enough to prevent significant agreement between experiment and computation. However, it shows that we were misunderstanding something about the fundamental nature of detonation reflection. To address this misunderstanding, further experimentation was performed with reflected detonation waves in the GALCIT detonation tube, or GDT. The setup of the GDT is described in this chapter, and the results are presented in chapters 4 and 5. The primary improvement of the GDT over the driven-thin tube is that the GDT has windows which allow for optical access to the detonation wave.

3.2 GDT Construction

The GDT is a 7.6 m long, 280 mm inner-diameter detonation tube equipped with a 152.4 mm wide test section and two quartz windows to provide optical access (see Akbar, 1997 and Kaneshige, 1999 for a complete description of this facility). The possibility of shock wave–boundary layer interaction motivated the design and

construction of a splitter plate that raised the effective floor of the test section to the center of the windows. This allowed any interaction of the shock wave with the boundary layer to be observed. The geometry of the GDT, test section, and splitter plate is illustrated in figure 3.1. The test section has a rectangular cross section; this differs from the geometry used in the driven-thin detonation experiments in which the cross section was circular. However, considering the radius of curvature of the driven-thin specimen tubes of 63.5 mm was much larger than the expected boundary layer thickness and detonation cell size, we expect the general flow features to be similar in the two experiments.

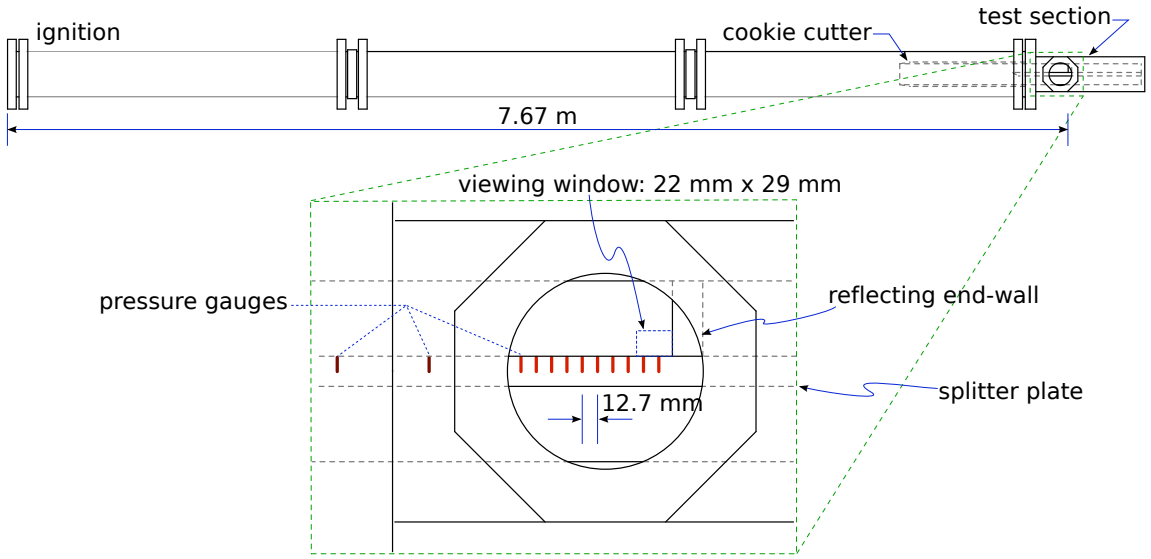

Figure 3.1: An overview of the GDT experimental facility, with inset showing test section details.

Details of the splitter plate are as follows (and are included in figure 3.2). It is a 6061-T6 aluminum plate 150.0 mm wide, 1070 mm long, and 25.4 mm thick with a leading edge sharpened to a 15° point to minimize flow disturbance. It was pinned to the GDT test section by three 12.7 mm steel alloy dowels through existing port locations. A false wall with a thickness of 50.8 mm was bolted to the plate using four 1/2”-20 bolts. This wall served as the location of normal detonation reflection. There were gaps of width less than 0.5 mm between the splitter plate and the walls of the test section. Similarly, there was a gap between the top of the splitter plate end-wall and

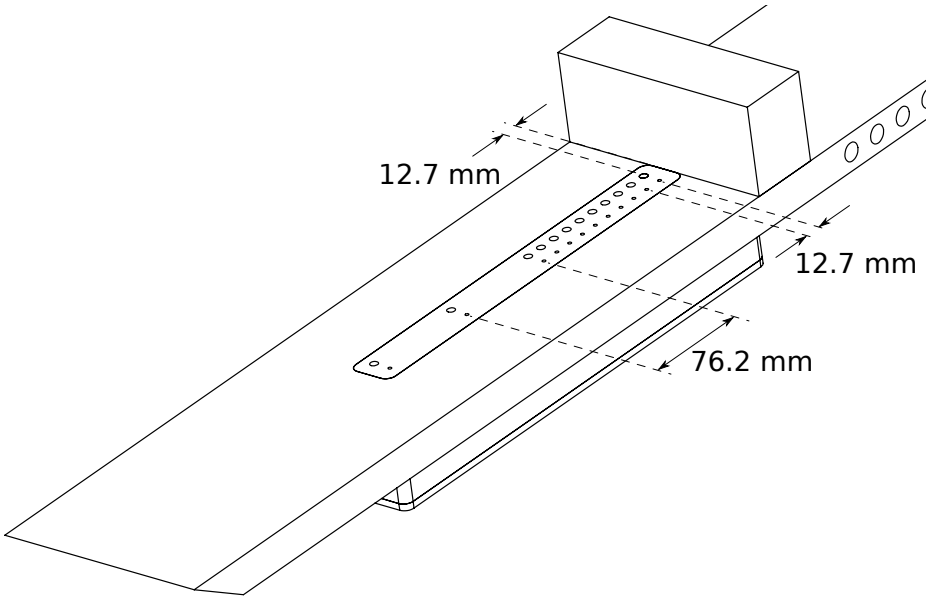

Figure 3.2: Three-dimensional view of the splitter plate used in the GDT.

the ceiling of the test section of width less than 1 mm. Gas was able to flow through these gaps, but given that the gap widths were much less than the other relevant physical dimensions (such as the width of the plate) and because schlieren images do not show a flow disturbance, these gaps were deemed unable to substantially affect the overall flow field. A full set of drawings for the splitter plate are included in appendix C.

In addition to raising the test section floor to the center of the windows, the splitter plate served to house a suite of pressure and heat-flux gauges with 12.7 mm spacing in a removable measurement gauge box to achieve highly resolved measurements of the flow field behind the incident detonation and reflected shock waves. In addition to the three PCB 113A24 pressure sensors mounted in the GDT, twelve PCB 113B26 piezoelectric pressure gauges were located in a line 12.7 mm from the center of the plate with locations relative to the reflecting end-wall, as explicated in table 3.1. Pressure sensor models 113A24 were amplified by a PCB 482A22 ICP sensor signal conditioner, and models 113B26 were amplified by a PCB 483A signal conditioner. All pressure gauges have a 6.4 mm diameter and maximum error of 1.3% as determined from calibration data. These are high-frequency response gauges with a reported

resonant frequency above 500 kHz (PCB, 2009); this fast response makes them ideal for measuring the pressure resulting from shock and detonation waves.

Twelve surface junction thermocouples identical to those employed by Sanderson and Sturtevant (2002) were located at identical axial locations as the pressure gauges and 12.7 mm on the opposite side of center from the pressure gauges. These thermocouples measured heat-flux to the walls inside the test section. The thermocouples were connected to a TrikTek Model 205B instrumentation amplifier with a response time of 7.5 μs to a unit step input. The gauge response time is 0.5 μs and thus the amplifiers dominate the overall response time. The gauges themselves were epoxied into the measurement gauge box and the gauges were sanded to be flush with the surface of the box. The heat-flux gauge resistance was then measured, and if the sanding process caused the gauge resistance to exceed 3 Ω the gauge was removed and replaced. Calibration efforts along the lines of Mohammed et al. (2010, 2011) would be necessary to better deduce the gauge response. The spectral method employed by Sanderson and Sturtevant (2002) for reducing the heat-flux data is also employed here. Table 3.1 contains the locations of the pressure and heat-flux gauges, but measurement locations are also given on relevant plots (such as shown in figure 4.1). All signals were recorded using four National Instruments PXI-6133 S Series Multifunction DAQ cards at a rate of 2.5 MHz. The PXI cards were connected to the signal amplifiers by NI TB-2709 SMB terminal blocks and were housed in an NI PXI-1062Q chassis controlled by an NI PXIe-8375 MXI-Express card.

3.3 Flow Visualization

A Z-type schlieren system (Settles, 2001) was used to visualize the detonation and reflected shock behavior. Multiple schlieren arrangements were used with differing components and dimensions; details of each are expounded below. In each configuration we desired to take high resolution images of the incident detonation and reflected shock wave, with an emphasis on exploring the possibility of reflected shock wave–boundary layer interaction. There are two primary difficulties inherent to imaging

Table 3.1: Pressure and heat-flux gauge placement for all experiments performed in the GDT.

Gauge Number	Type	Model	Amplifier	Distance From Reflection (mm)
1	Pressure	113A24	PCB 482A22	4889
2	Pressure	113A24	PCB 482A22	3060
3	Pressure	113A24	PCB 482A22	1206
4	Pressure	113B26	PCB 483A	279
5	Pressure	113B26	PCB 483A	203
6	Pressure	113B26	PCB 483A	127
7	Pressure	113B26	PCB 483A	114
8	Pressure	113B26	PCB 483A	102
9	Pressure	113B26	PCB 483A	89
10	Pressure	113B26	PCB 483A	76
11	Pressure	113B26	PCB 483A	64
12	Pressure	113B26	PCB 483A	51
13	Pressure	113B26	PCB 483A	38
14	Pressure	113B26	PCB 483A	25
15	Pressure	113B26	PCB 483A	13
16	Heat-flux	N/A	TrikTek 205B	279
17	Heat-flux	N/A	TrikTek 205B	203
18	Heat-flux	N/A	TrikTek 205B	127
19	Heat-flux	N/A	TrikTek 205B	114
20	Heat-flux	N/A	TrikTek 205B	102
21	Heat-flux	N/A	TrikTek 205B	89
22	Heat-flux	N/A	TrikTek 205B	76
23	Heat-flux	N/A	TrikTek 205B	64
24	Heat-flux	N/A	TrikTek 205B	51
25	Heat-flux	N/A	TrikTek 205B	38
26	Heat-flux	N/A	TrikTek 205B	25
27	Heat-flux	N/A	TrikTek 205B	13

gaseous detonation waves that any schlieren system employed must overcome:

1. The fastest detonation visualized was a 93% hydrogen-7% oxygen mixture with a Chapman-Jouguet speed of 3756 m/s. Supposing a 30 mm wide physical field of view mapped to a 1260 pixel-wide sensor, an exposure time of 6.3 ns is needed to limit wave motion to one pixel. Fortunately other relevant speeds (such as the maximum fluid velocity or the reflected shock speed) are slower and the field of view is adjustable, but we still need image exposure times below 100 ns to adequately freeze the flow.

2. Gaseous detonations produce large amounts of light that can overwhelm the light from a schlieren system. The light thus produced can be approximated as broadband white light that emanates in all directions from the test section. Preventing this light from entering the camera sensor requires filtering the light in front of the camera to limit the light to a narrow wavelength, baffling the light so that only collimated light reaches the camera, using a short camera exposure time to reduce the amount of unwanted light, or a combination of all three.

To combat these difficulties, multiple configurations using different light sources and cameras were investigated to determine the optimal method of visualizing the flow field. Two general schlieren configurations were employed that were distinguished by their depth of focus. The first system, termed the unfocused system, had a depth of focus much larger than the test section width while the second, called the focused system, had a depth of focus smaller than the test section width. The details of each are outlined below. In both systems, alignment of the collimated light through the test section was achieved by placing two identical objects of known dimensions (such as a calibration block or ruler) flush with the reflecting end-wall, one on each side of the test section. If only one object was visible in the recorded image, then the light was determined to be passing straight through the test section.

3.3.1 Unfocused Schlieren

The schematic shown in figure 3.3 depicts the setup used to record schlieren images with a large depth of focus. Different optical lengths were used to produce different effects, so figure 3.3 is a representative case. Other cases used different numbers of turning mirrors as needed to allow the schlieren system to fit in the physical dimensions of the laboratory. For all cases, the light source, camera, and mirrors were placed to minimize the turning angles for the collimating and focusing mirrors. Another design consideration was that the light path was maneuvered such that the light directly entered the camera. This was ensured by placing the final mirror (the focusing mirror in figure 3.3) at the same height and transverse position as the camera. These considerations served to limit the introduced optical distortion.

The depth of focus, Δz, of this system is

$$\Delta z = \frac{\phi}{\alpha} = \frac{\phi f_1}{b} \sim 300 \text{ mm} \tag{3.1}$$

where ϕ is the acceptable diameter of the circle-of-confusion (which was taken to be on the order of 1 mm), f_1 is the focal length of the collimating mirror (which was 1500 mm for all cases as shown in table 3.2), b is the light source size (which was approximately 5 mm for each light source used in the unfocused schlieren systems), and $\alpha = b/f_1$ is the aperture angle of the light source (Settles, 2001). Since this value for Δz is larger than the 76 mm half-width test section, we can approximate the schlieren system as having an infinite depth of field. This implies that all disturbances in the density field across the test section will be integrated equally and will uniformly influence the resulting schlieren image. The relative strengths and weaknesses of this system are outlined in section 3.3.3.

Figure 3.3 depicts the relevant optical lengths used for each configuration. The focal length, $f_1 = 1500$ mm, was chosen to increase the depth of focus per equation (3.1). Focal length f_2 and distance d_{kc} were selected to yield a suitable image

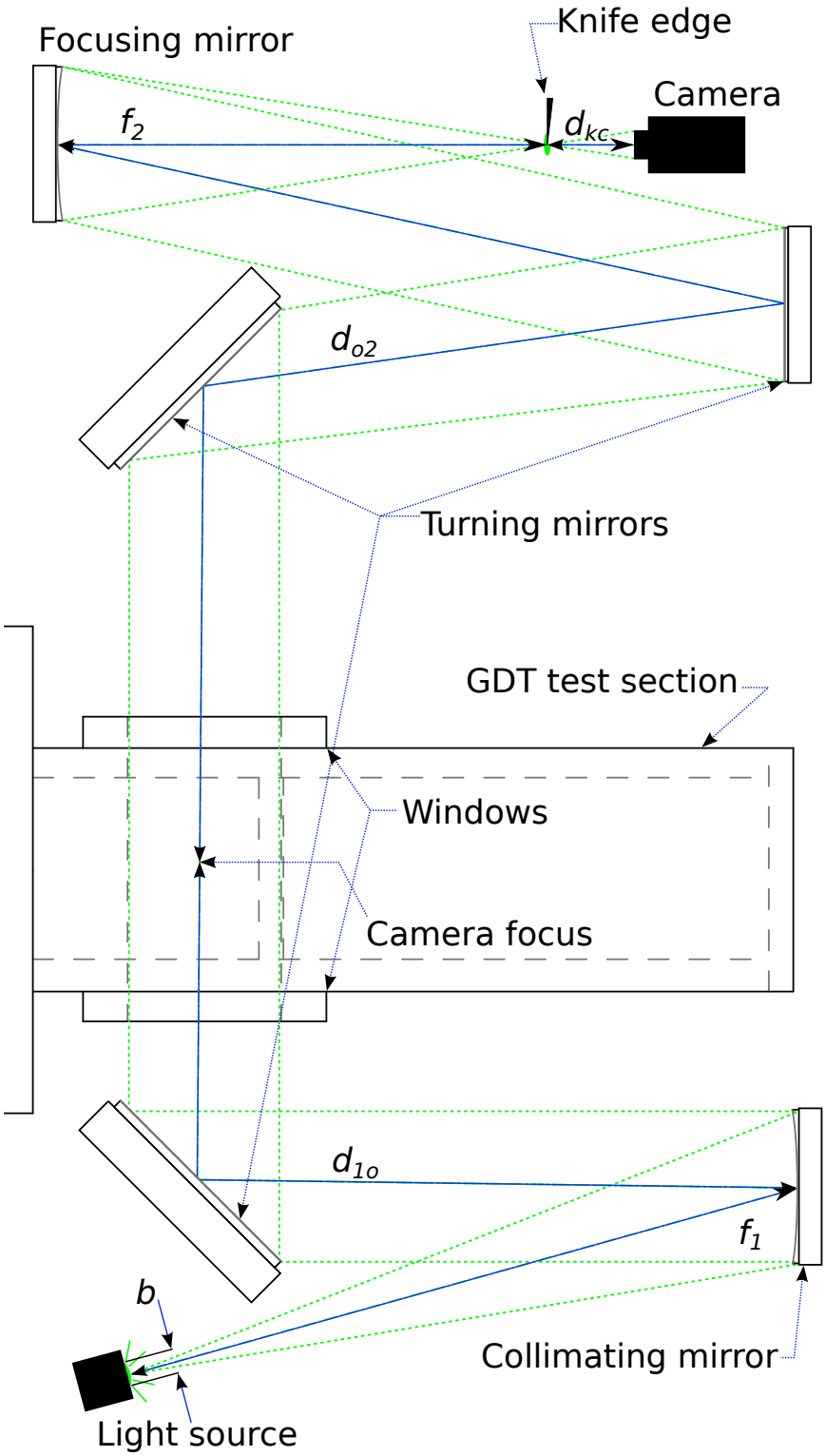

Figure 3.3: Representative schematic of schlieren visualization system as viewed from above. Different systems used more or fewer turning mirrors. Mirror placements are not to scale.

magnification per

$$M = \frac{d_{kc}}{f_2} \tag{3.2}$$

where d_{kc} is the distance between the schlieren cut-off and f_2 is the focal length of the focusing mirror as illustrated in figure 3.3. Proper focus also requires

$$\frac{1}{f_2} = \frac{1}{d_{o2}} + \frac{1}{f_2 + d_{kc}} \tag{3.3}$$

where d_{o2} is the distance between the schlieren object and the focusing mirror. This implies

$$d_{o2} = (f_2 + d_{kc})\,\frac{f_2}{d_{kc}} = f_2\frac{1+M}{M} \tag{3.4}$$

and thus all optical lengths are determined by the focal lengths f_1 and f_2 and the magnification M.

In general, larger values of f_2 were preferred since schlieren sensitivity, S, is proportional to f_2 as given by

$$S = \frac{f_2}{A} \tag{3.5}$$

where A is the unobstructed height of the source image. As shown in table 3.2, different values for f_2 and M were selected depending on whether a large field of view was desired (as effected with a small magnification), or a small field of view was desired to reveal finer structures in the flow field.

Four different cameras and light sources were used in the unfocused scheme as we sought to find the best visualization system; these are specified in table 3.2. Note that each system uses different path lengths and thus achieves different sensitivities and magnifications. Therefore, a length scale is included on all schlieren images to ensure each image clearly shows relevant dimensions. Details for each system with apposite images are included in appendix D. Here we discuss system #4, which yielded the

best images. The light source was a Photogenics PL1000DRC flash lamp with an exposure time of 1 ms. The light was collected and directed into a fiber-optic cable using a 7 mm diameter lens. The opposite end of the fiber had a 5 mm lens that directed the light towards the focusing mirror. The camera used was a Specialised Imaging SIMD16 Ultra Fast Framing Camera. The SIMD16 recorded 16 1280 x 960 pixel 12 bit images for each experiment using intensified CCD sensors set to intensify the image with a gain of 7. The SIMD16 allowed for essentially arbitrary exposure time and frame rate. The exposure time was set to 20 ns for all experiments to freeze the flow, and a frame rate was chosen based on the predicted wave speeds. The procedure used to trigger the light source and camera is included in section 3.4. The camera has a monitor signal that was recorded using the same data acquisition system that recorded the pressure and heat-flux signals, so that it was known precisely when the camera was imaging. After the experiment, the recorded schlieren images were gray-scale balanced to account for differences between the intensified CCD sensors. The USAF 1951 target shown in figure 3.4 was used to quantify the resolving power of this system to be 223 μm horizontally and 125 μm vertically as measured with the target at the center of the test section. Multiple examples of detonation images captured with this system are included in chapter 4.

Table 3.2: Details of unfocused schlieren configurations.

#	Light source	Camera	f_1 (mm)	f_2 (mm)	M	t_{exp} (ns)
1	Sparker	Nikon D200	1500	1600	0.5	300
2	SLD1332V	Phantom v7.10	1500	1600	2	50
3	SMART Cavilux	Phantom v7.10	1500	1000	0.5	10
4	PL1000DRC	SI SIMD16	1500	1000	1	20

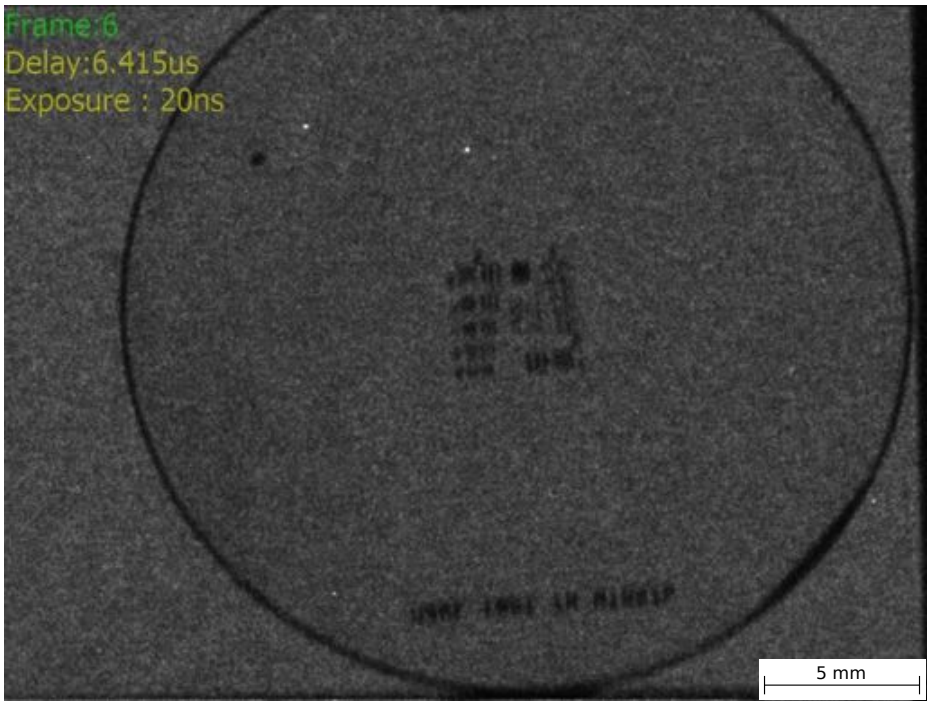

Figure 3.4: Image of the USAF 1951 target used to determine the resolving power of the unfocused schlieren system.

3.3.2 Focused Schlieren

By increasing the height of the light source, b, and decreasing the collimating focal length, f_1, the depth of focus is decreased per the equation

$$\Delta z = \frac{\phi f_1}{b}. \tag{3.6}$$

Decreasing the depth of focus is generally something to be avoided for the reasons discussed next in section 3.3.3. However, as shown later in section 5.2.2, it proved necessary to obtain a focusing effect in the wave visualization. The same basic design shown in figure 3.3 still applies, but now the light is not collimated. Instead, the light diverges from the collimating mirror at the aperture angle

$$\alpha = \frac{b}{f_1}. \tag{3.7}$$

This divergence implies that considerable care must be taken in selecting optical components and path lengths. Details of the focused schlieren light paths and selection of optical components are included in appendix D.

Two configurations were employed, with specifications included in table 3.3. Both systems are detailed in appendix D, but here we will only discuss system #6, which produced the best images. The light source from this system was an EverGreen70 Q-switched pulsed PIV laser that emitted two 10 ns duration laser pulses with 532 nm wavelength, 70 mJ pulse energy, and 3 mm beam diameter. To create an extended source, the laser light was expanded by a cylindrical lens to create a laser sheet that impinged on either a white screen or an engineered optical diffuser with a diameter of 25.4 mm and a diffusion angle of 20°. In both cases, the light was scattered and collected by the collimating mirror in the same fashion as the unfocused system shown in figure 3.3. This system used a PCO.2000 14 bit PIV camera with a resolution of 2048 x 2048 pixels. The triggering procedure is given in section 3.4. A photodetector was used to monitor the laser pulses so that the precise image time was always known. Because a PIV laser and camera were used, two images were recorded for each experiment. The USAF 1951 target was used to determine that this system had a horizontal resolution of 63 μm and a vertical resolution of 44 μm in the center of the test section and less than 250 μm at the windows. An example of the focusing effect achieved with an extended light source is shown in figure 3.6. Multiple examples of these focused images are included in chapter 5.

Table 3.3: Details of focused schlieren configurations.

#	Light source	Camera	b (mm)	f_1 (mm)	f_2 (mm)	M	t_{exp} (ns)
5	HardSoft IL-106G	Nikon D200	50	500	750	1	250
6	EverGreen70	PCO.2000	25	500	1000	1	10

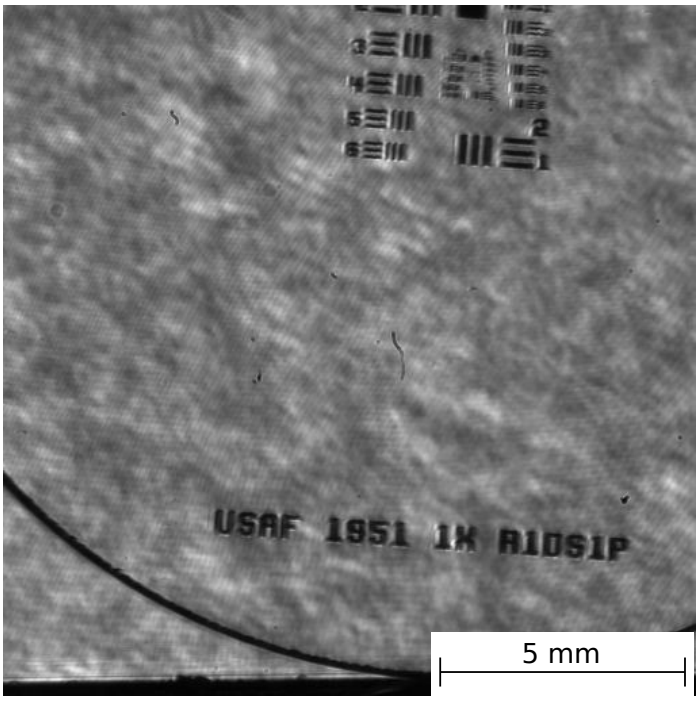

Figure 3.5: Image of the USAF 1951 target used to determine the resolving power of the focused schlieren system.

3.3.3 Visualization Discussion

The flow fields produced in detonation experiments are three-dimensional. This complicates visualization because it can be difficult to understand a picture in which three-dimensional structures have been reduced to a two-dimensional image. Austin (2003), whose work is shown in figure 1.2, and others have avoided this by using a narrow detonation facility to suppress the three-dimensional detonation structure. This was not possible in our case because we were interested in examining the boundary layer profile on the splitter plate behind the detonation, and this would be affected by the side walls in a narrow facility. In an unfocused schlieren system, the boundary layer on the splitter plate can be obstructed by the boundary layers on the windows through which we examine the flow. Thus, ideally, the schlieren system used would be a focused system to image a two-dimensional slice of the three-dimensional flow. In reality, however, there are experimental difficulties in using the focused schlieren system. The primary three are:

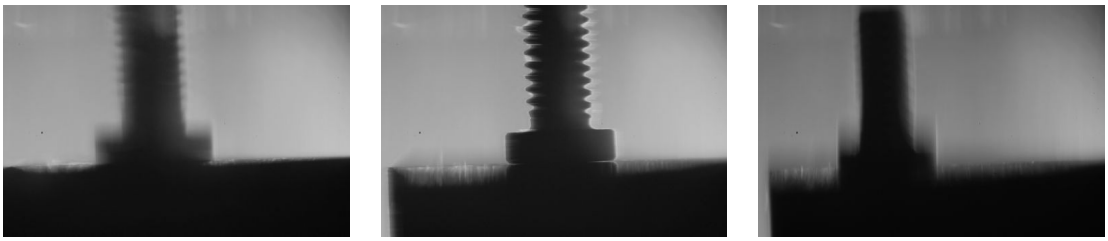

(a) (b) (c)

Figure 3.6: Example of the focusing effect obtained using an extended source with schlieren visualization system #5. A 4-40 screw is located (a) adjacent to the window near the light source, (b) in the center of the test section, and (c) adjacent to the window near the camera.

1. Baffling is no longer an option. In section 3.3 it was mentioned that baffling is often used to reduce the amount of unwanted light that reaches the camera. Unfortunately, baffling works on the principle that non-collimated light is obstructed, and focused schlieren operates on the principle that the source light is not collimated.

2. The divergence angle α in focused schlieren systems results in a large portion of the light not impinging on the focusing mirror for practically-sized optics. This implies that a brighter light source or longer exposure time is needed to achieve a brightness similar to that obtained for a similar unfocused schlieren system. This constriction means that the best quality images occur when the collimating mirror to focusing mirror path length

$$d = d_{1o} + d_{o2} = d_{1o} + f_2 \frac{1+M}{M} \leq d_{1o} + f_2 \tag{3.8}$$

   is minimized.

3. As given in equation (3.5), the sensitivity of the schlieren system increases linearly with the focal length, f_2. Unfortunately, this is at odds with the previous criteria in which small path lengths are desired to limit light loss, and a compromise between light loss and sensitivity must be achieved. Appendix D explores this problem in detail and optimizes the path lengths used in table 3.3.

3.4 GDT Experiment Procedure

The following process was used for performing experiments in the GDT. The tube was initially evacuated to pressure below 100 mTorr and then filled via the method of partial pressures to the desired initial pressure and composition. A circulation pump was used to mix the gas for 5 minutes. After the reactants were injected and mixed, a sequence of events was initiated and controlled by an eight-channel BNC 575 pulse delay generator in a manner detailed by Akbar (1997). This automated process began by injecting a mixture of acetylene and oxygen into the ignition end of the tube from gas bottles at initial pressure between 15 and 20 psi. The injection period was 4.500 s, after which there was a settling period of 0.500 s. Immediately following the settling period, two capacitors with a total capacitance of 2 μF charged to 9 kV discharged through an 80 μm diameter copper wire located in the ignition end. This vaporized the copper wire and created a blast wave in the acetylene-oxygen mixture, thereby initiating a detonation. This wave propagated from the acetylene-oxygen into the test mixture and continued to propagate towards the opposite end of the tube in the manner described in section 1.1. Stoichiometric hydrogen-oxygen, ethylene-oxygen, and hydrogen-nitrous oxide test mixtures were examined at different fill pressures, diluents, and diluent percentages. A shot list of all experiments performed and the checklist used are included in appendix C.

The signal sent to discharge the capacitors also triggered the data acquisition system that began recording the pressure and heat-flux data for a period of 12 ms; this was ample time for the detonation to propagate into the test section, impinge upon the end-wall, and the reflected shock to return back to the ignition end. To obtain images of the detonation and shock waves, it was necessary to trigger the light source and camera with microsecond accuracy. This was accomplished by using the pressure signals to determine when the detonation was in the field of view. This procedure was complicated by the electromagnetic pulse created by the capacitor discharge used to initiate detonation, which created a voltage spike in the pressure measurements several times greater than the actual pressure signals created by the

detonation. Hence a Tektronix TDS 640A four-channel oscilloscope was used, because it has the capability of accepting two separate trigger signals with a programmable minimum allowed delay between each signal. The first trigger was provided by the fire signal. A minimum delay of 2 ms was prescribed before the second trigger, which was given by a suitable pressure sensor, would trigger the oscilloscope. This second trigger caused the oscilloscope to produce an output signal that triggered a four-channel BNC model 565 pulse delay generator. This delay generator controlled the light source and camera and accounted for the delays inherent to each visualization component. The EverGreen70 laser used in visualization system #6, for example, had a 137 μs delay between triggering the laser and light being emitted, due to the delay inherent to the Q-switch.

3.5 Summary

The construction of the GALCIT detonation tube (GDT) is described with an emphasis on the splitter plate that was designed and constructed for the experiments discussed in chapters 4 and 5. This plate housed an array of pressure and heat-flux sensors to gather information about the incident detonation and reflected shock wave created when the detonation impinged on the false wall mounted to the splitter plate. The GDT allows for optical access to the waves, and multiple Z-type schlieren systems were assembled. Six different light source/camera/optical length combinations were used. These six systems fell into two general schlieren schemes differentiated by depth of focus. The first system used a long depth of focus to create an essentially unfocused schlieren system. The best images with this scheme were obtained using a SIMD16 camera to capture sixteen-frame movies that are presented in chapter 4. The second system used a light source of height greater than or equal to 25 mm to produce a narrow depth of field to focus on the flow disturbances in the center of the test section. The best images in this scheme were obtained by using a PIV laser and camera to capture two high-resolution images per experiment. Descriptions of all unfocused and focused schlieren systems are presented in appendix D. Although

an ideal schlieren system would not be affected by flow on the side walls (just as the focused schlieren is not), practical considerations limited the usefulness of the focused schlieren scheme.

Chapter 4

Detonation Reflection

4.1 Introduction

The experimental findings discussed in section 1.2.3 revealed that the reflected shock wave created when a detonation orthogonally impinges upon an end-wall has a speed and strength that is not explained by the one-dimensional inviscid non-reacting model presented in section 1.2.2. This discrepancy is not limited to the specific case of 50 kPa fill pressure with stoichiometric ethylene-oxygen (examined in figure 1.9), as will be shown in this chapter. The research presented here examines the origin of this discrepancy and formulates a more accurate model for reflected detonation behavior.

The GDT described in chapter 3 was used to gather data to examine the shock wave created when a detonation undergoes normal reflection. As discussed in chapter 3, three categories of data were recorded for each experiment performed in the GDT: time-resolved pressure measurements, time-resolved heat-flux measurements, and up to 16 images of the detonation and/or reflected shock waves where the number of images depended on the type of visualization system employed. In total, 270 detonation experiments were performed. To parse these results, the data were divided into two portions to examine two aspects of detonation waves. First, in this chapter, we use a selection of the most apposite pressure and image data to inspect the speed and strength of the incident detonation and reflected shock, as well as the qualitative behaviors of these waves, so that the inconsistency presented above may be resolved. Second, in chapter 5, we use the heat-flux and image data to analyze the bound-

ary layer induced by the incident detonation wave, with an emphasis on examining the possibility of shock wave–boundary layer interaction for reflected detonations. A complete list of recorded data is included in appendix E.

4.2 Reflected Detonation Data

A selected shot list of 19 detonations is given in table 4.1. These experiments were chosen from the complete list of 270 experiments because they were successful in recording simultaneous pressure and heat-flux data, along with 16 images of the incident detonation and reflected shock using the unfocused schlieren visualization system #4 described in section 3.3.1. Pairing the pressure data with the 16 images recorded using the SIMD16 framing camera provides for a more complete understanding of the detonation and shock behavior than the pressure data alone. These tests explored the effect of initial pressure, fuel, and dilution on the incident detonation and reflected shock waves.

4.2.1 Pressure Data

Figure 4.1 shows pressure signals obtained using the experimental assembly described in section 3.2 for two different experiments, shot numbers 2152 and 2179. Both of these experiments were detonations of stoichiometric hydrogen-oxygen at fill pressure 25 kPa. Two shots with identical fill conditions are shown to illustrate the repeatability of the pressure measurements. This plot shows features present in all detonation measurements and will serve as a representative case in describing how the waves were analyzed. In figure 4.1, the detonation first arrives at the gauge located 127 mm from the end-wall as observed by the pressure jump shortly after 0.05 ms. The detonation propagates towards the end-wall, causing pressure increases in each subsequent gauge. Shortly after the detonation arrives at the pressure gauge nearest the end-wall (13 mm from the point of reflection), a second pressure increase is observed in this gauge, marking the arrival of the reflected shock wave. The shock travels back towards the point of ignition, causing a second increase in each pressure measurement.

Table 4.1: Initial experimental conditions used in reflected detonation analysis. Theoretical values were computed with the Shock and Detonation Toolbox.

Experiment Parameters			Theoretical Conditions	
Shot Number	p_1 (kPa)	Mixture	U_{CJ} (m/s)	U_{R0} (m/s)
2163	10	$2H_2$-O_2	2711	1026
2164	10	$2H_2$-O_2-3Ar	1838	717
2166	10	$2H_2$-O_2-12Ar	1503	644
2167	10	$2H_2$-O_2-$3N_2$	1986	770
2168	10	$2H_2$-O_2-$1.5CO_2$	1774	670
2152	25	$2H_2$-O_2	2760	1049
2179	25	$2H_2$-O_2	2760	1049
2161	25	$2H_2$-O_2-3Ar	1872	736
2162	25	$2H_2$-O_2-12Ar	1521	662
2160	25	$2H_2$-O_2-$3N_2$	2012	784
2158	25	$2H_2$-O_2-$1.5CO_2$	1795	680
2180	50	$2H_2$-O_2	2798	1066
2186	50	$2H_2$-O_2	2798	1066
2170	50	$2H_2$-O_2-3Ar	1897	750
2169	50	$2H_2$-O_2-12Ar	1533	676
2171	50	$2H_2$-O_2-$3N_2$	2030	795
2181	50	$2H_2$-O_2-$1.5CO_2$	1811	688
2188	50	C_2H_4-$3O_2$	2340	887
2189	50	C_2H_4-$3O_2$-$4CO_2$	1662	620

Data spikes seen in shot 2179 are due to cabling loosened by the detonation.

A similar pressure profile was observed for all detonation experiments. Figure 4.2, for example, shows pressure measurements taken during shot number 2162. The flammable mixture was still at fill pressure 25 kPa, but the mixture was stoichiometric hydrogen-oxygen with 80% argon dilution. The dilution served to increase the detonation cell size. Qualitatively, the pressure data looks very similar to the data for shots 2152 and 2179. The primary difference was a lower frequency content as caused by the larger cell size. This may be observed in the fast Fourier transform shown in figure 4.3. The transform was performed using pressure data from the gauge located 127 mm from the end-wall with data taken over the first 10 μs after the arrival of the detonation (the gauge 127 mm from the end-wall was chosen so that there would enough time to gather adequate frequency data before the arrival of the reflected

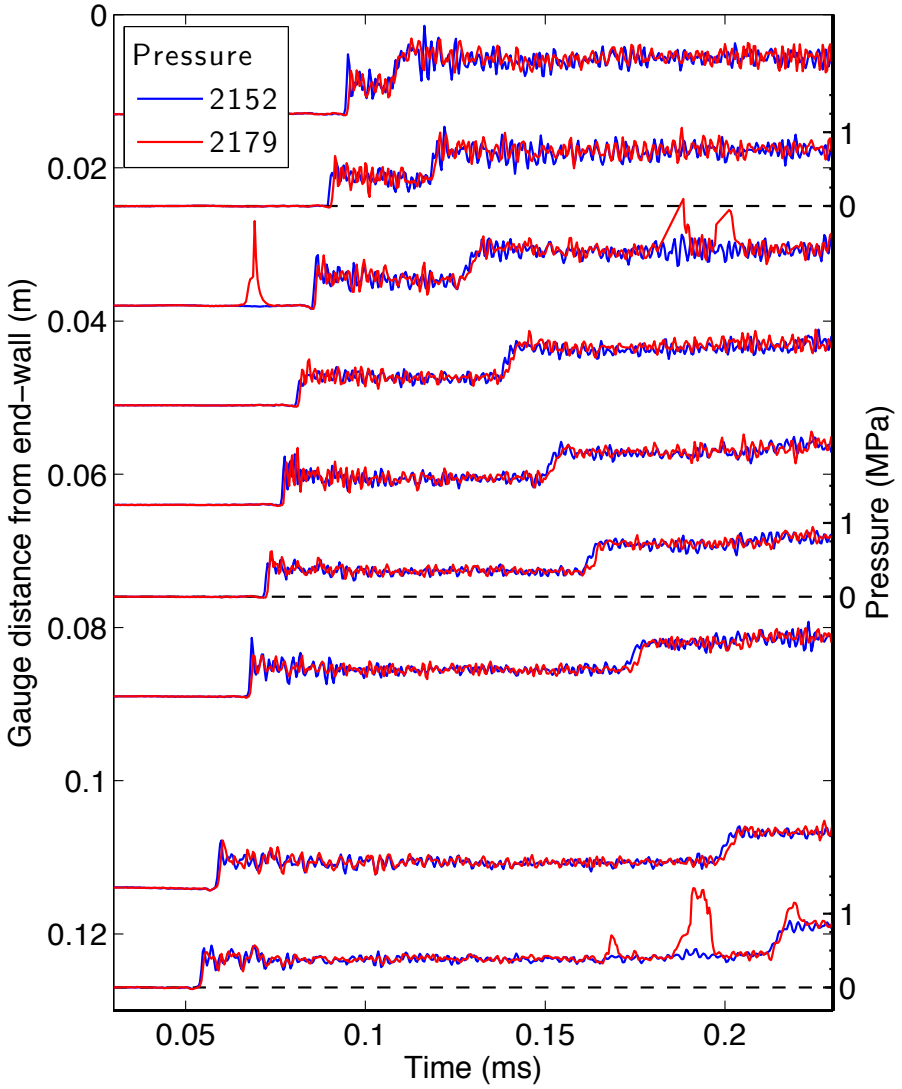

Figure 4.1: Pressure measurements for shots 2152 and 2179. The initial composition for both experiments was stoichiometric hydrogen-oxygen at fill pressure 25 kPa. Data from two experiments are shown to illustrate the repeatability in the experiment. Data spikes, such as seen in the gauge 38 mm from the end-wall in shot 2179, are due to cabling loosened by the detonation.

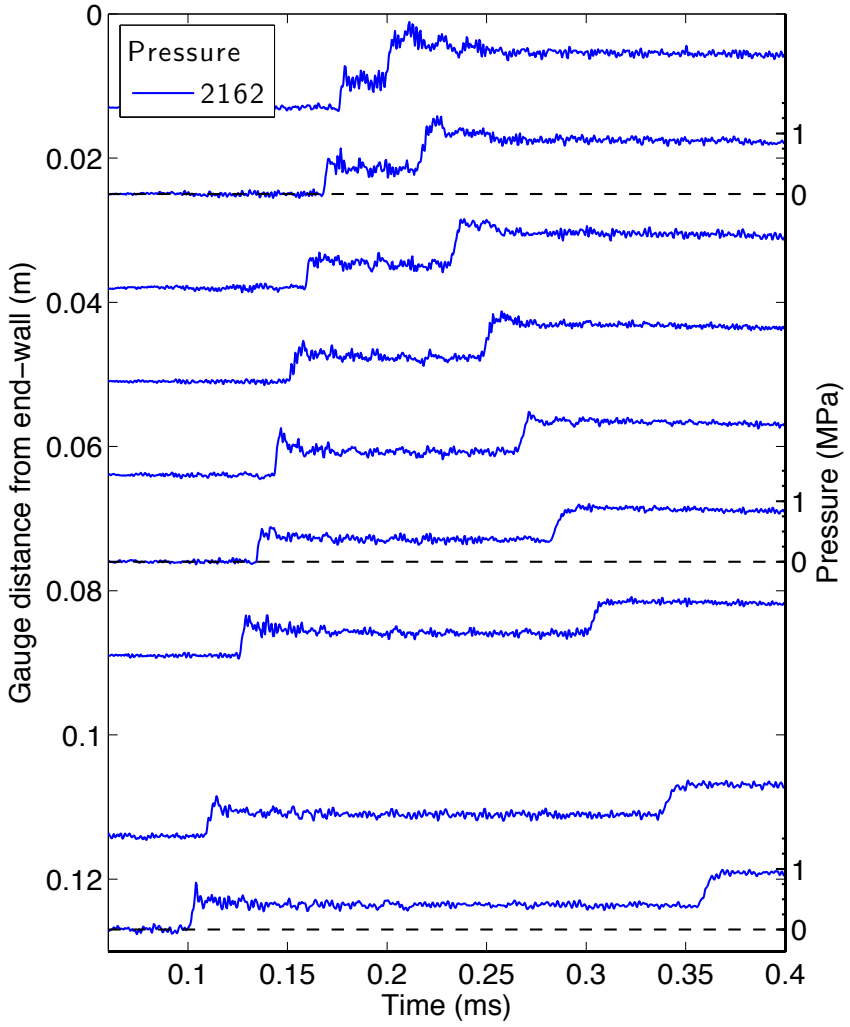

Figure 4.2: Pressure measurements for shot 2162. The initial composition was stoichiometric hydrogen-oxygen with 80% argon dilution at fill pressure 25 kPa.

shock). As the transverse waves behind the detonation front impinge upon the sidewalls, they create pressure spikes. When the cell size is larger, these spikes occur less often. This effect is exaggerated when the cell size is further increased, as seen in figure 4.4, which shows shot number 2166 with the fill pressure lowered to 10 kPa.

In order to address the inaccuracy in the pressure model, we used the time of arrival of the incident detonation and reflected shock wave combined with the known gauge location to calculate the speed of the incident detonation and the reflected shock waves. However, the pressure signals exhibited a rise-time of several microseconds,

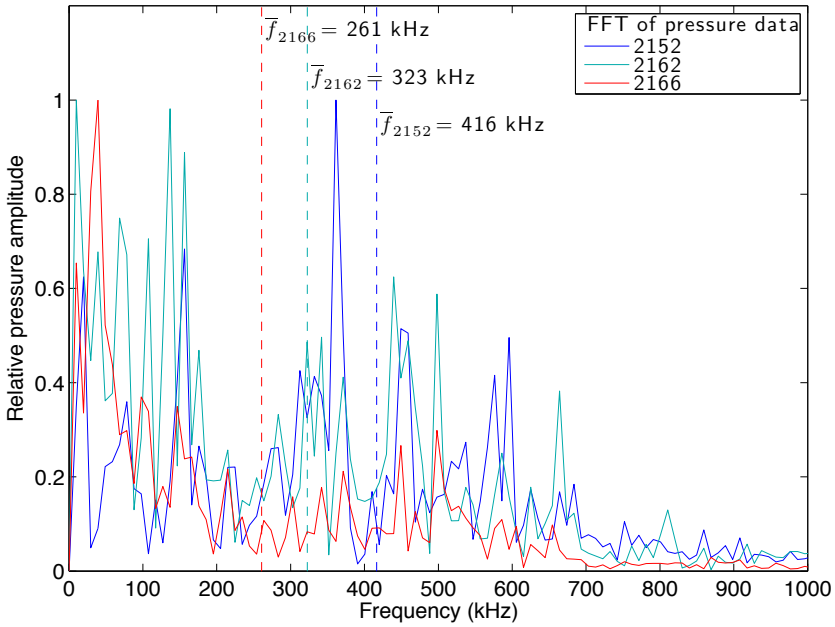

Figure 4.3: Fast Fourier transform of pressure measurements for shots 2152, 2162, and 2166.

complicating the selection of a single wave arrival time. The pressure signals from shot 2152 (as seen in figure 4.1), for example, had a mean rise-time of 1.0 μs for the incident detonation and 5.1 μs for the reflected shock. Thus we desired to formulate a procedure to determine the wave arrival times that was both robust enough to handle the noise in the signals, and was resistant to the errors inherent in manual selection.

To address these factors, the following method was implemented to obtain wave arrival times that accounted for the finite signal rise-times. For each gauge and each experiment, two pairs of times were manually chosen such that the first pair windowed the detonation arrival (that is the first time, t_{w1}, was clearly before detonation arrival and the second time, t_{w2}, was clearly after detonation arrival), and the second pair windowed the reflected shock arrival. For each time interval, $[t_{w1}, t_{w2}]$, times $t_{5\%}$ and $t_{95\%}$ were chosen such that

$$t_{window,1} < t_{5\%} < t_{95\%} < t_{window,2} \tag{4.1}$$

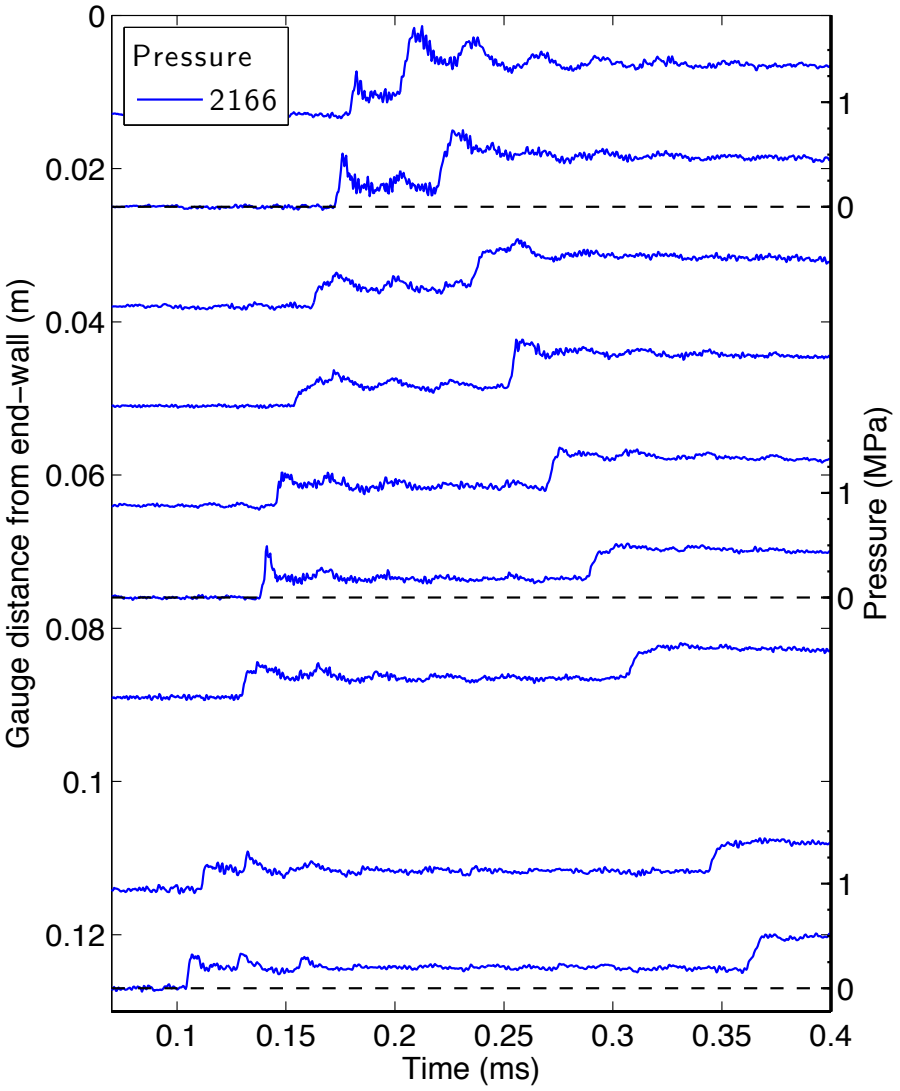

Figure 4.4: Pressure measurements for shot 2166. The initial composition was stoichiometric hydrogen-oxygen with 80% argon dilution at fill pressure 10 kPa.

and the pressure was such that

$$p\left(t_{5\%}\right) = p_{min} + 0.05\left(p_{max} - p_{min}\right) \tag{4.2}$$

$$p\left(t_{95\%}\right) = p_{min} + 0.95\left(p_{max} - p_{min}\right) \tag{4.3}$$

where p_{min} and p_{max} are the minimum and maximum pressures in the closed interval $[t_{w1}, t_{w2}]$. In this manner, a mean time of arrival and an approximation of the signal rise-time may be determined that is not significantly affected by small changes in the manually chosen t_w. Figure 4.5 shows the same data that were plotted in figure 4.1, with the 5% and 95% arrival times given in dashed black lines as calculated with this method. The time of arrival, t_{ta}, is defined to be

$$t_{ta} = t_{5\%} \tag{4.4}$$

to mark the leading edge of the wave arrival. The uncertainty in the time of arrival measurement is calculated from the signal rise time

$$\Delta t_{ta} = t_{95\%} - t_{5\%}. \tag{4.5}$$

To completely account for possible measurement uncertainties, we must also include the finite size of the pressure gauges. The gauge radius of 3.2 mm was used as a maximum uncertainty in gauge location for all pressure measurements. The location of the gauges relative to the reflecting end-wall was known to within 0.1 mm, and thus the finite gauge size dominates the overall uncertainty.

With the gauge locations, wave arrival times, and measurement uncertainties known, we are prepared to examine the speed of the incident detonation and reflected shock and make comparisons to the theories previously presented. Also plotted in figure 4.5 is the predicted pressure as determined by the idealized reflected shock model. Here we observe that the reflected shock arrival times are not well predicted by this model. It is curious that the difference in predicted arrival time was large even at the gauge nearest the end-wall (where the arrival time was 3.1 μs or 33%

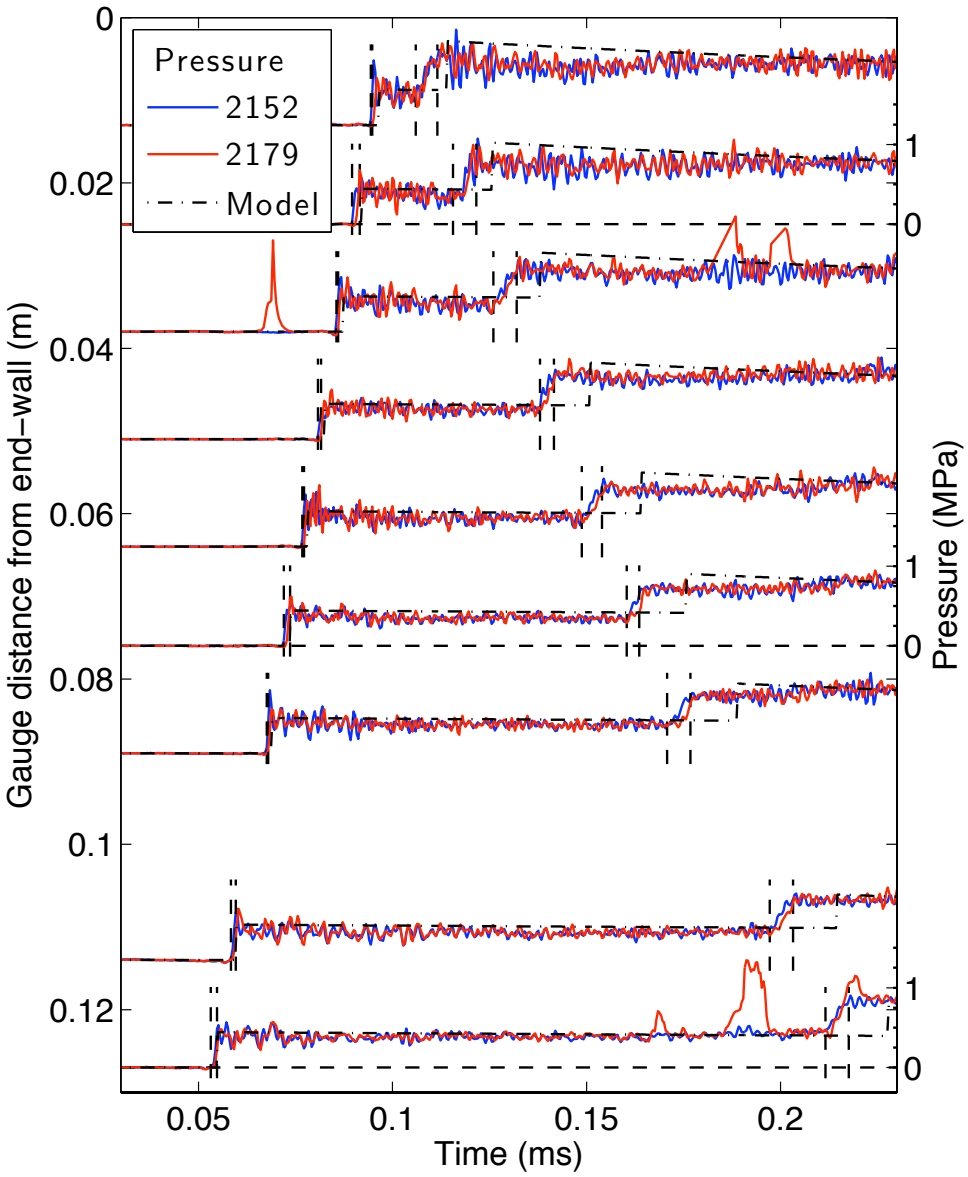

Figure 4.5: Pressure measurements for shots 2152 and 2179 with 5%-95% arrival times for shot 2152 shown as dashed black lines. The one-dimensional non-reacting pressure model is also shown. The initial composition was stoichiometric hydrogen-oxygen at fill pressure 25 kPa.

late). This is surprising because it implies the reflected shock is much faster at the end-wall than was predicted, and that this speed decays considerably so that later gauges do not show the same percent difference (the idealized pressure model for the gauge located 127 mm from the end-wall, for example, is 11 μs but only 9.6% late). The pattern of the reflected shock model being late is consistent among all detonation experiments performed. This disparity in speed is examined in detail in conjunction with the schlieren images in section 4.4.

4.2.2 High-Speed Imaging

The raw image file for shot 2152 is shown in figure 4.6. The 16 frames comprising a single movie are tiled left-to-right, top-to-bottom, so as to view the entire recording. Counting the frames sequentially from left-to-right, top-to-bottom, the first 6 frames show the detonation propagating from the left to the reflecting end-wall located at the right-most edge of each frame; the floor of the splitter plate is barely visible along the bottom edge of each frame. The detonation is seen to impinge upon the end-wall at the approximate time of the 7^{th} frame. Frames 8 to 16 then show the reflected shock wave propagating back to the left. The frames shown in figure 4.6 are slightly tilted as evidenced by the reflecting end-wall being off-vertical. This represents a misalignment between the camera and the detonation tube.

In contrast to the pressure measurements, the time of measurement for each image is known with great accuracy (the exposure time for all images was 20 ns and the time that the camera began each frame was directly recorded as described in section 3.3.1), but the wave location in each image must now be determined. The procedure for doing this was as follows. First, if applicable, each frame was rotated and cropped so that the end-wall was straight and just visible at the right-edge of the image. Second, the mean transverse gray-scale value was determined as a function of distance from the end-wall by taking a vertical average of the image intensity. Third, the waves were windowed, and $x_{5\%}$ and $x_{95\%}$ values were determined analogously to the method described in the previous section (4.2.1). Specifically, for each manually selected

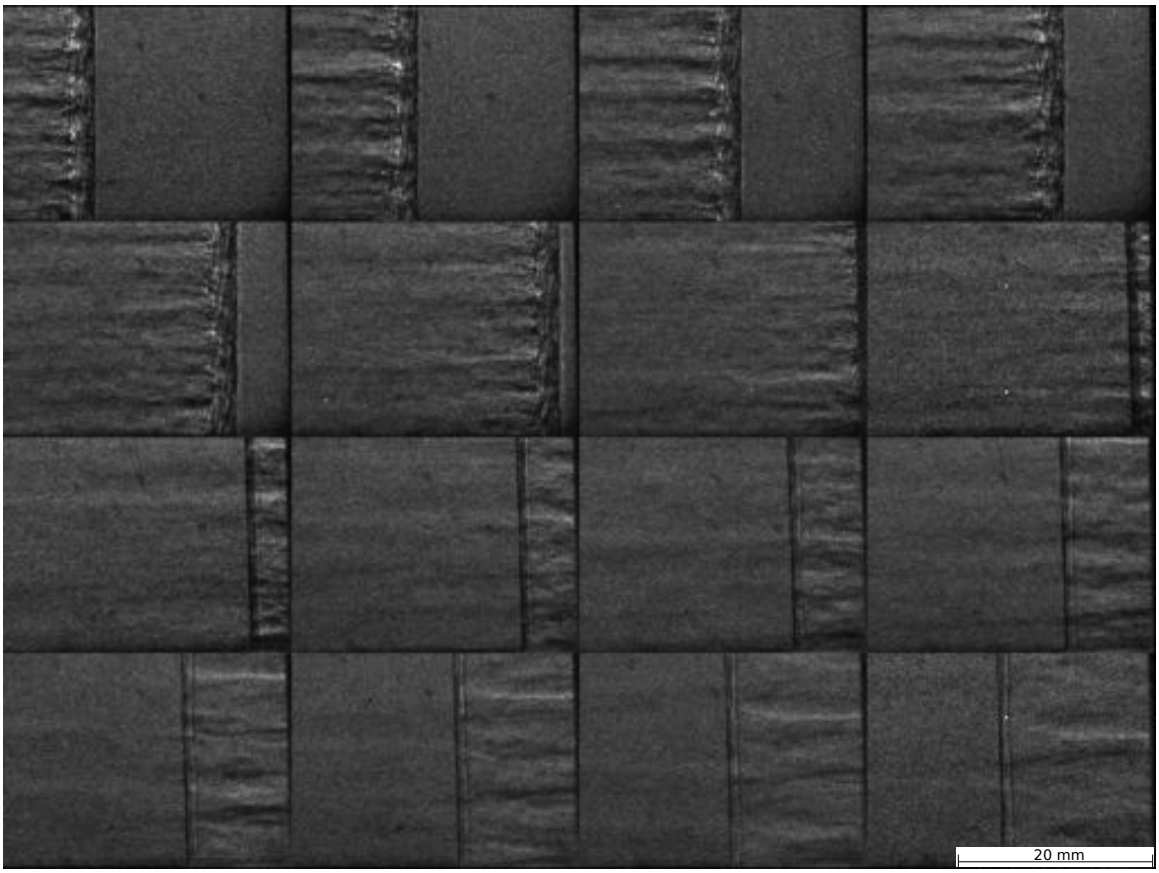

Figure 4.6: Schlieren images of incident detonation and reflected shock for shot 2152. The initial composition was stoichiometric hydrogen-oxygen at initial pressure 25 kPa. The exposure time was 20 ns, the intra-frame time was 1.27 μs, and each frame is approximately 29 mm wide as described in section 3.3.1. Images are placed chronologically left-to-right, top-to-bottom.

window $[x_{w1}, x_{w2}]$, locations $x_{5\%}$ and $x_{95\%}$ are found such that

$$x_{w1} < x_{5\%} < x_{95\%} < x_{w2} \tag{4.6}$$

and

$$\overline{I}\left(x_{5\%}\right) = \overline{I}_{max} - 0.05\left(\overline{I}_{max} - \overline{I}_{min}\right) \tag{4.7}$$

$$\overline{I}\left(x_{95\%}\right) = \overline{I}_{max} - 0.95\left(\overline{I}_{max} - \overline{I}_{min}\right) \tag{4.8}$$

where $\overline{I}$ is the image intensity averaged across the span-wise direction (the vertical

direction in the image) and $\overline{I}_{min}$ and $\overline{I}_{max}$ are the associated minimum and maximum mean intensity values in the closed interval $[x_{w1}, x_{w2}]$. Note that the sign differences in these equations, compared to equations (4.2) and (4.3), are due to the image intensity decreasing through the detonation and shock waves. A sample frame from shot 2152 with associated averaged image intensity and 5%-95% location window is shown in figure 4.7. The black line near the right-hand edge of figure 4.7 represents the location of the end-wall, which was also determined from the images.

Before examining the arrival data in detail, it is enlightening to use the image data to inspect the qualitative behavior of the incident detonation and reflected shock waves. Figures 4.8–4.13 show cropped and rotated image data from 17 detonations covering most of the cases given in table 4.1, and five of the 16 total frames are included for each experiment. Figure 4.8 contains undiluted hydrogen-oxygen detonations at fill pressures of 10, 25, and 50 kPa and will serve as the baseline case to contrast with the other experiments. In these undiluted mixtures, we see a nearly planar detonation front propagating towards the wall (frame 1) and a nearly planar reflected shock exiting (frames 2–5). Although the three-dimensional structures of the detonation waves are largely concealed in these images, due to the schlieren integration through the width of the test section, the transverse waves behind the detonations are still visible. The detonation cell size is increased by lowering the pressure and adding a diluent (Strehlow, 1969a,b). The effect of adding argon dilution is shown in figure 4.9 (50% argon dilution) and figure 4.10 (80% argon dilution). In these figures, the three-dimensional detonation structure as viewed in previous detonation experiments (such as the work of Austin, 2003) is clearly visible, particularly the transverse waves, which appear as horizontal stripes across the images. These transverse waves travel behind the detonation at the fluid velocity. After the reflected shock wave passes through the transverse waves, the mean lateral fluid velocity is zero, and therefore we observe the motion of the transverse waves freeze and slowly dissipate. This effect is particularly visible in the 50% argon dilution cases at fill pressures 25 and 50 kPa shown in figures 4.9(b) and (c). This behavior had not been previously photographed.

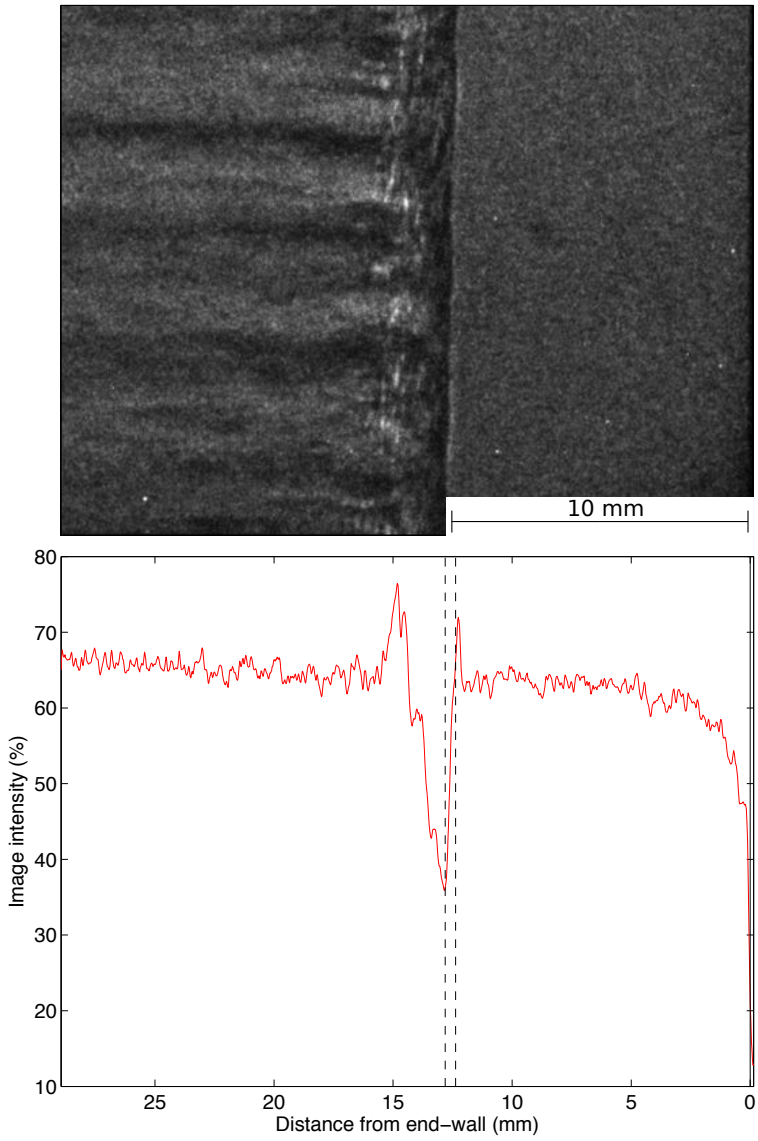

Figure 4.7: Schlieren image of incident detonation for shot 2152 with vertically-averaged image intensity and determined wave location window. The solid black line shows the location of the end-wall and the dashed black lines represent the location of the detonation with uncertainty.

Figures 4.11 and 4.12 show the effect of different dilutions on the incident detonation and reflected shock waves. Both nitrogen and carbon dioxide dilution produce an irregular detonation structure (Strehlow, 1967) as is visible in these images. The detonation irregularity induced with 33% carbon dioxide dilution as shown in figure 4.12 is particularly pronounced, leading to incident and reflected waves that are highly distorted. These distortions are not accounted for in any of the one-dimensional theories presented in chapter 1, and their effect on the wave speeds is discussed in section 4.4.

One component of every reflected shock image that is not accounted for by the idealized reflected shock theory is that the reflected shock exhibits a thickness and three-dimensional structure of its own. This thickness is present in all reflected shock waves examined and its origin is examined in section 4.4.3.

4.3 Wave Speed Determination

Using the methods outlined in section 4.2, wave arrival data with uncertainties were recorded for each initial condition given in table 4.1. With these data, we constructed location-time diagrams with uncertainty bars specifying the measurement uncertainty; an example of this is given in figure 4.14 for the representative shot numbers 2152 and 2166. Using these measurements, we may now determine the relevant wave speeds of the incident detonation and reflected shock through first- and second-order polynomial fits, respectively.

Weighted nonlinear regression was used to fit the arrival data for the detonation wave to a first-order polynomial of the form

$$X_{det}(t) = U_{det}\,(t_0 - t) \tag{4.9}$$

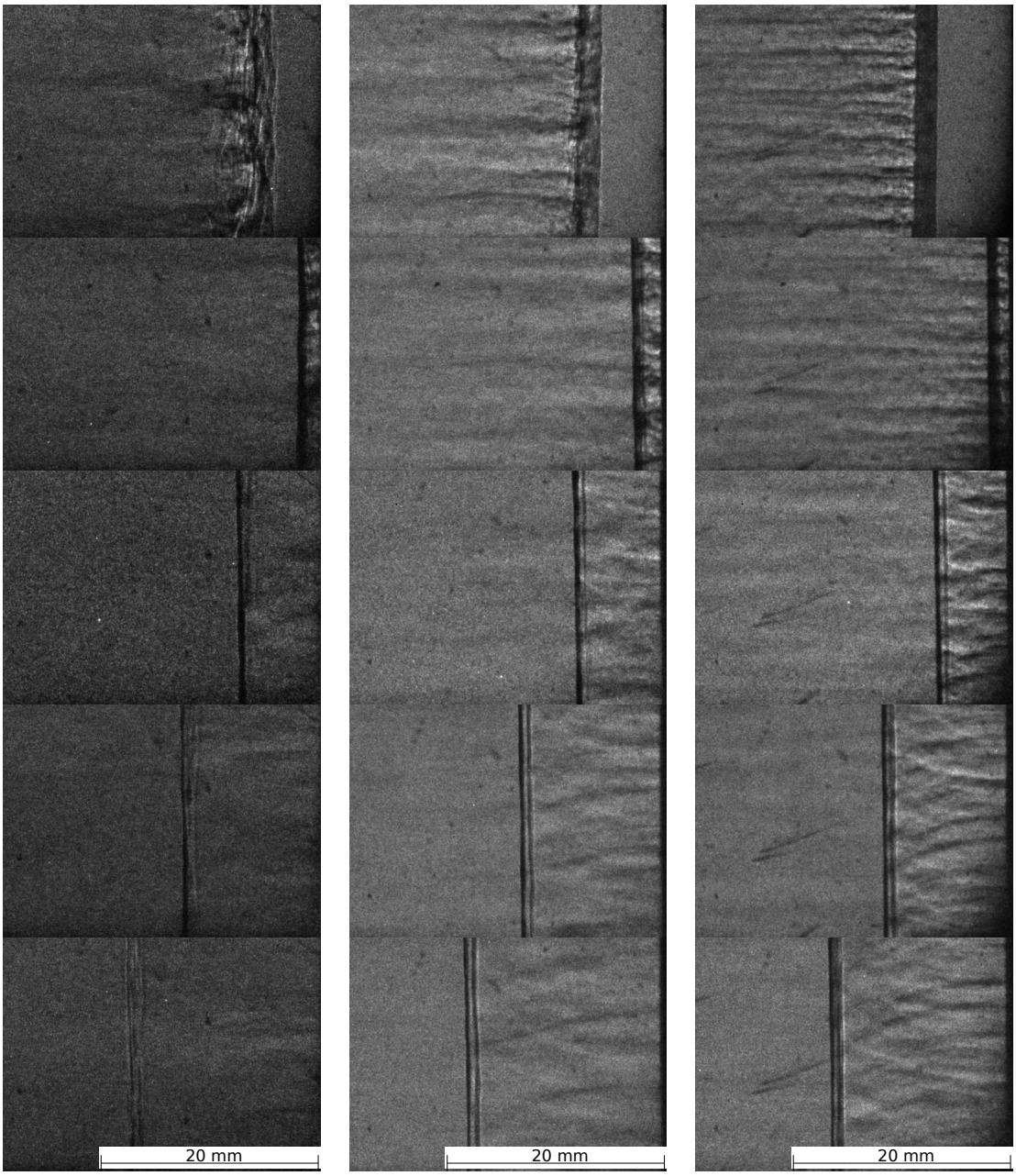

(a) (b) (c)

Figure 4.8: Schlieren images of incident detonation and reflected shock wave for shots (a) 2163, (b) 2179, and (c) 2180. The initial mixture was stoichiometric hydrogen-oxygen with no diluent at fill pressure 10, 25, and 50 kPa, respectively.

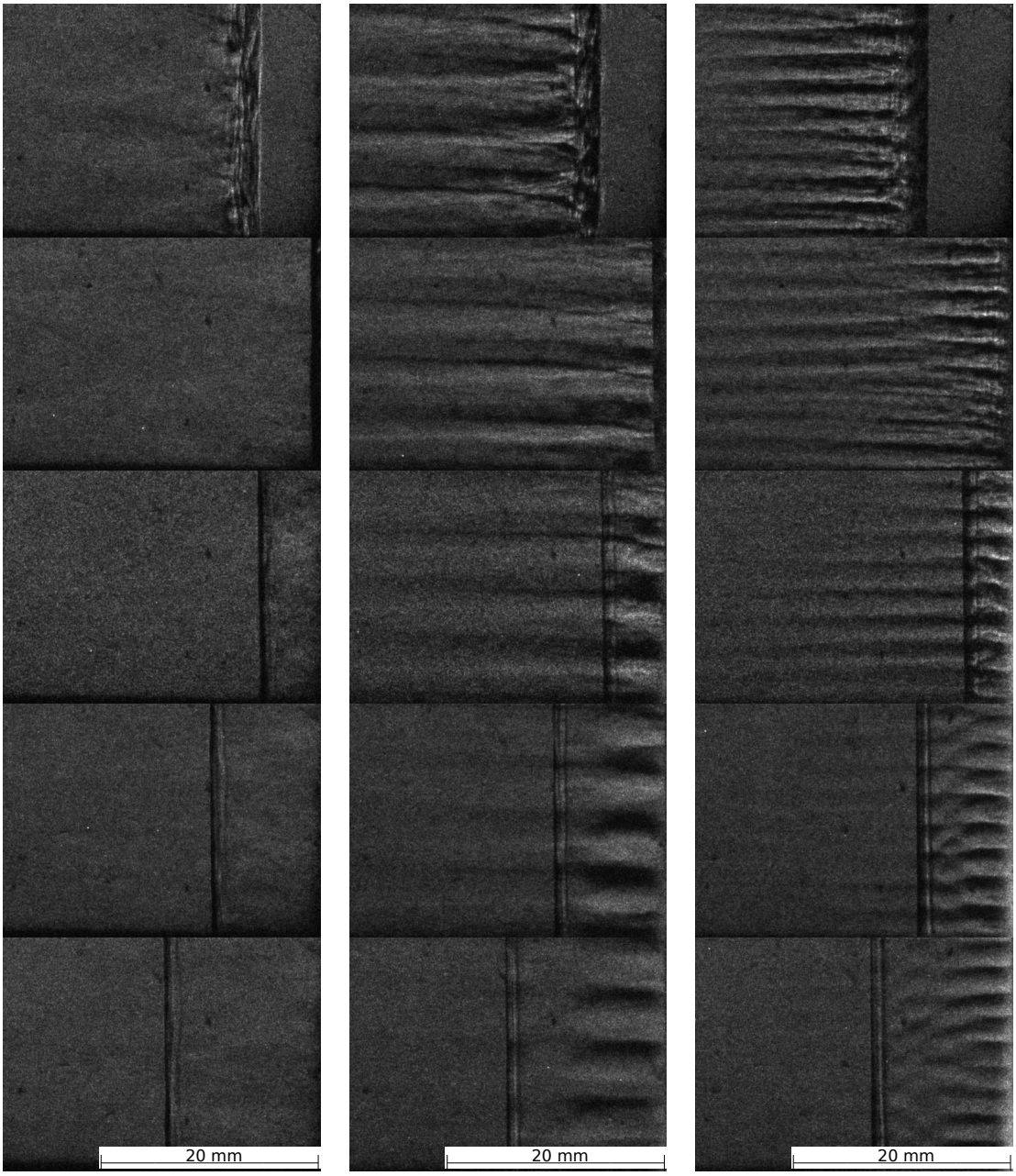

(a) (b) (c)

Figure 4.9: Schlieren images of incident detonation and reflected shock wave for shots (a) 2164, (b) 2161, and (c) 2170. The initial mixture was stoichiometric hydrogen-oxygen with 50% argon dilution at fill pressure 10, 25, and 50 kPa, respectively.

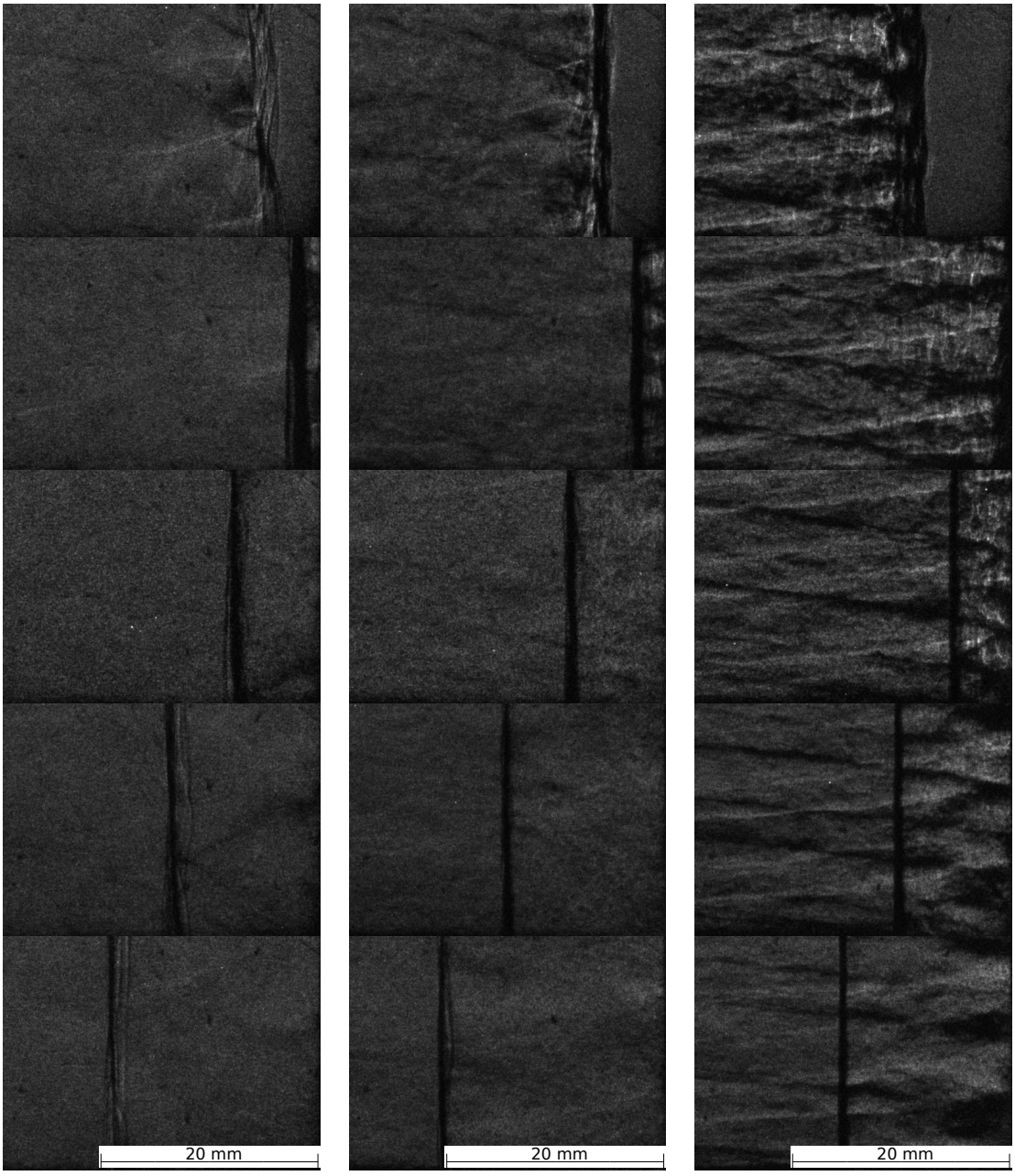

(a) (b) (c)

Figure 4.10: Schlieren images of incident detonation and reflected shock wave for shots (a) 2166, (b) 2162, and (c) 2169. The initial mixture was stoichiometric hydrogen-oxygen with 80% argon dilution at fill pressure 10, 25, and 50 kPa, respectively.

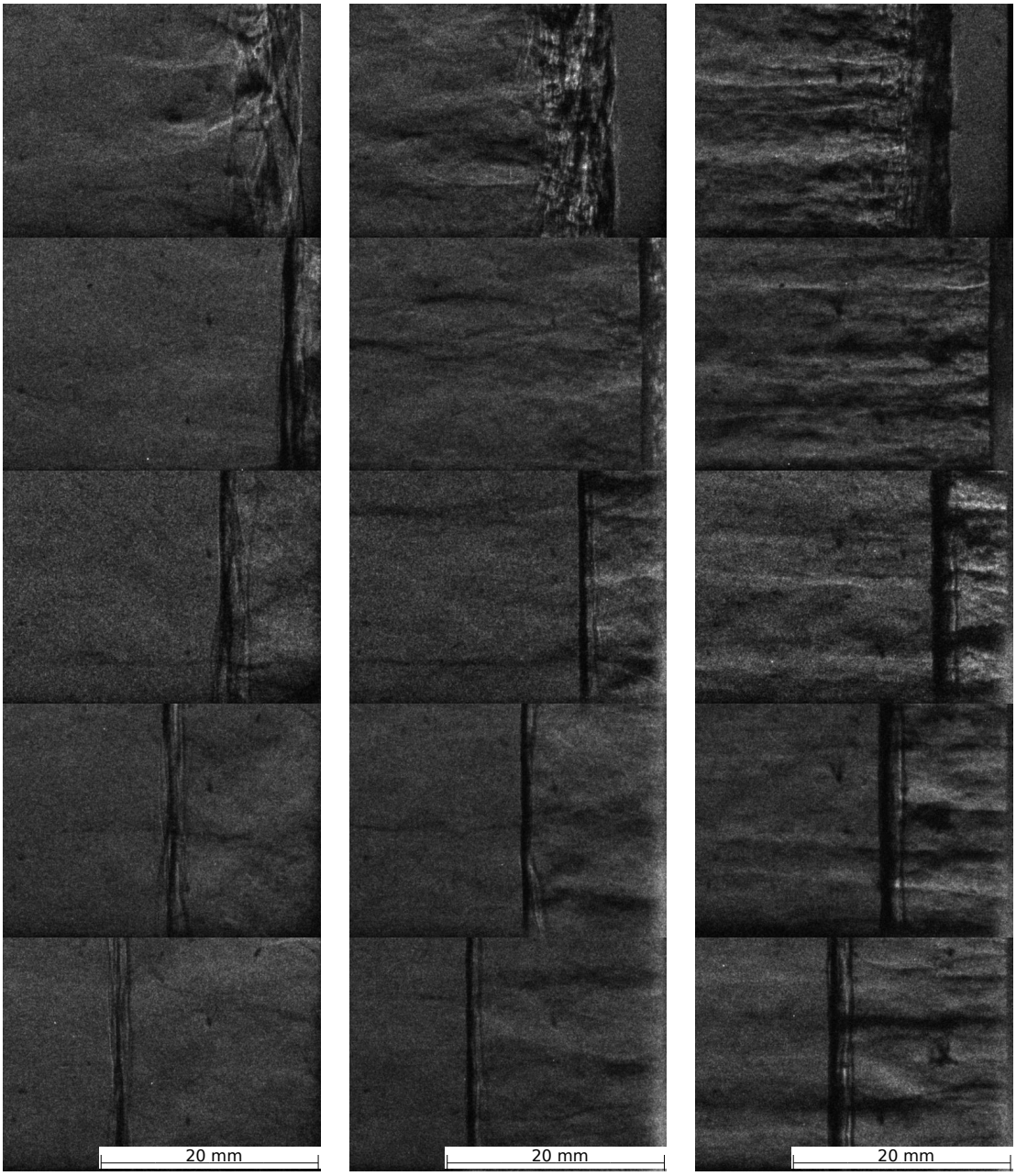

(a) (b) (c)

Figure 4.11: Schlieren images of incident detonation and reflected shock wave for shots (a) 2167, (b) 2160, and (c) 2171. The initial mixture was stoichiometric hydrogen-oxygen with 50% nitrogen dilution at fill pressure 10, 25, and 50 kPa, respectively.

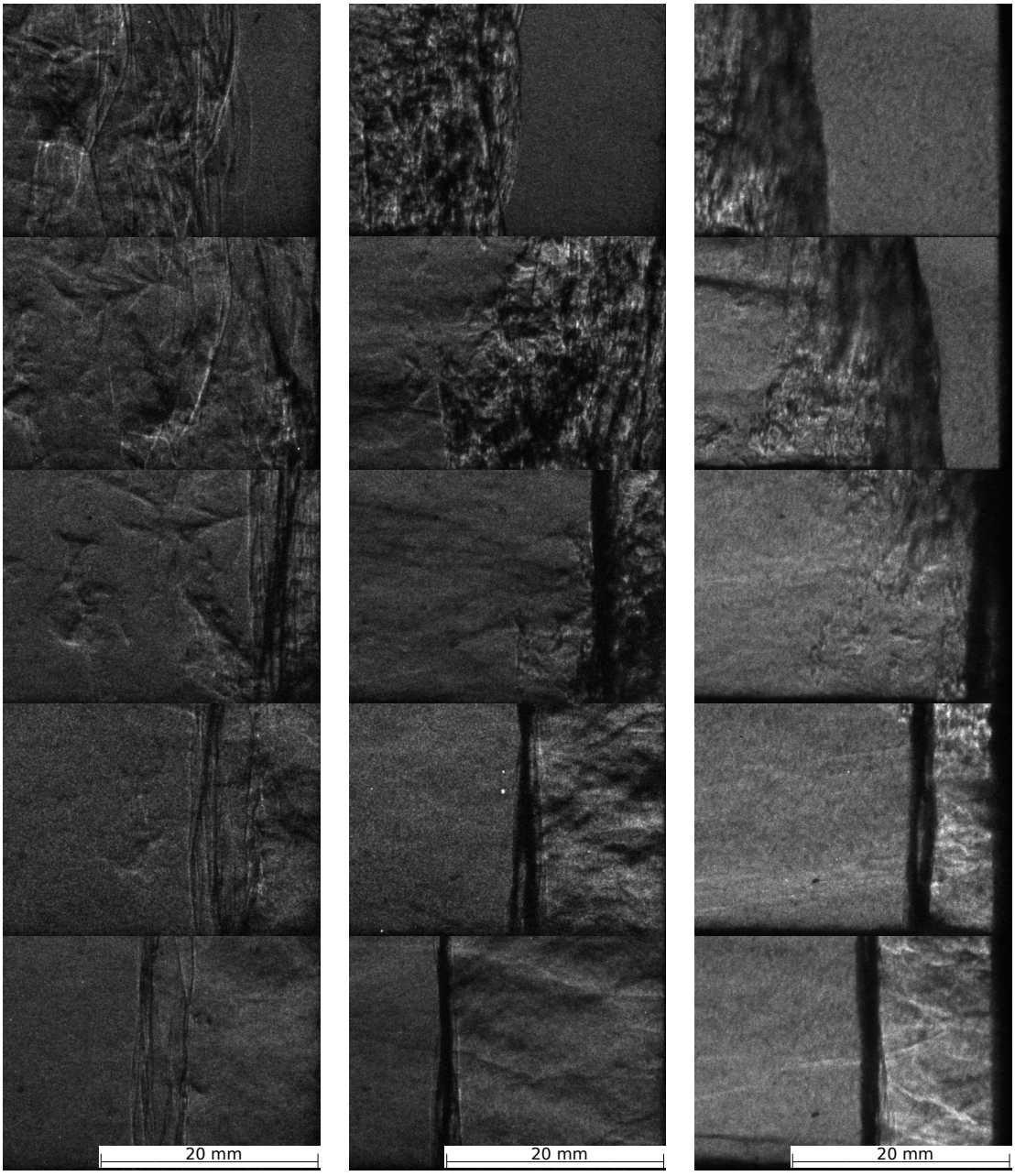

(a) (b) (c)

Figure 4.12: Schlieren images of incident detonation and reflected shock wave for shots (a) 2168, (b) 2158, and (c) 2181. The initial mixture was stoichiometric hydrogen-oxygen with 33% carbon dioxide dilution at fill pressure 10, 25, and 50 kPa, respectively.

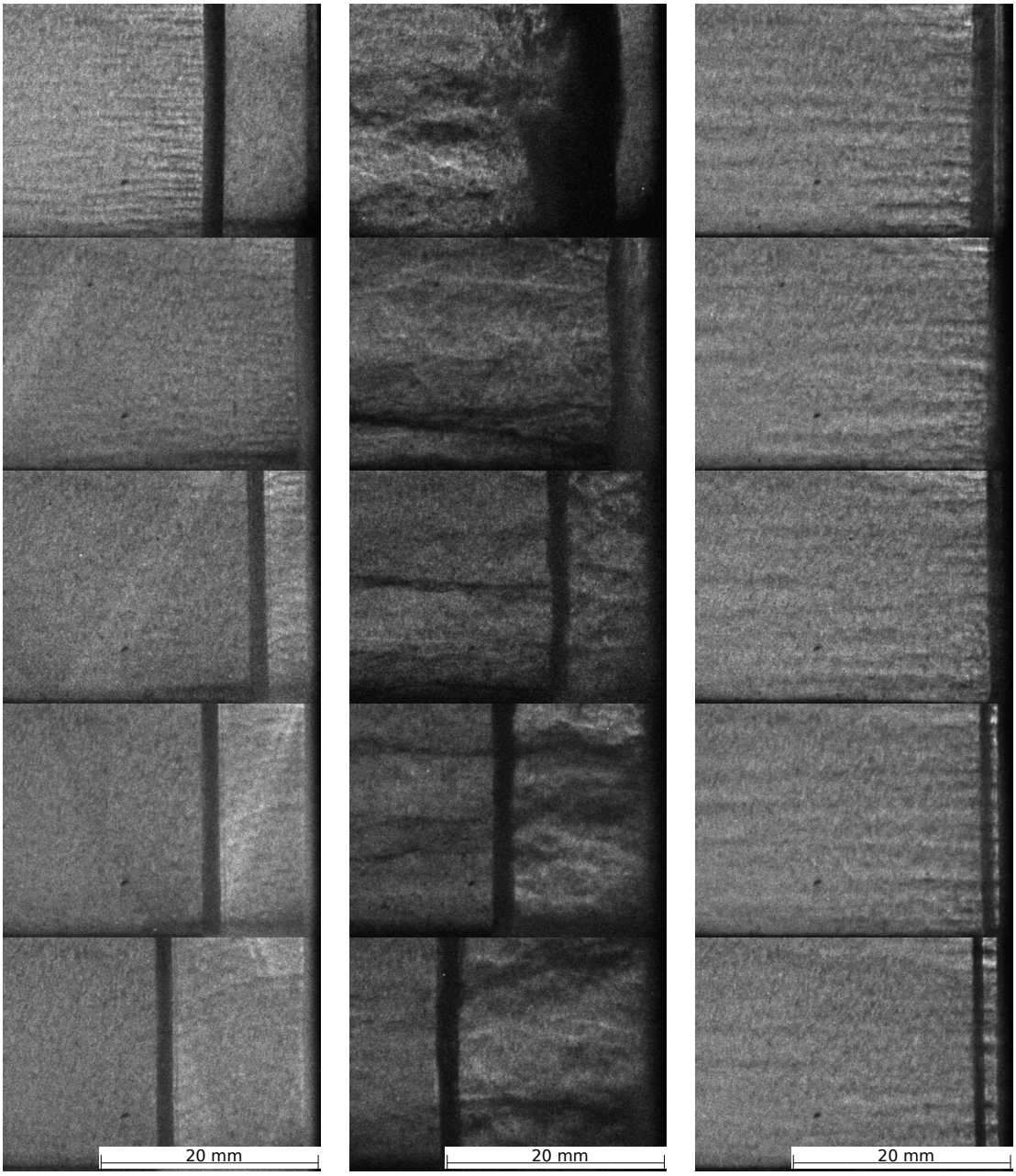

(a) (b) (c)

Figure 4.13: Schlieren images of incident detonation and reflected shock wave for shots (a) 2188, (b) 2189, and (c) 2186. The initial mixture was stoichiometric ethylene-oxygen with 0% and 50% carbon dioxide for shots 2188 and 2189, respectively, and stoichiometric hydrogen-oxygen for shot 2186, all at fill pressure 50 kPa.

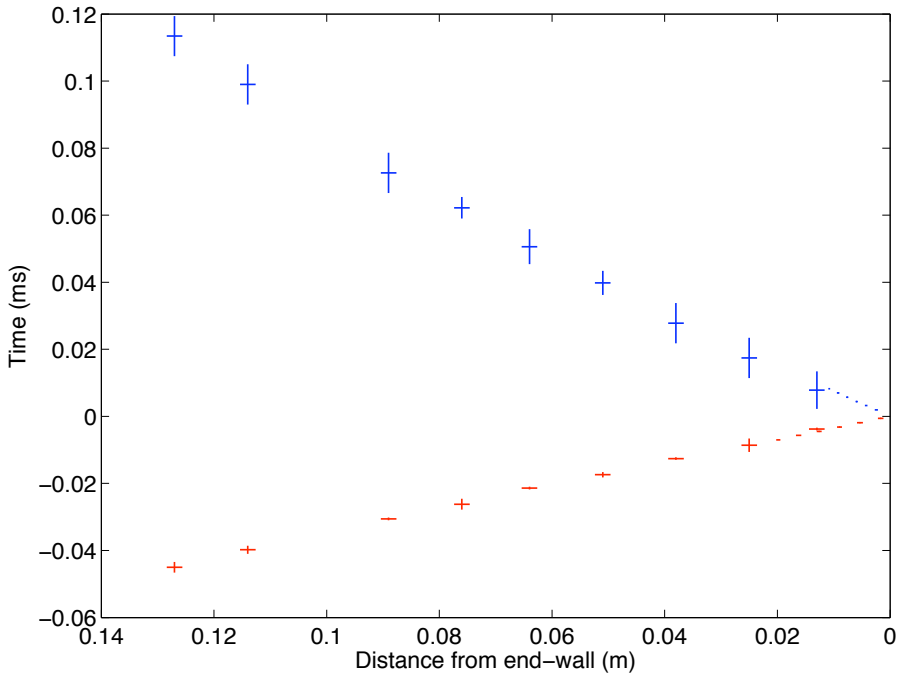

(a)

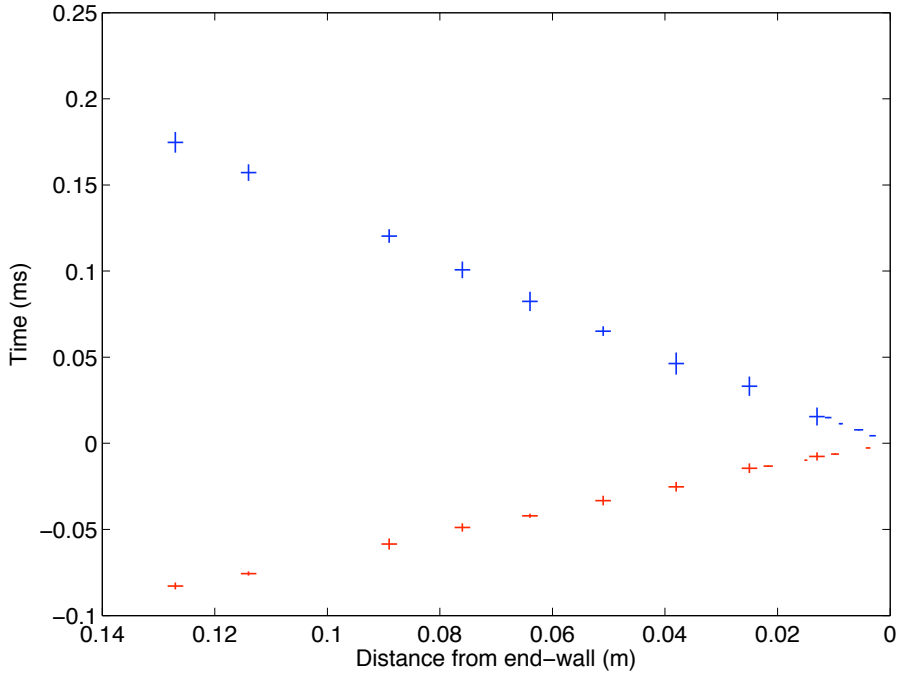

(b)

Figure 4.14: x-t diagram showing detonation and shock arrivals, with uncertainties, for representative shots (a) 2152 and (b) 2166. The detonation is shown in red propagating towards the reflecting end-wall at the right, and the reflected shock is shown in blue propagating back. The points clustered near the end-wall correspond to arrivals taken from the image files, and the points farther away correspond to arrivals taken from the pressure measurements.

where $X_{det}(t)$ is the location of the detonation relative to the reflecting end-wall as a function of time. The measured location and time arrival data were used to determine the fit parameters U_{det} and t_0, representing the experimental detonation speed and time the detonation impinges upon the end-wall, respectively. Using the Matlab nonlinear regression function `lsqnonlin`, the values U_{det} and t_0 were chosen to minimize the quantity, e, defined to be

$$e = \sqrt{\sum_i \left[\left(x_i - X_{det}\left(t_i\right)\right) \cdot w_i\right]^2} \tag{4.10}$$

for known (x_i, t_i) data with weighting, w_i, given by the uncertainties in the x_i and t_i data:

$$w_i = \left[\left(U_{det} \cdot \Delta t_i\right)^2 + \left(\Delta x_i\right)^2\right]^{-1/2}. \tag{4.11}$$

The standard error, s_e, is determined from the residual and Jacobian of the nonlinear regression. Generally, the standard error of the i^{th} fit parameter is calculated by

$$s_{e,i} = \sqrt{\frac{\hat{\epsilon}}{N} \sum_j R_{ij}^{-1} \cdot R_{ij}^{-1}} \tag{4.12}$$

where $\hat{\epsilon}$ is the normalized residual of the nonlinear regression, N is the number of degrees of freedom in the parameter fit,[1] and R is the upper triangle decomposition of the Jacobian of the regression.

A similar process was used to determine the reflected shock speed and acceleration at the end-wall with associated standard errors using a second-order polynomial of the form

$$X_{rs}(t) = U_{rs}\left(t - t_0\right) + \frac{1}{2} a_{rs}\left(t - t_0\right)^2 \tag{4.13}$$

where $X_{rs}(t)$ is the location of the reflected shock wave relative to the reflecting

[1] $N = N_p + N_i - 2$ for N_p pressure arrival times and N_i image location data points using a two parameter fit.

end-wall as a function of time, and t_0 is the time the detonation impinges upon the end-wall as determined by the fit to the detonation data. The fit parameters, U_{rs} and a_{rs}, represent the speed and acceleration of the reflected shock wave at the moment of detonation reflection. The determined detonation and shock fit parameters are given in tables 4.2 and 4.3 and are analyzed next.

4.4 Discussion

The determined wave speeds and schlieren images allow us to draw several conclusions regarding the detonation and reflected shock data. First, we compare our measured wave speeds to the theoretical Chapman-Jouguet speed. Second, we examine the reflected shock wave speeds and compare them to the idealized detonation reflection model. Third, we formulate a new model for the reflected shock wave that accounts for the non-zero reaction zone thickness; this new model is much more successful than the idealized model at predicting the speed of the reflected shock near the end-wall. Fourth, we deduce the source of the shock wave thickness noted in images of the reflected shock.

4.4.1 Detonation Speed

Table 4.2 gives the detonation speeds, U_{det}, with uncertainties obtained from the pressure measurements and high-speed schlieren images compared to the theoretical Chapman-Jouguet detonation speed, U_{CJ}; these data are also plotted in figure 4.15. The experimental measurements are in excellent alignment with the CJ theory, and the only experiments that show substantial deviations are shots 2168 and 2189. The source of these discrepancies is obvious when we examine the corresponding schlieren images. Figures 4.12(a) and 4.13(b) show images from the high-speed videos of shots 2168 and 2189, respectively. The large cellular structure caused by low pressure (in the case of shot 2168) or carbon dioxide dilution (shots 2168 and 2189) effects a wave structure that is poorly approximated by a one-dimensional model.

Table 4.2: Detonation speeds fit to pressure and image data compared to the theoretical Chapman-Jouguet speed. The value Δ_{CJ} is the difference of the CJ speed relative to the fit detonation speed.

Experiment Parameters				Theoretical Conditions	
Shot Number	p_1 (kPa)	Mixture	U_{det} (m/s)	U_{CJ} (m/s)	Δ_{CJ} (%)
2163	10	$2H_2$-O_2	2861 ± 19	2711	-5.2
2164	10	$2H_2$-O_2-3Ar	1838 ± 6	1838	0.0
2166	10	$2H_2$-O_2-12Ar	1533 ± 15	1503	-2.0
2167	10	$2H_2$-O_2-$3N_2$	1976 ± 9	1986	0.5
2168	10	$2H_2$-O_2-$1.5CO_2$	1924 ± 46	1774	-7.8
2152	25	$2H_2$-O_2	2830 ± 12	2760	-2.5
2179	25	$2H_2$-O_2	2830 ± 10	2760	-2.5
2161	25	$2H_2$-O_2-3Ar	1902 ± 6	1872	-1.6
2162	25	$2H_2$-O_2-12Ar	1535 ± 4	1521	-1.0
2160	25	$2H_2$-O_2-$3N_2$	2082 ± 11	2012	-3.4
2158	25	$2H_2$-O_2-$1.5CO_2$	1865 ± 12	1795	-3.8
2180	50	$2H_2$-O_2	2799 ± 9	2798	-0.0
2186	50	$2H_2$-O_2	2831 ± 18	2798	-1.2
2170	50	$2H_2$-O_2-3Ar	1898 ± 3	1897	-0.0
2169	50	$2H_2$-O_2-12Ar	1523 ± 2	1533	0.7
2171	50	$2H_2$-O_2-$3N_2$	2060 ± 9	2030	-1.5
2181	50	$2H_2$-O_2-$1.5CO_2$	1886 ± 17	1811	-4.0
2188	50	C_2H_4-$3O_2$	2350 ± 4	2340	-0.4
2189	50	C_2H_4-$3O_2$-$4CO_2$	1814 ± 6	1662	-8.4

Hence, moderate differences exist between the measured detonation speed and the Chapman-Jouguet theory in a few cases.

For the most part, however, the measured detonation speed is extremely close to the theoretical CJ speed. This corroborates previous detonation research wherein the CJ theory worked well to predict global properties, such as the average detonation speed, even when considering irregular detonations (see, for example, Strehlow, 1967). The accuracy of the CJ speed also showed that the experimental conditions and data acquisition were precisely implemented.

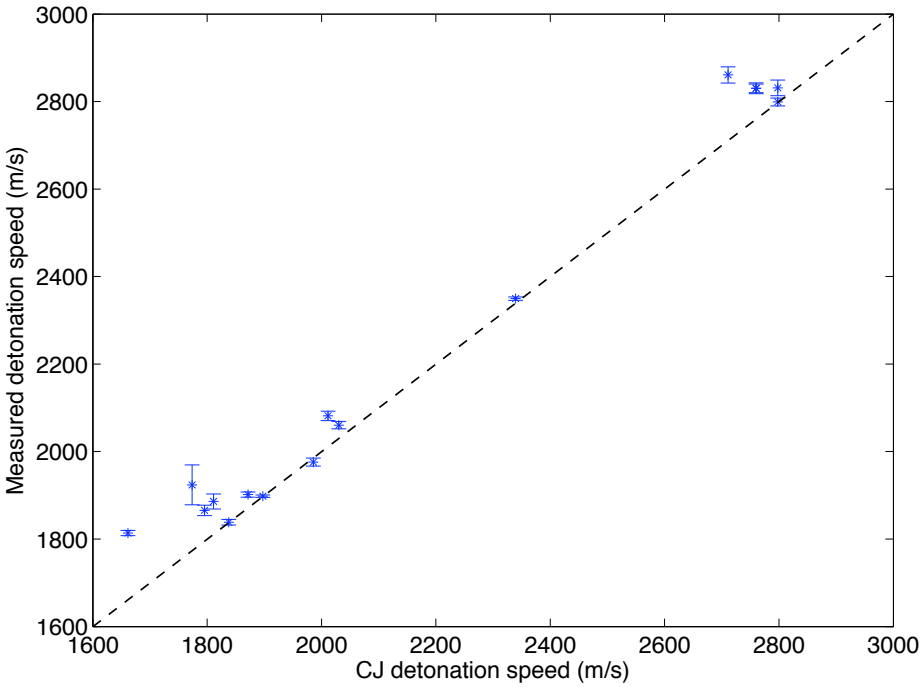

Figure 4.15: Measured detonation speed compared to the theoretical CJ detonation speed. The dashed black line corresponds to $U_{measured} = U_{predicted}$.

4.4.2 Reflected Shock Speed

Table 4.3 shows the fit reflected shock speeds, U_{rs}, and accelerations, a_{rs}, with uncertainties. To compare these speeds to the idealized reflected shock model, the same nonlinear fit used to analyze the data was applied to the shock model, with location data extracted at identical times as used in the experimental fits. This gave ideal reflected shock speeds, U_{rsi}, and accelerations, a_{rsi}, extrapolated to the end-wall for each experiment. In table 4.3 (and also later in table 4.4 and figure 4.18) we can see that this idealized reflected shock theory does not accurately predict the reflected shock speed. We observe that the predicted speed was slower than the measured speed in every test, with a mean error for these conditions of 22% and a minimum error of 12%. These errors are highlighted in figure 4.16(a) and (b), where the x-t diagrams for shots 2152 and 2166 were appended to include the predicted detonation and shock locations. In these figures and subsequent discussion, the idealized reflected shock model is termed the no reaction zone shock.

In addition to being suboptimal for predicting detonation-driven damage, this sub-

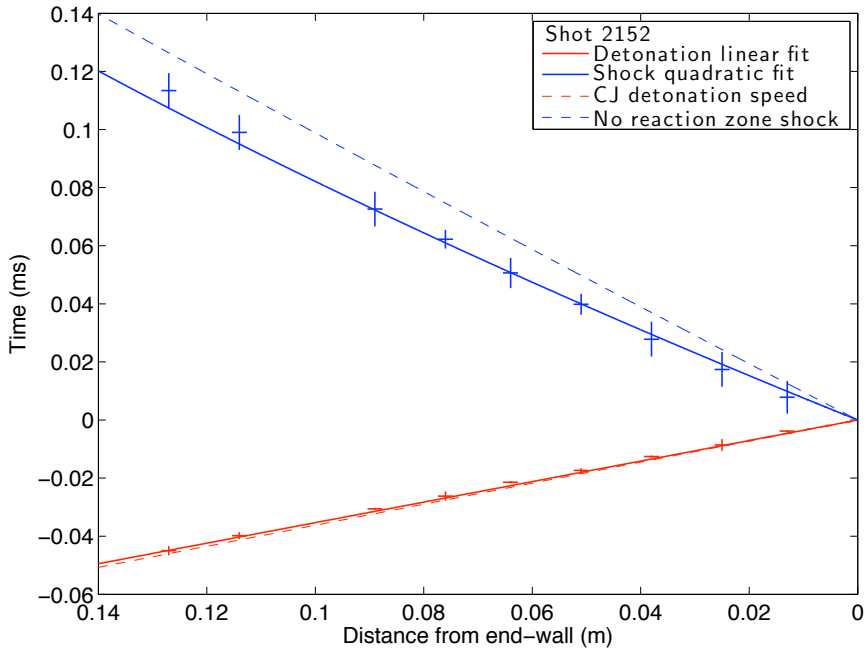

(a)

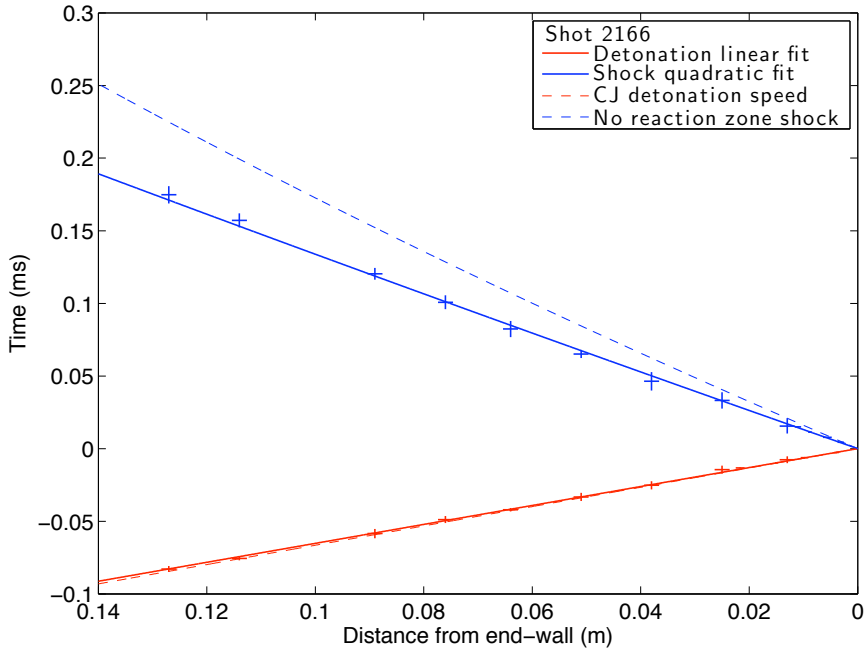

(b)

Figure 4.16: x-t diagram showing detonation and shock arrivals with uncertainties for shot (a) 2152 and (b) 2166, with predicted detonation locations, and shock locations from the idealized reflected shock model with no reaction zone.

Table 4.3: Reflected shock speed and acceleration extrapolated to the reflecting end-wall for the pressure and image data and the idealized no reaction zone reflected shock model.

Experiment Parameters			Quadratic Fit to Shock Data		No Reaction Zone Shock Model	
Shot Number	p_1 (kPa)	Mixture	U_{rs} (m/s)	a_{rs} (km/s^2)	U_{rsi} (m/s)	a_{rsi} (km/s^2)
2163	10	$2H_2$-O_2	1365 ± 18	-3005 ± 840	1014 ± 1	-521 ± 10
2164	10	$2H_2$-O_2-3Ar	913 ± 11	-1014 ± 86	693 ± 3	-600 ± 16
2166	10	$2H_2$-O_2-12Ar	765 ± 5	-262 ± 75	627 ± 4	-552 ± 17
2167	10	$2H_2$-O_2-$3N_2$	1025 ± 5	-2007 ± 303	751 ± 3	-616 ± 14
2168	10	$2H_2$-O_2-$1.5CO_2$	847 ± 20	-752 ± 114	642 ± 4	-549 ± 17
2152	25	$2H_2$-O_2	1331 ± 3	-2752 ± 488	1037 ± 1	-513 ± 9
2179	25	$2H_2$-O_2	1361 ± 12	-3198 ± 689	1037 ± 1	-513 ± 9
2161	25	$2H_2$-O_2-3Ar	894 ± 7	-891 ± 108	712 ± 3	-612 ± 15
2162	25	$2H_2$-O_2-12Ar	794 ± 4	-413 ± 29	648 ± 4	-573 ± 17
2160	25	$2H_2$-O_2-$3N_2$	1052 ± 8	-1622 ± 172	765 ± 3	-623 ± 14
2158	25	$2H_2$-O_2-$1.5CO_2$	959 ± 22	-1328 ± 210	653 ± 4	-557 ± 16
2180	50	$2H_2$-O_2	1208 ± 4	-1928 ± 424	1055 ± 1	-499 ± 10
2186	50	$2H_2$-O_2	1582 ± 94	-4143 ± 792	1055 ± 1	-499 ± 10
2170	50	$2H_2$-O_2-3Ar	844 ± 2	-607 ± 61	727 ± 3	-622 ± 15
2169	50	$2H_2$-O_2-12Ar	782 ± 3	-311 ± 112	663 ± 4	-586 ± 16
2171	50	$2H_2$-O_2-$3N_2$	1004 ± 9	-1195 ± 61	776 ± 2	-630 ± 14
2181	50	$2H_2$-O_2-$1.5CO_2$	919 ± 12	-1097 ± 98	662 ± 4	-565 ± 17
2188	50	C_2H_4-$3O_2$	1040 ± 17	-1008 ± 181	860 ± 2	-630 ± 11
2189	50	C_2H_4-$3O_2$-$4CO_2$	878 ± 8	-1043 ± 96	584 ± 5	-512 ± 19

stantial under-prediction in the reflected detonation speed indicates that this model is lacking a fundamental element of the gasdynamics of detonation reflection. In considering the origin of this discrepancy, two primary assumptions of the reflected shock model stand out as potential sources of error. The first possible source is the inviscid assumption inherent to the idealized model. We initially believed that shock wave–boundary layer interaction might be responsible for the discrepancy, and the reasoning behind this hypothesis and the related analysis is included in chapter 5. The second possible source of error is the assumption that the incident detonation was approximated as having zero thickness. Here we consider the effect of relaxing this assumption to allow for a detonation with a finite length reaction zone, as allowed for in the ZND model introduced in section 1.1.2.

As seen in figure 1.5, the ZND detonation profile contains a region behind the detonation front called the induction zone where the gas has been shocked to the von Neumann point (point 2_{VN} in figure 1.4), but most of the chemical reactions have not occurred. As shown in the x-t diagram given in figure 4.17, when the detonation impinges upon the end-wall, the reflected shock will first pass through this unreacted induction zone. The higher pressures and temperatures behind the reflected shock cause the reaction time-scales to decrease substantially. Thus the ZND model suggests that for times soon after the incident detonation impinges upon the end-wall there will be a detonation that propagates through the ZND profile. The chemical reaction will vanish as the reflected wave passes into the products already processed by the detonation, but for regions near the end-wall the chemical reaction will boost the speed of the reflected wave. Near the end-wall, we can therefore approximate the reflected wave speed in the lab-fixed frame of reference as

$$U_{rsr} = U_{CJ,vn} - u_2 \tag{4.14}$$

where $U_{CJ,vn}$ is the theoretical Chapman-Jouguet detonation speed for gases initially at the von Neumann point and u_2 is the fluid velocity behind the detonation. The increased speed of the reflected wave will cause an expansion wave to develop behind

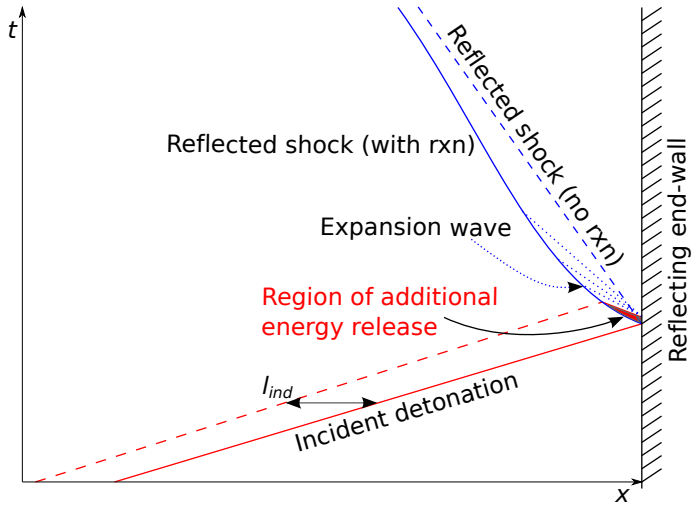

Figure 4.17: Space-time diagram of the reflected shock passing through the induction zone. The unreacted region behind the reflected shock serves to increase the speed of the shock near the reflecting end-wall.

the reflected shock to decelerate the gas to zero velocity at the end-wall. This will diminish the speed of the reflected wave as observed in the data as a strong deceleration of the reflected shock at the end-wall.

These results are included in table 4.4 and illustrated graphically in figure 4.18 under the variable U_{rsr}. We see that in almost every case the reacting reflected shock model gives the most accurate predictions of the reflected shock speed, with a mean absolute difference of 6.3% for the cases considered. The largest differences occurred for shot numbers 2180, 2186, 2170, and 2188. All of these tests were 50 kPa fill pressure mixtures where the reacting shock model over-predicted the reflected shock speed. Shots 2180 and 2186 were both stoichiometric hydrogen-oxygen without dilution, shot 2170 was hydrogen-oxygen with 50% argon, and shot 2188 was stoichiometric ethylene-oxygen without dilution. Shot 2186 operated the SIMD16 framing camera with a frame rate of 4 million frames per second, an order of magnitude larger than other experiments; this provided multiple images while the reflected shock was millimeters from the reflecting end-wall. Based on the mixtures of these shots we see that the reacting shock model was least successful when the chemical induction time was at a minimum, as occurs for higher pressures and less dilution. The fact that

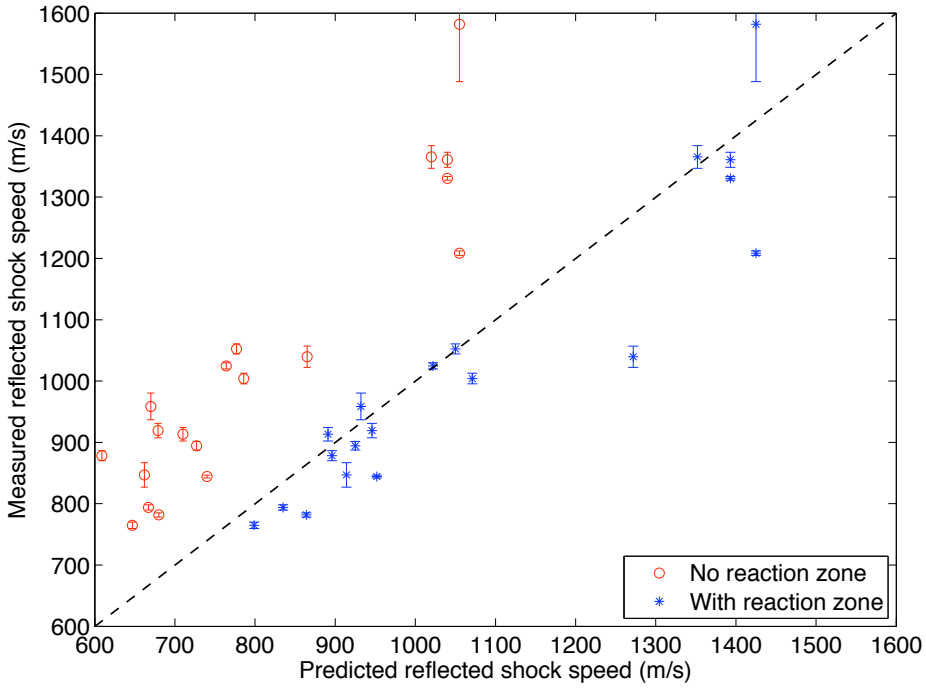

Figure 4.18: Measured reflected shock speed compared to the predicted reflected shock speed for the two methods described. The dashed black line corresponds to $U_{measured} = U_{predicted}$.

the model over-predicted the speed when the induction time was small is explained when we consider the assumptions inherent to the reacting reflected shock theory; it is at these conditions that the energy contribution after the reflected shock has passed through the induction zone would be at a minimum. A more accurate model would require that post-detonation conditions be treated as a volume that explodes, with thickness determined by the induction length. However, given that the current reacting shock model incorporates a more complete understanding of the one-dimensional ZND detonation structure to accurately predict the reflected shock speed for most conditions considered (especially the 10 and 25 kPa fill pressure conditions), we believe that the source of the reflected shock wave discrepancy has been determined.

As given in table 4.3, the reflected shock is rapidly decelerating as it propagates away from the end-wall. In figure 4.19 we examine the speed of the reflected shock using measurements taken when the reflected shock was more than 100 mm from the

Table 4.4: Reflected shock speeds fit to pressure and image data compared to the idealized no reaction zone reflected shock speed and the reacting shock speed. The values Δ_{rsi} and Δ_{rsr} are the difference of the idealized reflected shock speed and reacting shock speed relative to the fit shock speed.

Experiment Parameters				Theoretical Conditions			
Shot Number	p_1 (kPa)	Mixture	U_{rs} (m/s)	U_{rsi} (m/s)	Δ_{rsi} (%)	U_{rsr} (m/s)	Δ_{rsr} (%)
2163	10	$2H_2$-O_2	1365 ± 18	1020 ± 1	-25.3	1352	-1.0
2164	10	$2H_2$-O_2-3Ar	913 ± 11	710 ± 1	-22.2	891	-2.4
2166	10	$2H_2$-O_2-12Ar	765 ± 5	647 ± 1	-15.4	799	4.5
2167	10	$2H_2$-O_2-$3N_2$	1025 ± 5	764 ± 1	-25.4	1022	-0.3
2168	10	$2H_2$-O_2-$1.5CO_2$	847 ± 20	662 ± 1	-21.8	914	7.9
2152	25	$2H_2$-O_2	1331 ± 3	1040 ± 3	-21.8	1393	4.7
2179	25	$2H_2$-O_2	1361 ± 12	1040 ± 3	-23.6	1393	2.4
2161	25	$2H_2$-O_2-3Ar	894 ± 7	727 ± 1	-18.7	925	3.4
2162	25	$2H_2$-O_2-12Ar	794 ± 4	667 ± 1	-16.0	835	5.2
2160	25	$2H_2$-O_2-$3N_2$	1052 ± 8	777 ± 1	-26.2	1050	-0.2
2158	25	$2H_2$-O_2-$1.5CO_2$	959 ± 22	670 ± 1	-30.1	932	-2.8
2180	50	$2H_2$-O_2	1208 ± 4	1055 ± 2	-12.7	1425	17.9
2186	50	$2H_2$-O_2	1582 ± 94	1055 ± 2	-33.3	1425	-9.9
2170	50	$2H_2$-O_2-3Ar	844 ± 2	740 ± 1	-12.4	952	12.8
2169	50	$2H_2$-O_2-12Ar	782 ± 3	680 ± 1	-13.0	864	10.5
2171	50	$2H_2$-O_2-$3N_2$	1004 ± 9	786 ± 1	-21.7	1071	6.7
2181	50	$2H_2$-O_2-$1.5CO_2$	919 ± 12	679 ± 1	-26.1	946	2.9
2188	50	C_2H_4-$3O_2$	1040 ± 17	865 ± 1	-16.8	1272	22.4
2189	50	C_2H_4-$3O_2$-$4CO_2$	878 ± 8	609 ± 1	-30.7	896	2.0

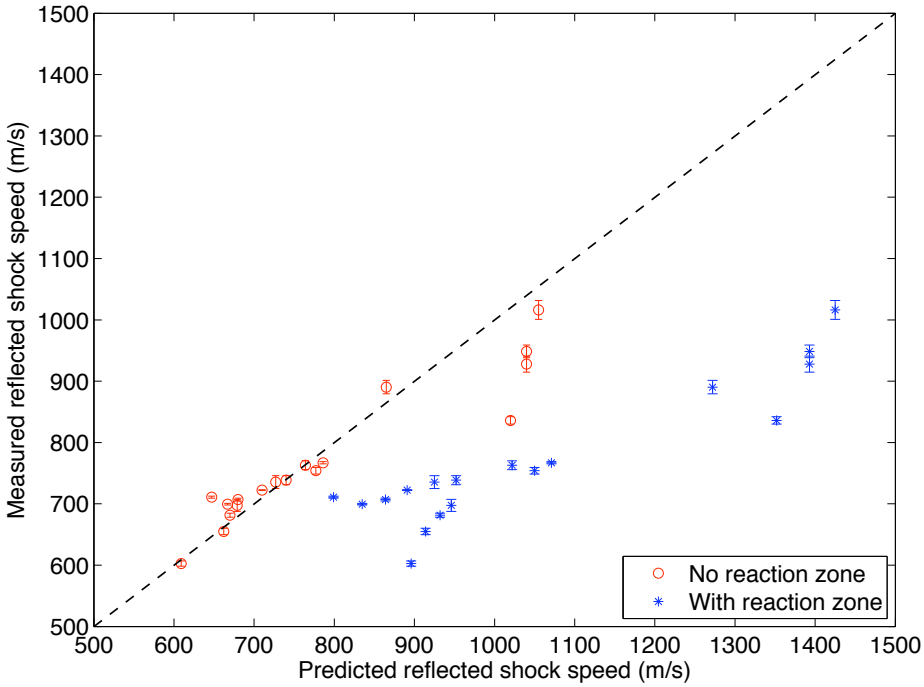

Figure 4.19: Measured reflected shock speed compared to the predicted reflected shock speed after the shock has traveled 100 mm for the two methods described. The dashed black line corresponds to $U_{measured} = U_{predicted}$.

end-wall. We have fit the shock location and time of arrival data to a first-order polynomial of the form

$$X_{rs}(t) = U_{rs}\,(t - t_0) \tag{4.15}$$

where U_{rs} and t_0 are the fit parameters. Using this fit speed, we observe that after the reflected shock has traveled at least 100 mm, its speed matches that of the no reaction zone shock model. We thus conclude that for times long after reflection has occurred, the reflected shock wave travels at the speed predicted by the model without considering the reaction zone. The effect of the acceleration at the end-wall is to offset the shock location by a distance $x_{off} = U_{rs}t_0$. This distance is on the order of 10 mm for the cases considered; it is interesting to note that this offset distance is caused by the induction zone behind the detonation wave which has a thickness on the order of 100 μm.

4.4.3 Reflected Shock Thickness

When examining images of the reflected shock wave, we observe that, like the detonation, the reflected shock exhibits a thickness and three-dimensional structure. In most experiments, the schlieren images seem to portray two reflected shock waves, one immediately behind the other. For the present discussion, we define the distance from the front of the first apparent shock to the back of the second apparent shock as the reflected shock thickness. Qualitatively, we observe that thicker incident waves result in thicker reflected waves (compare shot 2180 to shot 2168, for example). We also observe that the reflected shock thickness is approximately constant for the imaged location (consider the reflected shock progression of shot 2161, for example). It is difficult to quantify this effect because the nebulous term "optical wave thickness" is a measurement based off of uncalibrated intensities of schlieren images, and it would not be feasible to quantify using the current visualization system when the three-dimensional instabilities dominate the flow. It appears, however, that the perceived optical thickness of the reflected wave corresponds to the thickness of the incident wave multiplied by the density ratio. For shots 2179 and 2180, we use the method discussed in section 4.2.2 to determine the wave beginning and also the wave end; these shots were chosen because it was relatively easy to quantify the beginning and end of the detonation and shock waves. We may thereby determine an optical thickness for both the incident detonation, l_{det}, and the reflected shock l_{rs}. We see that the thickness of the shock wave is approximately equal to

$$l_{rs} \approx l_{det} \frac{\rho_2}{\rho_R} \tag{4.16}$$

for the cases considered. This reveals the source of the shock thickness to be the incident detonation structure, and the reduced thickness of the shock relative to the detonation is caused by the increased density. These cases are summarized in table 4.5. Note that, because this shock thickness corresponds to times on the order of 1 μs, it is not responsible for the $\sim$ 5 μs rise-times observed in the pressure measurements. The source of the longer rise time for the reflected shock wave was

Table 4.5: Approximate optical thickness of detonation and reflected shock for selected experiments as determined by schlieren images.

Experiment Parameters			Theoretical Conditions	
Shot Number	l_{det} (mm)	l_{rs} (mm)	$l_{det}\frac{\rho_2}{\rho_R}$ (mm)	Δ_{thick} (%)
2179	2.7	1.4	1.2	12%
2180	2.2	1.0	1.0	0%

not definitively determined, but it is likely caused by the variable reflected shock strength through the velocity boundary layer induced by the incident detonation as discussed in chapter 5. This variable strength will result in a non-uniform pressure that will take time to equilibrate.

4.5 Conclusions

Pressure and image data were gathered from reflected detonation experiments. These measurements were used to determine time of arrival of the detonation and reflected shock waves (from the pressure measurements) and wave locations (from the image data) in a manner that quantifies the uncertainty in the measurements. Nonlinear regression was used to determine the experimental speeds of the incident detonation and reflected shock wave in a manner that incorporated the measurement uncertainties.

These speeds were compared to the Chapman-Jouguet theory (for the detonation) and the idealized inviscid non-reacting reflected shock model. It was shown that the Chapman-Jouguet theory predicted the speed of the incident detonation for all experimental cases considered, even when the cell size was large. We also observed that the idealized reflected shock model consistently predicts a reflected shock speed that is too slow for times soon after reflection. This discrepancy indicates that the detonation wave reflection process is more complicated than allowed for by this inviscid non-reacting reflection model. This inaccuracy was resolved when we considered the one-dimensional ZND detonation structure. When we examined the case of a reflecting ZND detonation, it was apparent that the reflected shock wave would first pass

through the unreacted induction zone and thus, for times soon after reflection, there would be a reaction zone behind the reflected shock that would give it an increased speed. This speed was approximated as the detonation speed for gases at the von Neumann point reduced by the fluid velocity behind the detonation. This approximated speed was most accurate in predicting the reflected shock speed at the end-wall when the induction times were longest. These results would extend to reflected detonation waves in vessels with a circular cross section, so long as the radius of curvature of the tube wall was much larger than other relevant length scales. Therefore, we believe that the source of the previously noted discrepancy in the idealized non-reacting inviscid reflected shock wave model has been determined.

Chapter 5

Examining the Boundary Layer Behind Detonations

5.1 Introduction

During the examination of the reflected shock wave created when a detonation normally impinges upon an end-wall, it was initially suspected that the reflected shock wave was interacting with the boundary layer induced by the flow established by the incident detonation, resulting in shock wave bifurcation as illustrated in figure 5.2. The unfocused schlieren images of reflected detonation waves presented in chapter 4 seemed to indicate that bifurcation was not occurring. However, it was possible that the observed thickness of the reflected shock (as discussed in section 4.4.3) was in fact reflected shock bifurcation that was occurring on the viewing windows, and thereby obstructing any such interaction that was also occurring on the test section floor. Our desire to investigate this possibility prompted the development of the focused schlieren system discussed in section 3.3.2, which would allow us to view any shock wave–boundary layer interaction on the test section floor with minimal interference from any similar interaction occurring on the windows. This chapter discusses the results from the focused schlieren system and confirms the conclusion based on the unfocused schlieren images: shock wave–boundary layer interaction does not occur for any reflected detonation case considered. As will be discussed in section 5.2, the absence of bifurcation was initially unexpected; the reason for the absence is ex-

plained by considering the thermal and viscous boundary layers existing behind the incident detonation, as determined from a solution to the laminar boundary layer equations governing flow behind a shock wave. Finally, we use heat-flux data to examine the boundary layer induced by the incident detonation, and compare the data to predicted laminar and turbulent heat-flux results in the form of Stanton-Reynolds number plots. It is shown that the heat-flux measurements exhibit the closest agreement to a turbulent fit, but that fluctuations in the measured heat transfer imply that the results are not conclusive.

5.2 Shock Wave Bifurcation

5.2.1 Shock Bifurcation Theory

Reflected shock wave bifurcation has been extensively studied in shock tubes as it pertains to shock tube performance (Mark, 1957, Strehlow and Cohen, 1959, Taylor and Hornung, 1981, Weber et al., 1995, Davis and Sturtevant, 2000, Petersen and Hanson, 2006), ignition (Yungster, 1992, Yamashita et al., 2012), and DDT (Gamezo et al., 2005). Figure 5.1(a) shows an illustration of the basic flow features present at the side-wall behind the incident wave through which the reflected shock must propagate. The reflected shock will be affected by the reduced velocity in the boundary layer, but the extent to which it is affected depends on the fluid properties and reflected shock conditions. If bifurcation does not occur, then the reflected shock may bend forward due to the slower fluid speed into which the shock is propagating; the important thing to note about this interaction is that it is local and will not substantially affect the flow outside the boundary layer. If bifurcation does occur, the interaction will not be confined to the boundary layer and will grow to fill the entire tube. In either case, the reflected shock Mach number will change through the boundary layer and will produce a vertical gradient in fluid properties behind the reflected shock.

The characteristic flow features of normally reflected shock bifurcation are illustrated in figure 5.2. The present analysis relates to the geometry of a reflected shock

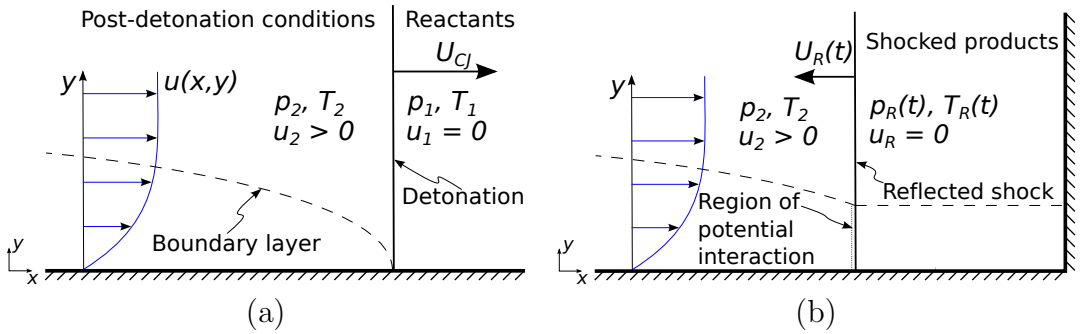

Figure 5.1: (a) Illustration of extant flow features near the side-wall behind the incident detonation. (b) A reflected shock that does not bifurcate; the gradient in fluid properties through the boundary layer in front of the reflected shock will result in a gradient in fluid properties behind the reflected shock and may result in shock wave–boundary layer interaction.

wave in a rectangular duct such as examined experimentally in chapters 2 and 4, but similar flow fields will also be observed in vessels with other cross sections so long as the radius of curvature is much larger than the height of the observed flow features. In certain experimental conditions, the reflected shock splits into a lambda shock due to interaction with the boundary layer created by the incident wave, and this lambda shock structure can grow to be many times larger than the boundary layer. Mark (1958) developed the foundational theory that explains and predicts under what conditions bifurcation will occur. Mark argues that bifurcation occurs because the stagnation pressure in the boundary layer in the reflected shock-fixed frame is less than the pressure behind the primary reflected shock. This creates a separated bubble of gas that is at a lower pressure than the gas in the free-stream, and is thereby accelerated in the direction that the reflected shock wave propagates. The condition of bifurcation is thus given as:

$$p_{0,bl} \geq p_R \qquad \Rightarrow \qquad \text{no bifurcation} \tag{5.1}$$

$$p_{0,bl} < p_R \qquad \Rightarrow \qquad \text{bifurcation} \tag{5.2}$$

where $p_{0,bl}$ is the stagnation pressure in the reflected shock-fixed frame in the boundary layer after it has been processed by the reflected shock wave. This stagnation pressure may be calculated using the conditions behind the incident wave and the reflected

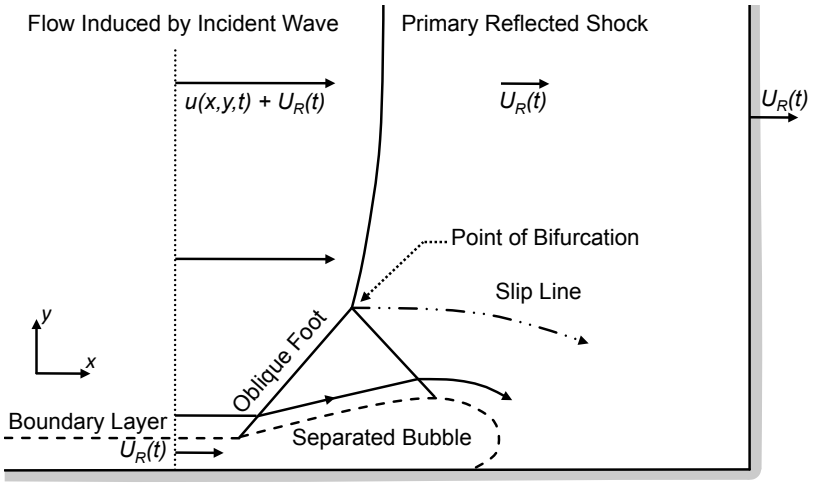

Figure 5.2: Archetypical reflected shock wave bifurcation drafted in the shock-fixed frame.

shock Mach number with the shock-jump conditions:

$$p_{0,bl} = p_2 \left[\frac{\left(\frac{\gamma+1}{2} M_{rs}^2\right)^{\gamma}}{\frac{2\gamma}{\gamma+1} M_{rs}^2 - \frac{\gamma-1}{\gamma+1}} \right]^{\frac{1}{\gamma-1}} \tag{5.3}$$

where p_2 is the pressure behind the incident wave and M_{rs} is the Mach number of the reflected shock. In shock tube experiments, the reflected shock Mach number does not change substantially through the boundary layer. In detonation experiments, however, the large thermal gradient caused by the high free-stream temperature implies that M_{rs} will vary dramatically through the boundary layer. From this equation, we see that lower values of the ratio of specific heats, γ, produces bifurcation under a wider range of shock Mach numbers. This result has also been confirmed with shock tube experiments such as those by Taylor and Hornung (1981). This suggests that reflected detonation waves, which have an especially low value of γ, will readily bifurcate.

Ziegler (2011) performed two-dimensional viscous compressible reactive computations of an incident detonation wave reflecting from a planar end-wall to examine the possibility of shock wave bifurcation for the detonation case. These simulations utilized the fluid-solver framework AMROC version 2.0 (such as used by Pantano

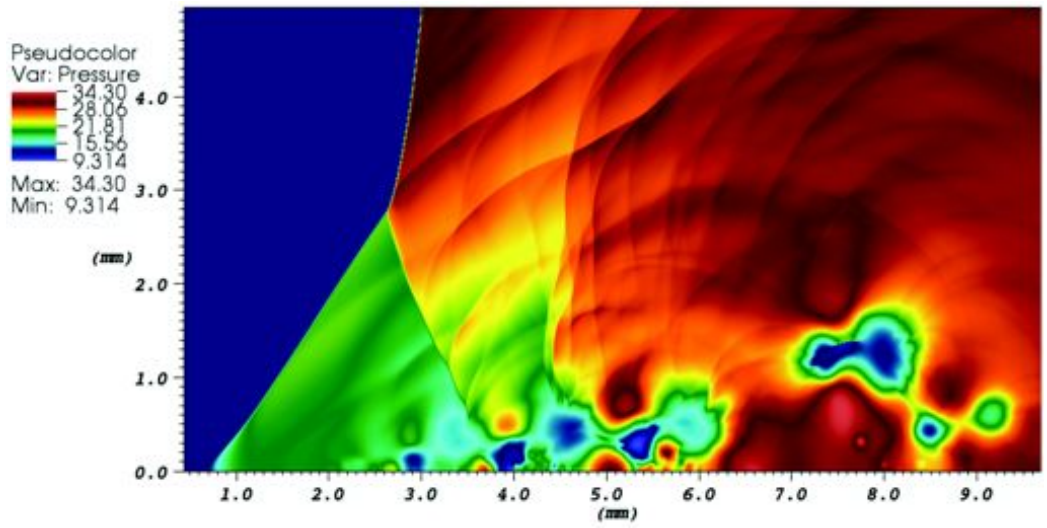

Figure 5.3: Computed reflected detonation wave exhibiting shock wave bifurcation. A detonation of stoichiometric hydrogen-oxygen with 70% argon dilution and fill pressure of 50 kPa was initially propagating to the right where it impinged on an end-wall. The bifurcated reflected shock is now observed propagating to the left. Figure by Ziegler (2011), used with permission.

et al., 2006, Matheou et al., 2010), integrated into the Virtual Test Facility (Deiterding et al., 2007), and utilizing a hybrid 6$^{\text{th}}$-order accurate Centered-Difference (CD)/WENO finite difference method (Ziegler et al., 2011) in a 40 x 40 mm domain. The case of stoichiometric hydrogen-oxygen with 70% argon dilution at fill pressure 50 kPa was chosen, and a simple thermochemical mechanism was designed to model the chemical reactions. These simulations predicted bifurcation would occur for the reflected detonation wave case, and an example image from these results is included in figure 5.3. However, although these simulations did use a no-slip boundary condition at the side-wall, the side-wall was assumed to be adiabatic, implying that there was not a significant thermal gradient through the velocity boundary layer.

None of the above analyses fully replicated the experimental detonation conditions. The initial analysis by Mark (1957), for example, assumes the temperature is constant and equal to the initial conditions. This assumption is clearly invalid for the detonation case. The simulations of Ziegler (2011) did not incorporate the cold-wall boundary condition, and thus the temperature, sound-speed, and Mach number profiles through the velocity boundary layer were not correctly reproduced. As shown

in equation (5.3), the Mach number can play a critical role in determining whether or not bifurcation occurs. Thus, with prior analyses not providing a definite answer one way or the other, we conducted reflected detonation experiments to determine if bifurcation would occur.

5.2.2 Bifurcation Experimental Results

The GDT described in chapter 3 with the focused schlieren system was used to record images of reflected detonations and to investigate the possibility of reflected shock wave–boundary layer interaction. Table 5.1 shows all cases considered with this system, and figure 5.4 shows an example pair of images recorded with the PCO.2000 camera during a reflected detonation experiment of stoichiometric hydrogen-oxygen at fill pressure 25 kPa. In the top frame of figure 5.4 we see the detonation propagating to the right, and the bottom frame shows the reflected shock propagating back to the left. Note that bifurcation is not observed; this result was consistent for all detonation experiments performed. Figures 5.5 and 5.6, for example, show reflected detonation waves of undiluted stoichiometric hydrogen-oxygen at fill pressures 10 and 40 kPa. Figures 5.7 and 5.8 show reflected detonations of stoichiometric hydrogen-oxygen with 50% and 67% argon dilution and fill pressure of 40 kPa; in these images, the reflected shock was observed to bend forward through the decreased velocity in the boundary layer, but no bifurcation was observed.

In order to conclude the investigation into shock wave bifurcation, it was deemed prudent to produce and visualize a case when bifurcation did actually occur. To accomplish this, the GDT was operated with a test mixture and conditions that were known to produce reflected shock wave bifurcation. Under these conditions, the acetylene-oxygen injection system produced a shock wave in the test mixture instead of a detonation. Two examples of the resulting interaction are shown in figures 5.10 (which used an unfocused schlieren system) and 5.9 (taken using a focused schlieren system). These images show the classic features of reflected shock wave bifurcation illustrated in figure 5.2.

Table 5.1: Initial experimental conditions used in shock wave–boundary layer analysis. Theoretical values were computed with the Shock and Detonation Toolbox.

Experiment Parameters			Theoretical Conditions	
Shot Number	p_1 (kPa)	Mixture	U_{CJ} (m/s)	U_{R0} (m/s)
2088	10	$2H_2$-O_2	2711	1026
2089	10	$2H_2$-O_2	2711	1026
2106	10	$2H_2$-O_2-3Ar	1838	717
2107	10	$2H_2$-O_2-6Ar	1664	668
2084	25	$2H_2$-O_2	2760	1049
2085	25	$2H_2$-O_2	2760	1049
2090	25	$2H_2$-O_2	2711	1026
2117	25	$2H_2$-O_2	2711	1026
2119	25	$2H_2$-O_2	2711	1026
2120	25	$2H_2$-O_2	2711	1026
2104	25	$2H_2$-O_2-3Ar	1872	736
2103	25	$2H_2$-O_2-6Ar	1691	686
2102	25	$2H_2$-O_2-15Ar	1457	661
2115	25	$2H_2$-O_2-15Ar	1457	661
2091	40	$2H_2$-O_2	2786	1061
2092	40	$2H_2$-O_2	2786	1061
2093	40	$2H_2$-O_2-3Ar	1889	746
2095	40	$2H_2$-O_2-3Ar	1889	746
2097	40	$2H_2$-O_2-6Ar	1705	696
2098	40	$2H_2$-O_2-6Ar	1705	696
2099	40	$2H_2$-O_2-15Ar	1462	670
2100	40	$2H_2$-O_2-15Ar	1462	670
2101	40	$2H_2$-O_2-15Ar	1462	670
2125	25	C_2H_4-$3O_2$	2306	869
2134	25	C_2H_4-$3O_2$	2306	869
2140	25	C_2H_4-$3O_2$	2306	869
2141	25	C_2H_4-$3O_2$	2306	869
2003	15	N_2O	N/A	N/A
2042	15	N_2O	N/A	N/A
2044	15	N_2O	N/A	N/A
2045	15	N_2O	N/A	N/A
2055	15	N_2O	N/A	N/A

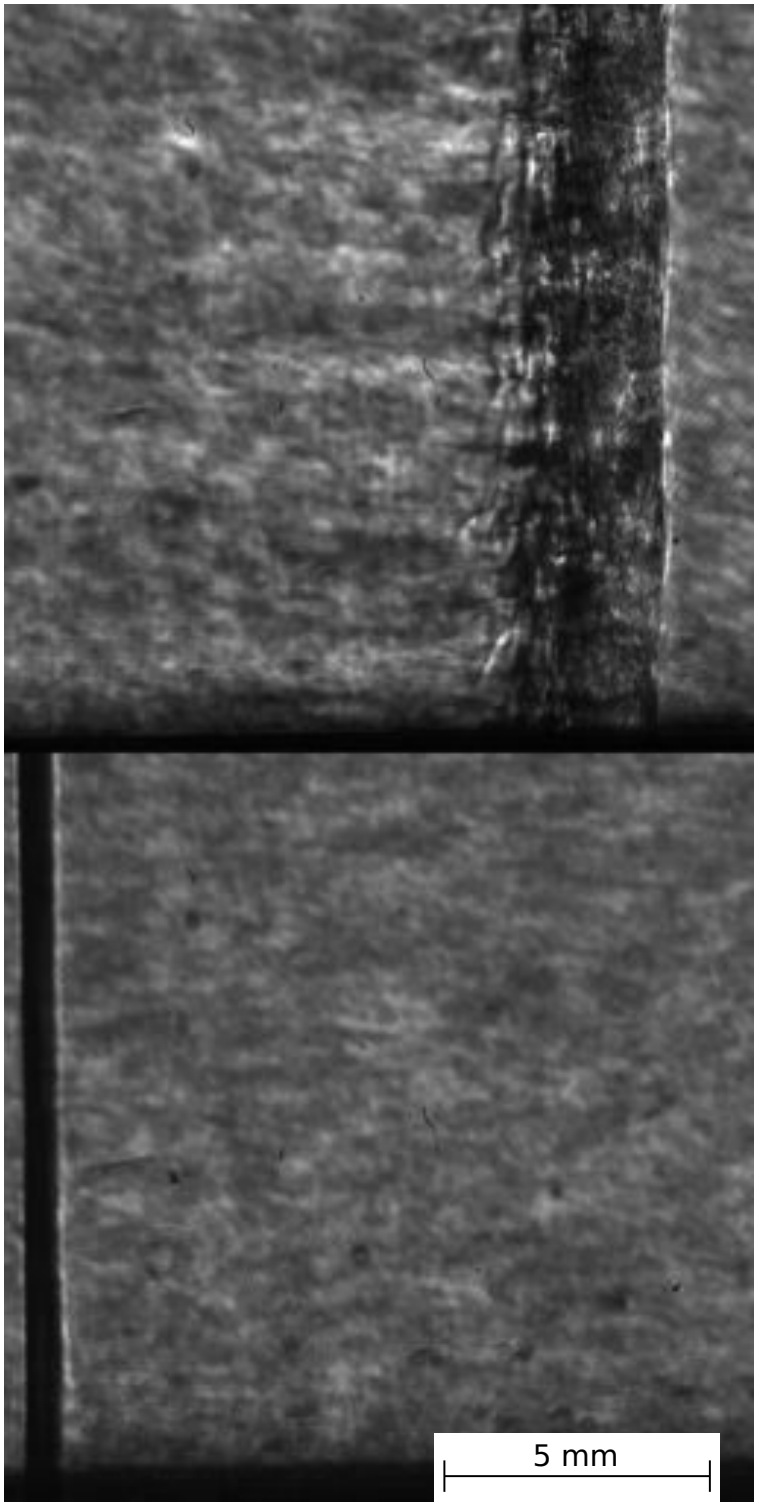

Figure 5.4: Focused schlieren image of shot 2120 of a detonation in stoichiometric hydrogen-oxygen with 10 kPa fill pressure. The top image shows the detonation propagating to the right, and the bottom image shows the reflected shock propagating back to the left.

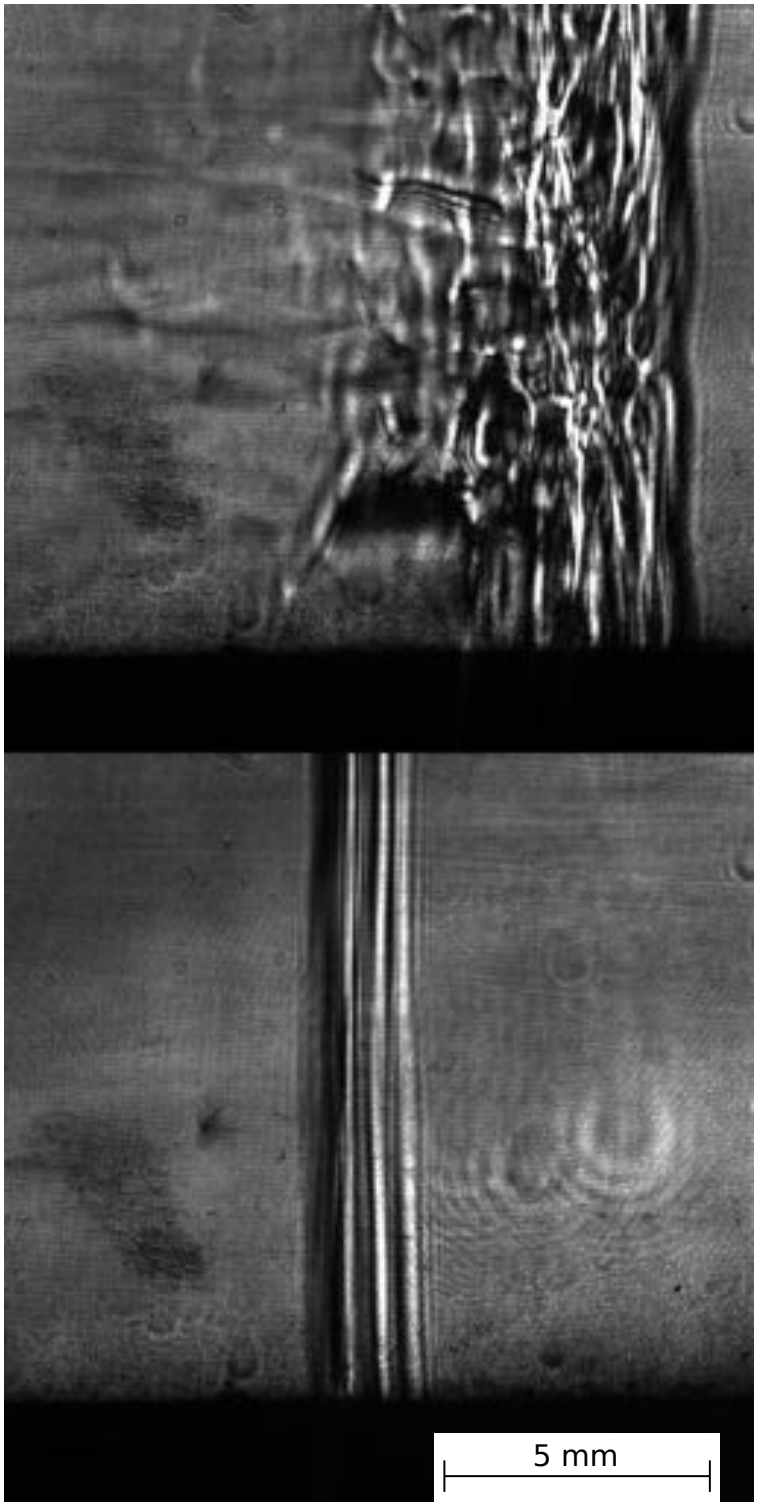

Figure 5.5: Focused schlieren image of shot 2089 of a detonation in stoichiometric hydrogen-oxygen with 10 kPa fill pressure. The top image shows the detonation propagating to the right, and the bottom image shows the reflected shock propagating back to the left.

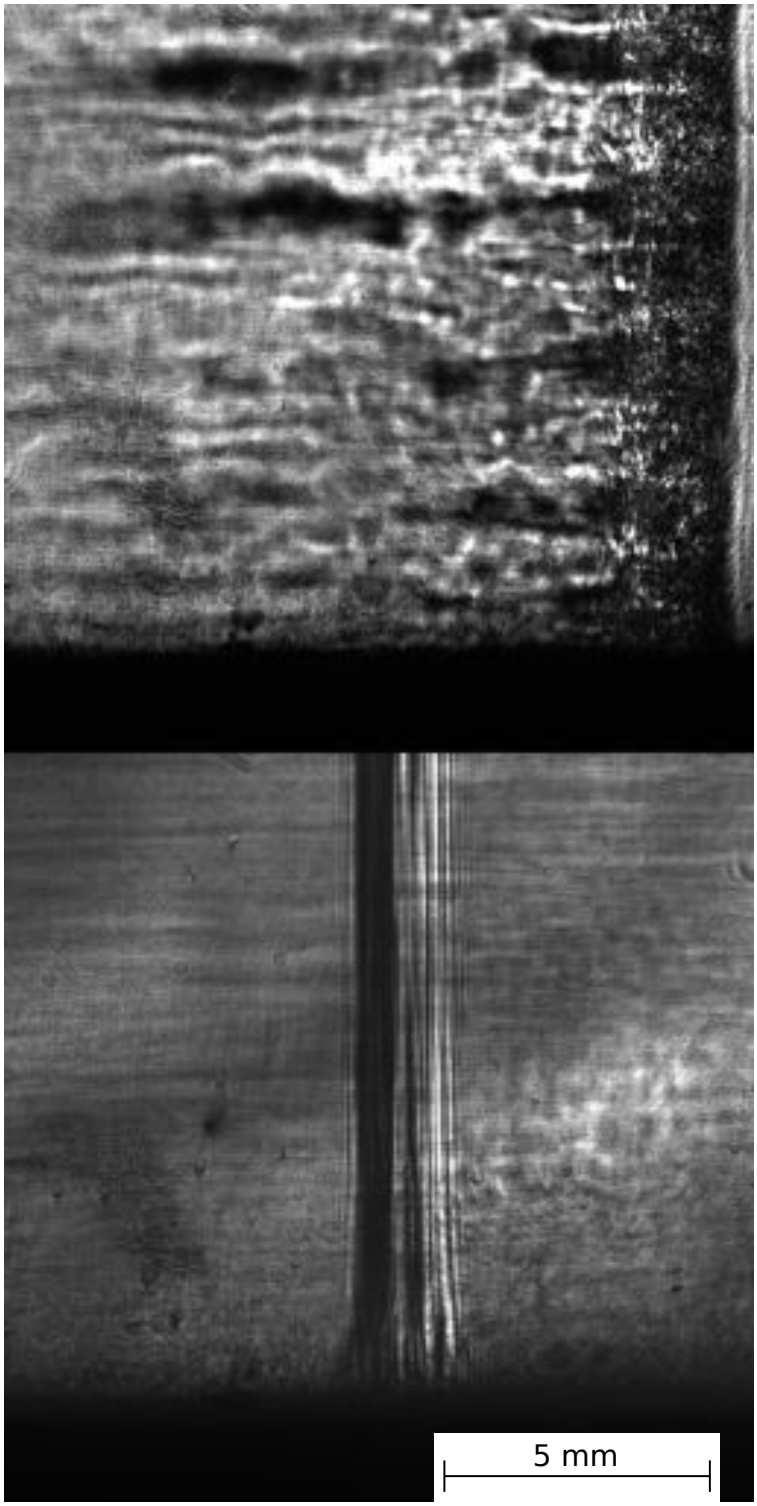

Figure 5.6: Focused schlieren image of shot 2092 of a detonation in stoichiometric hydrogen-oxygen with 40 kPa fill pressure. The top image shows the detonation propagating to the right, and the bottom image shows the reflected shock propagating back to the left.

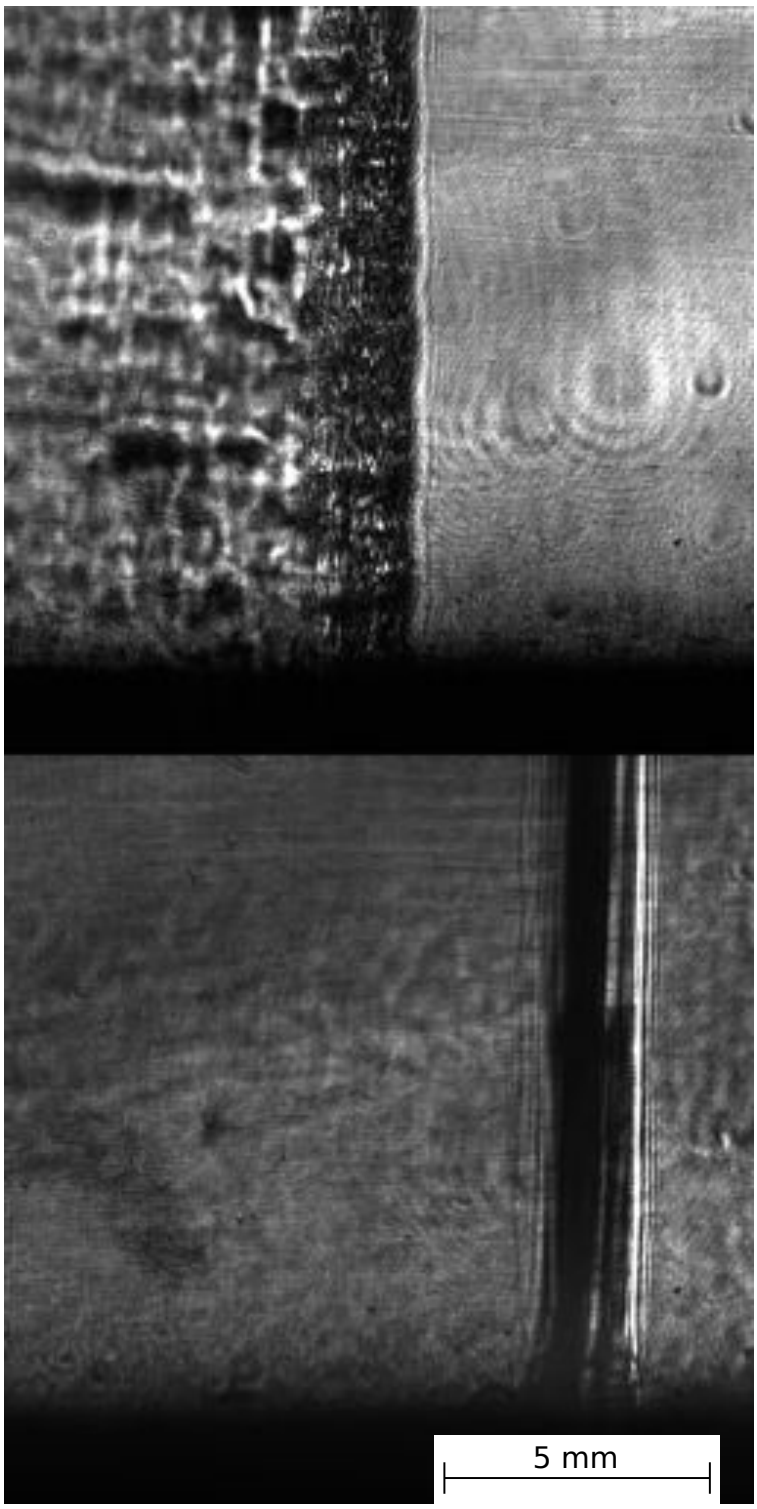

Figure 5.7: Focused schlieren image of shot 2095 of a detonation in stoichiometric hydrogen-oxygen with 50% argon dilution at a fill pressure of 40 kPa. The top image shows the detonation propagating to the right, and the bottom image shows the reflected shock propagating back to the left.

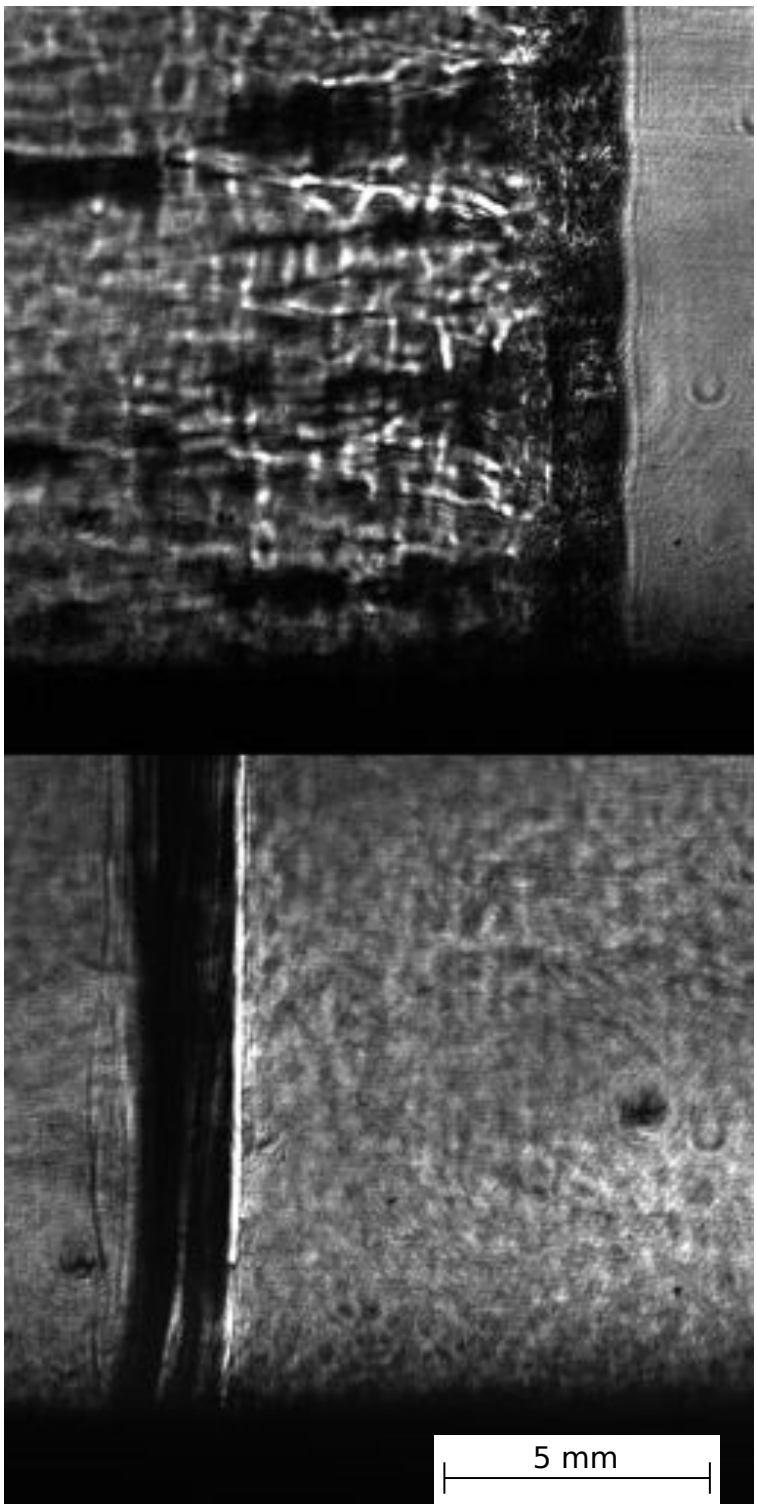

Figure 5.8: Focused schlieren image of shot 2098 of a detonation in stoichiometric hydrogen-oxygen with 67% argon dilution at a fill pressure of 40 kPa. The top image shows the detonation propagating to the right, and the bottom image shows the reflected shock propagating back to the left.

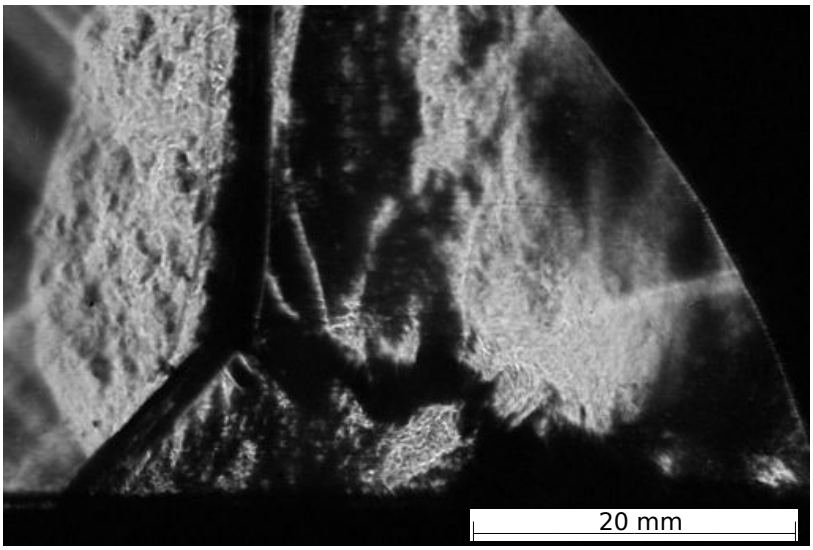

Figure 5.9: Unfocused schlieren image of shot 2003 of a reflected shock in pure nitrous oxide at fill pressure 15 kPa using schlieren visualization system #1.

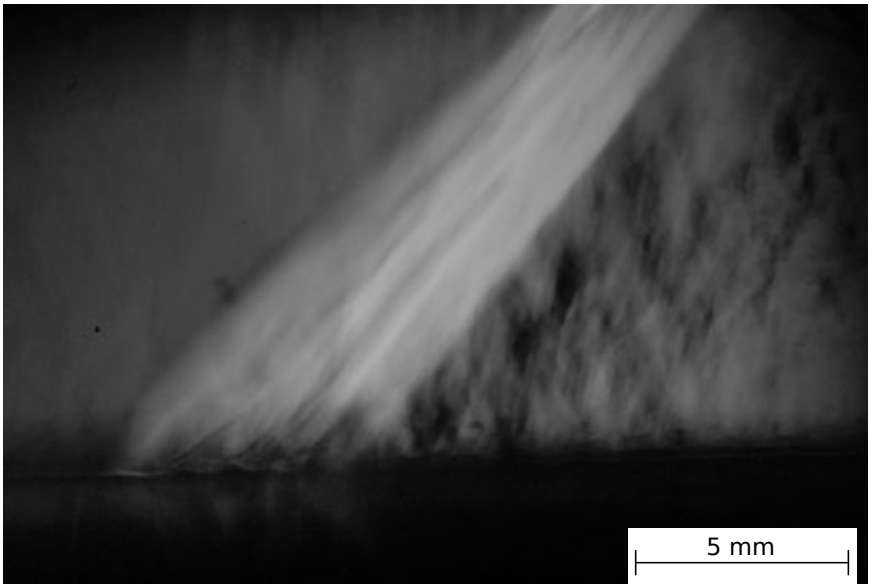

Figure 5.10: Focused schlieren image of shot 2044 of a reflected shock in pure nitrous oxide at fill pressure 15 kPa using schlieren visualization system #5.

The effects of the bifurcated lambda shock may be seen in pressure measurements, such as those shown in figure 5.11. Here we see two distinct pressure increases from the shock bifurcation, representing each leg of the lambda shock. For example, considering the pressure signal for the gauge located 38 mm from the end-wall, we see the incident shock arrive at time $t_2 = -0.04$ ms, and then the reflected bifurcated oblique shocks arrive at times $t_3 = 0.16$ ms and $t_4 = 0.26$ ms. Considering that figures 5.4–5.8 show none of the characteristics of bifurcation seen in figures 5.9 and 5.10, and that the pressure measurements examined in chapter 4 do not follow the qualitative trends observed in the experiments in which bifurcation was known to occur, we conclude that reflected shock wave bifurcation did not occur in any of the detonation experiments performed. To examine the reason for this, we will consider a laminar boundary layer solution for the flow field behind a detonation wave.

5.3 Laminar Boundary Layer Analysis

We now consider the boundary layer growth behind a detonation using the wave-fixed frame of reference shown in figure 5.12. In order to make the problem practical to solve analytically, we neglected all multi-dimensional aspects of the detonation and treated it as a planar shock wave propagating at speed U_{CJ} with post-shock conditions equal to the Chapman-Jouguet state.

A complete derivation of the compressible two-dimensional steady free-stream boundary layer equations is included in appendix F; here we highlight the techniques and assumptions used in the derivation, and discuss the results. We begin by using the Levy-Lees transformation to transition from (x, y, t) to (ζ, η, τ) via

$$\zeta(x,t) = 1 - \frac{x}{X_D(t)} \tag{5.4}$$

$$\eta(x,y,t) = \frac{\displaystyle\int_0^y \frac{\rho(x,y',t)}{\rho_2} dy'}{\delta(x,t)} \tag{5.5}$$

$$\tau(t) = \frac{tU_{CJ}}{L} \tag{5.6}$$

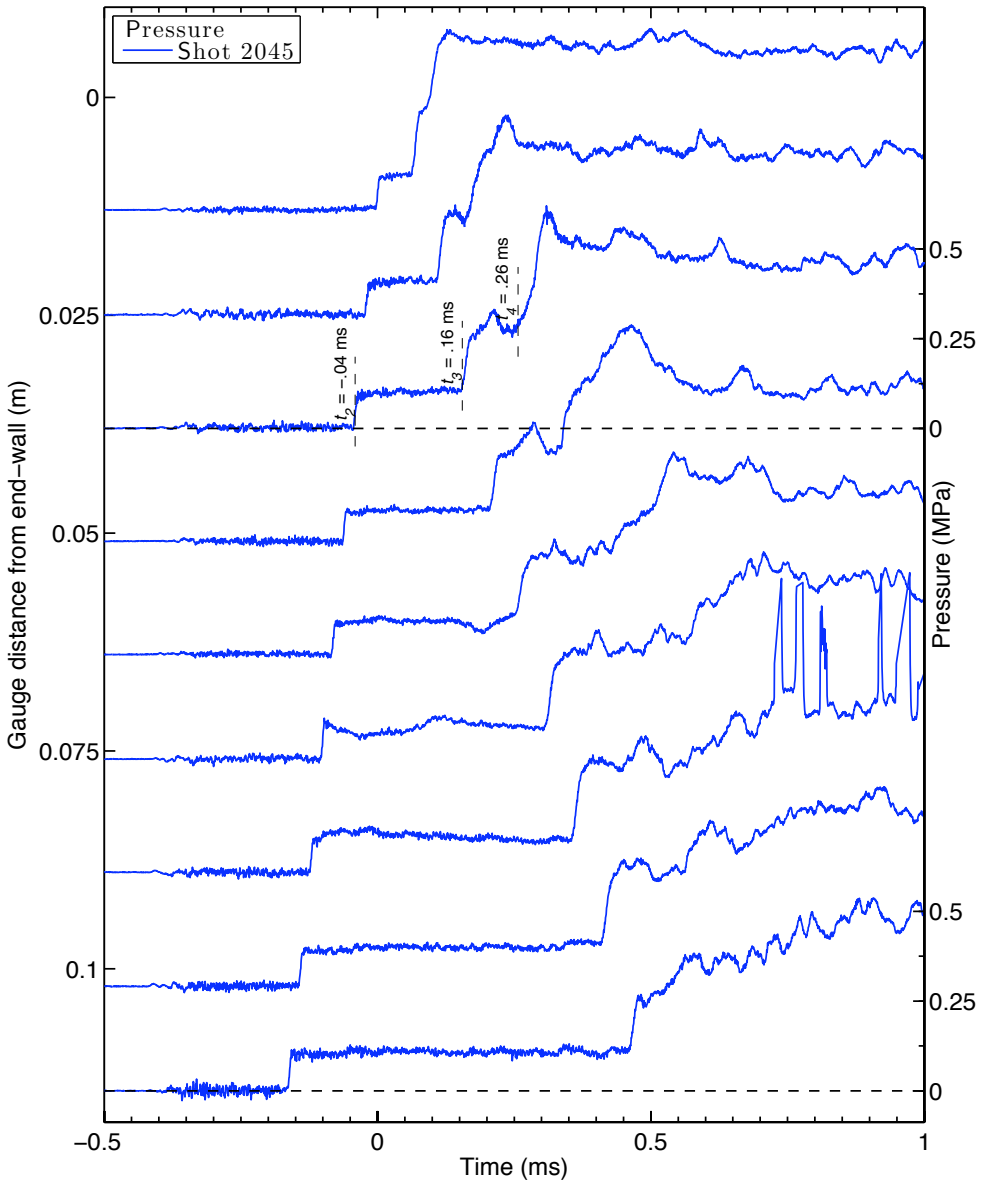

Figure 5.11: Pressure measurements for shot 2045 of a shock in pure nitrous oxide at fill pressure 15 kPa in which bifurcation occurred. The incident shock arrives at time t_2, the leading shock of the bifurcated foot arrives at time t_3, and the trailing bifurcated shock arrives at time t_4.

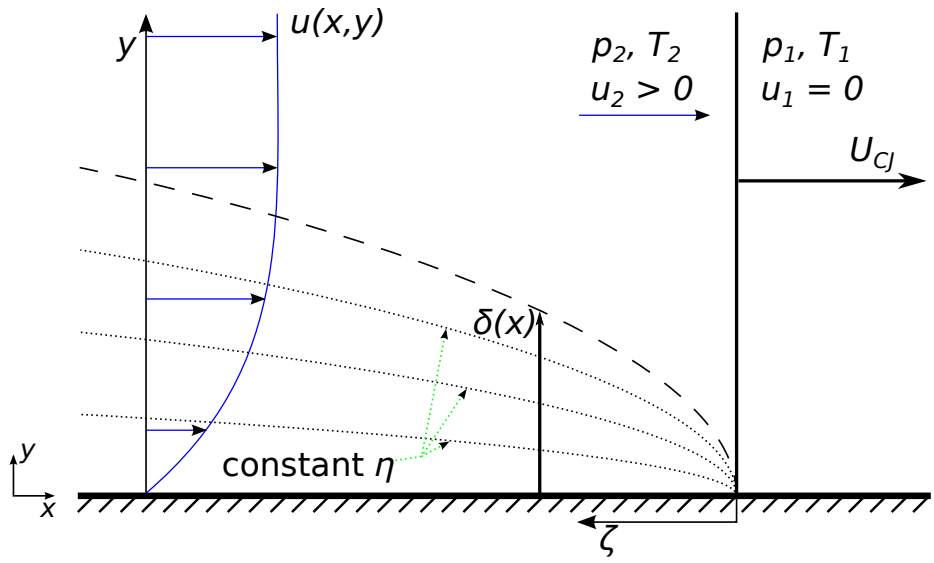

Figure 5.12: Frame of reference used for boundary layer calculations.

where $X_D(t)$ is the location of the detonation, $\delta(x,t)$ is the boundary layer thickness, and ρ, U_{CJ}, and L are the gas density, detonation speed, and detonation tube length, respectively. We may then use the compressible stream function Ψ defined to be

$$\Psi(\zeta,\eta,\tau) = u_2\delta(\zeta,\tau)\, f(\eta) \tag{5.7}$$

such that

$$\rho u = \rho_2 \frac{\partial \Psi}{\partial y} \tag{5.8}$$

$$\rho v = -\rho_2 \left[\frac{\partial \Psi}{\partial x} + \frac{\partial}{\partial t}(\eta\delta)\right]. \tag{5.9}$$

Then if we use

$$\delta(\zeta,\tau) = \sqrt{\frac{\mu_2 L\tau\zeta}{\rho_2 U_{CJ}}} \tag{5.10}$$

the conservation of mass and momentum equations become

$$(Cf_{\eta\eta})_\eta + \frac{1}{2}\left(\eta - \frac{u_2}{U_{CJ}}f\right) f_{\eta\eta} = 0 \tag{5.11}$$

where subscript η represents the derivative with respect to η and C is the Chapman-Rubesin parameter defined by

$$C = \frac{\rho\mu}{\rho_2\mu_2}. \tag{5.12}$$

The boundary conditions are no-flow at the side-wall, and the free-stream condition $u = u_2$ implies

$$f(0) = f_\eta(0) = 0 \tag{5.13}$$

$$\lim_{\eta\to\infty} f_\eta(\eta) = 1. \tag{5.14}$$

Taking the Chapman-Rubesin parameter to be unity, we arrive at the classic equation for boundary layer growth behind a shock wave (Schlichting, 1979):

$$f_{\eta\eta\eta} + \frac{1}{2}\left(\eta - \frac{u_2}{U_{CJ}} f\right) f_{\eta\eta} = 0. \tag{5.15}$$

A similar analysis may be applied to the conservation of energy equation to produce

$$g_{\eta\eta} + \frac{Pr}{2}\left(\eta - \frac{u_2}{U_{CJ}} f\right) g_\eta = -PrEc f_{\eta\eta}^2. \tag{5.16}$$

Here g is the enthalpy non-dimensionalized by the free-stream enthalpy

$$g(\eta) = \frac{h(\eta)}{h_2}; \tag{5.17}$$

Pr is the Prandtl number, defined to be the ratio of viscous diffusion to thermal diffusion computed from

$$Pr = \frac{c_p\mu}{k} \tag{5.18}$$

where c_p is the specific heat at constant pressure, μ is the dynamic viscosity, and k is the thermal conductivity; and Ec is the Eckert number, which is the ratio of kinetic energy to free-stream enthalpy

$$Ec = \frac{u_2^2}{c_p T_2}. \tag{5.19}$$

The boundary conditions are given by the known post-detonation free-stream conditions at the limit as $\eta \to \infty$ and the cold-wall boundary condition of a fixed wall temperature at $\eta = 0$.

$$g(0) = \frac{T_w}{T_2} \tag{5.20}$$

$$\lim_{\eta \to \infty} g(\eta) = 1. \tag{5.21}$$

The solutions to Equations 5.15 and 5.17 were obtained using the Matlab function `ode45` combined with a shooting technique to implement the boundary conditions. The resulting velocity and temperature profiles are plotted in figure 5.13 for the specific case of a stoichiometric hydrogen-oxygen detonation at fill pressure 25 kPa. Once the temperature profile is known, the heat-flux to the wall may be computed using

$$\dot{q} = k \left. \frac{dT}{dy} \right|_{y=0} \tag{5.22}$$

where k is the thermal conductivity in the fluid. This predicted heat-flux is compared with the measured heat-flux behind detonations in section 5.4.

The reason bifurcation did not occur in the detonation experiments lies in the stagnation pressure profile through the boundary layer, as plotted in figure 5.14. The ratio of the stagnation pressure in the reflected shock-fixed frame to the pressure behind the main portion of the reflected shock wave is plotted through the boundary layer alongside the Mach number of the reflected shock. We observe that the pressure ratio is strictly greater than 1, implying that the no-bifurcation criteria given in

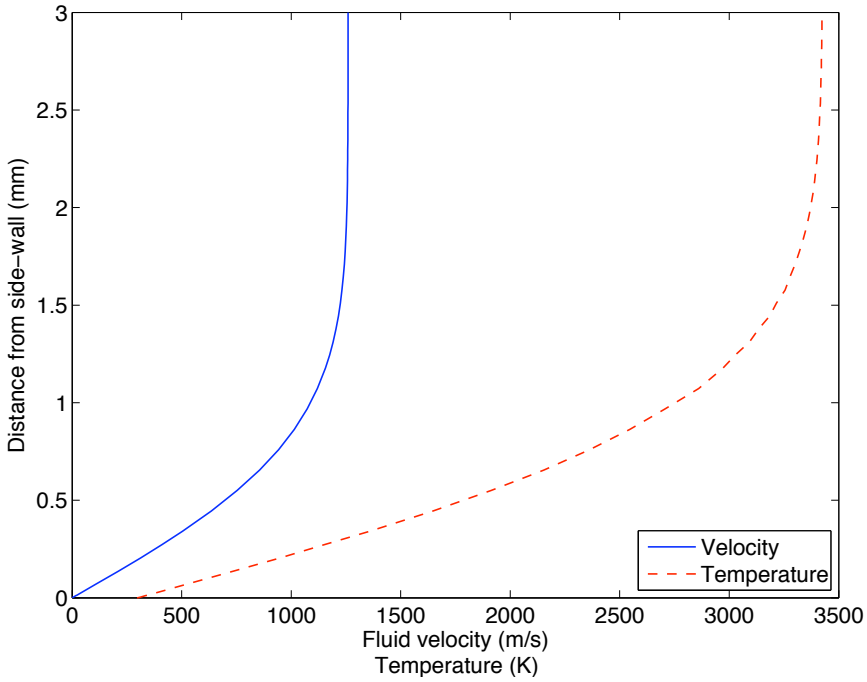

Figure 5.13: Solution of the laminar boundary layer equations for flow behind a shock wave with post-shock conditions matching a stoichiometric hydrogen-oxygen detonation with fill pressure 25 kPa computed 1 m behind the detonation.

equation (5.1) is satisfied and bifurcation of the reflected shock wave does not occur. The cold-wall boundary condition causes the Mach number of the reflected shock wave to be larger at the wall than in the free-stream, even though the speed is decreased at the wall. The increased Mach number effects the increased stagnation pressure and prevents bifurcation of the reflected shock wave.

We can also use the laminar boundary layer analysis to examine the theoretical implications of an adiabatic wall as shown in figure 5.15. By replacing the cold-wall boundary condition with the requirement that

$$\left.\frac{dT}{dy}\right|_{y=0} = 0 \tag{5.23}$$

corresponding to an adiabatic wall, we observe a considerable difference in the temperature profile as plotted in figure 5.15(a). With an adiabatic wall, viscous dissipation serves to increase the temperature in the boundary layer. This implies that the reflected shock Mach number in the boundary layer is much smaller for the case of an

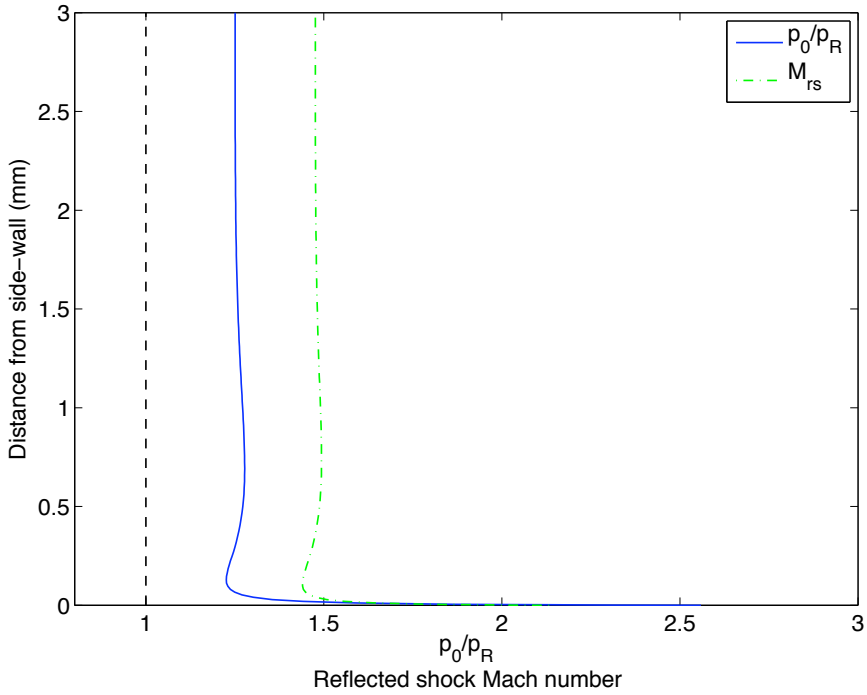

Figure 5.14: Stagnation pressure ratio and reflected shock Mach number profiles in the shock-fixed frame plotted through a laminar boundary layer 1 m behind a detonation as computed for conditions matching a stoichiometric hydrogen-oxygen detonation with fill pressure 25 kPa.

adiabatic wall. This in turn affects the stagnation pressure ratio across the reflected shock as plotted in figure 5.15(b). The decreased reflected shock Mach number causes a corresponding decrease in the stagnation pressure computed in the shock-fixed frame such that the stagnation pressure dips below the pressure computed at the reflecting end-wall. Therefore, the criteria for bifurcation given in equation (5.2) is satisfied for the case of an adiabatic wall. This agrees with the computational results of Ziegler (2011) (which were performed using an adiabatic wall).

5.4 Heat-Flux Data

Heat-flux measurements were performed to investigate the nature of the boundary layer behind the incident detonation wave. The most reliable results with the best signal-to-noise ratio were obtained for experimental conditions where the free-stream temperature was large–this eliminated the highly diluted cases from consideration–

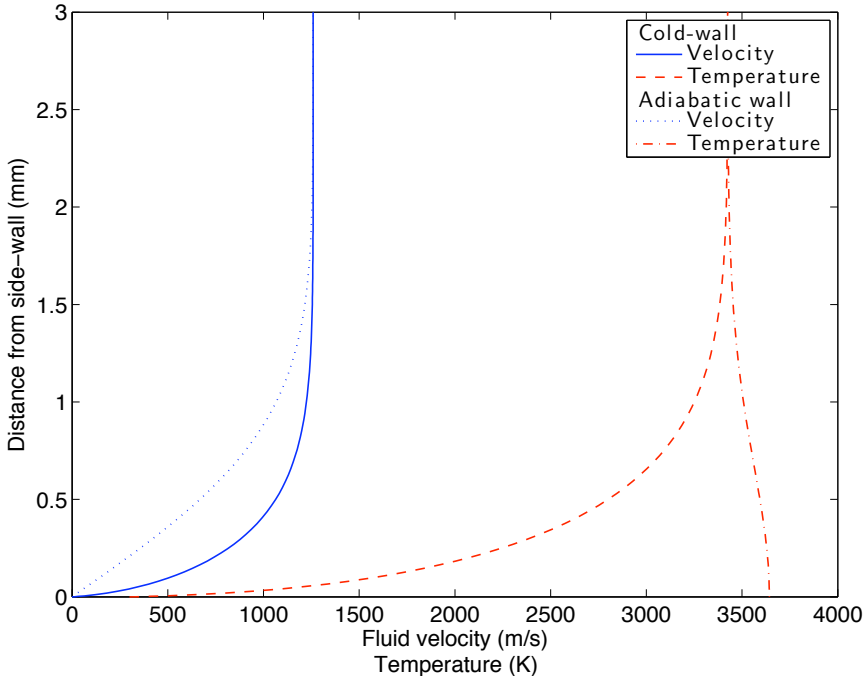

(a)

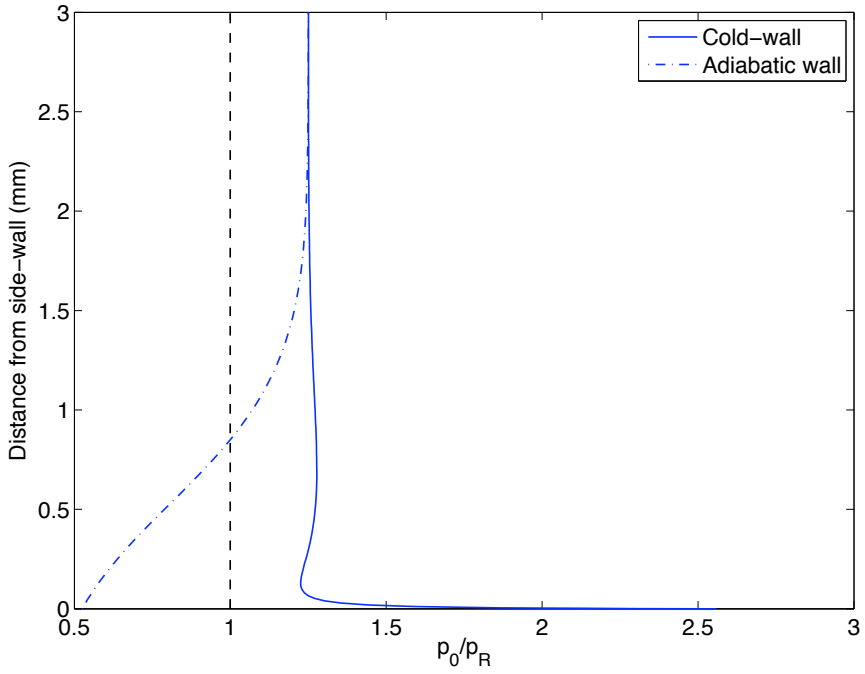

(b)

Figure 5.15: The effect of an adiabatic wall boundary condition is examined in (a) the velocity and temperature profiles and (b) the stagnation pressure ratio divided by the pressure at the reflecting end-wall. Conditions are those of a laminar boundary layer 1 m behind a stoichiometric hydrogen-oxygen detonation with fill pressure 25 kPa.

Table 5.2: Initial experimental conditions used in the heat-flux analysis. Theoretical values were computed with the Shock and Detonation Toolbox.

Experiment Parameters			Theoretical Conditions	
Shot Number	p_1 (kPa)	Mixture	u_2 (m/s)	T_2 (K)
2089	10	$2H_2$-O_2	1239	3272
2090	25	$2H_2$-O_2	1260	3425
2119	25	$2H_2$-O_2	1260	3425
2120	25	$2H_2$-O_2	1260	3425
2104	25	$2H_2$-O_2-3Ar	840	3179
2091	40	$2H_2$-O_2	1270	3508
2093	40	$2H_2$-O_2-3Ar	846	3245
2180	50	$2H_2$-O_2	1276	3548
2123	25	C_2H_4-$3O_2$	1063	3684
2124	25	C_2H_4-$3O_2$	1063	3684
2125	25	C_2H_4-$3O_2$	1063	3684
2188	50	C_2H_4-$3O_2$	1067	3783

and we focused on the experimental conditions given in table 5.2.

Figure 5.16 portrays the time-resolved heat-flux data for shot 2090 compared to the laminar boundary layer results as seen in figure 5.13. The dashed vertical lines correspond to the arrival window for the incident detonation and reflected shock waves as determined from the pressure signals using the method described in section 4.2.1. The incident detonation wave is clearly marked by a spike in both measured and predicted heat transfer–the highest heat transfer is measured immediately behind the detonation front when the boundary layer is thinnest. We observe that the reflected shock serves to moderately increase the heat transfer due to the increase in temperature associated with the reflected shock. The data are compared in more detail below. In comparison to the results of Liu et al. (1983), who performed simulations on the laminar boundary layer behind detonation waves, and Laderman et al. (1962), who performed experiments, we see that our results follow similar trends and share the same order of magnitude. Laderman et al. (1962), for example, measured a heat-flux of approximately 8 MW/m^2 100 μs behind a stoichiometric hydrogen-oxygen detonation of fill pressure 101 kPa; this is on the same order of magnitude as our results (we measure a heat-flux of approximately 10 MW/m^2 100 μs behind a stoichiometric

hydrogen-oxygen detonation of fill pressure 50 kPa).

A typical method used to analyze heat transfer data for high-speed flow is to non-dimensionalize the data and plot it in Stanton number-Reynolds number form, where the Stanton and Reynolds numbers are computed from

$$Re = \frac{\rho_2 u_2^2 \left(t - t_a\right)}{\mu_2} \tag{5.24}$$

$$St = \frac{\dot{q}}{\left(h_2 - h_w\right) \rho_2 u_2} \tag{5.25}$$

and where t_a is the arrival time of the detonation as determined using the method described in section 4.2 (Petersen and Hanson, 2003). Appropriate thermodynamic conditions were computed using the GRI30 mechanism and the Shock and Detonation Toolbox. Because we are most interested in examining the boundary layer profile behind the incident detonation, we will focus our analysis on gauges with the furthest spacing from the reflecting end-wall that provide the longest test time between detonation and shock arrivals. Heat-flux results from shots 2090, 2119, and 2120 for four gauge locations are given in figure 5.17. These shot numbers all correspond to a stoichiometric hydrogen-oxygen detonation at fill pressure 25 kPa. Figure 5.18 shows similar data for the higher fill pressure conditions. We observe that the general trends in the heat-transfer data were repeatable between shots and gauge locations, with differences between specific gauges primarily due to high amplitude oscillations in the measured Stanton number; these fluctuations had relative magnitudes up to 25%. Also plotted is a turbulent Stanton-Reynolds number relationship using the Reynolds analogy to obtain a relationship between the Stanton number and the skin friction coefficient, C_f,

$$St \approx \frac{C_f}{2Pr^{2/3}} \frac{T_{aw} - T_w}{T_2 - T_w} \tag{5.26}$$

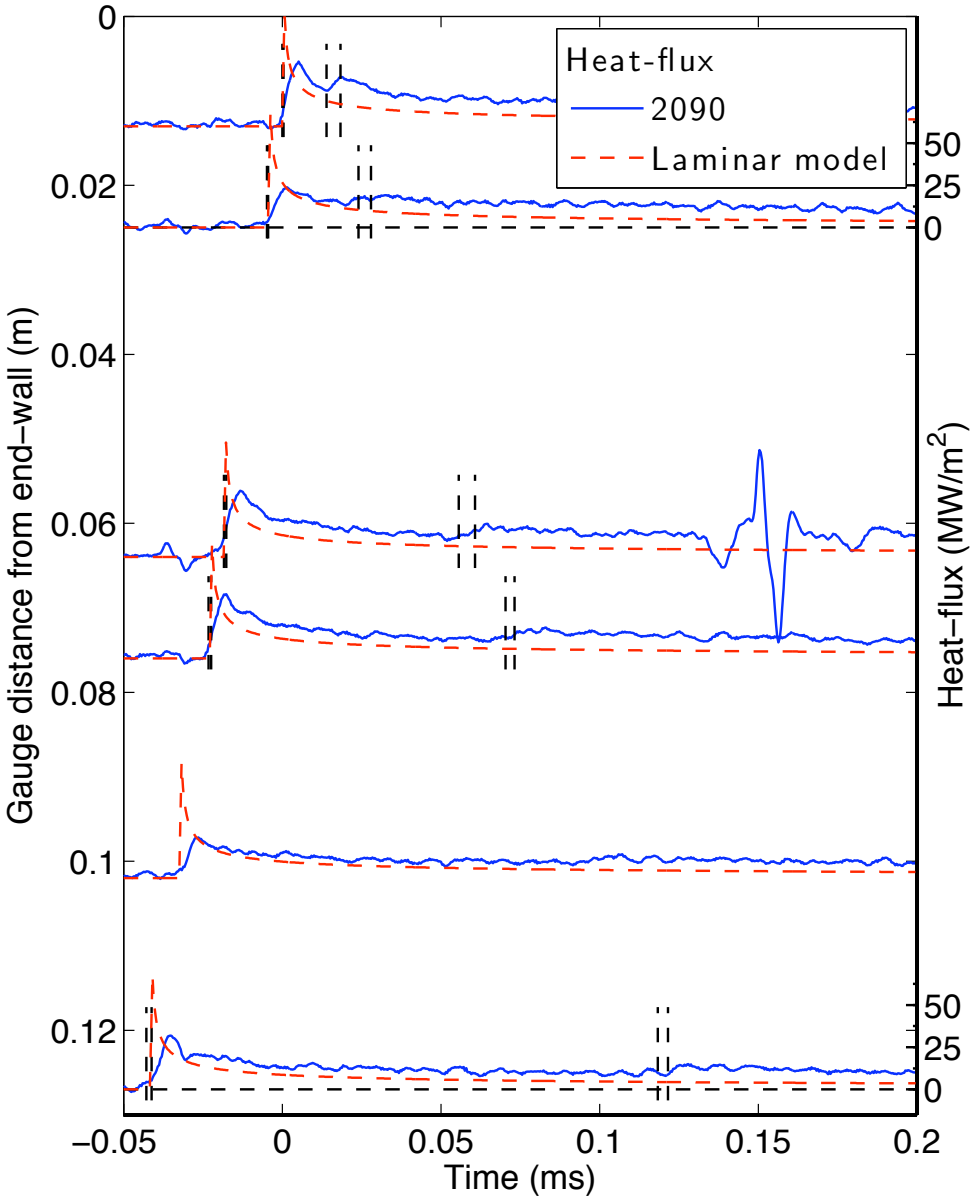

Figure 5.16: Heat-flux results for shot 2090, a stoichiometric hydrogen-oxygen detonation of fill pressure 25 kPa. Experimental measurements (blue) are compared to the laminar boundary layer heat-flux model (red). The vertical dashed lines represent detonation and reflected shock arrival windows.

where $T_w = 300$ K is the temperature of the wall and T_{aw} is the temperature of an adiabatic wall. T_{aw} is computed using

$$T_{aw} = T_2 \left(1 + \sqrt{Pr} \frac{\gamma_{2,eq} - 1}{2} M_2^2 \right). \tag{5.27}$$

This was combined with a turbulent relationship for the skin friction coefficient as determined by Schlichting (1979):

$$C_f = \frac{0.0592}{Re^{1/5}} \tag{5.28}$$

to compute the turbulent Stanton-Reynolds line shown.

Glass and Patterson (1955) report that laminar boundary layer growth in a shock tube can occur even in the presence of transverse waves such as seen in detonations. Further, the computational laminar boundary layer solution of Liu et al. (1983) obtains agreement with the experimental results of Laderman et al. (1962) to approximately 50%. However, in all experiments performed in this study, we observed that the turbulence fit functions as a better predictor for the measured heat-flux results than the laminar boundary layer solution for Reynolds numbers above approximately 10^5. Per the work of Tanaki et al. (2009) and of Petersen and Hanson (2003), we would expect transition to occur between Reynolds numbers of $0.6 \cdot 10^6 < Re_{tr} < 3 \cdot 10^6$. We do not see a sharp rise in heat-flux as might be expected of turbulent transition; however, we do observe an increase in the frequency and peak-to-peak amplitude of the oscillations in the Stanton number beginning at a Reynolds number of approximately 10^5, which may indicate transition has occurred. Unfortunately, the fluctuations in the data make any concrete conclusion as to the nature of the boundary layer impossible. As the transverse waves impinge upon the side-wall, we would expect the thickness of the boundary layer to be affected. This might be responsible for the observed fluctuations in heat-flux, and implies that both laminar and turbulent fits considered are highly idealized situations.

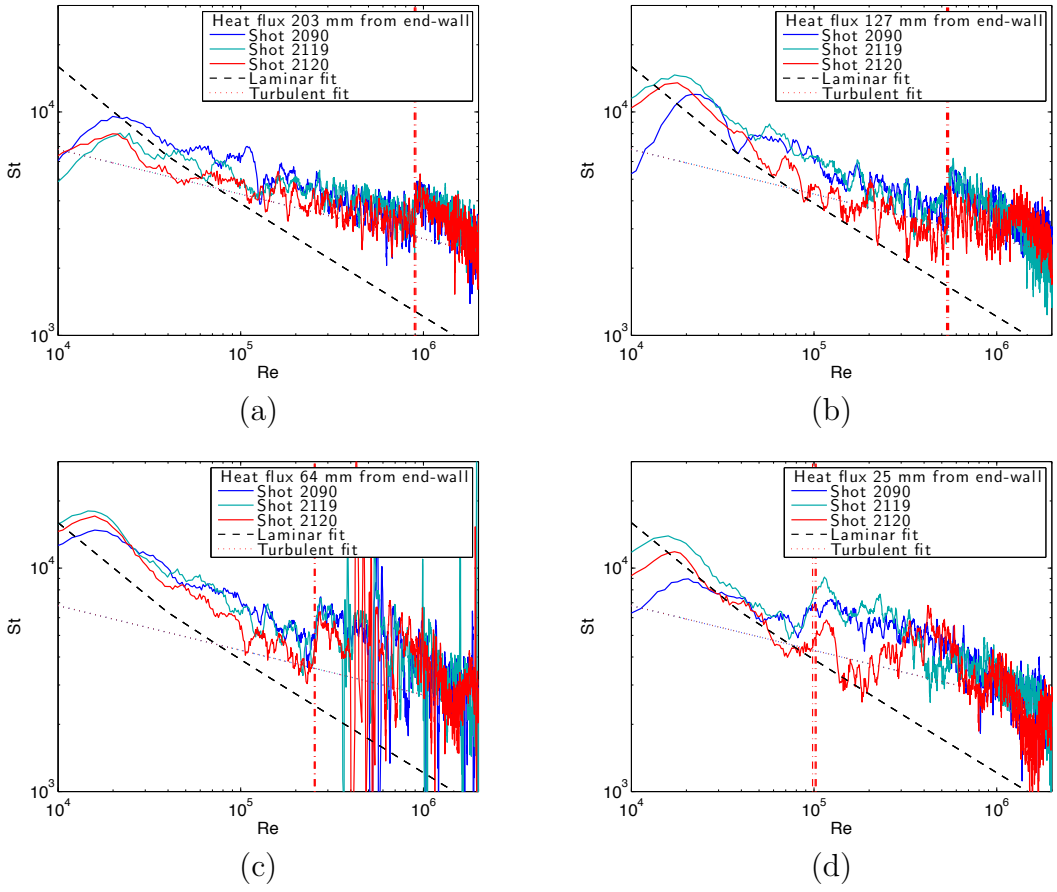

Figure 5.17: Stanton number-Reynolds number plots for shot numbers 2090, 2119, and 2120, stoichiometric hydrogen-oxygen detonations at fill pressure 25 kPa. Experimental measurements are for heat-flux gauges located (a) 203, (b) 127, (c) 64, and (d) 25 mm from the reflecting end-wall. Also plotted are the laminar boundary layer solution and a turbulence model. The reflected shock wave arrives at the Reynolds number corresponding to the vertical dashed line.

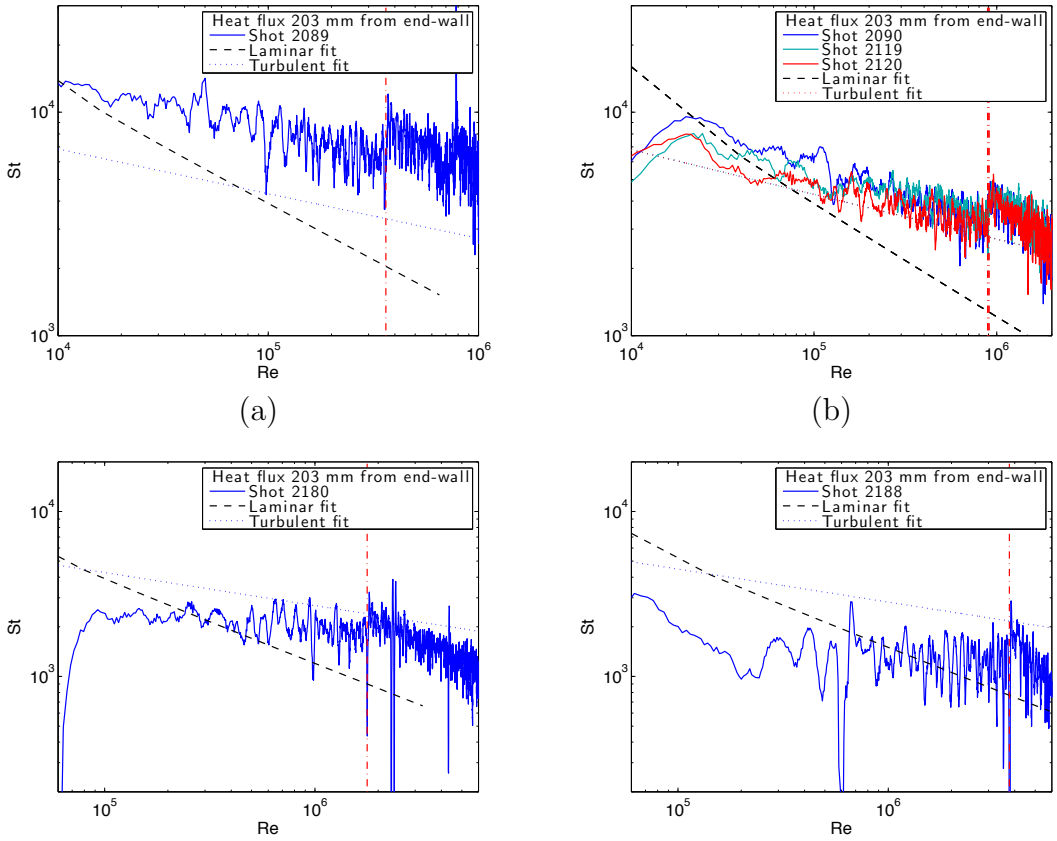

Figure 5.18: Stanton number-Reynolds number plots for heat-flux gauges located 203 mm from the reflecting end-wall for test numbers (a) 2089; (b) 2090, 2119, and 2120; (c) 2180; and (d) 2188. Also plotted are the laminar boundary layer solution and a turbulence model. The reflected shock wave arrives at the Reynolds number corresponding to the vertical dashed line.

5.5 Conclusions

It was initially suspected that the shock wave created when a detonation impinged upon an end-wall may interact with the boundary layer induced by the incident detonation. A focused schlieren system was assembled to investigate this possibility and, through analysis of the focused schlieren images with the pressure traces, it was shown that detonations did not bifurcate for any case considered. An analytical boundary layer solution was employed to show that the strong thermal boundary layer present behind the detonation inhibits bifurcation by increasing the reflected shock Mach number in the boundary layer. The increase in Mach number serves to increase the stagnation pressure in the boundary layer in the reflected shock-fixed frame; this stagnation pressure increase prevents flow separation and, in turn, bifurcation.

Heat-flux gauges were used to examine the behavior of the boundary layer induced by the incident detonation. It was shown that heat loads to the side-wall were on the order of 10 MW/m^2 and that the largest heat loads occurred immediately behind the detonation when the boundary layer is thinnest. The experimental heat-flux was best predicted using a turbulent relationship for the heat transfer, but the large fluctuations present in the heat transfer data prevent us from drawing definitive conclusions as to the nature of the boundary layer.

Chapter 6

Conclusions

Gaseous detonation reflection off a planar end-wall was examined to investigate detonation-driven material response and the gasdynamics of detonation reflection.

6.1 Detonation-Driven Plastic Deformation

Experiments were performed to characterize the elastic and plastic deformation of thin-walled stainless steel tubes subjected to internal gaseous detonation. This work built on previous research described in Karnesky (2010), but used a different specimen tube material that was better characterized at the high strain, high strain-rate deformation regime that typifies detonation-driven deformation. In these experiments a ripple pattern was observed for the intermediate fill pressure of 200 kPa with stoichiometric hydrogen-oxygen, but a ripple pattern was not observed for the larger fill pressure of 300 kPa. Using a single degree of freedom model, this behavior was explicated as only occurring for experimental conditions when the peak stress developed during the elastic oscillation induced by the incident detonation is of the same magnitude as the internal pressure existing behind the reflected shock wave.

The deformation data gathered in these experiments were used as a metric to determine the success or failure of a two-dimensional finite element analysis performed in LS-DYNA. This FEA model used standard Johnson-Cook material properties to incorporate strain-rate hardening, and a previously developed pressure loading model for the pressures caused by incident detonation and reflected shock loading.

It was shown that this provided quantitatively accurate comparisons to both the time-resolved strains and the residual plastic strains as measured in the detonation experiments. The comparison was best for the 300 kPa fill pressure case shown in figure 6.1 when the elastic oscillations are not important.

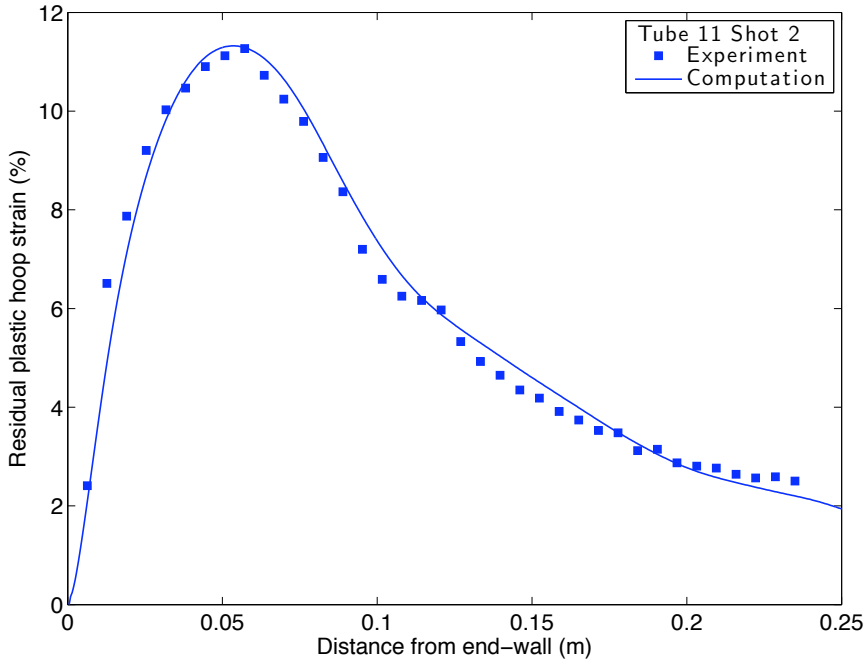

Figure 6.1: Comparison of measured and computed residual plastic deformation after the first detonation of stoichiometric ethylene-oxygen with fill pressure 300 kPa in specimen tube 11.

6.2 Reflected Detonation Waves

During the examination of the detonation-driven material response, it was determined that the reflected shock model used in the finite element simulations was inaccurate for times soon after detonation reflection. This indicated that our present understanding of reflected detonation waves was incomplete, and motivated reflected detonation experiments in the GALCIT detonation tube using pressure measurements, such as shown in figure 6.2, and schlieren images, such as shown in figure 6.3, to gather precise information on the behavior of the reflected shock wave. These measurements were combined to construct space-time diagrams as evinced in figure 6.4(a). The

experiments demonstrated that the reflected wave was much faster than predicted by the previously developed reflected detonation model for times immediately after reflection occurred. This was explained by considering the ZND detonation profile that includes a reaction zone of finite thickness. When a detonation impinges upon an end-wall, the reflected shock will first pass through the unreacted induction zone behind the detonation front. The gas in this induction zone will explode and, by comparing the speeds expected from such an explosion, it was concluded that this chemical reaction is responsible for the increased reflected shock speed; the agreement between this model and experimental measurements is shown in figure 6.4(b).

6.3 Investigation of Shock Wave–Boundary Layer Interaction

It was initially suspected that reflected detonations might undergo reflected shock wave–boundary layer interaction in the form of shock bifurcation. A finite source size focused schlieren system was assembled to investigate this possibility without the images being substantially affected by the flow on the detonation tube windows. Using this system, it was shown that bifurcation did not occur for any detonation experiments performed. An analytical boundary layer solution explained this as being due to the large thermal gradient present through the velocity boundary; this serves to increase the Mach number of the reflected shock wave in the boundary layer, which in turn results in a large stagnation pressure behind the reflected shock. Heat-flux gauges were used to examine the behavior of the boundary layer induced by the incident detonation. Heat loads to the side-wall were on the order of 10 MW/m^2, and the largest heat loads occurred immediately behind the detonation when the boundary layer is thinnest. The experimental heat-flux was best predicted using a turbulent relationship for the heat transfer such as shown in figure 6.5, but the large fluctuations in measured heat transfer data made it impossible to draw conclusions as to the nature of the boundary layer behind gaseous detonation waves. Further

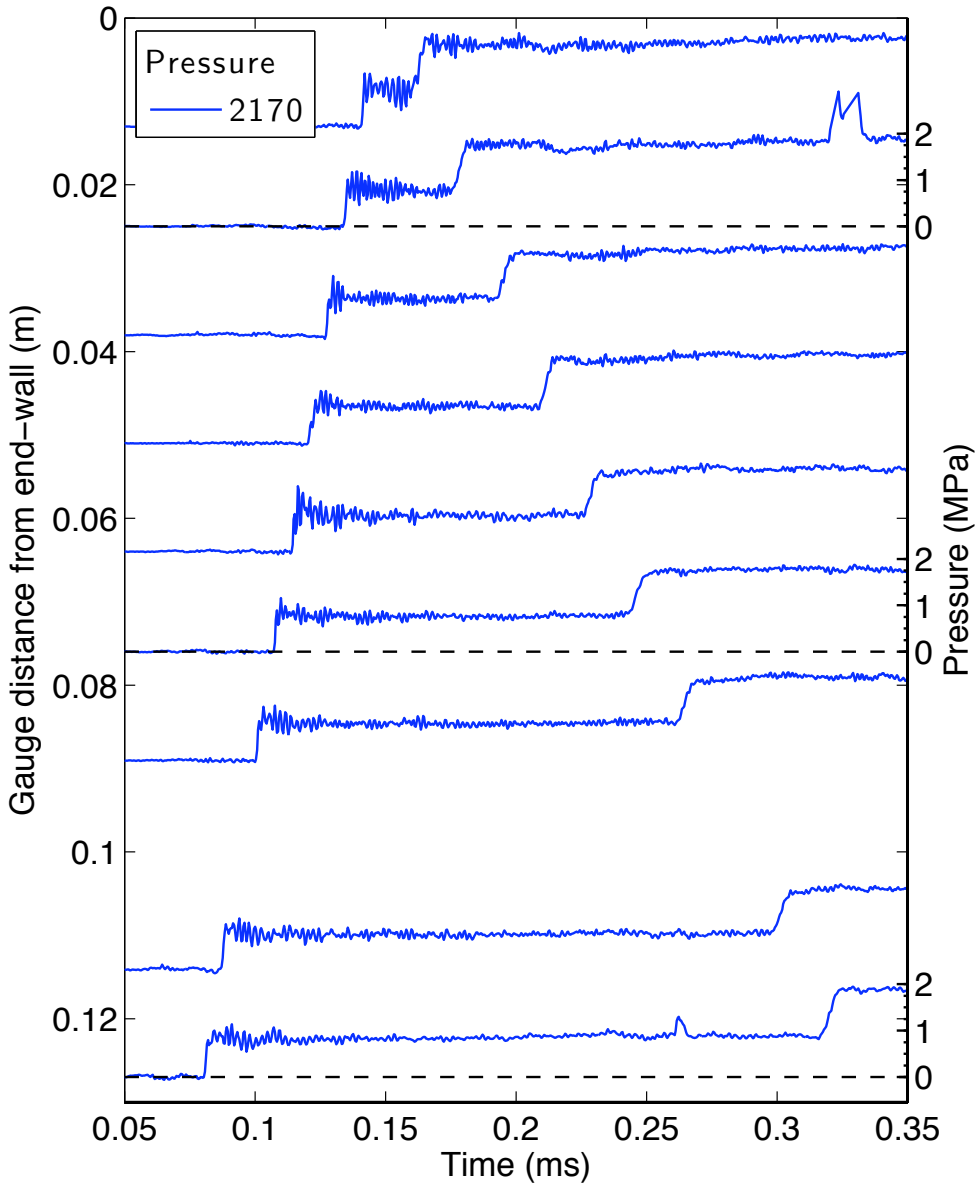

Figure 6.2: Time-resolved pressure measurements for shot 2170, a detonation of stoichiometric hydrogen-oxygen with 50% argon dilution at fill pressure 50 kPa.

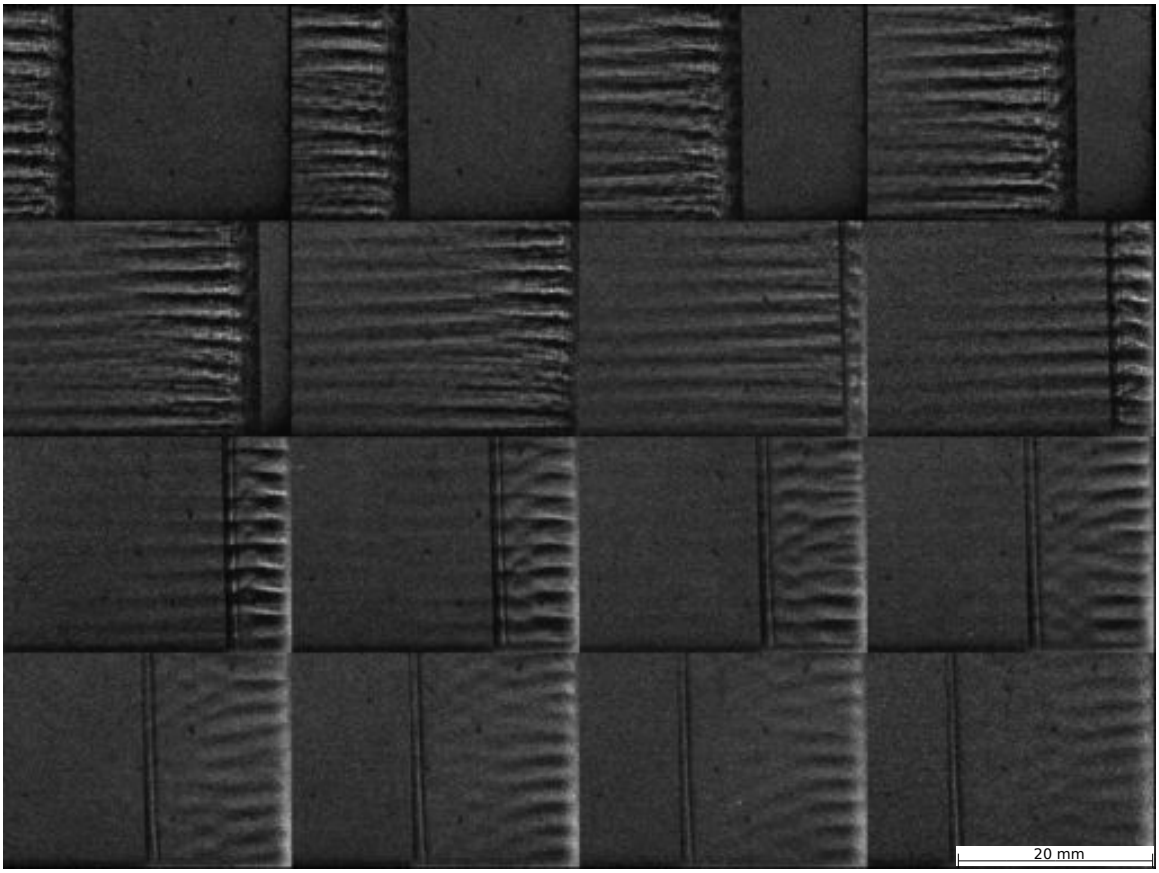

Figure 6.3: Unfocused schlieren visualization of shot 2170, a detonation of stoichiometric hydrogen-oxygen with 50% argon dilution at fill pressure 50 kPa. Sixteen frames are shown ordered left-to-right, top-to-bottom.

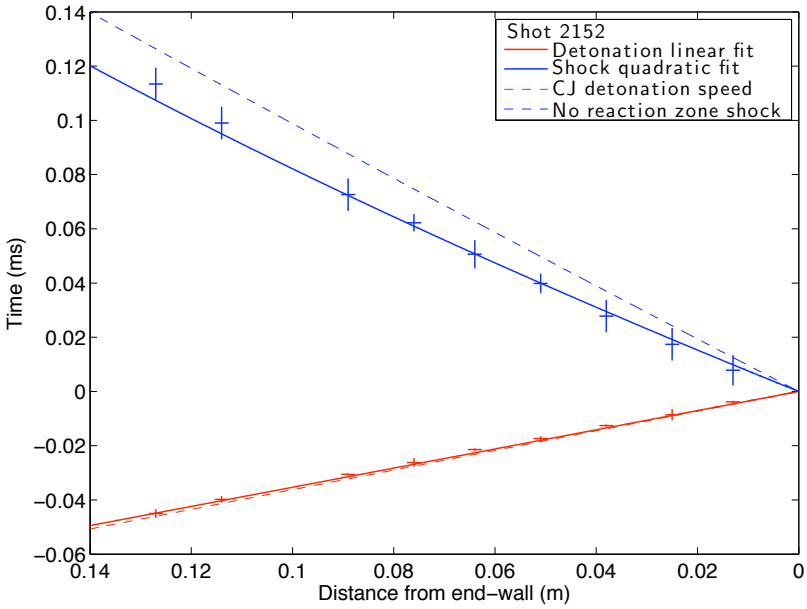

(a)

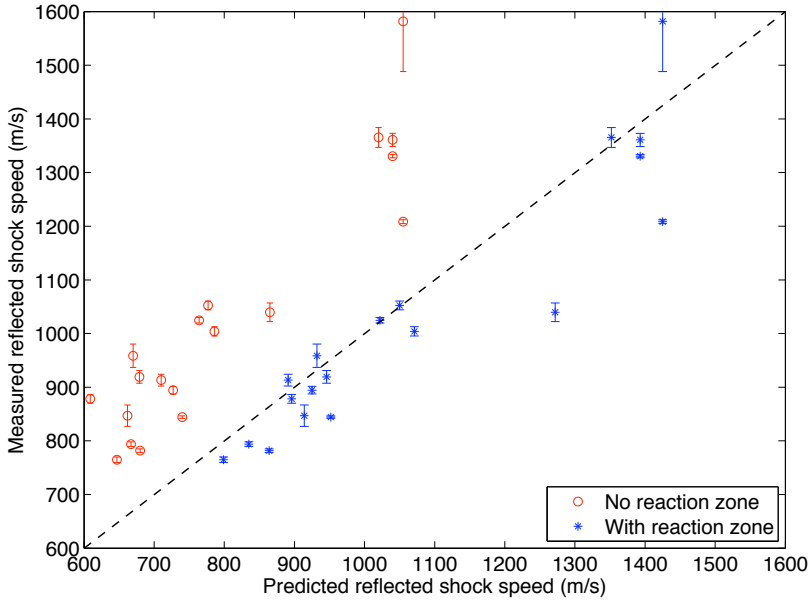

(b)

Figure 6.4: (a) x-t diagram showing detonation and shock arrivals; we observe that the measured reflected shock speed is much faster than predicted by the no reaction zone model. (b) Measured reflected shock speeds compared to predicted reflected shock speeds; this illustrates the importance of considering the reaction zone behind the reflected shock wave for times soon after detonation reflection. The dashed black line corresponds to $U_{measured} = U_{predicted}$..

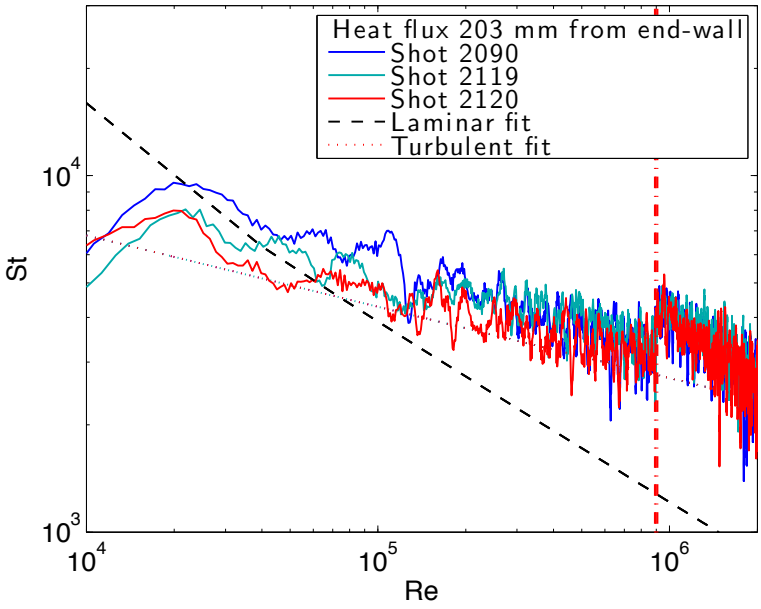

Figure 6.5: Stanton number-Reynolds number plot for heat-flux gauges located 203 mm from the reflecting end-wall for test numbers 2090, 2119, and 2120. Also plotted are the laminar boundary layer solution and a turbulence model.

work is needed to examine the boundary layer induced by detonations, and to study the effect of the transverse waves behind the detonation front on the boundary layer growth to properly interpret these heat transfer results.

6.4 Possibilities for Future Work

In the material response computations performed in the present work, the material deformation was decoupled from the internal gasdynamics of the reflected detonation wave. A simulation that coupled the fluid and solid mechanics would allow for a more accurate understanding of the effect of the material motion caused by the detonation on the reflected shock wave, and would incorporate other effects, such as the overall shortening of the tube as caused by the material deformation. These factors would be particularly important if the deformation resulting from the incident detonation were increased, such as would be the case if the fill pressure were increased.

Visualizing the reflected detonation allowed us to identify a key aspect that gov-

erns the behavior of the reflected shock wave near the location of reflection, but it did not result in a comprehensive model to predict the side-wall pressure resulting from the reflected shock wave. One part of the present work that could be improved is the computational modeling of the reflected detonation wave. Building upon detonation simulations such as those performed by Ziegler (2011) would help a superior reflected detonation model to be realized. Such a simulation would require two- or three-dimensional computation of a reflected detonation that included the cellular detonation structure, viscosity, and a thermally conducting side-wall. This represents considerable computational expense, but it would enhance the present understanding of reflected detonation waves and help to elucidate experimental observations such as the reflected shock thickness discussed in section 4.4.3. This level of simulation is also required to examine the effect of the cellular structure on boundary layer development behind the detonation.

Bibliography

R. Akbar. *Mach Reflection of Gaseous Detonations*. PhD dissertation, Rensselaer Polytechnic Institute, 1997. 67, 81

J.M. Austin. *The Role of Instability in Gaseous Detonation*. PhD dissertation, California Institute of Technology, 2003. x, 3, 4, 79, 95

R. Becker. Stoßwelle und detonation. *Zeitschrift für Physik*, 8(1):321–362, 1922. 8

W.M. Beltman and J.E. Shepherd. Linear elastic response of tubes to internal detonation loading. *Journal of Sound and Vibration*, 252(4):617–655, 2002. 1, 19, 22, 23, 25

E.M. Braun, F.K. Lu, and D.R. Wilson. Airbreathing rotating detonation wave engine cycle analysis. In *46th AIAA/ASME/SAE/ASEE Joint Propulsion Conference & Exhibit*, Nashville, TN, July 25-28 2010. 2

E. Oran Brigham. *The Fast Fourier Transform and Its Applications*. Prentice-Hall, Englewood Cliffs, New Jersey, 1st edition, 1974. ISBN 0-13-307496-X. 42

S. Browne, J. Ziegler, and J.E. Shepherd. Numerical solution methods for shock and detonation jump conditions. Technical Report FM2006-006, Graduate Aeronautical Laboratories California Institute of Technology, February 2008. 8, 17

A. Camargo, H.D. Ng, J. Chao, and J.H.S. Lee. Propagation of near-limit gaseous detonations in small diameter tubes. *Shock Waves*, 20:499–508, 2010. 27

A.J. Chabai and R.J. Emrich. Transition from laminar to turbulent flow in the shock tube boundary layer. *Bulletin of the American Physical Society*, 3:291, 1958. 29

D.L. Chapman. On the rate of explosion in gases. *Philosophical Magazine*, 47:90–104, 1899. 5

J.P. Davis and B. Sturtevant. Separation length in high-enthalpy shock/boundary-layer interaction. *Physics of Fluids*, 12(10):2661–2687, October 2000. 120

R. Deiterding, F. Cirak, S.P. Mauch, and D.I. Meiron. A virtual test facility for simulating detonation- and shock-induced deformation and fracture of thin flexible shells. *International Journal for Multiscale Computational Engineering*, 5(1):47–63, 2007. 123

W. Döring. On detonation processes in gases. *Annals of Physics*, 43:421–436, 1943. 9

J.A. Fay. Two-dimensional gaseous detonations: velocity deficit. *Physics of Fluids*, 2 (283), 1959. 27

W. Fickett and W. C. Davis. *Detonation*. University of California Press, Berkeley, CA, 1979. 1, 3, 8, 9

V.N. Gamezo, A.M. Khokhlov, and E.S. Oran. The influence of shock bifurcations on shock-flame interactions and DDT. *Combustion and Flame*, 126:1810–1826, 2001. 28

V.N. Gamezo, E.S. Oran, and A.M. Khokhlov. Three-dimensional reactive shock bifurcations. *Proceedings of the Combustion Institute*, 30:1841–1847, 2005. 120

I.I. Glass and G.N. Patterson. A theoretical and experimental study of shock-tube flows. *Journal of the Aeronautical Sciences*, 22(2), February 1955. 143

D.G. Goodwin. Cantera – an open-source, extensible software suite for CVD process simulations. *Electrochemical Society*, pages 155–162, 2003. 8

G.R. Johnson and W.H. Cook. A constitutive model and data for metals subjected to large strains, high strain rates and high temperatures. In *Proceedings of the 7th International Symposium on Ballistics*, The Hague, The Netherlands, 1983. 26

E. Jouguet. On the propagation of chemical reactions in gases. *Journal de Mathematiques Pures et Appliquees*, 1:347–425, 1905. 5

K. Kailasanath. Review of propulsion applications of detonation waves. *AIAA Journal*, 38(9):1698–1708, September 2000. 2

M.J. Kaneshige. *Gaseous Detonation Initiation and Stabilization by Hypervelocity Projectiles*. PhD dissertation, California Institute of Technology, 1999. 67

J. Karnesky. *Detonation Induced Strain in Tubes*. PhD dissertation, California Institute of Technology, 2010. v, 2, 19, 23, 24, 30, 31, 33, 44, 62, 65, 66, 147

J. Karnesky, J. Damazo, K. Chow-Yee, A. Rusinek, and J.E. Shepherd. Plastic deformation due to reflected detonation. *International Journal of Solids and Structures*, 50(1):97–110, 2013. 1, 19, 20, 23, 24, 26, 30, 31, 52

A.H. Keil. Introduction to underwater explosion research. Technical Report GACIA/PA35818, Norfolk Naval Ship Yard, Portsmouth, Virginia, 1956. 22

A.H. Keil. The response of ships to underwater explosions. In *Society of naval architects and marine engineers annual meeting*, New York, NY, November 16-17 1961. 23

M. Kuznetsov, A. Lelyakin, and W. Breitung. Numerical simulation of radiolysis gas detonations in a bwr exhaust pipe and mechanical response of the piping to the detonation pressure loads. In L. Angermann, editor, *Numerical simulations - Examples and applications in computational fluid dynamics*, chapter 19. InTech, 2010. 22

A.J. Laderman, G.J. Hecht, and A.K. Oppenheim. Thin film thermometry in detonation research. In C.M. Herzfeld, editor, *Temperature - its measurement and control in science and industry*, volume 3. Reinhold Publishing Corp, London, 1962. 140, 143

J.H.S. Lee. *The Detonation Phenomenon*. Cambridge University Press, 2008. ISBN 978-0-521-89723-5. 3

S. Lee, F. Barthelat, J.W. Hutchinson, and H.D. Espinosa. Dynamic failure of metallic pyramidal truss core materials – experiments and modeling. *International Journal of Plasticity*, 22:2118–2145, 2006. 27

Z. Liang, J. Karnesky, and J.E. Shepherd. Structural response to reflected detonations and deflagration-to-detonation transition in H_2-N_2O mixtures. Technical Report FM2006-003, Graduate Aeronautical Laboratories California Institute of Technology, August 2006. 31

S.W. Liu and H. Mirels. Numerical solutions for unsteady laminar boundary layers behind blast waves. *Physics of Fluids*, 23(681), 1980. 28

W.S. Liu, X.X. Du, and I.I. Glass. Laminar boundary layers behind detonation waves. *Proceedings of the Royal Society of London Series A, Mathematical and Physical Sciences*, 387(1793):331–349, June 1983. 28, 140, 143, 471, 472, 479

Livermore Software. *LS–DYNA User's Manual, version 971*. Livermore Software Technology Corporation, Livermore, CA, 2005. 60

F.K. Lu, E.M. Braun, L. Massa, and D.R. Wilson. Rotating detonation wave propulsion experimental challenges, modeling, and engine concepts. In *47th AIAA/ASME/SAE/ASEE Joint Propulsion Conference & Exhibit*, San Diego, CA, July 31-August 3 2011. 2

H. Mark. The interaction of a reflected shock wave with the boundary layer in a shock tube. *Journal of the Aeronautical Sciences*, pages 304–306, April 1957. 120, 123

H. Mark. The interaction of a reflected shock wave with the boundary layer in a shock tube. Technical Report TM1418, National Advisory Committee for Aeronautics, March 1958. 28, 121

G. Matheou, A.M. Bonanos, C. Pantano, and P.E. Dimotakis. Large-eddy simulation of mixing in a recirculating shear flow. *Journal of Fluid Mechanics*, 646:375–414, 2010. 123

M. Mirzaei, H. Biglari, and M. Salavatian. Analytical and numerical modeling of the transient elasto-dynamic response of a cylindrical tube to internal gaseous detonation. *International Journal of Pressure Vessels and Piping*, 83:531–539, 2006. 22

H.A. Mohammed, H. Salleh, and M.Z. Yusoff. Determination of the effusivity of different scratched coaxial temperature sensors under hypersonic flow. *International Journal of Thermophysics*, 31:2305–2322, 2010. 70

H.A. Mohammed, H. Salleh, and M.Z. Yusoff. The effect of scratch technique on the thermal-product value of temperature sensors. *Thermophysics and Aeromechanics*, 18(1):51–64, 2011. 70

M.A. Nettleton. *Gaseous Detonations*. Chapman and Hall, NY, 1987. 10

J. Von Neumann and A.H. Taub. *Collected Works of J. von Neumann: General Editor, A.H. Taub*, volume 6. Pergamon Press, New York, 1942. 9

G.N. Nurick and J.B. Martin. Deformation of thin plates subjected to impulsive loading - a review: Part I: Theoretical considerations. *International Journal of Impact Engineering*, 8(2):159–170, 1989a. 23

G.N. Nurick and J.B. Martin. Deformation of thin plates subjected to impulsive loading - a review: Part II: Experimental studies. *International Journal of Impact Engineering*, 8(2):171–186, 1989b. 23

E.S. Oran and V.N. Gamezo. Origins of the deflagration-to-detonation transition in gas-phase combustion. *Combustion and Flame*, 148:4–47, October 2006. 1

C. Pantano, R. Deiterding, D.J. Hill, and D.I. Pullin. A low numerical dissipation

patch-based adaptive mesh refinement method for large-eddy simulation of compressible flows. *Journal of Computational Physics*, 221(1):63–87, 2006. 122

PCB. *Operating Manual for Quartz Pressure Sensors*. PCB Piezotronics, Depew, NY, 2009. Document Number 21354, Revision B. 70

E.L. Petersen and R.K. Hanson. Improved turbulent boundary-layer model for shock tubes. *AIAA Journal*, 41(7):1314–1322, 2003. 141, 143

E.L. Petersen and R.K. Hanson. Measurement of reflected-shock bifurcation over a wide range of gas composition and pressure. *Shock Waves*, 15:333–40, 2006. 120

F. Pintgen and J.E. Shepherd. Elastic and plastic structural response of thin tubes to deflagration-to-detonation transition events. Technical Report FM2005-008, Graduate Aeronautical Laboratories California Institute of Technology, April 2006a. 34

F. Pintgen and J.E. Shepherd. Structural response to deflagration-to-detonation transition events in a tube. Technical Report FM2005-005, Graduate Aeronautical Laboratories California Institute of Technology, May 2006b. 31

M.I. Radulescu and R.K. Hanson. Effect of heat loss on pulse-detonation-engine flow fields and performance. *Journal Of Propulsion And Power*, 21(2):274–285, Mar-Apr 2005. 13

R. Rajendran and K. Narasimhan. Deformation and fracture behavior of plate specimens subjected to underwater explosion–a review. *International Journal of Impact Engineering*, 32:1945–1963, 2006. 22

G.D. Roy, S.M. Frolov, A.A. Borisov, and D.W. Netzer. Pulse detonation propulsion: challenges, current status, and future perspective. *Progress in Energy and Combustion Science*, 30:545–672, 2004. 2

A. Rusinek and J.R. Klepaczko. Shear testing of a sheet steel at wide range of strain rates and a constitutive relation with strain-rate and temperature dependence of the flow stress. *International Journal of Plasticity*, 17:87–115, 2001. 31

S.R. Sanderson and B. Sturtevant. Transient heat flux measurement using a surface junction thermocouple. *Review of Scientific Instruments*, 73(7):2781–7, 2002. 70

H. Schlichting. *Boundary-Layer Theory*. McGraw-Hill, New York, 1979. 29, 135, 143, 471, 479

D. Schwer and K. Kailasanath. Numerical investigation of the physics of rotating-detonation-engines. *Proceedings of the Combustion Institute*, 33:2195–2202, 2011. 2

R.L. Scorah. On the thermodynamic theory of detonation. *Journal of Chemical Physics*, 3(7), 1935. 8

G.S. Settles. *Schlieren and Shadowgraph Techniques*. Springer-Verlag Berlin Heidelberg New York, 2001. 70, 73

J.E. Shepherd. Structural response of piping to internal gas detonation. *Journal of Pressure Vessel Technology*, 131(3):87–115, June 2009. 1, 23

J.E. Shepherd. *Dynamics of vapor explosions: rapid evaporation and instability of butane droplets exploding at the superheat limit*. PhD dissertation, California Institute of Technology, 1981. 232

J.E. Shepherd, A. Teodorcyzk, R. Knystautas, and J.H.S. Lee. Shock waves produced by reflected detonations. *Progress in Astronautics and Aeronautics*, 134:244–264, 1991. 1

T. Simkins. Resonance of flexural waves in gun tubes. Technical Report No. ARCCB-TR-87008, US Army Armament Research, Development and Engineering Center, 1987. 24

G.P. Smith, D.M. Golden, M. Frenlach, N.W. Mirarty, B. Eiteneer, M. Goldenberg, C. Thomas Bowman, R.K. Hanson, S. Song, W. Gardiner, V.V. Lissianski, and Z. Qin. Gri-mech 3.0. http://www.me.berkeley.edu/gri_mech/, 1999. Accessed 2010. 28

K. I. Stanyukovich. *Unsteady Motion of Continuous Media*. Pergamon Press, 1960. 16

R.A. Strehlow. Gas phase detonations: recent developments. In *154*$^{\text{th}}$ *meeting of the American Chemical Society*, Chicago, IL, September 1967. 97, 107

R.A. Strehlow. Transverse waves in detonations: I. spacing in the hydrogen-oxygen system. *AIAA Journal*, 7(2):492–496, 1969a. 4, 95

R.A. Strehlow. Transverse waves in detonations: Ii. structure and spacing in H_2-O_2, C_2H_2-O_2, C_2H_4-O_2 and CH_4-O_2 systems. *AIAA J*, 7(3):492–496, 1969b. 4, 95

R.A. Strehlow and A. Cohen. Limitations of the reflected shock technique for studying fast chemical reactions and its application to the observation of relaxation in nitrogen and oxygen. *Journal of Chemical Physics*, 30(1):257–265, 1959. 120

K. Tanaki, K. Inaba, and M. Yamamoto. Numerical investigation on transition of shock induced boundary layer. In *47*$^{\text{th}}$ *AIAA Aerospace Sciences Meeting*, Orlando, USA, January 5-8 2009. 29, 143

S. Tang. Dynamic response of a tube under moving pressure. In *The American Society of Civil Engineers*, volume 5, pages 97–122, 1965. 24

G.I. Taylor. The dynamics of the combustion products behind plane and spherical detonation fronts in explosives. *Philosophical Transactions of the Royal Society*, A200:235–247, 1950. 10

J.R. Taylor and H.G. Hornung. Real gas and wall roughness effects on the bifurcation of the shock reflected from the end wall of a tube. In *Proceedings of the 13*$^{\text{th}}$ *International Symposium on Shock Tubes and Waves*, Niagara Falls, USA, July 6-9 1981. 28, 120, 122

T.Chao and J.E. Shepherd. Comparison of fracture response of preflawed tubes under internal static and detonation loading. *Journal of Pressure Vessel Technology*, 126 (3):345–53, 2004. 1, 23

P.A. Thompson. *Compressible Fluid Dynamics*. McGraw-Hill, New York, 1972. Out of print from McGraw-Hill, but reprinted privately and available from the Rensselaer Union Bookstore, RPI, Troy, NY. TEL 518 276 6555. 5, 10

Vishay. *Strain gage installations with M-Bond 200 Adhesive*. Vishay Precision Group - Micro-Measurements, Raleigh, NC, 2005a. Application note B-129-8. 37

Vishay. *Surface preparation for strain gage bonding*. Vishay Precision Group - Micro-Measurements, Raleigh, NC, January 2005b. Application note B-127-14. 37

Vishay. *High elongation strain measurement*. Vishay Precision Group - Micro-Measurements, Raleigh, NC, April 2007. Application note TT-605. 38

Y.S. Weber, E.S. Oran, and J.P. Boris. The numerical simulation of shock bifurcation near the end wall of a shock tube. *Physics of Fluids*, 7(10):2475–2488, 1995. 120

H. Yamashita, J. Kasahara, Y. Sugiyama, and A. Matsuo. Visualization study of ignition modes behind bifurcated-reflected shock waves. *Combustion and Flame*, 159:2954–2966, 2012. 120

W. Young and R. Budynas. *Roark's formulas for stress and strain*. McGraw-Hill, New York, 7$^{\text{th}}$ edition, 2002. ISBN 0-07-072542-X. 52

S. Yungster. Numerical study of shock-wave/boundary-layer interactions in premixed combustible gases. *AIAA Journal*, 30(10):2379–2387, October 1992. 120

R. Zaera, J.A. Rodríguez-Martínez, A. Casado, J. Fernández-Sáez, A. Rusinek, and R. Pesci. A constitutive model for analyzing martensite formation in austenitic steels deforming at high strain rates. *International Journal of Plasticity*, 29:77–101, 2012. 26

Y.B. Zel'dovich. On the theory of the propagation of detonations in gaseous systems. *JETP*, 10:542–568, 1940. Available in translation as NACA TM 1261 (1950). 9

Y.B. Zel'dovich and A. S. Kompaneets. *Theory of Detonation*. Academic Press, NY, 1960. English translation of original Russian. 10

J. Ziegler. *Simulations of Compressible, Diffusive, Reactive Flows with Detailed Chemistry Using a High-Order Hybrid WENO-CD Scheme*. PhD thesis, California Institute of Technology, 2011. 122, 123, 138, 154

J. Ziegler, R. Deiterding, D. Pullin, and J.E. Shepherd. High-order hybrid scheme for compressive, viscous flows with detailed chemistry. *Journal of Computational Physics*, 230(20):7598–7630, 2011. 123

Appendix A

Driven-Thin Experimental Procedure and Data

Included here is the checklist and all data recorded during the driven-thin detonation experiments. All experiments were performed with Kliulai Chow-Yee.

A.1 Driven-Thin Checklist

Checklist for experiments performed in the driven-thin detonation tube in 26 Guggenheim, Caltech.

Operators: Jason Damazo and Kliulai Chow-Yee

1. Turn on data acquisition system.
2. Turn on vacuum pump and heat exchanger.
3. Open hand valves for gases.
4. Turn on gas key, evacuate line, turn off gas key.
5. Open bottle farm valves.
6. Open all electronic valves to evacuate specimen tube. Wait until $p_{\text{vacuum}} < 40$ mTorr. Zero fill pressure gauge.
7. Check position of rotary valve.

8. Turn on strain gauge signal conditioning amplifiers; zero strain gauges. In tube 9, the amplifiers used a signal gain of 50 with a strain gauge excitation voltage of 10 V. For tubes 10 and 11, the amplifiers used a signal gain of 10 with an excitation voltage of 10 V.
9. Close door to experiment room and seal room.
10. Turn on warning light.
11. Don ear protection.
12. Evacuate the gas fill line.
13. Pressurize the gas fill line with oxygen.
14. Open valves and fill the detonation tube with oxygen to the target oxygen fill pressure.
15. Evacuate the fill line.
16. Pressurize the gas fill line with ethylene.
17. Open valves and fill the detonation tube with ethylene to the target fill pressure.
18. Evacuate the fill line.
19. Run circulation pump for at least 5 minutes.
20. Record the pre-shot temperature and pressure.
21. Close all valves to seal the detonation tube.
22. Verify interlocks are green.
23. Arm data acquisition.
24. Arm glow-plug.
25. Turn on glow plug and wait for ignition. Fire!

26. Switch off glow-plug immediately after data acquisition triggers or 30 seconds have elapsed.

27. Open valve to pressure gauge after the temperature is below 30°C.

28. Record post shot pressure and temperature.

29. Evacuate vessel.

30. If it is the last shot of the day, reset the facility.

31. Record data to ASCII files.

32. Back-up data.

A.2 Tube 9 Data

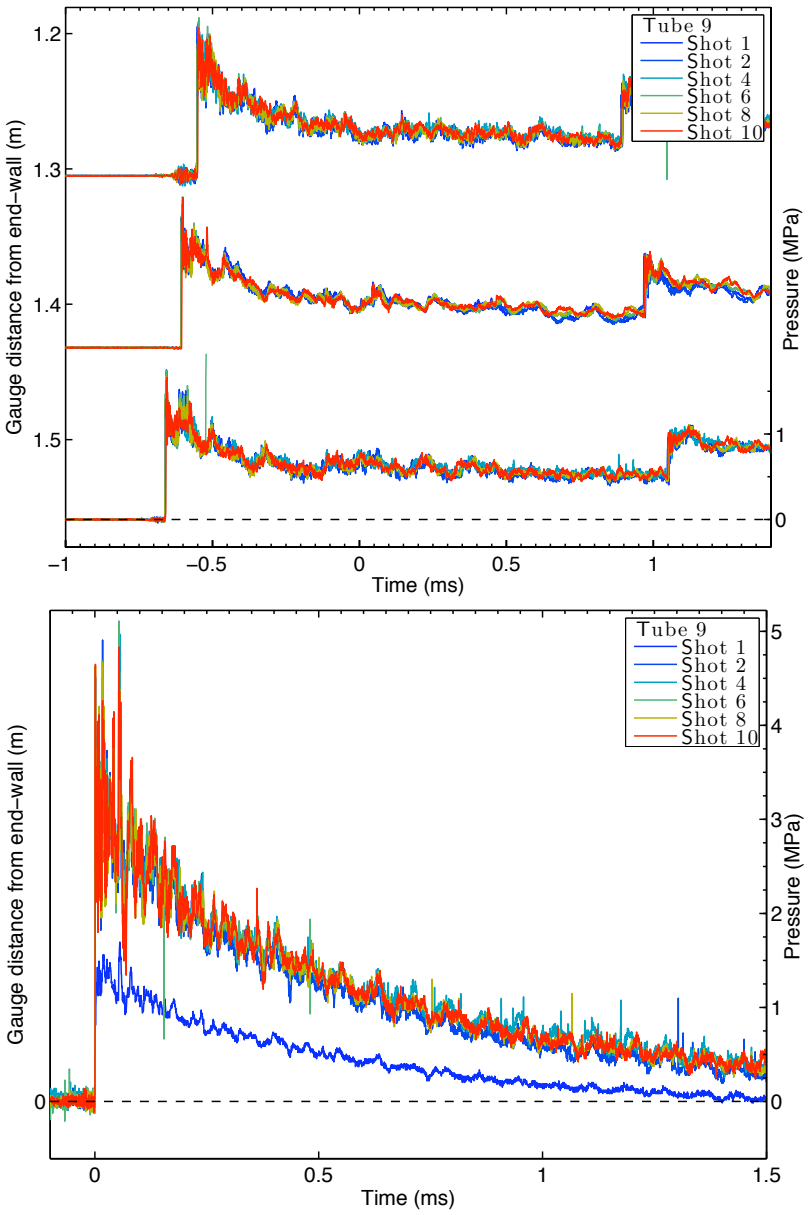

Figure A.1: Time-resolved pressure measurements from elastic shots in tube 9.

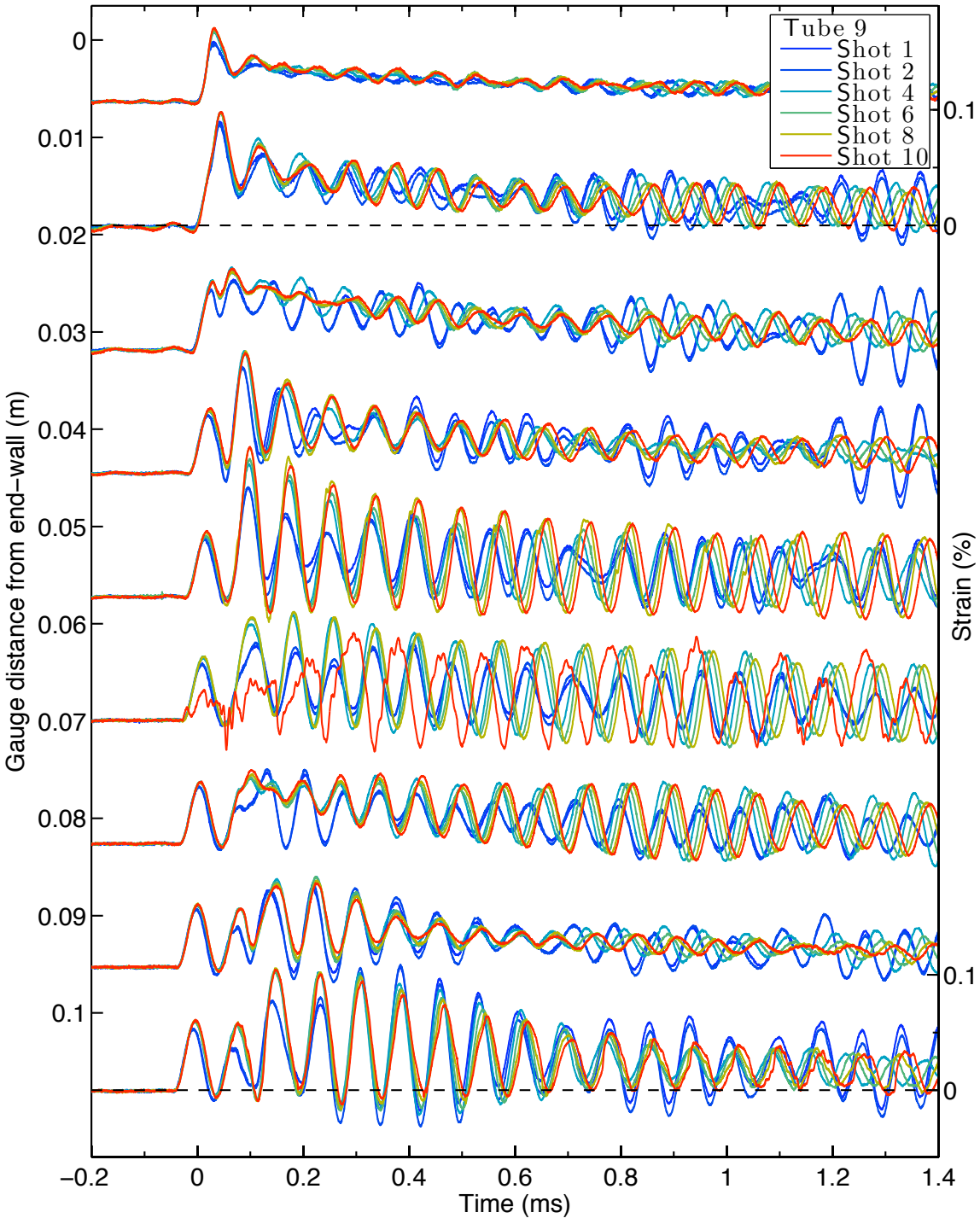

Figure A.2: Time-resolved elastic hoop strain measurements in tube 9, part 1.

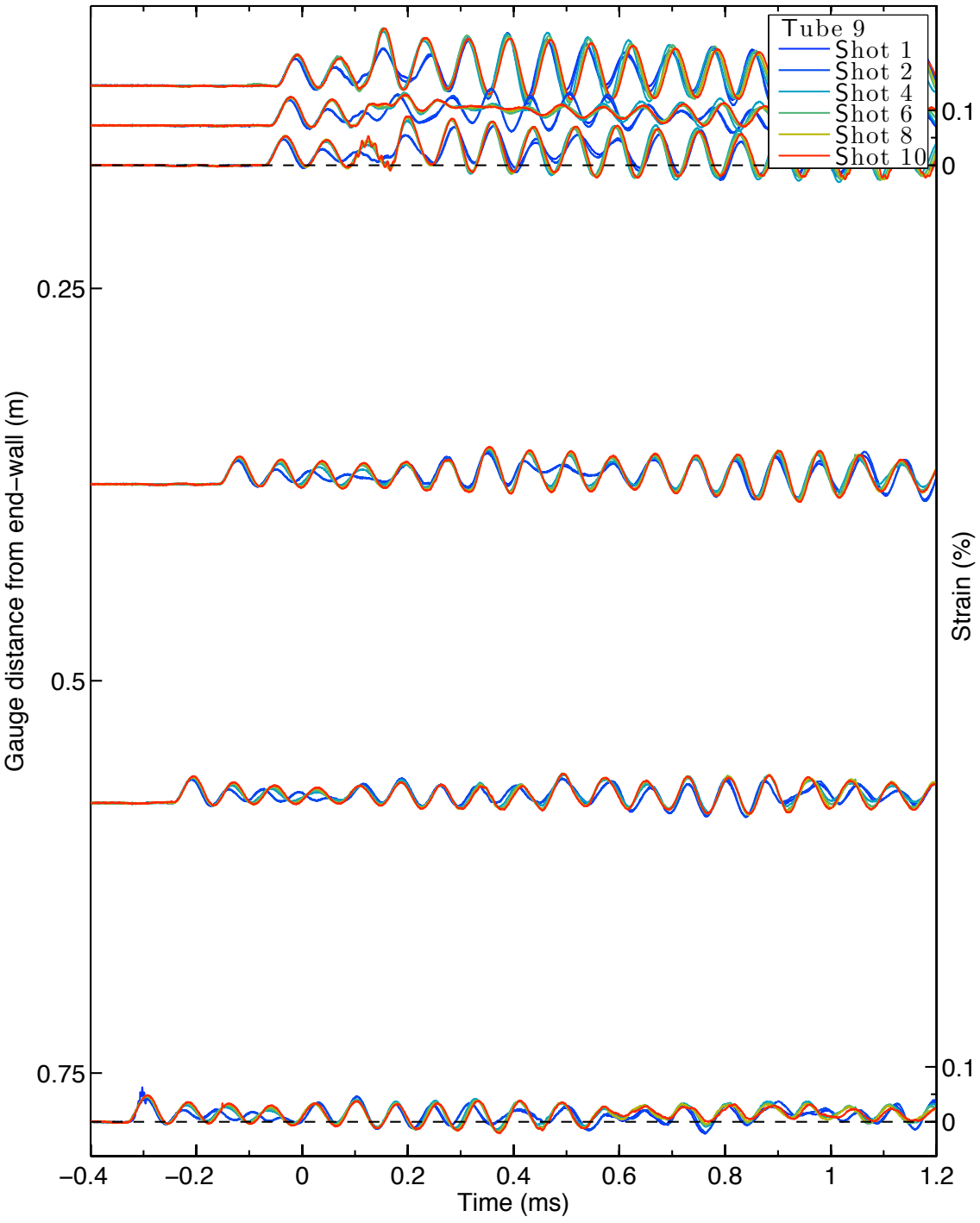

Figure A.3: Time-resolved elastic hoop strain measurements in tube 9, part 2.

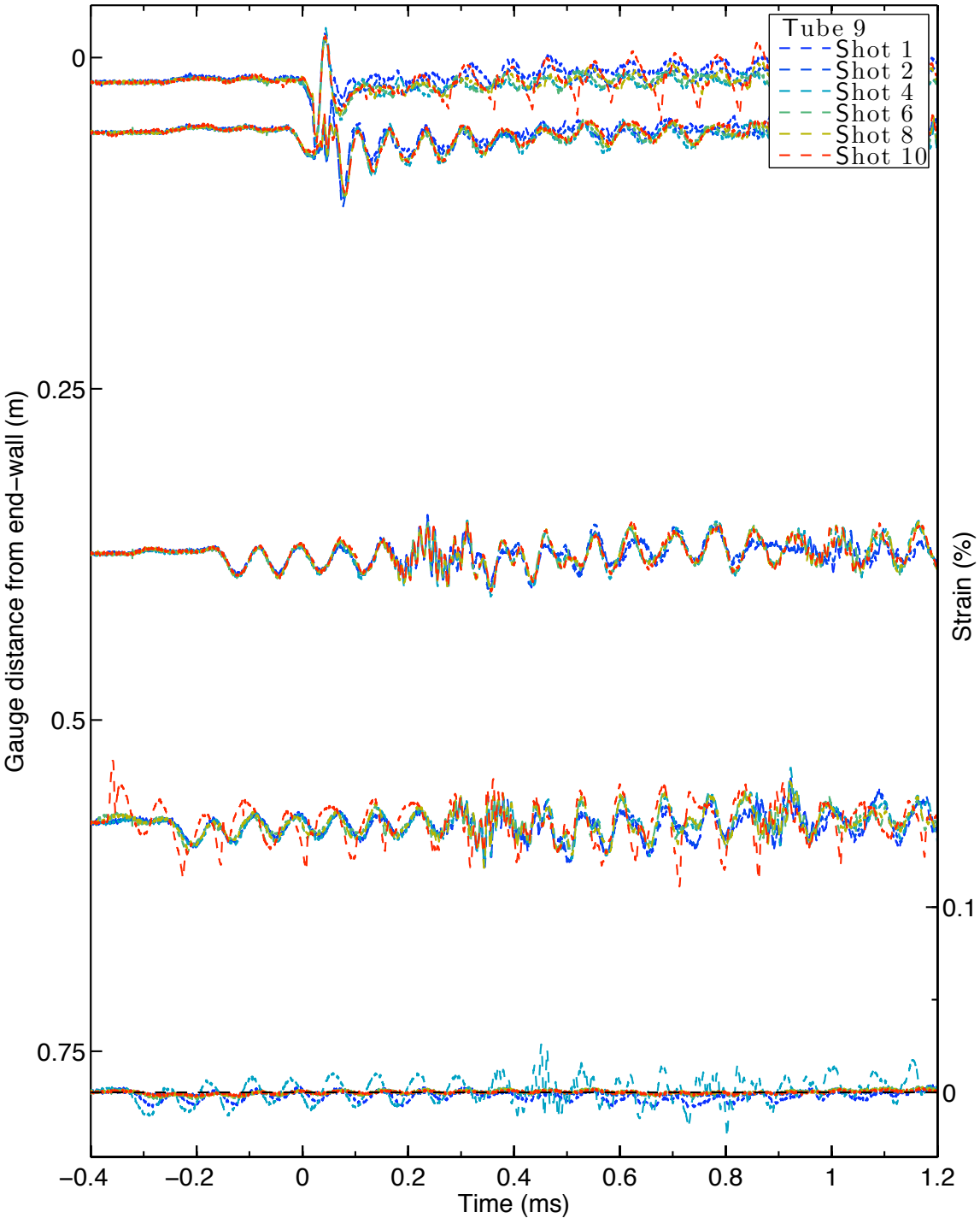

Figure A.4: Time-resolved elastic longitudinal strain measurements in tube 9.

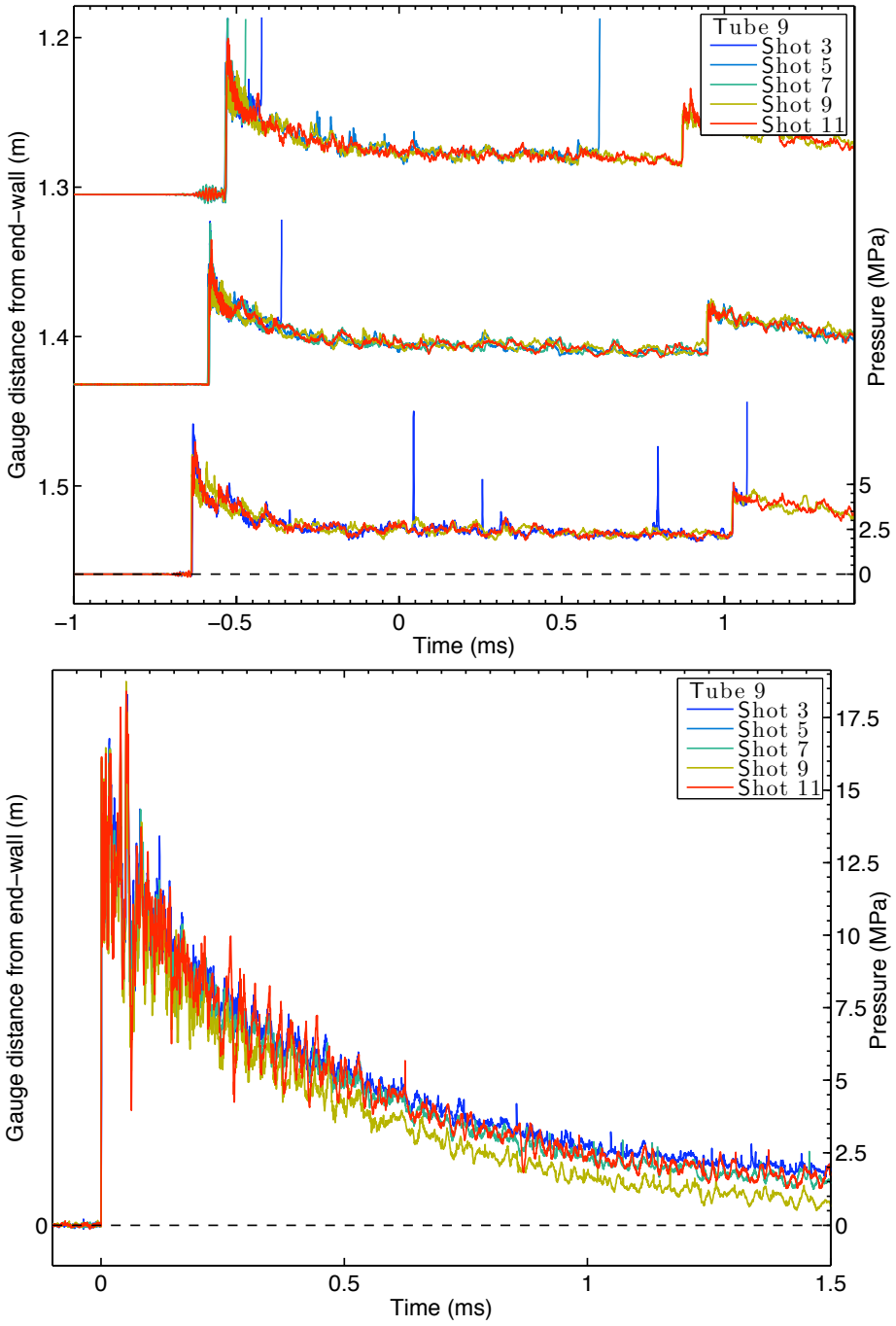

Figure A.5: Time-resolved pressure measurements from plastic shots in tube 9.

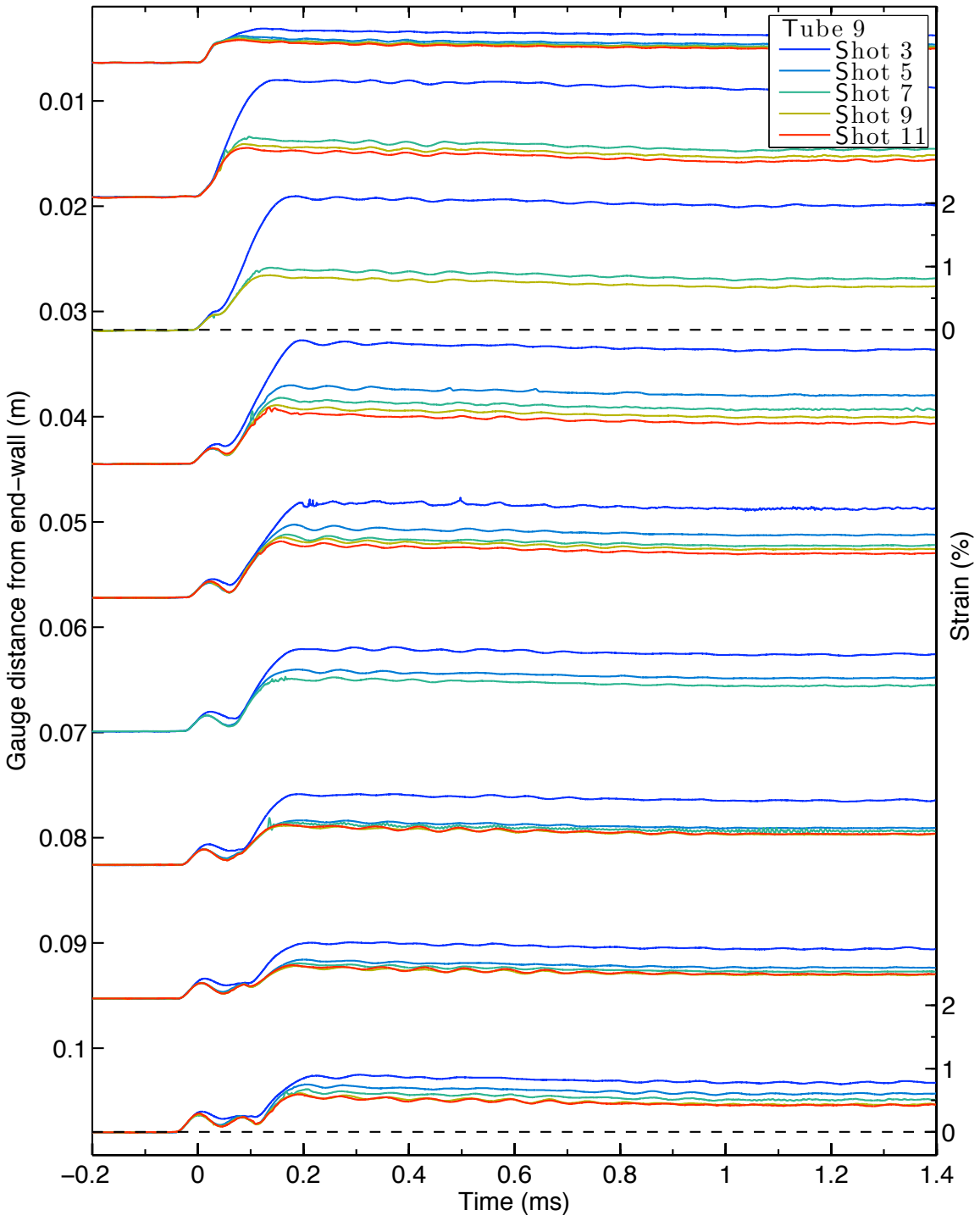

Figure A.6: Time-resolved plastic hoop strain measurements in tube 9, part 1.

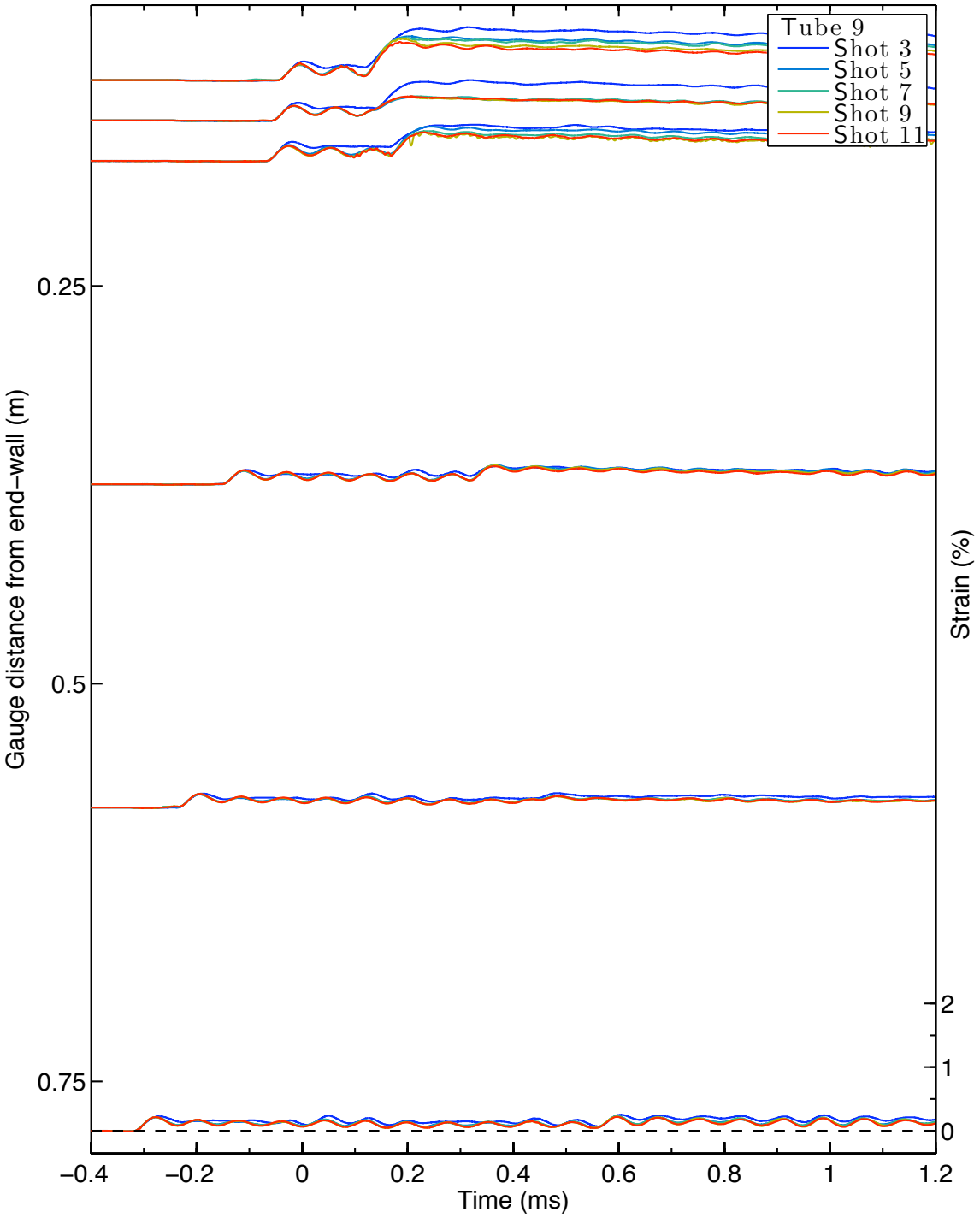

Figure A.7: Time-resolved plastic hoop strain measurements in tube 9, part 2.

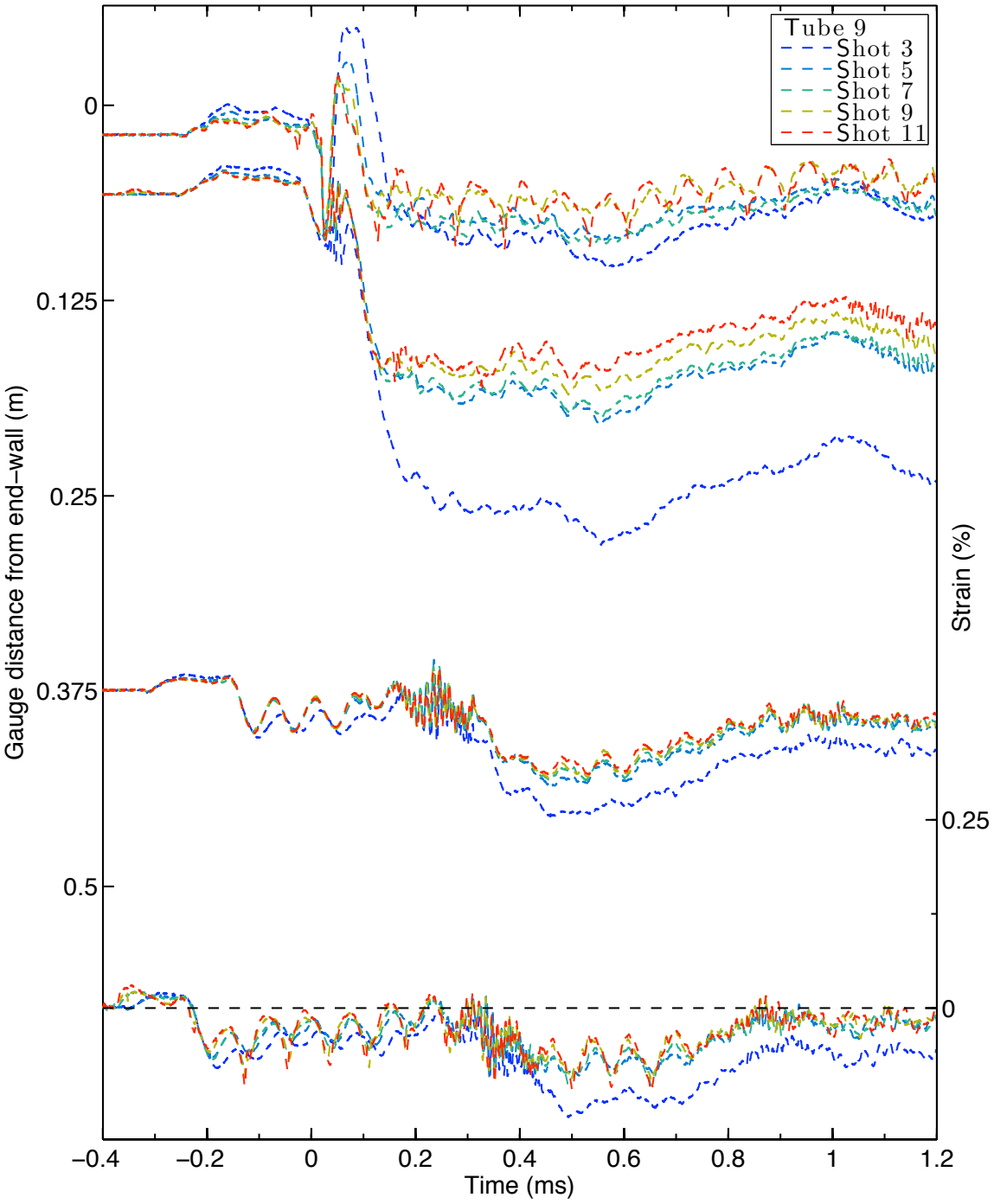

Figure A.8: Time-resolved plastic longitudinal strain measurements in tube 9.

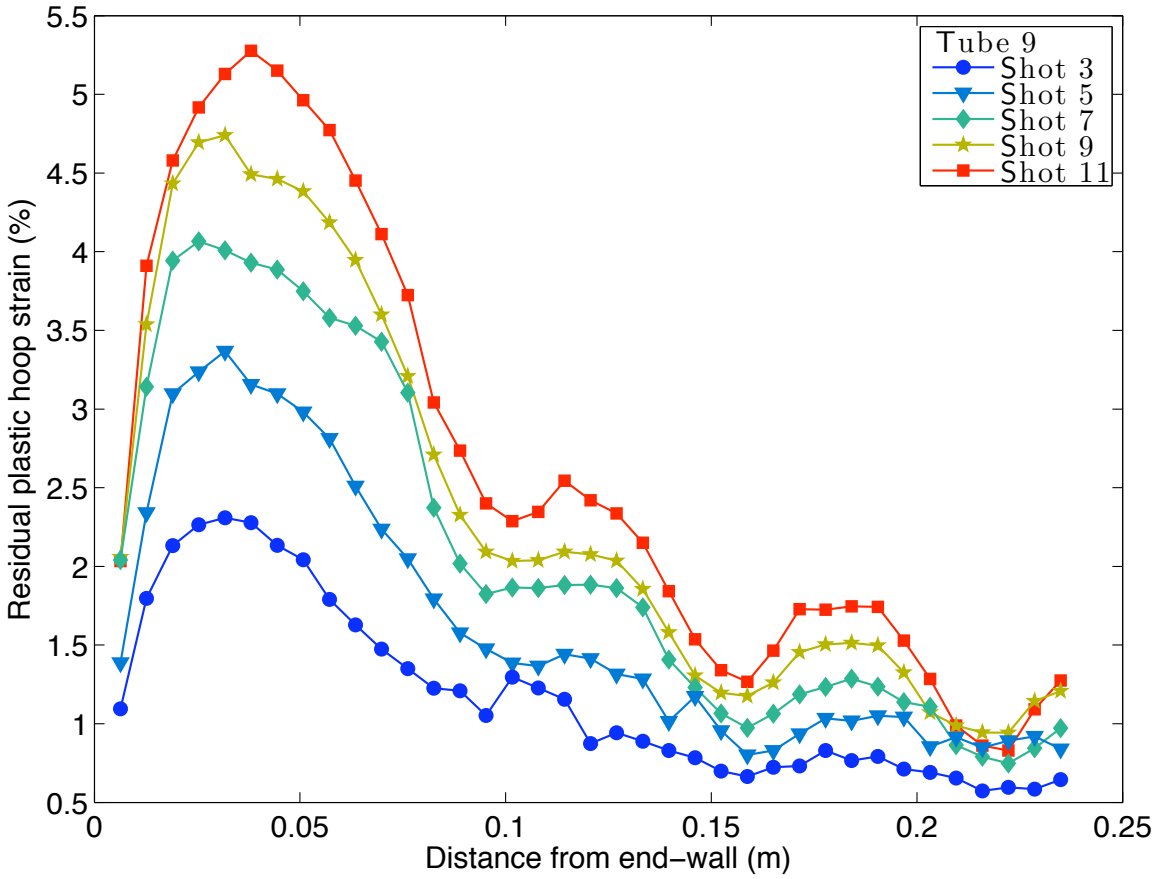

Figure A.9: Residual plastic hoop strain measurements in tube 9.

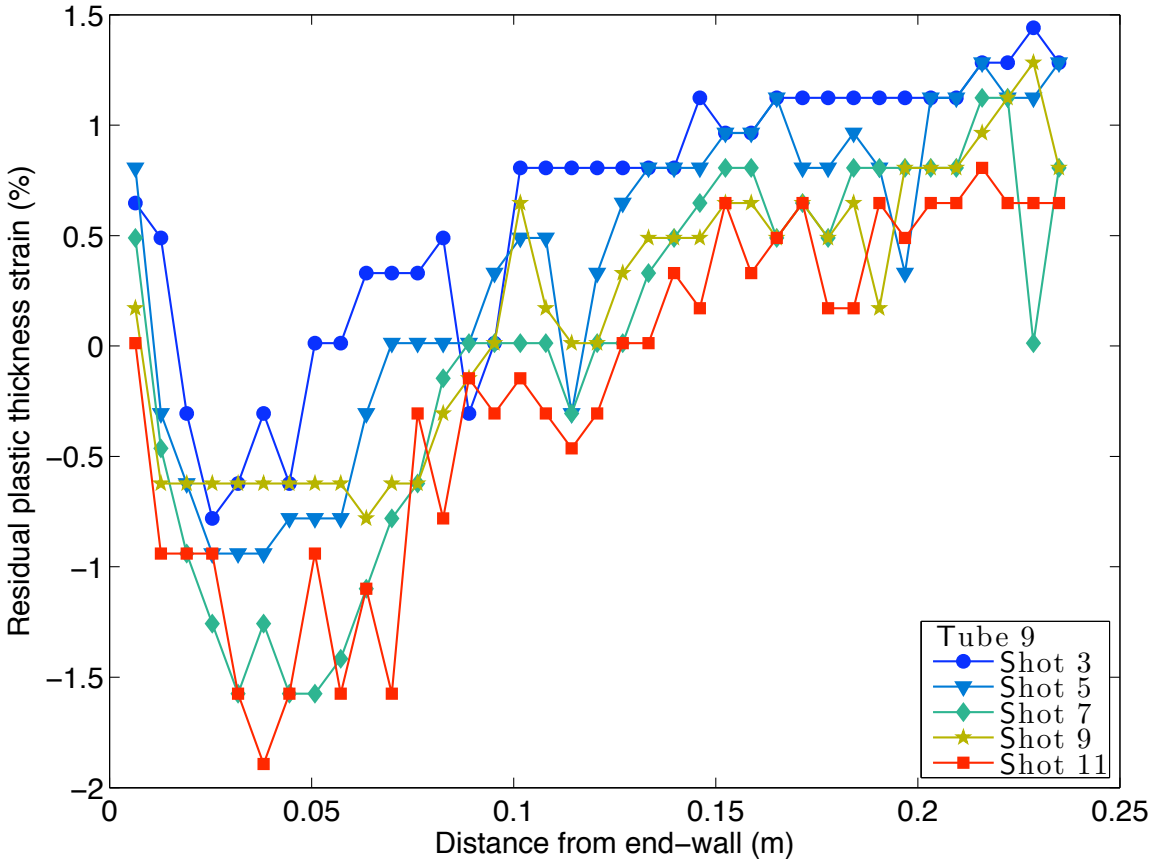

Figure A.10: Residual plastic thickness strain measurements in tube 9.

A.3 Tube 10 Data

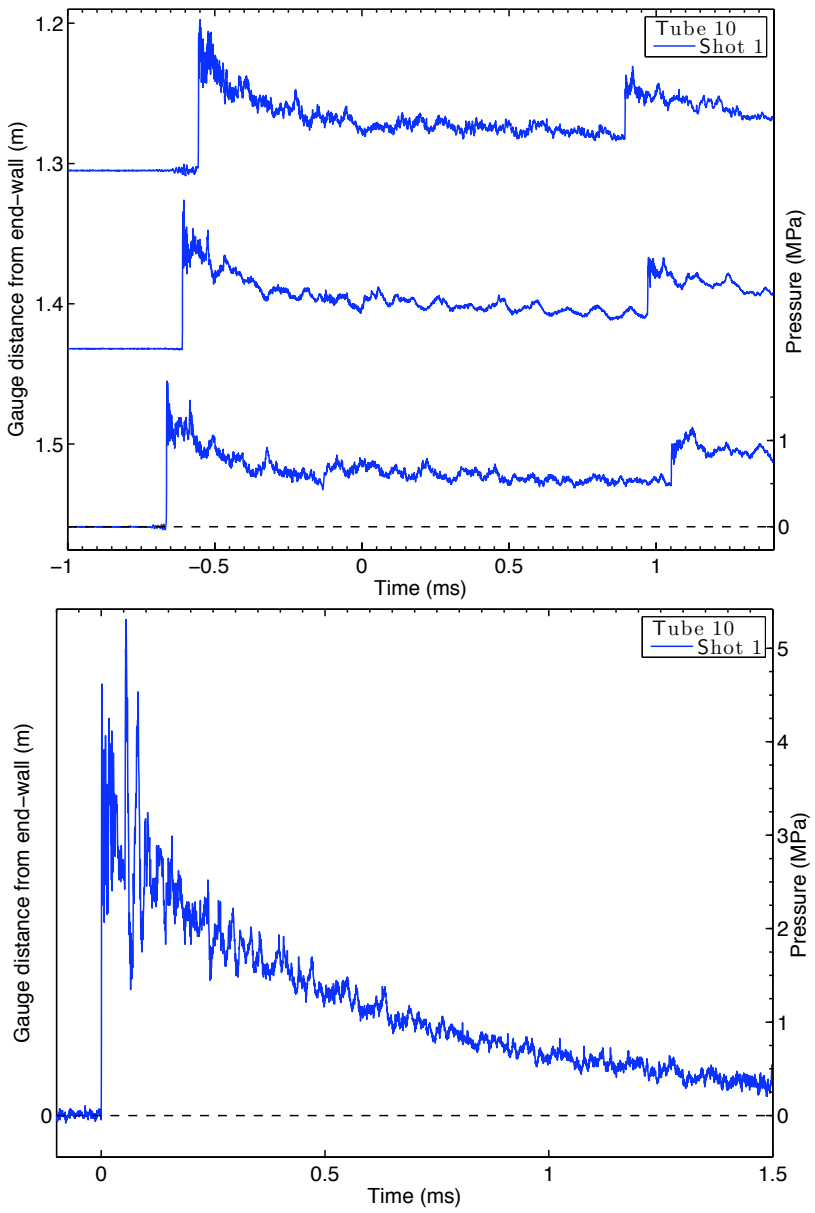

Figure A.11: Time-resolved pressure measurements from elastic shots in tube 10.

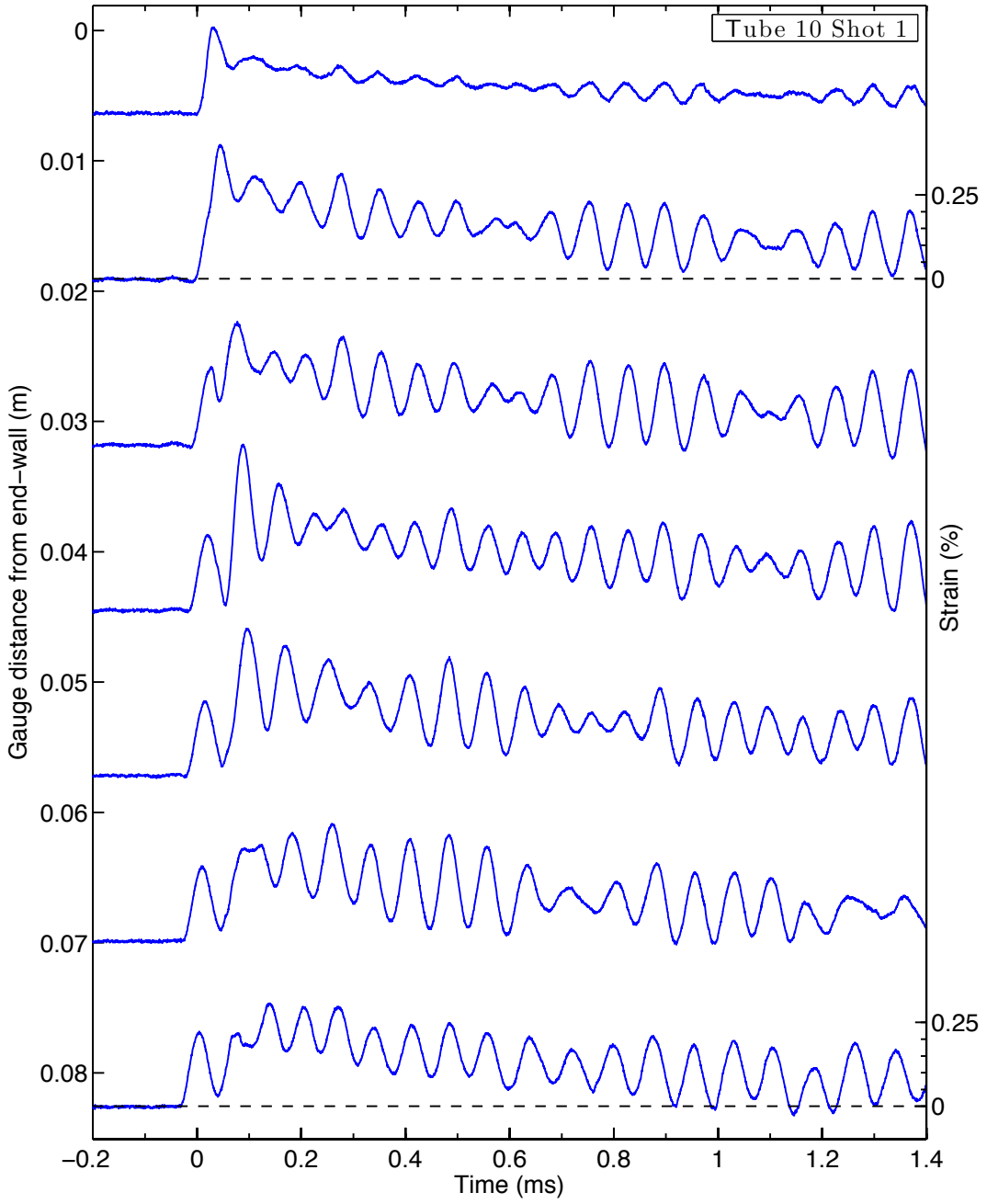

Figure A.12: Time-resolved elastic hoop strain measurements in tube 10, part 1.

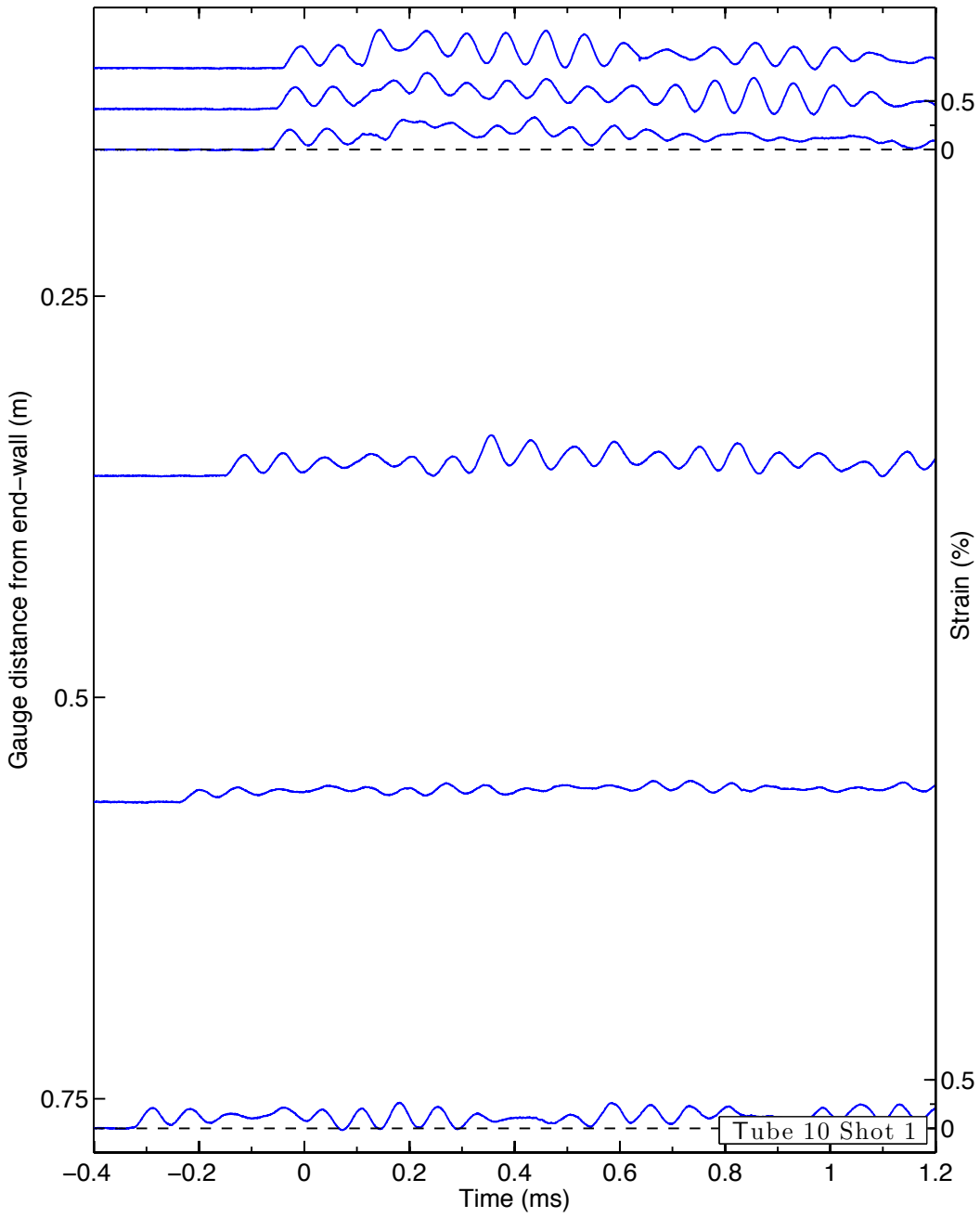

Figure A.13: Time-resolved elastic hoop strain measurements in tube 10, part 2.

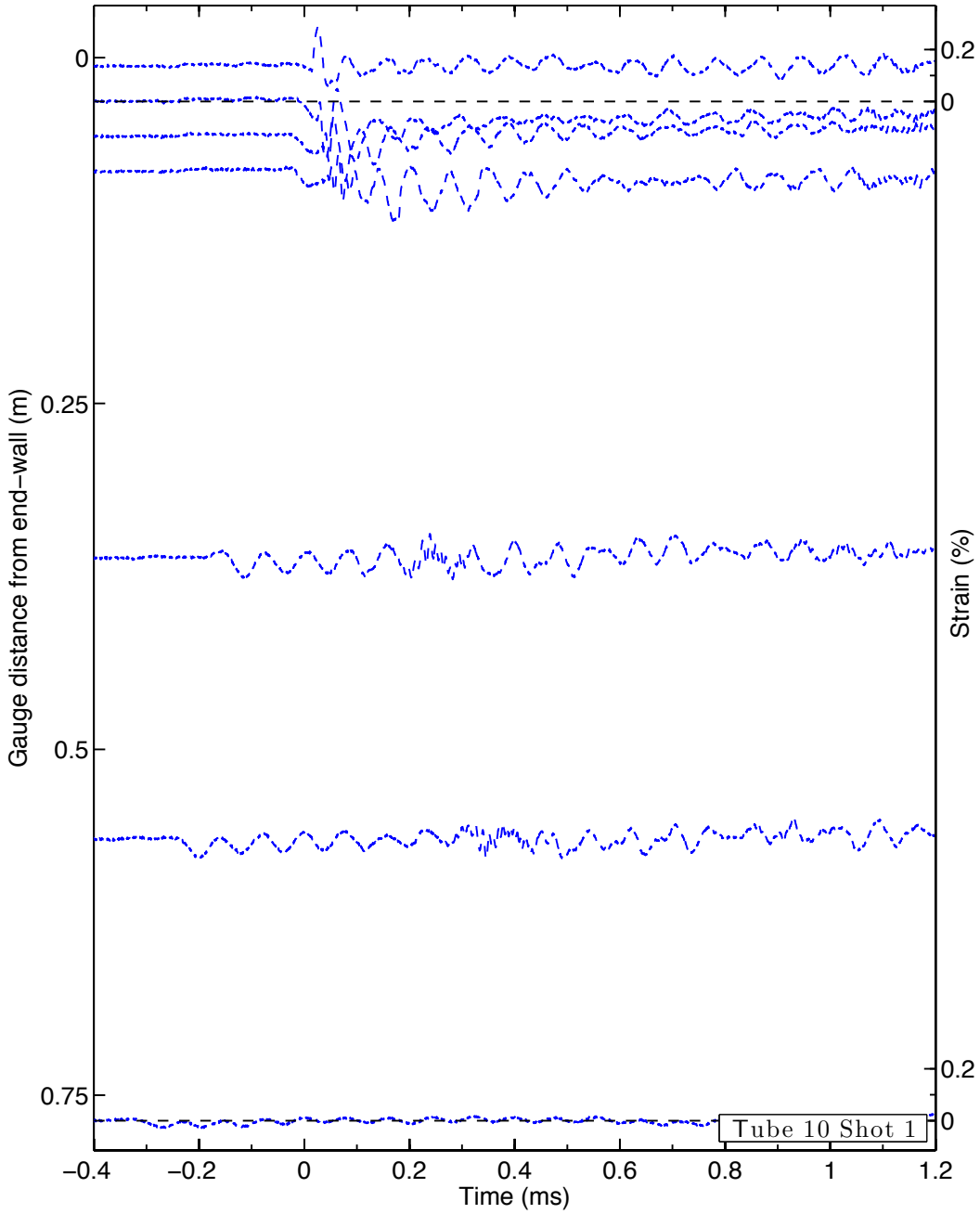

Figure A.14: Time-resolved elastic longitudinal strain measurements in tube 10.

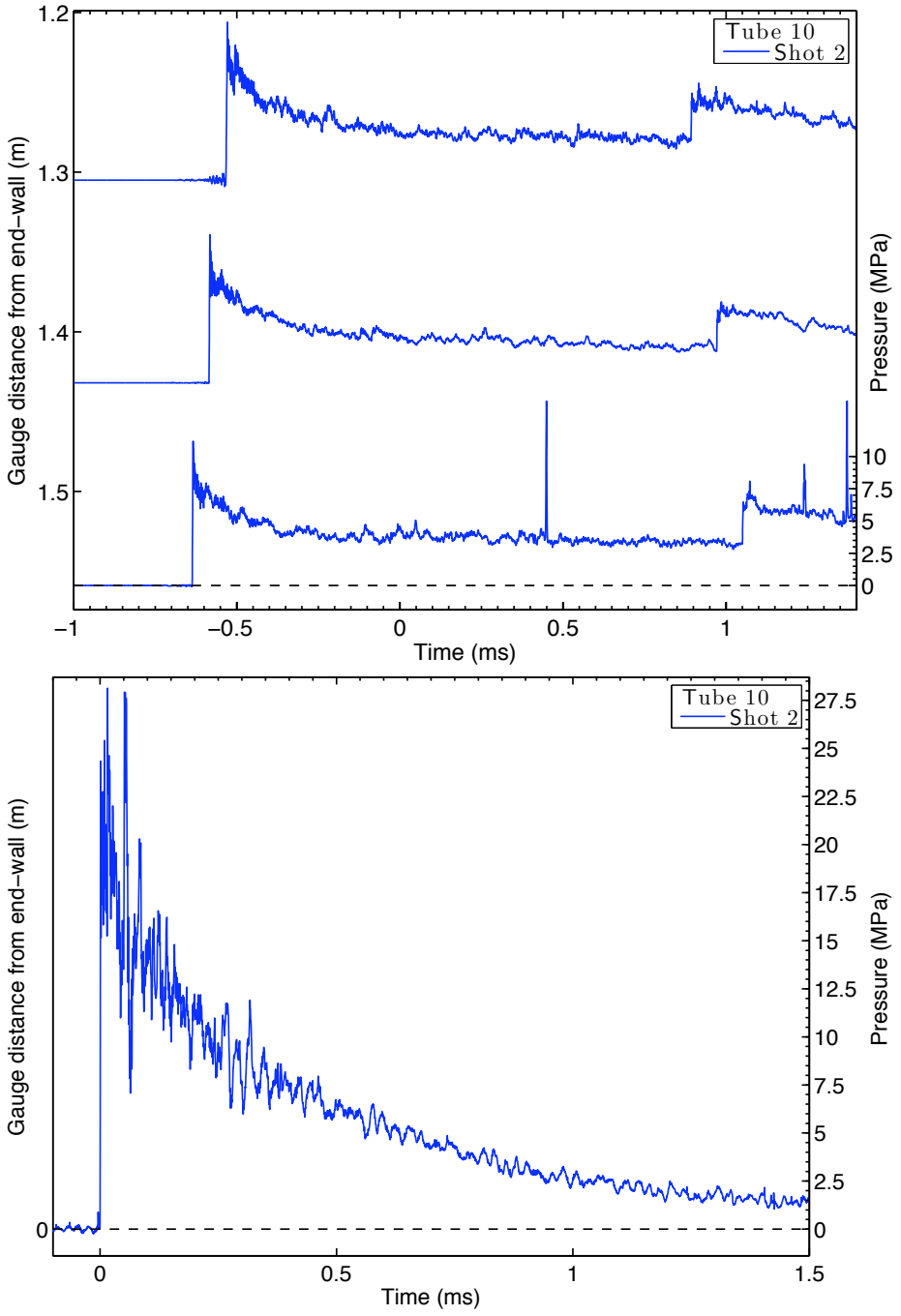

Figure A.15: Time-resolved pressure measurements from plastic shots in tube 10.

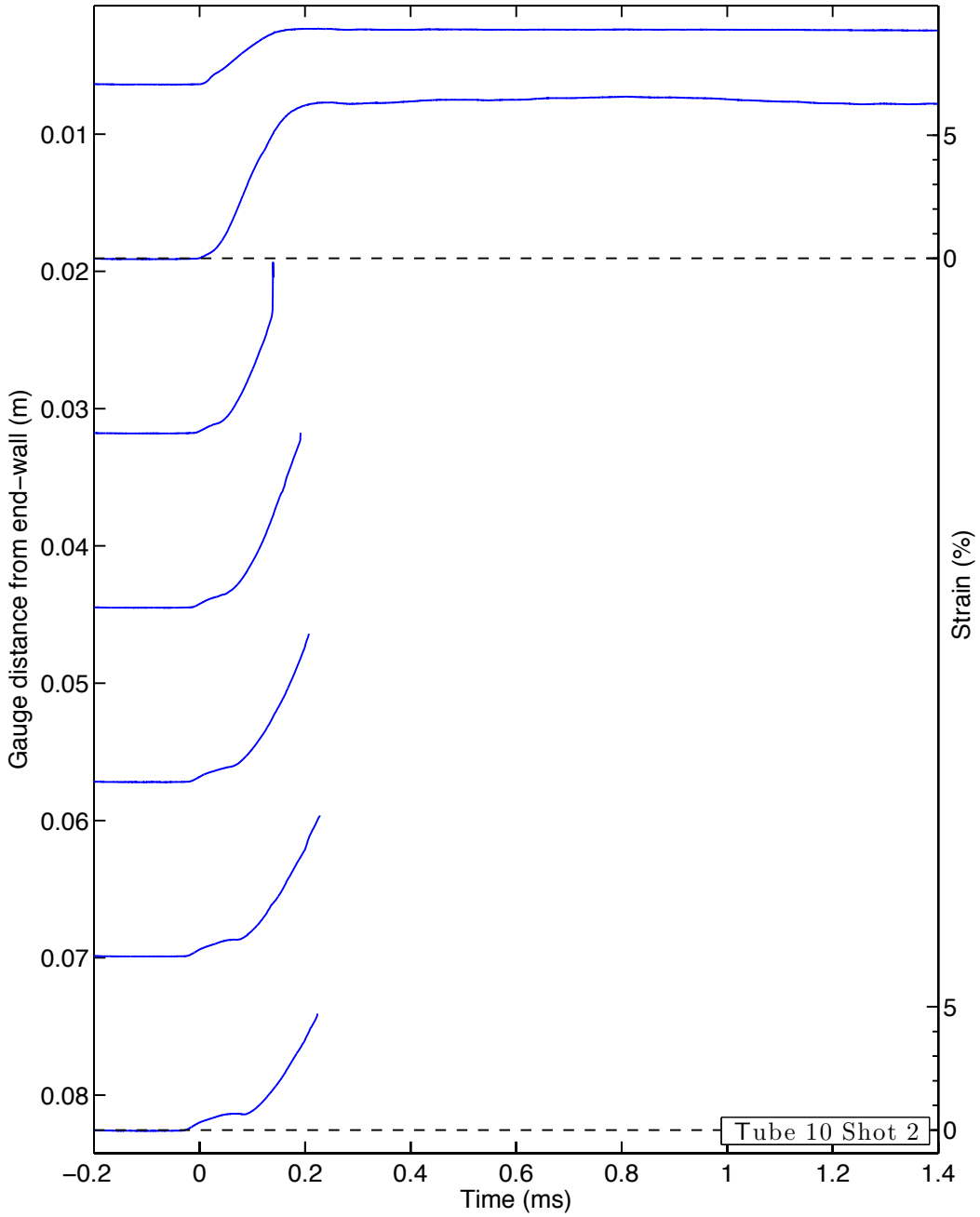

Figure A.16: Time-resolved plastic hoop strain measurements in tube 10, part 1.

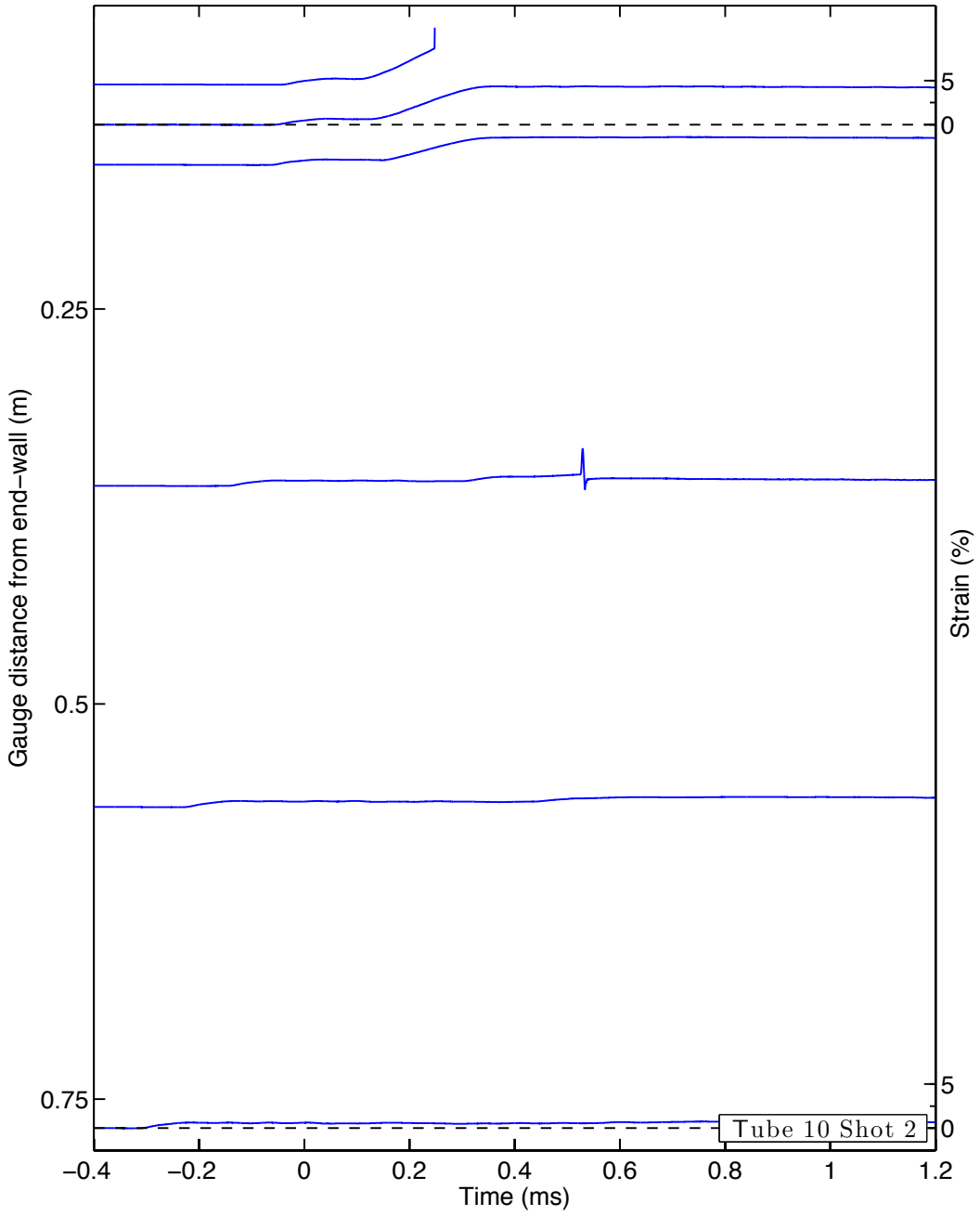

Figure A.17: Time-resolved plastic hoop strain measurements in tube 10, part 2.

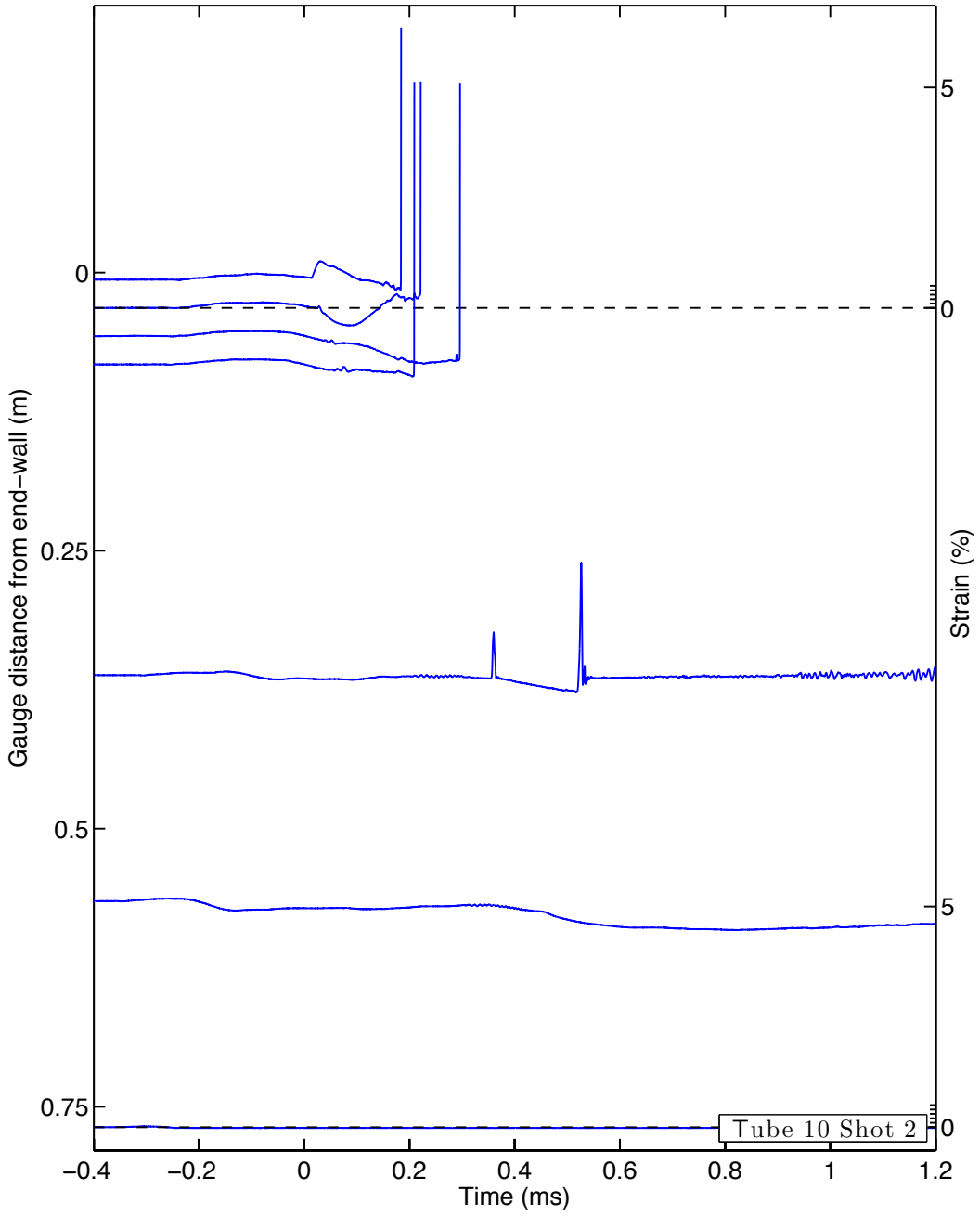

Figure A.18: Time-resolved plastic longitudinal strain measurements in tube 10.

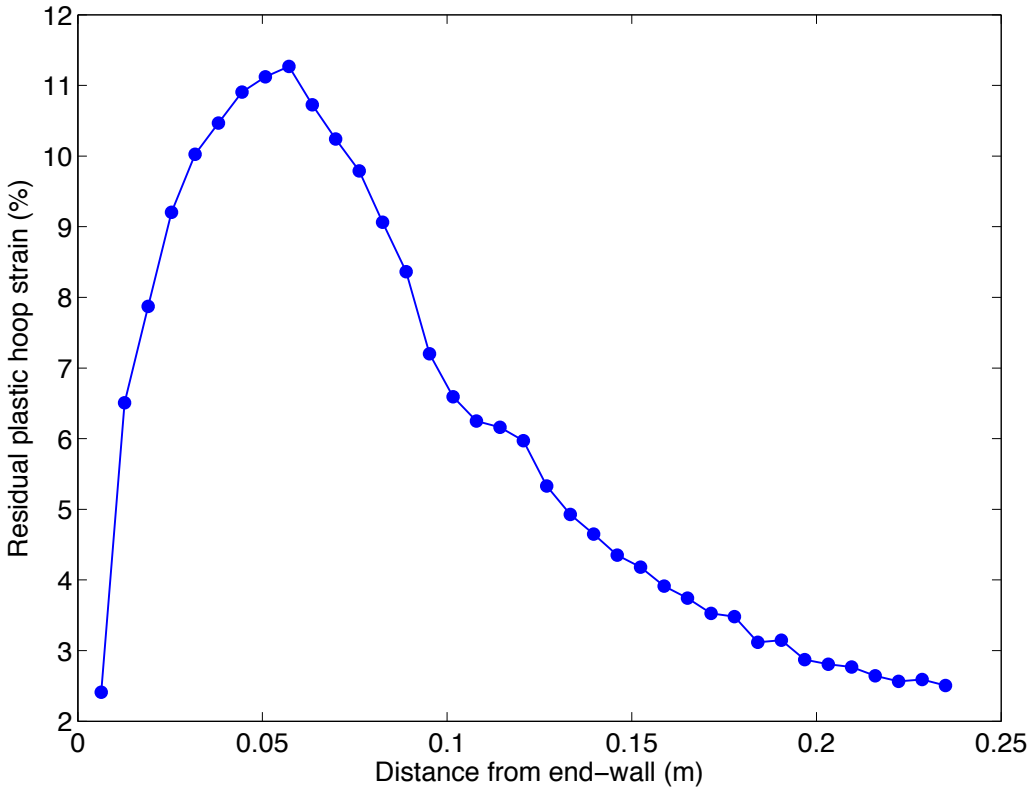

Figure A.19: Residual plastic hoop strain measurements in tube 10.

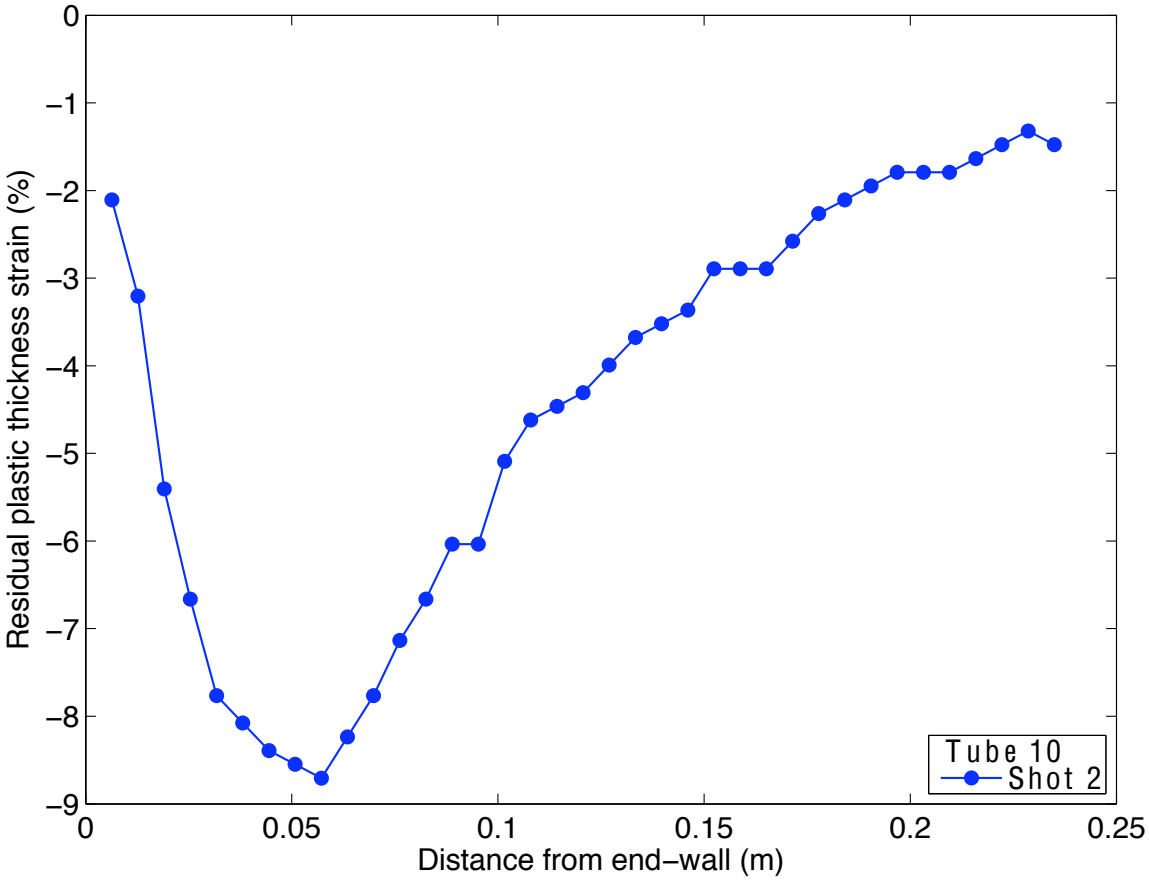

Figure A.20: Residual plastic thickness strain measurements in tube 10.

A.4 Tube 11 Data

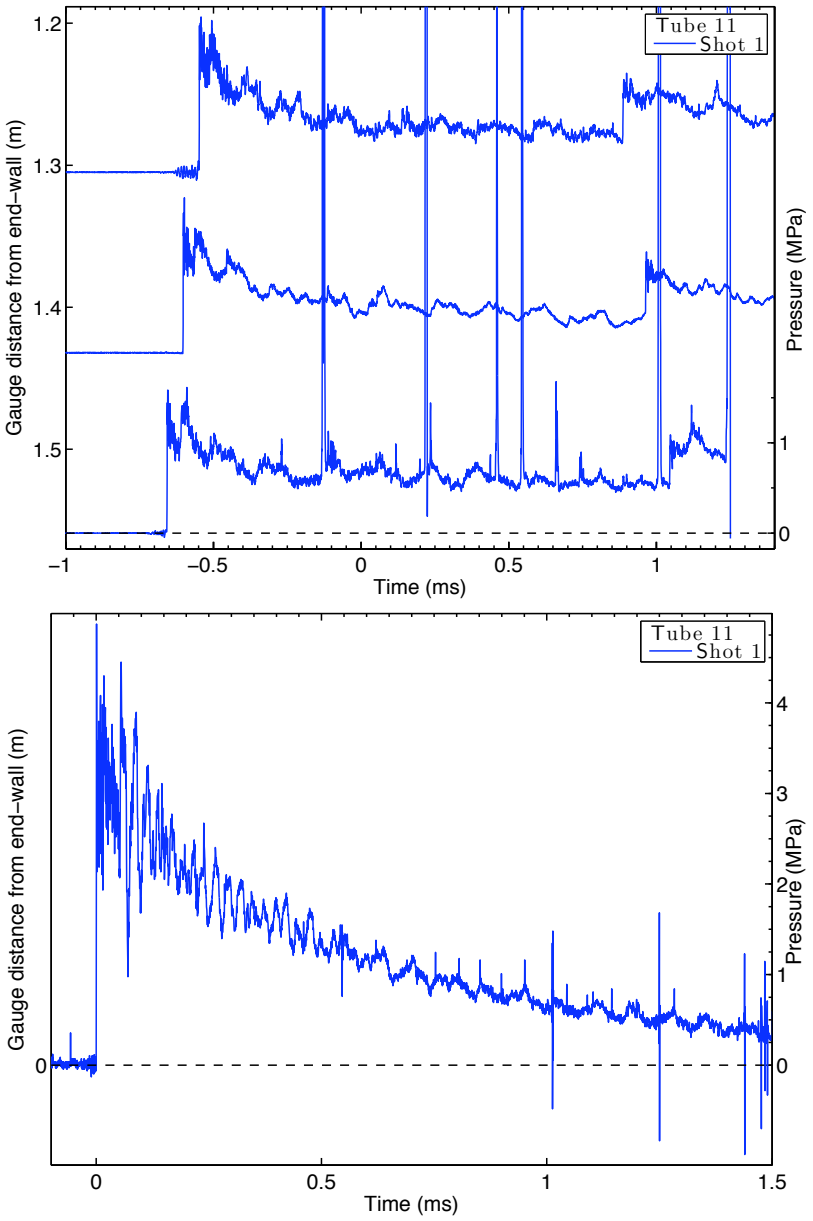

Figure A.21: Time-resolved pressure measurements from elastic shots in tube 11.

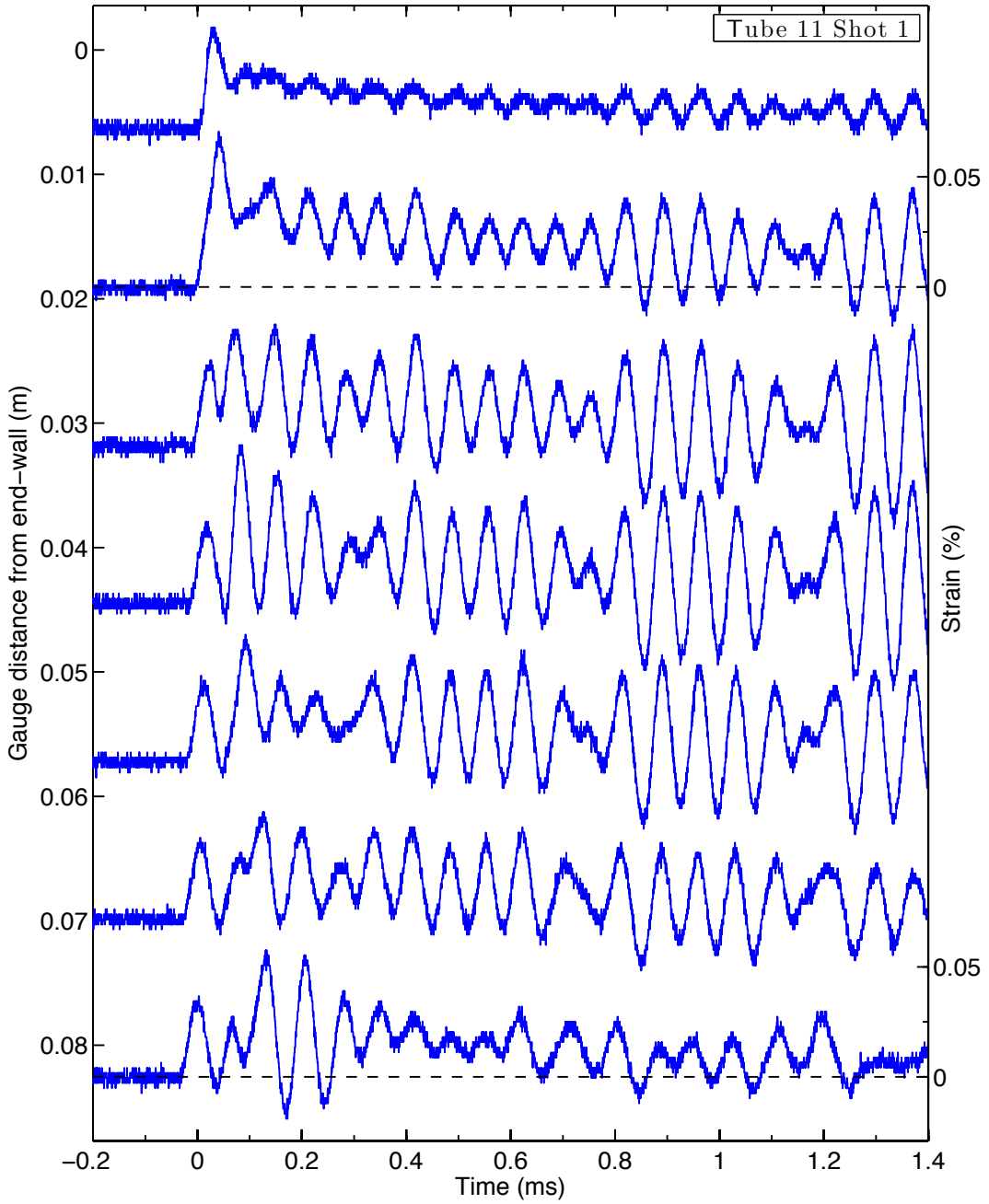

Figure A.22: Time-resolved elastic hoop strain measurements in tube 11, part 1.

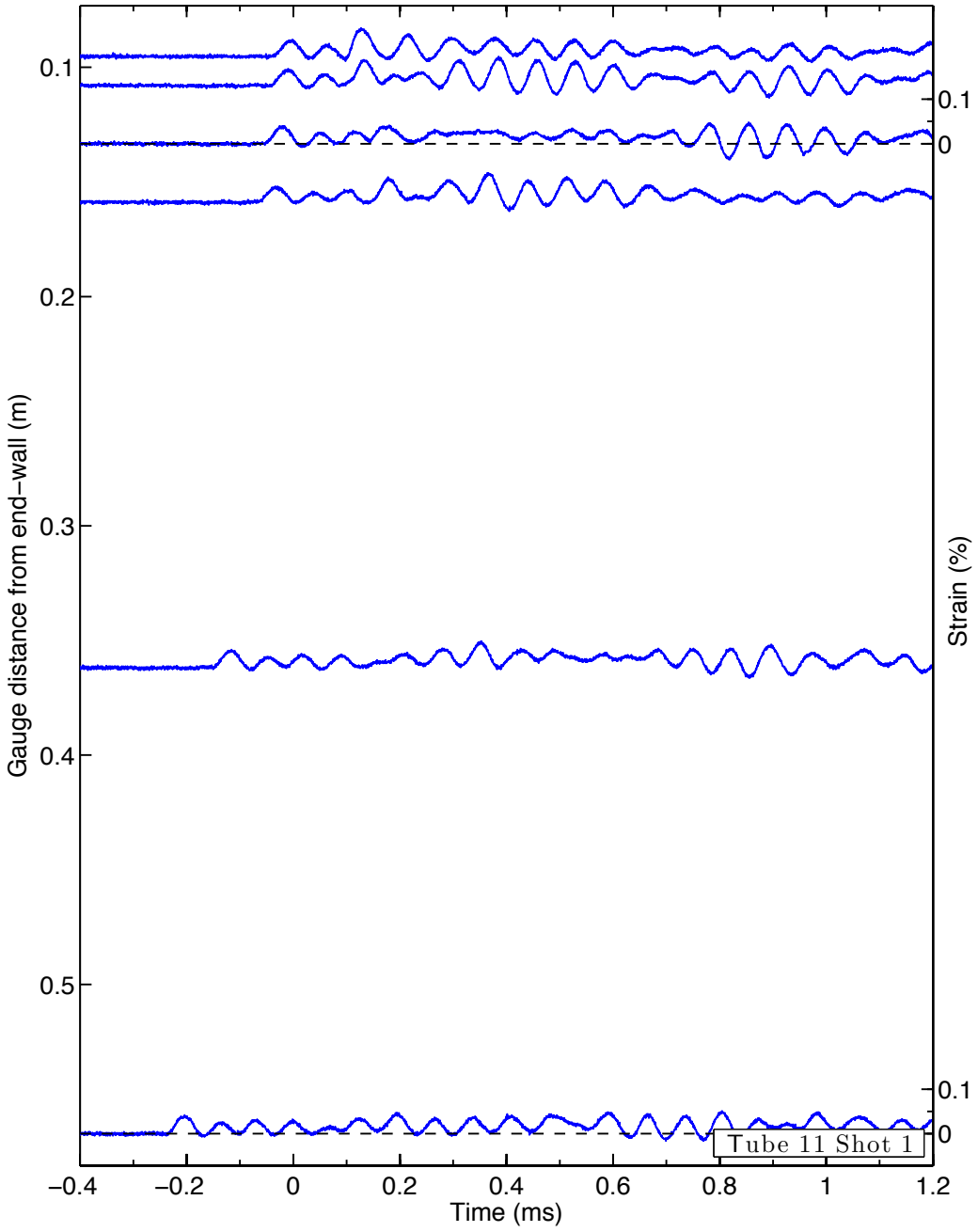

Figure A.23: Time-resolved elastic hoop strain measurements in tube 11, part 2.

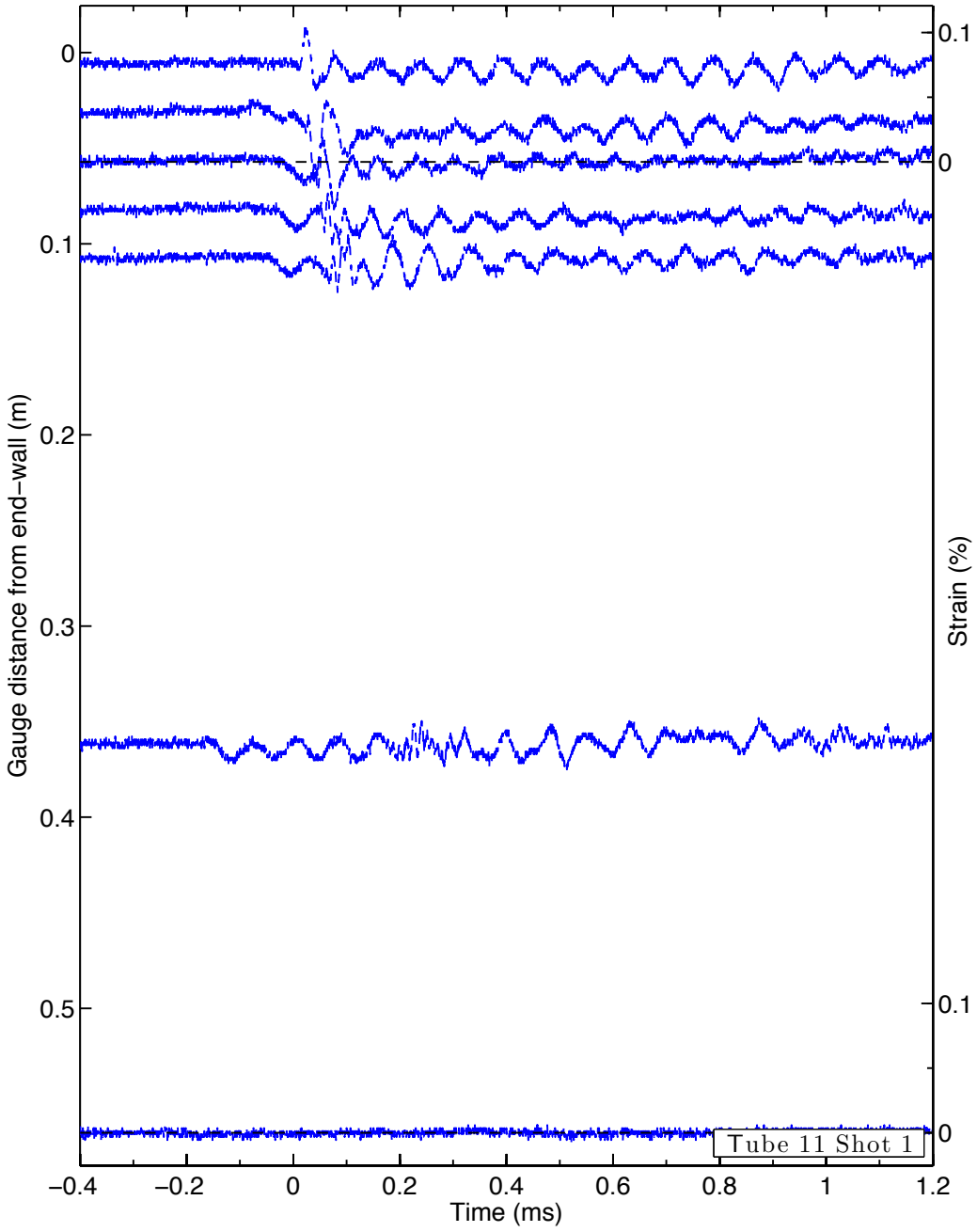

Figure A.24: Time-resolved elastic longitudinal strain measurements in tube 11.

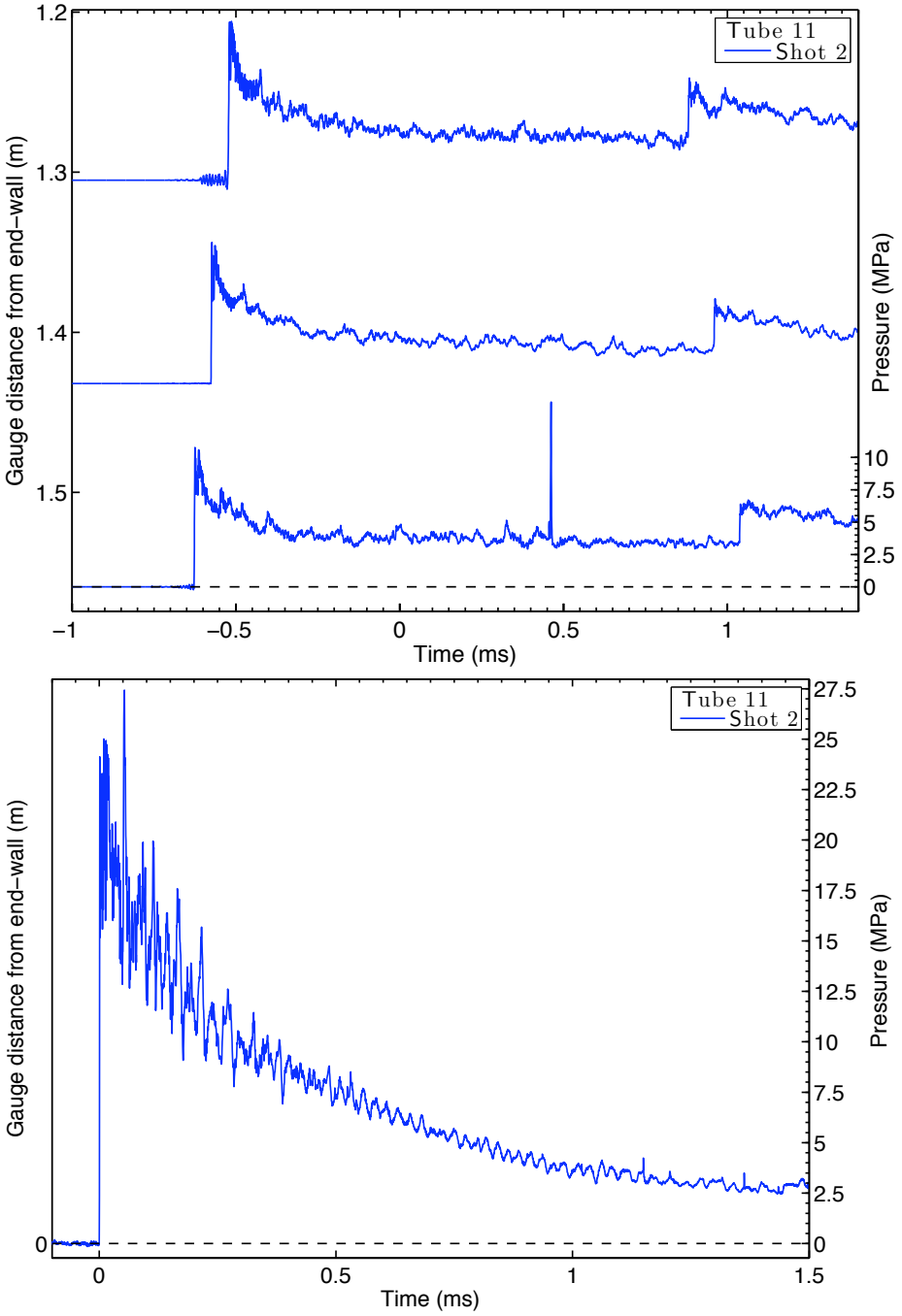

Figure A.25: Time-resolved pressure measurements from plastic shots in tube 11.

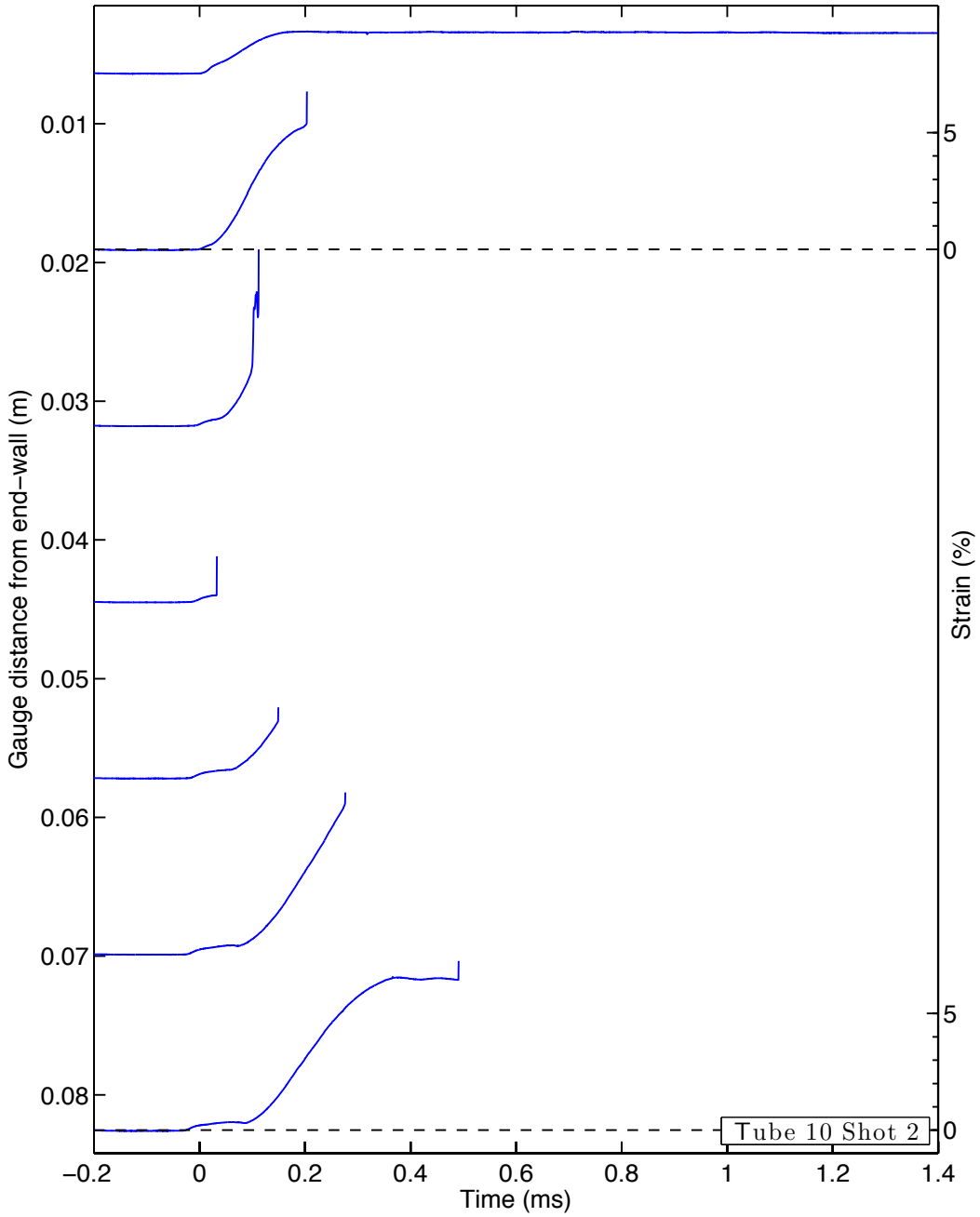

Figure A.26: Time-resolved plastic hoop strain measurements in tube 11, part 1.

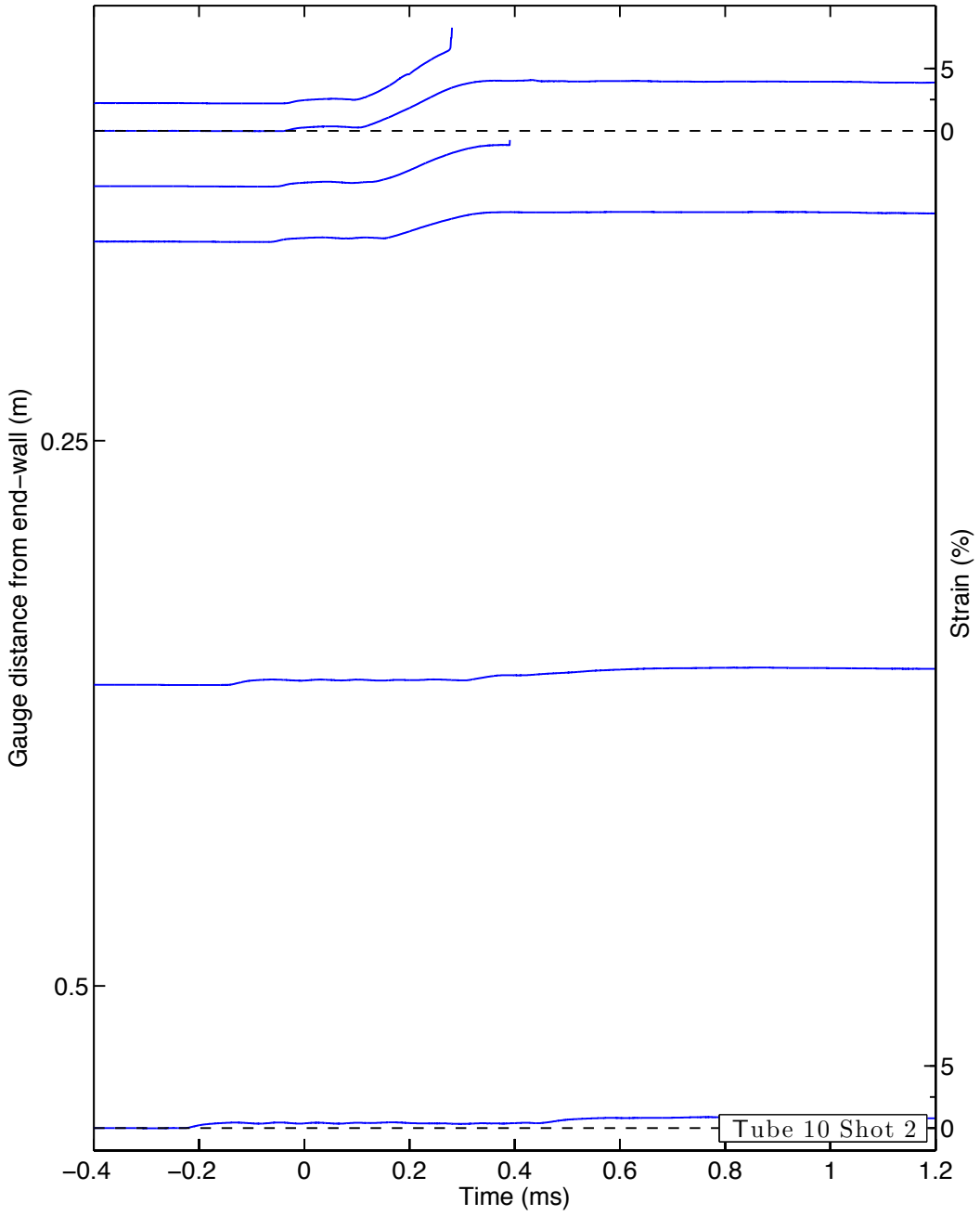

Figure A.27: Time-resolved plastic hoop strain measurements in tube 11, part 2.

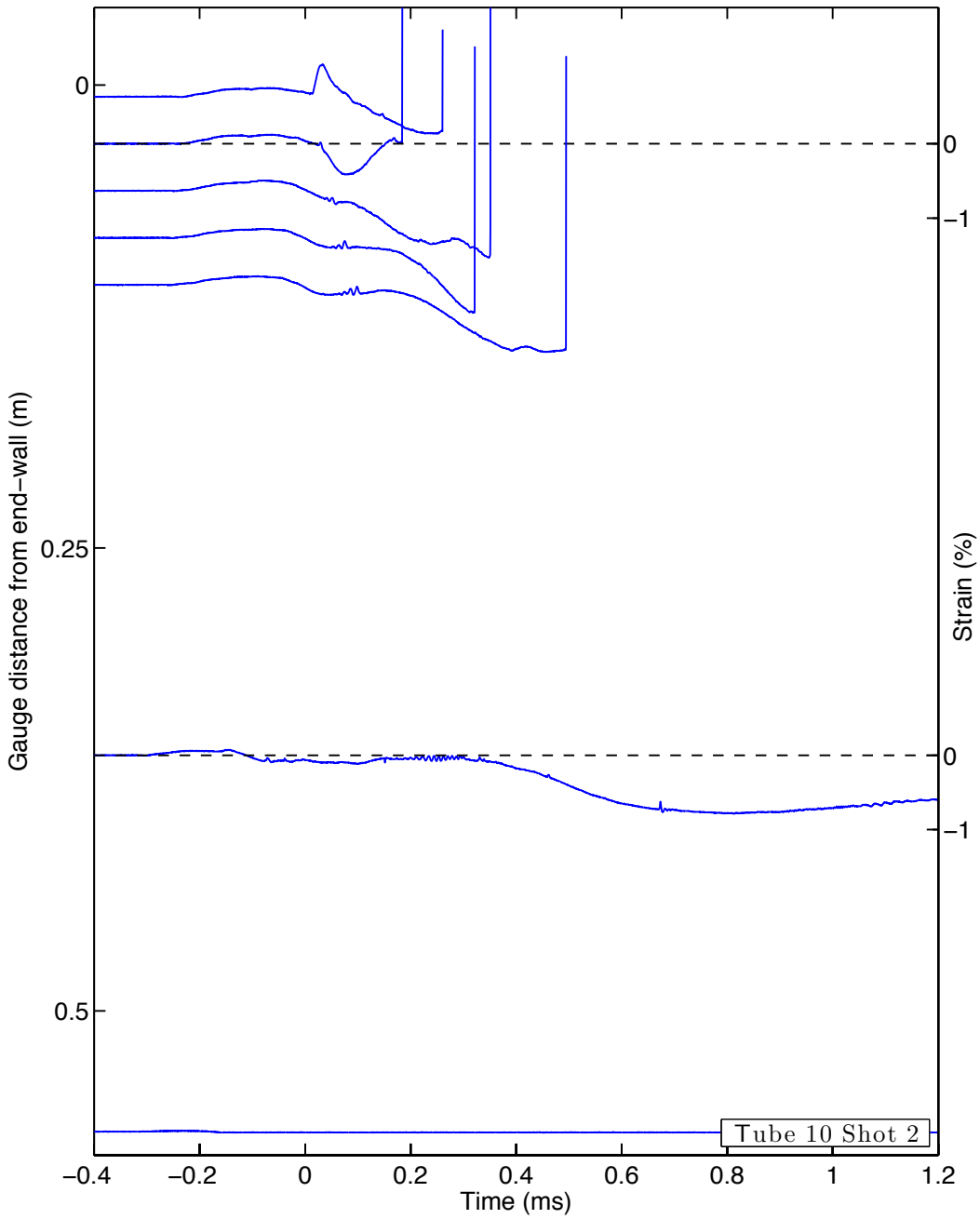

Figure A.28: Time-resolved plastic longitudinal strain measurements in tube 11.

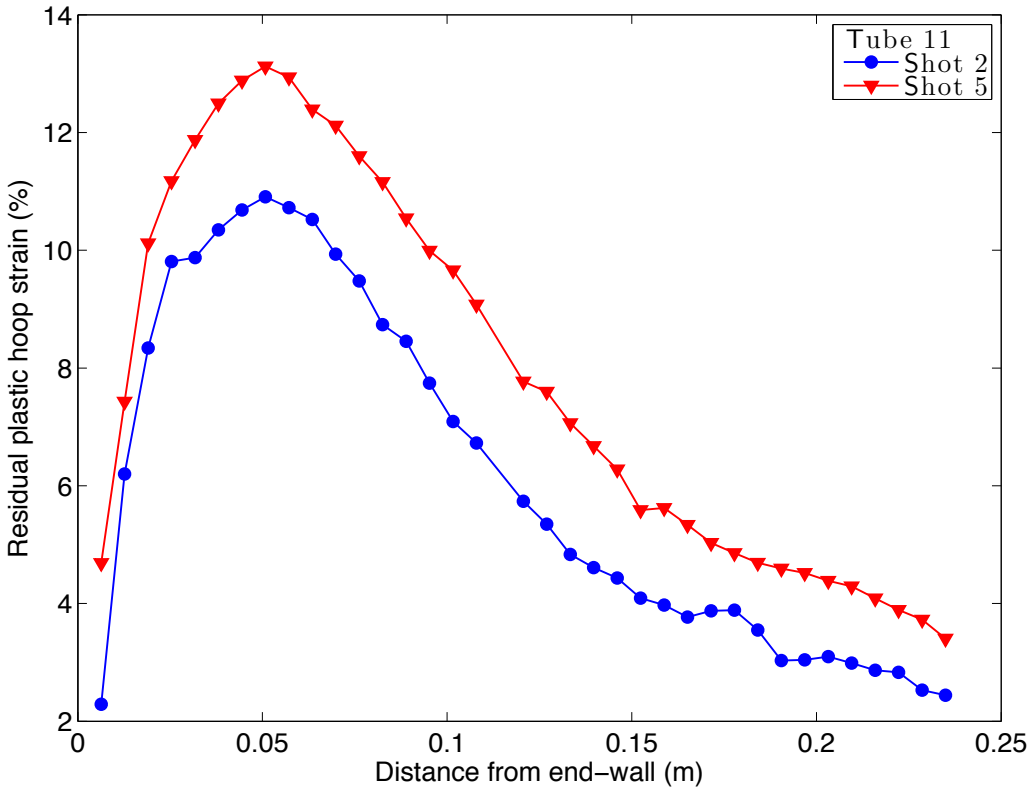

Figure A.29: Residual plastic hoop strain measurements in tube 11.

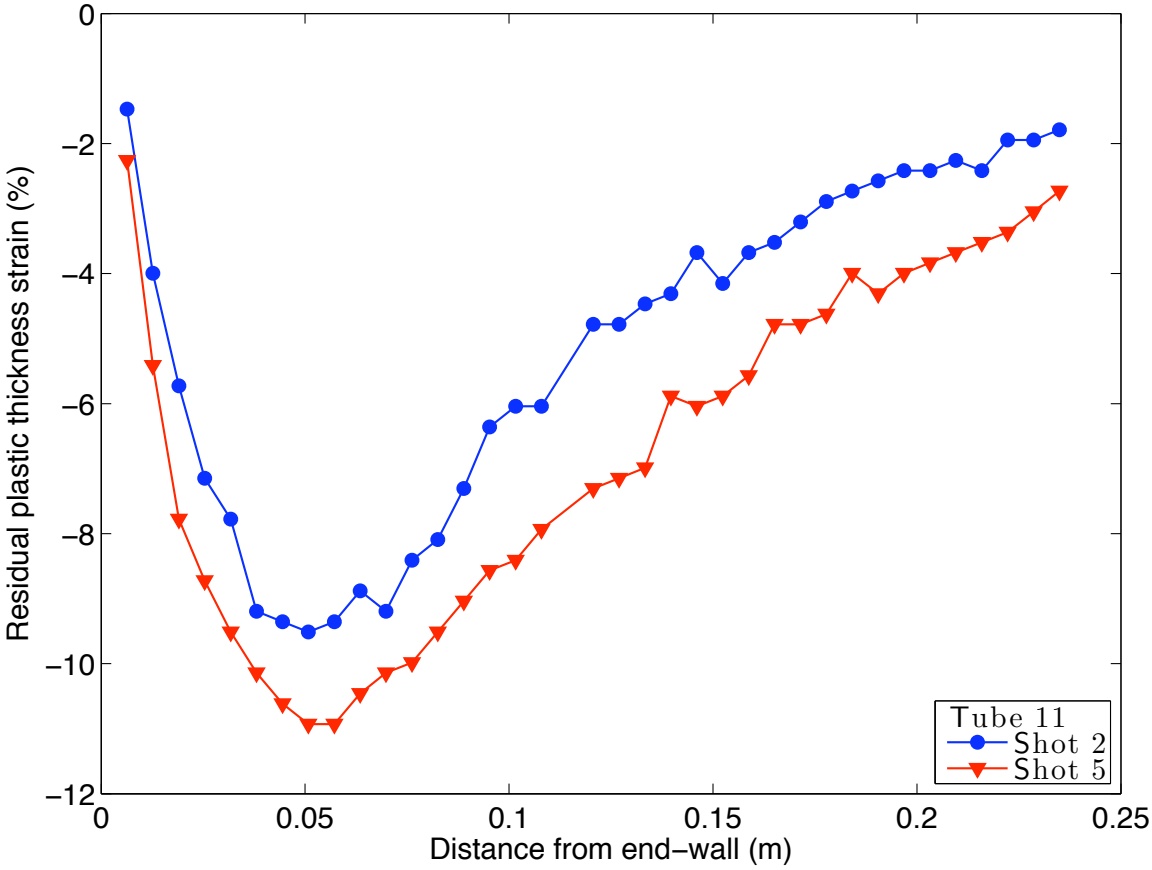

Figure A.30: Residual plastic thickness strain measurements in tube 11.

Appendix B

Single Degree of Freedom Model

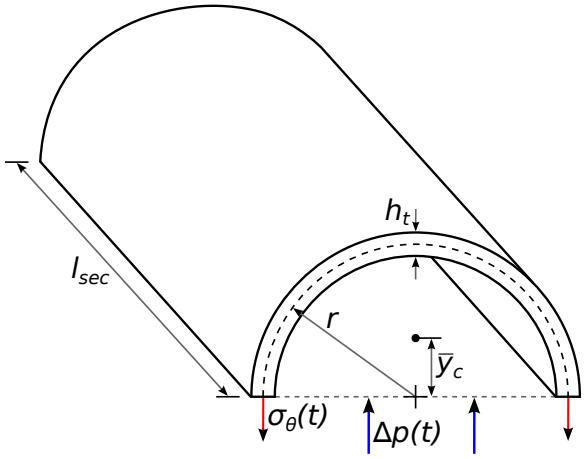

Figure B.1: Sketch of the forces applied to a thin-walled tube of infinite length.

The equations of motion for the single degree of freedom oscillator are derived here. Applying Newton's second law to the shell shown in figure B.1, we see

$$m_{sec}\frac{d^2\overline{y}_c}{dt^2} = 2rl_{sec}\Delta p(t) - 2h_t l_{sec}\sigma_\theta(t) \tag{B.1}$$

where m_{sec} is the mass of the tube section, $\overline{y}_c$ is the location of the centroid of the tube, r is the tube radius, l_{sec} is the length of the tube section, $\Delta p(t)$ is the time-dependent difference in pressure across the tube wall, h_t is the thickness of the tube, and $\sigma_\theta(t)$ is the time-dependent hoop stress in the shell wall. Using the density of the tube, ρ_t, we see

$$\pi r h_t l_{sec} \rho_t \frac{d^2\overline{y}_c}{dt^2} = 2 r l_{sec} \Delta p(t) - 2 h_t l_{sec} \sigma_\theta(t) \tag{B.2}$$

$$\frac{\pi}{2} \frac{d^2\overline{y}_c}{dt^2} = \frac{\Delta p(t)}{\rho_t h_t} - \frac{\sigma_\theta(t)}{\rho_t r}. \tag{B.3}$$

The location of the centroid for a half-circle is given by

$$\overline{y}_c = \frac{2r}{\pi} \tag{B.4}$$

implying

$$\frac{d^2\overline{y}_c}{dt^2} = \frac{2}{\pi}\frac{d^2 r}{dt^2} = \frac{2}{\pi}\frac{d^2 r'}{dt^2} \tag{B.5}$$

with $r' = r - r_0$, since $d^2 r_0/dt^2 = 0$. Thus we have

$$\frac{d^2 r'}{dt^2} = \frac{\Delta p(t)}{\rho_t h_t} - \frac{\sigma_\theta(t)}{\rho_t r}. \tag{B.6}$$

The hoop stress can be determined from

$$\sigma_\theta = \begin{cases} E_1 \epsilon_\theta & \sigma \leq \sigma_y \\ \sigma_y + E_2 \left(\epsilon - \epsilon_y\right) & \sigma > \sigma_y \end{cases} \tag{B.7}$$

where σ_y is the yield stress tracked by the additional equation

$$\frac{d\sigma_y}{dt} = \frac{d\sigma_y}{d\sigma_\theta}\frac{d\epsilon_\theta}{dt} \tag{B.8}$$

with

$$\frac{d\sigma_y}{d\sigma_\theta} = \begin{cases} 1 & \sigma \geq \sigma_y \\ 0 & \sigma < \sigma_y \end{cases}. \tag{B.9}$$

The equation for σ_θ assumes a state of unidirectional stress. This is justified since the tube thickness, h_t, is much smaller than the other dimensions, r and L. The large radius implies that stresses normal to the tube surface are much smaller than the hoop stress term, and, if we consider the dynamic loading of a location far from a restricting boundary condition as is the case for most of the tube if L is large, axial stress will only come from the inertia of the tube wall; this is also much less than the hoop stress term because the small thickness implies the mass of the tube per unit length is negligible relative to the pressure and hoop stress terms.

Appendix C

GDT Experimental Procedure and Drawings

Contained herein are the checklist, shot list, and drawing files pertaining to experiments performed in the GALCIT detonation tube. A description of the visualization systems employed is included in appendix D and all data gathered are included in appendix E.

C.1 GDT Checklist

Checklist for experiments performed in the GALCIT detonation tube.

Operator: Jason Damazo

Beginning of shot series

1. Turn on vacuum pump and heat exchanger.
2. Turn on desired bottles in bottle farm.
3. Turn on driver gases, record regulator settings.
4. Tighten endplate bolts.

Preparation and pump down

5. Load firing plug with wire.
6. Check that clamp bolts are snug and clamp movement is clear.

7. Pressurize hydraulics to 3500 psi, make sure all clamps engage backing plate surface.
8. Enable Main Control Panel power.
9. Turn on Main Control Panel 12 V relay.
10. Open valves: E1, T1, T2, T3, V1, V2, V3, MKS, G1, and N1.
11. Close valve: L1.
12. Wait for pressure to drop below 100 mTorr.
13. Zero fill pressure gauge.
14. Close valves: V1, V2, and V3.
15. Record final vacuum pressure.

Gas fill

16. Turn on warning lights and check that doors are closed (Laboratory access is restricted).
17. Don ear protection.
18. Fill GDT until internal pressure meets desired fill pressure, record achieved pressures.
19. Close valves: G1 and N1.
20. Turn on mixing pump, mix for 5 minutes.
21. Close valves: E1, T1, T2, T3, and MKS.

Firing procedure

22. Switch off 12 V relay.
23. Check that 'Fire Ready' light is on.

24. Turn on wire exploder.
25. Turn on Charge switch.
26. Charge for 2 minutes.
27. Arm data acquisition.
28. Arm wire exploder key switch.
29. Fire: Press run on delay generator (wait for detonation to occur).
30. Turn off Charge switch.
31. Disarm wire exploder key switch.
32. Turn off wire exploder.
33. If no combustion, dilute mixture.
34. Turn off warning lights (Laboratory access is unrestricted).
35. Record shot time.

Cleanup

36. Switch on 12 V relay on Main Control Panel.
37. Open valve: MKS, record post-detonation pressure.
38. Open valves: V1, V2, V3, T1, T2, T3, and E1, wait for vacuum.
39. Turn off driver gases.
40. Turn off vacuum pump.
41. Open valve: L1.
42. Turn off bottles in bottle farm.
43. Back-up and convert data.

C.2 GDT Shotlist

Below is the shotlist for all detonations in the GDT during my tenure at Caltech (November 19, 2010–May 31, 2013). Initial tests (shots 1930–1962) were preliminary experiments performed before a splitter plate was designed; their primary purpose was to gain knowledge with the operation of the GDT and to take preliminary detonation and reflection pictures. Shot numbers 1963–2021 used an early implementation of the splitter plate that did not have pressure and heat-flux gauges. The remaining tests (2022–2199) were performed with the splitter plate that was equipped with pressure and heat-flux measurement gauges, however it was only beginning with shot 2071 that the new data acquisition system described in chapter 3 was obtained and all pressure and heat-flux data were recorded. The pressure gauge located 25.4 mm from the reflecting end-wall was incorrectly calibrated for shots 2022–2112.

Table C.1: Shot list for experiments performed in the GDT. The data column indicates what was recorded for a particular test: 'p' indicates that time-resolved pressure data were saved, 'q' represents time-resolve heat-flux data, and 'i' is an image or video.

Shot number	p_1 (kPa)	Mixture	Data	Visualization
1930	7	C2H2:1 O2:1		phoenix[1]
1931	10	C2H2:1 O2:1		phoenix
1932	∼5	C2H2:1 O2:1	i	phoenix
1933	13	C2H2:1 O2:1	i	phoenix
1934	9	C2H2:1 O2:1	i	phoenix
1935	12	C2H2:1 O2:1	i	greenarrow[2]

Continued on next page

[1]The "Phoenix" visualization system used the Phantom v7.10 equipped with a camera lens pointed at the GDT window to record a simple movie of the detonation.

[2]The "Green arrow" visualization system used the Phantom v7.10 with a 200 mW, 532 nm interferometer laser in a Z-type schlieren set-up.

Table C.1 – continued from previous page

Shot number	p_1 (kPa)	Mixture	Data	Visualization
1936	12	C2H2:1 O2:1	i	greenarrow
1937	12	C2H2:1 O2:1		storm
1938	12	C2H2:1 O2:1		storm
1939	12	C2H2:1 O2:1		storm
1940	12	C2H2:1 O2:1		storm
1941	12	C2H2:1 O2:1		storm
1942	12	C2H2:1 O2:1		storm
1943	12	C2H2:1 O2:1		storm
1944	20	H2:2 O2:1 AR:12	i	storm
1945	20	H2:2 O2:1 AR:12	i	storm
1946	20	H2:2 O2:1 AR:12		storm
1947	20	H2:2 O2:1 AR:12		storm
1948	15	H2:2 O2:1 AR:12	i	storm
1949	15	H2:2 O2:1 AR:12		storm
1950	15	H2:2 O2:1 AR:12	i	storm
1951	15	H2:2 O2:1 AR:12	i	storm
1952	15	H2:2 O2:1 AR:12	i	storm
1953	15	H2:2 O2:1 HE:12	i	storm
1954	15	H2:2 O2:1 HE:12	i	storm
1955	15	H2:2 O2:1 HE:12	i	storm
1956	15	H2:2 O2:1 HE:12	i	storm
1957	5	H2:2 O2:1		storm
1958	5	H2:2 O2:1	i	storm
1959	5	H2:2 O2:1	i	storm
1960	5	H2:2 O2:1	i	storm
1961	5	H2:2 O2:1		storm

Continued on next page

Table C.1 – continued from previous page

Shot number	p_1 (kPa)	Mixture	Data	Visualization
1962	5	H2:2 O2:1		storm
1963	15	H2:2 O2:1 AR:12	i	storm
1964	15	H2:2 O2:1 AR:12	i	storm
1965	15	H2:2 O2:1 AR:12	i	storm
1966	15	H2:2 O2:1 AR:12	i	storm
1967	15	H2:2 O2:1 AR:12	i	storm
1968	10	H2:2 O2:1	i	storm
1969	10	H2:2 O2:1	i	storm
1970	10	H2:2 O2:1		storm
1971	10	H2:2 O2:1	i	storm
1972	15	H2:2 O2:1 N2:12	i	storm
1973	15	H2:2 O2:1 N2:12	i	storm
1974	15	H2:2 O2:1 N2:12	i	storm
1975	15	H2:2 O2:1 N2:12	i	storm
1976	15	H2:2 O2:1	i	storm
1977	15	H2:2 O2:1	i	storm
1978	15	H2:2 O2:1	i	storm
1979	15	H2:2 O2:1	i	storm
1980	15	H2:14 O2:1	i	storm
1981	15	H2:14 O2:1	i	storm
1982	15	H2:14 O2:1	i	storm
1983	15	H2:14 O2:1	i	storm
1984	15	H2:14 O2:1	i	storm
1985	15	H2:13 O2:2	i	storm
1986	15	H2:13 O2:2		storm
1987	15	H2:13 O2:2	i	storm

Continued on next page

Table C.1 – continued from previous page

Shot number	p_1 (kPa)	Mixture	Data	Visualization
1988	15	H2:13 O2:2	i	storm
1989	15	H2:13 O2:2	i	storm
1990	15	H2:13 O2:2	i	storm
1991	15	H2:13 O2:2	i	storm
1992	25	air		storm
1993	25	air	i	storm
1994	25	air	i	storm
1995	25	air	i	storm
1996	25	air	i	storm
1997	25	air	i	storm
1998	25	air	i	storm
1999	25	air	i	storm
2000	25	air	i	storm
2001	15	N2O:1		storm
2002	15	N2O:1	i	storm
2003	15	N2O:1	i	storm
2004	15	H2:6 N2O:94	i	storm
2005	15	H2:6 N2O:94	i	storm
2006	16	H2:6 N2O:94	i	storm
2007	15	H2:6 N2O:94	i	storm
2008	15	H2:1 N2O:9	i	storm
2009	15	H2:1 N2O:9		storm
2010	15	H2:1 N2O:9		storm
2011	15	H2:1 N2O:9	i	storm
2012	10	H2:2 O2:1		storm
2013	15	H2:2 O2:1		greenlantern

Continued on next page

Table C.1 – continued from previous page

Shot number	p_1 (kPa)	Mixture	Data	Visualization
2014	15	H2:2 O2:1		greenlantern
2015	15	H2:2 O2:1		greenlantern
2016	15	H2:2 O2:1	i	greenlantern
2017	15	H2:2 O2:1	i	greenlantern
2018	15	H2:2 O2:1	i	greenlantern
2019	15	H2:1 N2O:9	i	greenlantern
2020	15	H2:1 N2O:9	i	greenlantern
2021	15	H2:1 N2O:9	i	greenlantern
2022	15	H2:1 N2O:9		greenlantern
2023	15	N2O:1	i	greenlantern
2024	15	N2O:1	i	greenlantern
2025	15	N2O:1	i	greenlantern
2026	15	N2O:1	i	greenlantern
2027	15	N2O:1	i	greenlantern
2028	15	H2:1 N2O:9	i	greenlantern
2029	15	H2:1 N2O:9	i	greenlantern
2030	15	H2:1 N2O:9	i	greenlantern
2031	15	N2O:1	i	greenlantern
2032	15	N2O:1	i	greenlantern
2033	15	N2O:1	i	greenlantern
2034	15	N2O:1	i	greenlantern
2035	16	air	i	greenlantern
2036	15	N2O:1	i	greenlantern
2037	14	air	i	greenlantern
2038	14	air	i	greenlantern
2039	15	air	i	greenlantern

Continued on next page

Table C.1 – continued from previous page

Shot number	p_1 (kPa)	Mixture	Data	Visualization
2040	∼100	air	i	greenlantern
2041	15	N2O:1	p,i	greenlantern
2042	15	N2O:1	p,i	greenlantern
2043	15	N2O:1	p,i	greenlantern
2044	15	N2O:1	p,i	greenlantern
2045	15	N2O:1	p,i	greenlantern
2046	15	N2O:1	p,i	greenlantern
2047	15	N2O:1	p,i	greenlantern
2048	15	H2:1 N2O:9	p	greenlantern
2049	15	H2:15 N2O:85	p	greenlantern
2050	15	H2:2 N2O:8	p	greenlantern
2051	15	H2:25 N2O:75	p	greenlantern
2052	15	H2:3 N2O:7	p	greenlantern
2053	15	H2:35 N2O:65	p	greenlantern
2054	15	N2O:1	p,i	greenlantern
2055	15	N2O:1	p,i	greenlantern
2056	15	N2O:1	p	greenlantern
2057	15	N2O:1	p,i	greenlantern
2058	15	HE:1	p,i	greenlantern
2059	15	HE:1	p,i	greenlantern
2060	15	HE:1	p,i	greenlantern
2061	15	H2:2 O2:1	p	greenlantern
2062	15	H2:2 O2:1	p	ghostintheshell
2063	15	H2:2 O2:1	p,i	ghostintheshell
2064	15	H2:2 O2:1	p,i	ghostintheshell
2065	15	H2:2 O2:1	p,i	ghostintheshell

Continued on next page

Table C.1 – continued from previous page

Shot number	p_1 (kPa)	Mixture	Data	Visualization
2066	15	H2:2 O2:1	p,i	ghostintheshell
2067	15	H2:2 O2:1	p,i	ghostintheshell
2068	15	H2:2 O2:1	p	ghostintheshell
2069	15	H2:2 O2:1	p,i	ghostintheshell
2070	15	H2:2 O2:1	p,i	ghostintheshell
2071	15	H2:2 O2:1	p,q	watchmen
2072	15	H2:2 O2:1	p,q	watchmen
2073	30	H2:2 O2:1	p,q	watchmen
2074	5	H2:2 O2:1	p,q	watchmen
2075	99	air		watchmen
2076	25	N2O:1	p,q	watchmen
2077	25	N2O:1	p,q,i	watchmen
2078	25	N2O:1	p,q,i	watchmen
2079	25	H2:2 O2:1	p,q,i	watchmen
2080	25	H2:2 O2:1	p,q,i	watchmen
2081	25	H2:2 O2:1	p,q	watchmen
2082	25	H2:2 O2:1	p,q	watchmen
2083	25	H2:2 O2:1	p,q	watchmen
2084	25	H2:2 O2:1	p,q,i	watchmen
2085	25	H2:2 O2:1	p,q,i	watchmen
2086	25	H2:2 O2:1	p,q,i	watchmen
2087	10	H2:2 O2:1	p,q	watchmen
2088	10	H2:2 O2:1	i	watchmen
2089	10	H2:2 O2:1	p,q,i	watchmen
2090	25	H2:2 O2:1	p,q,i	watchmen
2091	40	H2:2 O2:1	p,q,i	watchmen

Continued on next page

Table C.1 – continued from previous page

Shot number	p_1 (kPa)	Mixture	Data	Visualization
2092	40	H2:2 O2:1	p,q,i	watchmen
2093	40	H2:2 O2:1 AR:3	p,q,i	watchmen
2094	40	H2:2 O2:1 AR:3	p,q,i	watchmen
2095	40	H2:2 O2:1 AR:3	p,q,i	watchmen
2096	40	H2:2 O2:1 AR:6	p,q,i	watchmen
2097	40	H2:2 O2:1 AR:6	p,q,i	watchmen
2098	40	H2:2 O2:1 AR:6	p,q,i	watchmen
2099	40	H2:2 O2:1 AR:15	p,q,i	watchmen
2100	40	H2:2 O2:1 AR:15	p,q,i	watchmen
2101	40	H2:2 O2:1 AR:15	p,q,i	watchmen
2102	25	H2:2 O2:1 AR:15	p,q,i	watchmen
2103	25	H2:2 O2:1 AR:6	p,q,i	watchmen
2104	25	H2:2 O2:1 AR:3	p,q,i	watchmen
2105	10	H2:2 O2:1 AR:3	p,q,i	watchmen
2106	10	H2:2 O2:1 AR:3	p,q,i	watchmen
2107	10	H2:2 O2:1 AR:6	p,q,i	watchmen
2108	10	H2:2 O2:1 AR:15	p,q,i	watchmen
2109	10	H2:2 O2:1 AR:15	p,q,i	watchmen
2110	25	AR:1	p,q,i	watchmen
2111	25	AR:1	p,q,i	watchmen
2112	25	AR:1	p,q,i	watchmen
2113	25	AR:1	p,q,i	watchmen
2114	25	H2:2 O2:1 AR:15	p,q	watchmen
2115	25	H2:2 O2:1 AR:15	p,q,i	watchmen
2116	25	H2:2 O2:1	p,q	watchmen
2117	25	H2:2 O2:1	p,q,i	watchmen

Continued on next page

Table C.1 – continued from previous page

Shot number	p_1 (kPa)	Mixture	Data	Visualization
2118	25	H2:2 O2:1	p,q,i	watchmen
2119	25	H2:2 O2:1	p,q,i	watchmen
2120	25	H2:2 O2:1	p,q,i	watchmen
2121	10	AR:1	p,q	watchmen
2122	25	C2H4:1 O2:3	p,q	watchmen
2123	25	C2H4:1 O2:3	p,q,i	watchmen
2124	25	C2H4:1 O2:3	p,q,i	watchmen
2125	25	C2H4:1 O2:3	p,q,i	watchmen
2126	25	H2:2 O2:1	p,q	watchmen
2127	25	C2H4:1 O2:3	p,q	watchmen
2128	25	C2H4:1 O2:3	p,q,i	watchmen
2129	25	C2H4:1 O2:3	p,q,i	watchmen
2130	25	C2H4:1 O2:3	p,q,i	watchmen
2131	25	C2H4:1 O2:3	p,q,i	watchmen
2132	25	C2H4:1 O2:3	p,q,i	watchmen
2133	25	C2H4:1 O2:3	p,q,i	watchmen
2134	25	C2H4:1 O2:3	p,q,i	watchmen
2135	25	C2H4:1 O2:3	p,q,i	watchmen
2136	25	C2H4:1 O2:3	p,q,i	watchmen
2137	25	C2H4:1 O2:3	p,q,i	watchmen
2138	25	C2H4:1 O2:3	p,q,i	watchmen
2139	25	C2H4:1 O2:3	p,q,i	watchmen
2140	25	C2H4:1 O2:3	p,q,i	watchmen
2141	25	C2H4:1 O2:3	p,q,i	watchmen
2142	25	C2H4:1 O2:3	p,q	watchmen
2143	25	H2:2 O2:1	p,q	watchmen

Continued on next page

Table C.1 – continued from previous page

Shot number	p_1 (kPa)	Mixture	Data	Visualization
2144	25	H2:2 O2:1 CO2:3	p,q	watchmen
2145	25	H2:4 O2:2 CO2:3	p,q	watchmen
2146	25	H2:2 O2:1	p,q	sandman
2147	25	H2:2 O2:1	p,q	sandman
2148	25	H2:2 O2:1	p,q	sandman
2149	25	H2:2 O2:1	p,q	sandman
2150	25	H2:2 O2:1	p,q	sandman
2151	25	H2:2 O2:1	p,q,i	sandman
2152	25	H2:2 O2:1	p,q,i	sandman
2153	25	H2:2 O2:1 CO2:3	p,q	sandman
2154	25	H2:4 O2:2 CO2:3		sandman
2155	25	H2:2 O2:1 CO2:1	p,q	sandman
2156	25	H2:2 O2:1 CO2:1	p,q,i	sandman
2157	25	H2:2 O2:1 CO2:1	i	sandman
2158	25	H2:4 O2:2 CO2:3	p,q,i	sandman
2159	25	H2:2 O2:1 N2:3	p,q	sandman
2160	25	H2:2 O2:1 N2:3	p,q,i	sandman
2161	25	H2:2 O2:1 AR:3	p,q,i	sandman
2162	25	H2:2 O2:1 AR:12	p,q,i	sandman
2163	10	H2:2 O2:1	p,q,i	sandman
2164	10	H2:2 O2:1 AR:3	p,q,i	sandman
2165	10	H2:2 O2:1 AR:12	p,q	sandman
2166	10	H2:2 O2:1 AR:12	p,q,i	sandman
2167	10	H2:2 O2:1 N2:3	p,q,i	sandman
2168	10	H2:4 O2:2 CO2:3	p,q,i	sandman
2169	50	H2:2 O2:1 AR:12	p,q,i	sandman

Continued on next page

Table C.1 – continued from previous page

Shot number	p_1 (kPa)	Mixture	Data	Visualization
2170	50	H2:2 O2:1 AR:3	p,q,i	sandman
2171	50	H2:2 O2:1 N2:3	p,q,i	sandman
2172	50	H2:4 O2:2 CO2:3	p,q	sandman
2173	50	H2:4 O2:2 CO2:3	p,q	sandman
2174	50	H2:4 O2:2 CO2:3	p,q	sandman
2175	25	AR:1	p,q	sandman
2176	25	AR:1	p,q	sandman
2177	25	AR:1	p,q,i	sandman
2178	25	AR:1	p,q	sandman
2179	25	H2:2 O2:1	p,q,i	sandman
2180	50	H2:2 O2:1	p,q,i	sandman
2181	50	H2:4 O2:2 CO2:3	p,q,i	sandman
2182	25	AR:1	p,q	sandman
2183	25	AR:1	p,q	sandman
2184	25	AR:1	p,q,i	sandman
2185	25	CO2:1	p,q	sandman
2186	50	H2:2 O2:1	p,q,i	sandman
2187	50	H2:2 O2:1 AR:12	p,q,i	sandman
2188	50	C2H4:1 O2:3	p,q,i	sandman
2189	50	C2H4:1 O2:3 CO2:4	p,q,i	sandman
2190	25	H2:2 O2:1 AR:12	p,q	cyclops
2191	50	H2:2 O2:1 AR:27	p,q	cyclops
2192	25	H2:2 O2:1 AR:12	p,q	cyclops
2193	25	H2:2 O2:1 AR:12	p,q,i	cyclops
2194	25	H2:2 O2:1 AR:12	p,q	cyclops
2195	25	H2:2 O2:1 AR:12	p,q,i	cyclops

Continued on next page

Table C.1 – continued from previous page

Shot number	p_1 (kPa)	Mixture	Data	Visualization
2196	25	H2:2 O2:1	p,q,i	watchmen
2197	25	H2:2 O2:1	p,q,i	watchmen
2198	25	H2:2 O2:1	p,q,i	watchmen

C.3 Drawings

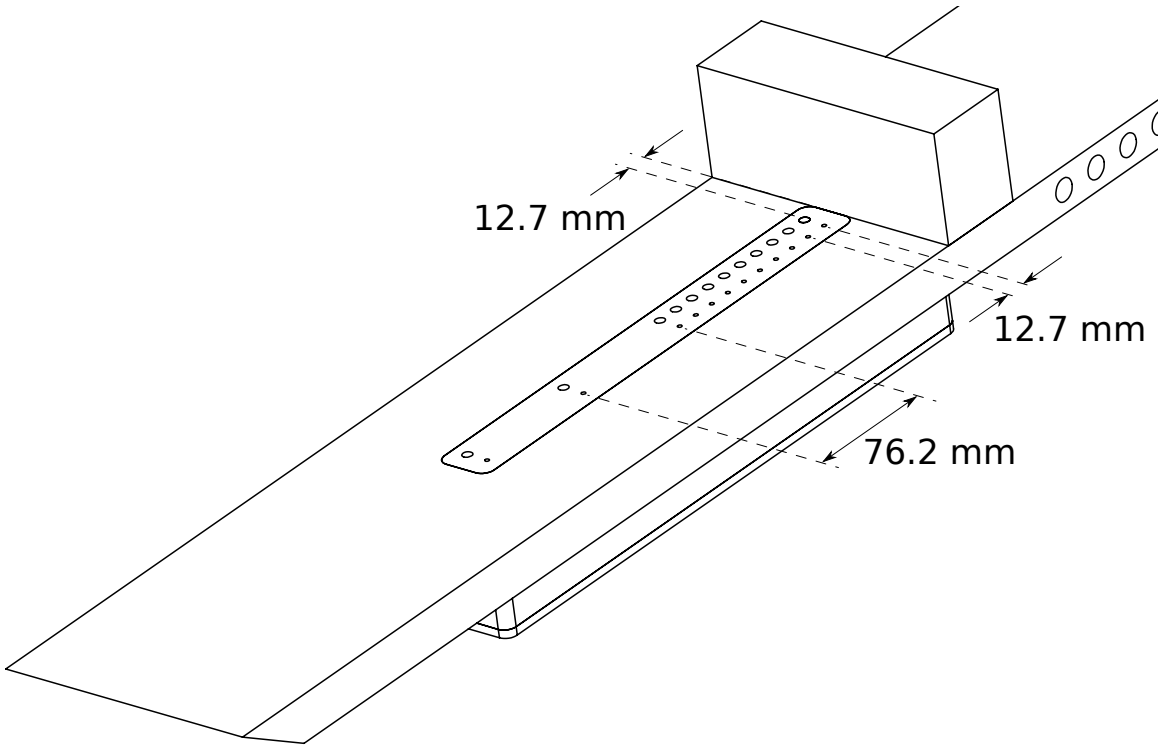

Figure C.1: Drawings of the GDT splitter plate, part 1.

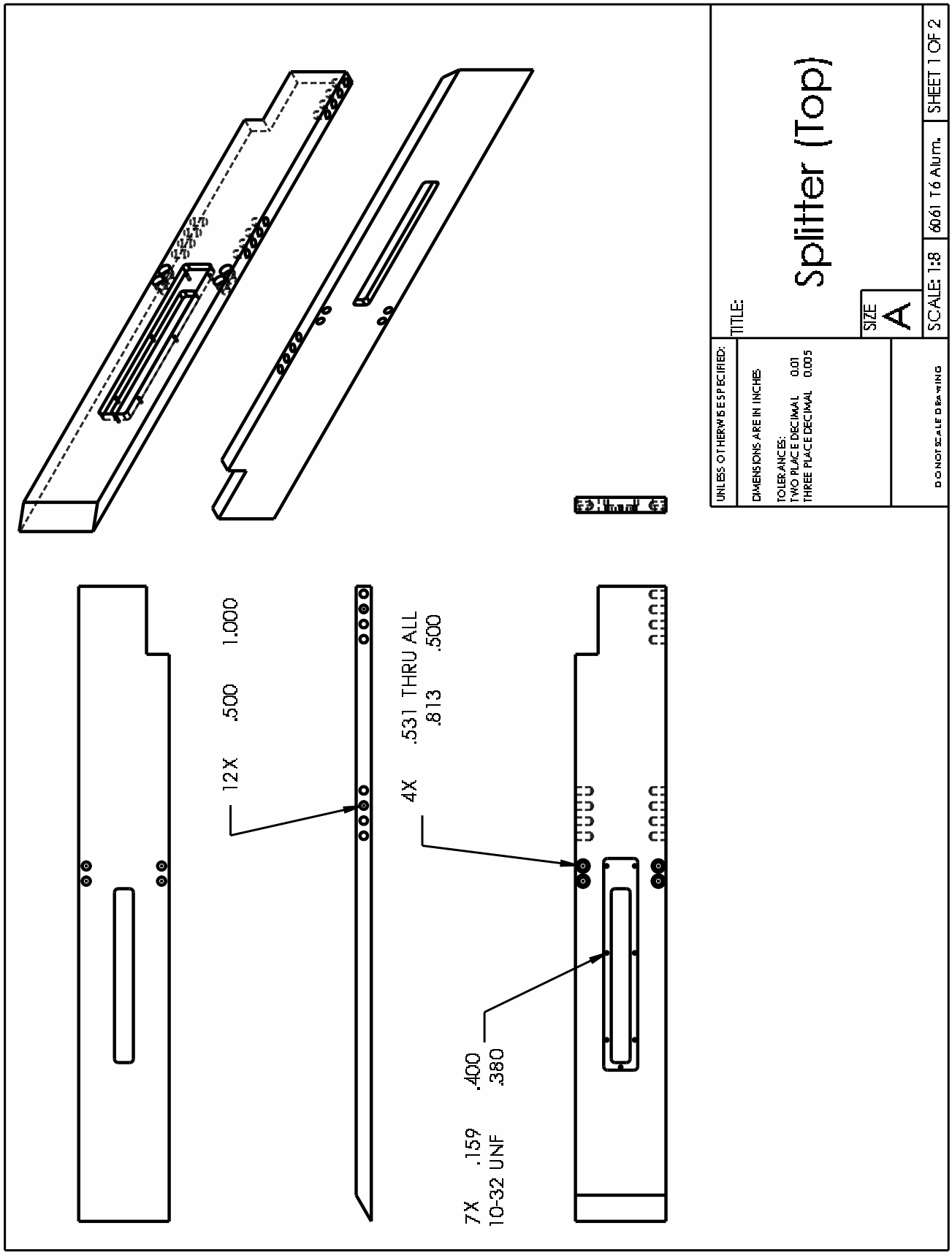

Figure C.2: Drawings of the GDT splitter plate, part 2.

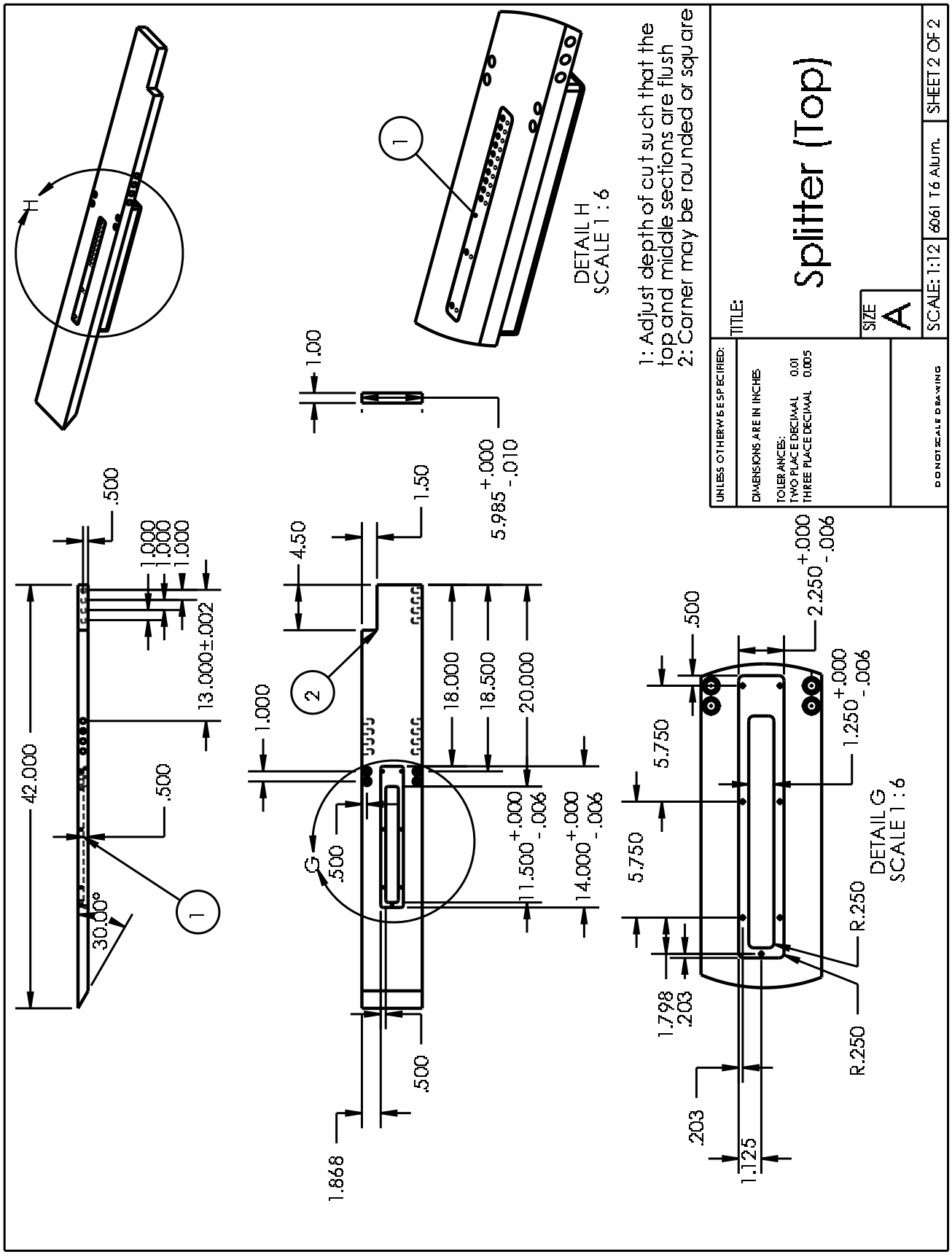

Figure C.3: Drawings of the GDT splitter plate, part 3.

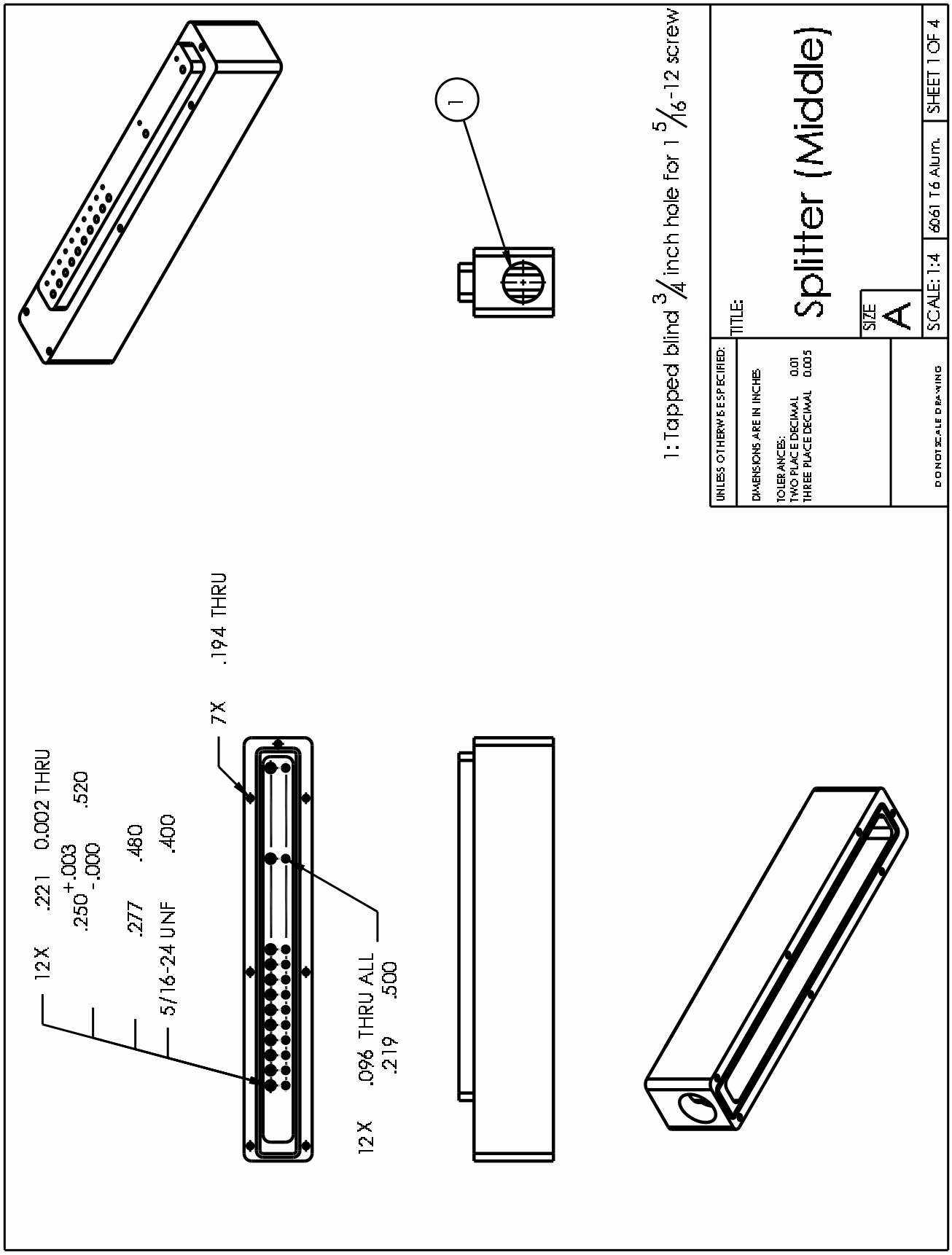

Figure C.4: Drawings of the GDT splitter plate, part 4.

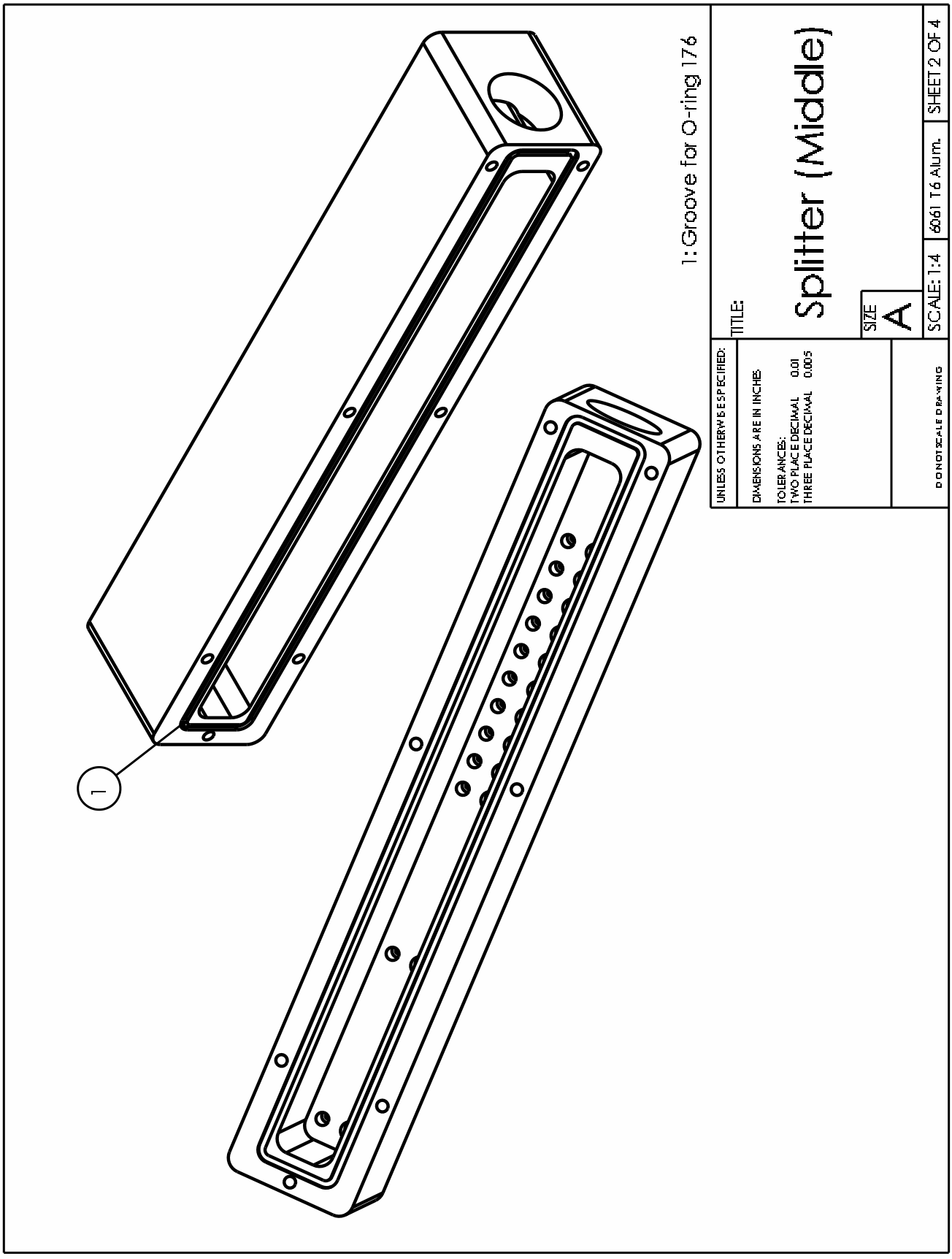

Figure C.5: Drawings of the GDT splitter plate, part 5.

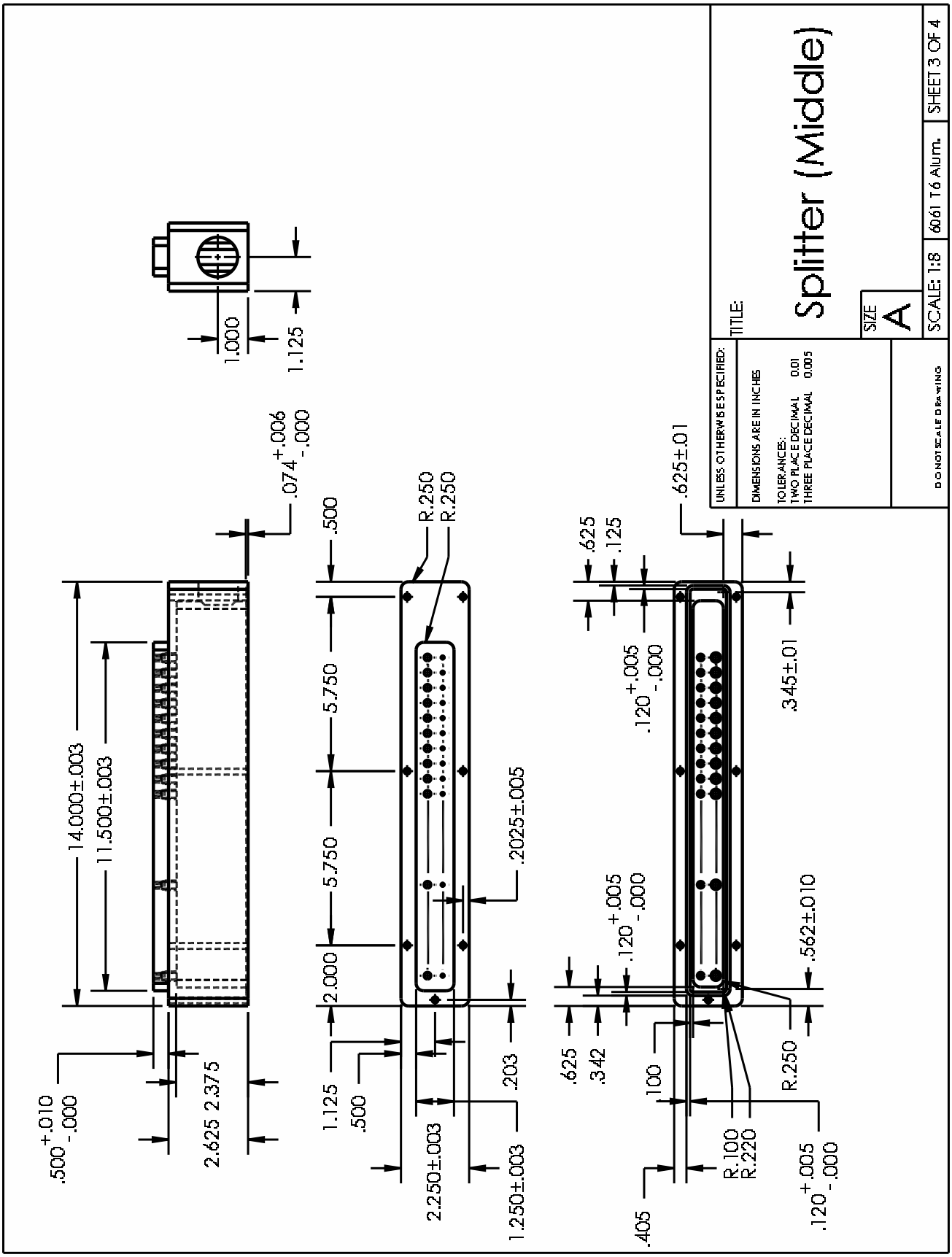

Figure C.6: Drawings of the GDT splitter plate, part 6.

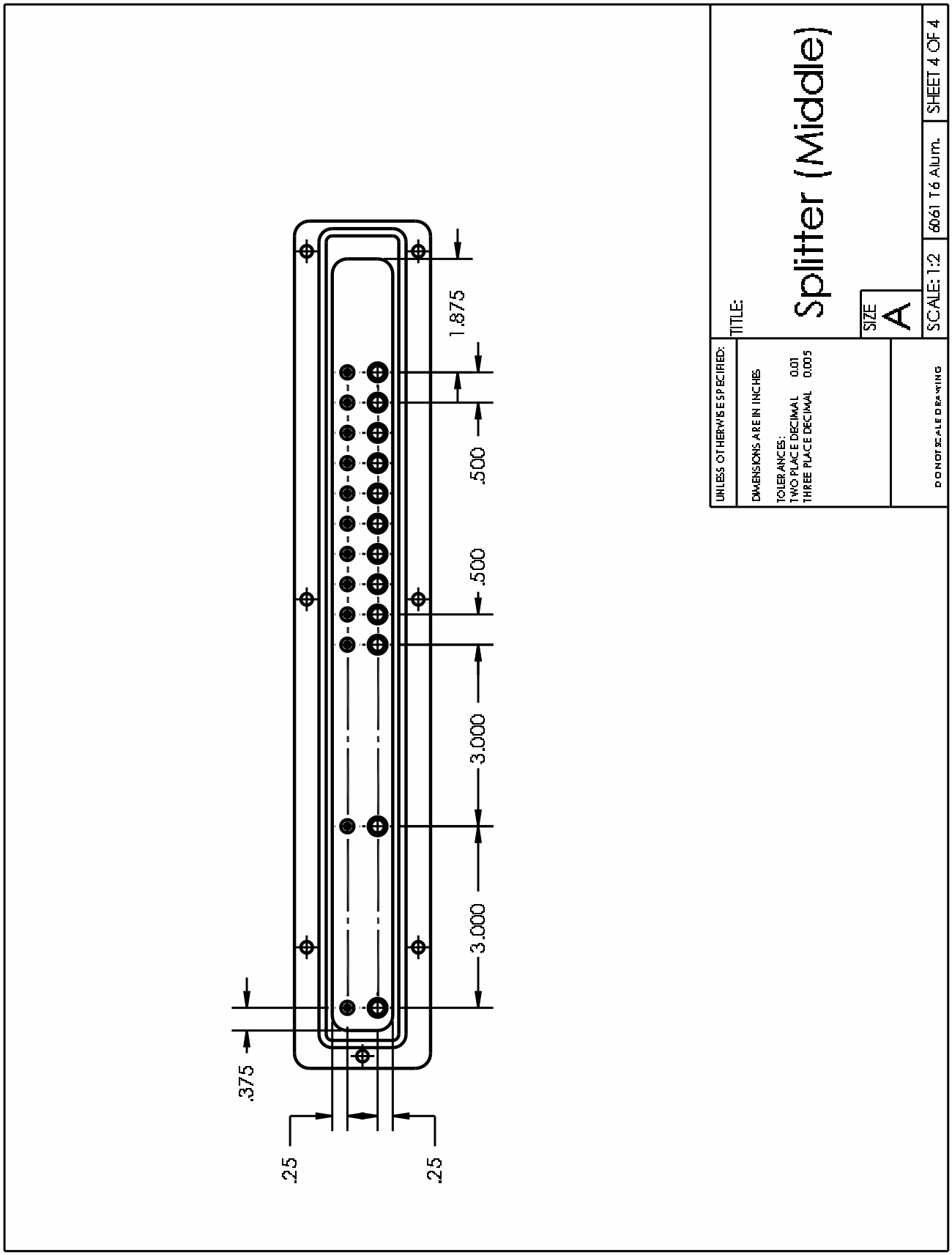

Figure C.7: Drawings of the GDT splitter plate, part 7.

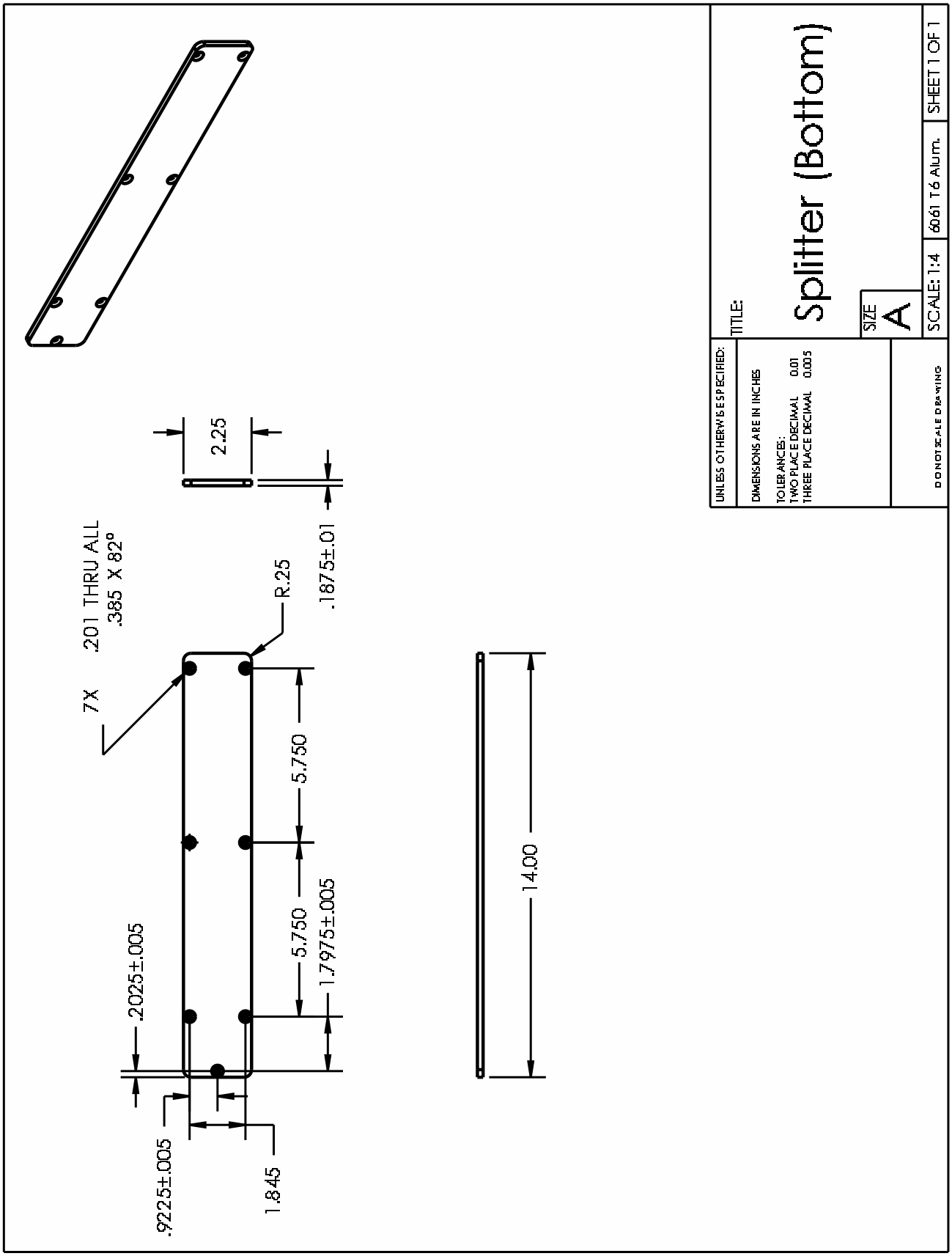

Figure C.8: Drawings of the GDT splitter plate, part 8.

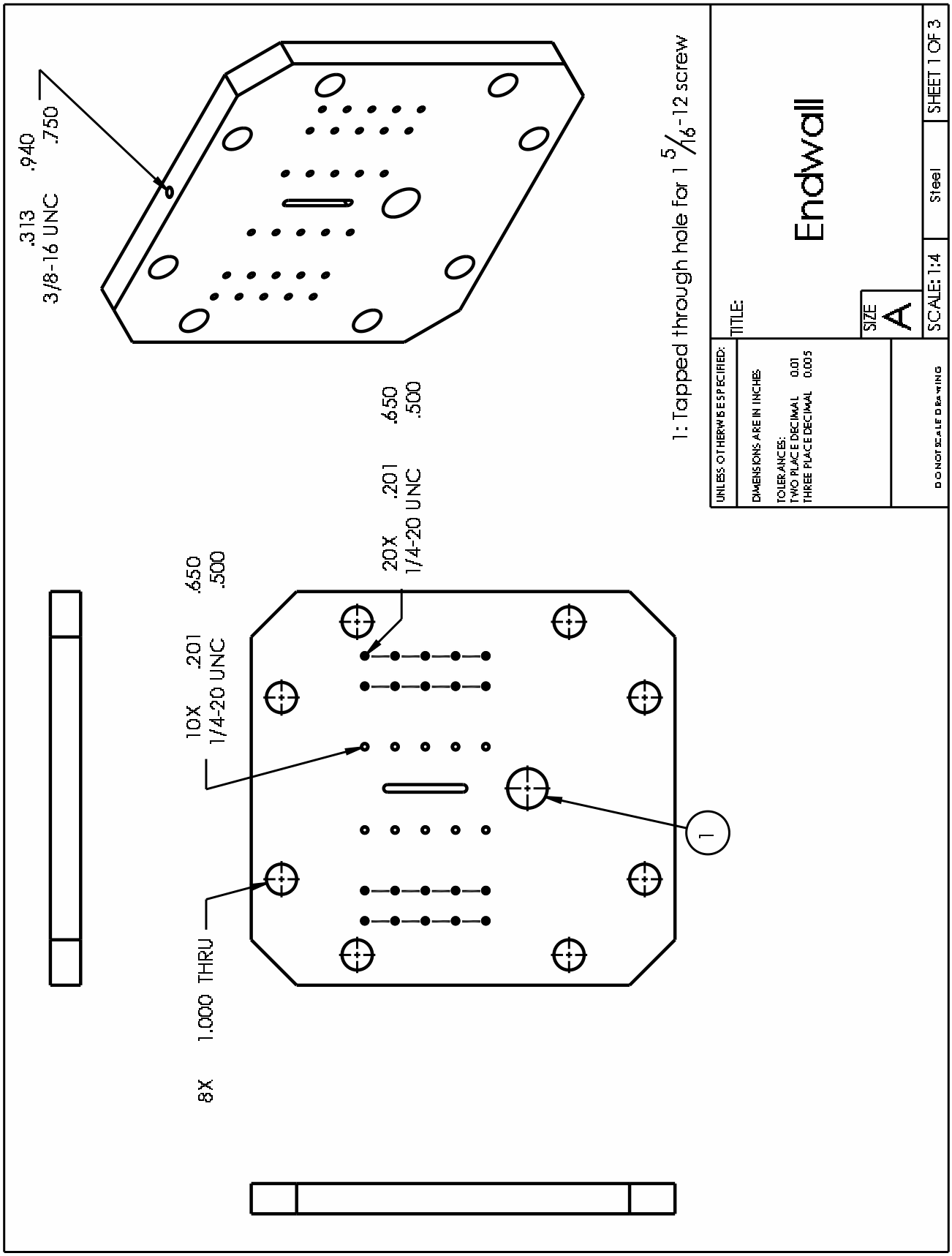

Figure C.9: Drawings of the GDT splitter plate, part 9.

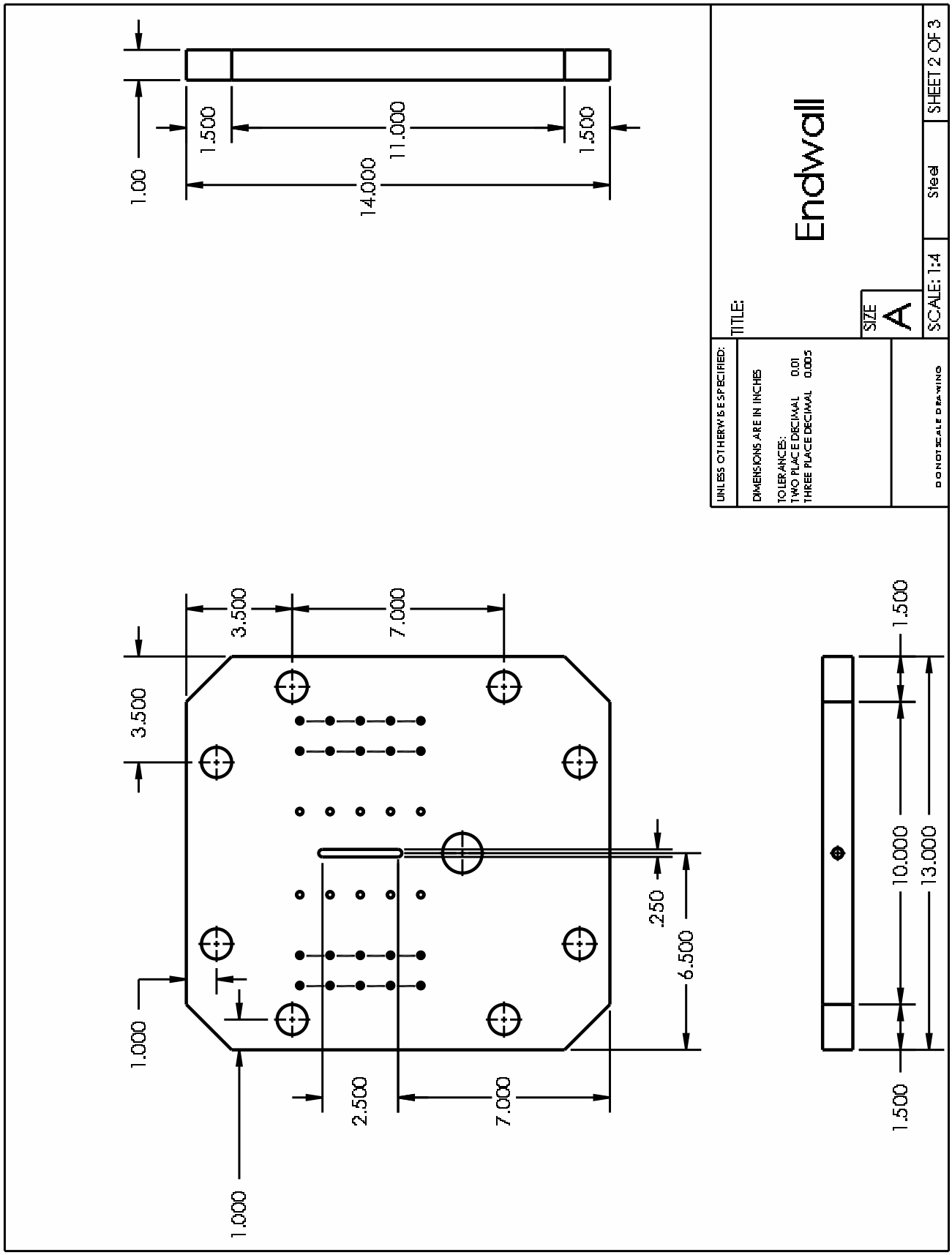

Figure C.10: Drawings of the GDT splitter plate, part 10.

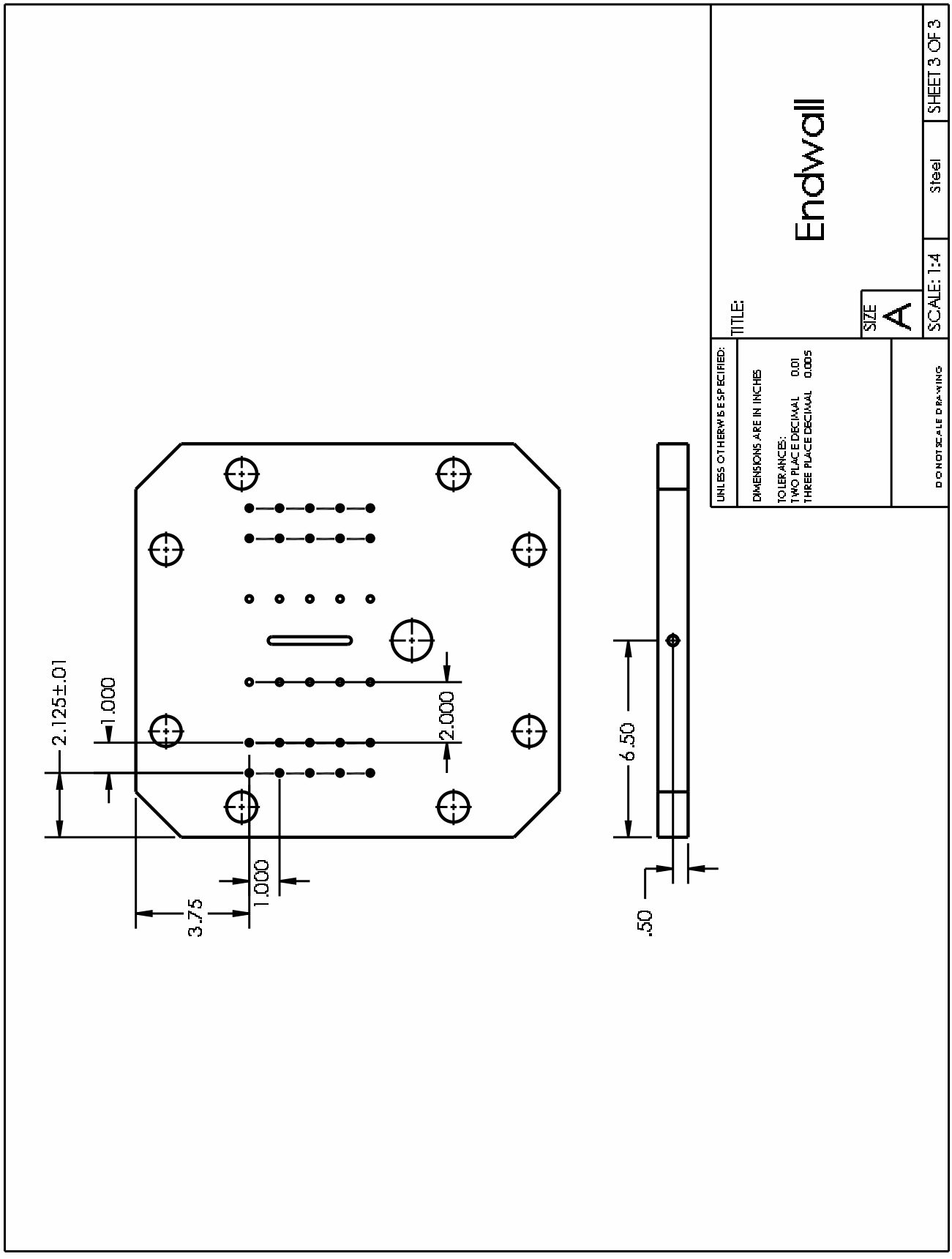

Figure C.11: Drawings of the GDT splitter plate, part 11.

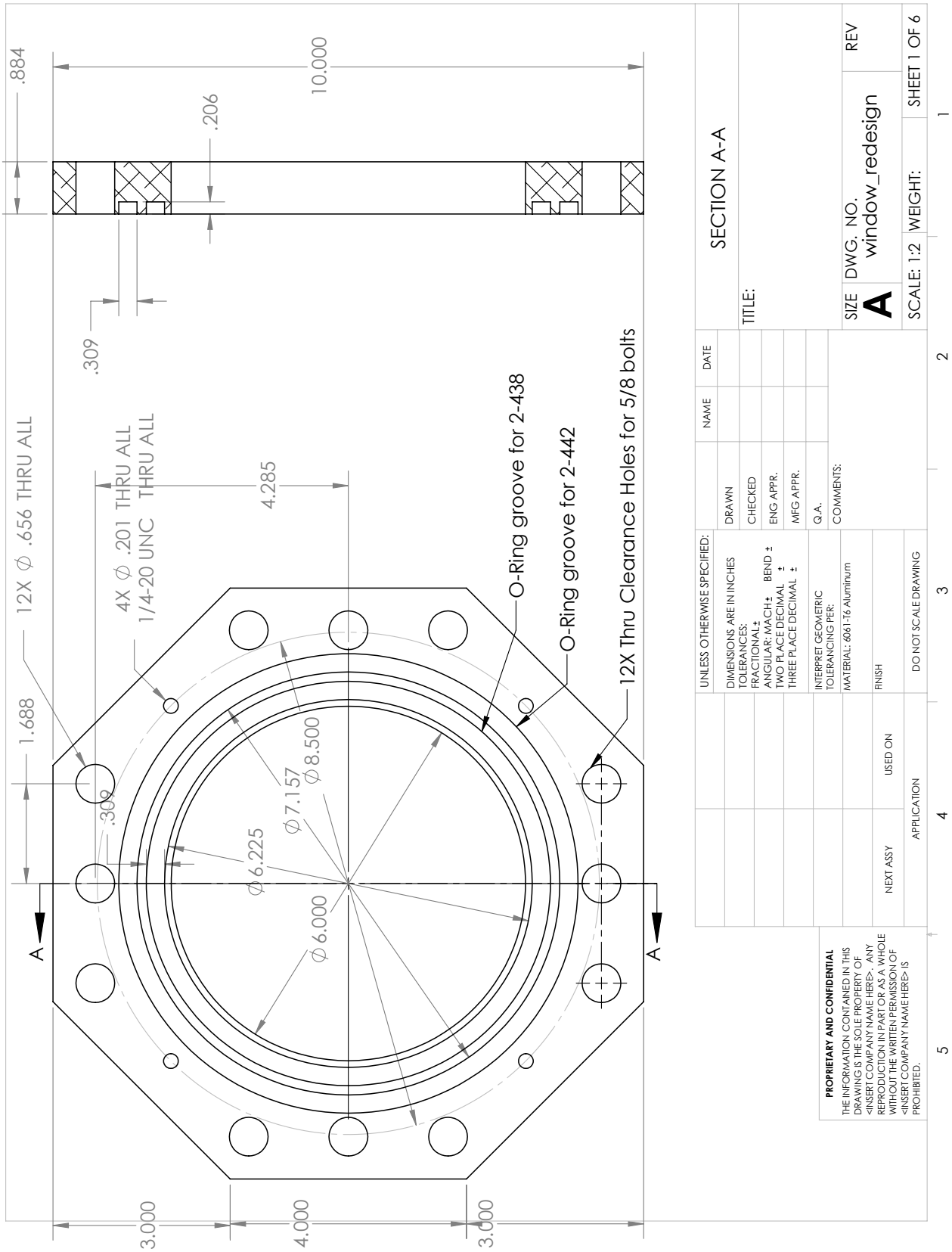

Figure C.12: Drawings of the redesigned GDT test section window, part 1.

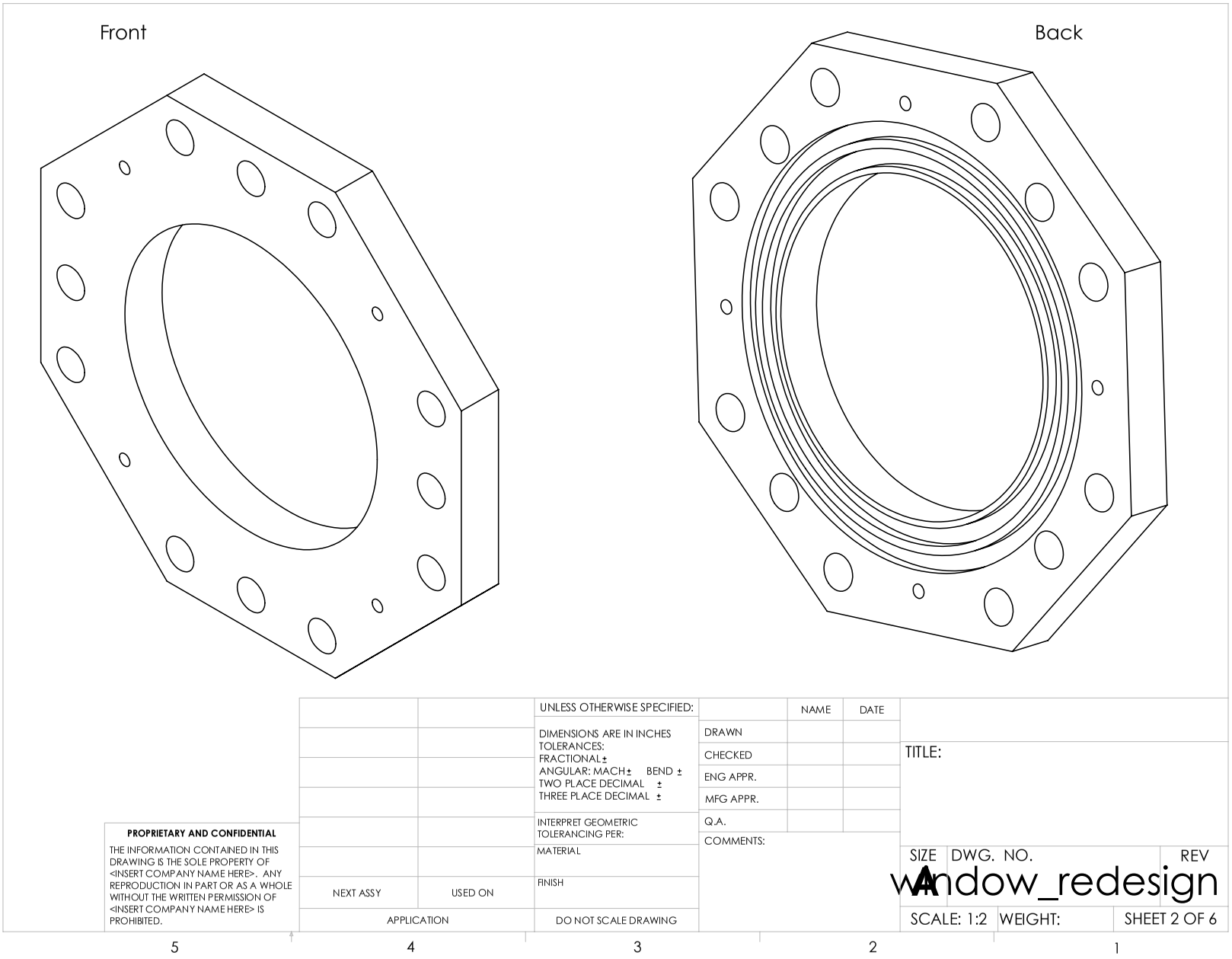

Figure C.13: Drawings of the redesigned GDT test section window, part 2.

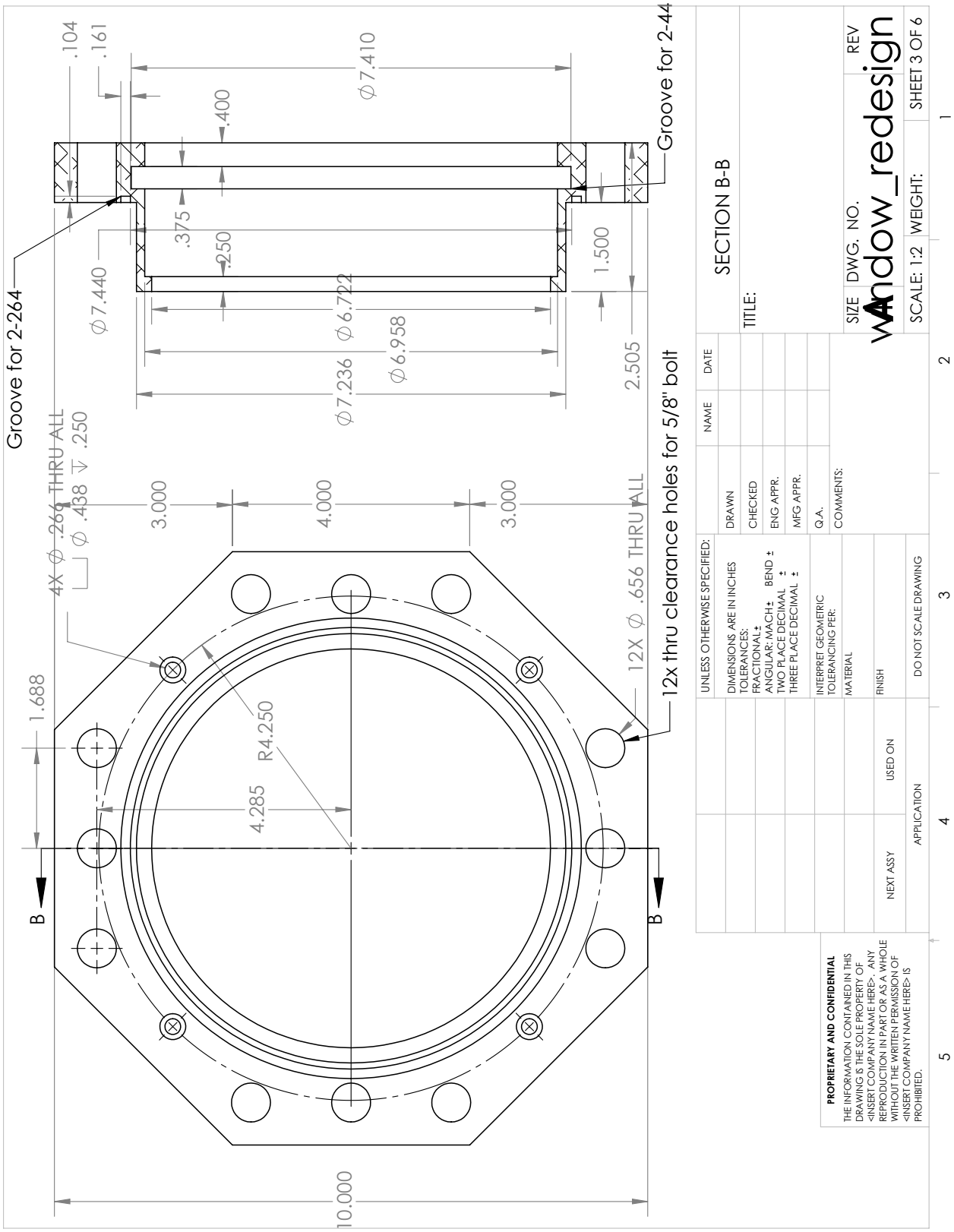

Figure C.14: Drawings of the redesigned GDT test section window, part 3.

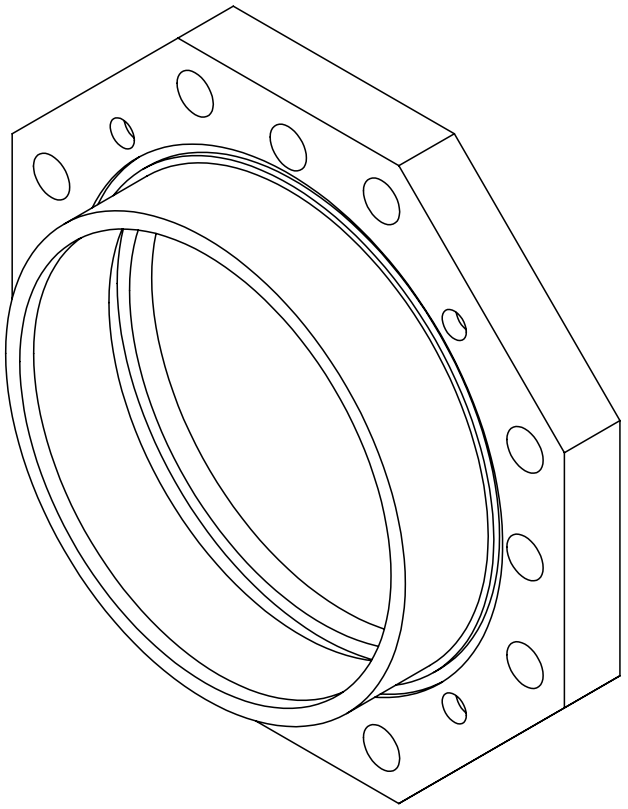

		UNLESS OTHERWISE SPECIFIED:		NAME	DATE
		DIMENSIONS ARE IN INCHES TOLERANCES: FRACTIONAL ± ANGULAR: MACH ± BEND ± TWO PLACE DECIMAL ± THREE PLACE DECIMAL ±	DRAWN		
			CHECKED		
			ENG APPR.		
			MFG APPR.		
		INTERPRET GEOMETRIC TOLERANCING PER:	Q.A.		
		MATERIAL	COMMENTS:		
NEXT ASSY	USED ON	FINISH			
APPLICATION		DO NOT SCALE DRAWING			

TITLE:

SIZE	DWG. NO.	REV
A	window_redesign	
SCALE: 1:2	WEIGHT:	SHEET 4 OF 6

5 4 3 2 1

Figure C.15: Drawings of the redesigned GDT test section window, part 4.

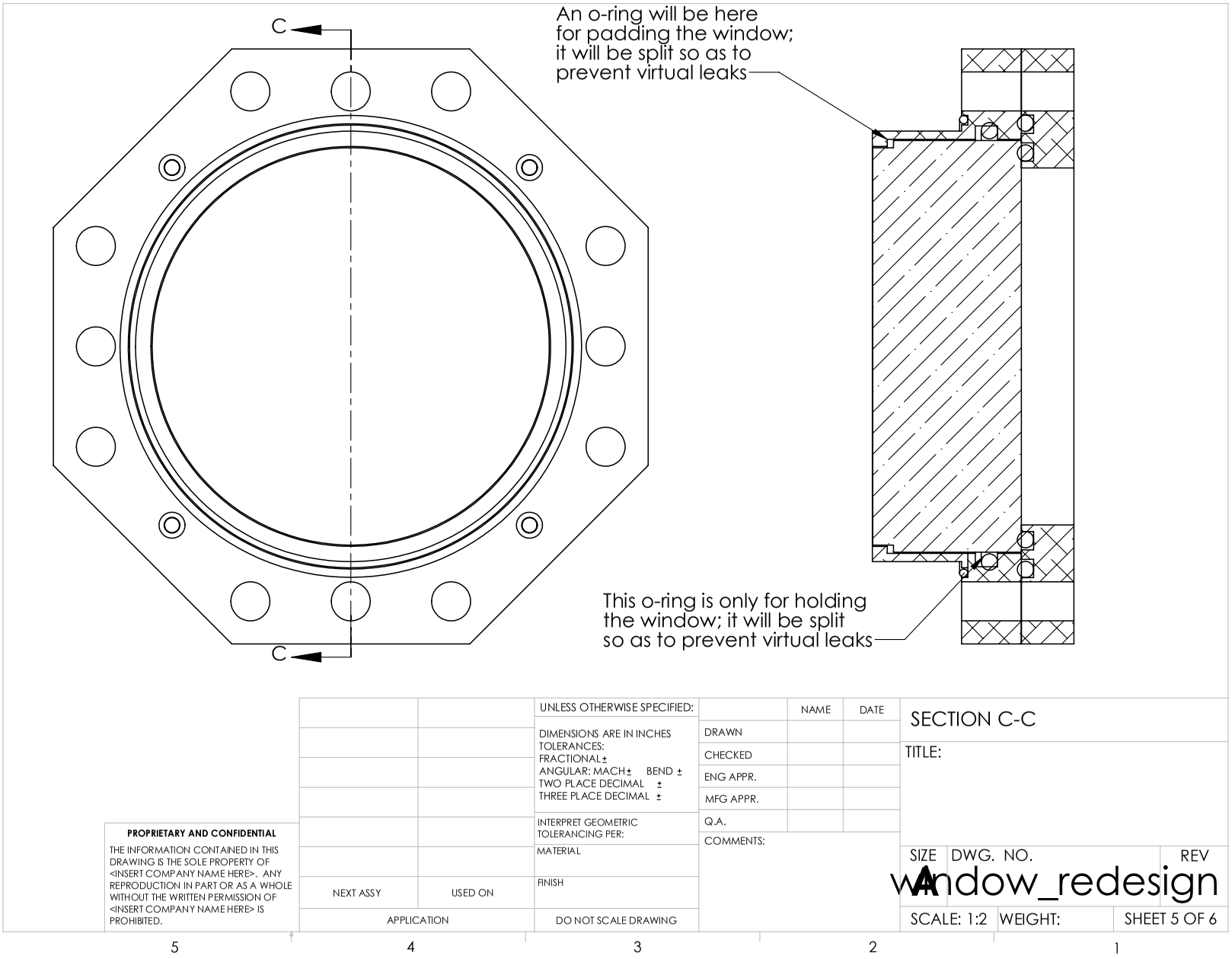

Figure C.16: Drawings of the redesigned GDT test section window, part 5.

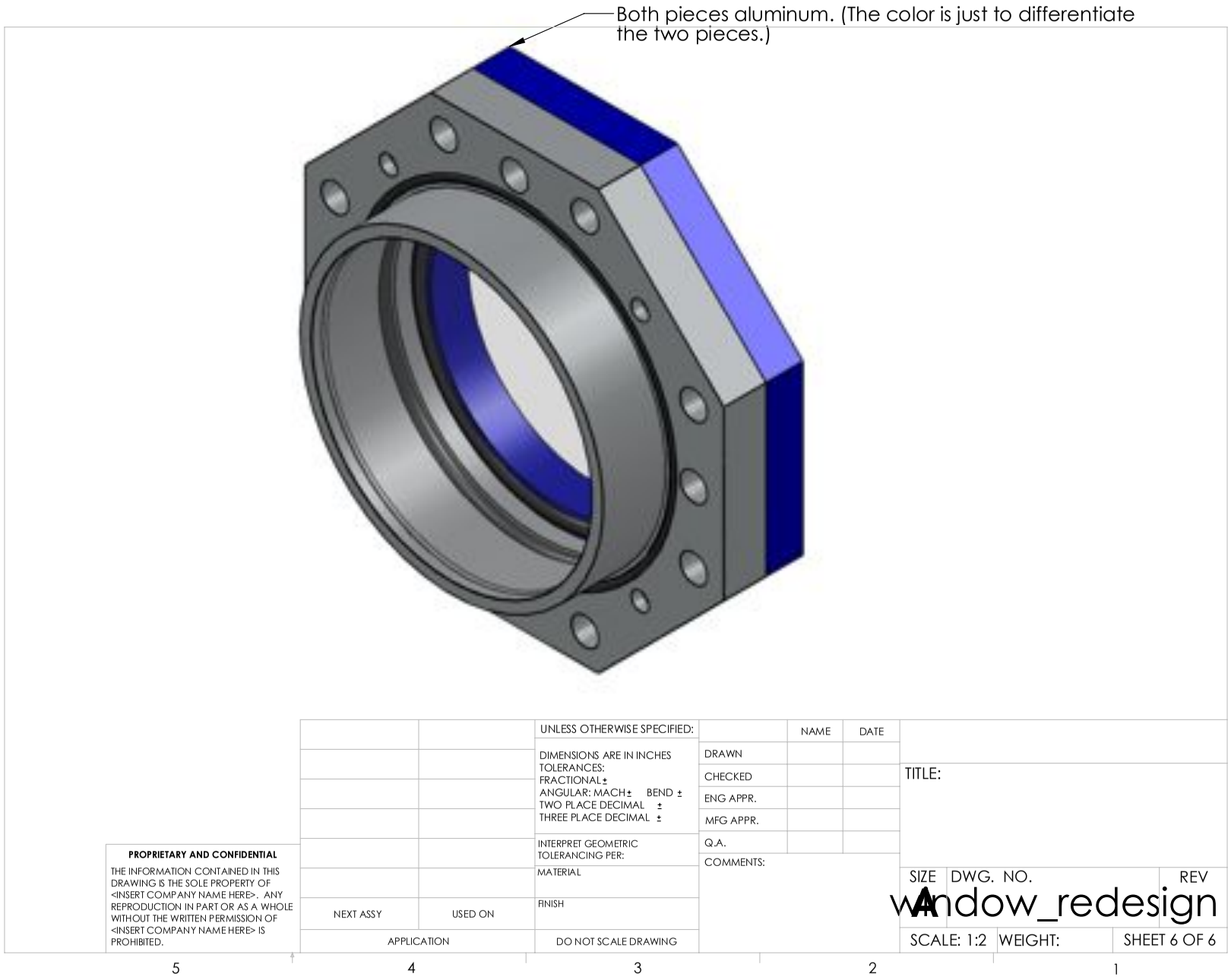

Figure C.17: Drawings of the redesigned GDT test section window, part 6.

Appendix D

Visualization Systems

Details for each visualization system employed are given below organized by type of system (focused or unfocused) and the light source used. A more complete set of images is included with the pressure and heat-flux data in appendix E.

D.1 Unfocused Schlieren Systems

A list of focal lengths and magnifications are shown in table D.1. A list of run conditions for each system is given in appendix C.

Table D.1: Details of unfocused schlieren configurations.

#	Light source	Camera	f_1 (mm)	f_2 (mm)	M	t_{exp} (ns)
1	Sparker	Nikon D200	1500	1600	0.5	300
2	SLD1332V	Phantom v7.10	1500	1600	2	50
3	SMART Cavilux	Phantom v7.10	1500	1000	0.5	10
4	PL1000DRC	SI SIMD16	1500	1000	1	20

D.1.1 Sparker

A sparker light source built by Shepherd (1981), nicknamed "Storm" in the data files, was used as a schlieren source to obtain pictures such as those shown below. The exposure time of 300 ns was a half-width, half-maximum value as recorded by a photodiode and should only be considered as an approximate exposure time. The

camera used was a 3872 x 2592 pixel Nikon D200. It was triggered off the exploding wire and the shutter remained open on the order of 50 ms. The sparker was then triggered off a pressure gauge with appropriate delay to produce the pictures.

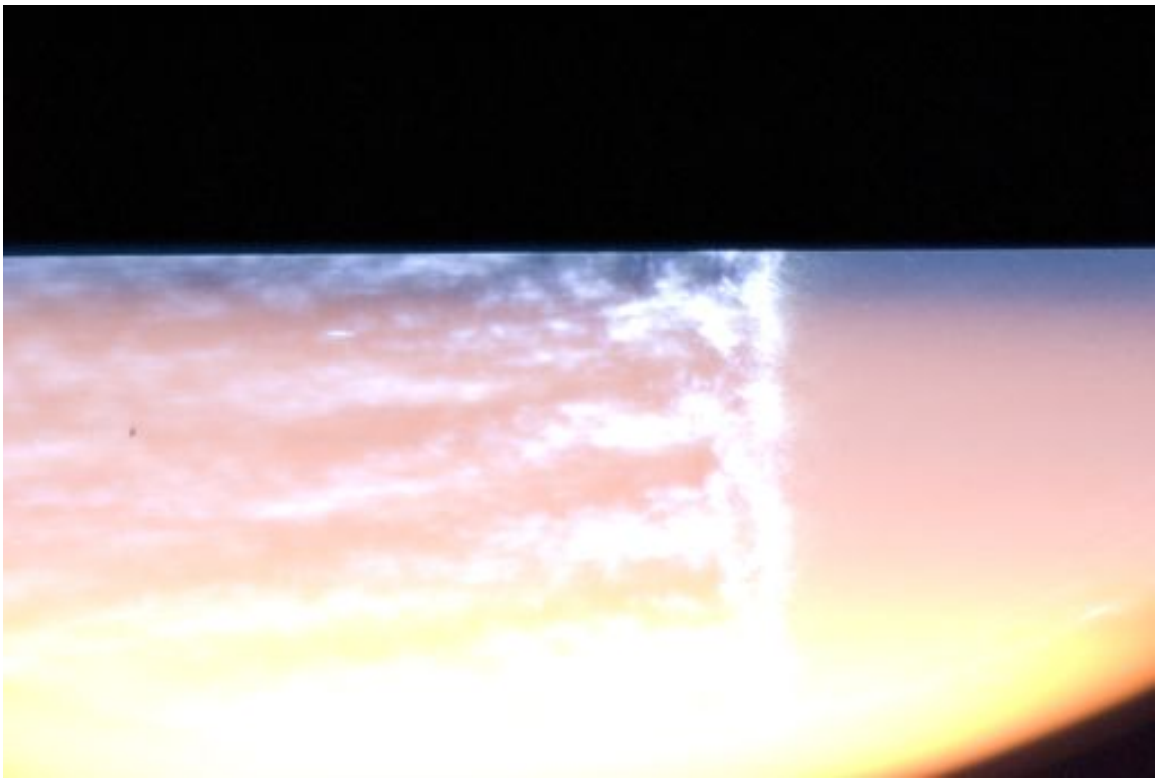

Figure D.1: Unfocused schlieren image of shot 1944. The field of view is approximately 45 mm wide.

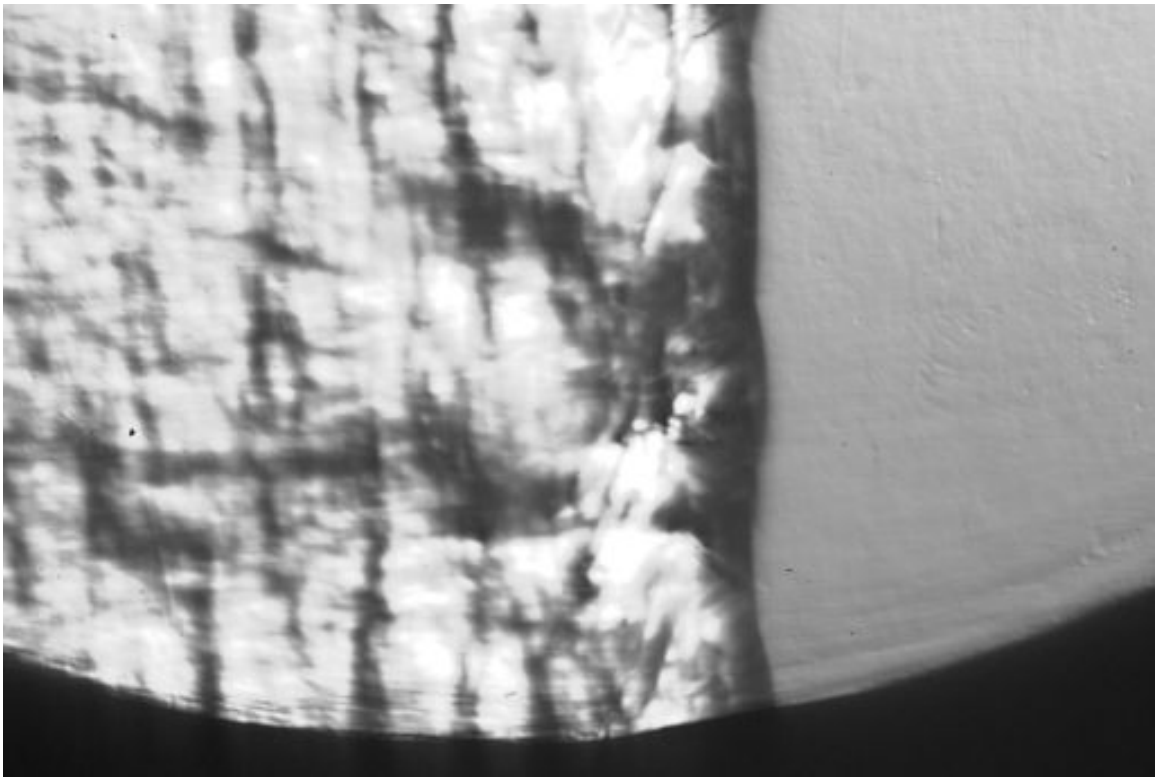

Figure D.2: Unfocused schlieren image of shot 1945. The field of view is approximately 45 mm wide.

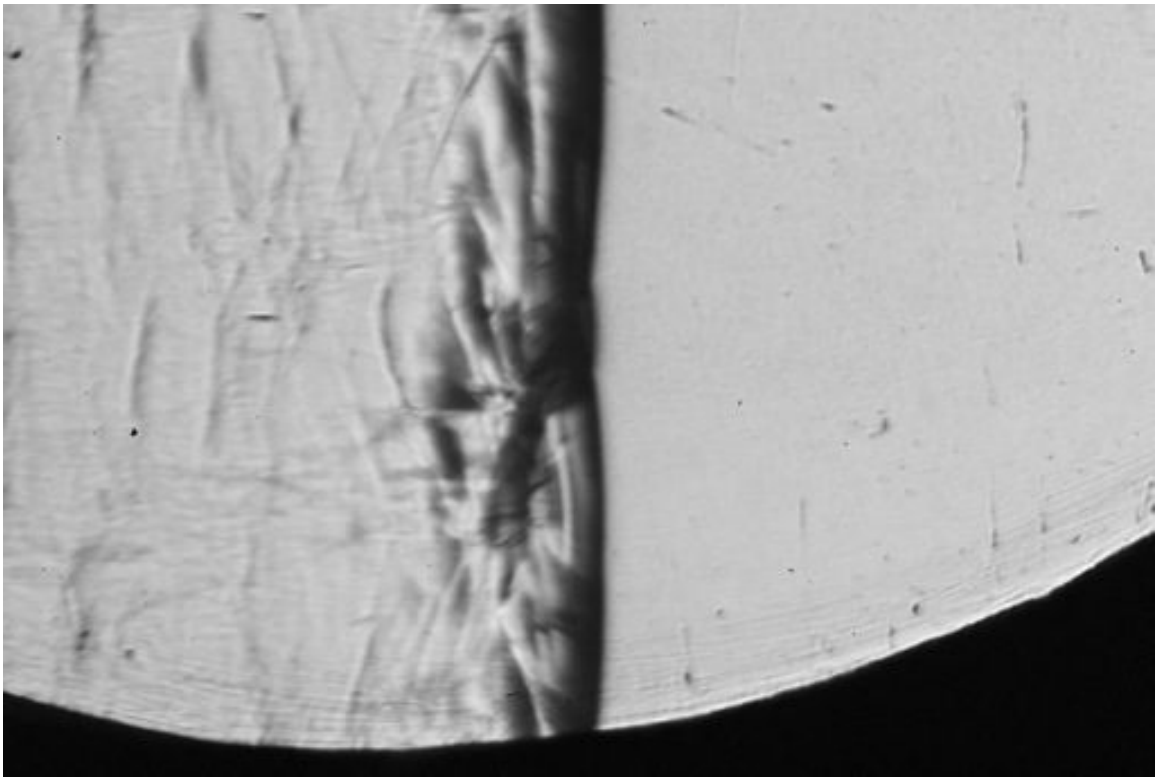

Figure D.3: Unfocused schlieren image of shot 1948. The field of view is approximately 45 mm wide.

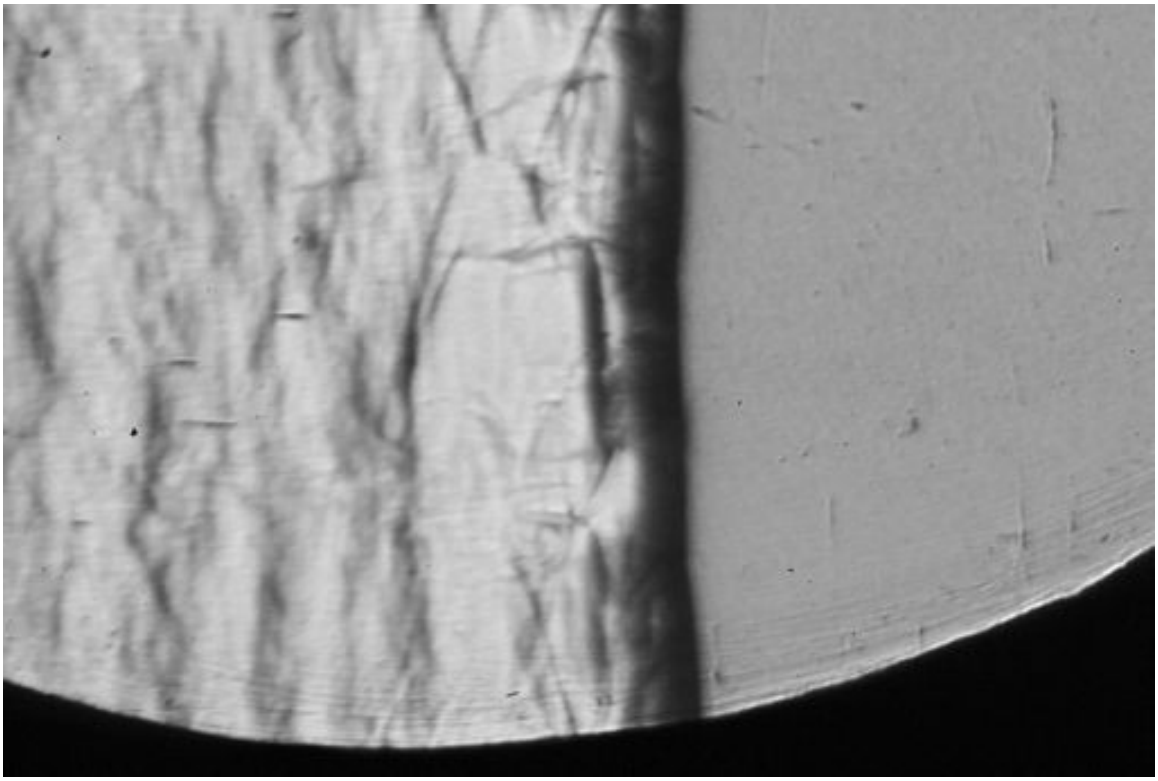

Figure D.4: Unfocused schlieren image of shot 1950. The field of view is approximately 45 mm wide.

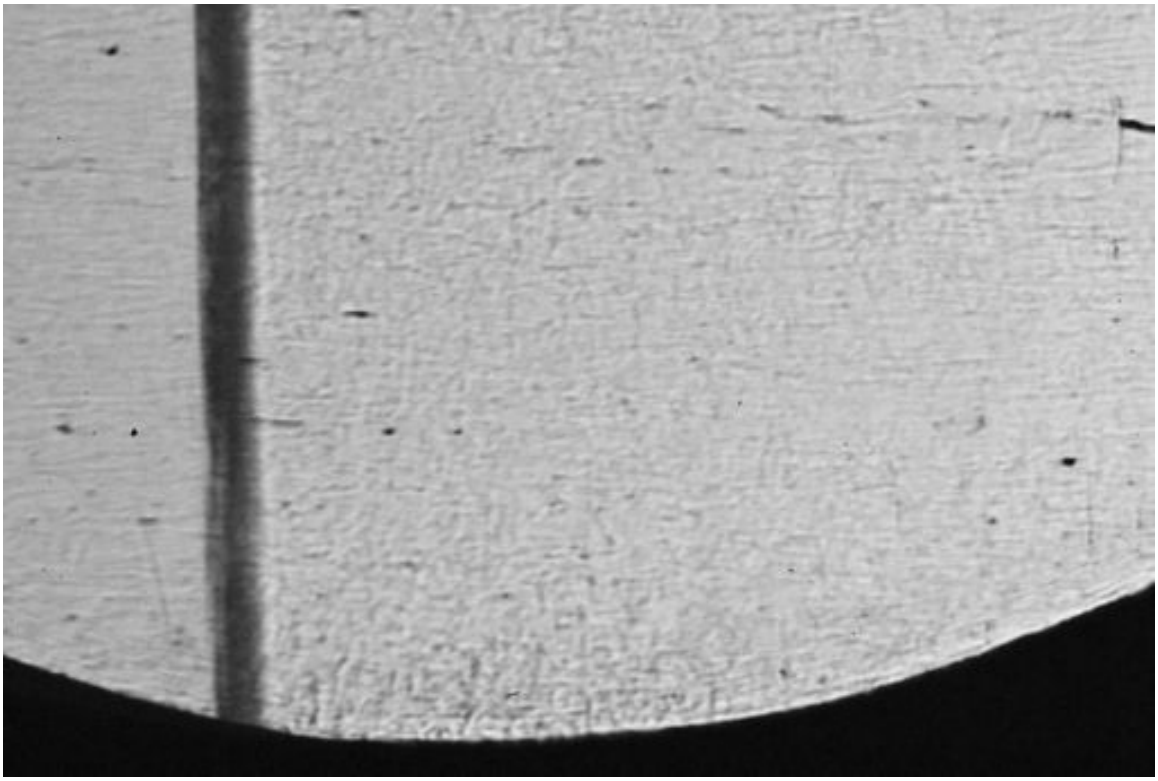

Figure D.5: Unfocused schlieren image of shot 1951. The field of view is approximately 45 mm wide.

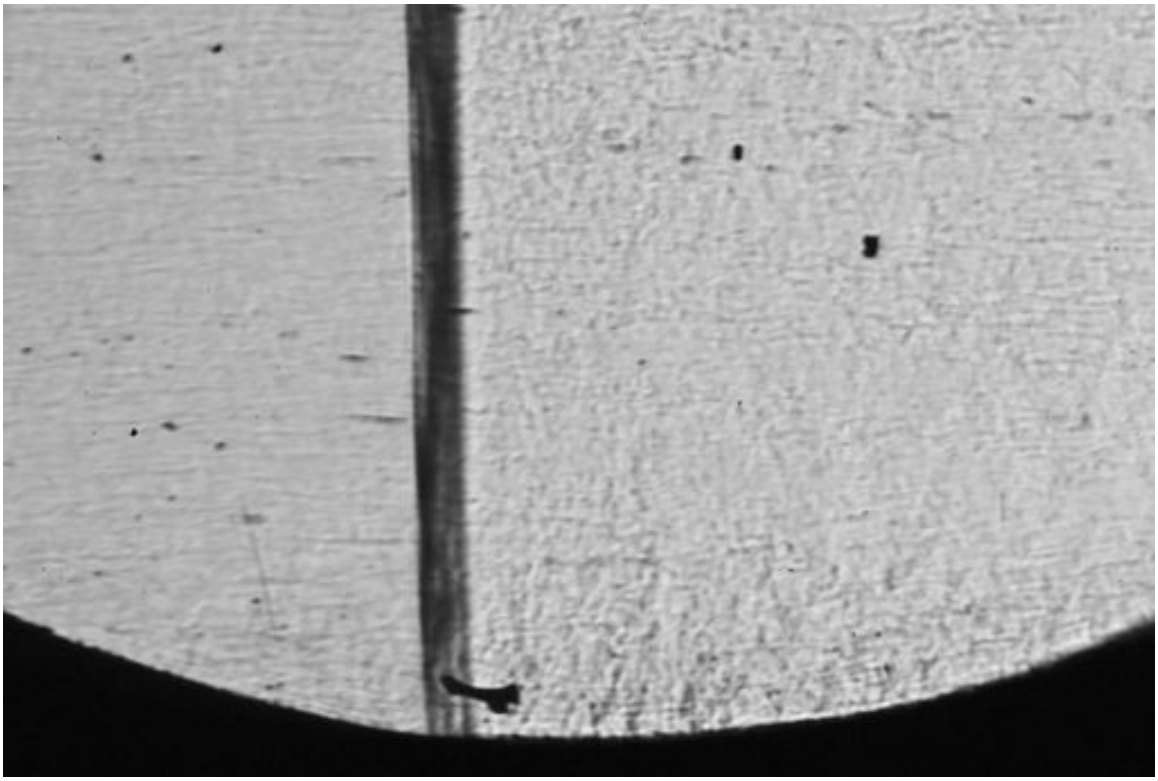

Figure D.6: Unfocused schlieren image of shot 1952. The field of view is approximately 45 mm wide.

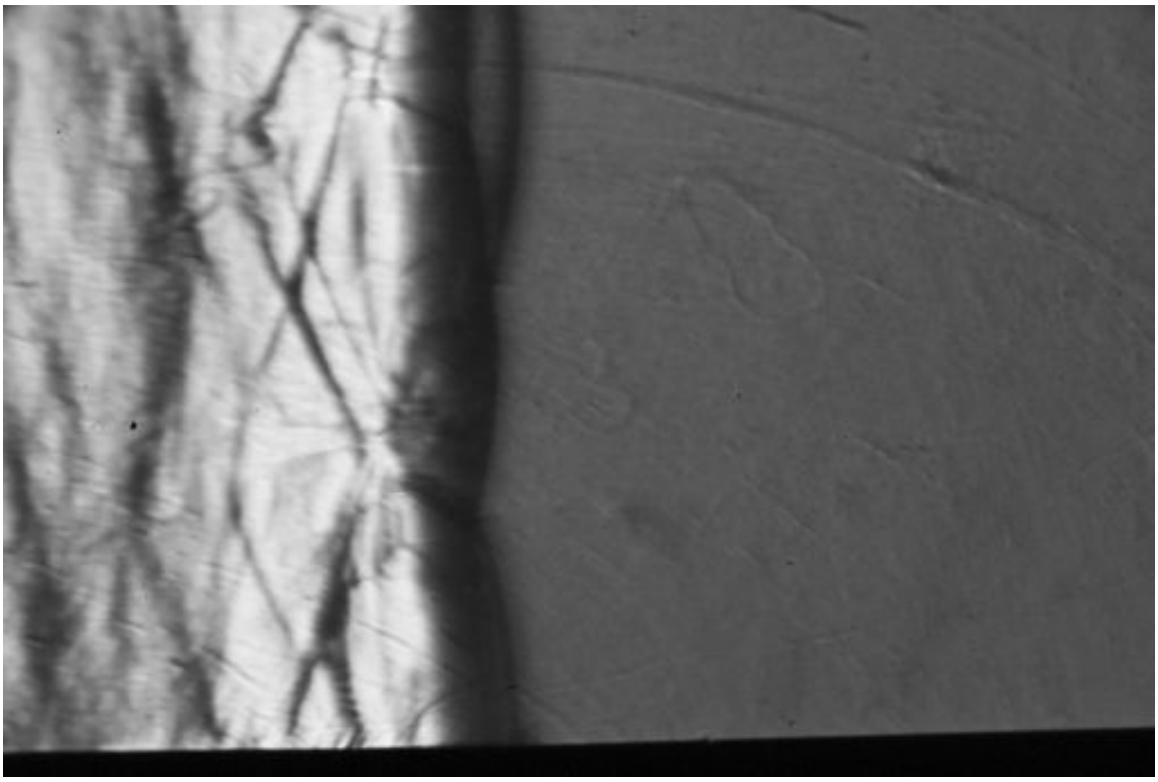

Figure D.7: Unfocused schlieren image of shot 1963. The field of view is approximately 45 mm wide.

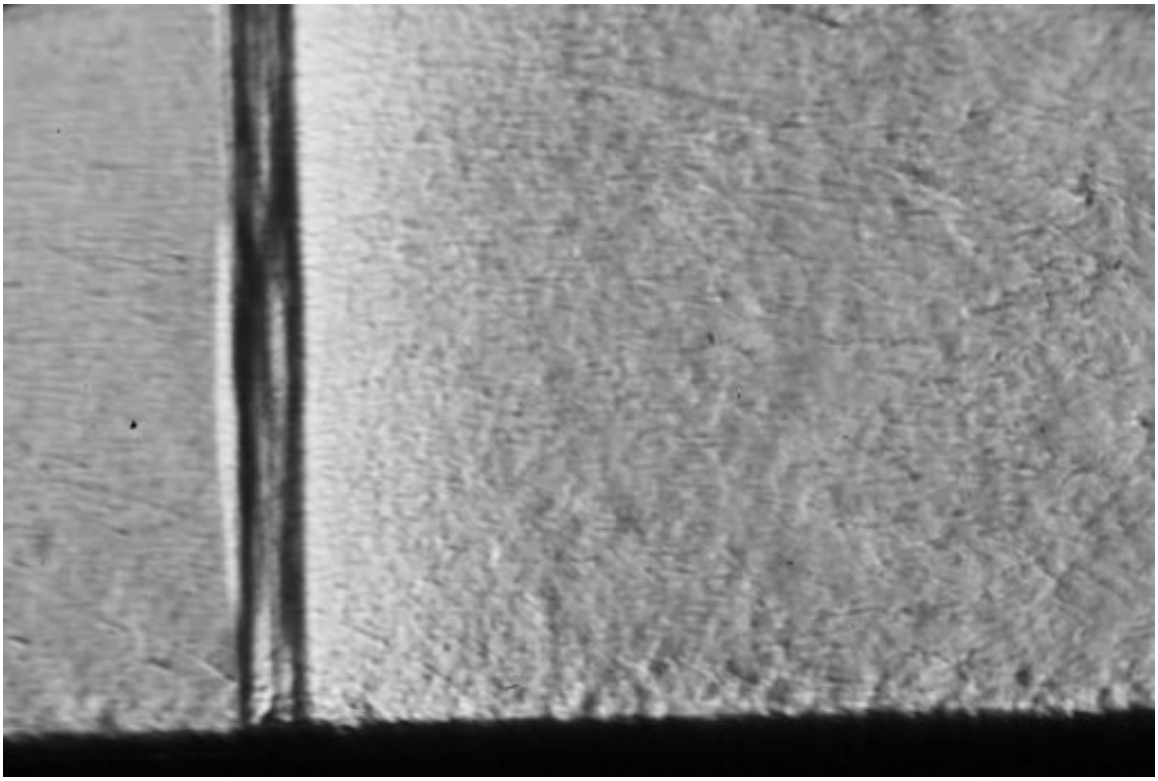

Figure D.8: Unfocused schlieren image of shot 1964. The field of view is approximately 45 mm wide.

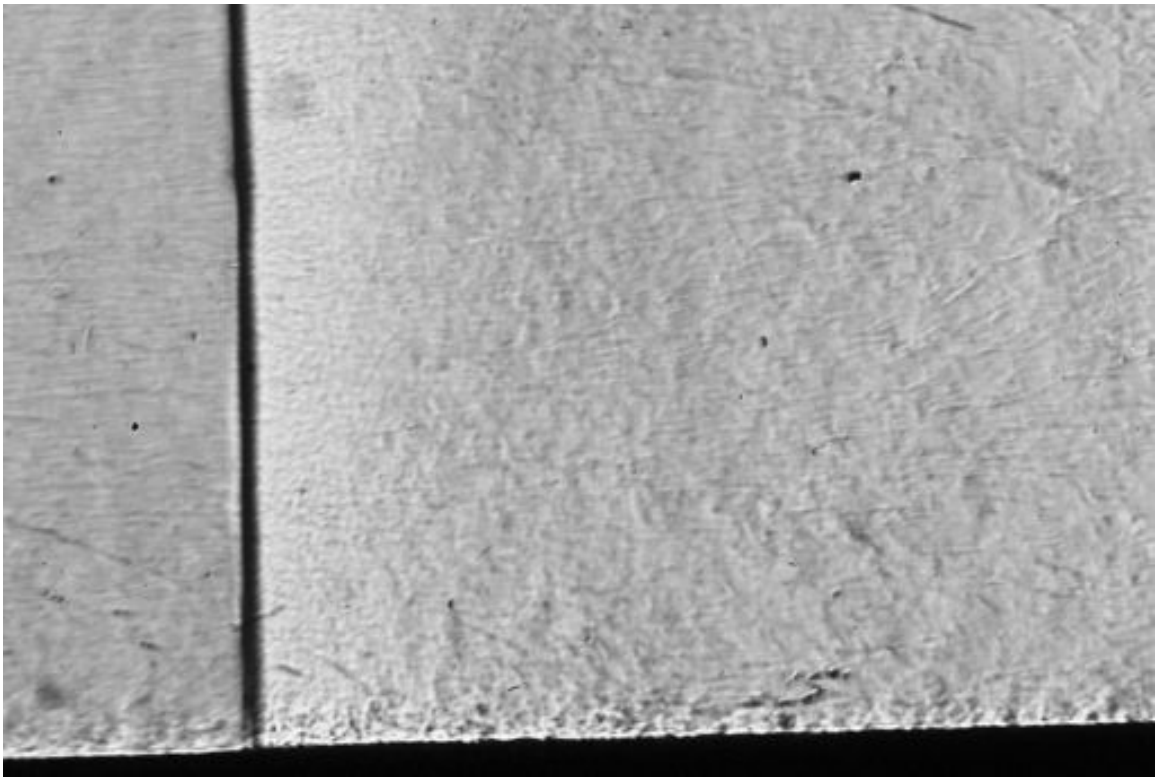

Figure D.9: Unfocused schlieren image of shot 1965. The field of view is approximately 45 mm wide.

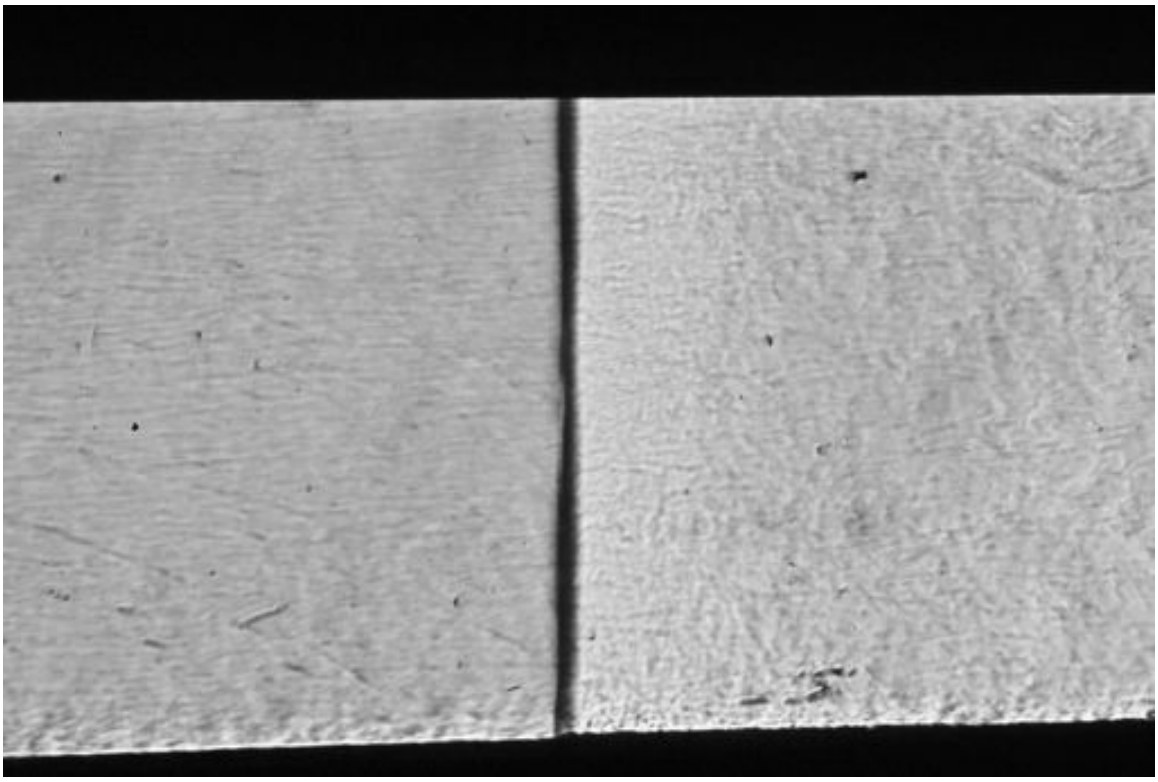

Figure D.10: Unfocused schlieren image of shot 1966. The field of view is approximately 45 mm wide.

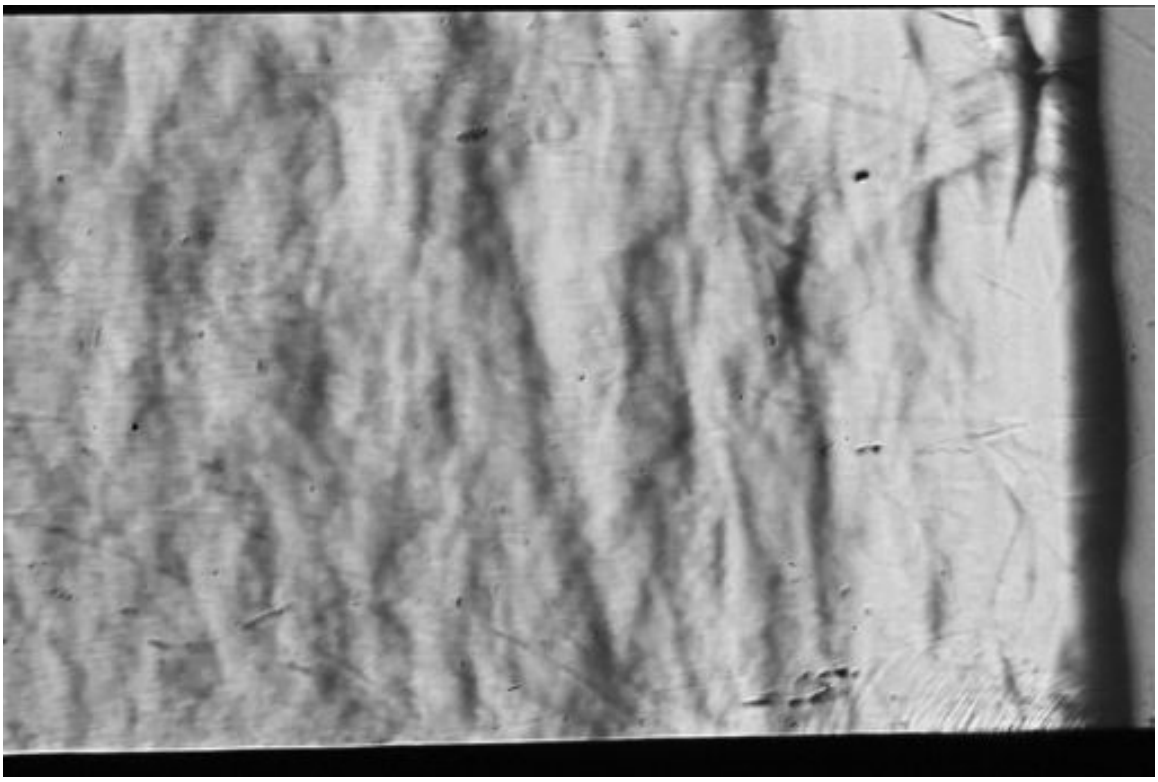

Figure D.11: Unfocused schlieren image of shot 1967. The field of view is approximately 45 mm wide.

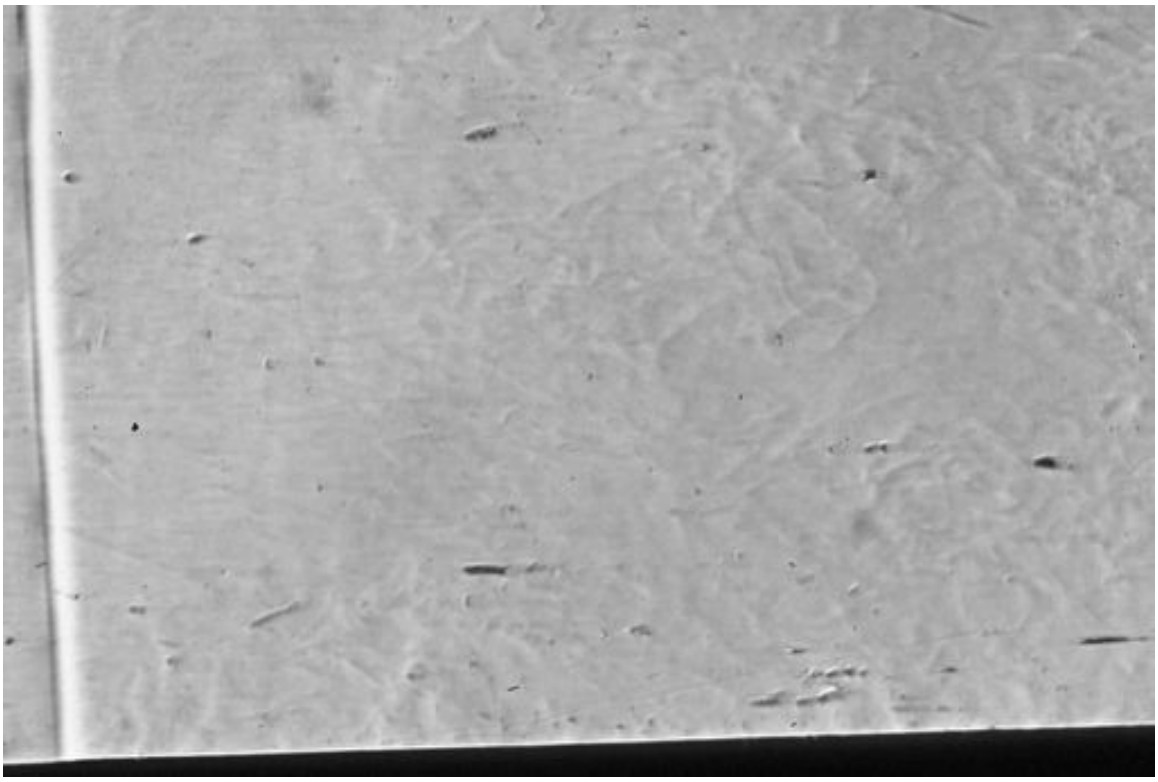

Figure D.12: Unfocused schlieren image of shot 1971. The field of view is approximately 45 mm wide.

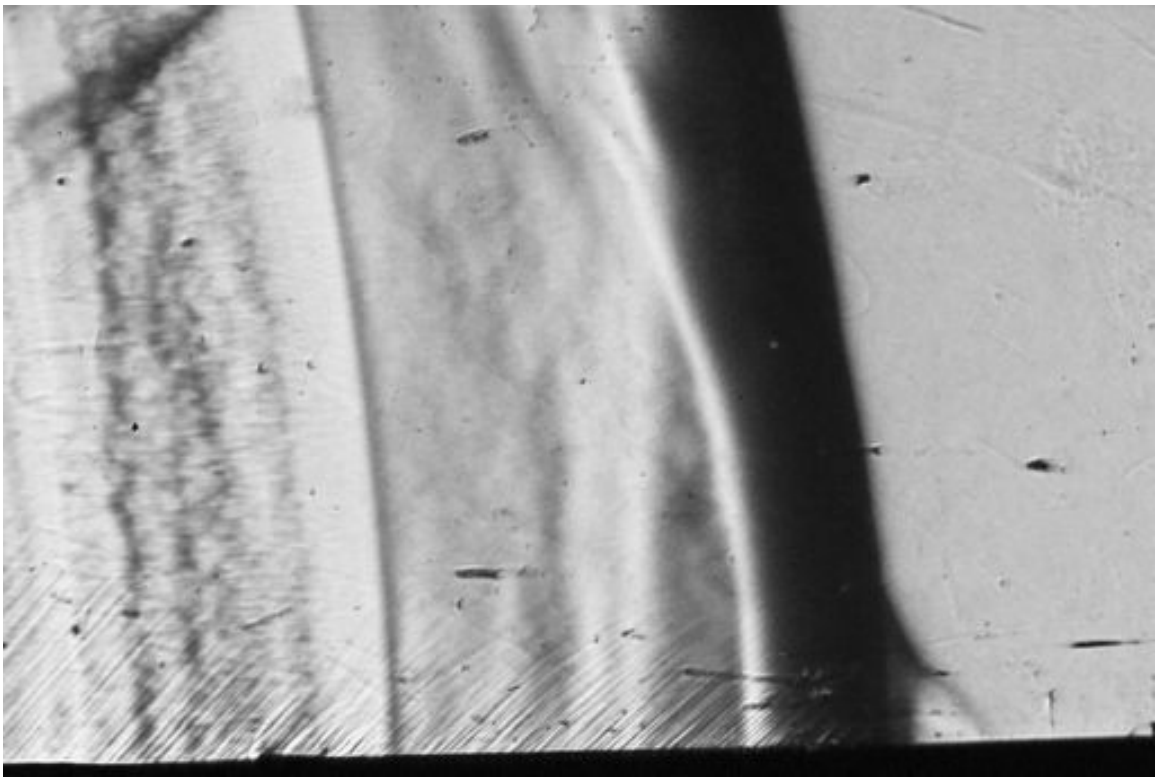

Figure D.13: Unfocused schlieren image of shot 1972. The field of view is approximately 45 mm wide.

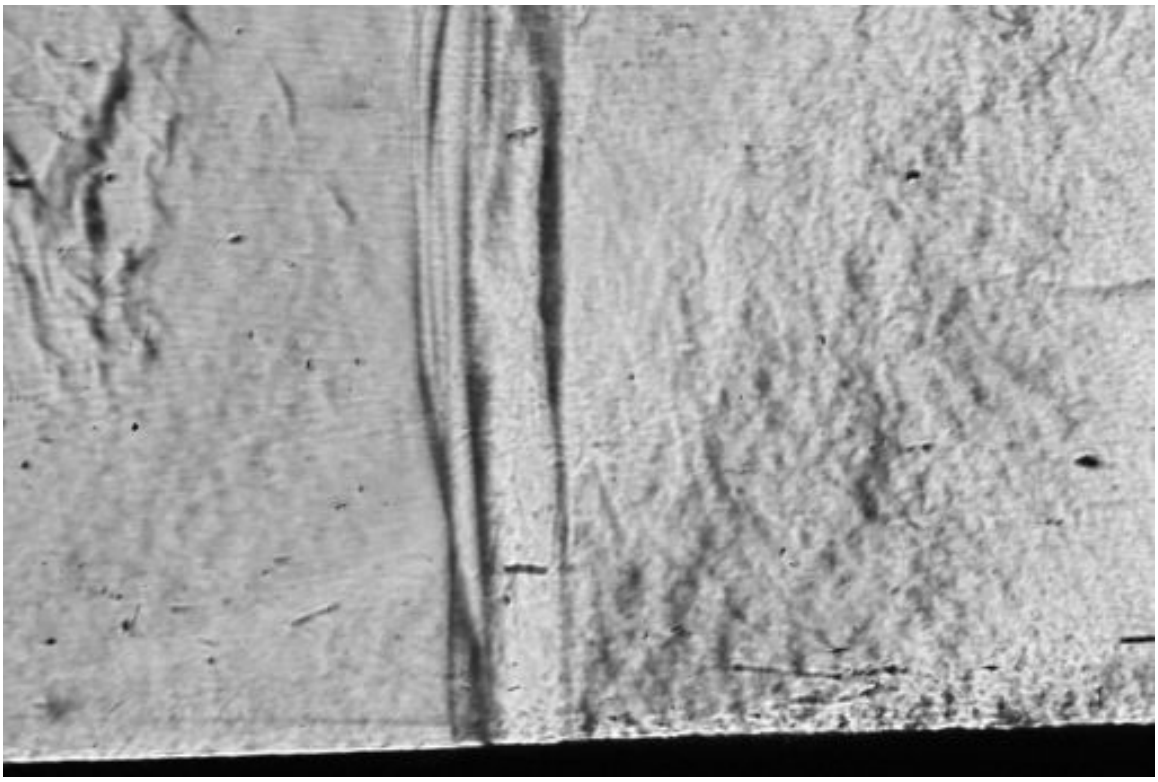

Figure D.14: Unfocused schlieren image of shot 1975. The field of view is approximately 45 mm wide.

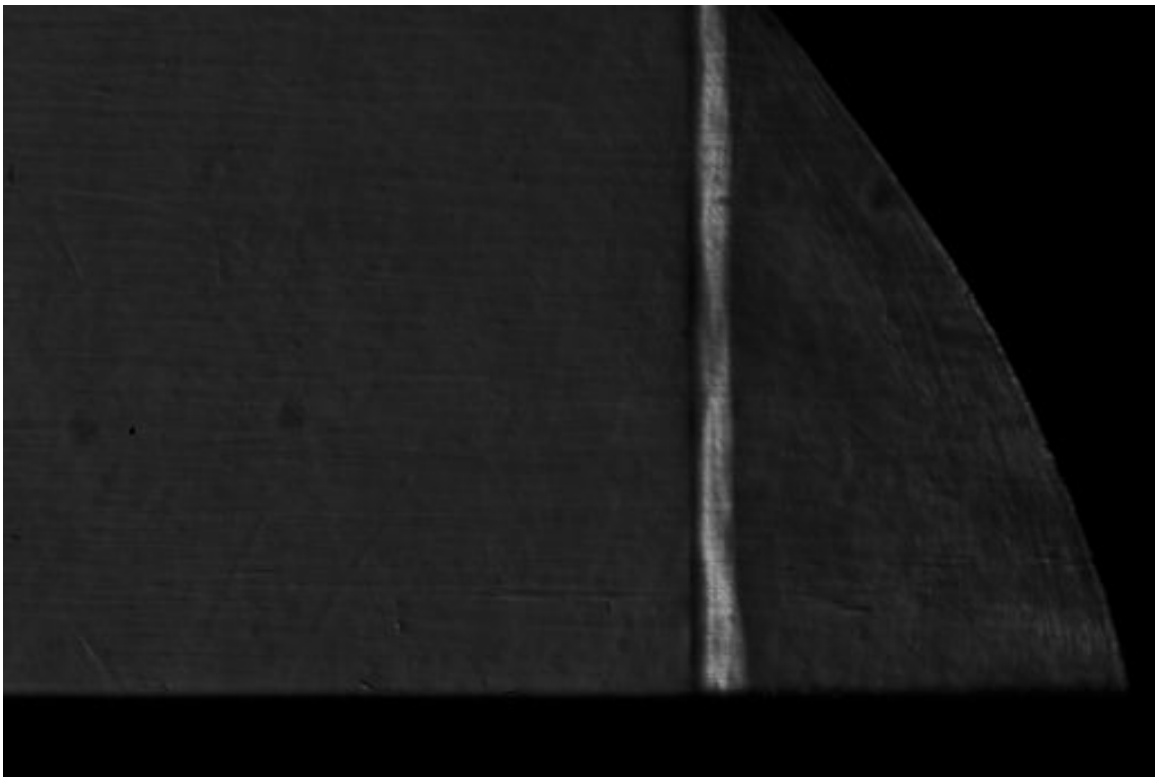

Figure D.15: Unfocused schlieren image of shot 1978. The field of view is approximately 45 mm wide.

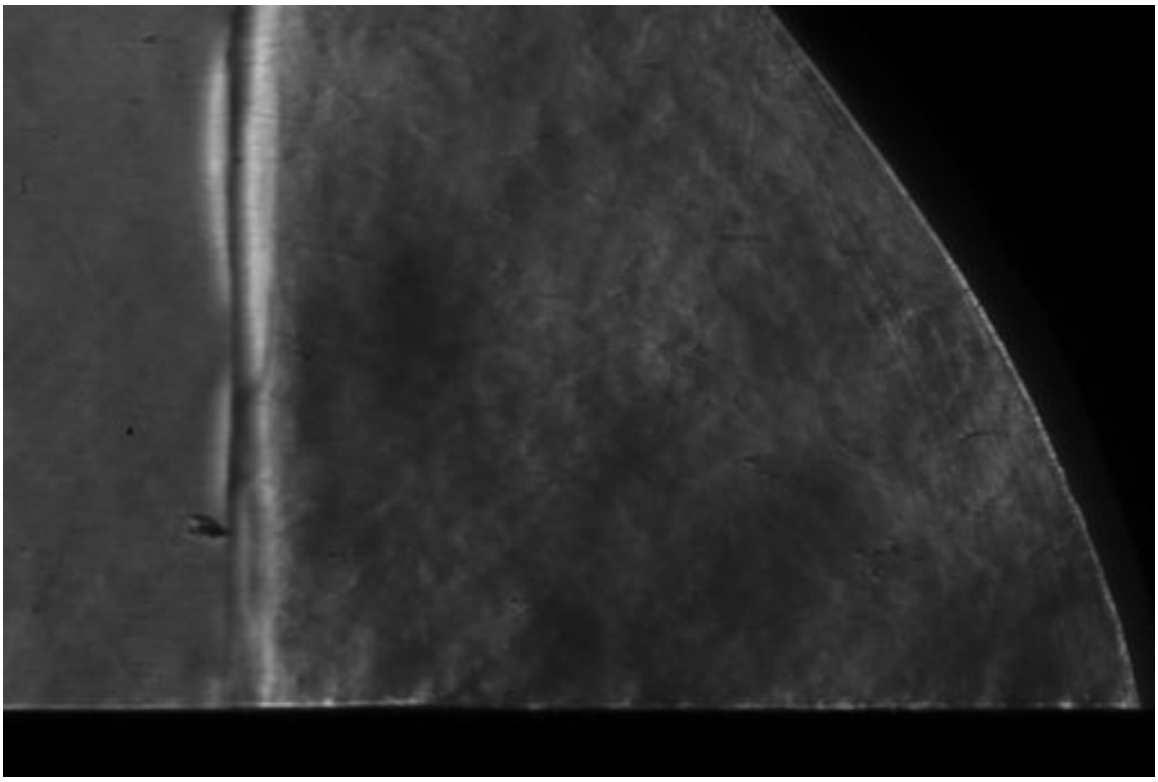

Figure D.16: Unfocused schlieren image of shot 1991. The field of view is approximately 45 mm wide.

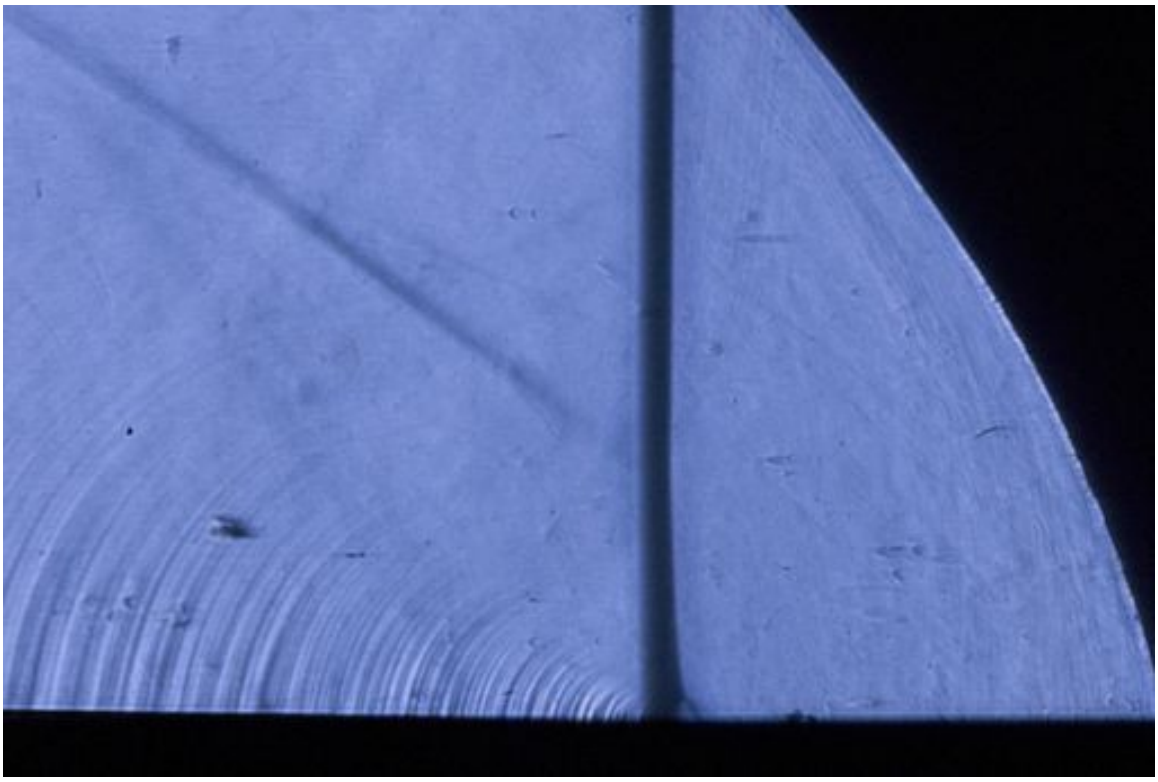

Figure D.17: Unfocused schlieren image of shot 1997. The field of view is approximately 45 mm wide.

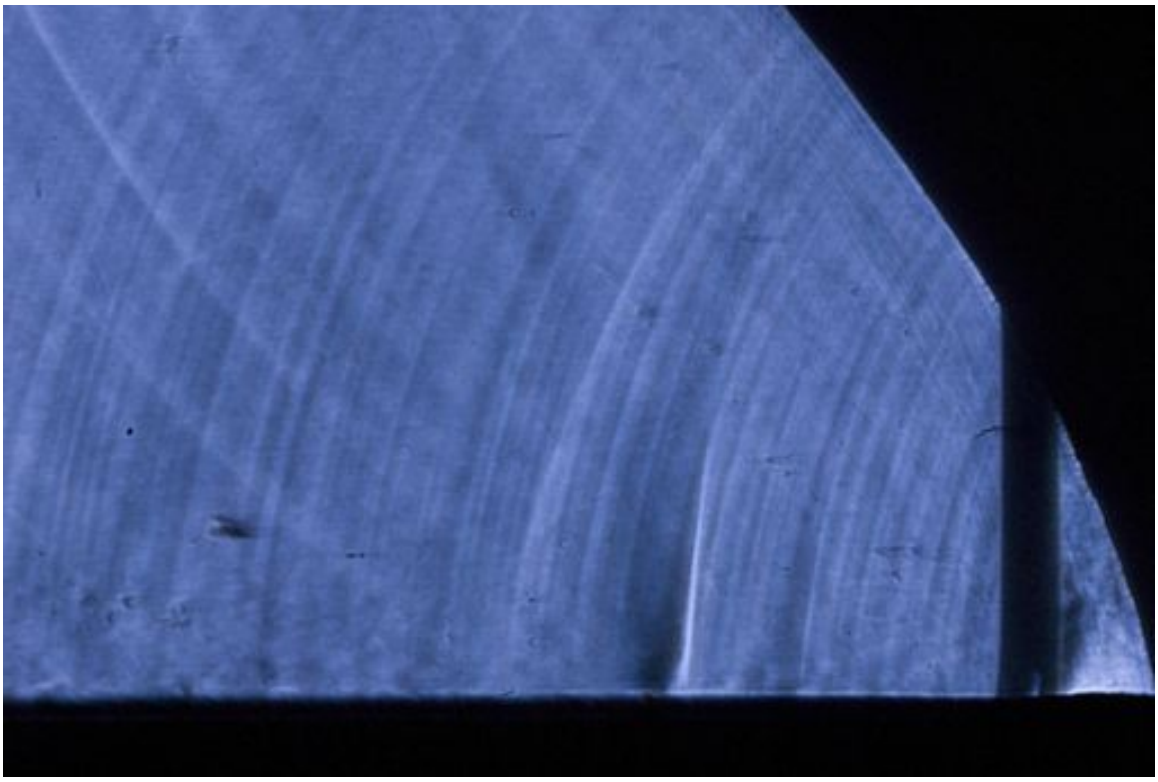

Figure D.18: Unfocused schlieren image of shot 1999. The field of view is approximately 45 mm wide.

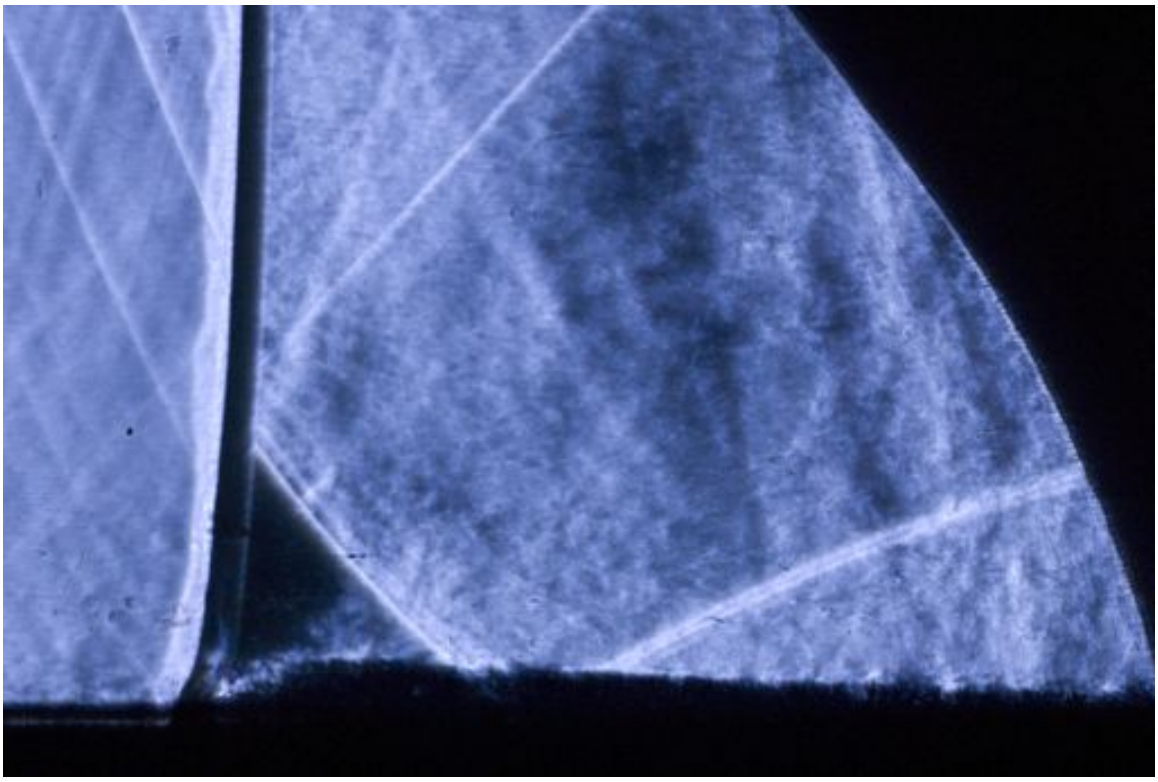

Figure D.19: Unfocused schlieren image of shot 2000. The field of view is approximately 45 mm wide.

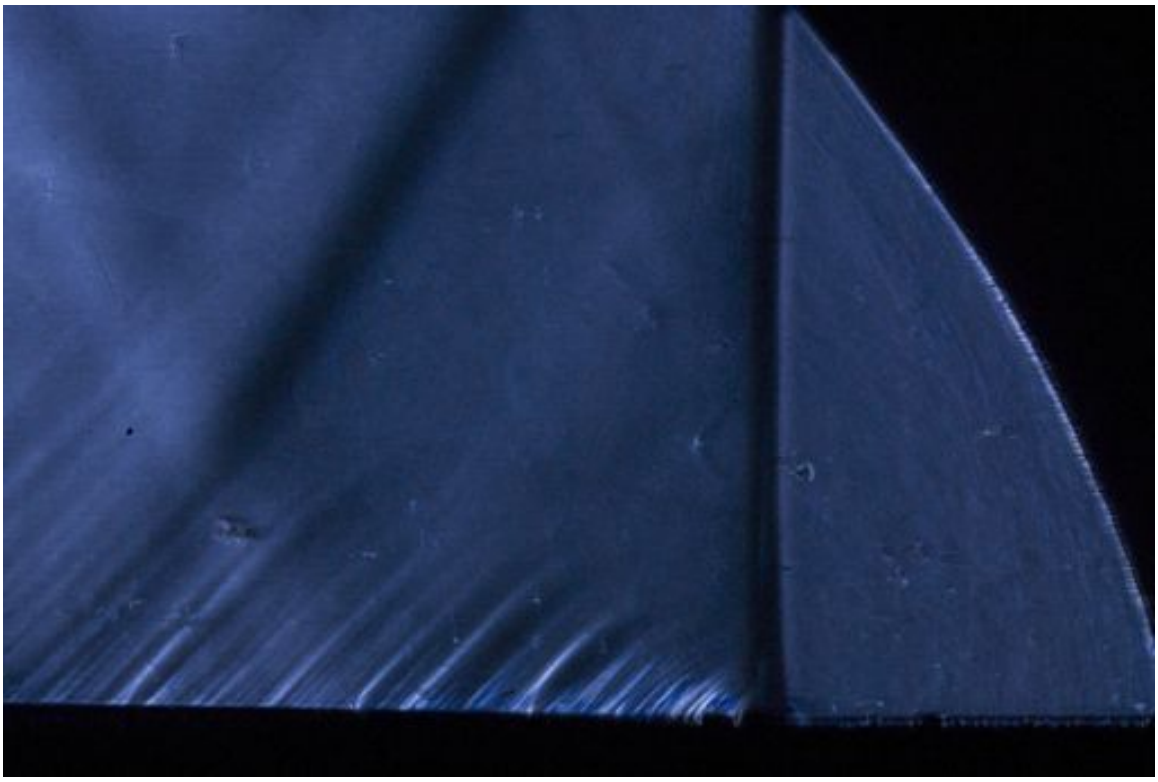

Figure D.20: Unfocused schlieren image of shot 2002. The field of view is approximately 45 mm wide.

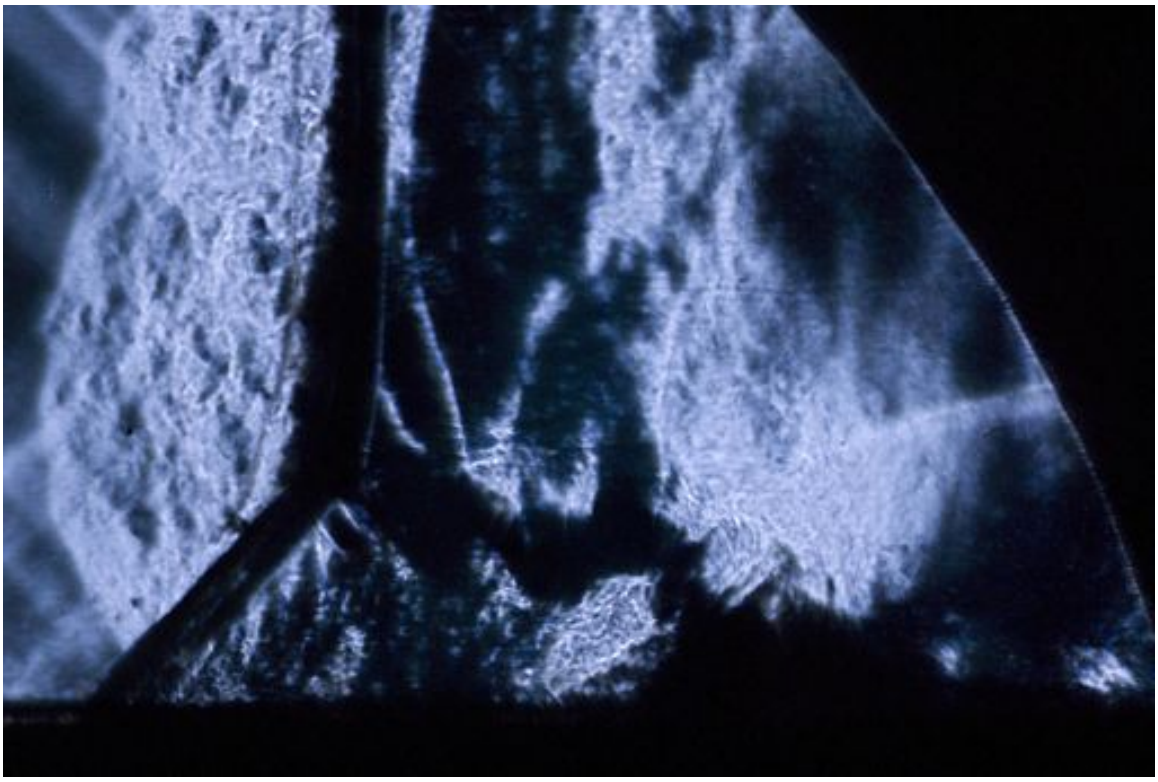

Figure D.21: Unfocused schlieren image of shot 2003. The field of view is approximately 45 mm wide.

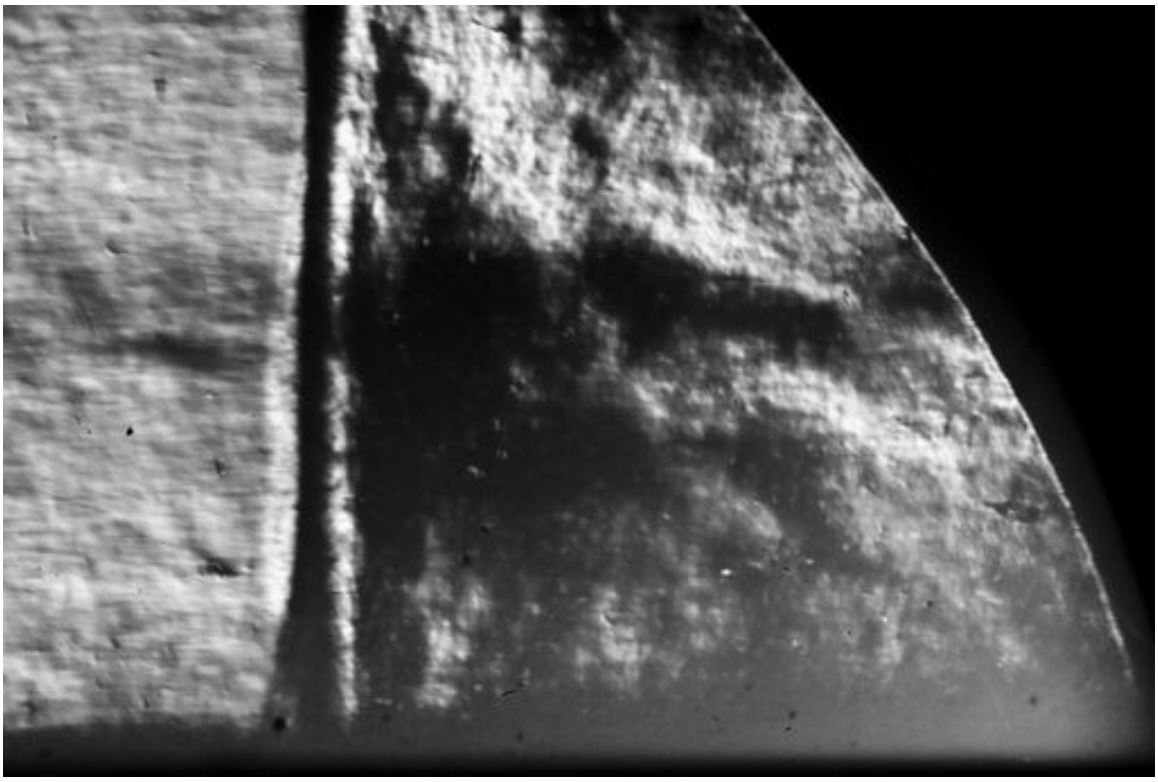

Figure D.22: Unfocused schlieren image of shot 2011. The field of view is approximately 45 mm wide.

D.1.2 SLD1332V

A Sony SLD1332V laser diode, nicknamed "Ghost in the Shell" in the data files, was used in conjunction with an LDP-V 03-100 UF3 current driver and a Phantom v7.10 high-speed camera to obtain images with a much shorter exposure time than was possible with the spark light source. A laser line filter was positioned in front of the camera; this made imaging detonation waves much easier. Both laser and camera were driven by a BNC delay generator that was triggered from a pressure signal. This visualization system was developed with Dr. Nick Parziale, who used it to great effect in the T5 hypervelocity wind tunnel.

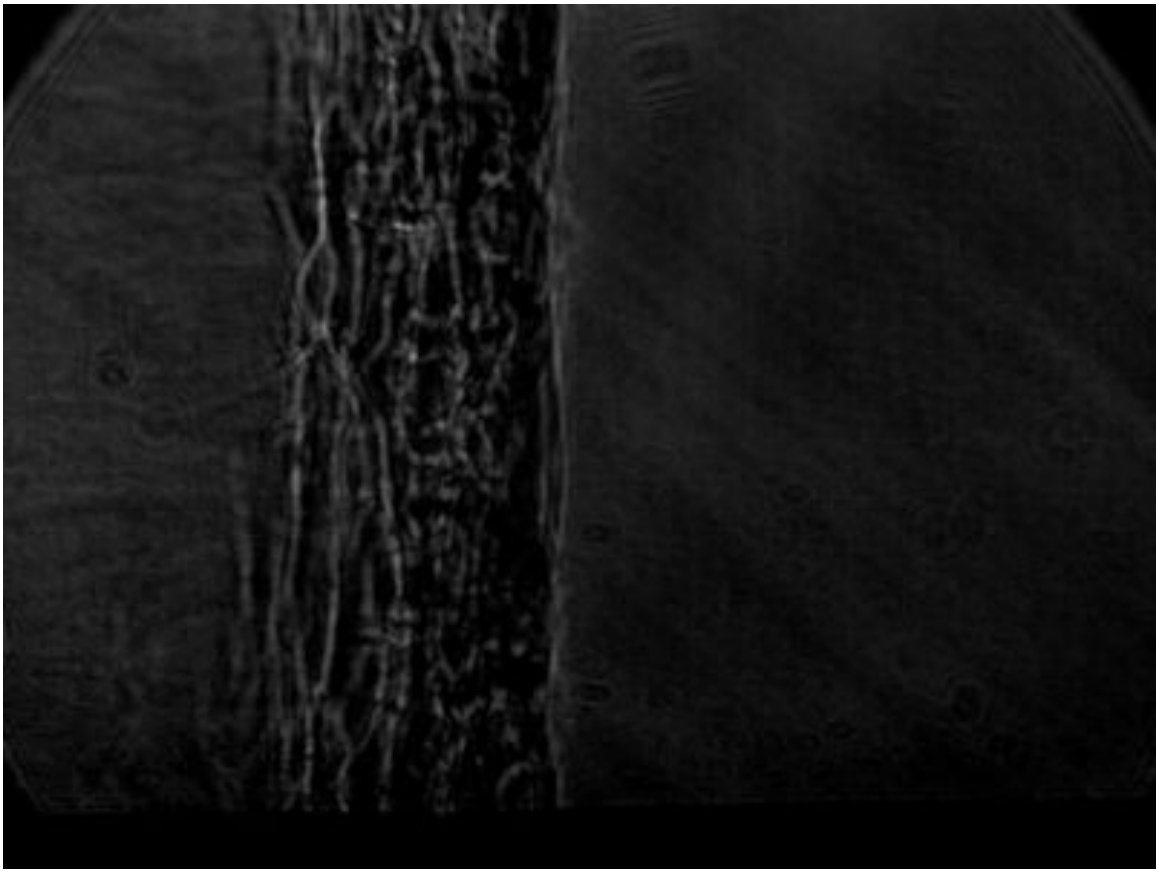

Figure D.23: Unfocused schlieren image of shot 2067. The field of view is approximately 10 mm wide.

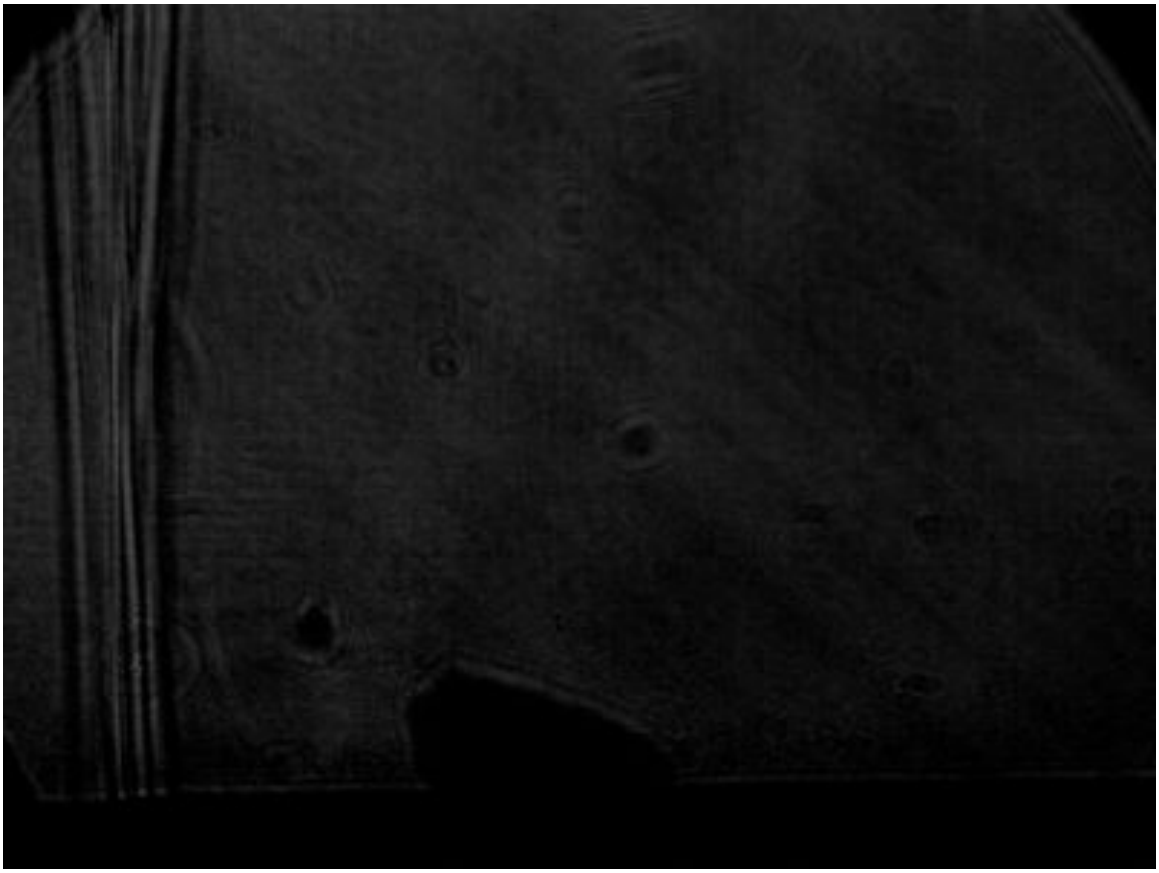

Figure D.24: Unfocused schlieren image of shot 2069. The field of view is approximately 10 mm wide.

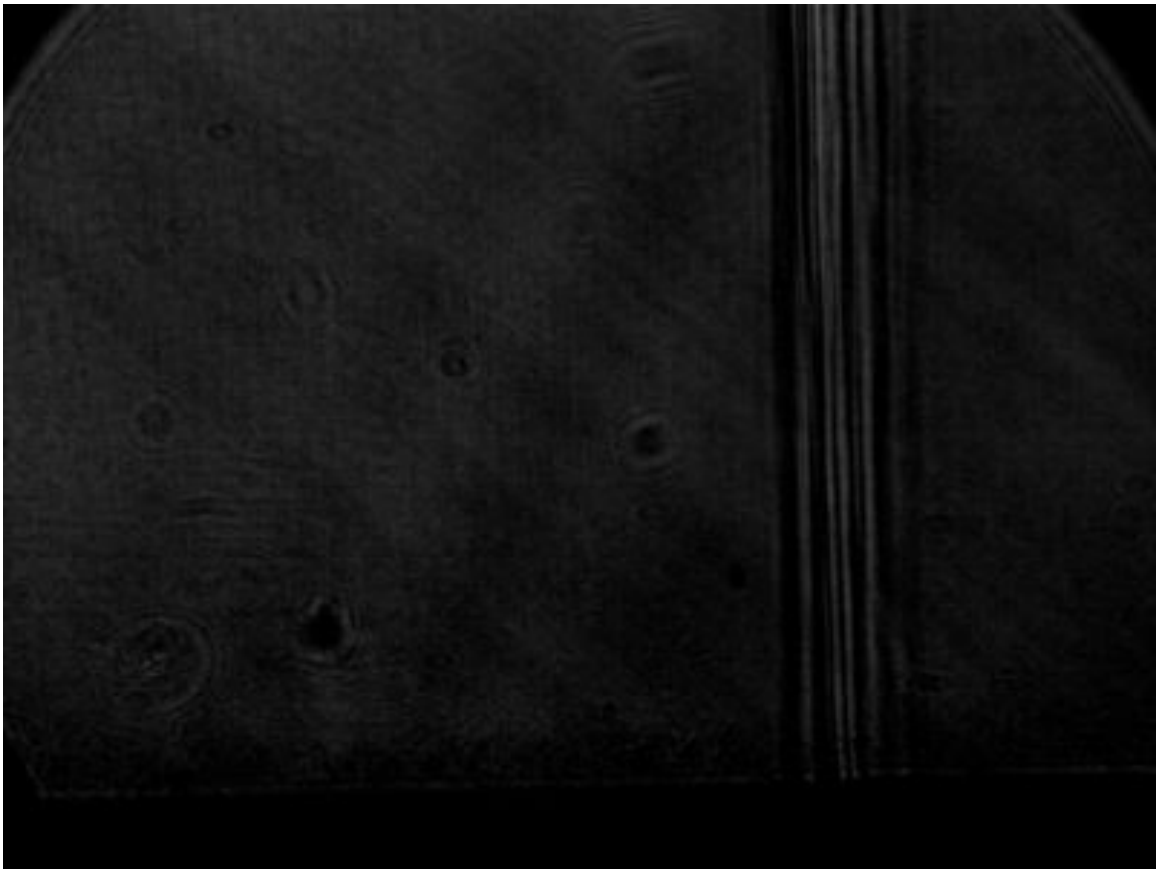

Figure D.25: Unfocused schlieren image of shot 2070. The field of view is approximately 10 mm wide.

D.1.3 SMART Cavilux

The SMART Cavliux laser, named "Cyclops" in the data files, was demoed for an afternoon to explore if it would be useful for detonation imaging. The laser was similar in capability to the SLD1332V system, but was slightly more user friendly in operation. The laser was run such that it would produce two sets of five 10 ns pulses in conjunction with the Phantom v7.10 camera. For an unknown reason, only four pulses were produced. In practice, it proved less useful than the SLD1332V laser.

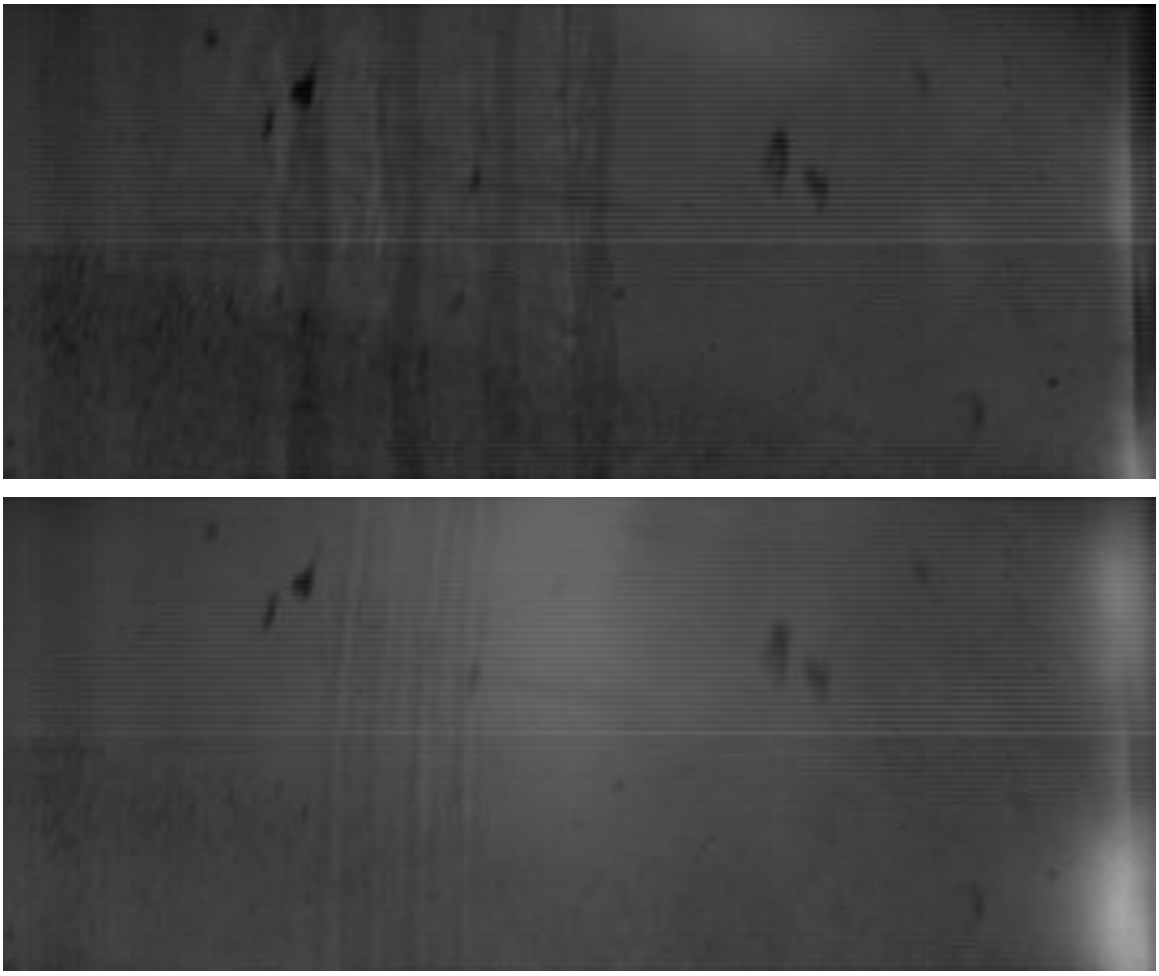

Figure D.26: Unfocused schlieren images of shot 2195. The field of view is approximately 66 mm wide.

D.1.4 PL1000DRC

The best images obtained were recorded using a PL1000DRC flash lamp with a SIMD16 Ultra Fast Framing Camera, nicknamed "Sandman." This allowed for 16 images at essentially arbitrary frame rate and exposure time. The light source was triggered off an upstream pressure gauge (so that it would have ample time to warm up and produce light). The camera, which had a trigger-to-picture delay time of 65 ns, was triggered off of a separate pressure gauge in the field of view. The low trigger-to-picture time meant that most every detonation performed resulted in a picture. The camera produced a 5 V output whenever the camera was recording an image; this signal was fed into the data acquisition system to relate the pressure signals and images. A USAF 1951 target was used to quantify the resolving power of this system to be 223 μm horizontally and 125 μm vertically as measured with the target at the center of the test section.

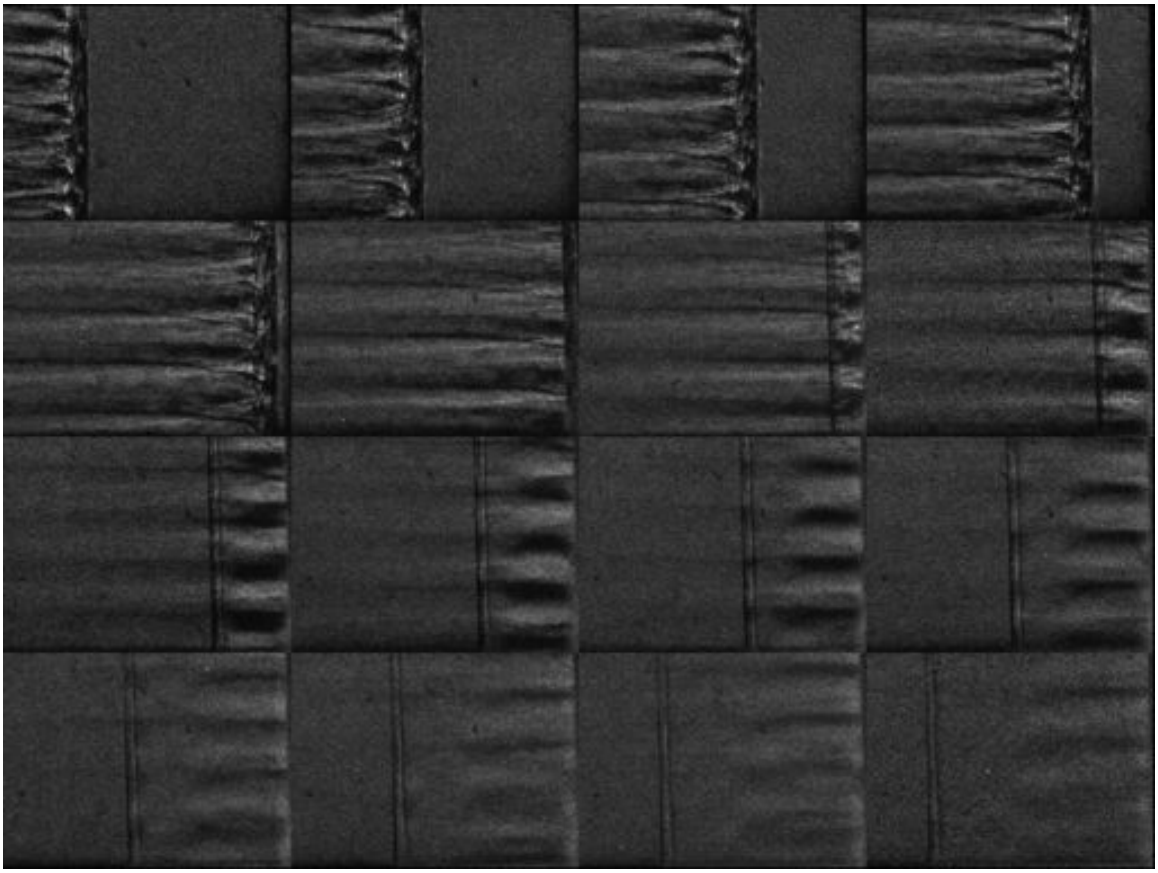

Figure D.27: Unfocused schlieren image of shot 2161. The field of view is approximately 30 mm wide.

D.2 Focused Schlieren Systems

Design considerations for a focused schlieren system as well as specifics for each focused visualization system employed are given below organized by the light source used. A list of focal lengths and magnifications are included in table D.2, although these sometimes changed between images and thus the scale for each individual picture should be checked. Run conditions are given in appendix C.

Table D.2: Details of focused schlieren configurations.

#	Light source	Camera	b (mm)	f_1 (mm)	f_2 (mm)	M	t_{exp} (ns)
5	HardSoft IL-106G	Nikon D200	50	500	750	1	250
6	EverGreen70	PCO.2000	25	500	1000	1	10

D.2.1 Focused Schlieren Design Considerations

Building a focused schlieren system requires more care than a similar unfocused system. Reducing the depth of focus (and thereby increasing the focusing effect) is achieved by increasing the camera aperture angle, α. This was accomplished by increasing the height of the schlieren source, b, as illustrated in figure D.28. The aperture angle of the source, α_s, (which may be larger than the camera aperture angle for reasons discussed later) may be calculated as follows:

$$\tan\frac{\alpha_s}{2} = \frac{b}{2f_1} \tag{D.1}$$

$$\Rightarrow \ \alpha_s \approx \frac{b}{f_1} \tag{D.2}$$

where f_1 is the focal length of the collimating optical element and the small angle approximation has been applied. However, this source aperture angle may be reduced if the schlieren object is too far from the focusing mirror. We observe that, in order for a given source aperture angle to have the optimal focusing effect, the maximum distance between the collimating optical element and the schlieren object, $d_{1s,max}$, is a function of f_1, ϕ_1, and b, where ϕ_1 is the diameter of the collimating element.

$$\tan\frac{\alpha_s}{2} = \frac{\phi_1}{2d_{1s,max}} \tag{D.3}$$

$$\Rightarrow \; d_{1s,max} = \frac{f_1\phi_1}{b} \tag{D.4}$$

If $d_{1s} > d_{1s,max}$, an effective aperture angle for the collimating optical element is determined by

$$\alpha_1 = \frac{\phi_1}{d_{1s}}. \tag{D.5}$$

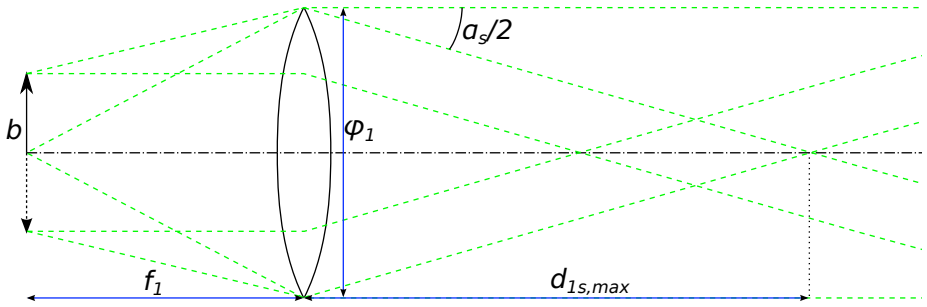

Figure D.28: The light source side of an extended schlieren system.

Figure D.29 depicts the camera side of the focused schlieren system. Similarly to the case of the schlieren object being too far from the collimating optical element, if the distance between the schlieren object and the focusing element, d_{s2}, is too large the light may not impinge upon the focusing optical element. In this case there is the

limiting distance, $d_{s2,max}$, determined by

$$d_{s2,max} = \frac{\phi_2}{\alpha} \tag{D.6}$$

$$= \frac{f_1 \phi_2}{b} \tag{D.7}$$

in the case that this distance is exceeded, there is an effective aperture angle, α_2, determined by

$$\alpha_2 = \frac{\phi_2}{d_{s2}} \tag{D.8}$$

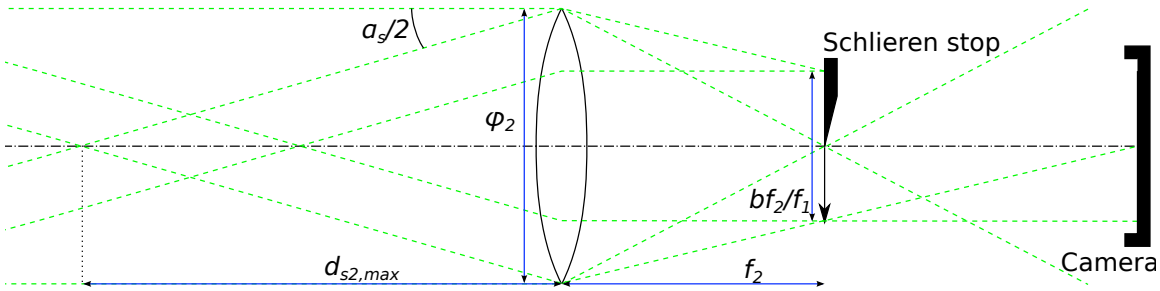

Figure D.29: The camera side of an extended schlieren system.

The true aperture angle, α, used to determine the depth of focus is the minimum of α_s, α_1, and α_2 given in equations (D.2), (D.5), and (D.8). The sensitivity of the schlieren system increases for increased d_{s2} and thus an optimal sensitivity for a given aperture angle may be determined:

$$d_{s2} = d_{s2,max} = \frac{\phi_1}{\alpha} = \frac{f_1 \phi_2}{b} \tag{D.9}$$

as illustrated in figure D.30; this choice also limits light loss. In practice, this distance was often exceeded to allow for greater schlieren sensitivity and to limit the effect of the test section floor discussed next.

As illustrated in figure D.31, increasing the aperture angle also results in a reduced illumination near the test section walls. For a given aperture angle and distance from

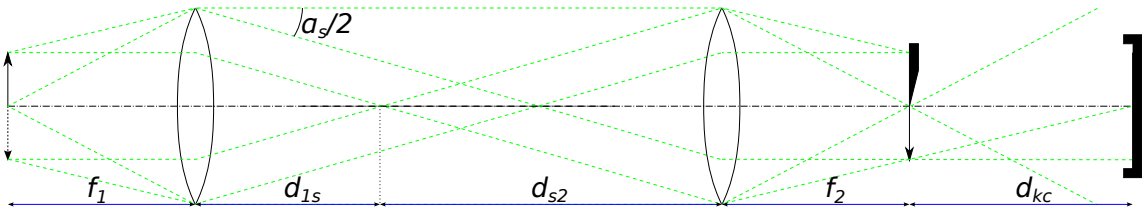

Figure D.30: An extended source schlieren system designed to obtain maximum sensitivity and depth of focus.

the side-wall, y, we can determine the fraction of light, ξ, transmitted through the test section of width w without impinging upon the wall from the equation

$$\xi = \frac{A'}{A} \tag{D.10}$$

$$A = \pi r_s^2 \tag{D.11}$$

$$r_s = \frac{\alpha w}{2} \tag{D.12}$$

$$A' = \begin{cases} A & \text{if } y \geq r_s \\ A - 2r_s^2 \cos^{-1}\left(\dfrac{y}{r_s}\right) + 2y\sqrt{r_s^2 - y^2} & \text{if } y < r_s \end{cases} \tag{D.13}$$

or defining y' as

$$y' = \frac{y}{r_s} \tag{D.14}$$

we have

$$\xi = \begin{cases} 1 & \text{if } y' \geq 1 \\ 1 - \dfrac{2}{\pi}\cos^{-1} y' + \dfrac{2y'}{\pi}\sqrt{1 - y'^2} & \text{if } y' < 1. \end{cases} \tag{D.15}$$

The above analysis assumed only one focusing element was employed (such as was the case in the current investigation). Adding further elements requires repeated consideration of each element to determine the limiting camera aperture angle.

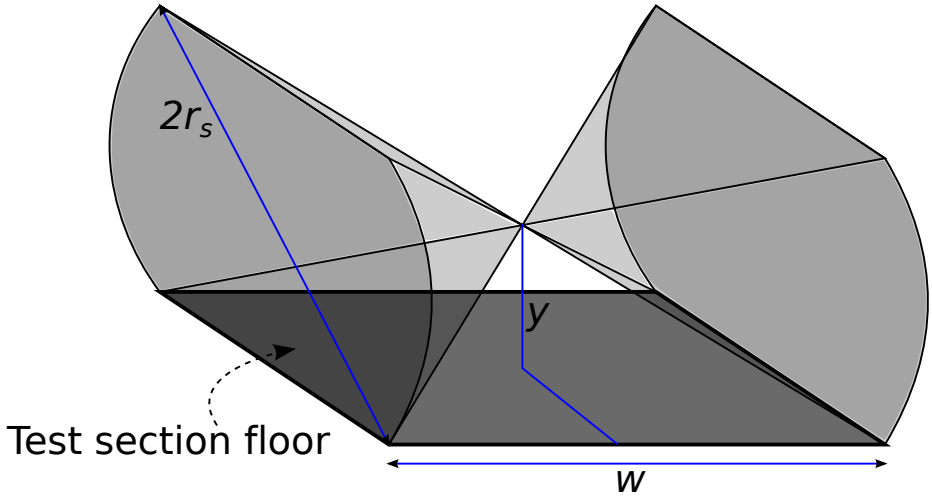

Figure D.31: The effect of the test section floor on the light paths.

D.2.2 HardSoft IL

This was a green LED light source, named the "Green Lantern" in data files, that was capable of producing light pulses down to 250 ns in duration. It was paired with the Nikon D200 camera discussed in section D.1.1. This source was ideal for use as a focused light source because of the shape of the LED array (which was 50 mm tall), and its ability to be pulsed. However, the light produced was not of short enough duration to adequately freeze the detonation, and the wavelength of the light was $\pm \sim 50$ nm making it impossible to adequately filter the light. For these reasons, this source was only used to visualize shock waves. The camera was triggered off of the exploding wire and the LED source triggered off of an appropriate pressure gauge. This visualization system was assembled and tested with the help of Jeff Odell.

Figure D.32: Focused schlieren image of shot 2042. The field of view is approximately 20 mm wide.

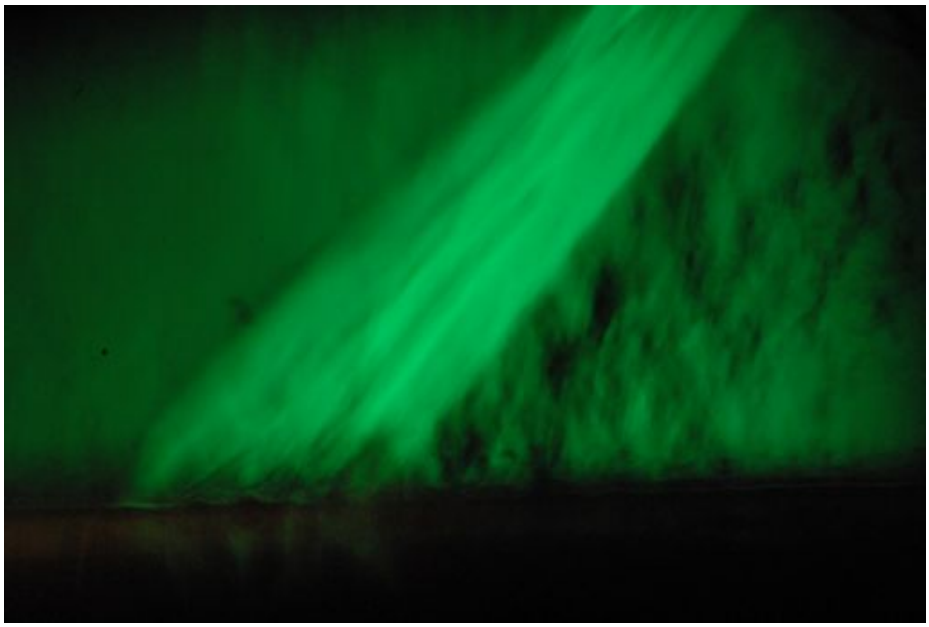

Figure D.33: Focused schlieren image of shot 2044. The field of view is approximately 20 mm wide.

Figure D.34: Focused schlieren image of shot 2045. The field of view is approximately 20 mm wide.

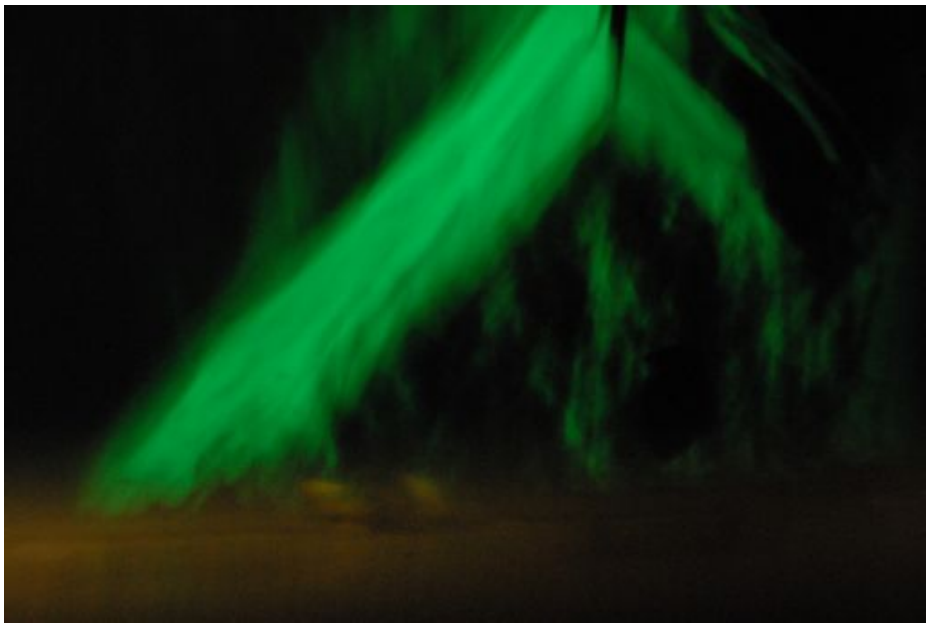

Figure D.35: Focused schlieren image of shot 2055. The field of view is approximately 20 mm wide.

D.2.3 EverGreen70

The EverGreen70 Q-switched pulsed PIV laser combined with the 4 megapixel 14 bit PCO.2000 camera produced some exceptional images. The laser emitted two 10 ns duration laser pulses at 530 nm wavelength with 70 mJ pulse energy. An extended source was created by expanding the beam with a cylindrical lens into a sheet that impinged on either a white screen or an engineered optical diffuser. The diffuser had a diameter of 25.4 mm and a diffusion angle of 20° to create a line of light that functioned as the schlieren source. The EverGreen70 required a delay of 135 μs between trigger and light emission. This made it difficult to time the images and frequently repeated tests were required to get a successful image. A USAF 1951 target was used to determine that this system had a horizontal resolution of 63 μm and a vertical resolution of 44 μm in the center of the test section and less than 250 μm at the windows.

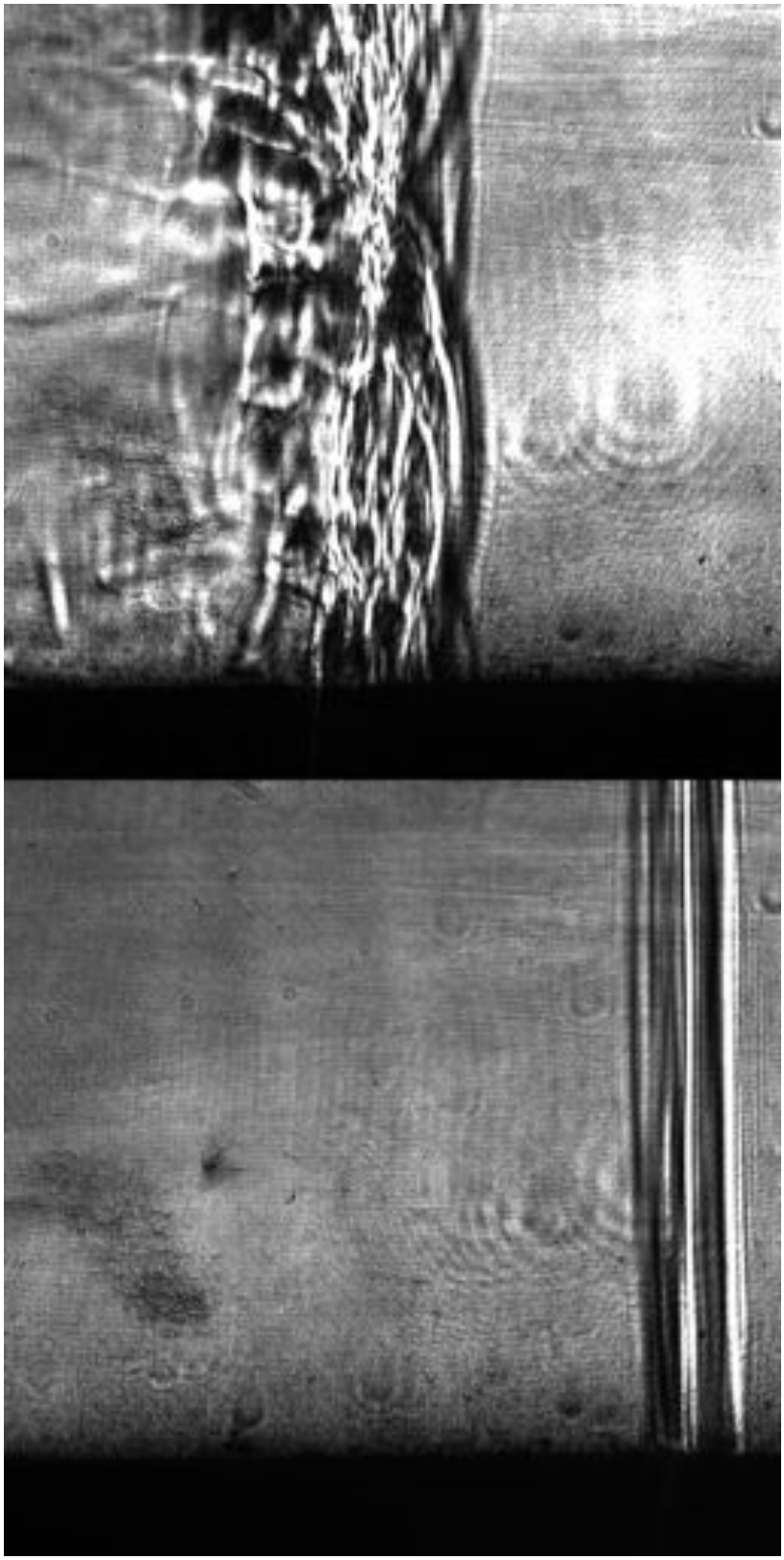

Figure D.36: Focused schlieren image of shot 2088. The field of view is approximately 14 mm wide.

Appendix E

GDT Pressure and Heat-Flux Data

A nearly complete set of data for the GDT experiments is included here. The data are organized by mixture and fill pressure. Pressure, heat-flux, and image data are included where appropriate. Signals that were dominated by noise and images that were indecipherable are not included.

E.1 Hydrogen-Oxygen

Figures E.1–E.51.

E.2 Hydrogen-Oxygen-Argon

Figures E.56–E.121.

E.3 Hydrogen-Oxygen-Nitrogen

Figures E.124–E.132.

E.4 Hydrogen-Oxygen-Carbon Dioxide

Figures E.136–E.147.

E.5 Hydrogen-Nitrous Oxide

Figure E.151.

E.6 Ethylene-Oxygen

Figures E.154–E.179.

E.7 Shock Waves

Figures E.183–E.189.

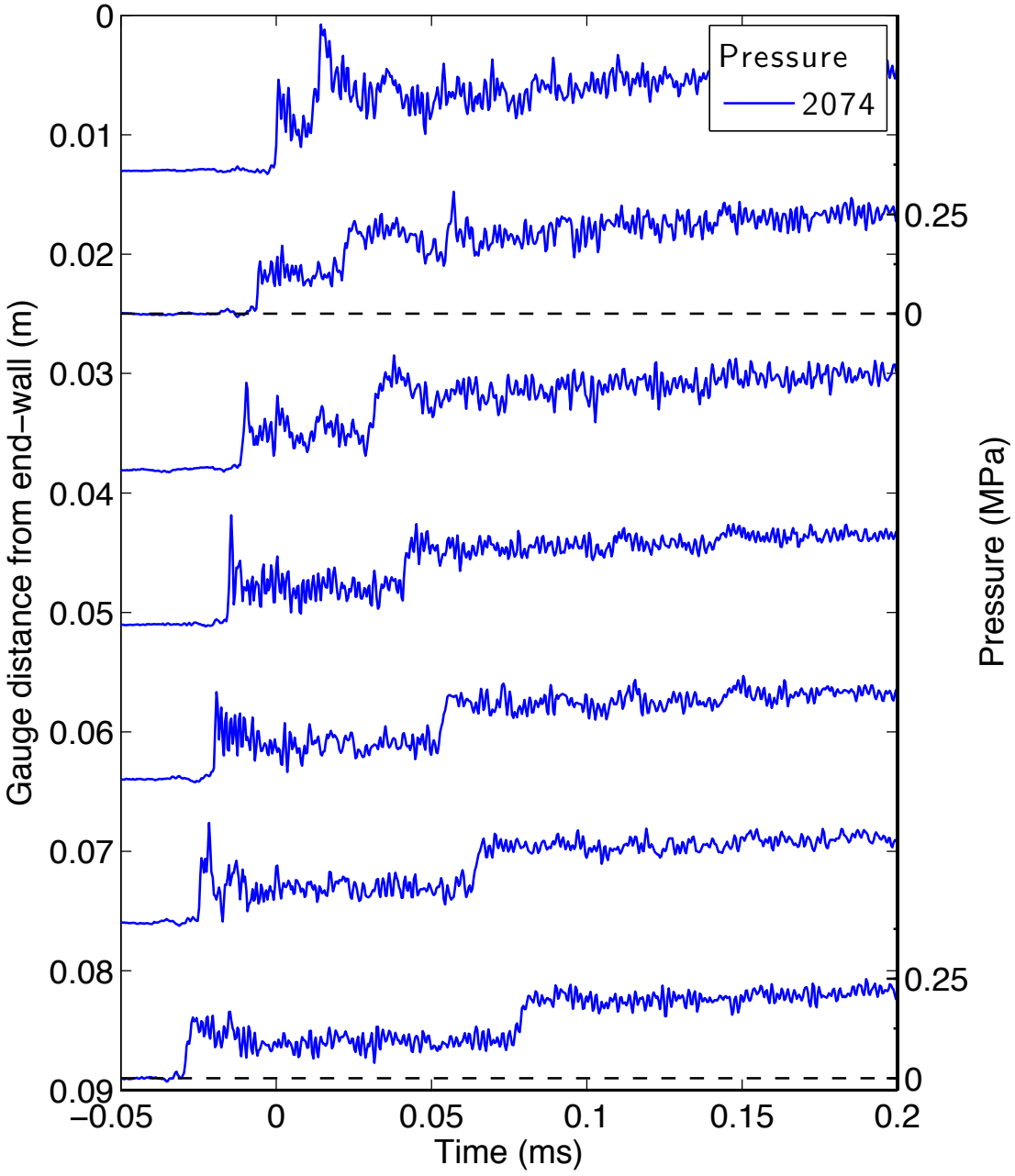

Figure E.1: Pressure traces for a detonation in stoichiometric hydrogen-oxygen at fill pressure 5 kPa, part 1.

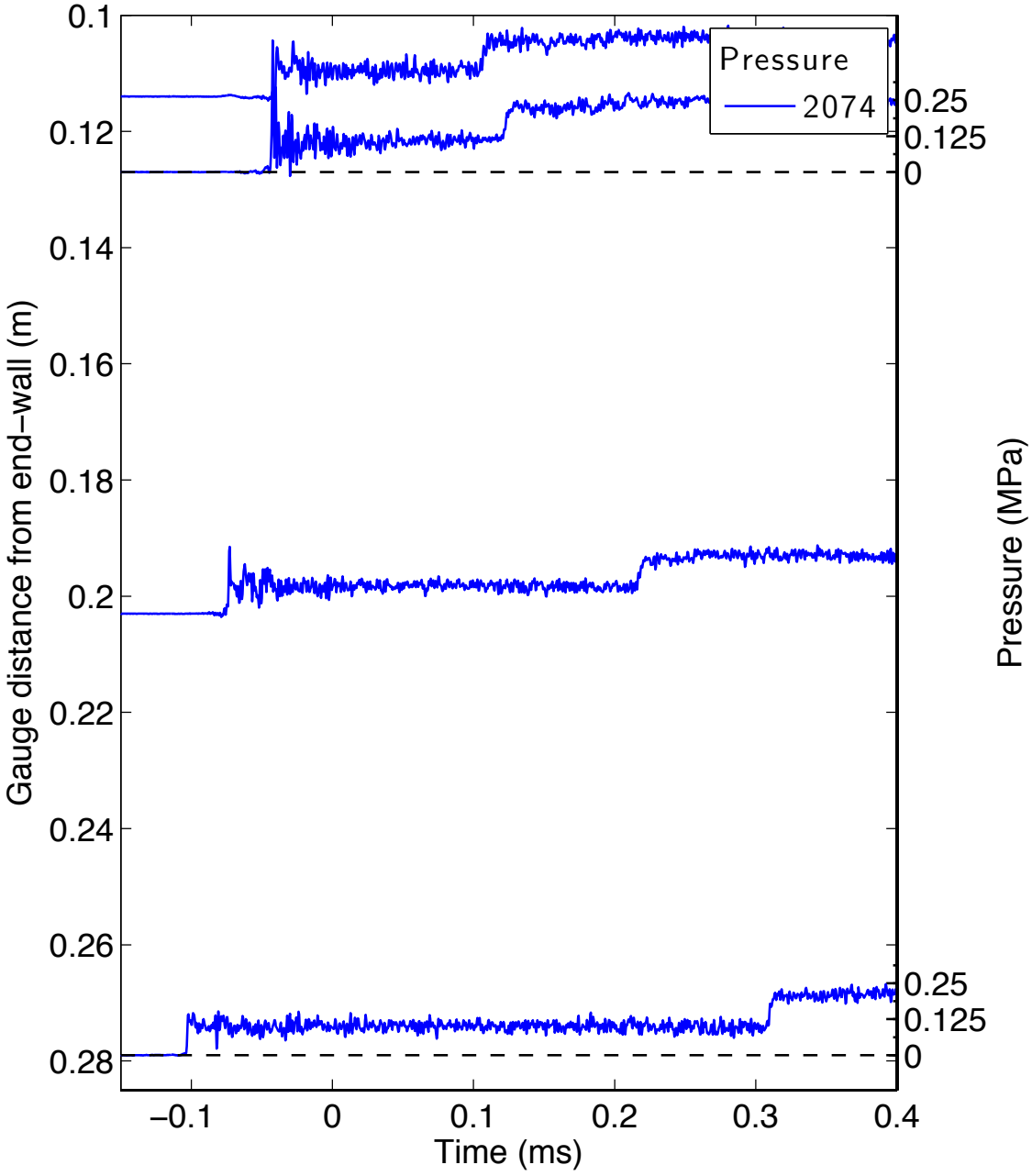

Figure E.2: Pressure traces for a detonation in stoichiometric hydrogen-oxygen at fill pressure 5 kPa, part 2.

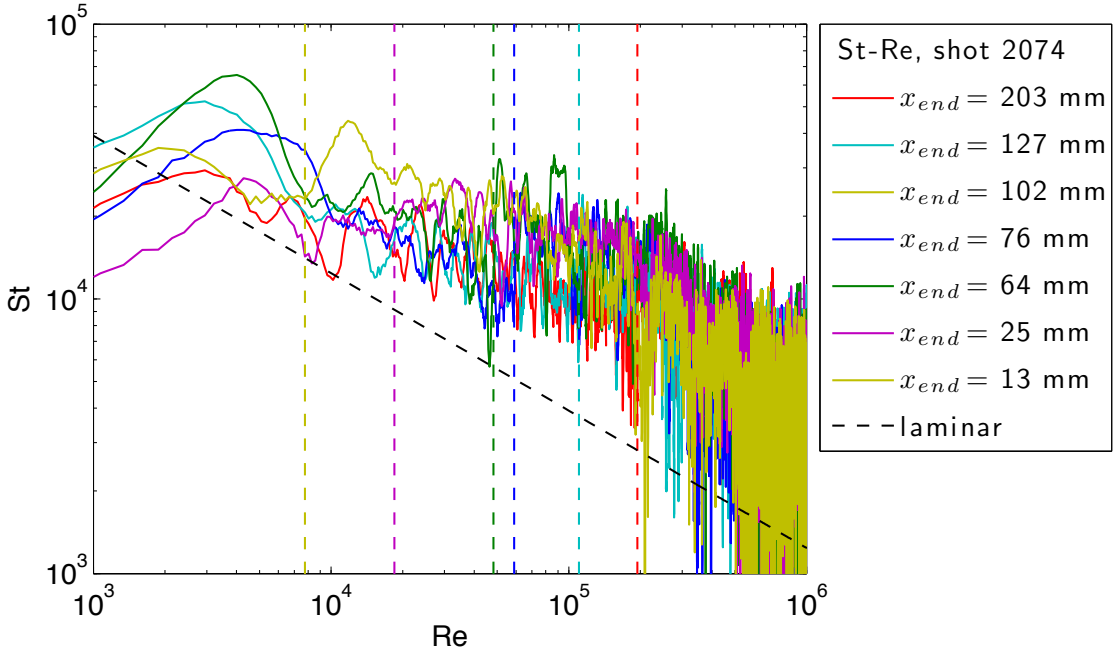

Figure E.3: Stanton-Reynolds number traces from shot 2074, a detonation in stoichiometric hydrogen-oxygen at fill pressure 5 kPa. The dashed vertical lines represent the arrival of the reflected shock wave.

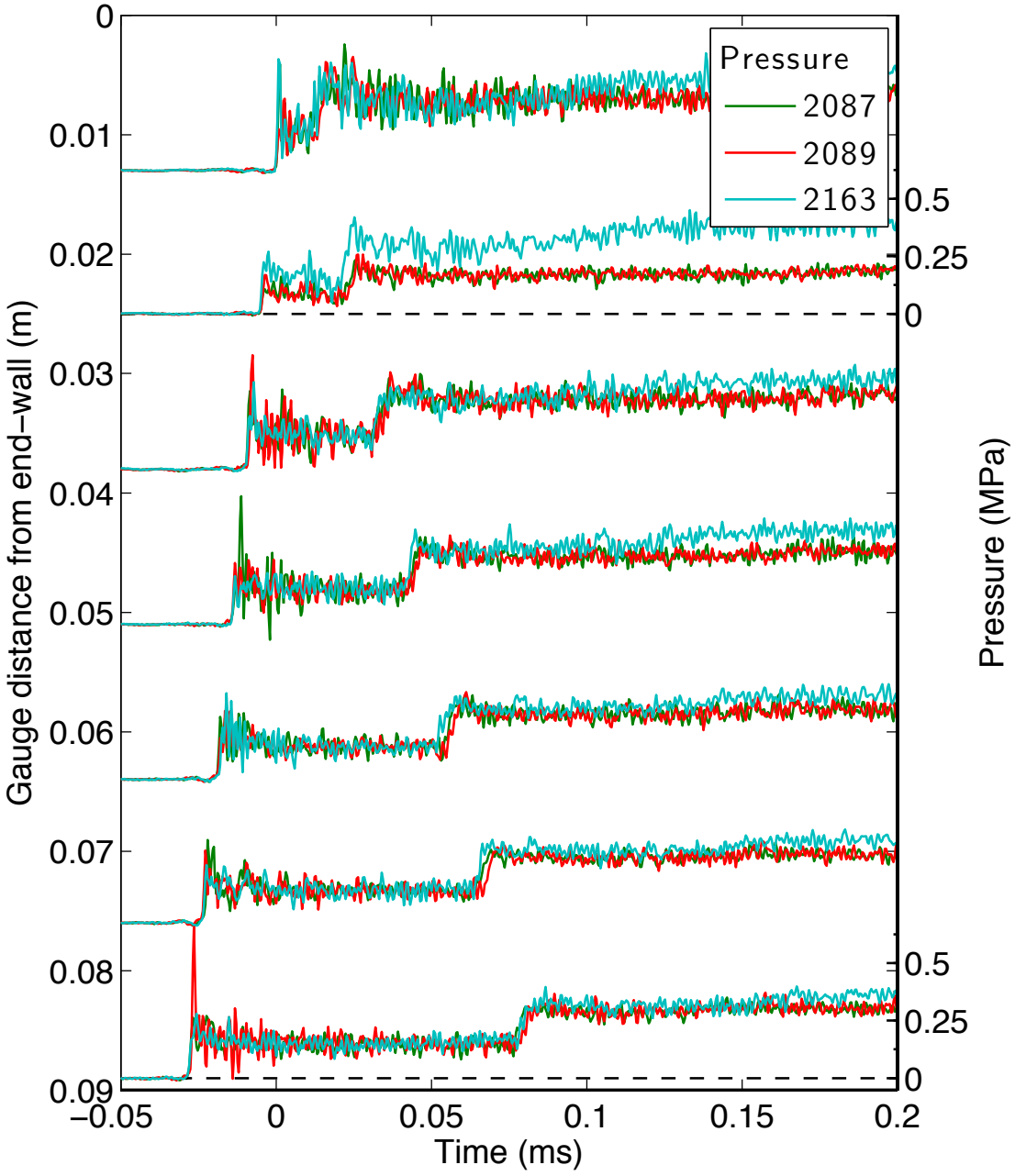

Figure E.4: Pressure traces for a detonation in stoichiometric hydrogen-oxygen at fill pressure 10 kPa, part 1.

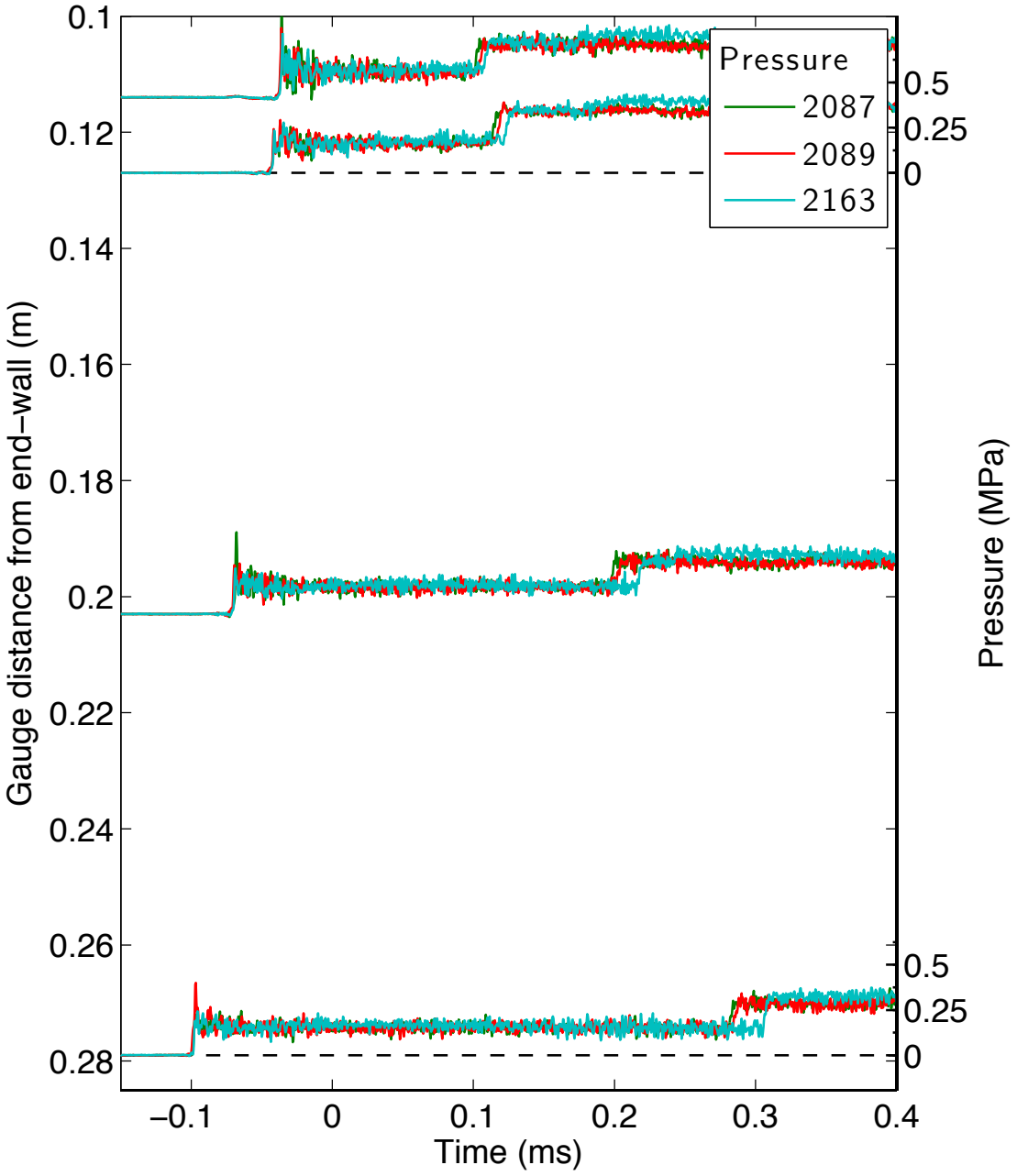

Figure E.5: Pressure traces for a detonation in stoichiometric hydrogen-oxygen at fill pressure 10 kPa, part 2.

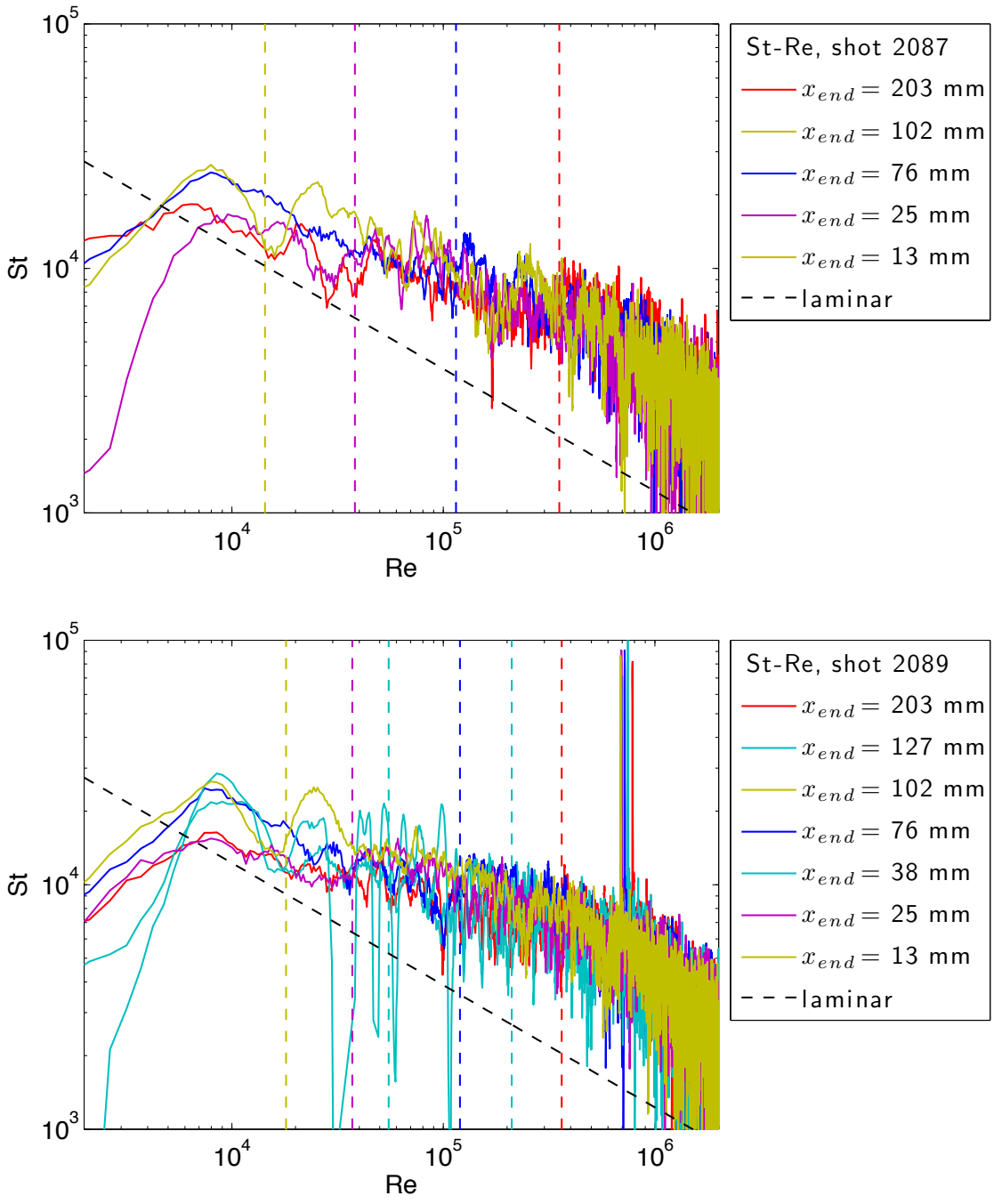

Figure E.6: Stanton-Reynolds number traces from shot 2089, a detonation in stoichiometric hydrogen-oxygen at fill pressure 10 kPa. The dashed vertical lines represent the arrival of the reflected shock wave.

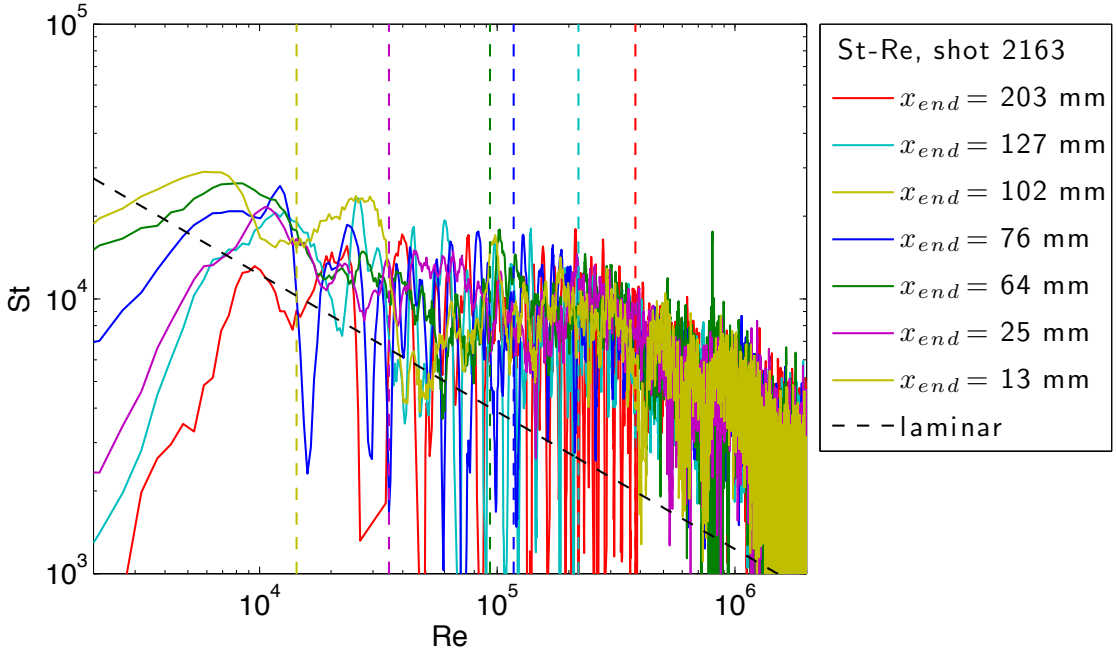

Figure E.7: Stanton-Reynolds number traces from shot 2163, a detonation in stoichiometric hydrogen-oxygen at fill pressure 10 kPa. The dashed vertical lines represent the arrival of the reflected shock wave.

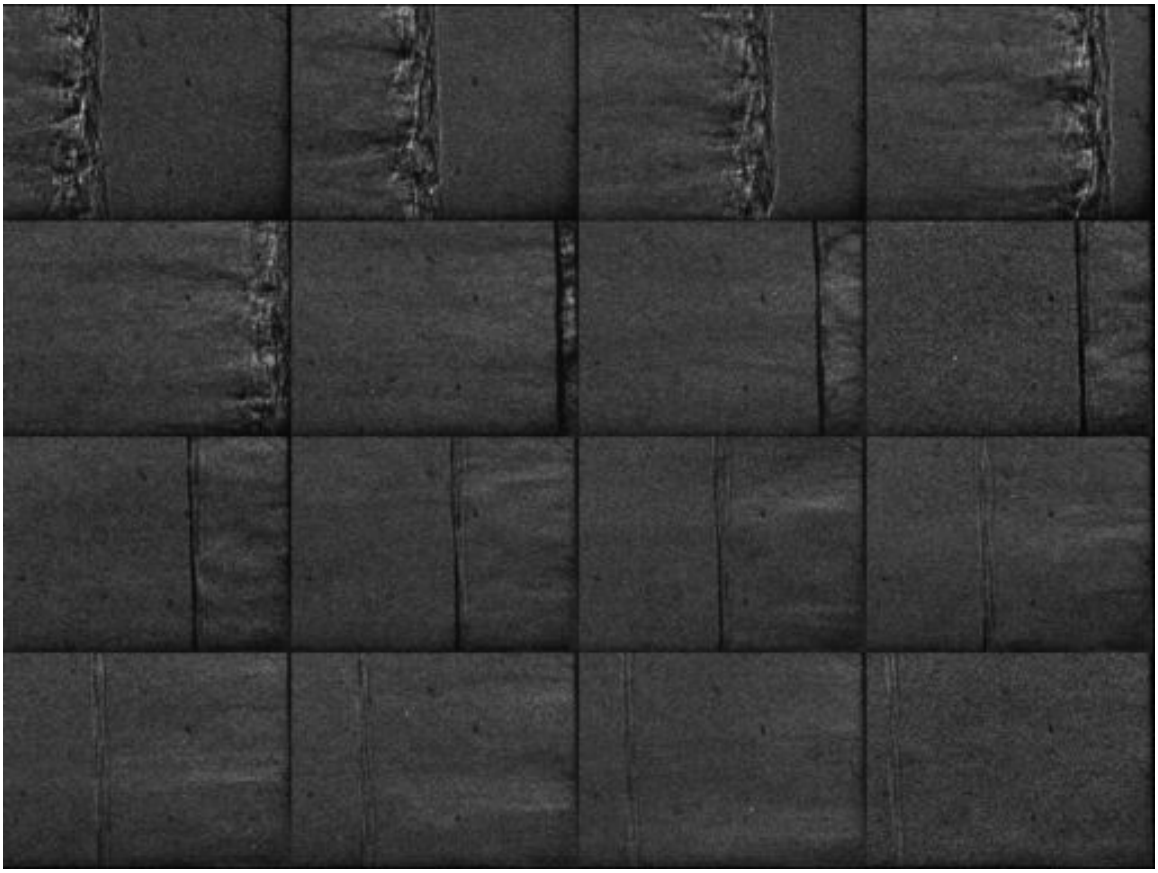

Figure E.8: Unfocused schlieren image of shot 2163. The field of view is approximately 30 mm wide.

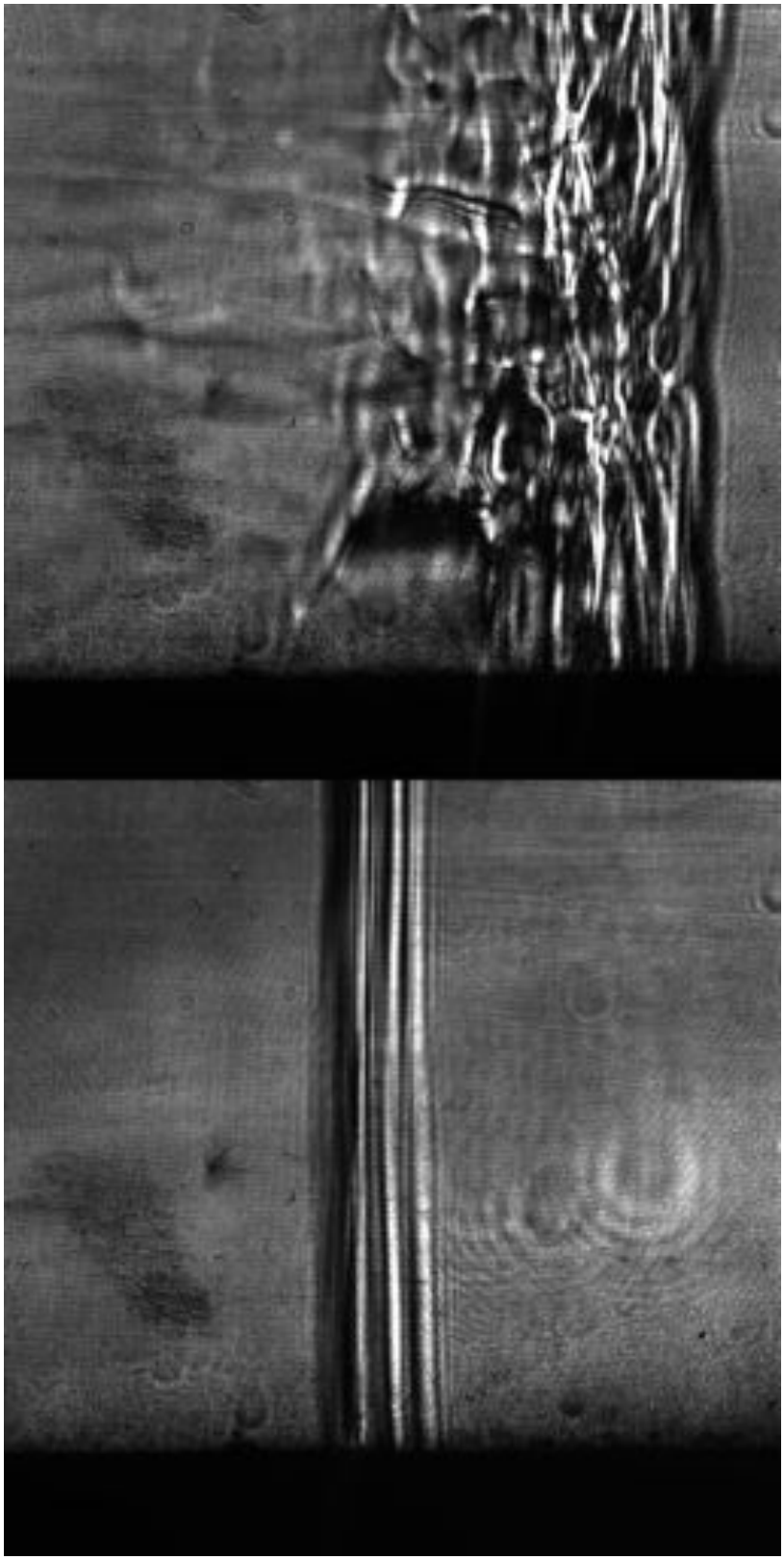

Figure E.9: Focused schlieren image of shot 2089. The field of view is approximately 14 mm wide.

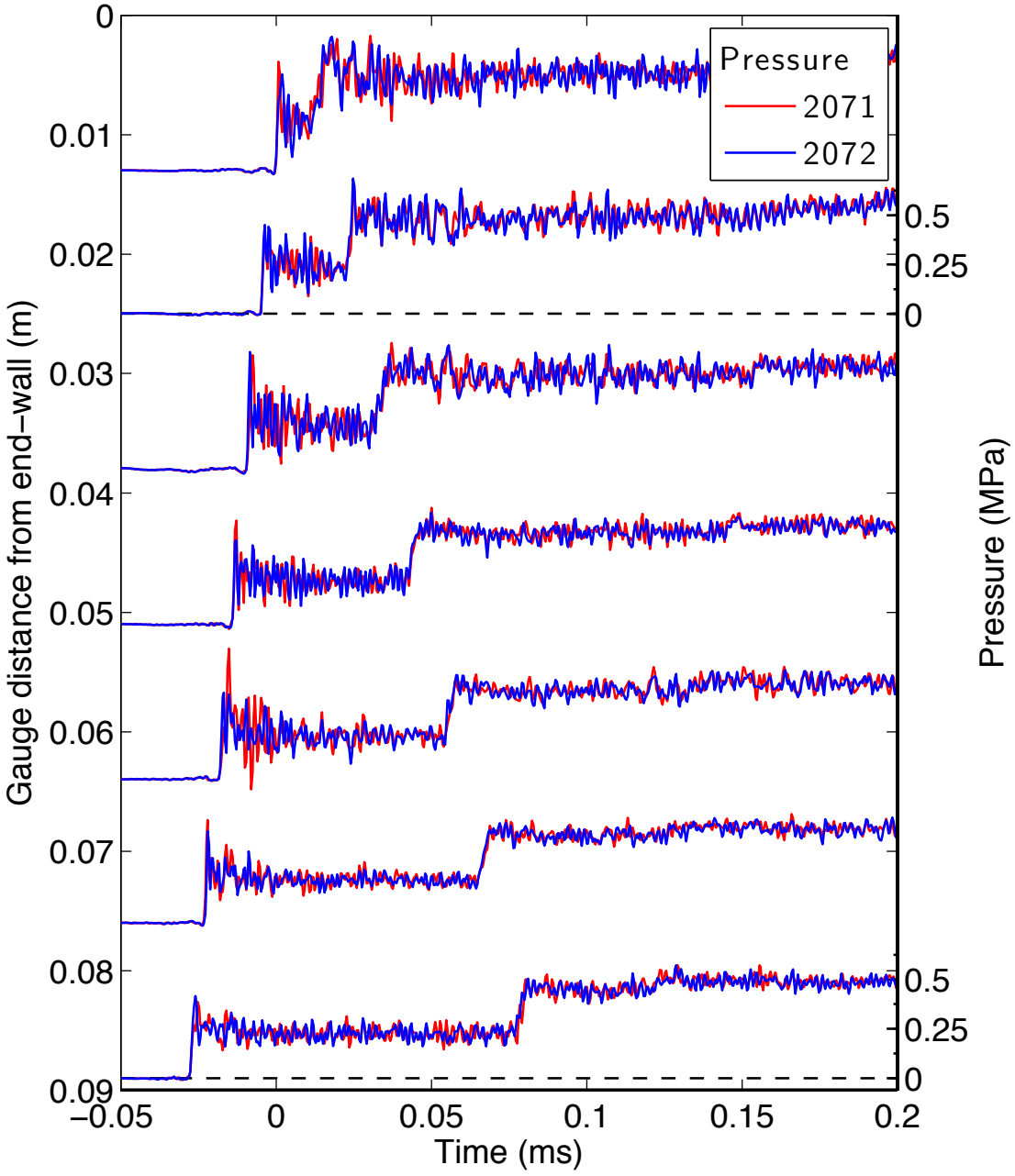

Figure E.10: Pressure traces for a detonation in stoichiometric hydrogen-oxygen at fill pressure 15 kPa, part 1.

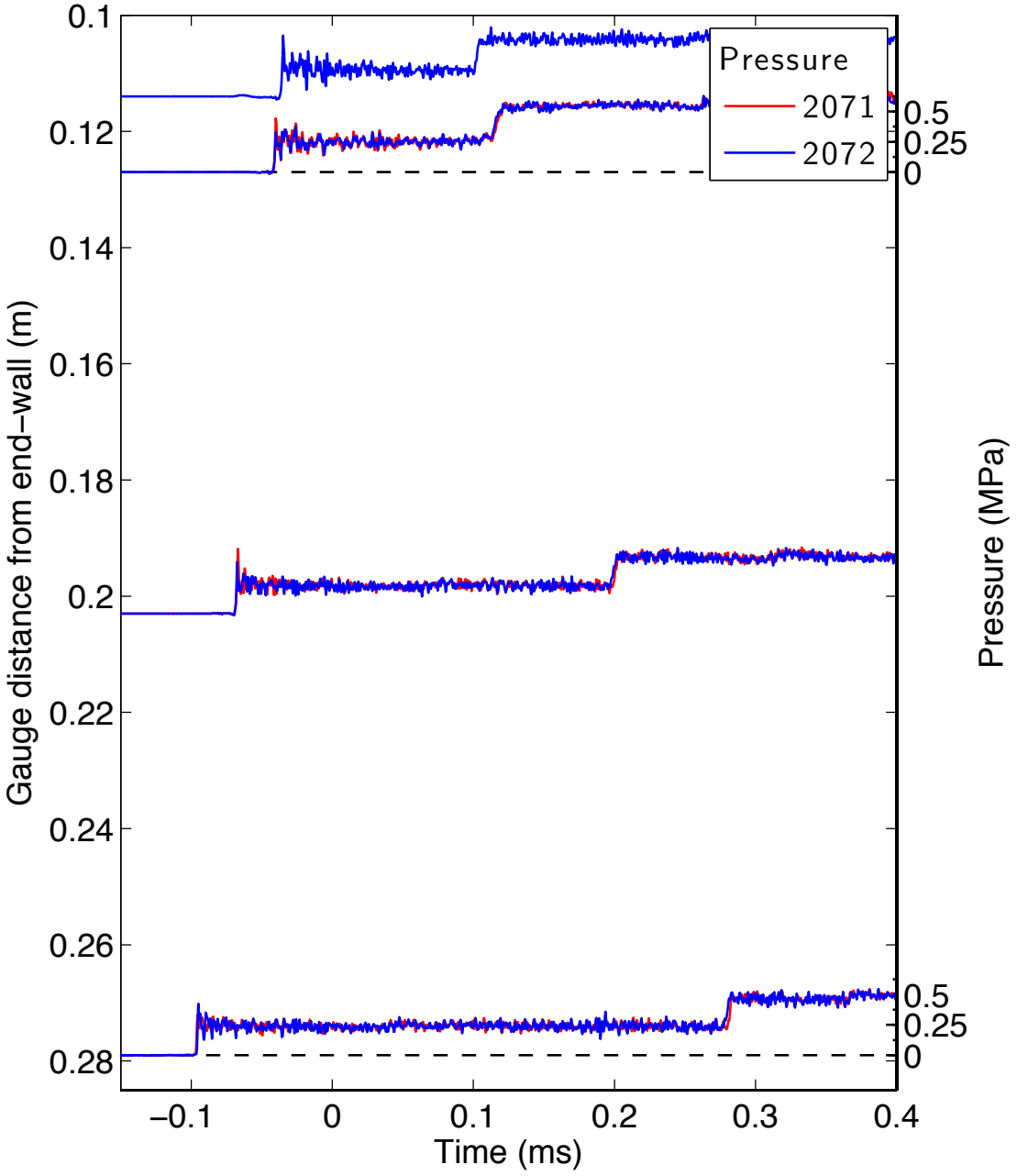

Figure E.11: Pressure traces for a detonation in stoichiometric hydrogen-oxygen at fill pressure 15 kPa, part 2.

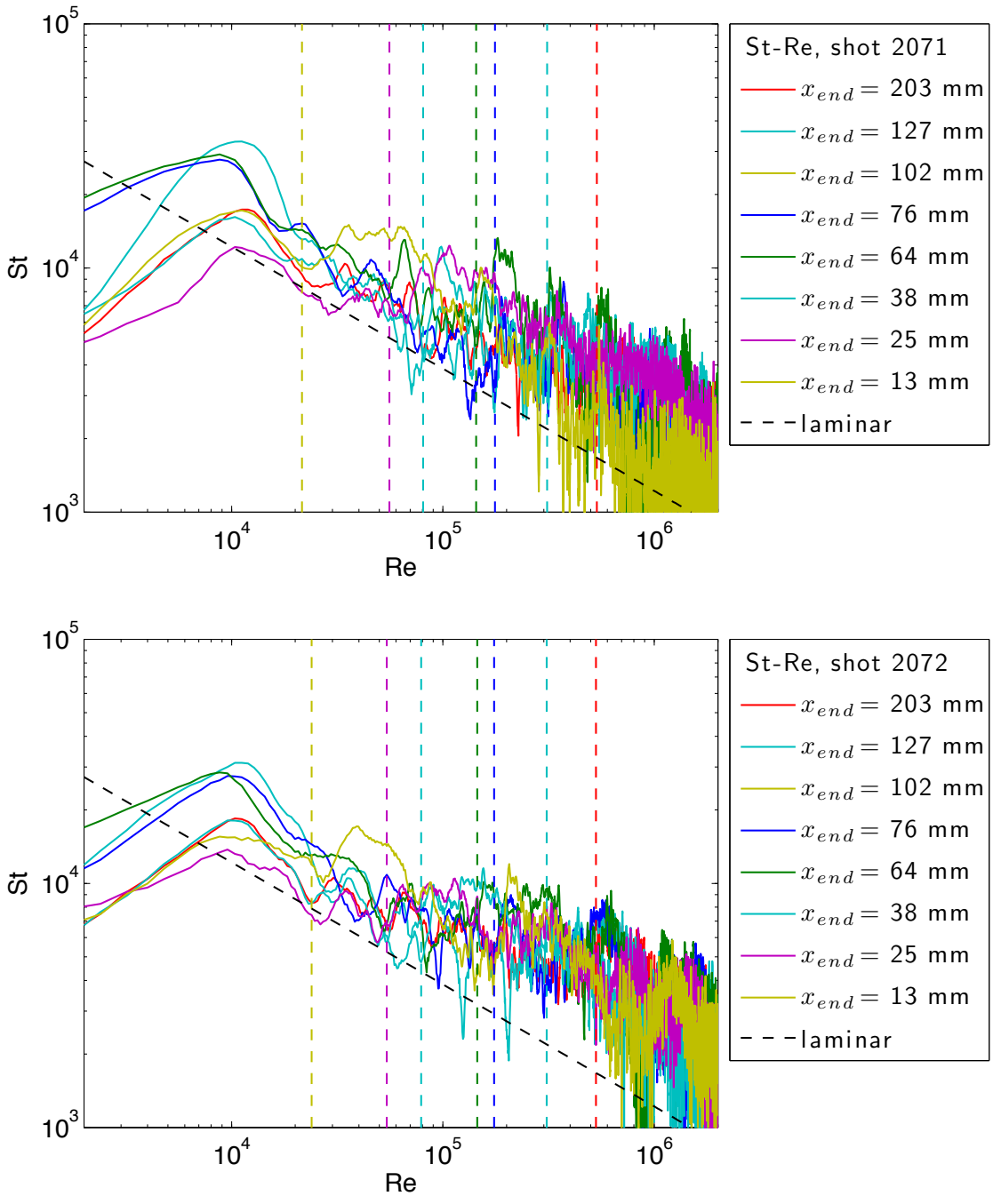

Figure E.12: Stanton-Reynolds number traces from shot 2072, a detonation in stoichiometric hydrogen-oxygen at fill pressure 15 kPa. The dashed vertical lines represent the arrival of the reflected shock wave.

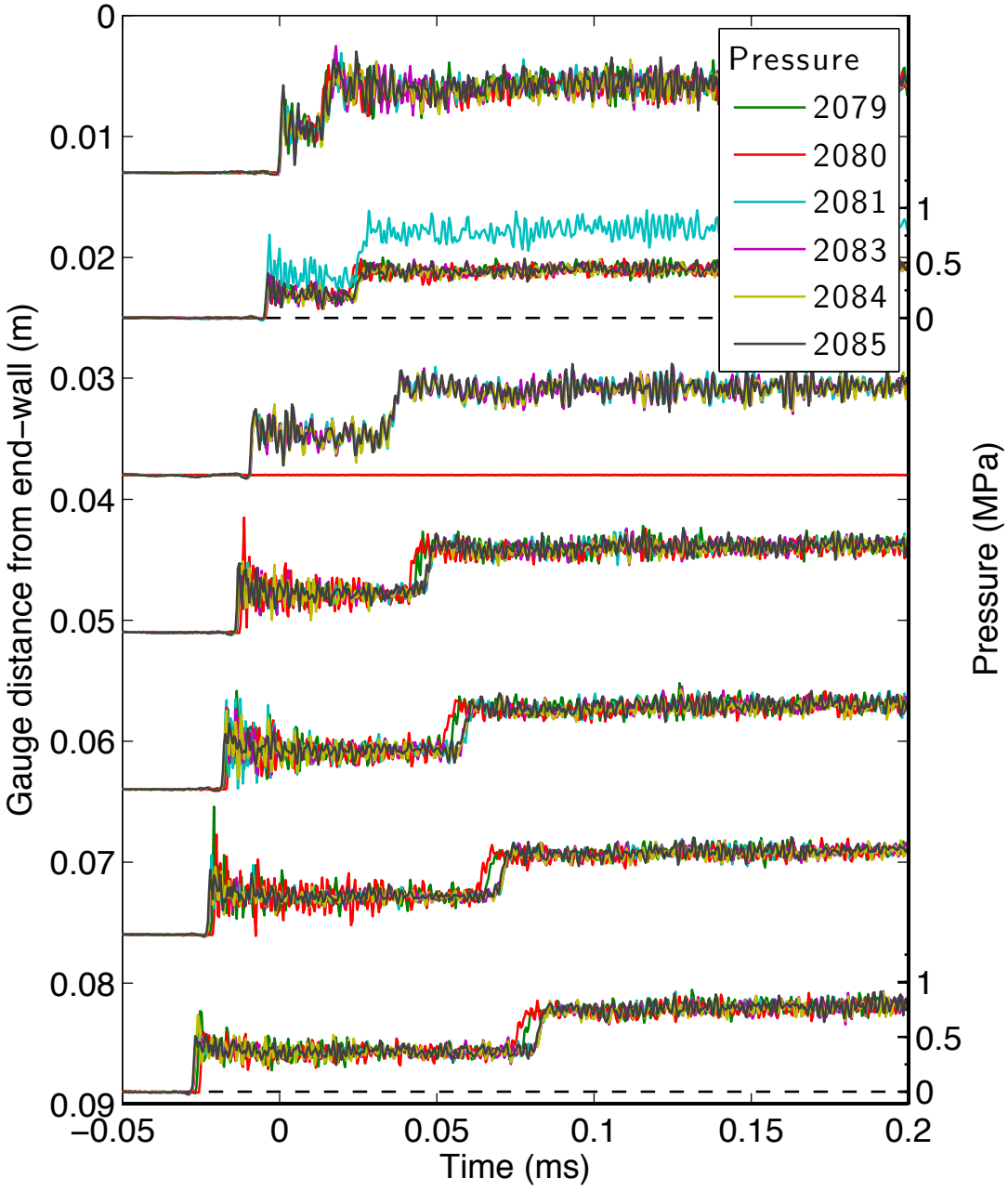

Figure E.13: Pressure traces for a detonation in stoichiometric hydrogen-oxygen at fill pressure 25 kPa, part 1.

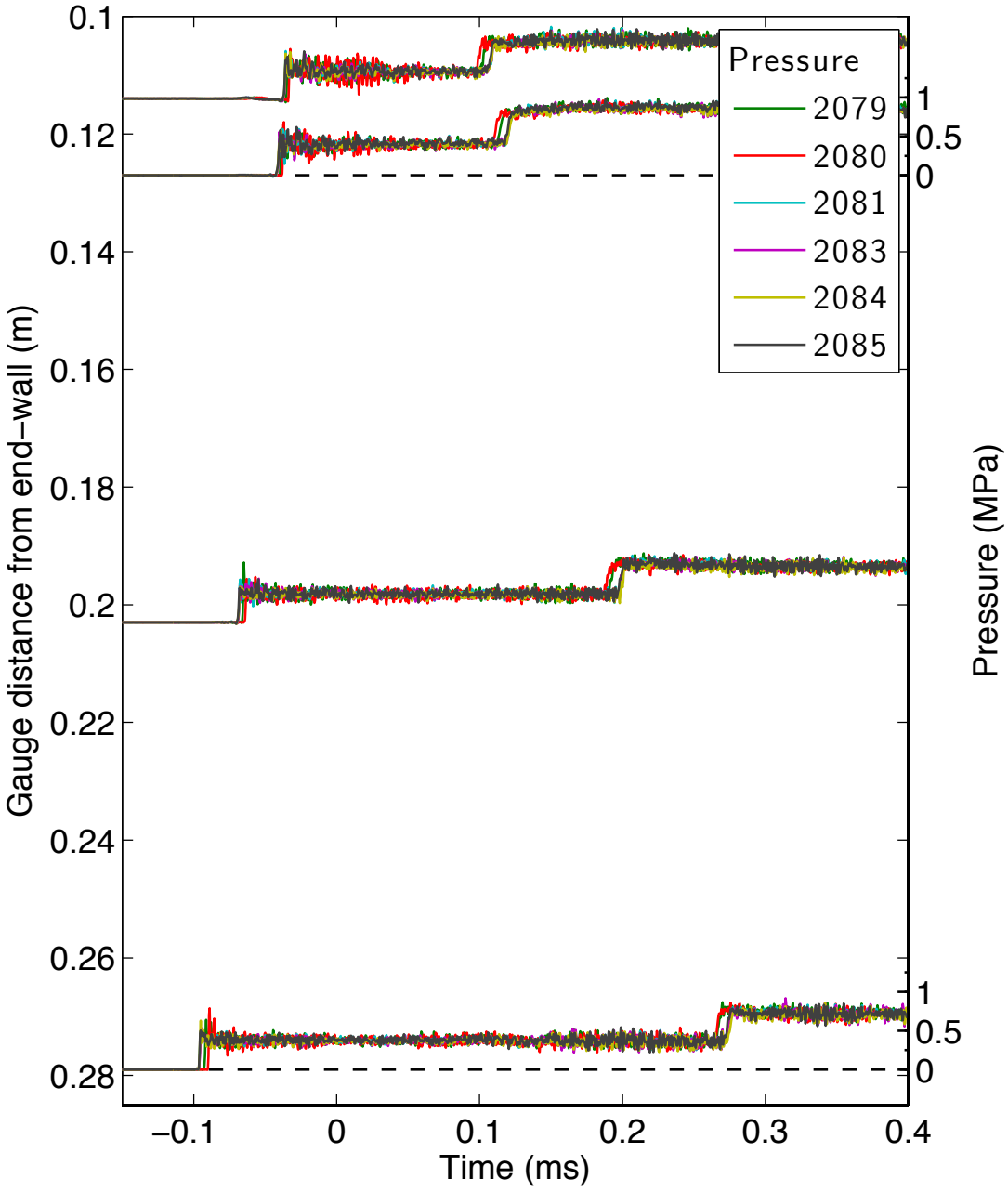

Figure E.14: Pressure traces for a detonation in stoichiometric hydrogen-oxygen at fill pressure 25 kPa, part 2.

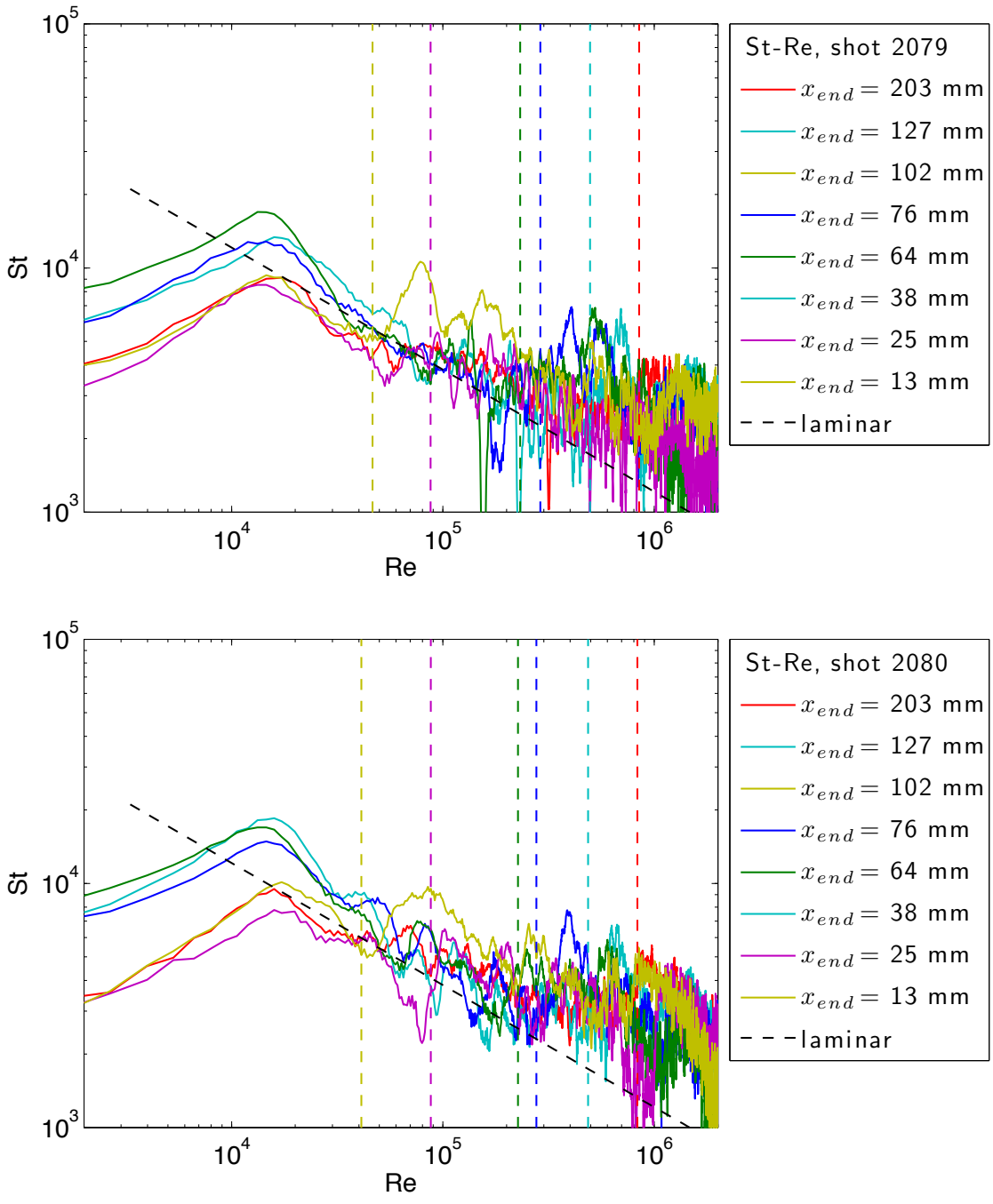

Figure E.15: Stanton-Reynolds number traces from shot 2080, a detonation in stoichiometric hydrogen-oxygen at fill pressure 25 kPa. The dashed vertical lines represent the arrival of the reflected shock wave.

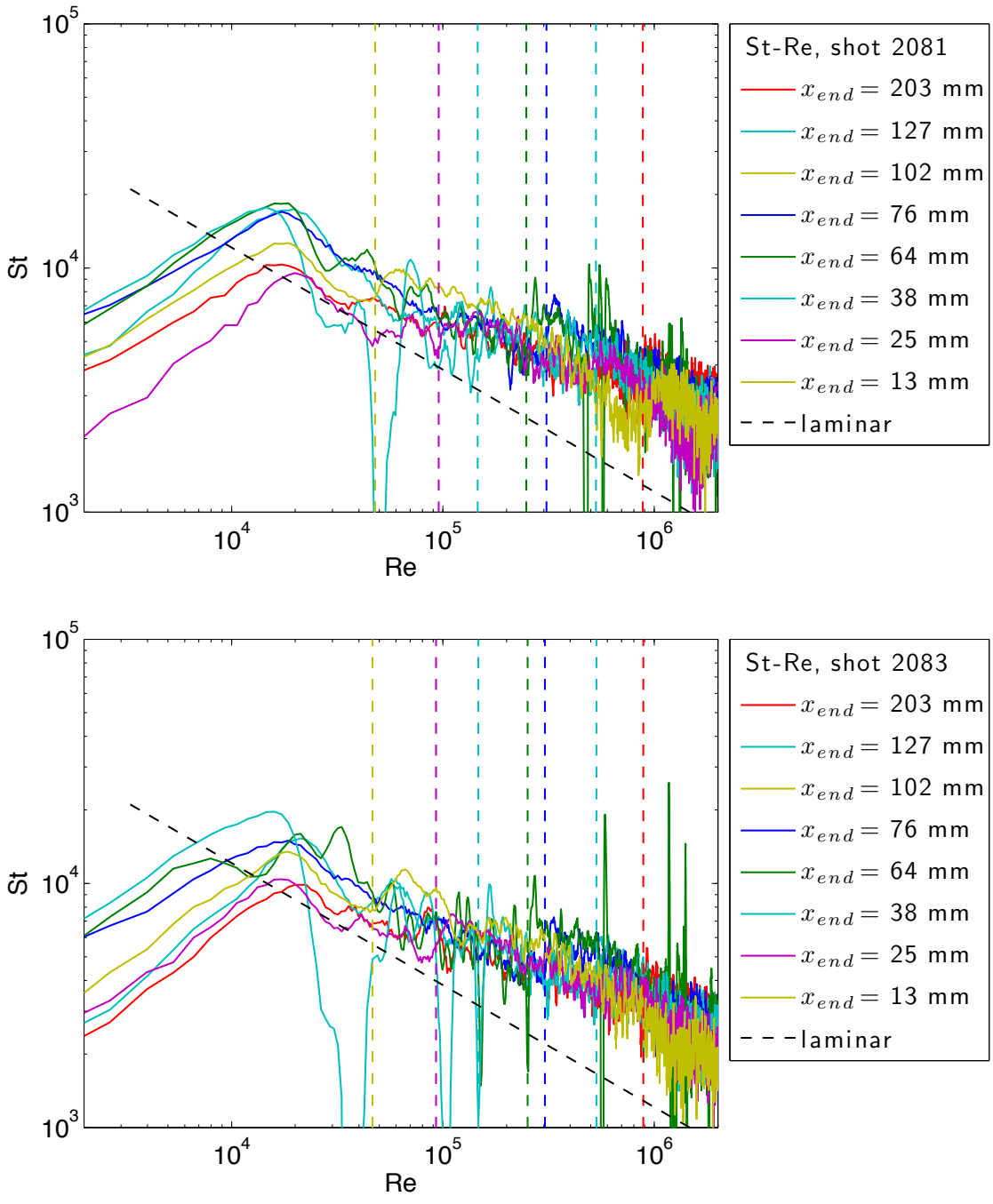

Figure E.16: Stanton-Reynolds number traces from shot 2083, a detonation in stoichiometric hydrogen-oxygen at fill pressure 25 kPa. The dashed vertical lines represent the arrival of the reflected shock wave.

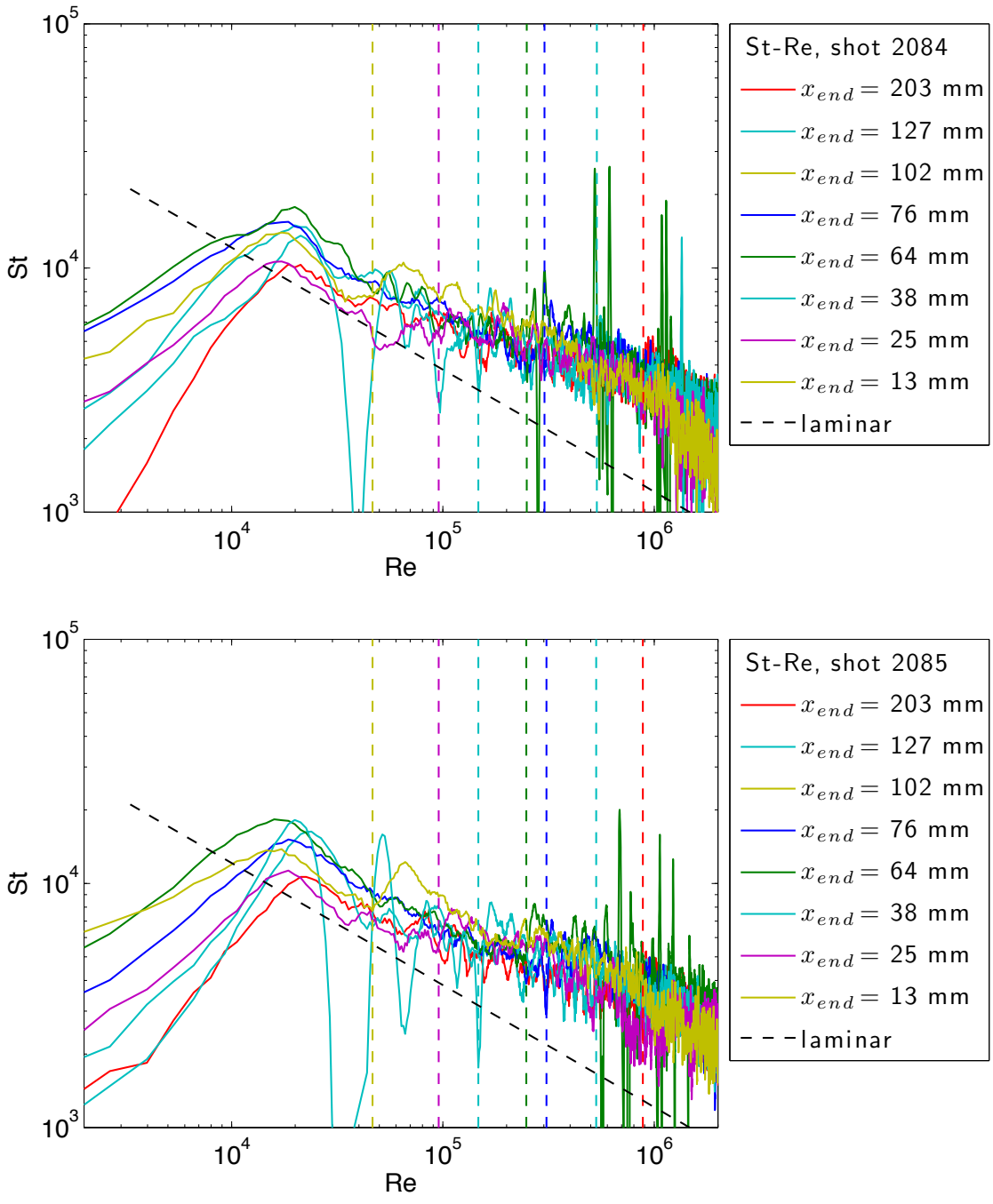

Figure E.17: Stanton-Reynolds number traces from shot 2085, a detonation in stoichiometric hydrogen-oxygen at fill pressure 25 kPa. The dashed vertical lines represent the arrival of the reflected shock wave.

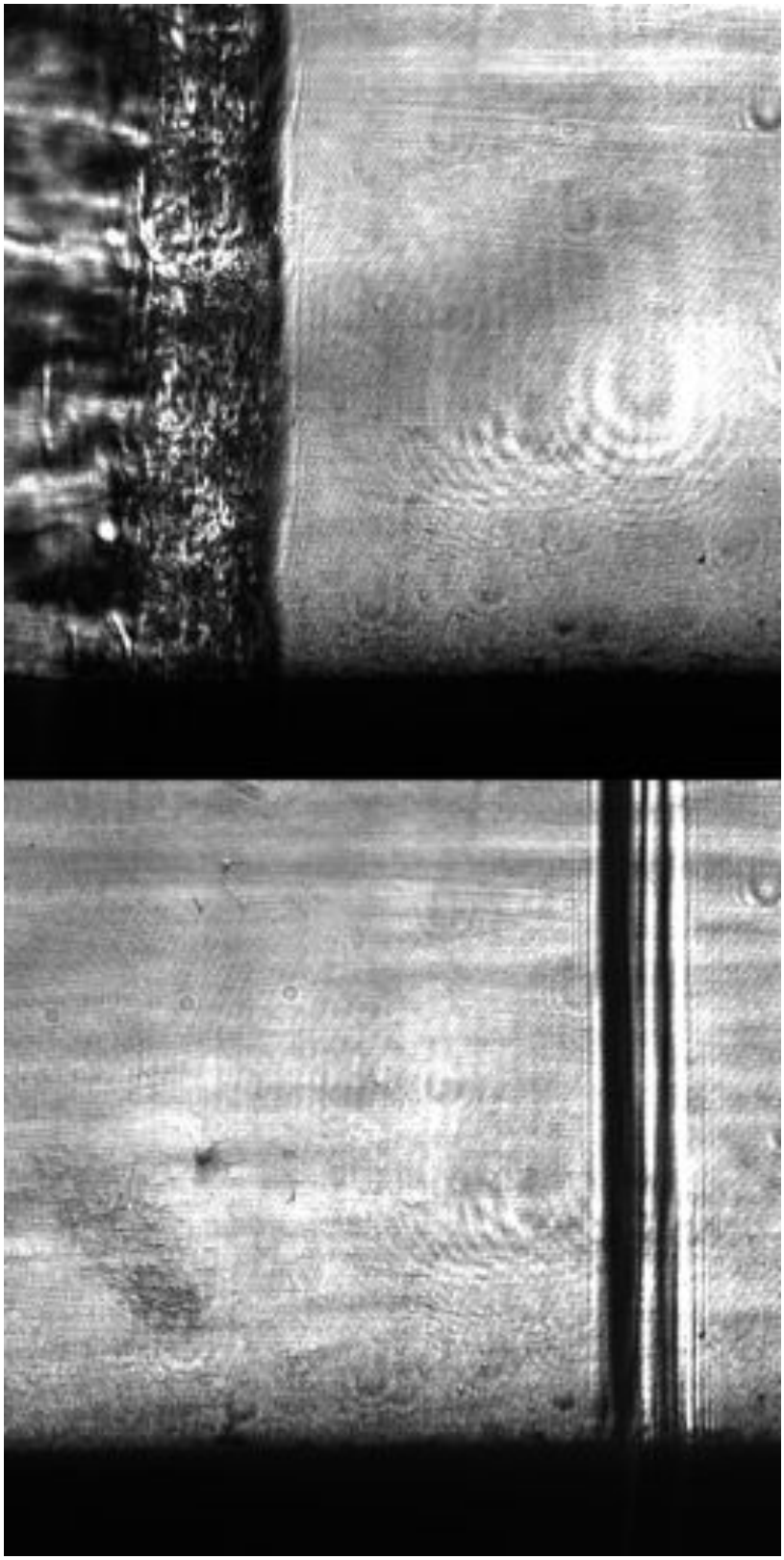

Figure E.18: Focused schlieren image of shot 2084. The field of view is approximately 14 mm wide.

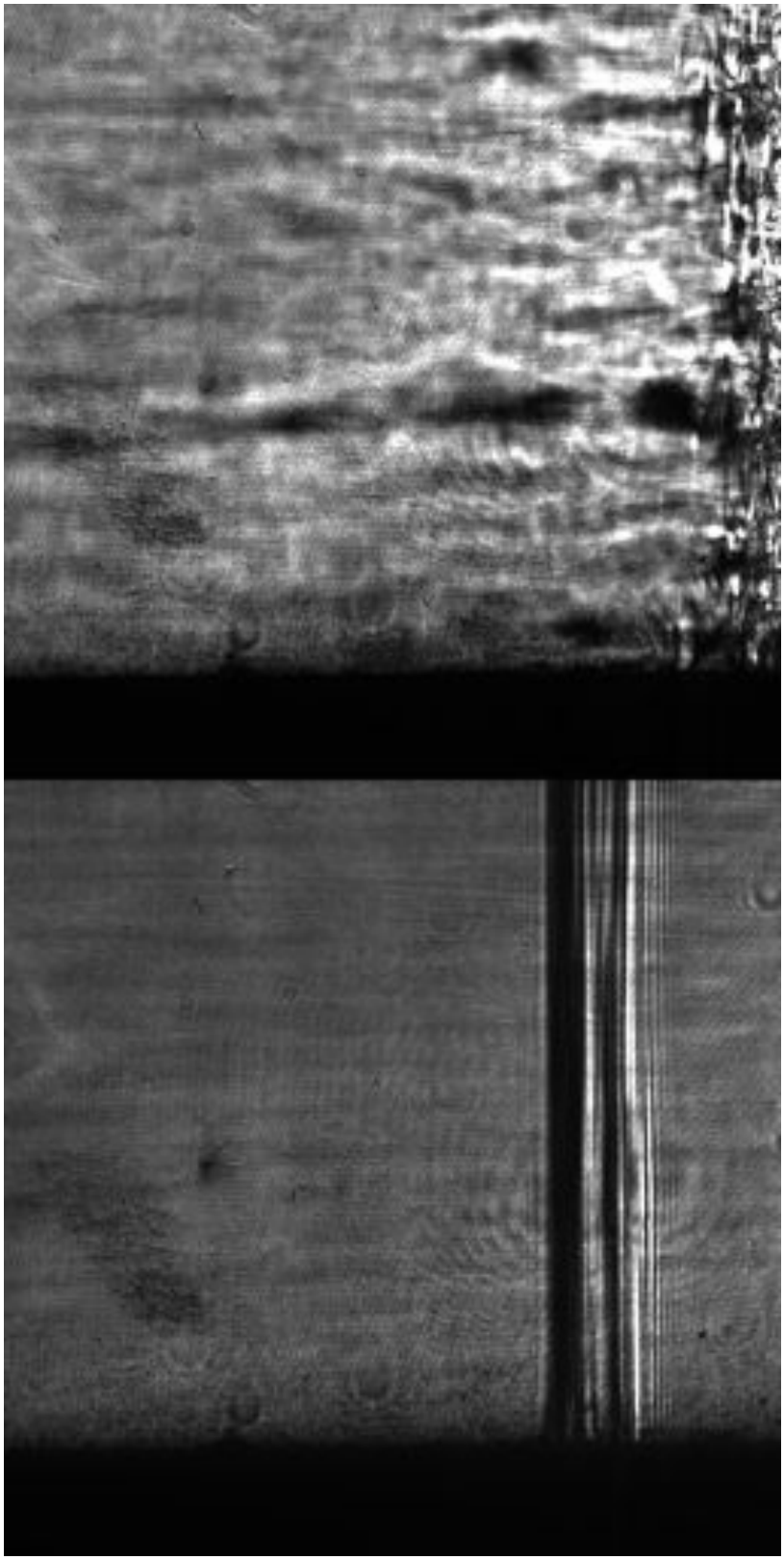

Figure E.19: Focused schlieren image of shot 2085. The field of view is approximately 14 mm wide.

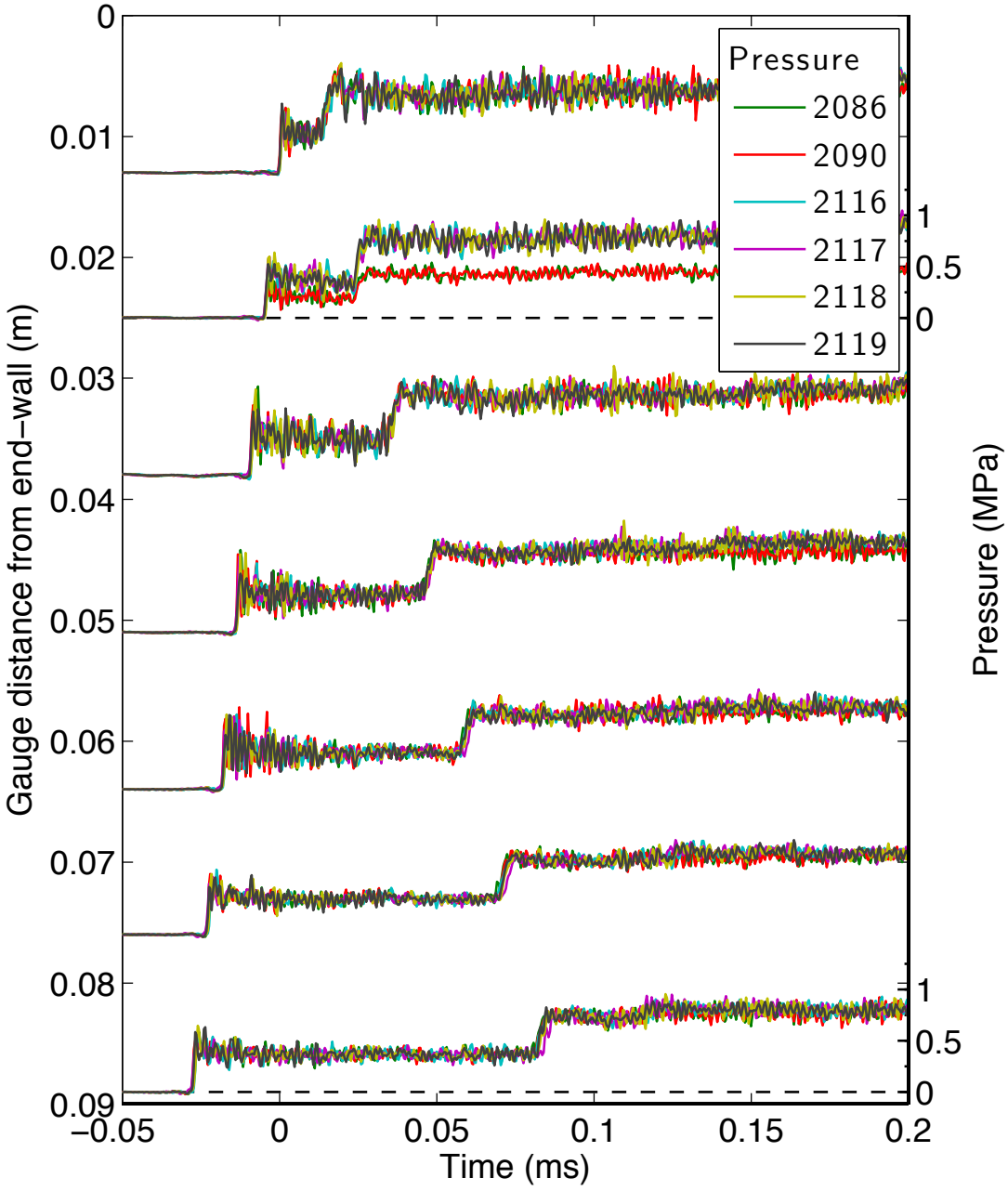

Figure E.20: Pressure traces for a detonation in stoichiometric hydrogen-oxygen at fill pressure 25 kPa, part 3.

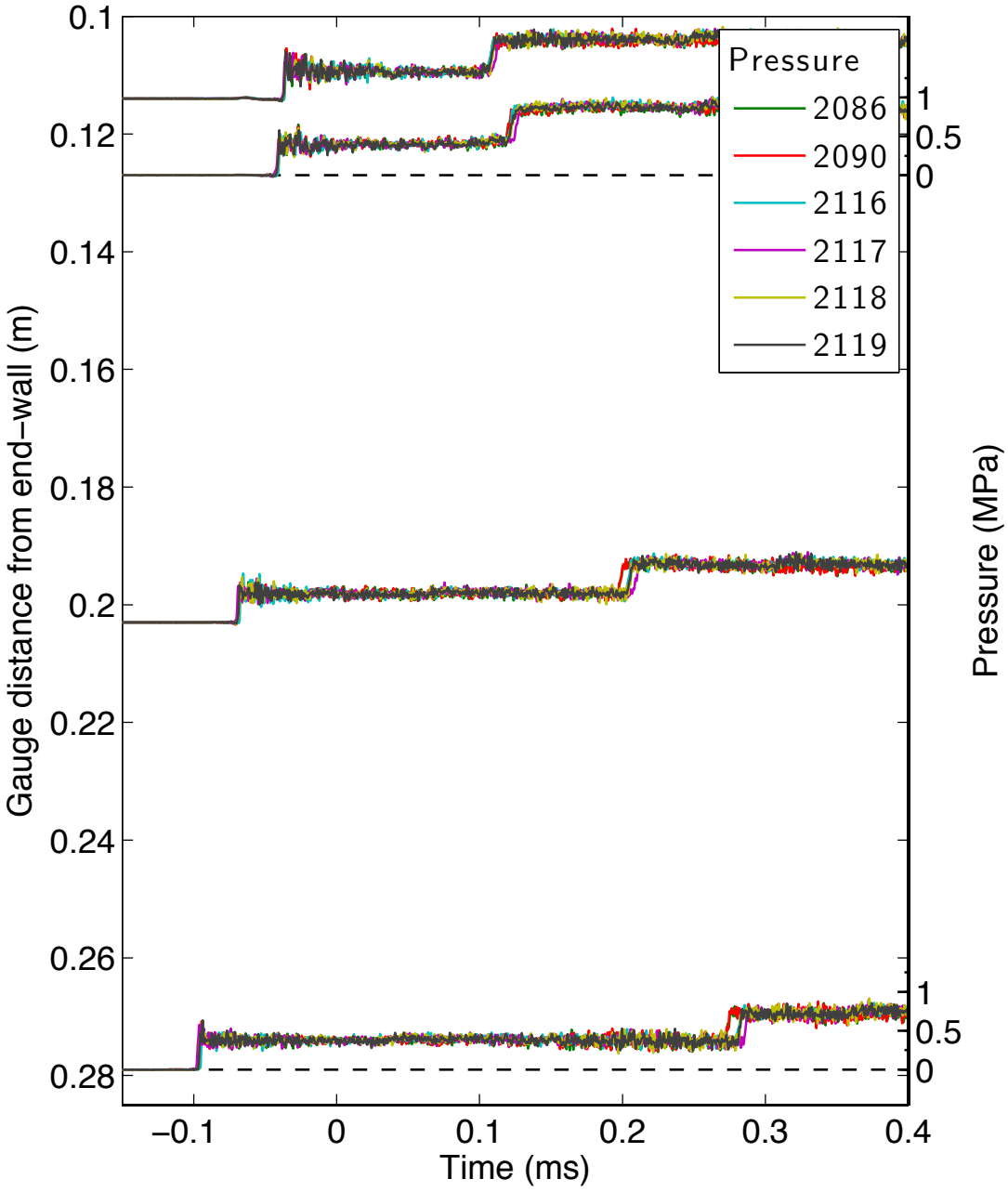

Figure E.21: Pressure traces for a detonation in stoichiometric hydrogen-oxygen at fill pressure 25 kPa, part 4.

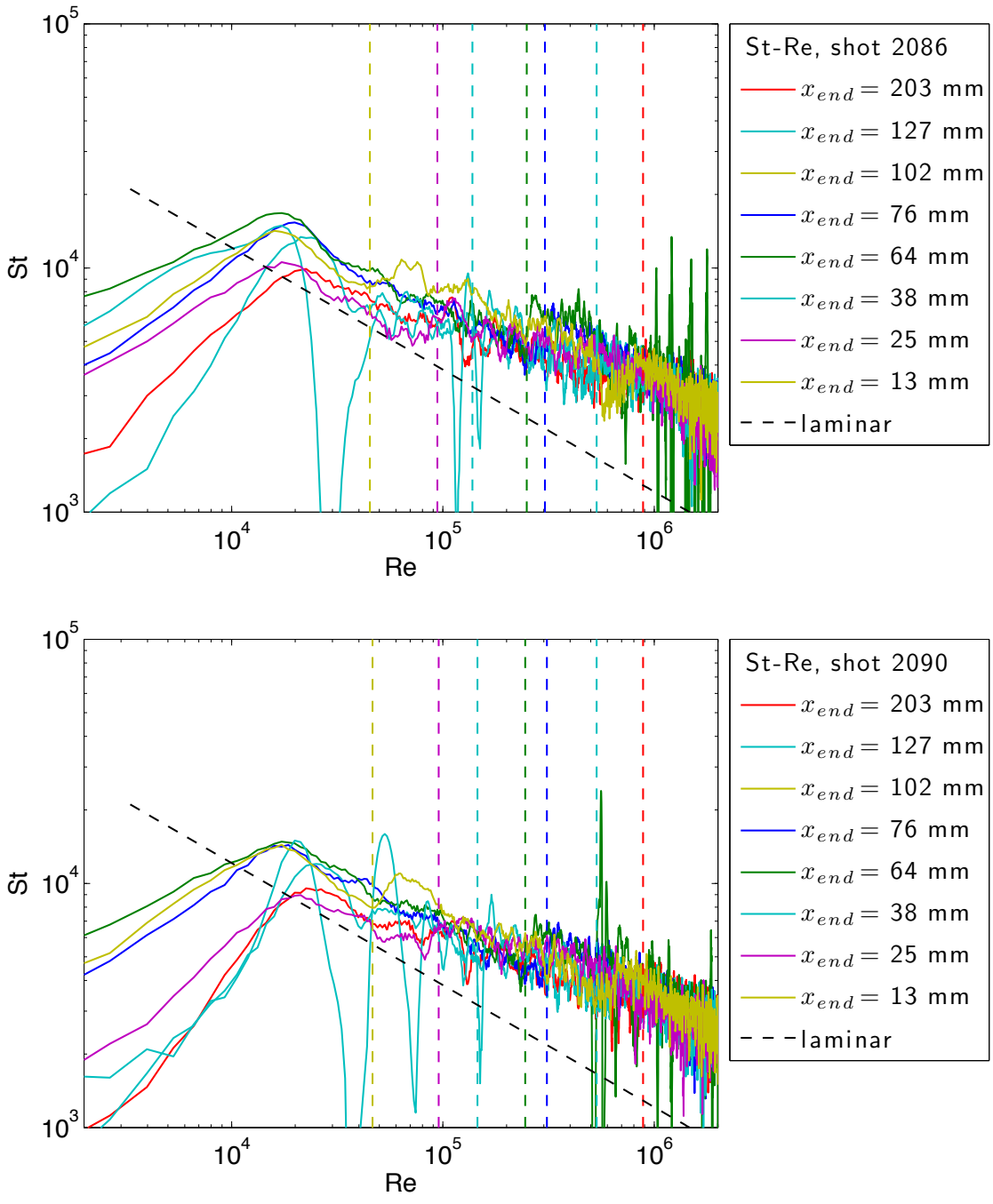

Figure E.22: Stanton-Reynolds number traces from shot 2090, a detonation in stoichiometric hydrogen-oxygen at fill pressure 25 kPa. The dashed vertical lines represent the arrival of the reflected shock wave.

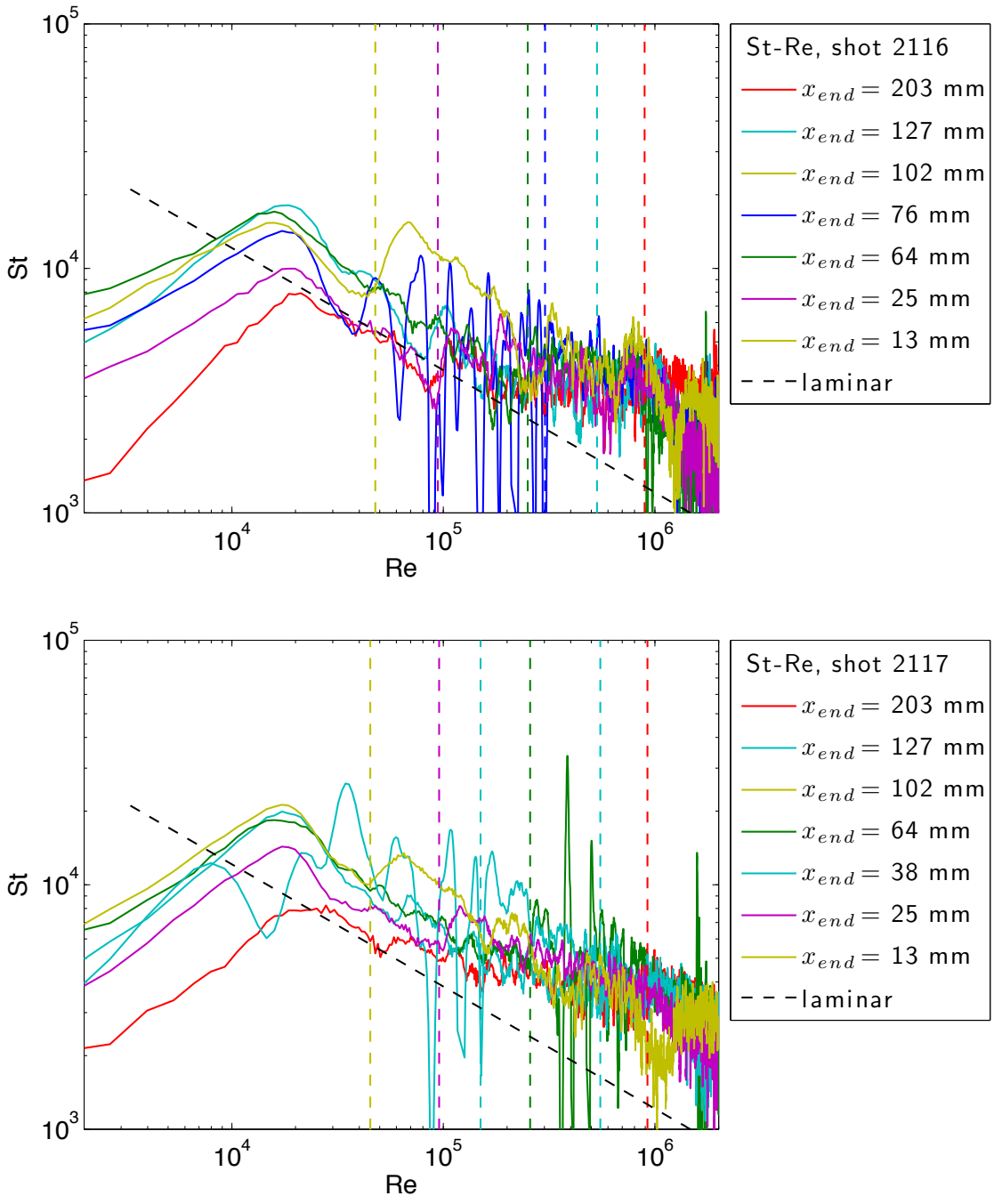

Figure E.23: Stanton-Reynolds number traces from shot 2117, a detonation in stoichiometric hydrogen-oxygen at fill pressure 25 kPa. The dashed vertical lines represent the arrival of the reflected shock wave.

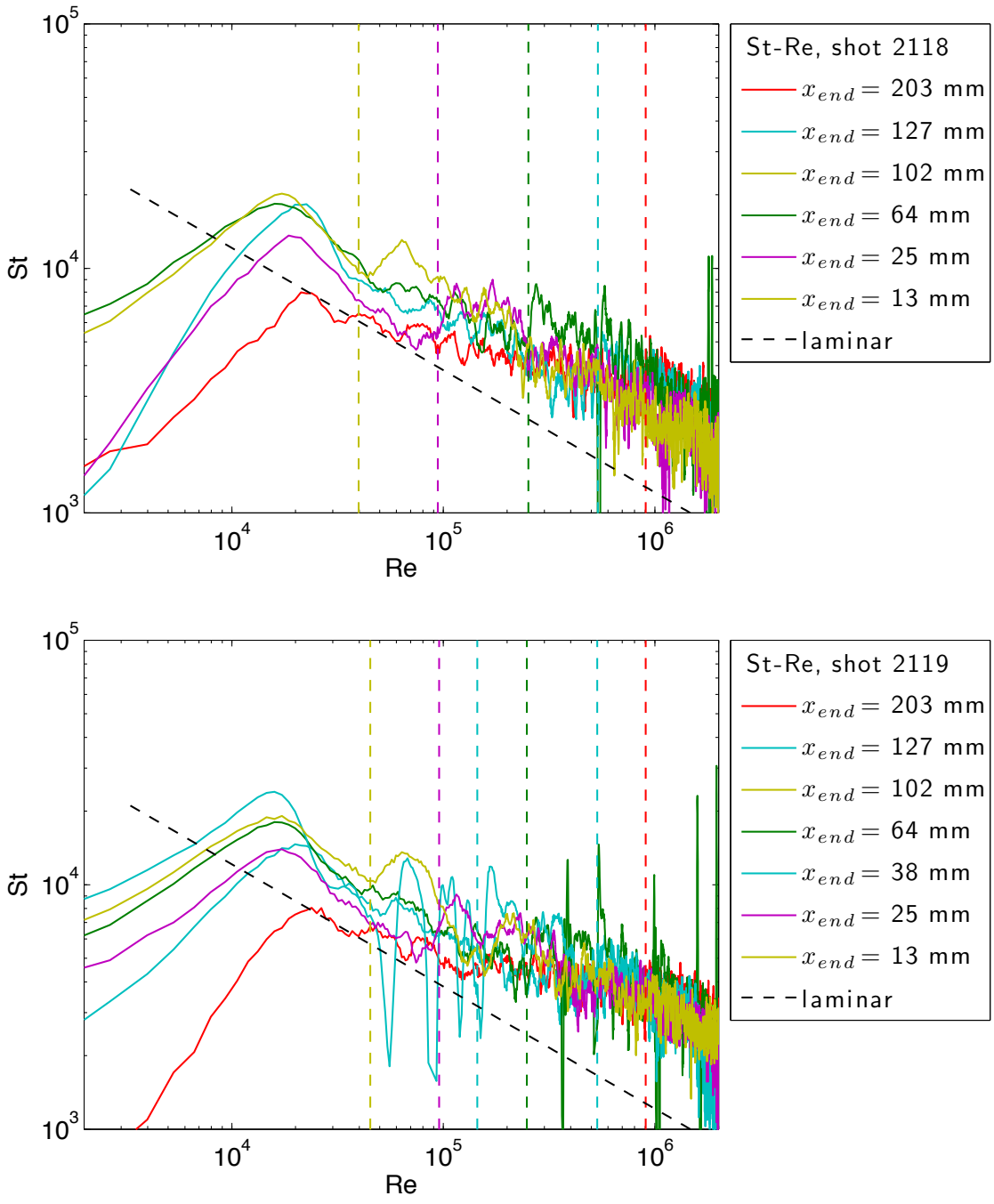

Figure E.24: Stanton-Reynolds number traces from shot 2119, a detonation in stoichiometric hydrogen-oxygen at fill pressure 25 kPa. The dashed vertical lines represent the arrival of the reflected shock wave.

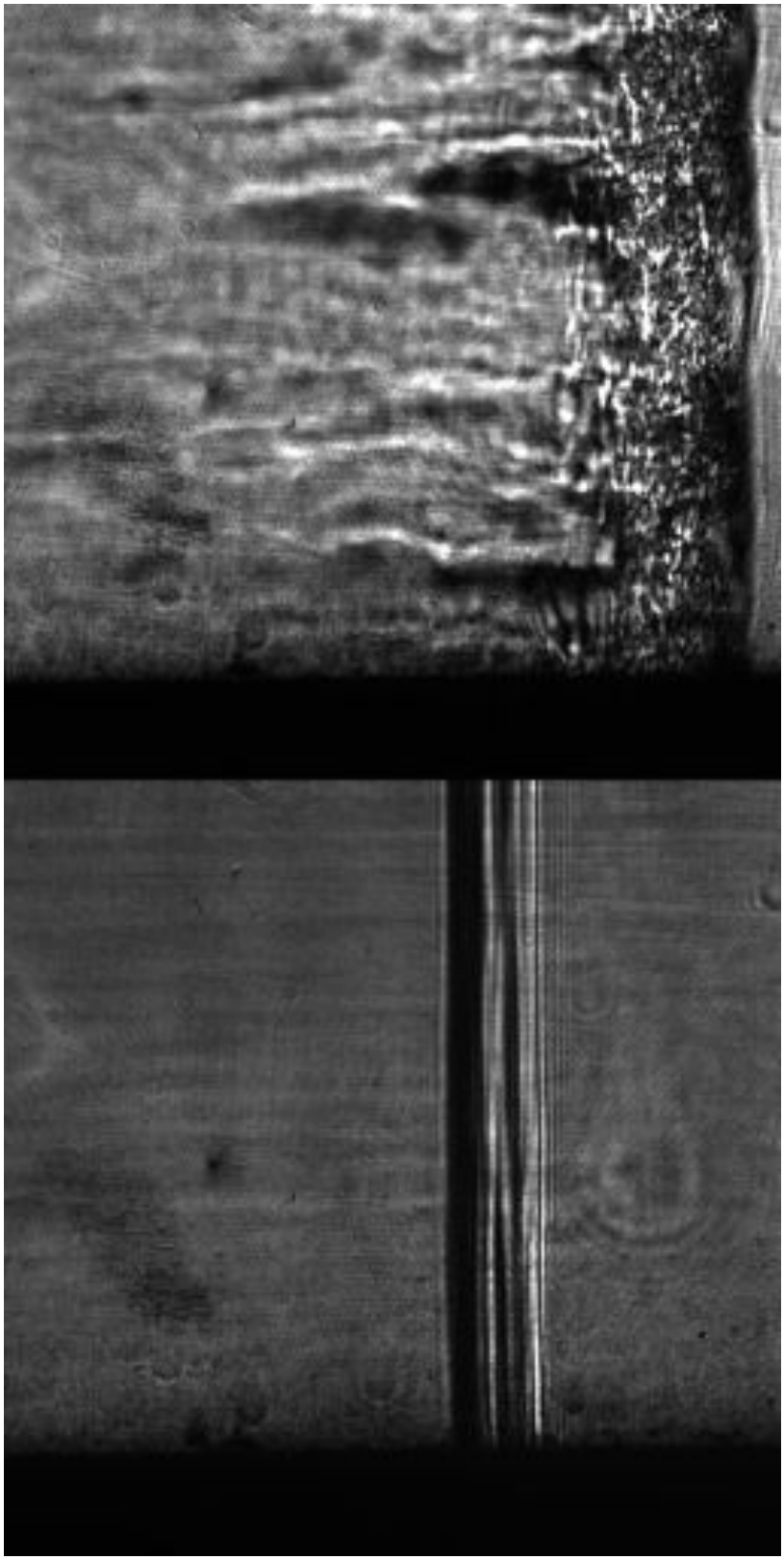

Figure E.25: Focused schlieren image of shot 2090. The field of view is approximately 14 mm wide.

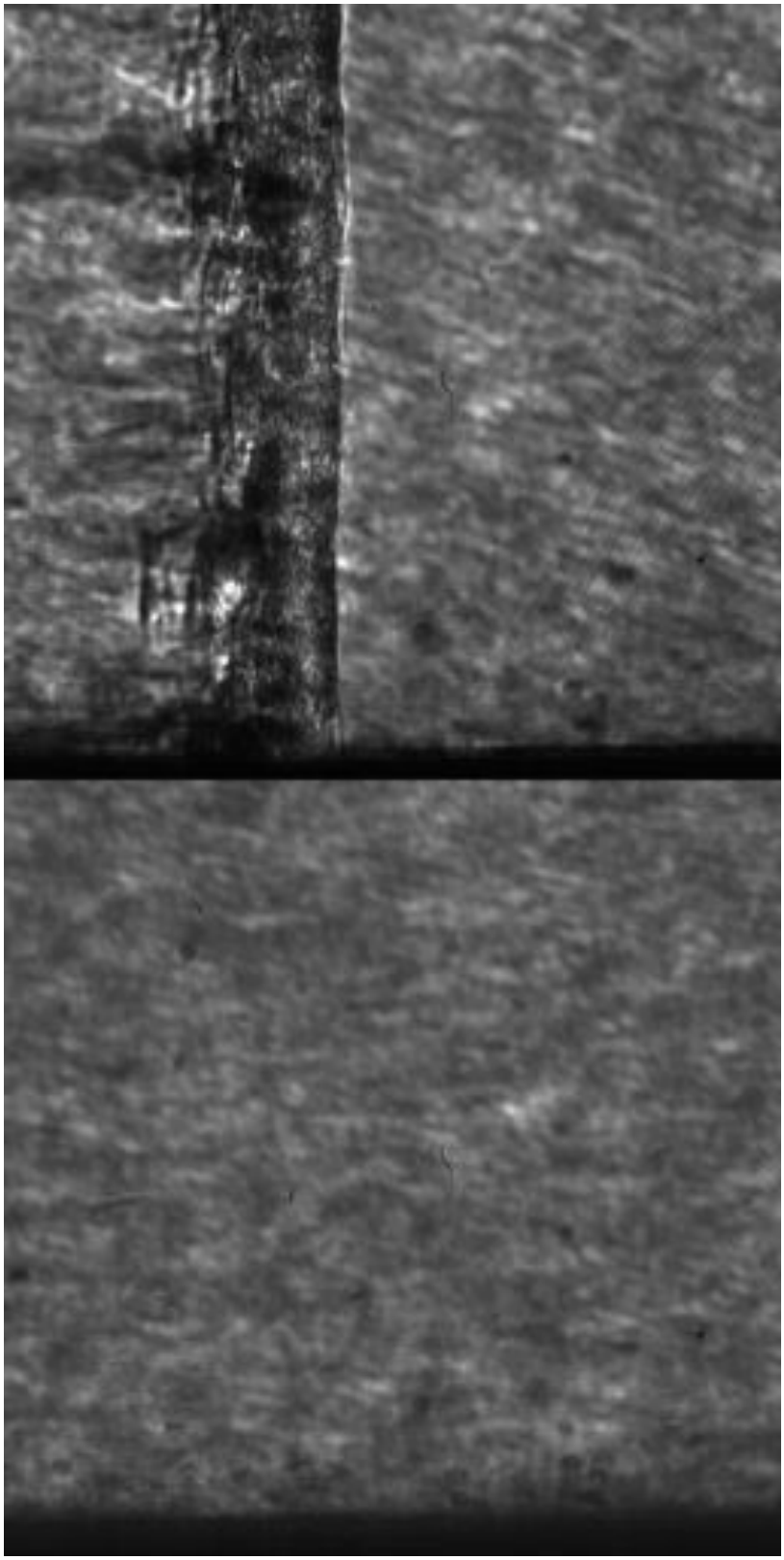

Figure E.26: Focused schlieren image of shot 2117. The field of view is approximately 14 mm wide.

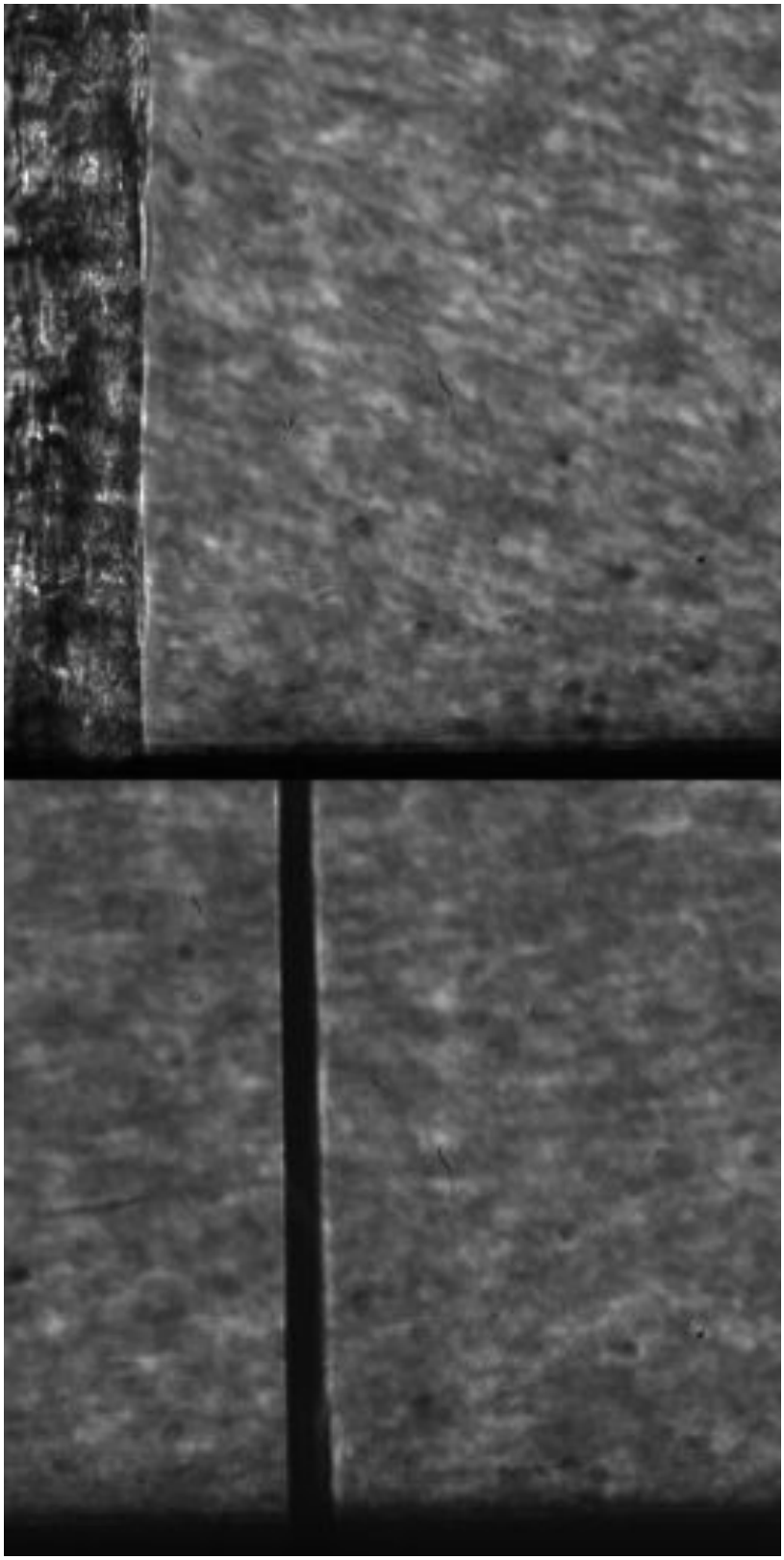

Figure E.27: Focused schlieren image of shot 2119. The field of view is approximately 14 mm wide.

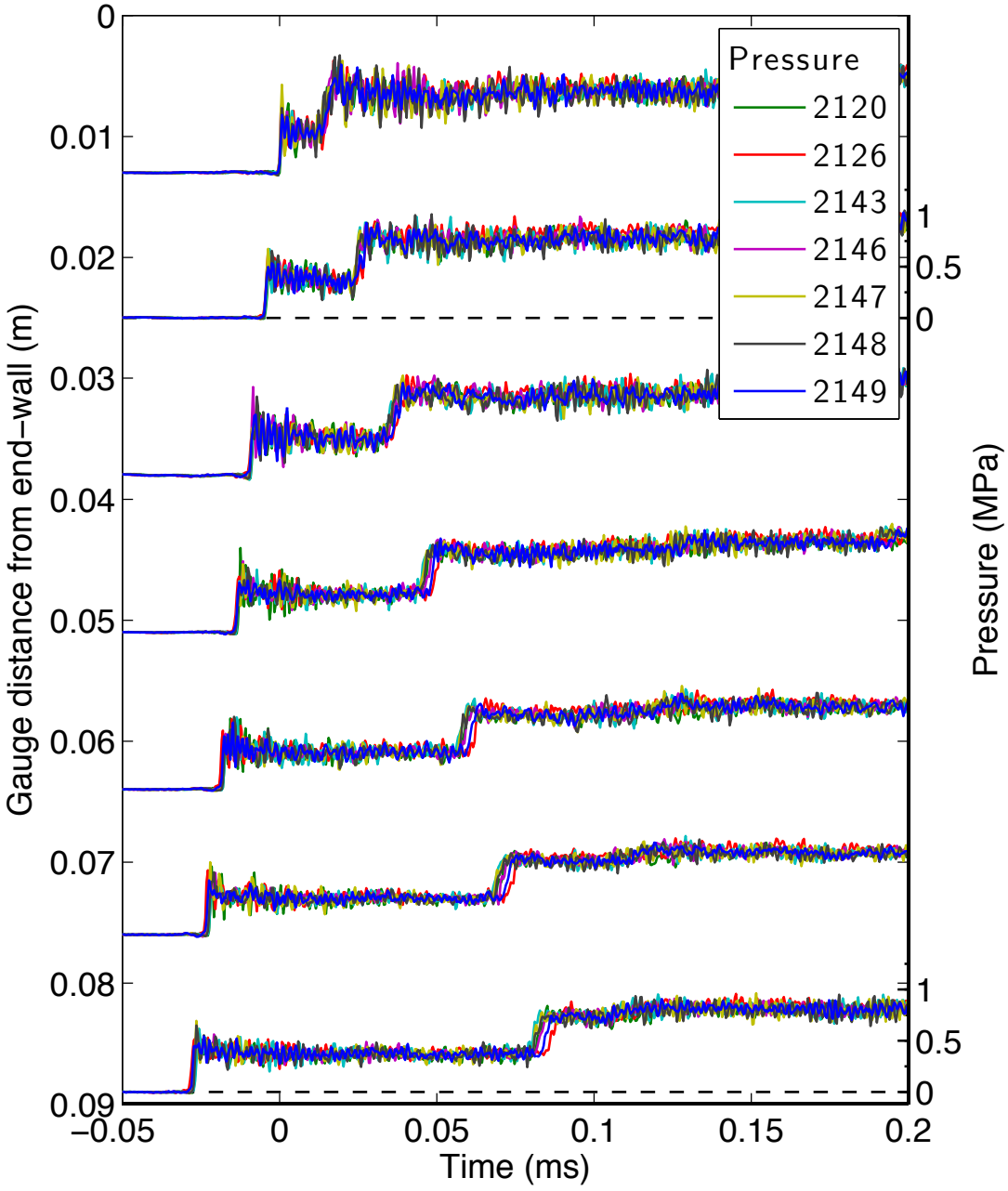

Figure E.28: Pressure traces for a detonation in stoichiometric hydrogen-oxygen at fill pressure 25 kPa, part 5.

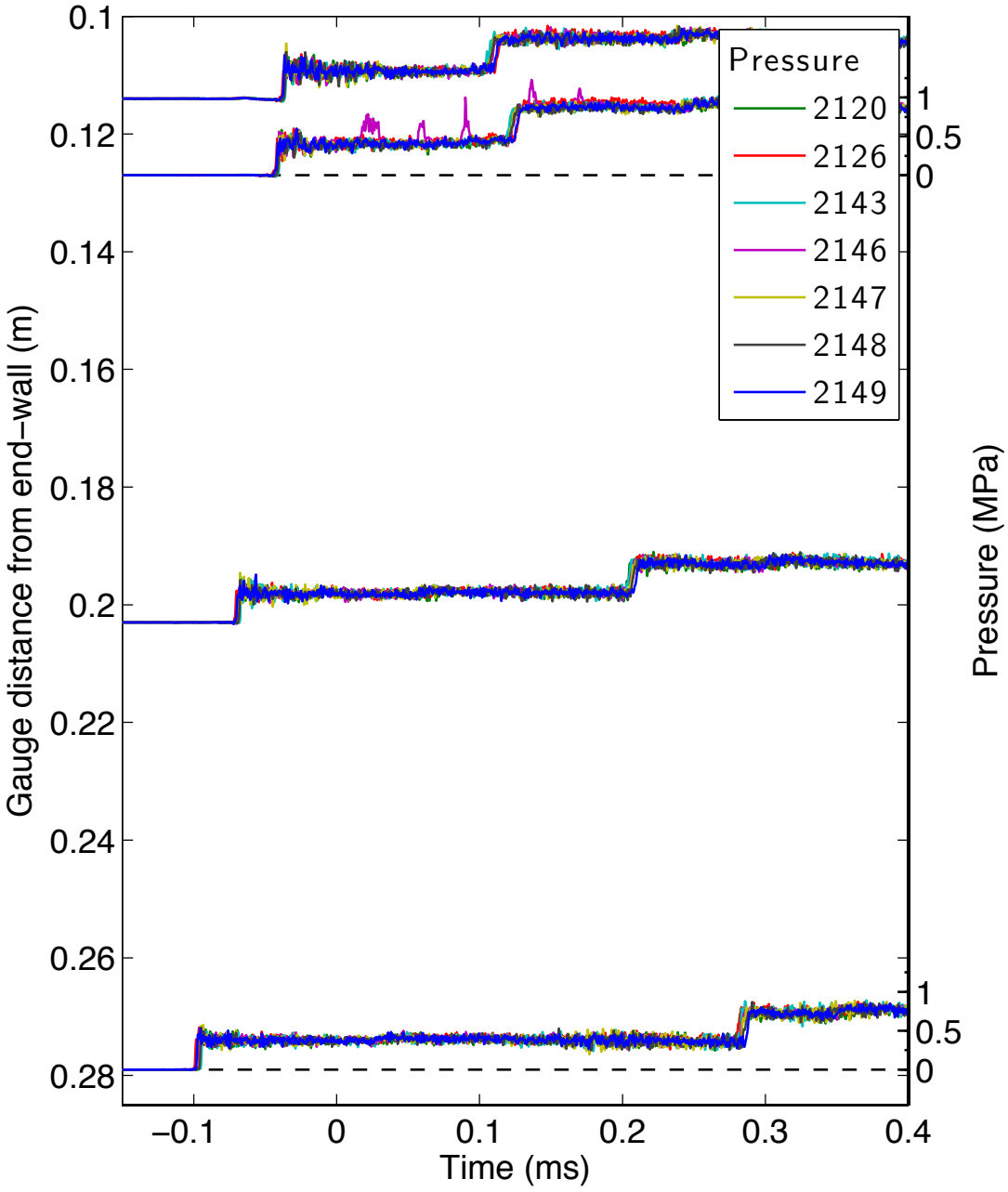

Figure E.29: Pressure traces for a detonation in stoichiometric hydrogen-oxygen at fill pressure 25 kPa, part 6.

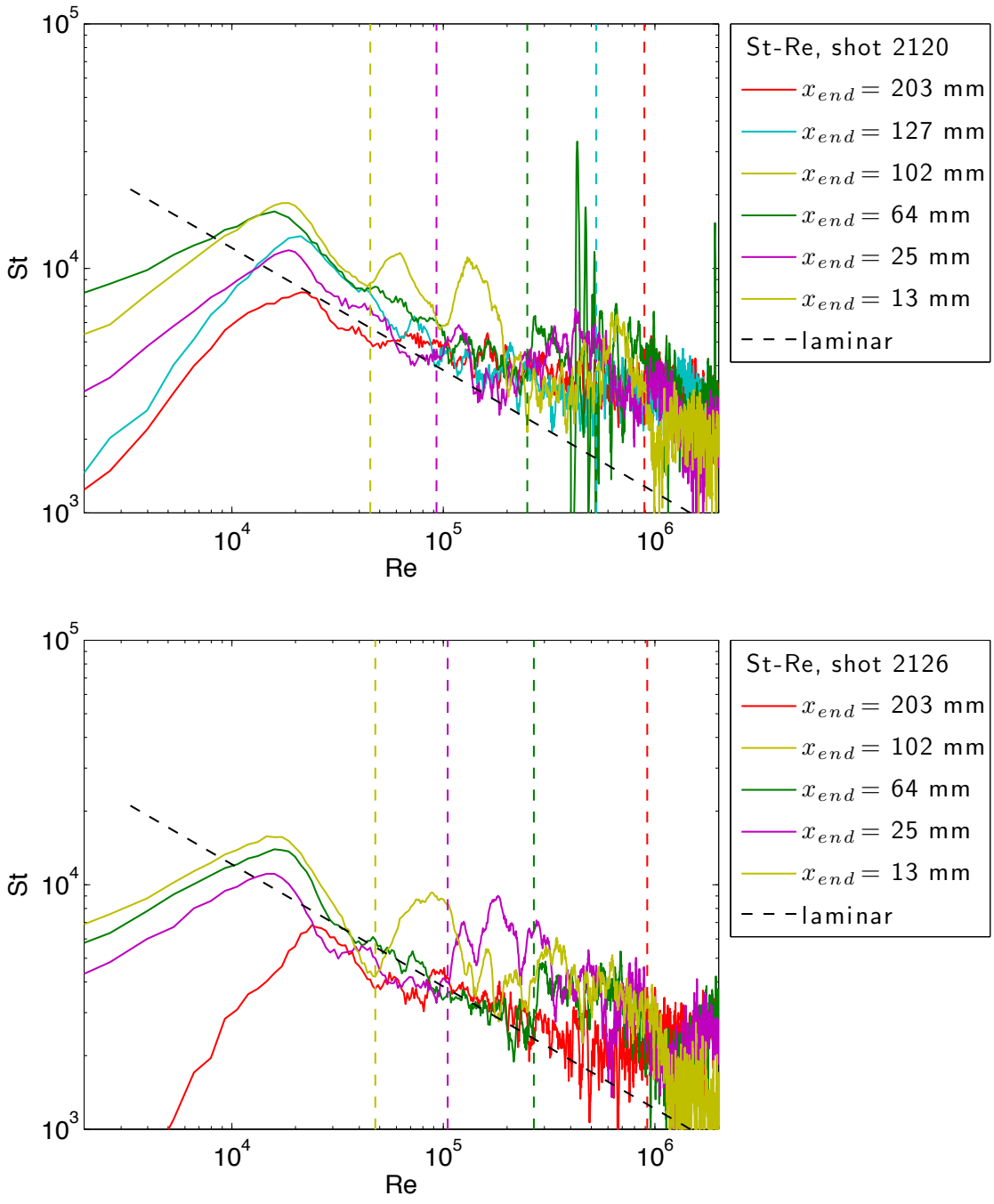

Figure E.30: Stanton-Reynolds number traces from shot 2126, a detonation in stoichiometric hydrogen-oxygen at fill pressure 25 kPa. The dashed vertical lines represent the arrival of the reflected shock wave.

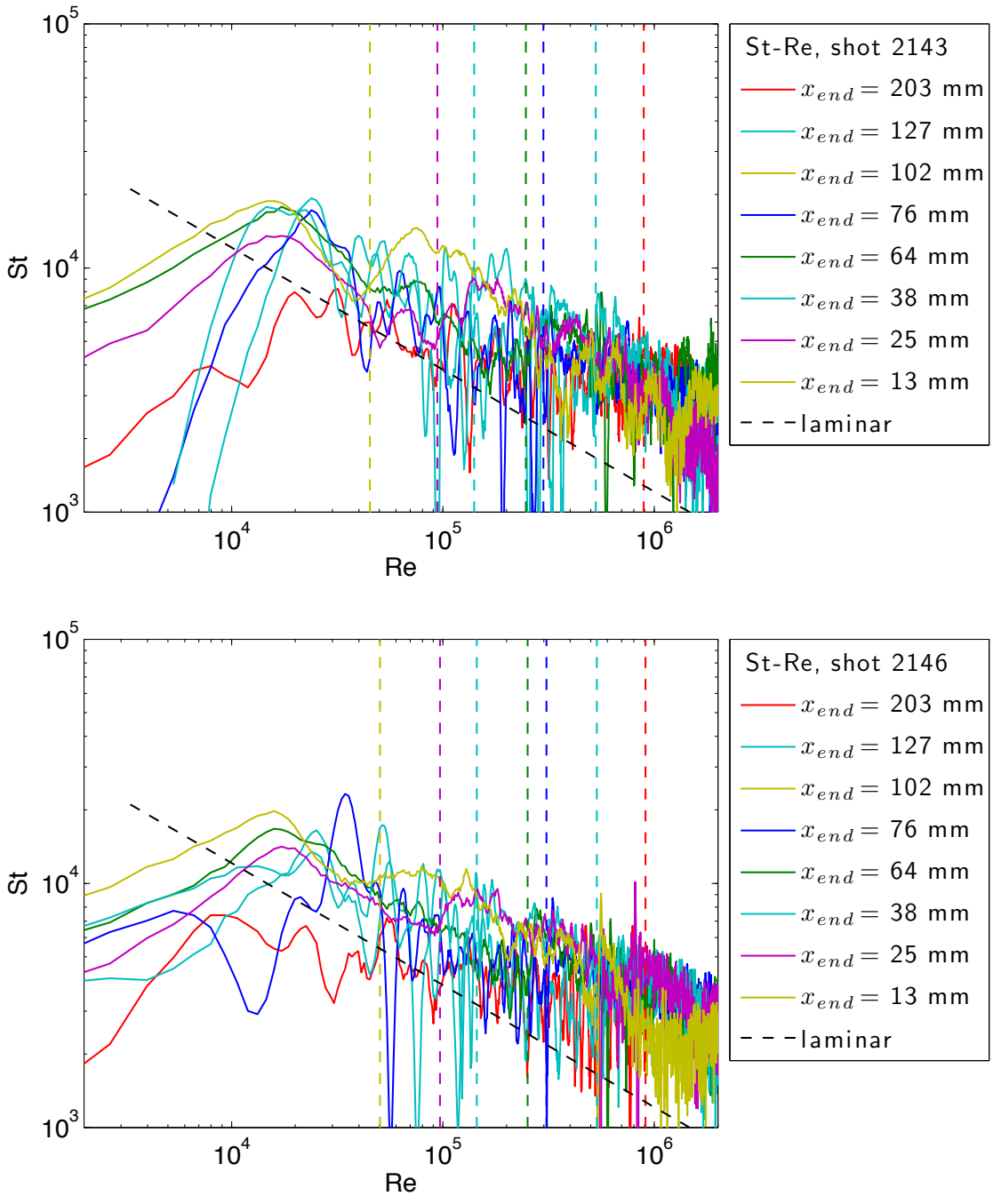

Figure E.31: Stanton-Reynolds number traces from shot 2146, a detonation in stoichiometric hydrogen-oxygen at fill pressure 25 kPa. The dashed vertical lines represent the arrival of the reflected shock wave.

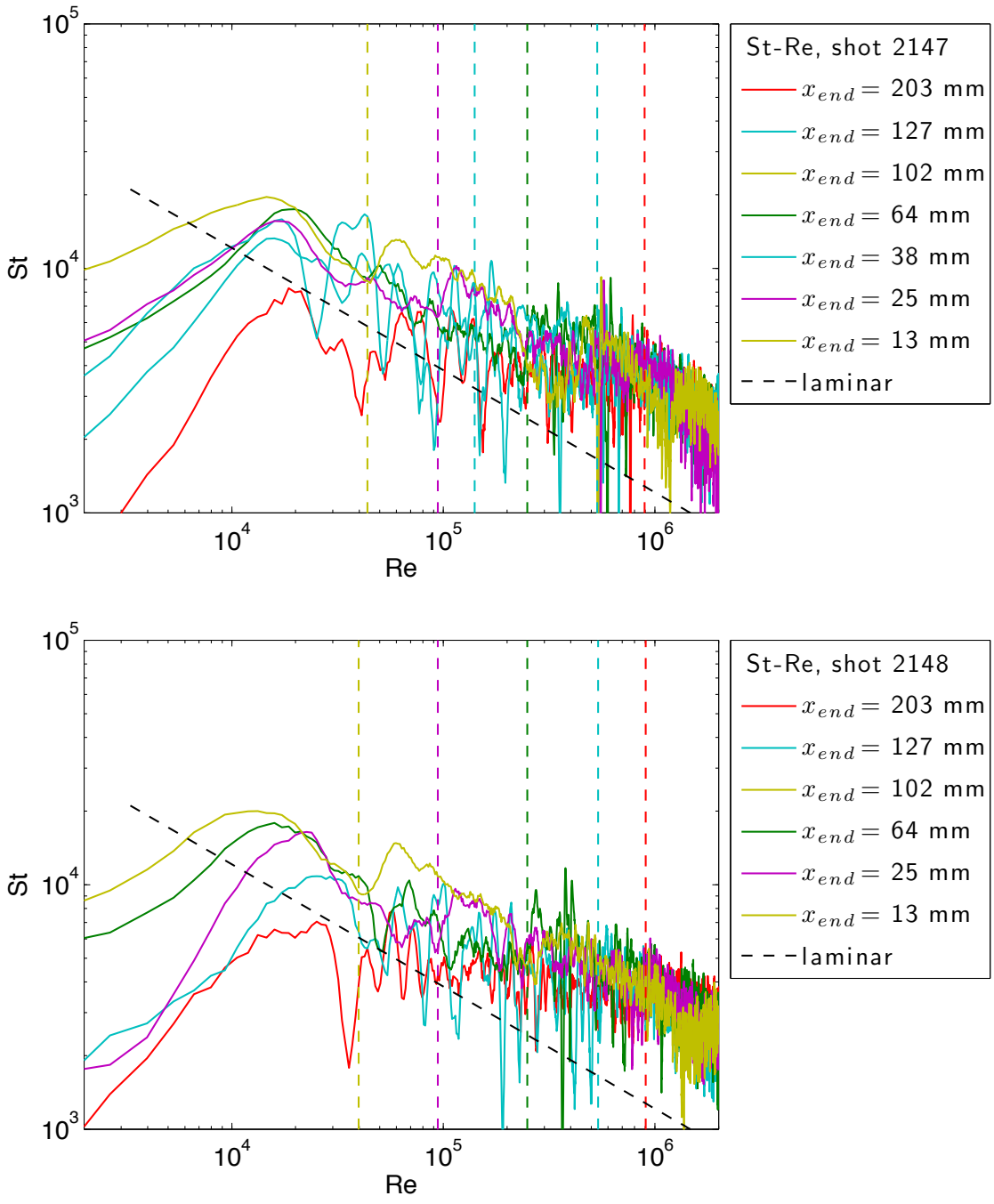

Figure E.32: Stanton-Reynolds number traces from shot 2148, a detonation in stoichiometric hydrogen-oxygen at fill pressure 25 kPa. The dashed vertical lines represent the arrival of the reflected shock wave.

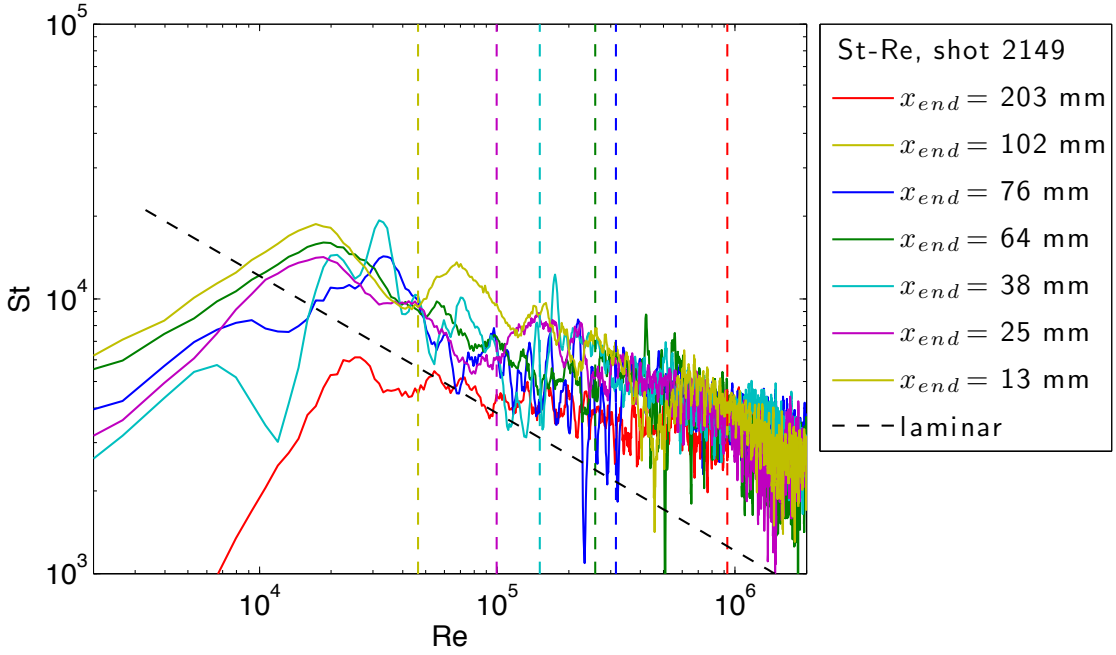

Figure E.33: Stanton-Reynolds number traces from shot 2149, a detonation in stoichiometric hydrogen-oxygen at fill pressure 25 kPa. The dashed vertical lines represent the arrival of the reflected shock wave.

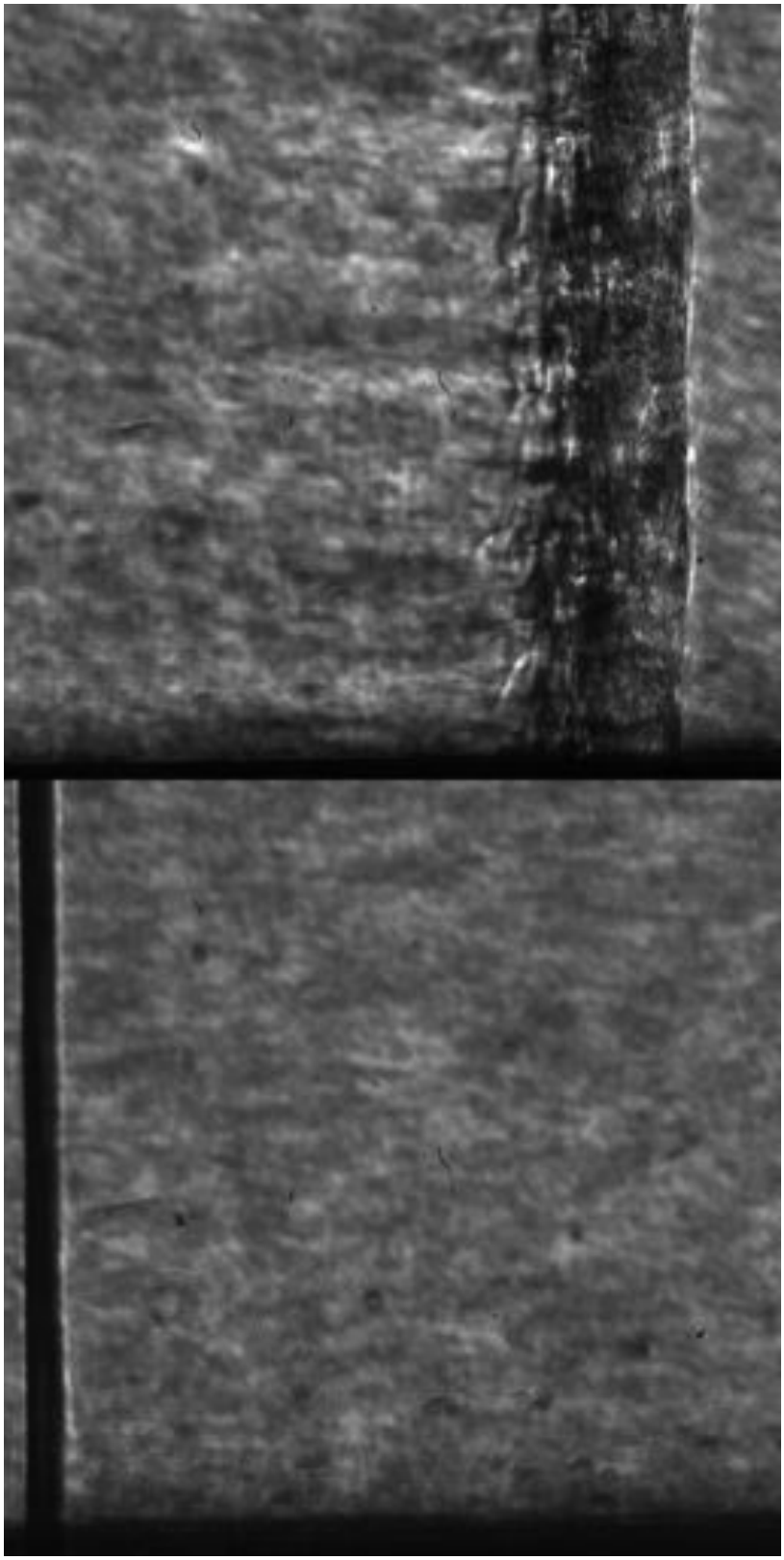

Figure E.34: Focused schlieren image of shot 2120. The field of view is approximately 14 mm wide.

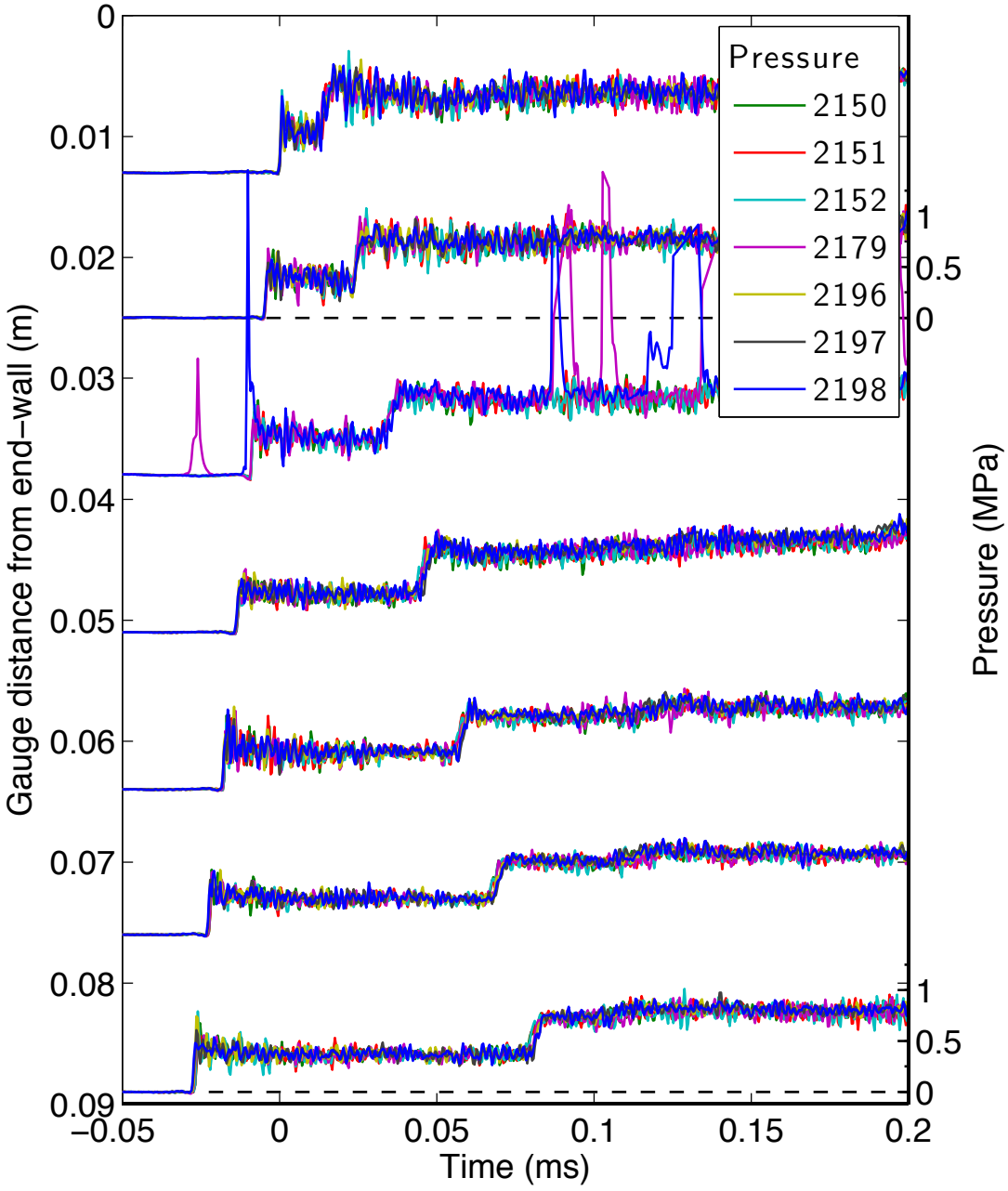

Figure E.35: Pressure traces for a detonation in stoichiometric hydrogen-oxygen at fill pressure 25 kPa, part 7.

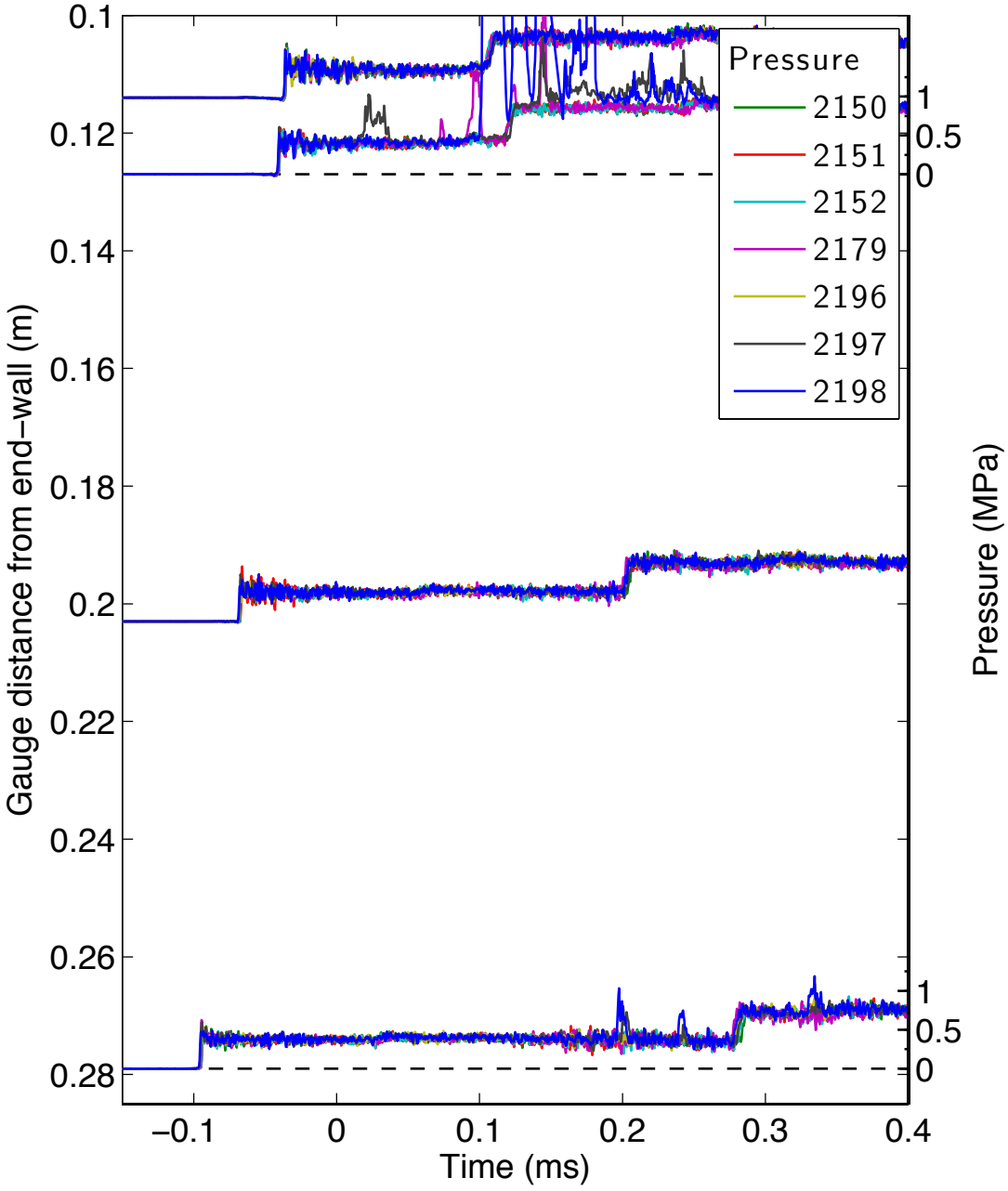

Figure E.36: Pressure traces for a detonation in stoichiometric hydrogen-oxygen at fill pressure 25 kPa, part 8.

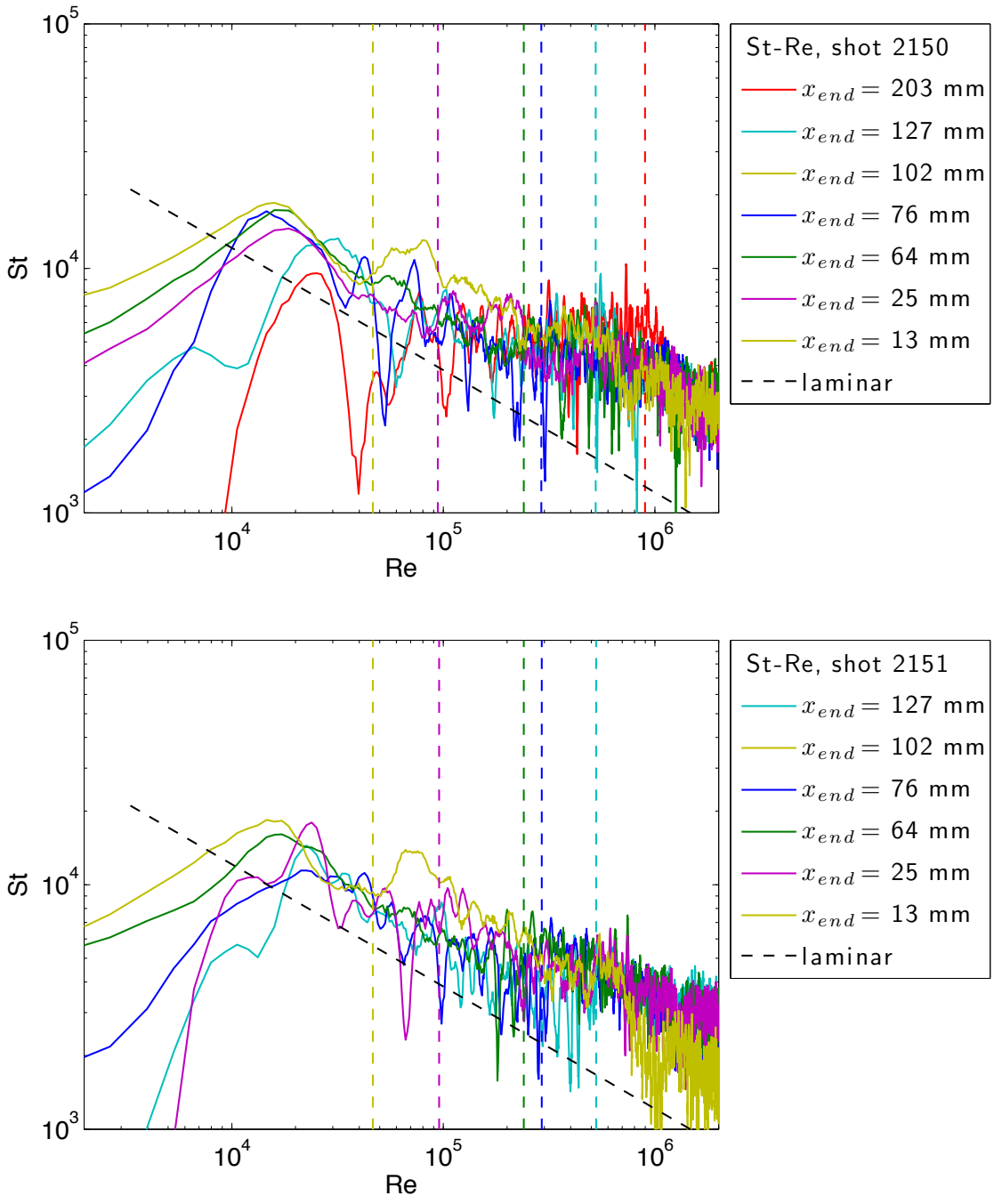

Figure E.37: Stanton-Reynolds number traces from shot 2151, a detonation in stoichiometric hydrogen-oxygen at fill pressure 25 kPa. The dashed vertical lines represent the arrival of the reflected shock wave.

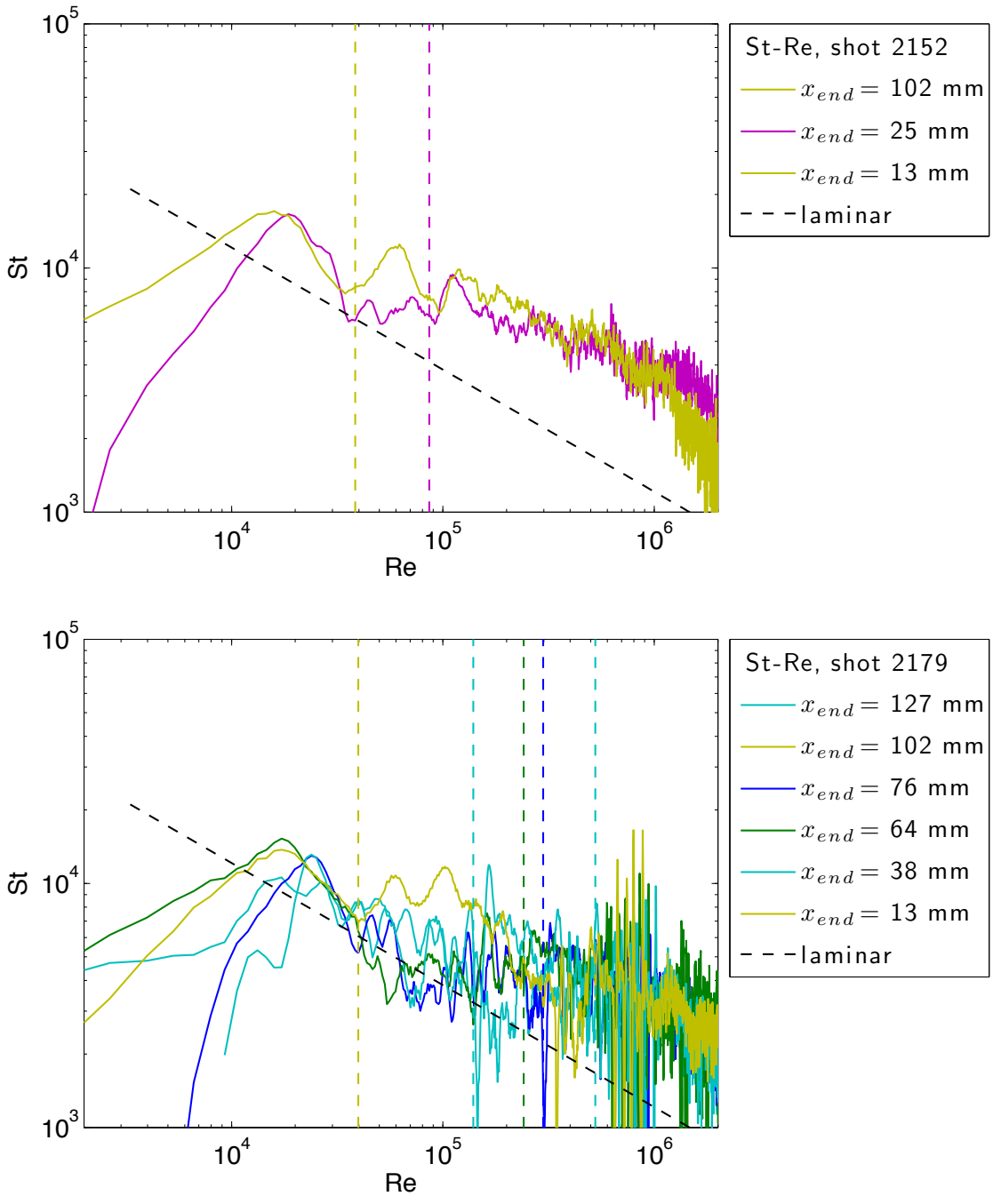

Figure E.38: Stanton-Reynolds number traces from shot 2179, a detonation in stoichiometric hydrogen-oxygen at fill pressure 25 kPa. The dashed vertical lines represent the arrival of the reflected shock wave.

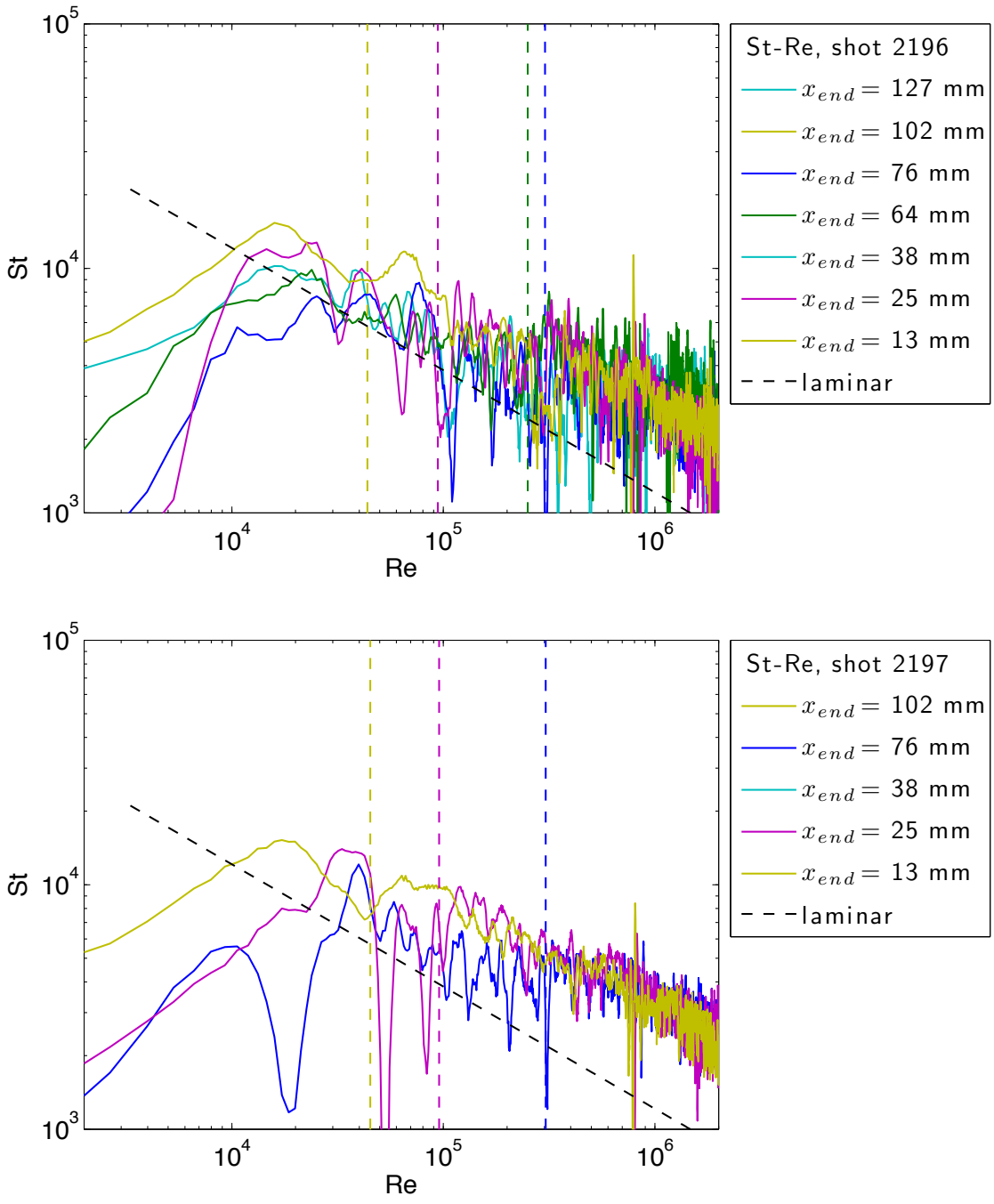

Figure E.39: Stanton-Reynolds number traces from shot 2197, a detonation in stoichiometric hydrogen-oxygen at fill pressure 25 kPa. The dashed vertical lines represent the arrival of the reflected shock wave.

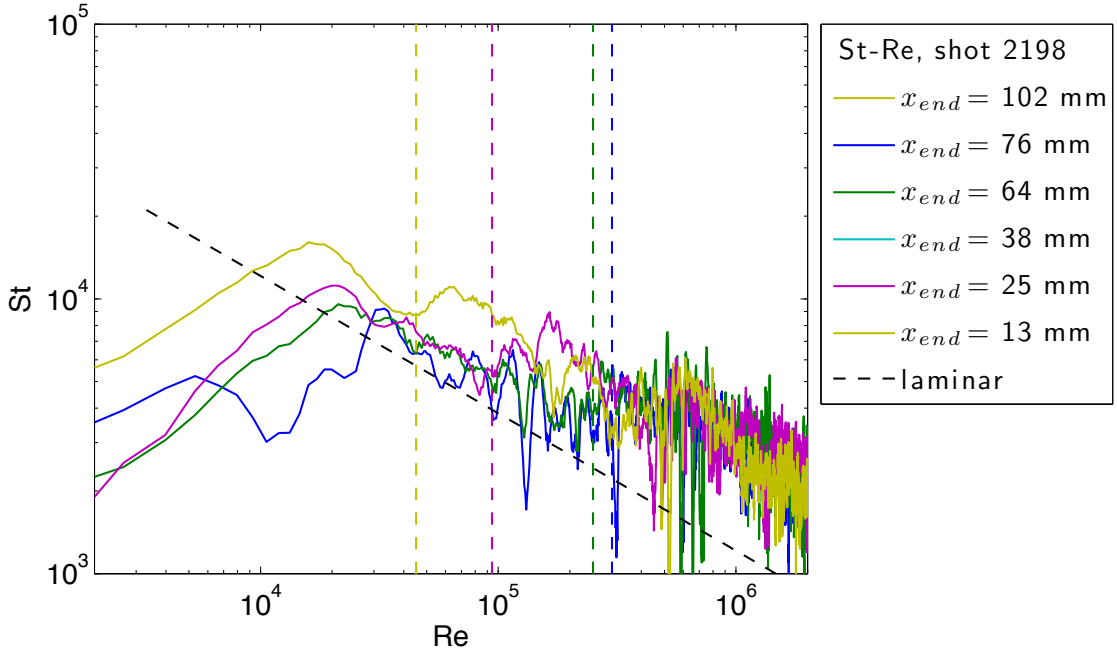

Figure E.40: Stanton-Reynolds number traces from shot 2198, a detonation in stoichiometric hydrogen-oxygen at fill pressure 25 kPa. The dashed vertical lines represent the arrival of the reflected shock wave.

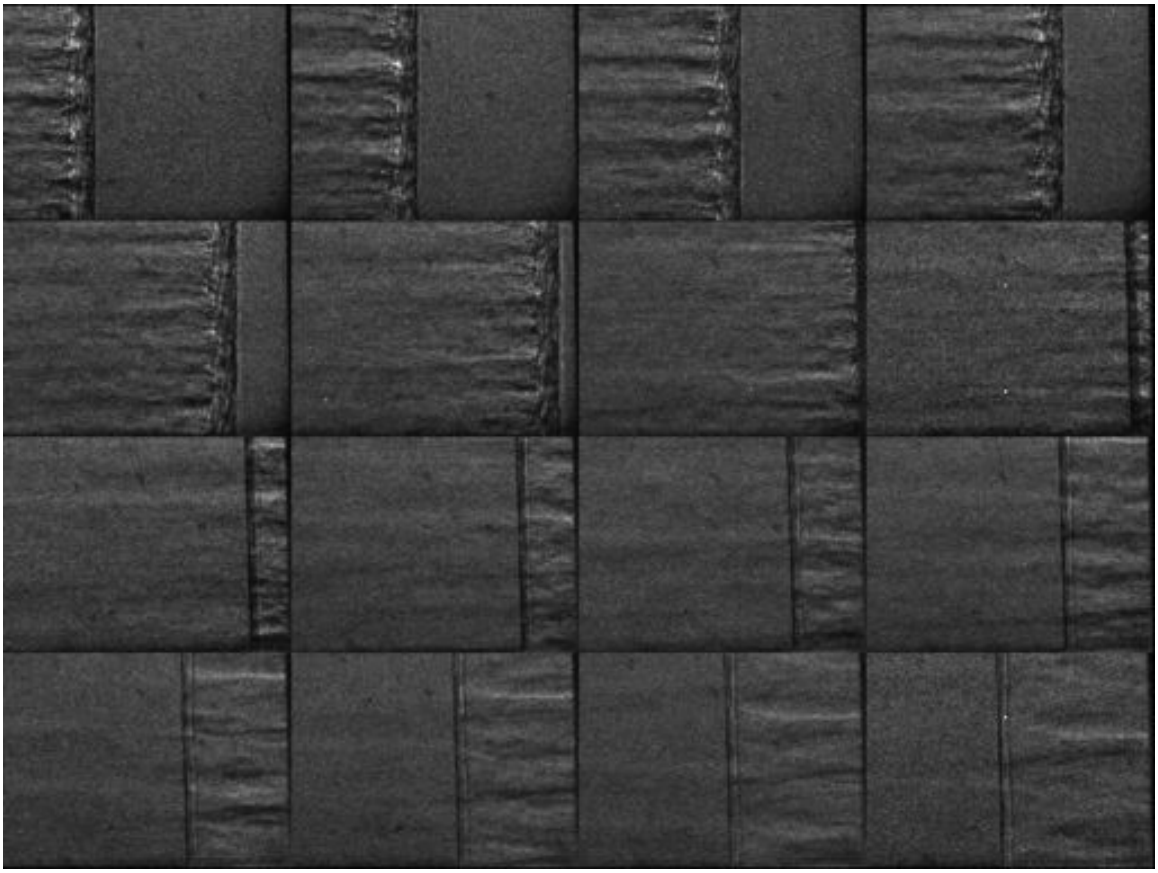

Figure E.41: Unfocused schlieren image of shot 2152. The field of view is approximately 30 mm wide.

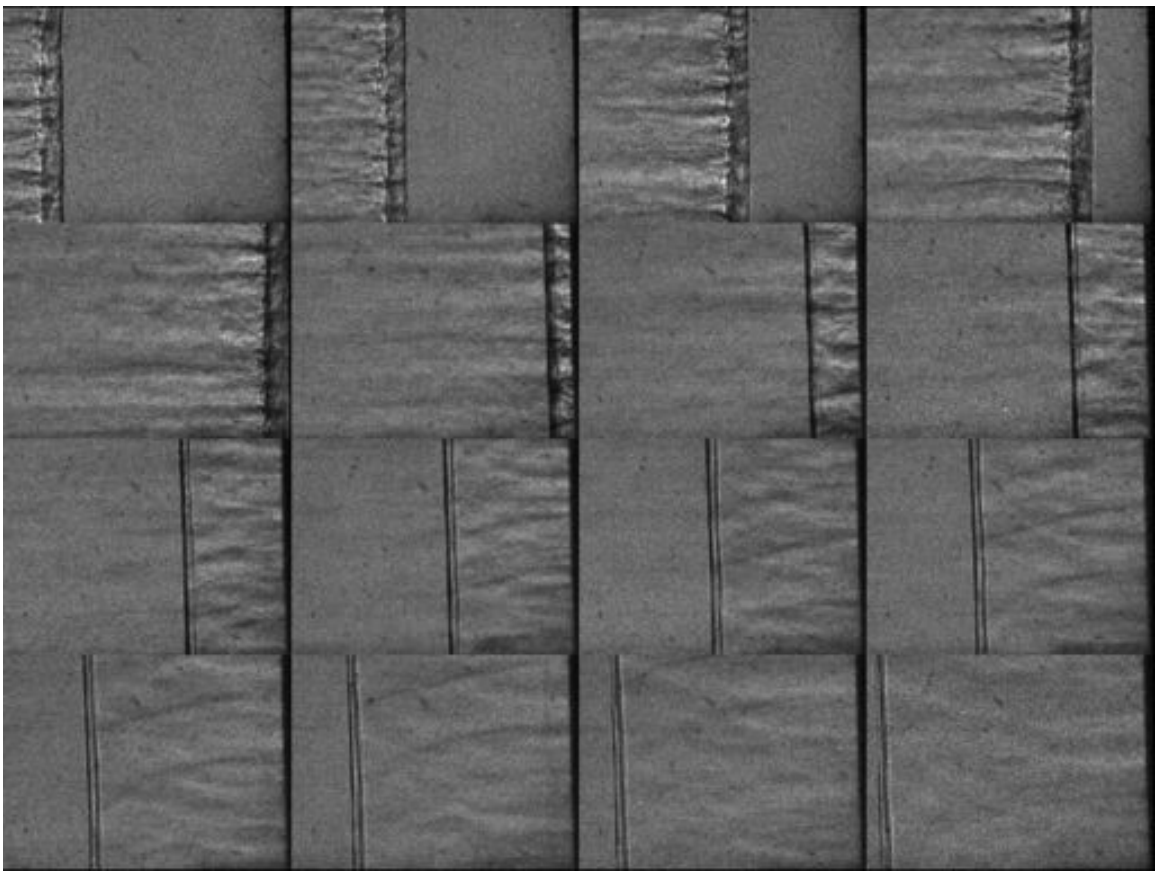

Figure E.42: Unfocused schlieren image of shot 2179. The field of view is approximately 30 mm wide.

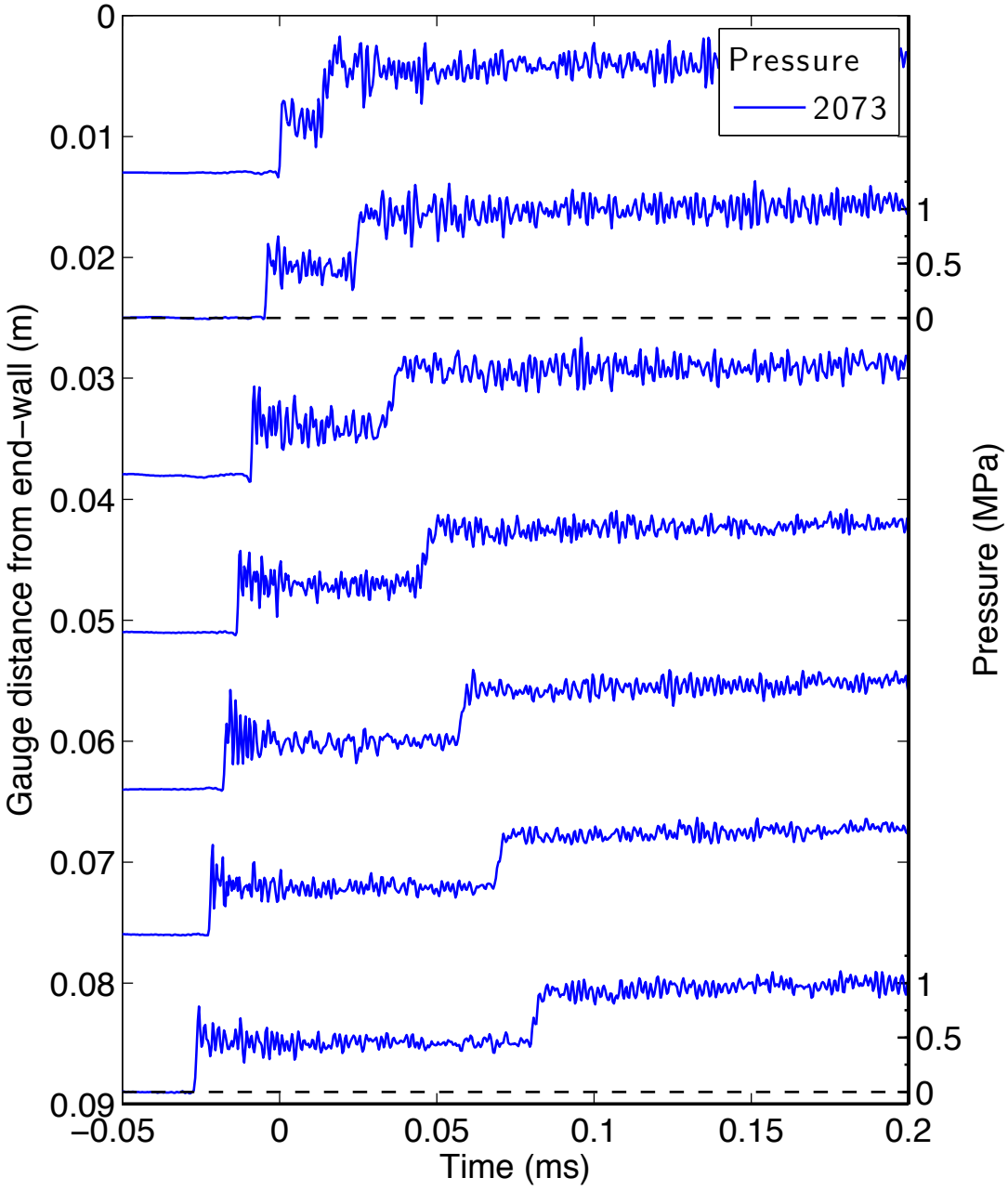

Figure E.43: Pressure traces for a detonation in stoichiometric hydrogen-oxygen at fill pressure 30 kPa, part 1.

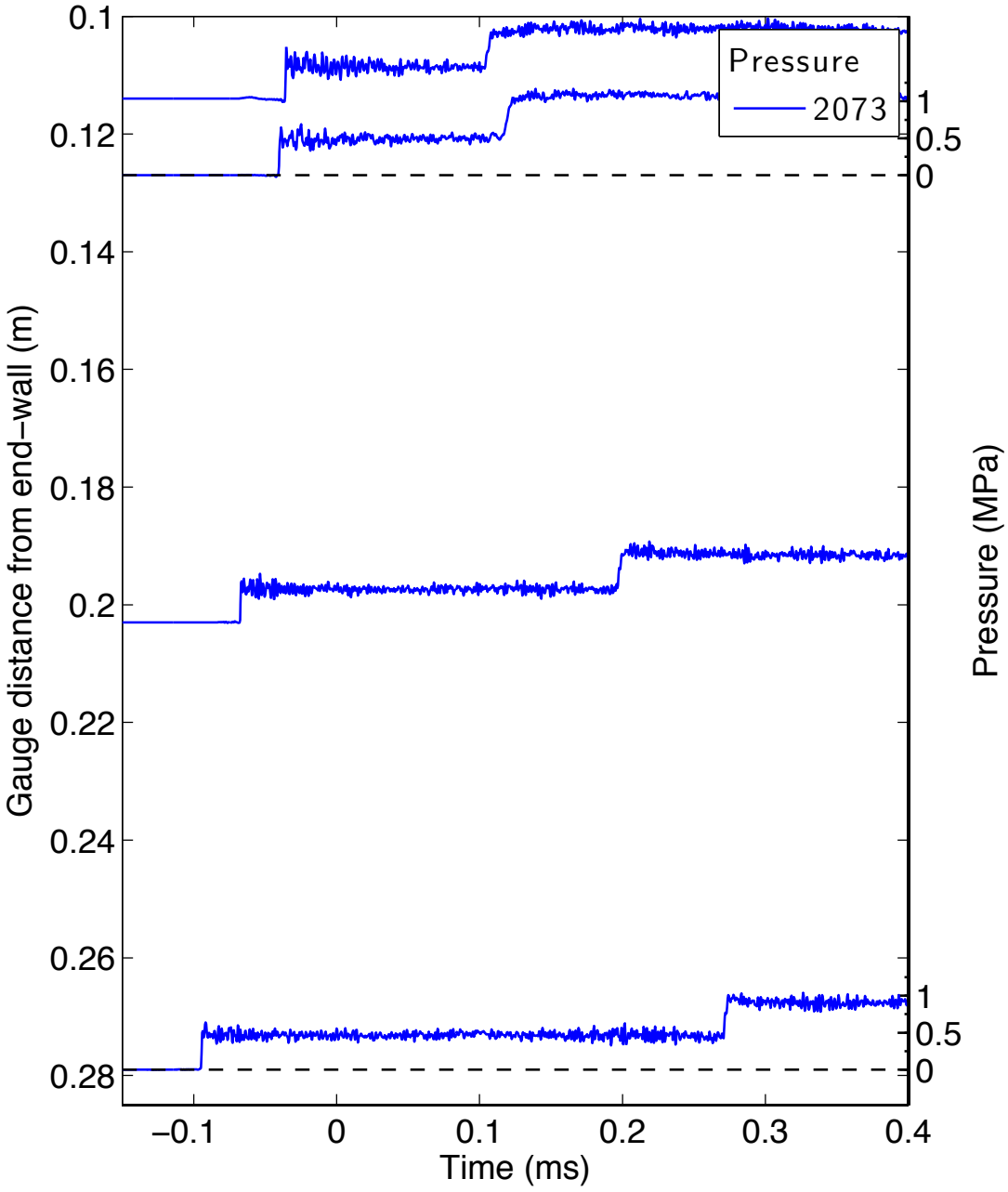

Figure E.44: Pressure traces for a detonation in stoichiometric hydrogen-oxygen at fill pressure 30 kPa, part 2.

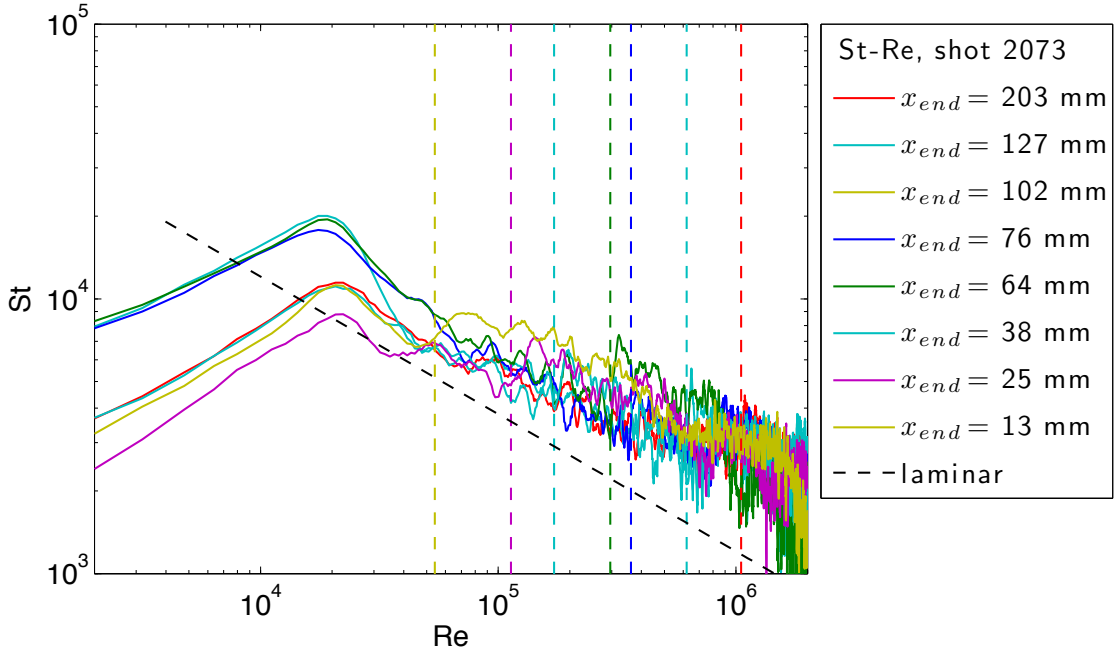

Figure E.45: Stanton-Reynolds number traces from shot 2073, a detonation in stoichiometric hydrogen-oxygen at fill pressure 30 kPa. The dashed vertical lines represent the arrival of the reflected shock wave.

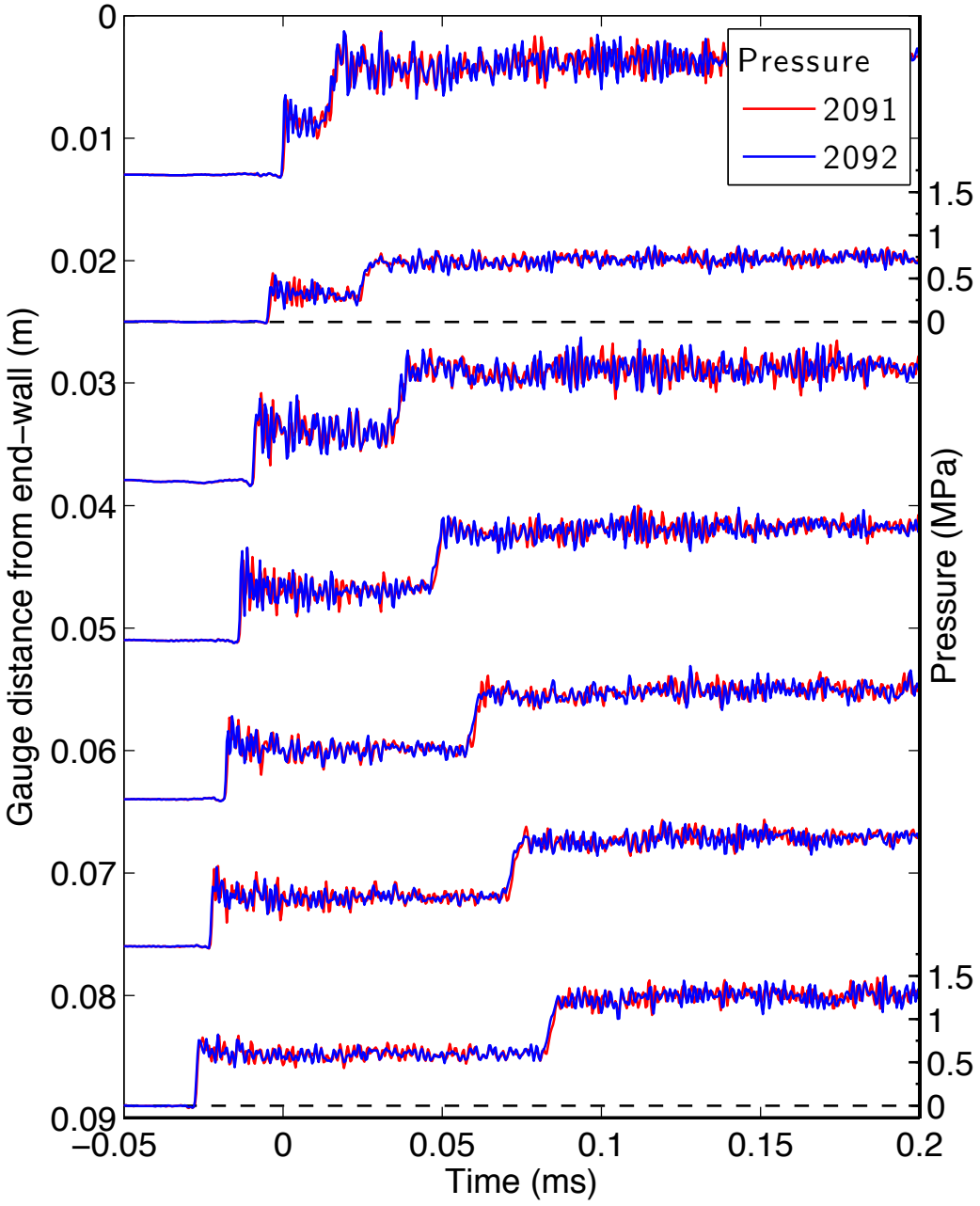

Figure E.46: Pressure traces for a detonation in stoichiometric hydrogen-oxygen at fill pressure 40 kPa, part 1.

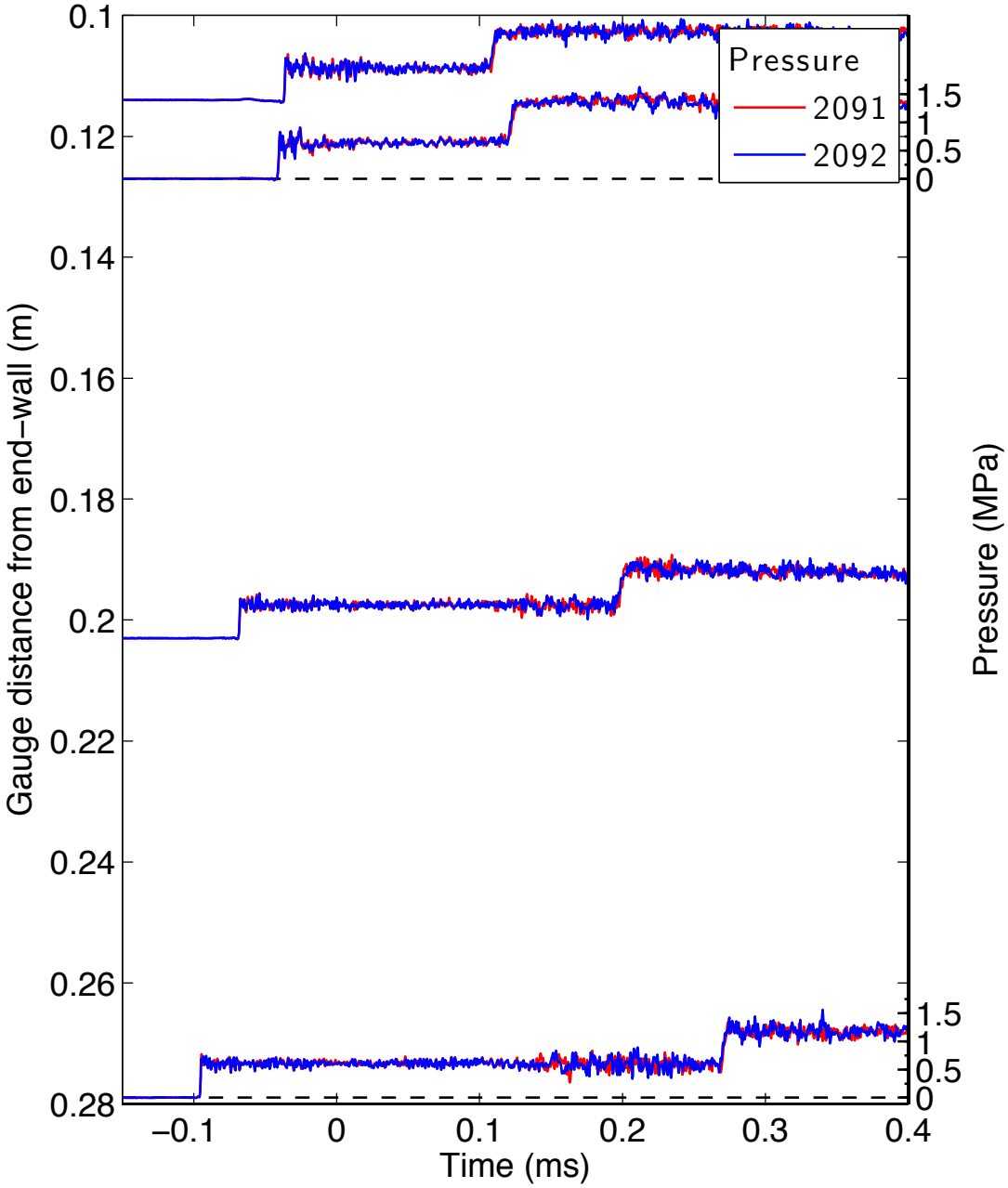

Figure E.47: Pressure traces for a detonation in stoichiometric hydrogen-oxygen at fill pressure 40 kPa, part 2.

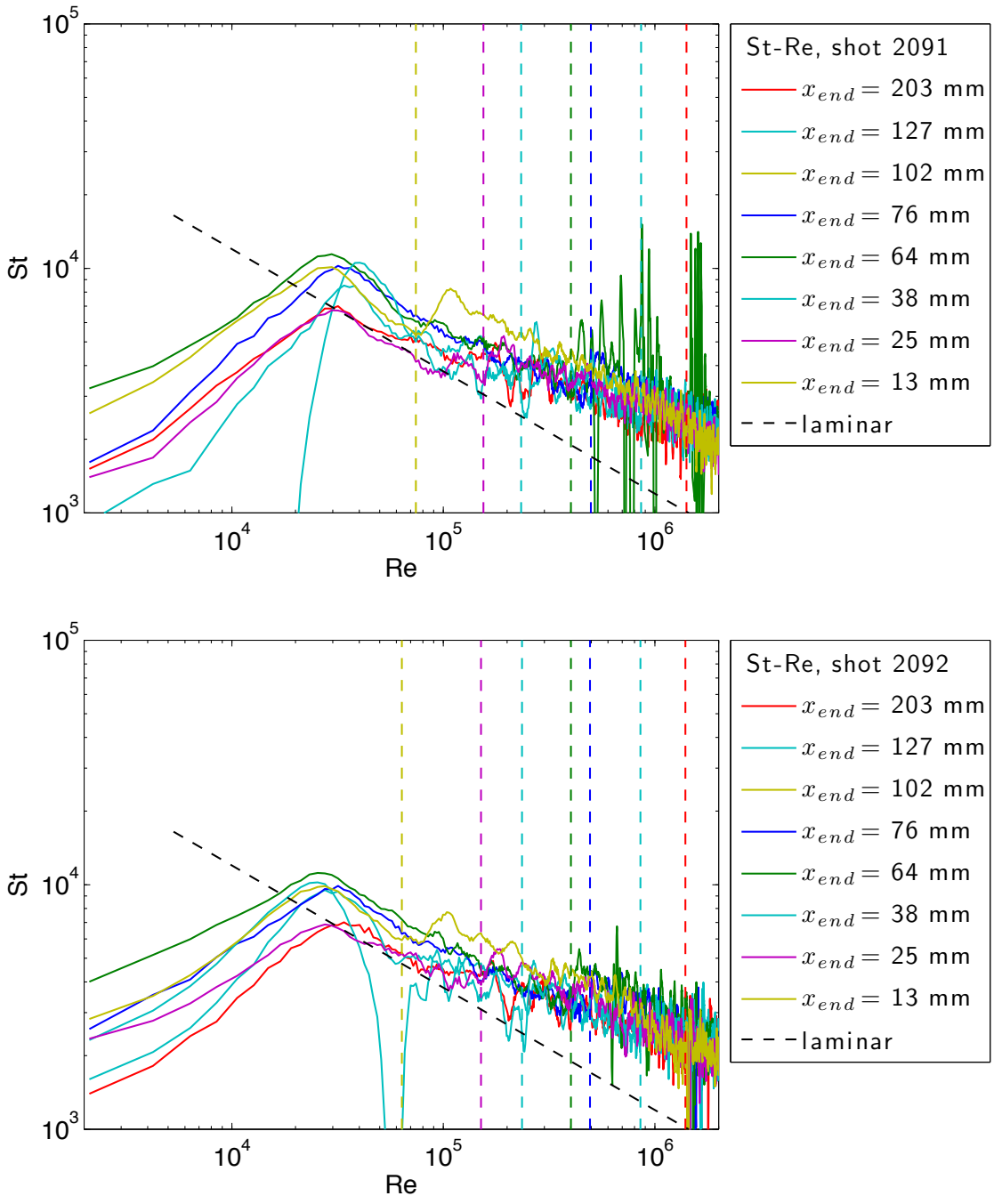

Figure E.48: Stanton-Reynolds number traces from shot 2092, a detonation in stoichiometric hydrogen-oxygen at fill pressure 40 kPa. The dashed vertical lines represent the arrival of the reflected shock wave.

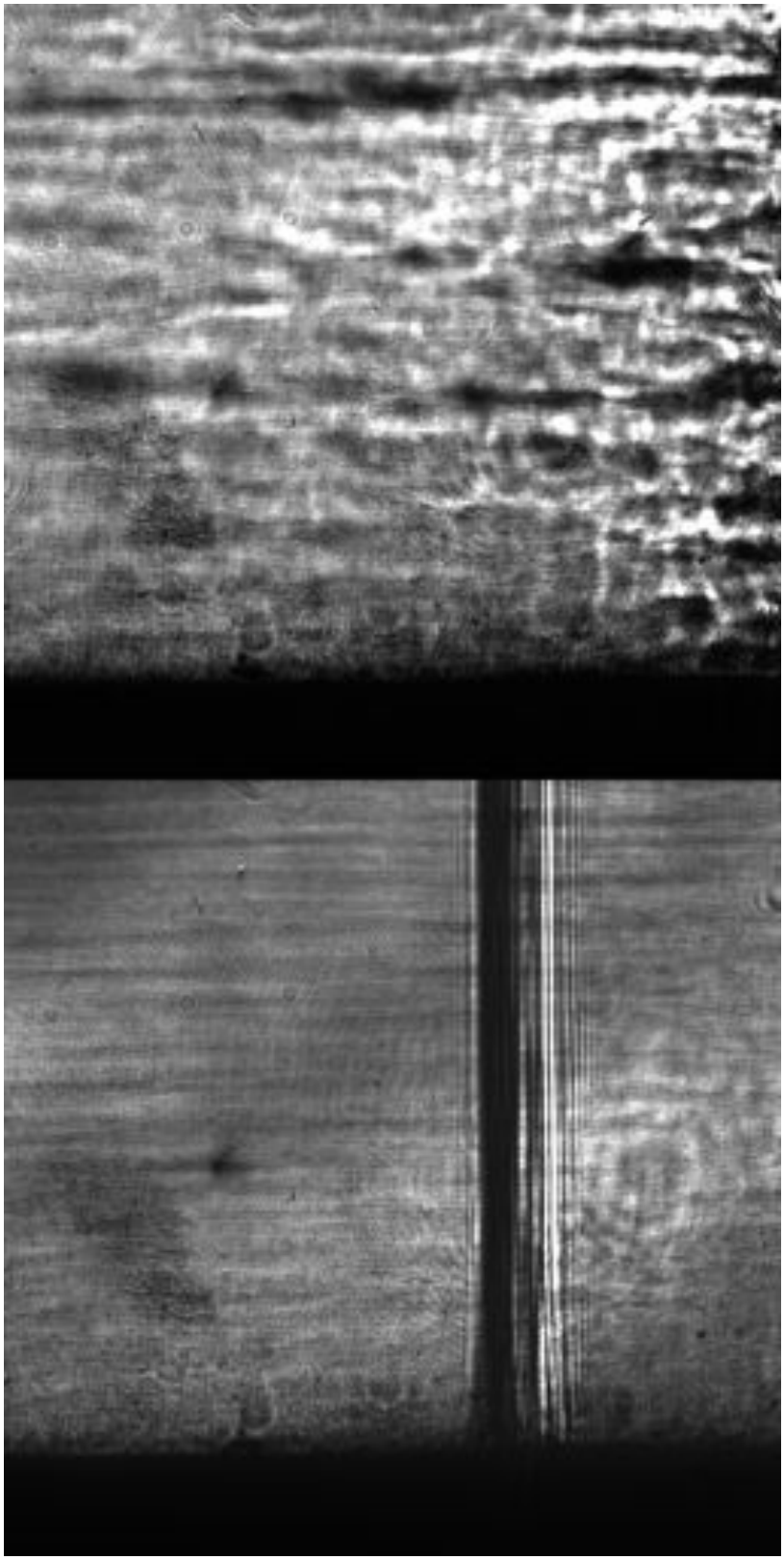

Figure E.49: Focused schlieren image of shot 2091. The field of view is approximately 14 mm wide.

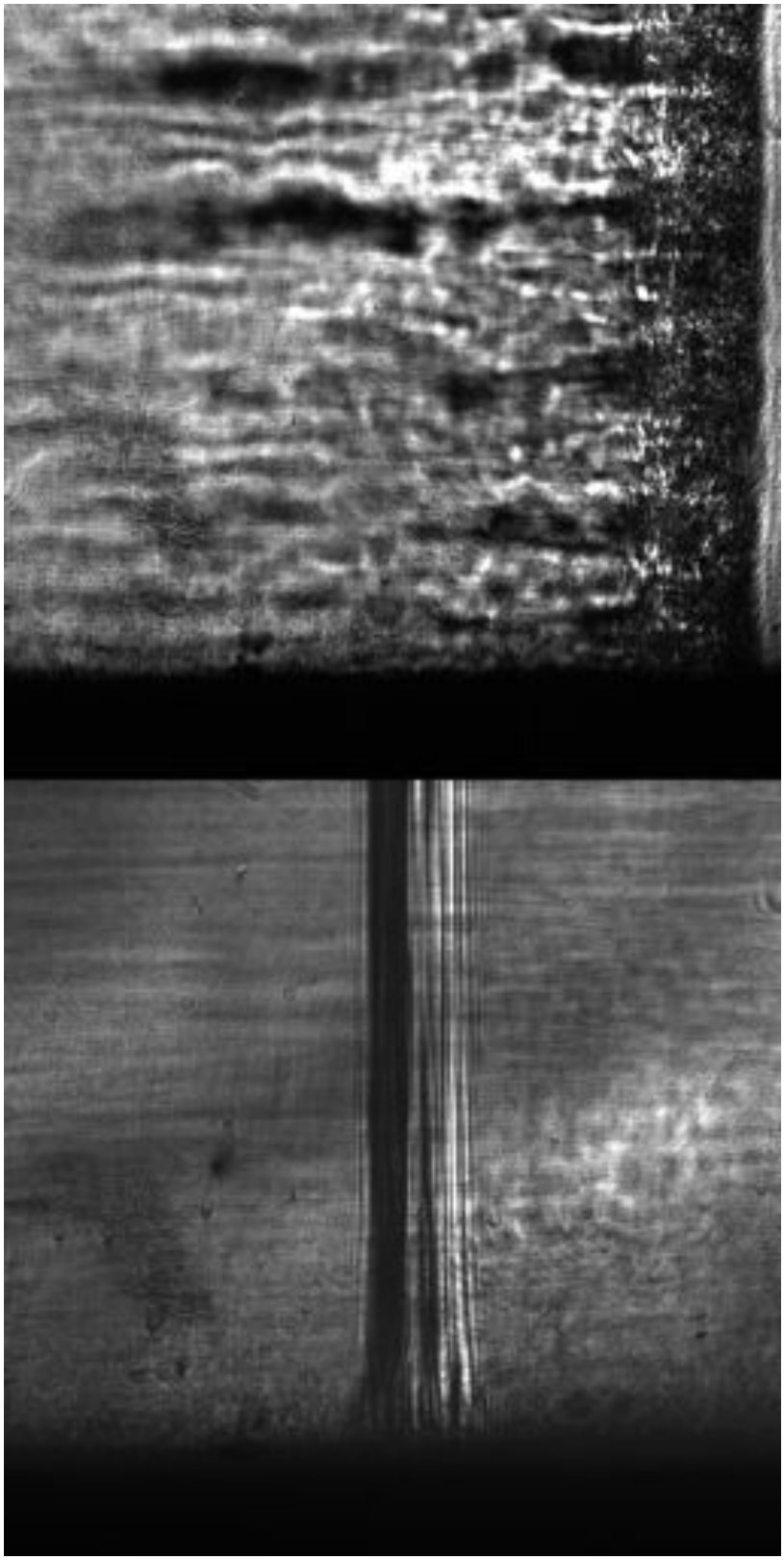

Figure E.50: Focused schlieren image of shot 2092. The field of view is approximately 14 mm wide.

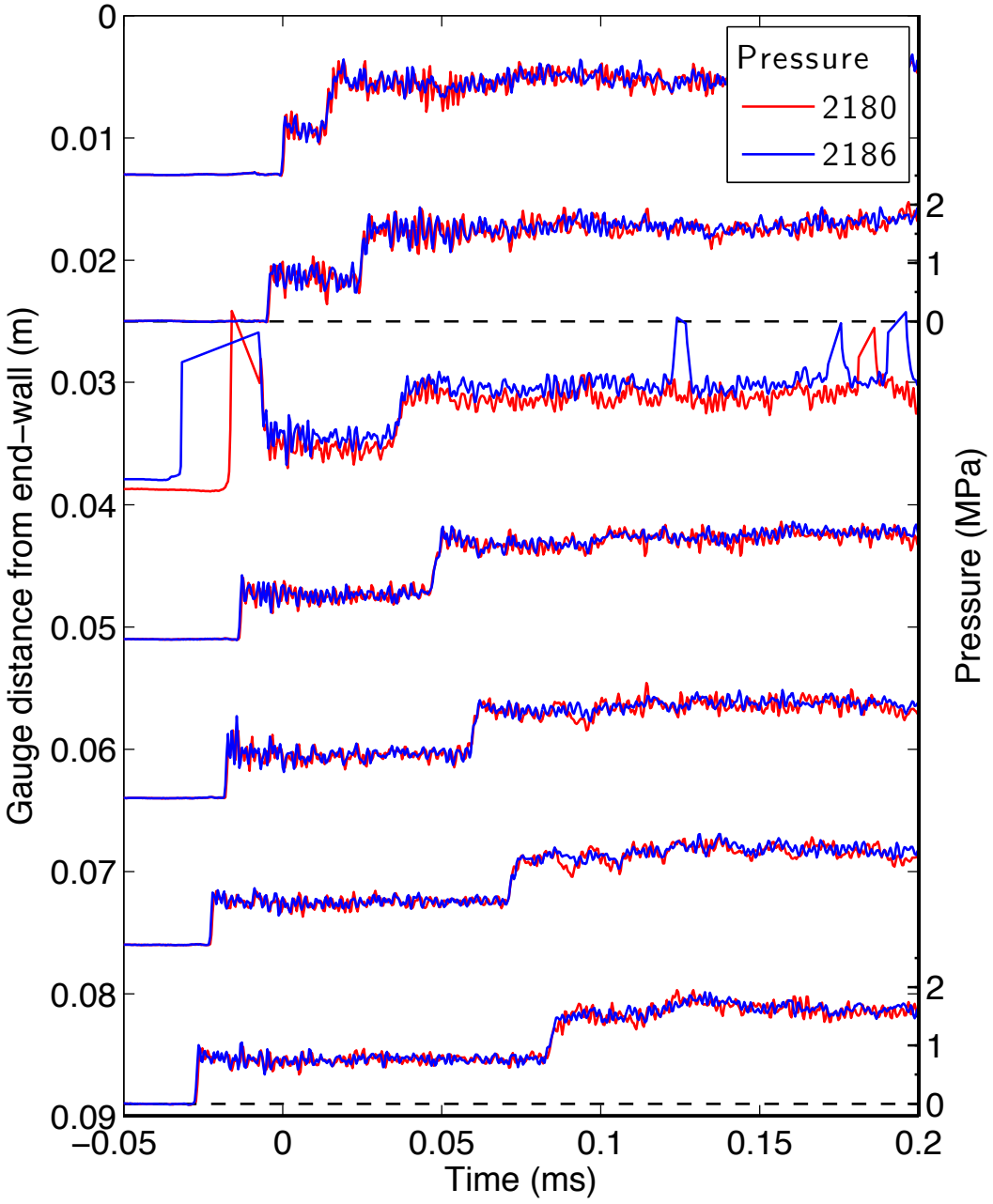

Figure E.51: Pressure traces for a detonation in stoichiometric hydrogen-oxygen at fill pressure 50 kPa, part 1.

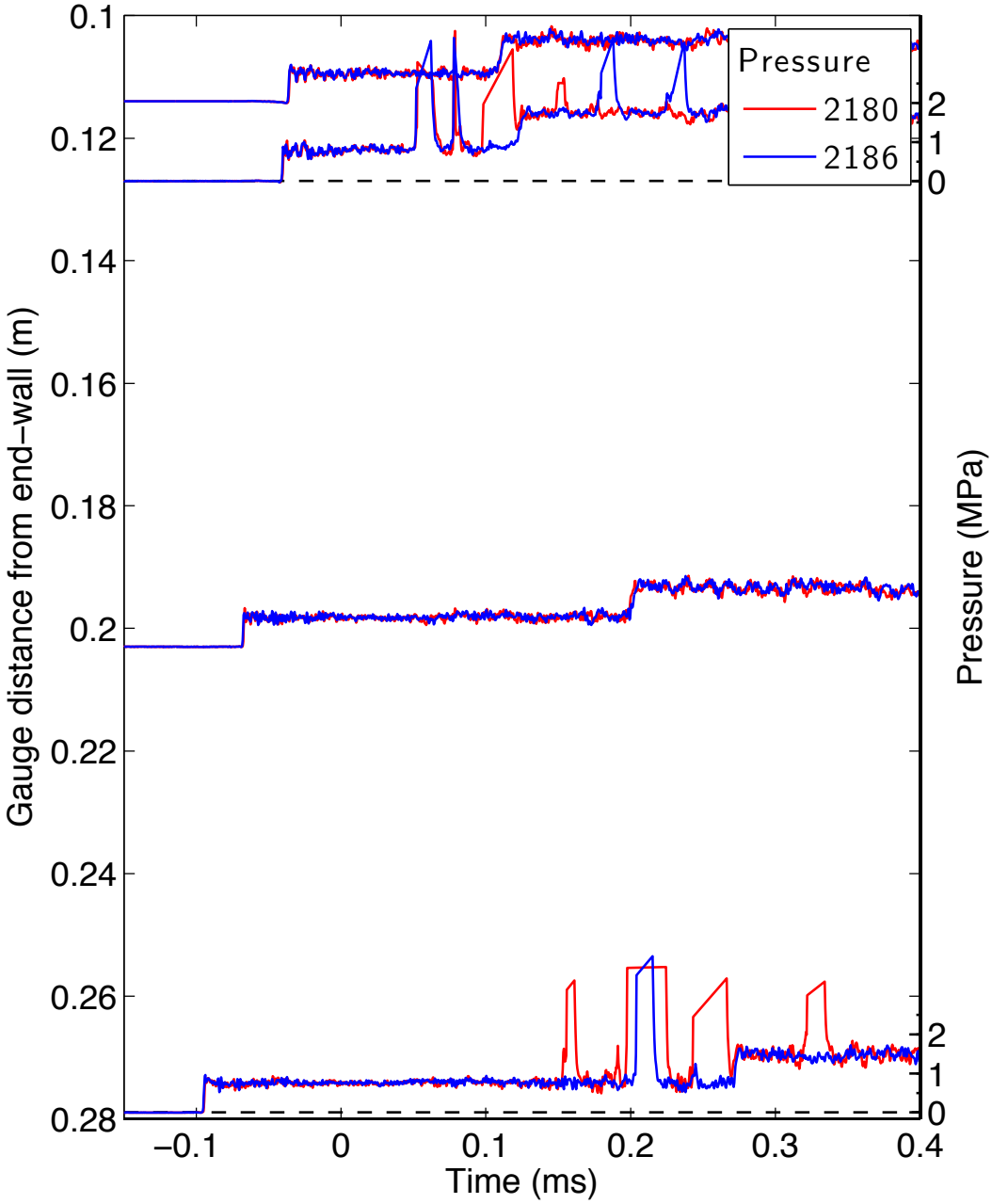

Figure E.52: Pressure traces for a detonation in stoichiometric hydrogen-oxygen at fill pressure 50 kPa, part 2.

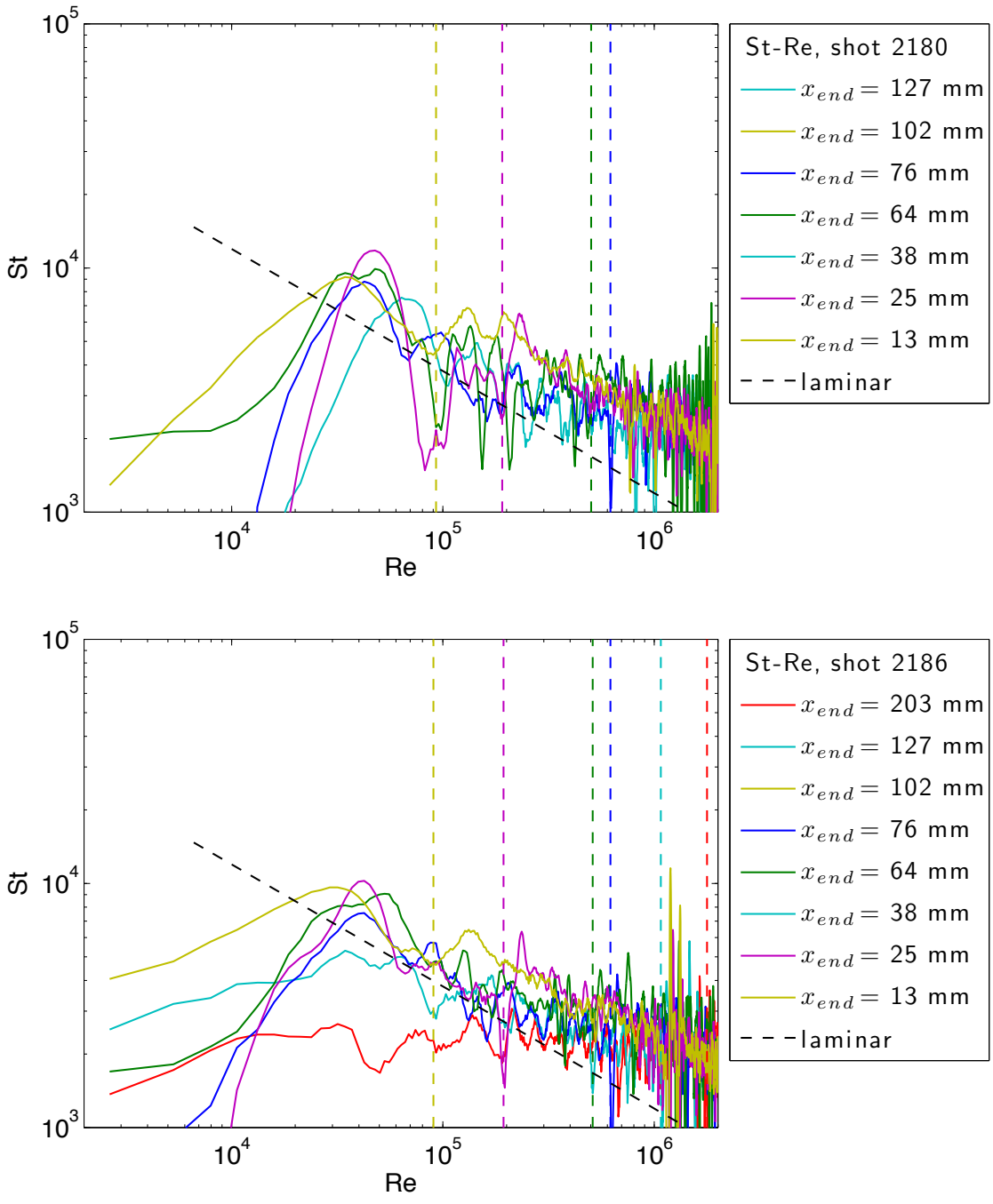

Figure E.53: Stanton-Reynolds number traces from shot 2186, a detonation in stoichiometric hydrogen-oxygen at fill pressure 50 kPa. The dashed vertical lines represent the arrival of the reflected shock wave.

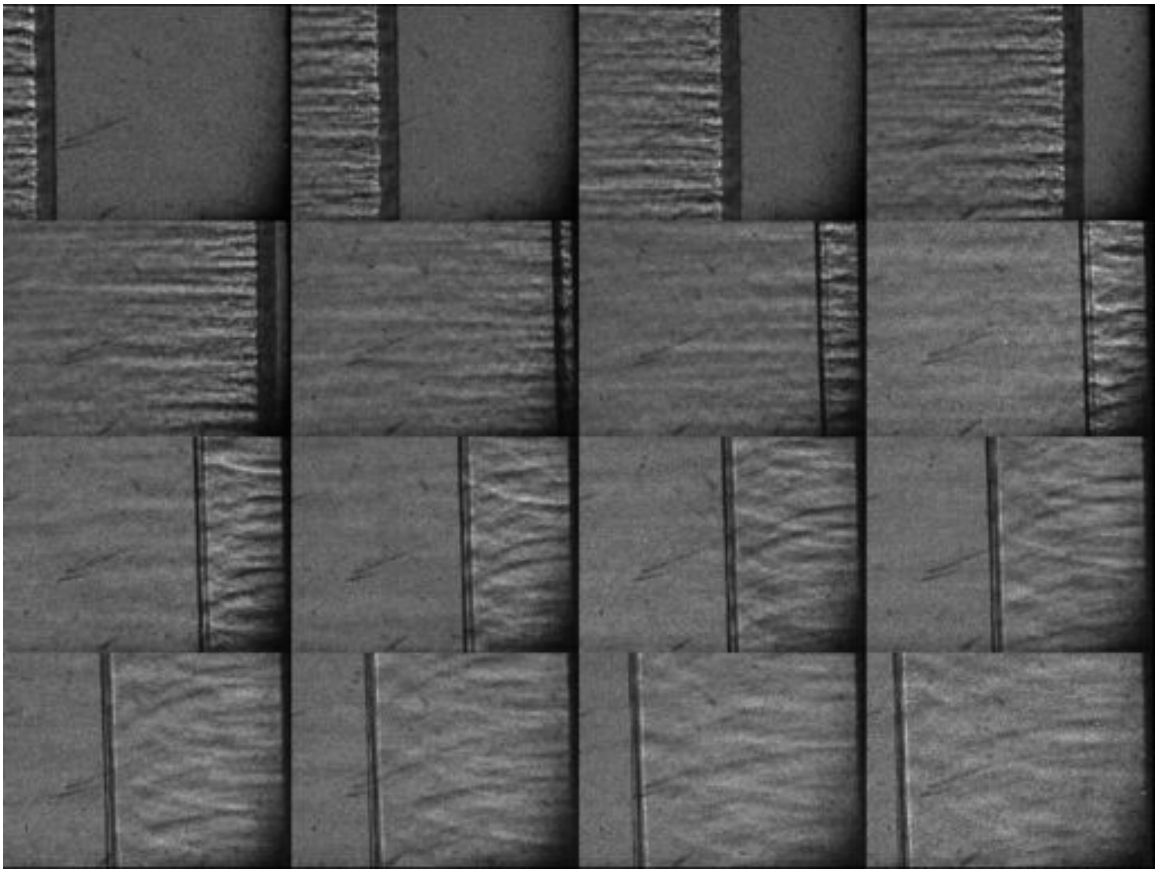

Figure E.54: Unfocused schlieren image of shot 2180. The field of view is approximately 30 mm wide.

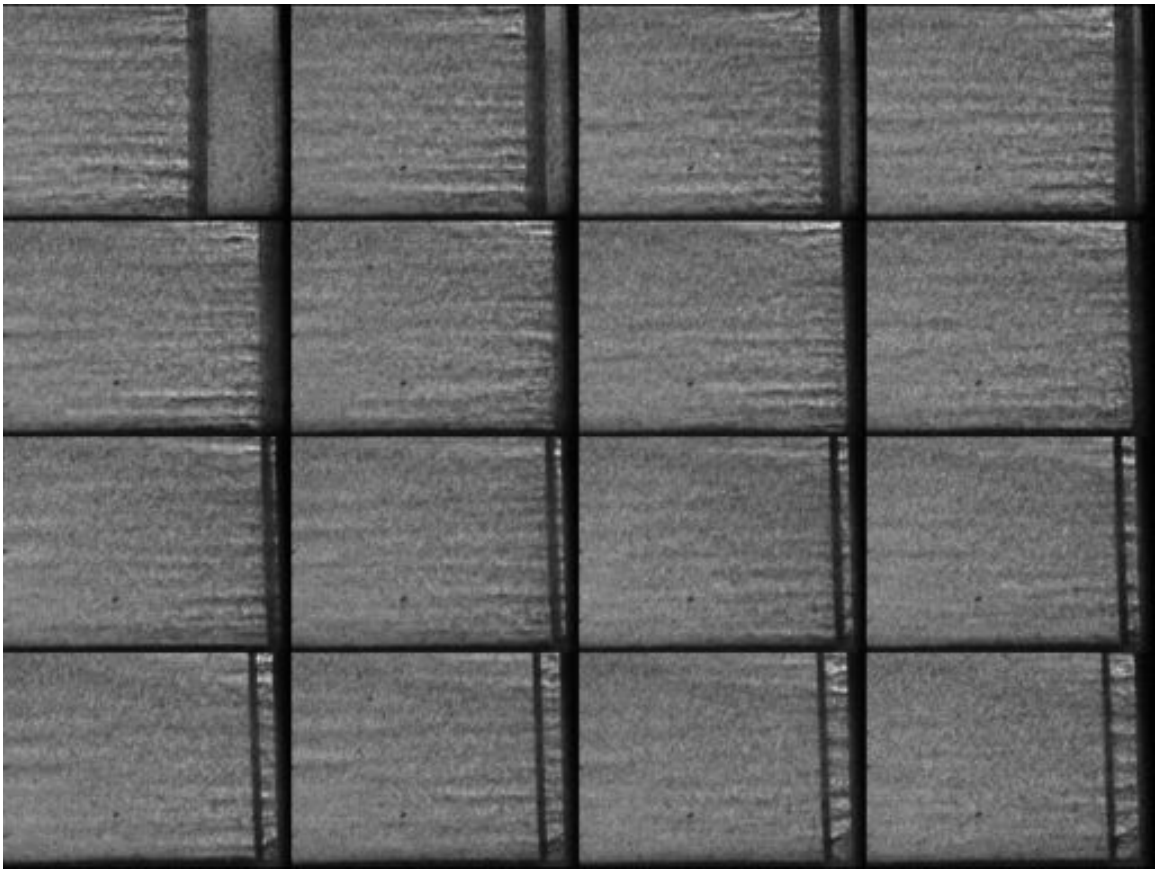

Figure E.55: Unfocused schlieren image of shot 2186. The field of view is approximately 30 mm wide.

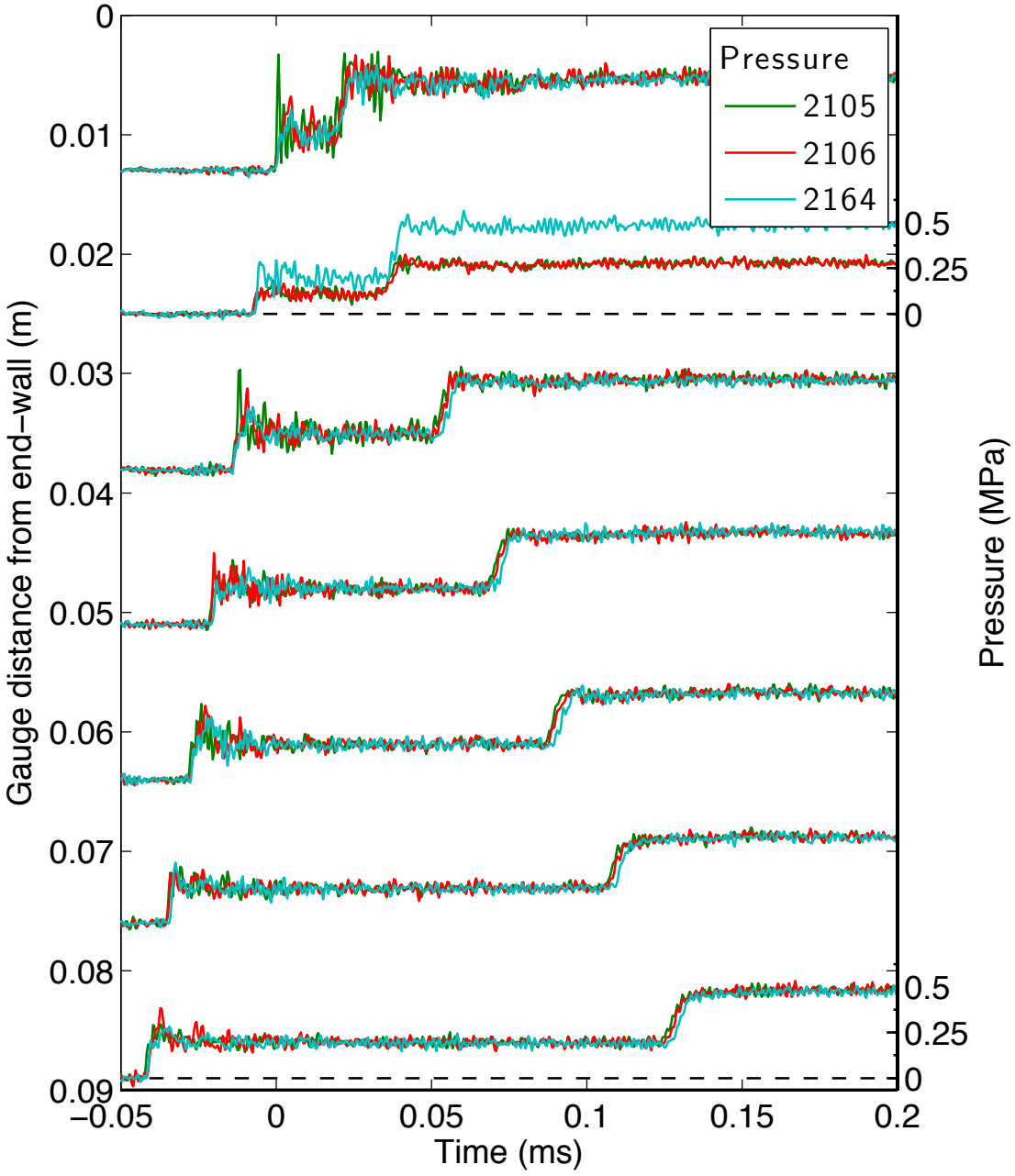

Figure E.56: Pressure traces for a detonation in stoichiometric hydrogen-oxygen with 50% argon dilution at fill pressure 10 kPa, part 1.

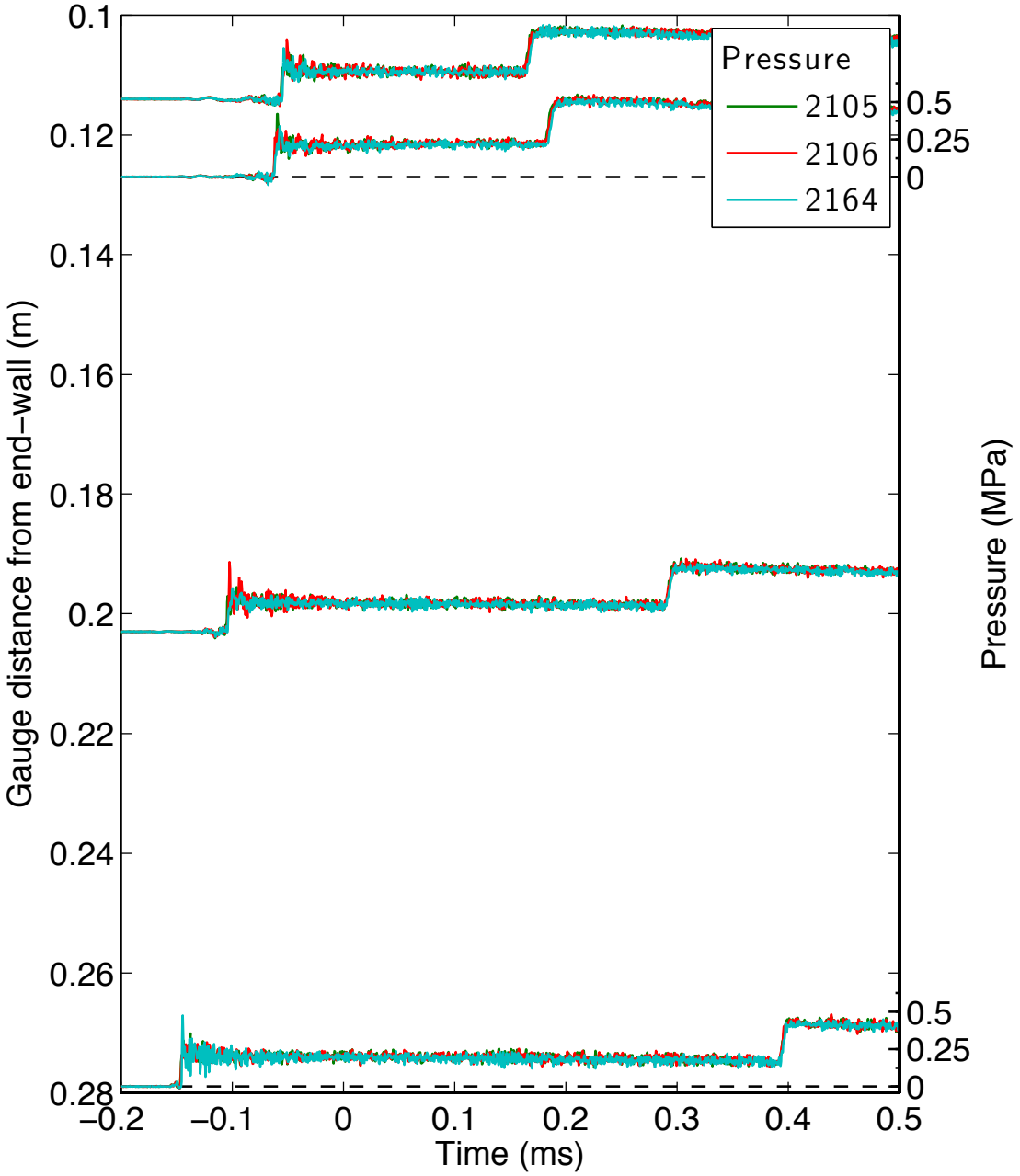

Figure E.57: Pressure traces for a detonation in stoichiometric hydrogen-oxygen with 50% argon dilution at fill pressure 10 kPa, part 2.

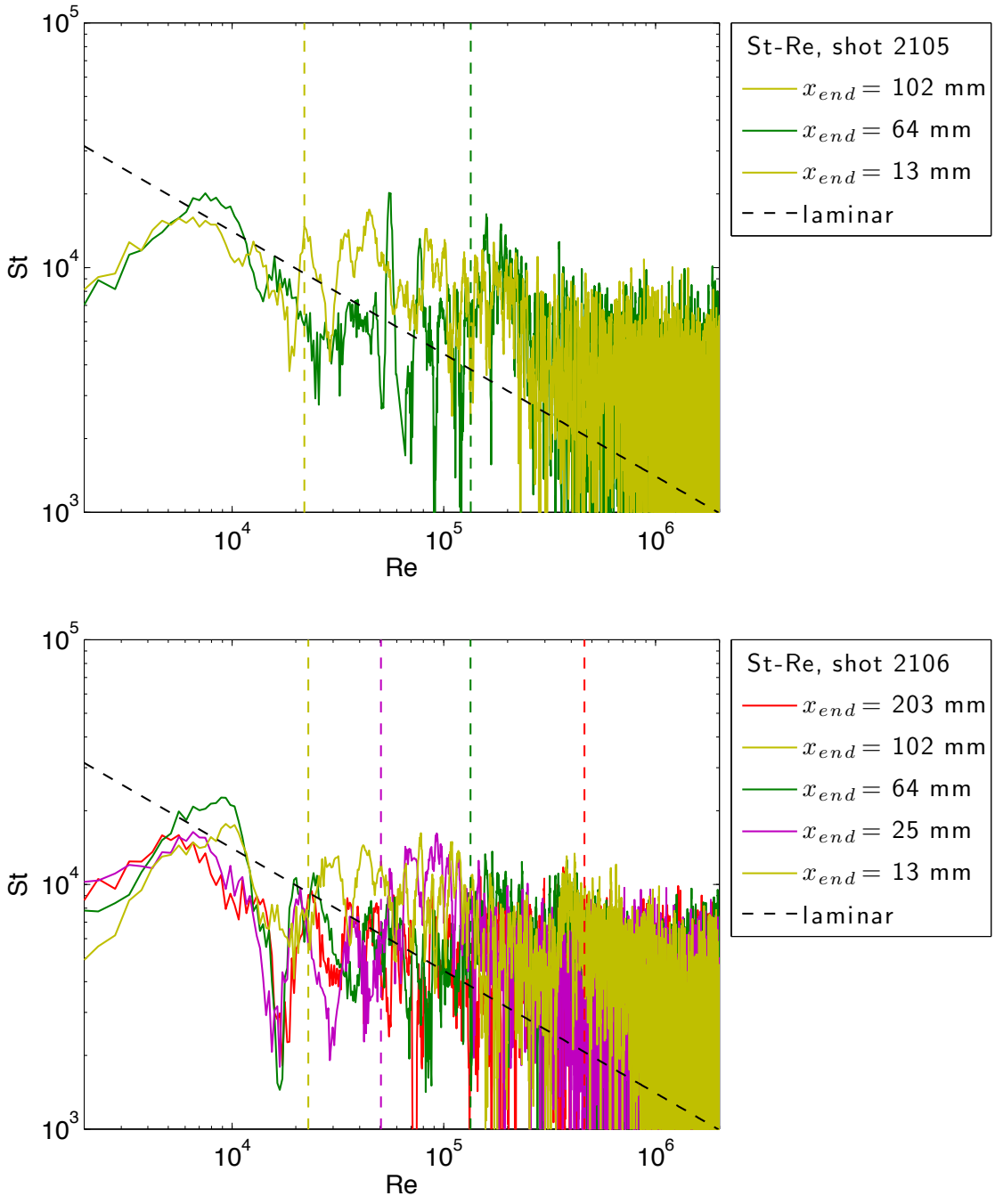

Figure E.58: Stanton-Reynolds number traces from shot 2106, a detonation in stoichiometric hydrogen-oxygen with 50% argon dilution at fill pressure 10 kPa. The dashed vertical lines represent the arrival of the reflected shock wave.

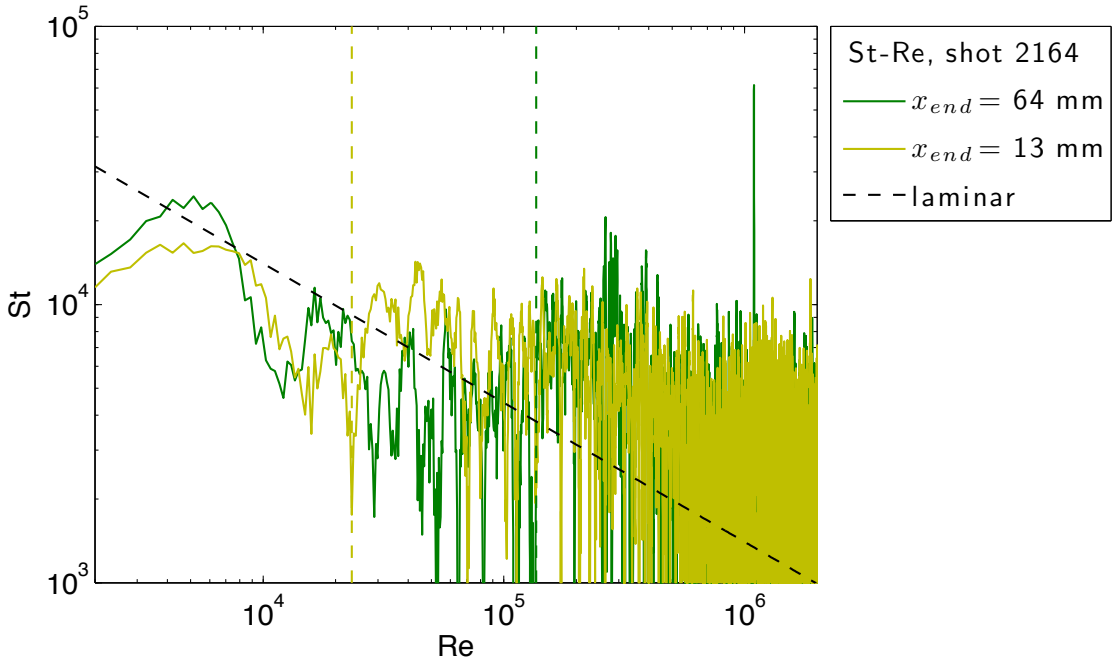

Figure E.59: Stanton-Reynolds number traces from shot 2164, a detonation in stoichiometric hydrogen-oxygen with 50% argon dilution at fill pressure 10 kPa. The dashed vertical lines represent the arrival of the reflected shock wave.

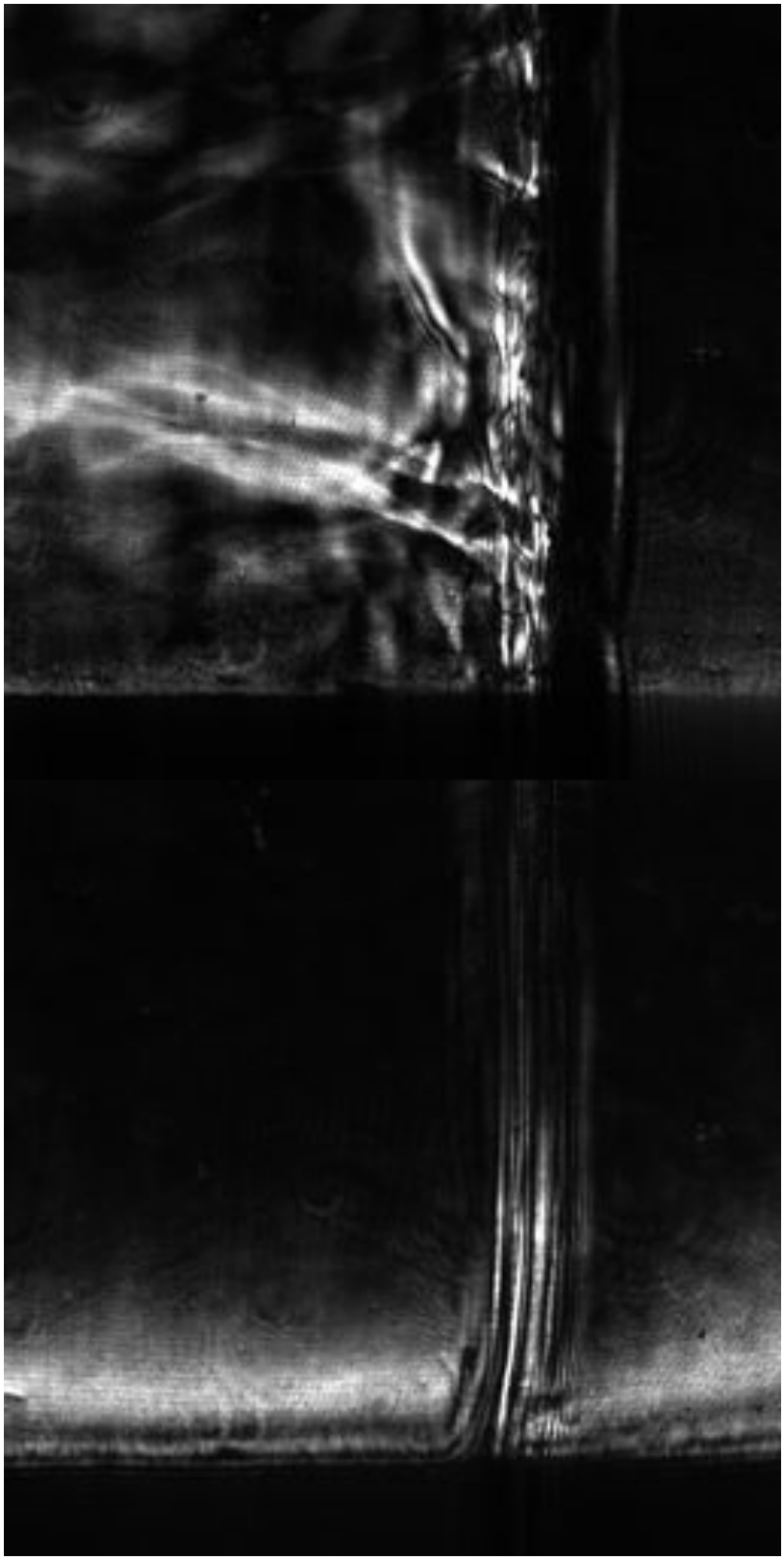

Figure E.60: Focused schlieren image of shot 2106. The field of view is approximately 14 mm wide.

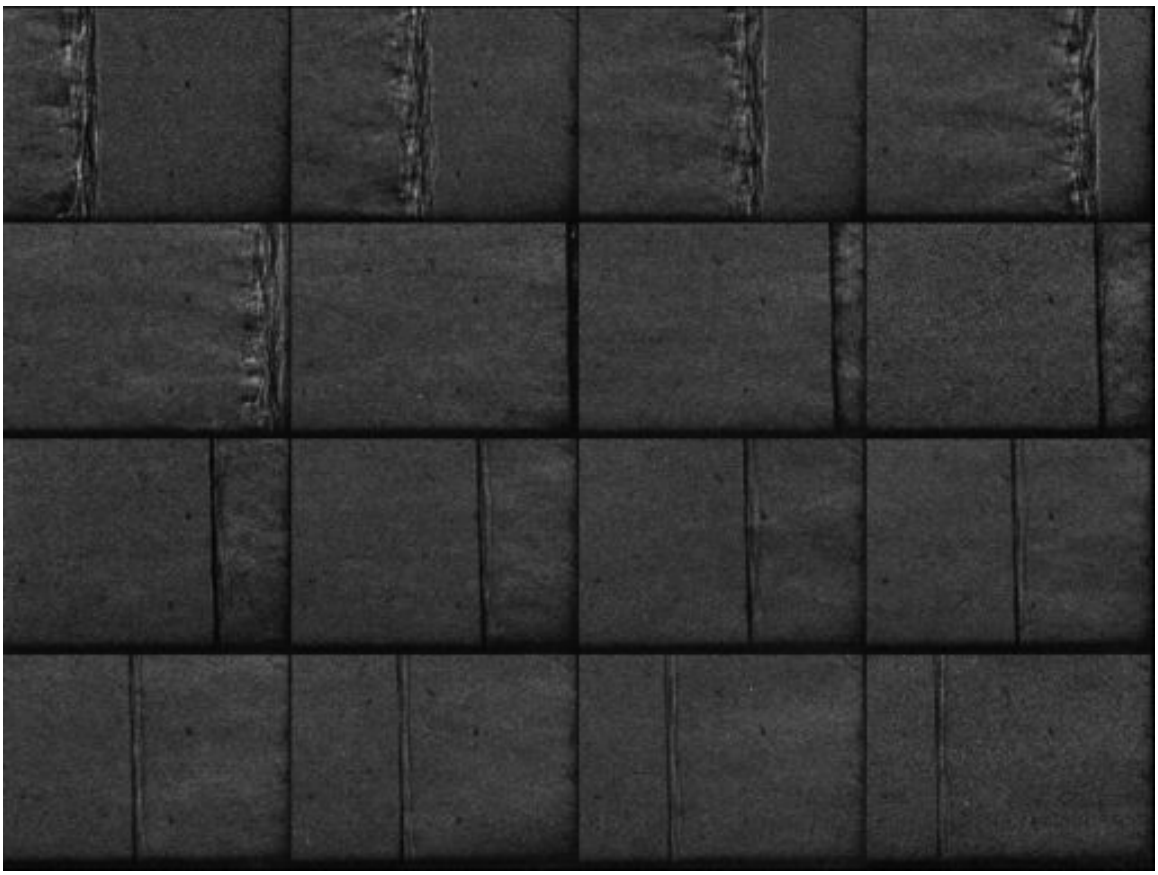

Figure E.61: Unfocused schlieren image of shot 2164. The field of view is approximately 30 mm wide.

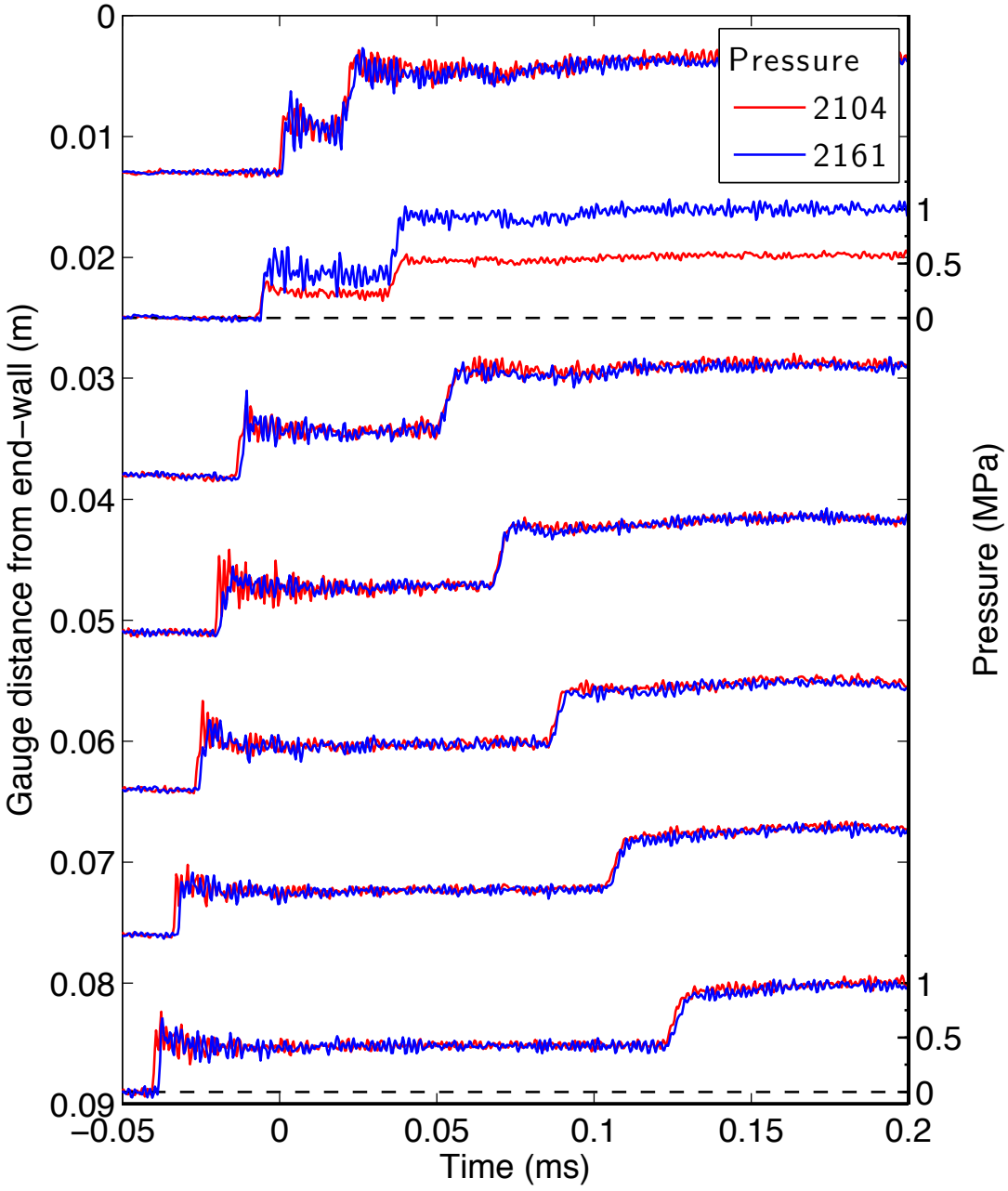

Figure E.62: Pressure traces for a detonation in stoichiometric hydrogen-oxygen with 50% argon dilution at fill pressure 25 kPa, part 1.

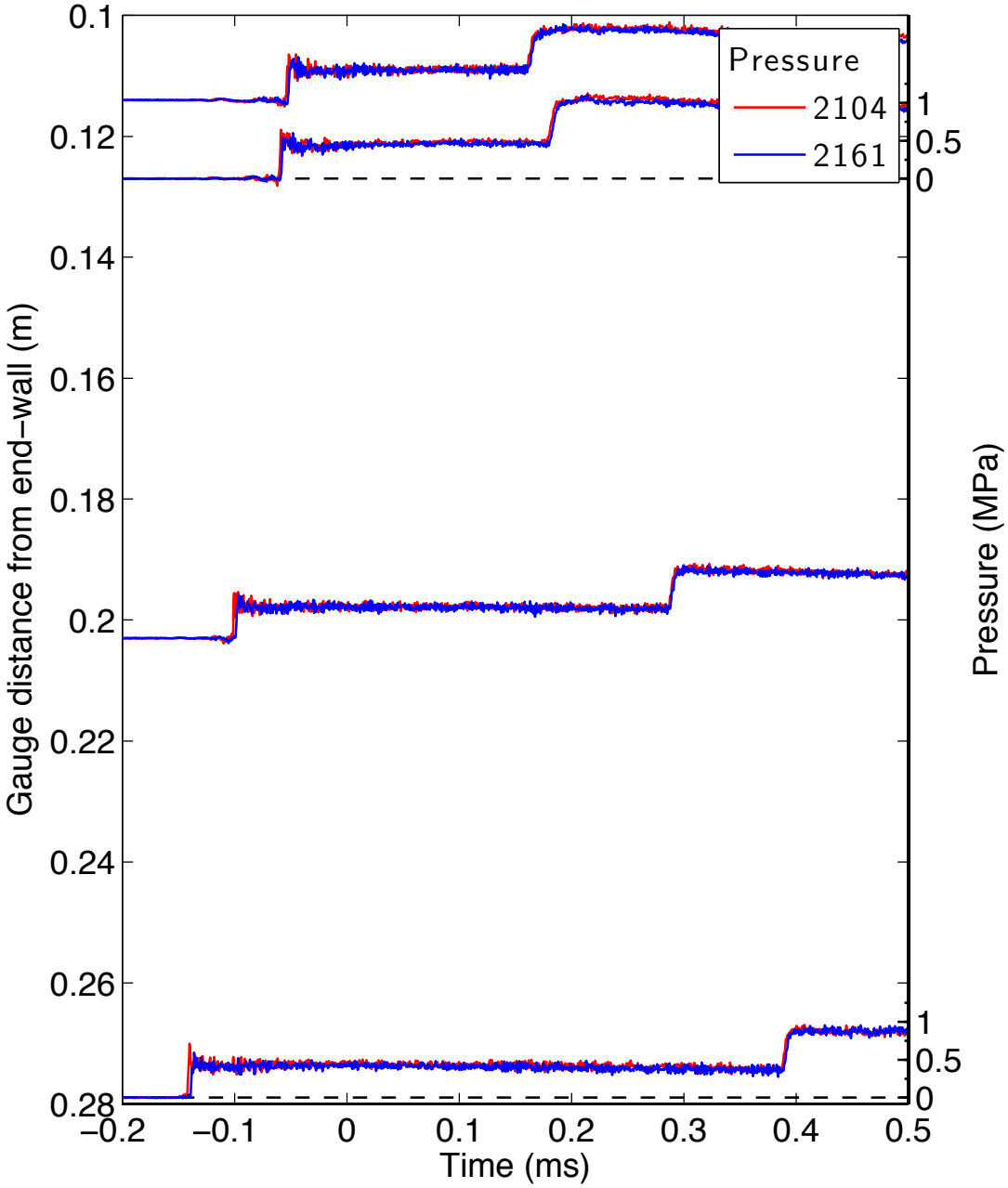

Figure E.63: Pressure traces for a detonation in stoichiometric hydrogen-oxygen with 50% argon dilution at fill pressure 25 kPa, part 2.

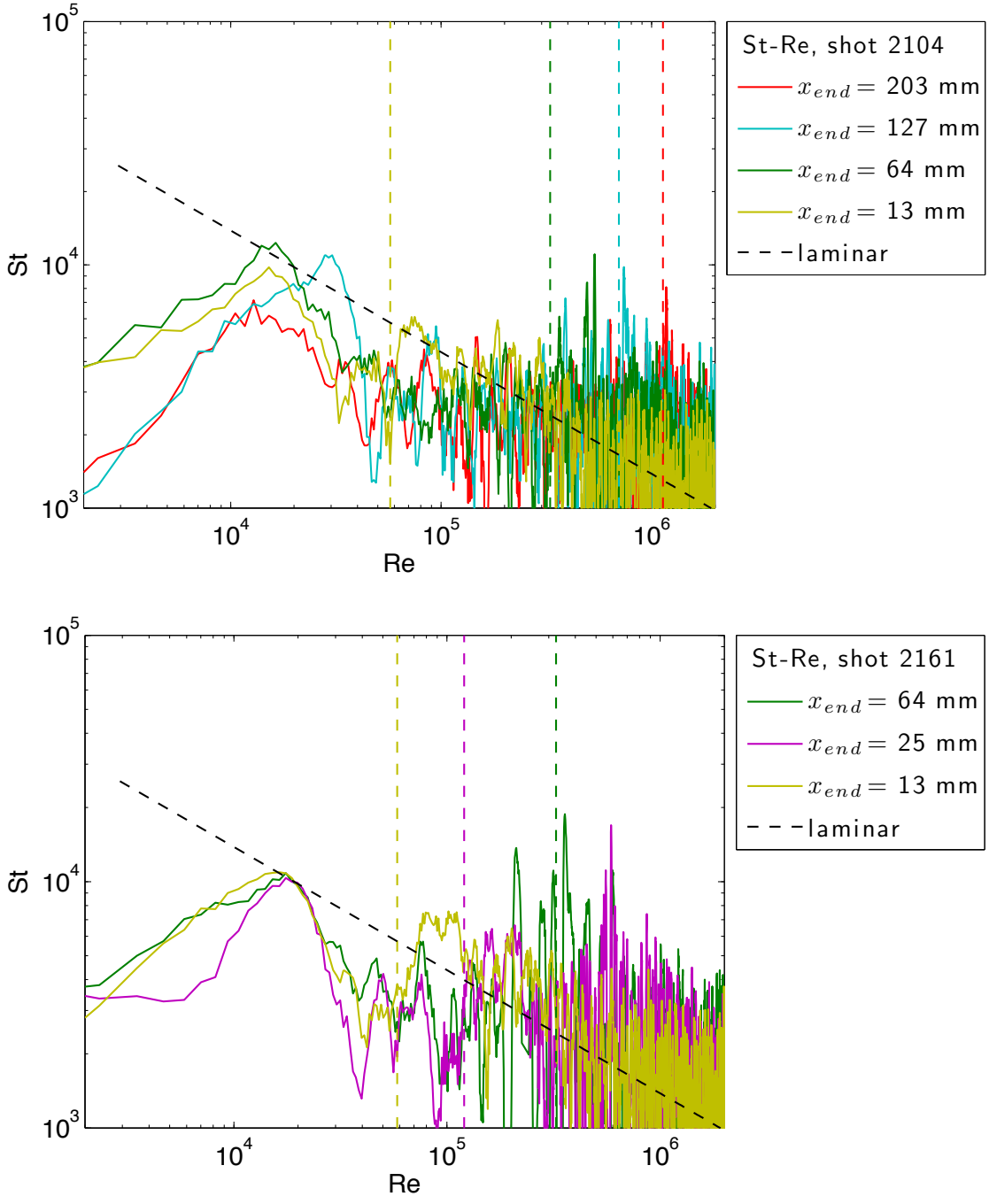

Figure E.64: Stanton-Reynolds number traces from shot 2161, a detonation in stoichiometric hydrogen-oxygen with 50% argon dilution at fill pressure 25 kPa. The dashed vertical lines represent the arrival of the reflected shock wave.

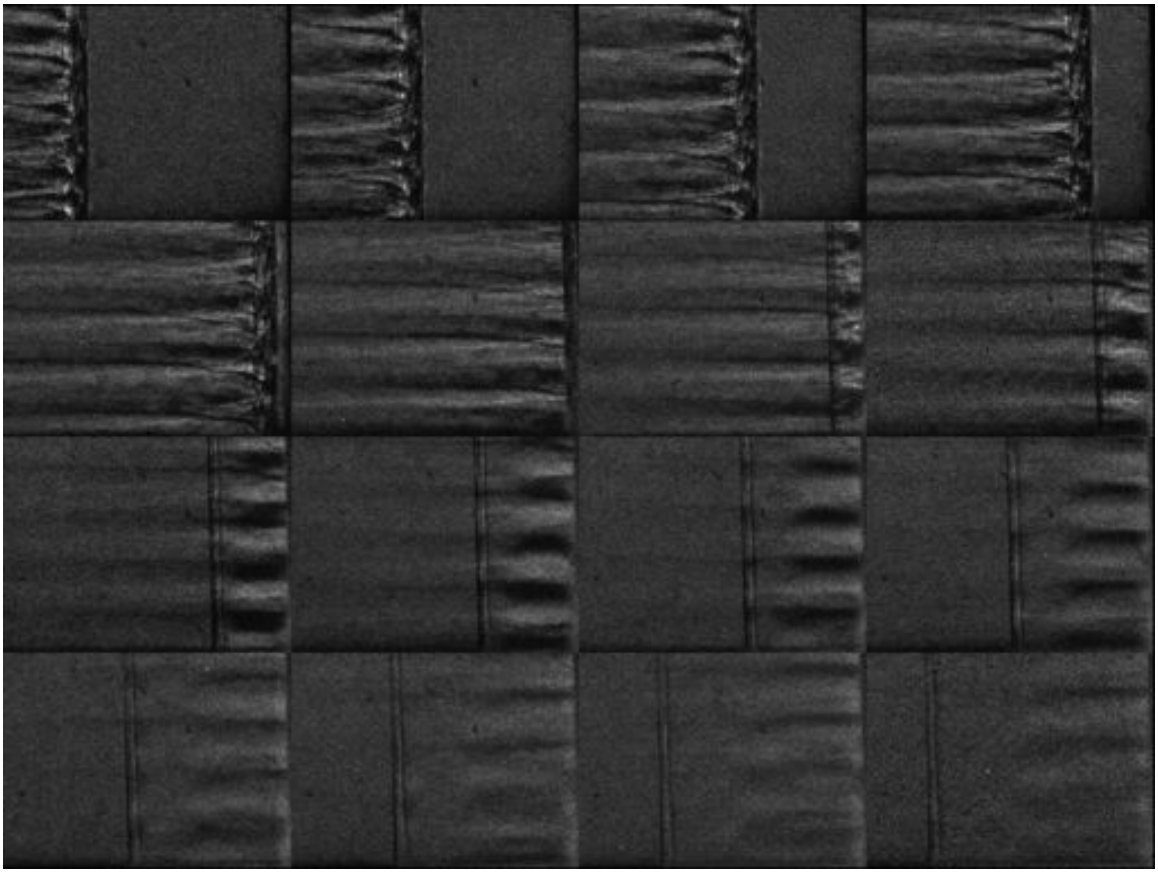

Figure E.65: Unfocused schlieren image of shot 2161. The field of view is approximately 30 mm wide.

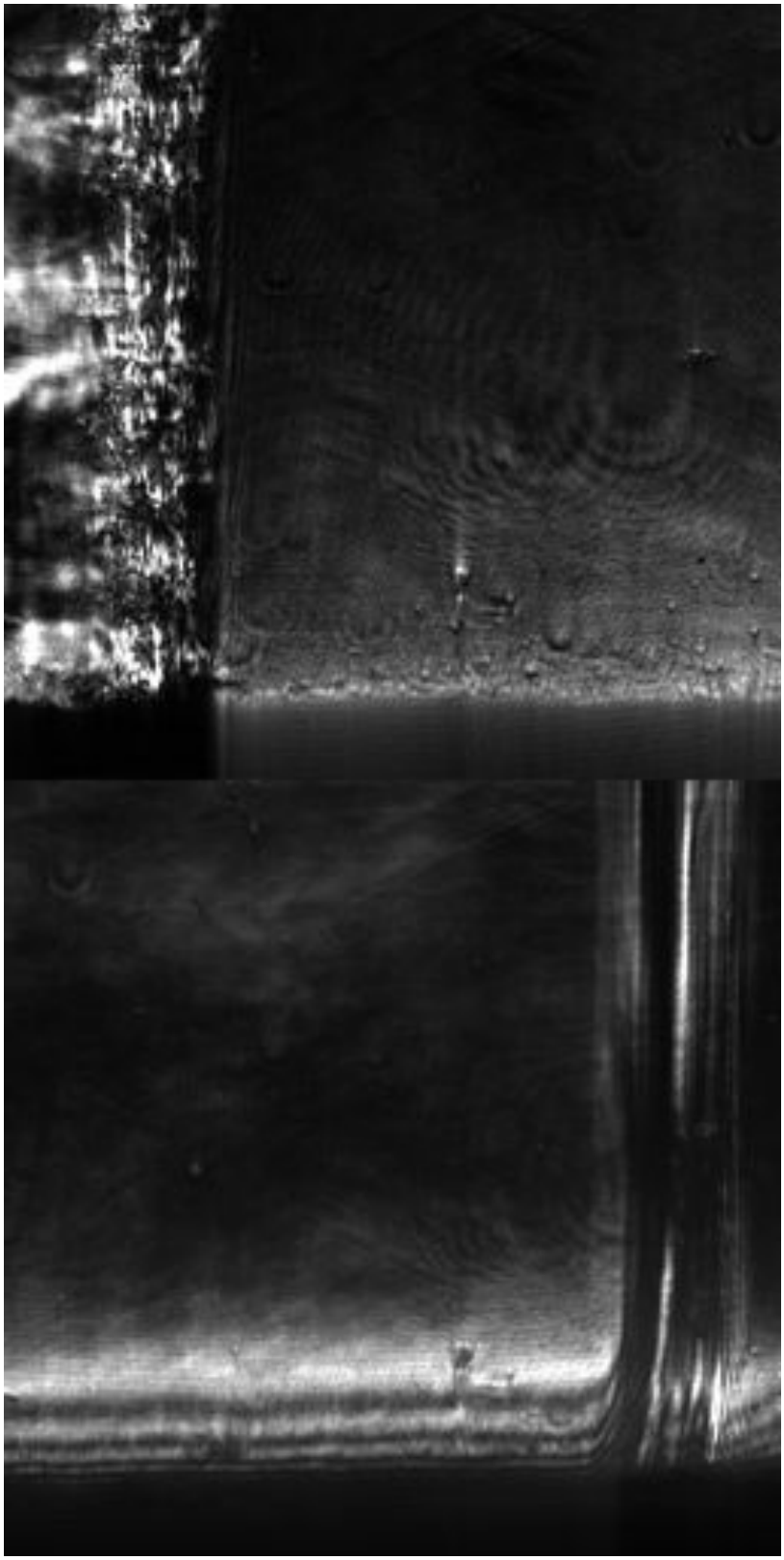

Figure E.66: Focused schlieren image of shot 2104. The field of view is approximately 14 mm wide.

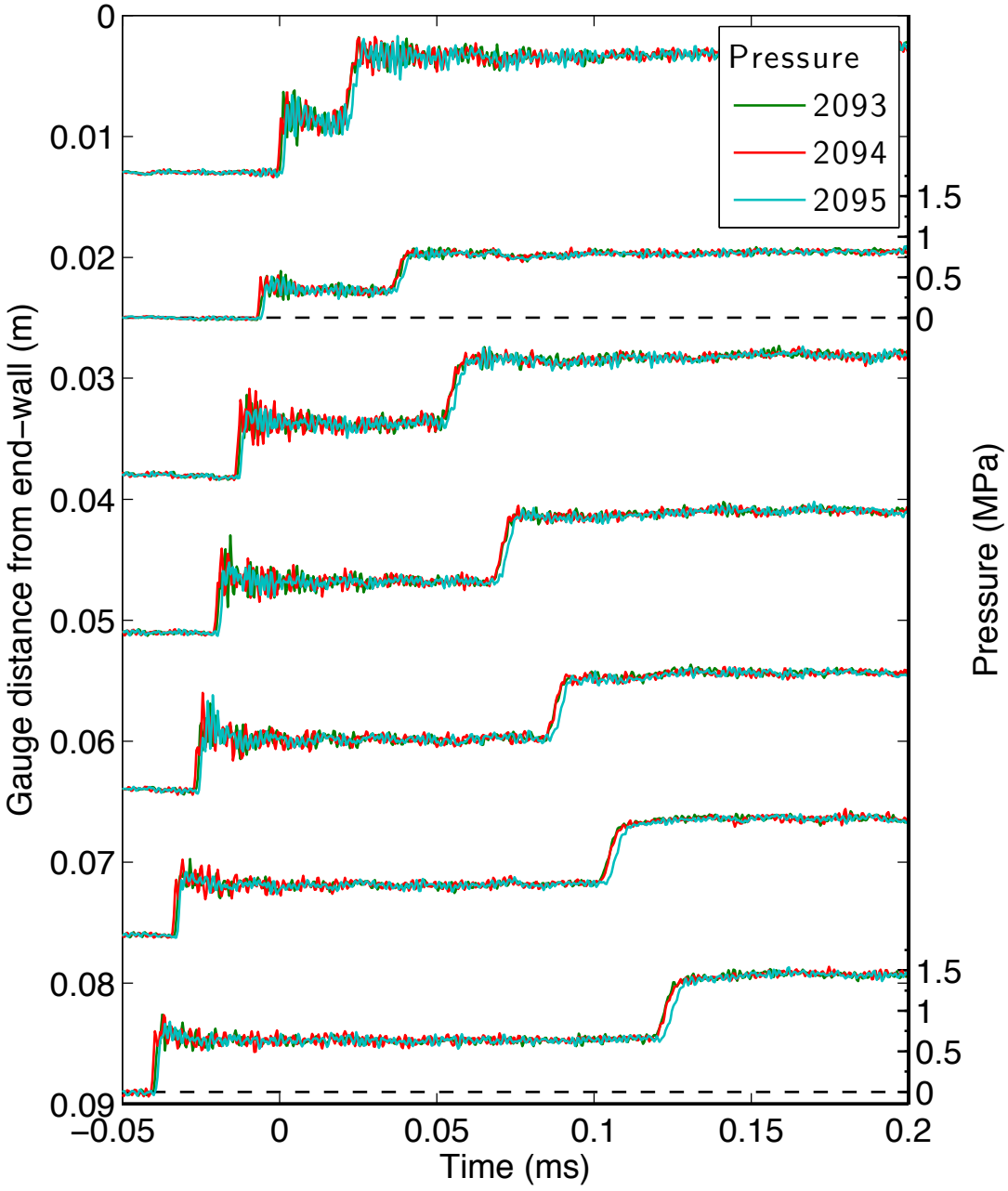

Figure E.67: Pressure traces for a detonation in stoichiometric hydrogen-oxygen with 50% argon dilution at fill pressure 40 kPa, part 1.

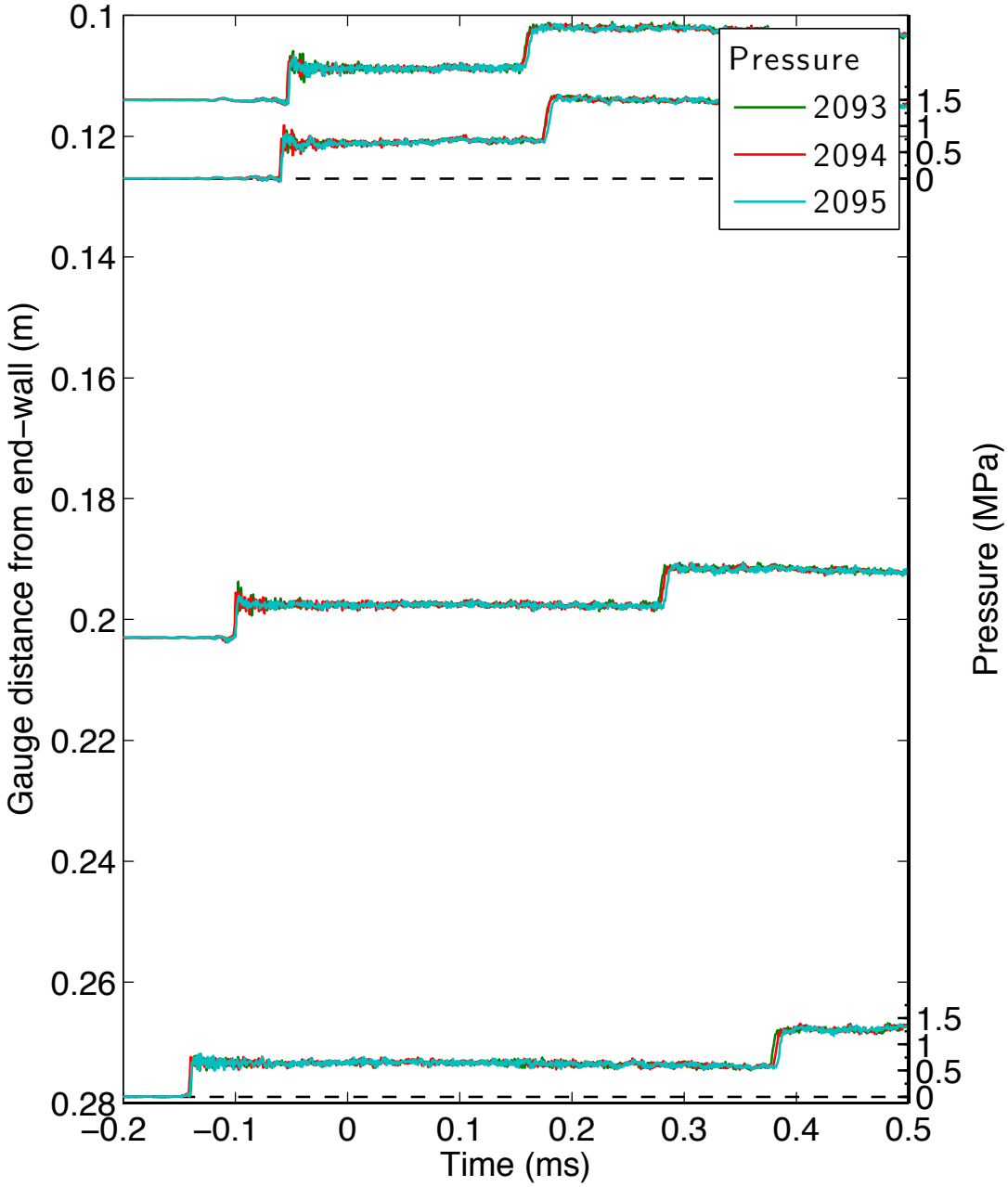

Figure E.68: Pressure traces for a detonation in stoichiometric hydrogen-oxygen with 50% argon dilution at fill pressure 40 kPa, part 2.

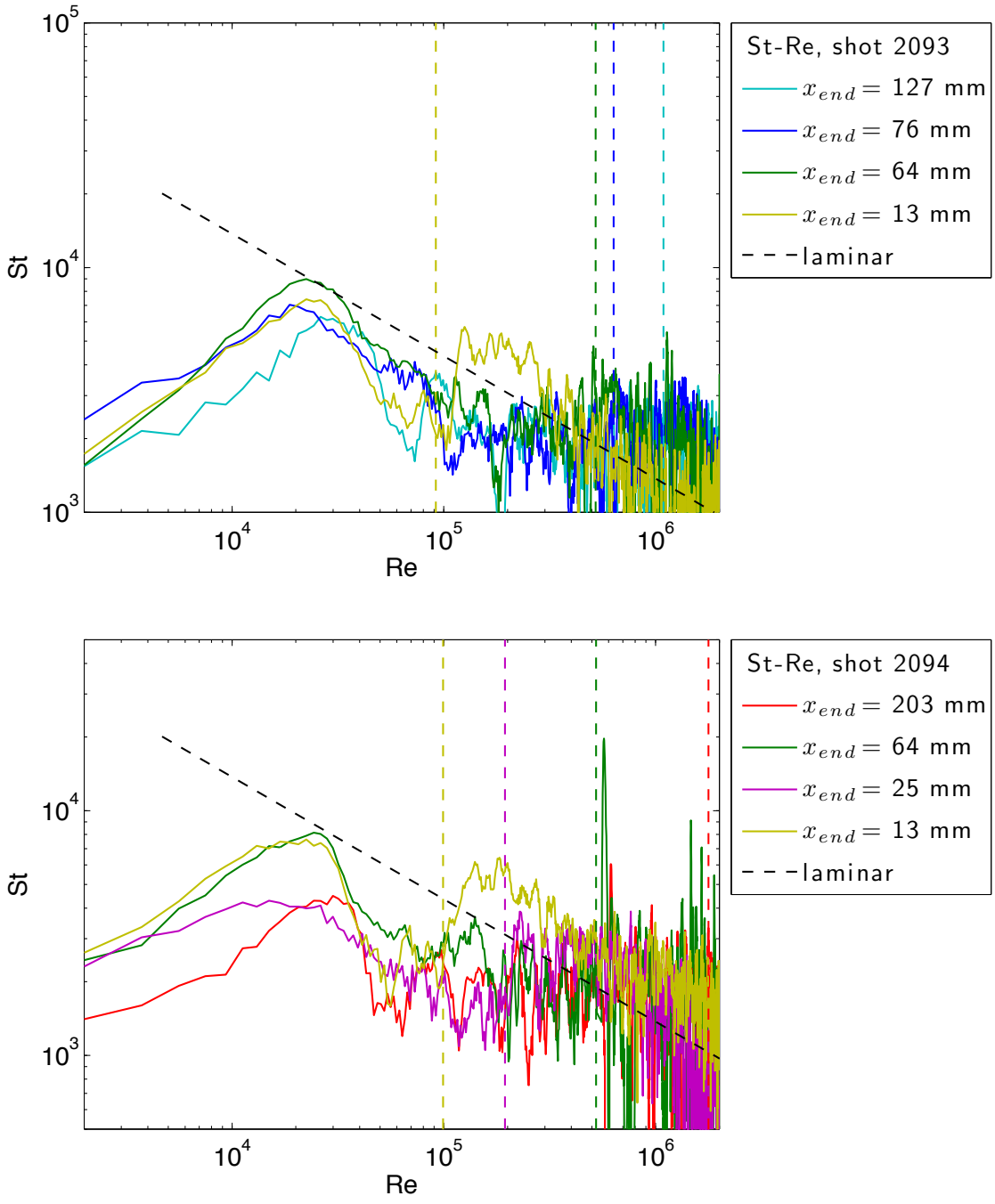

Figure E.69: Stanton-Reynolds number traces from shot 2094, a detonation in stoichiometric hydrogen-oxygen with 50% argon dilution at fill pressure 40 kPa. The dashed vertical lines represent the arrival of the reflected shock wave.

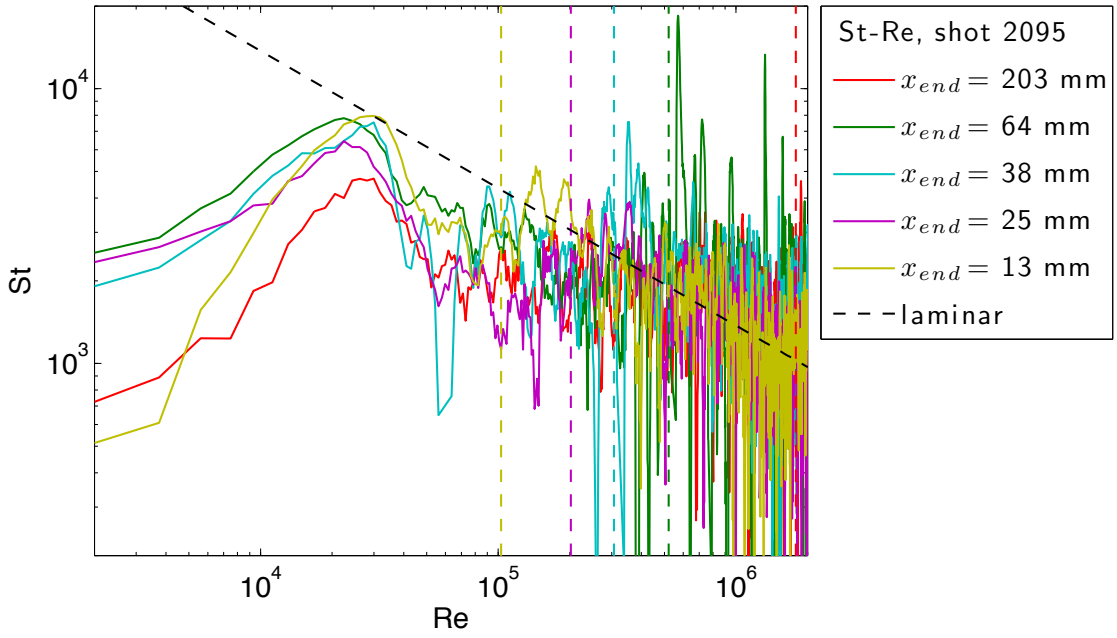

Figure E.70: Stanton-Reynolds number traces from shot 2095, a detonation in stoichiometric hydrogen-oxygen with 50% argon dilution at fill pressure 40 kPa. The dashed vertical lines represent the arrival of the reflected shock wave.

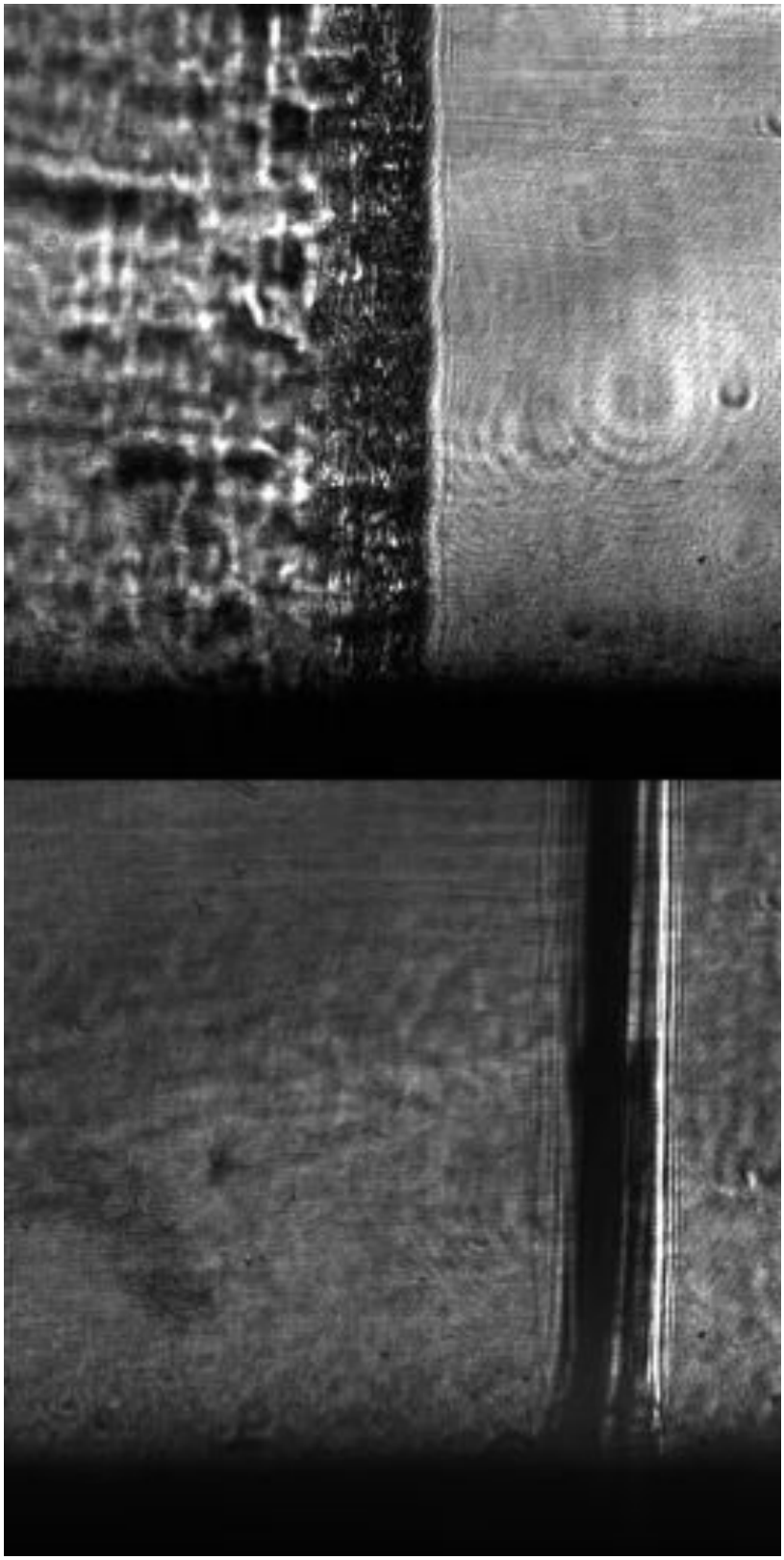

Figure E.71: Focused schlieren image of shot 2095. The field of view is approximately 14 mm wide.

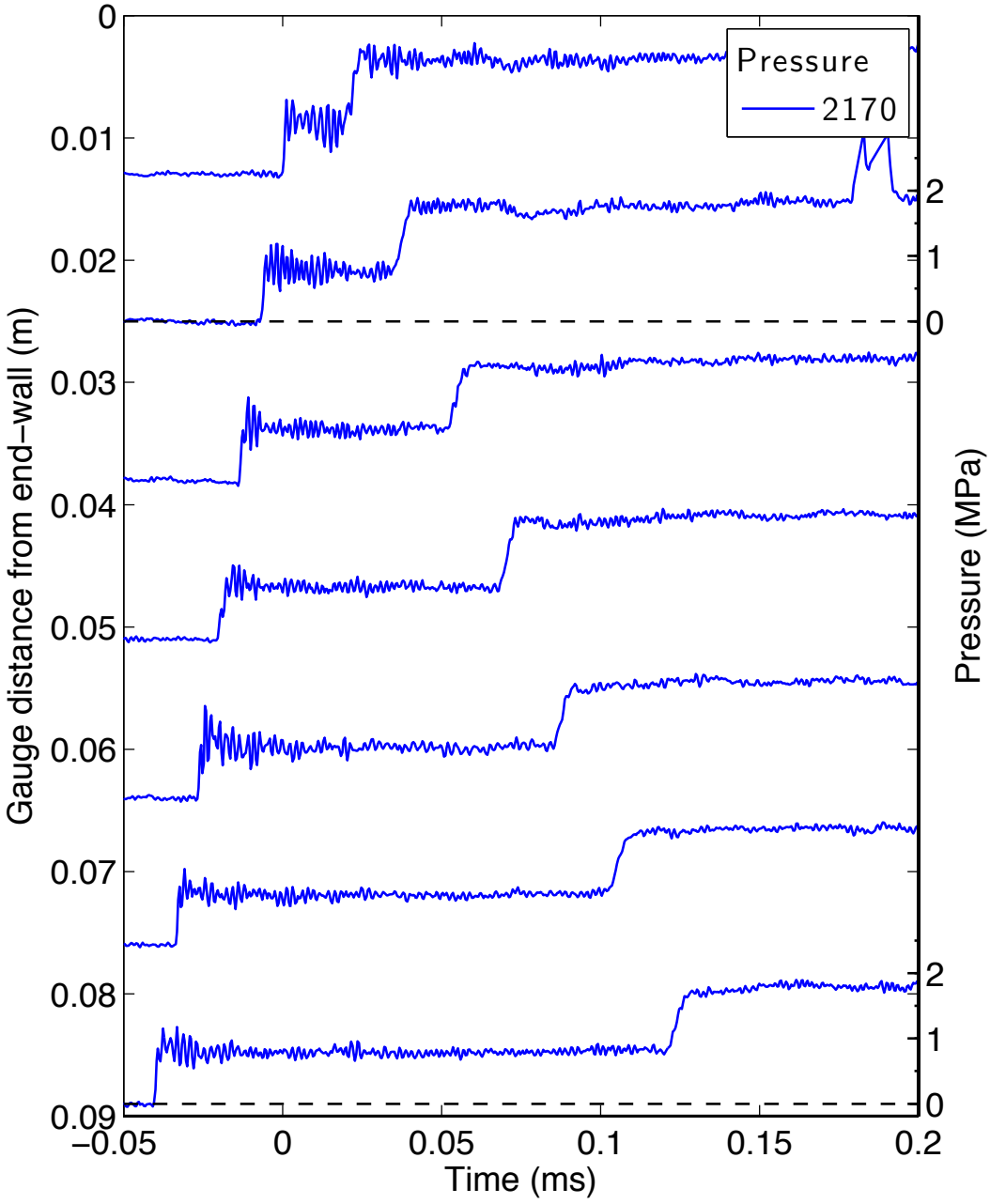

Figure E.72: Pressure traces for a detonation in stoichiometric hydrogen-oxygen with 50% argon dilution at fill pressure 50 kPa, part 1.

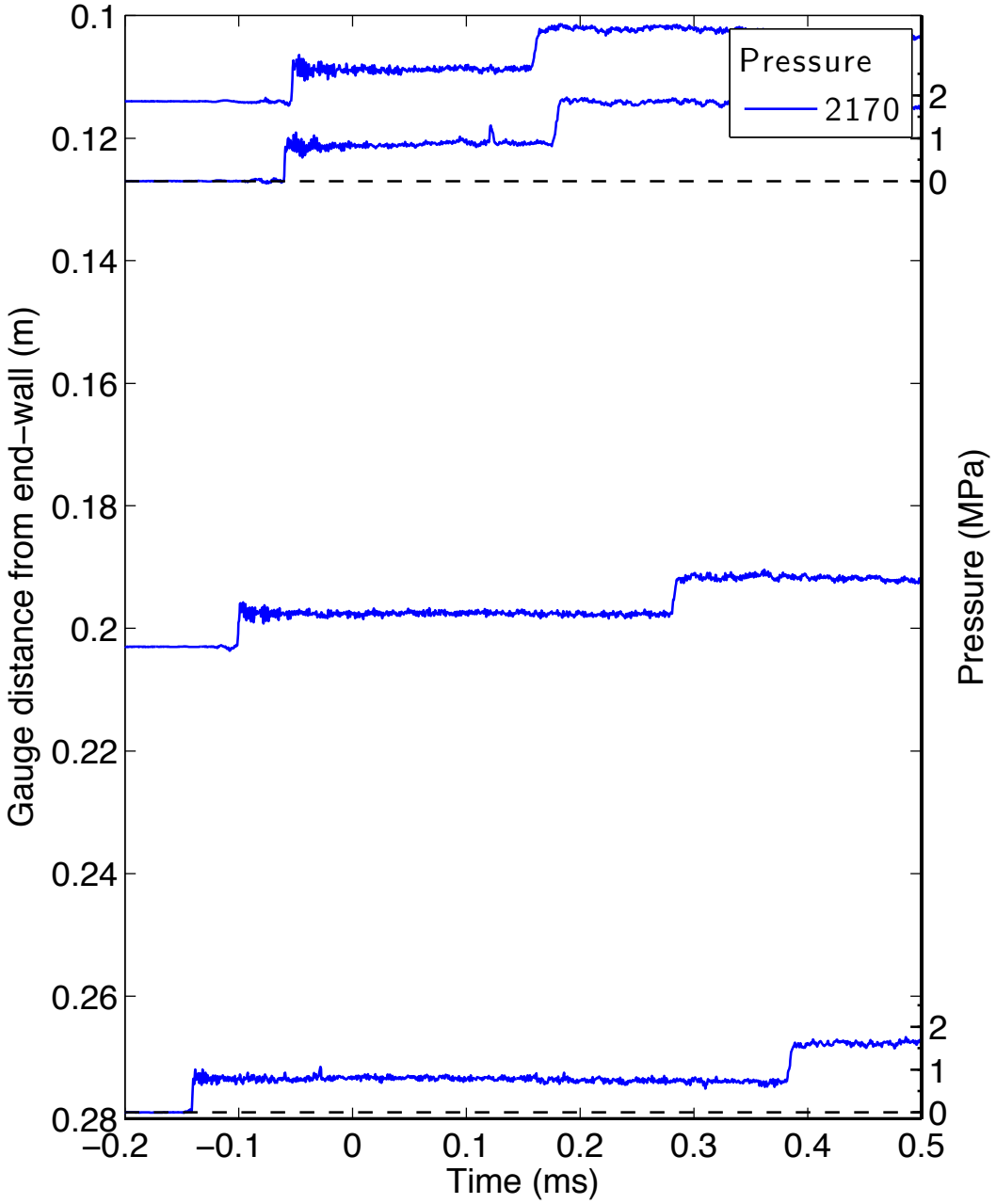

Figure E.73: Pressure traces for a detonation in stoichiometric hydrogen-oxygen with 50% argon dilution at fill pressure 50 kPa, part 2.

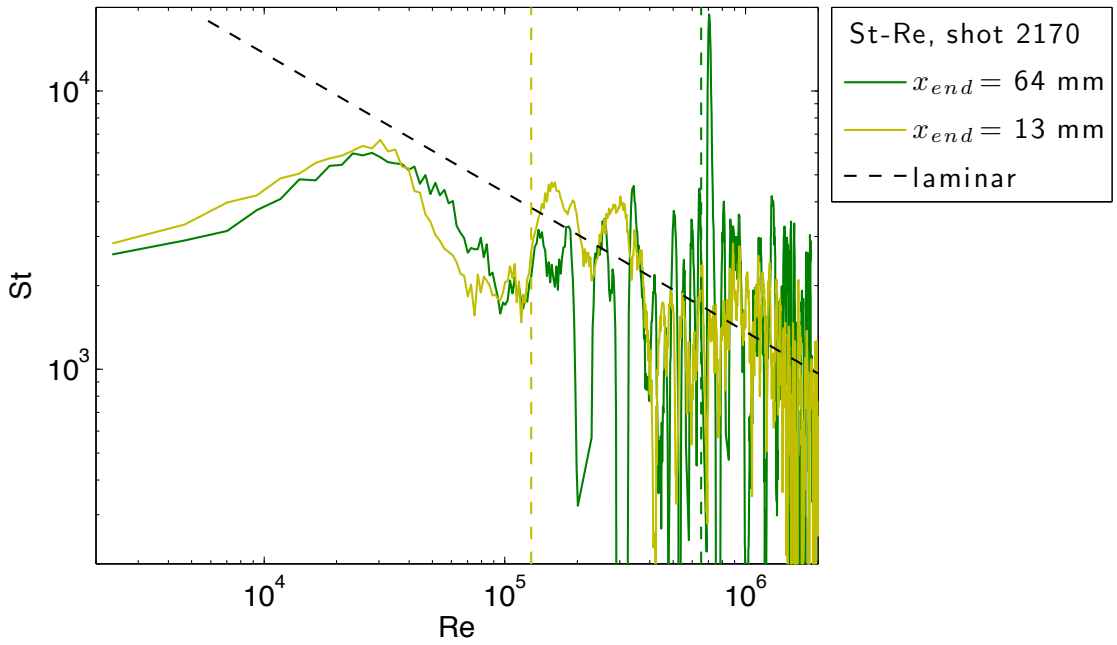

Figure E.74: Stanton-Reynolds number traces from shot 2170, a detonation in stoichiometric hydrogen-oxygen with 50% argon dilution at fill pressure 50 kPa. The dashed vertical lines represent the arrival of the reflected shock wave.

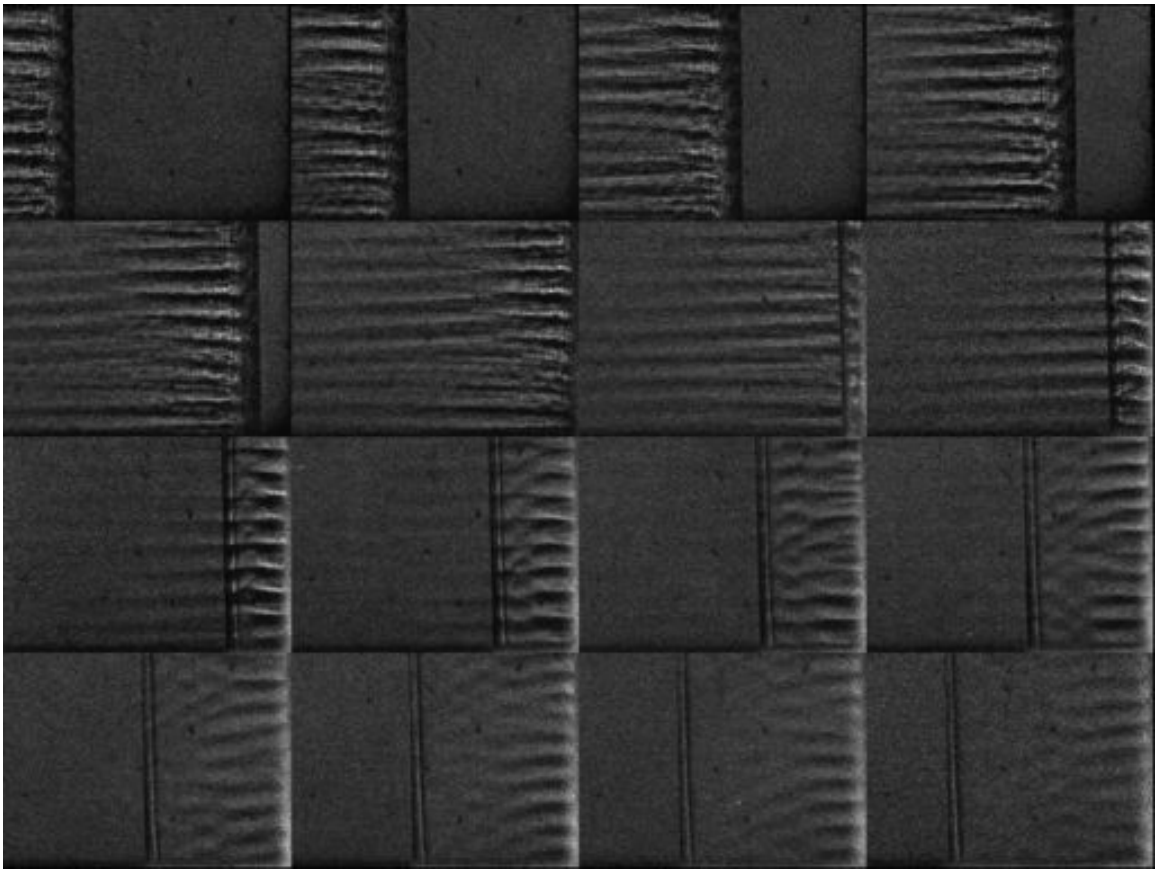

Figure E.75: Unfocused schlieren image of shot 2170. The field of view is approximately 30 mm wide.

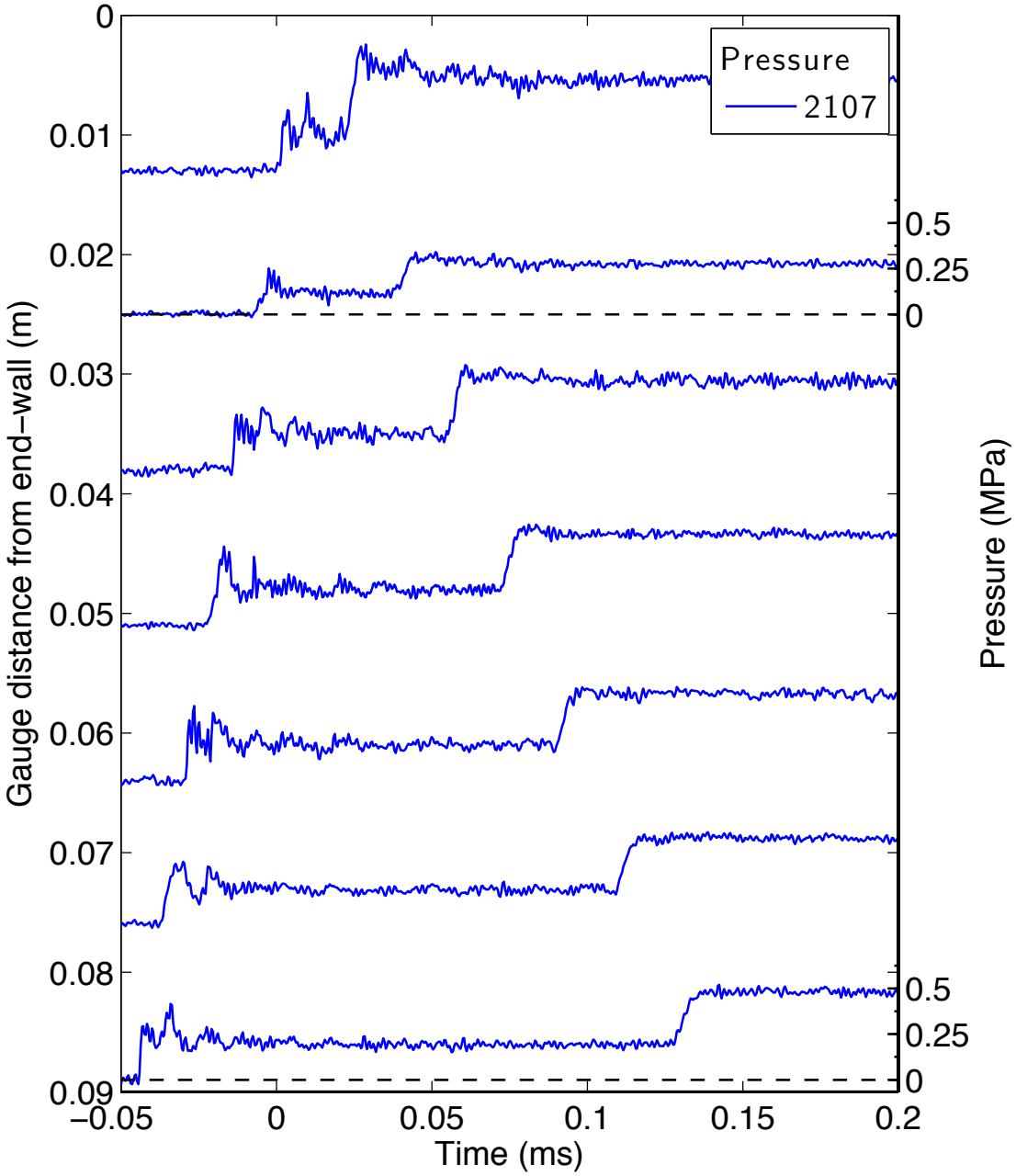

Figure E.76: Pressure traces for a detonation in stoichiometric hydrogen-oxygen with 67% argon dilution at fill pressure 10 kPa, part 1.

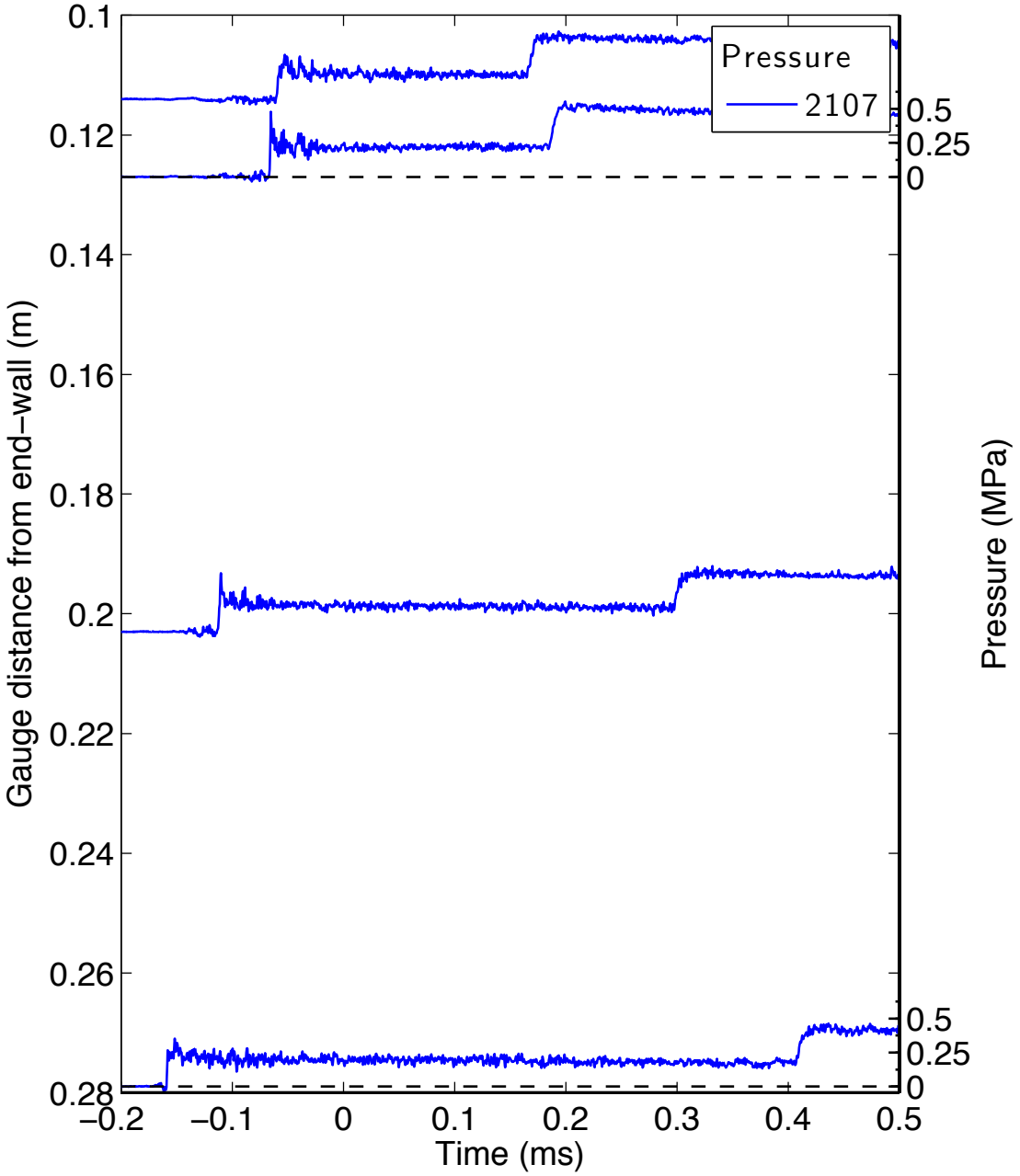

Figure E.77: Pressure traces for a detonation in stoichiometric hydrogen-oxygen with 67% argon dilution at fill pressure 10 kPa, part 2.

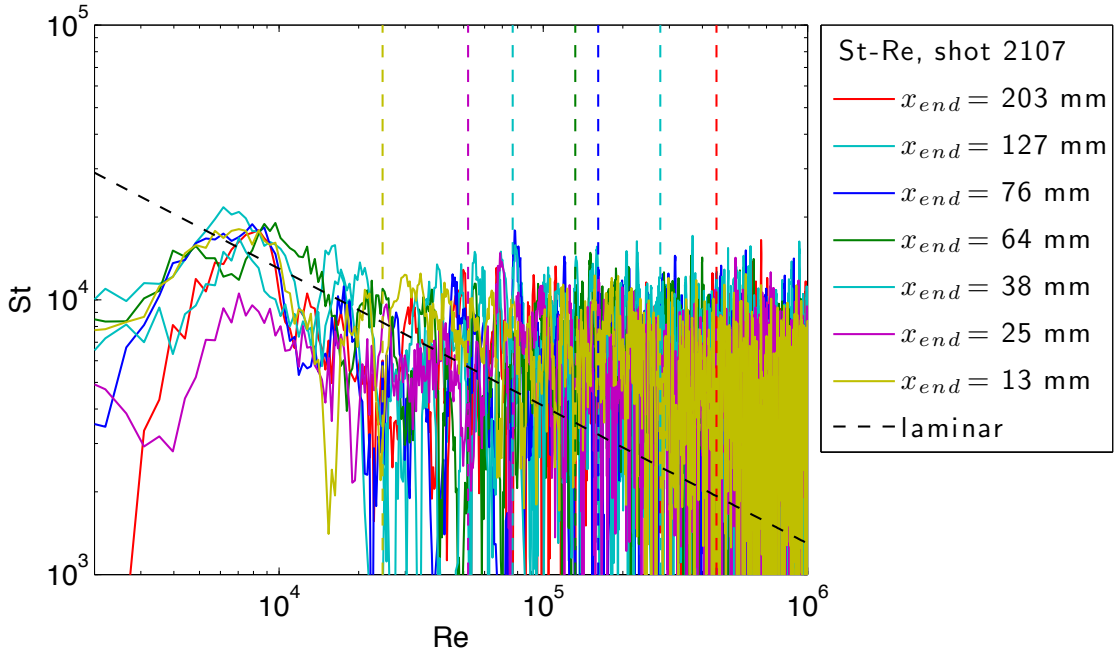

Figure E.78: Stanton-Reynolds number traces from shot 2107, a detonation in stoichiometric hydrogen-oxygen with 67% argon dilution at fill pressure 10 kPa. The dashed vertical lines represent the arrival of the reflected shock wave.

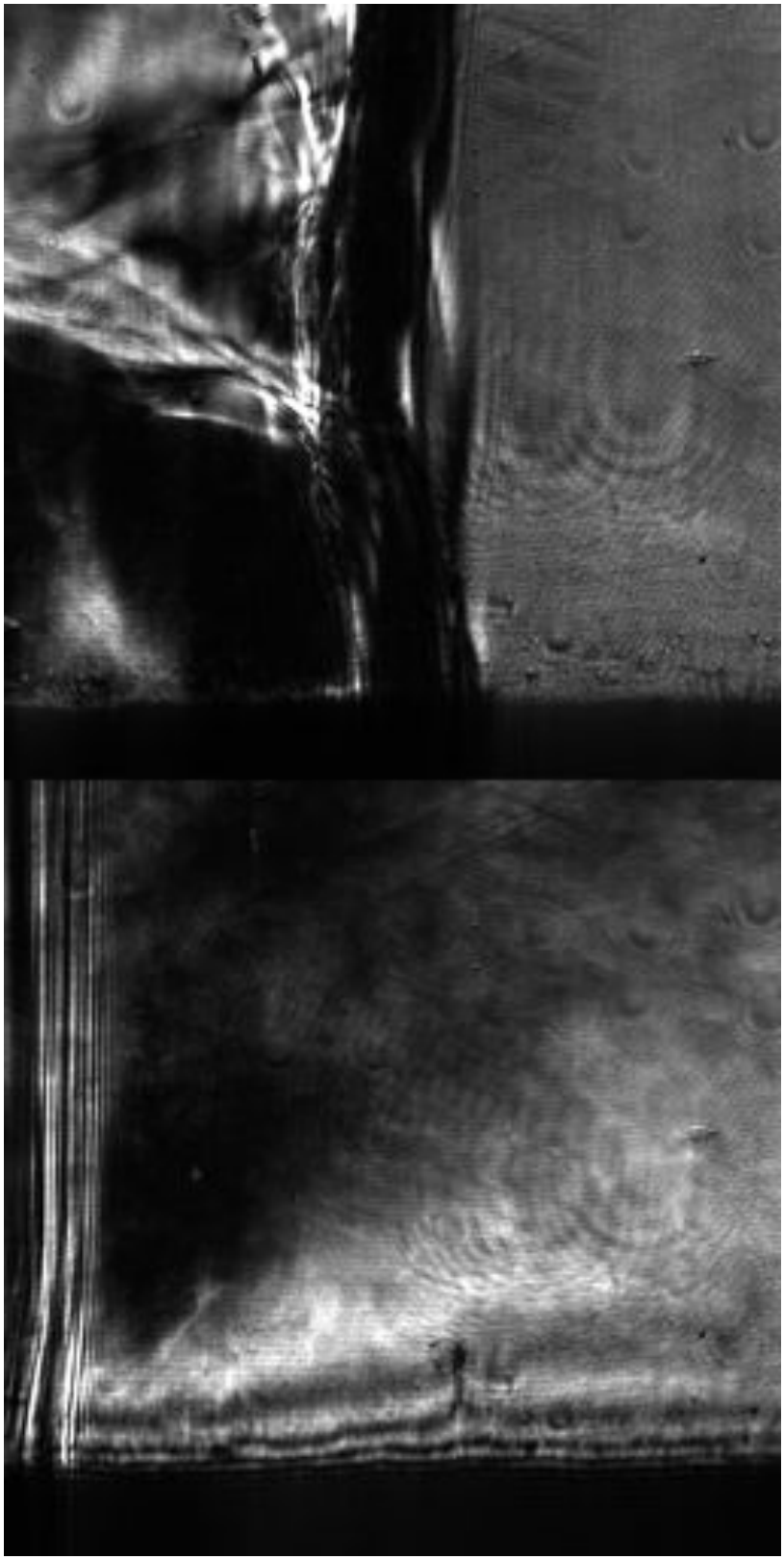

Figure E.79: Focused schlieren image of shot 2107. The field of view is approximately 14 mm wide.

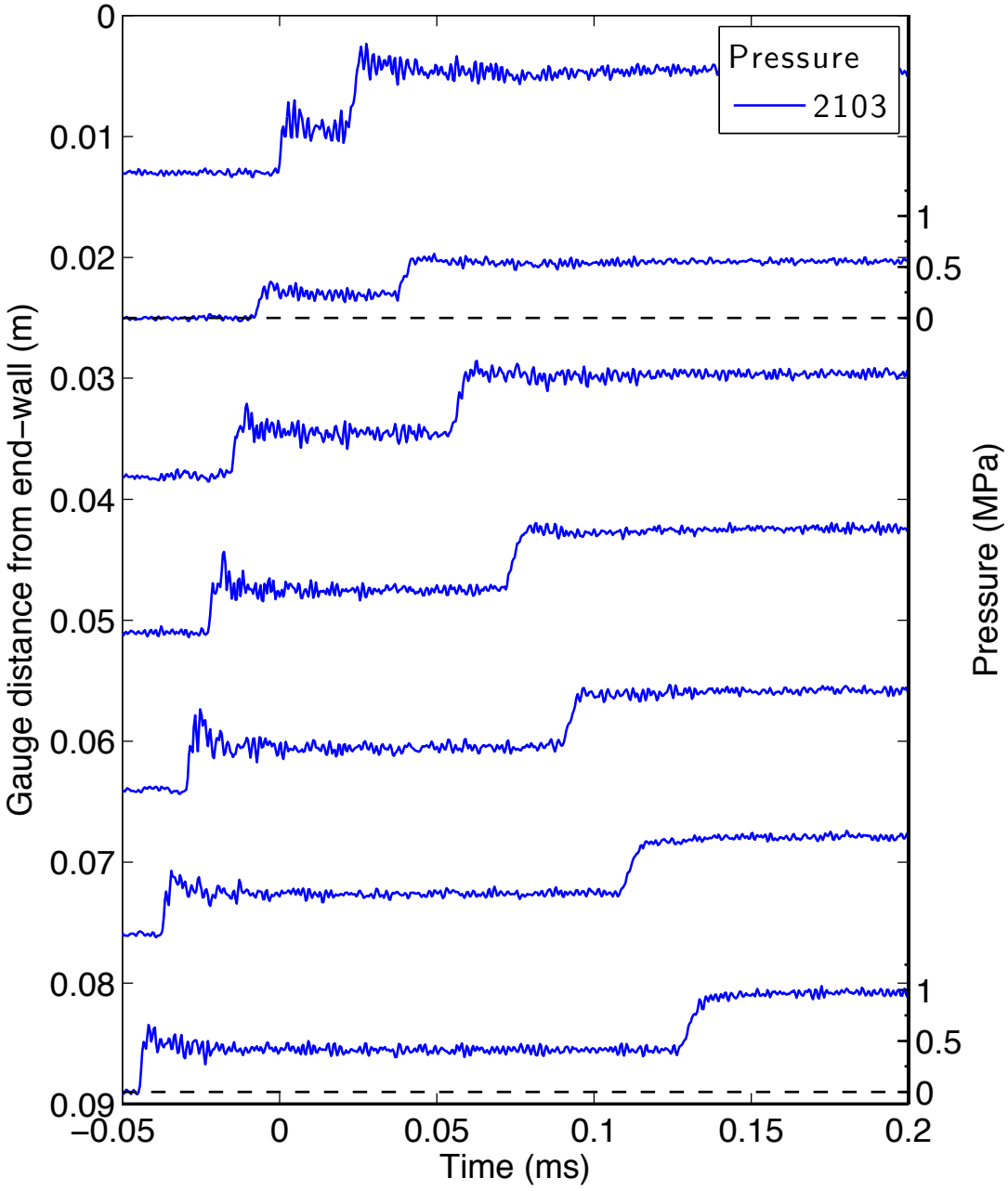

Figure E.80: Pressure traces for a detonation in stoichiometric hydrogen-oxygen with 67% argon dilution at fill pressure 25 kPa, part 1.

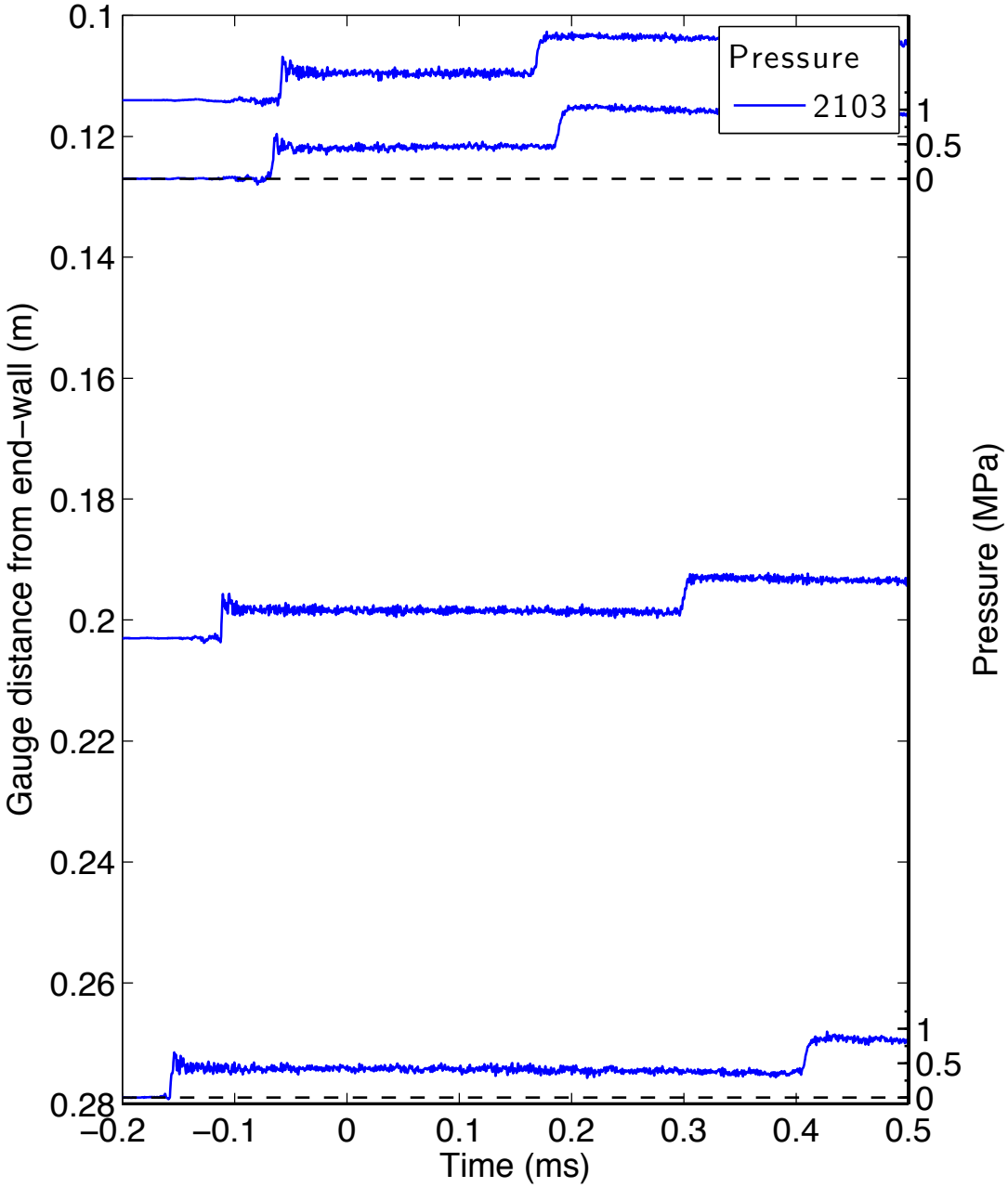

Figure E.81: Pressure traces for a detonation in stoichiometric hydrogen-oxygen with 67% argon dilution at fill pressure 25 kPa, part 2.

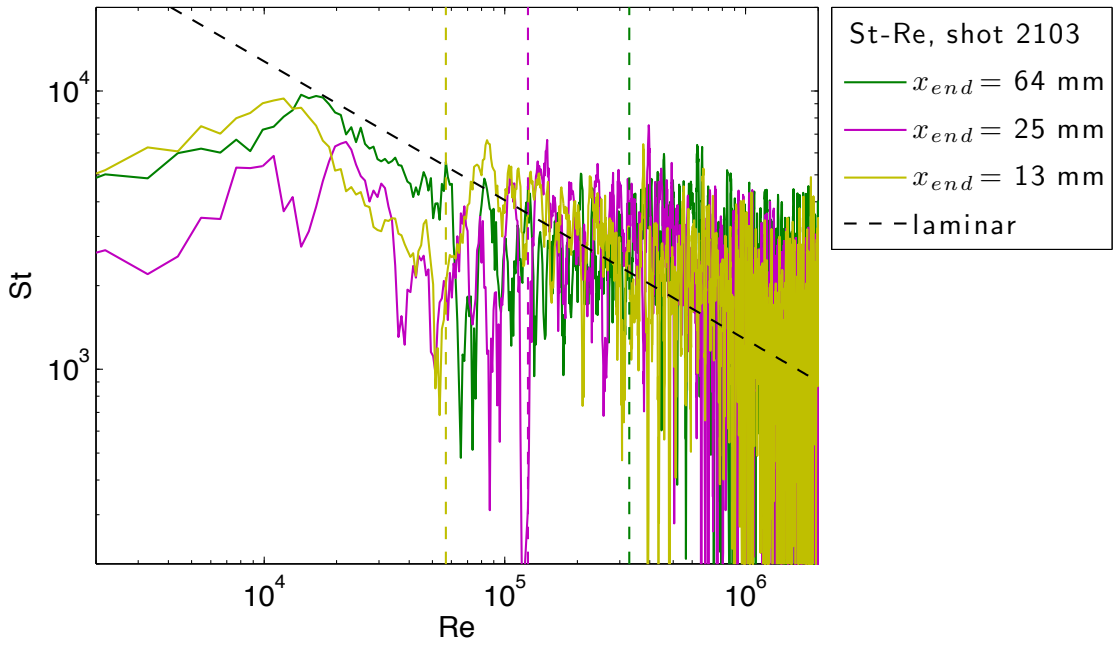

Figure E.82: Stanton-Reynolds number traces from shot 2103, a detonation in stoichiometric hydrogen-oxygen with 67% argon dilution at fill pressure 25 kPa. The dashed vertical lines represent the arrival of the reflected shock wave.

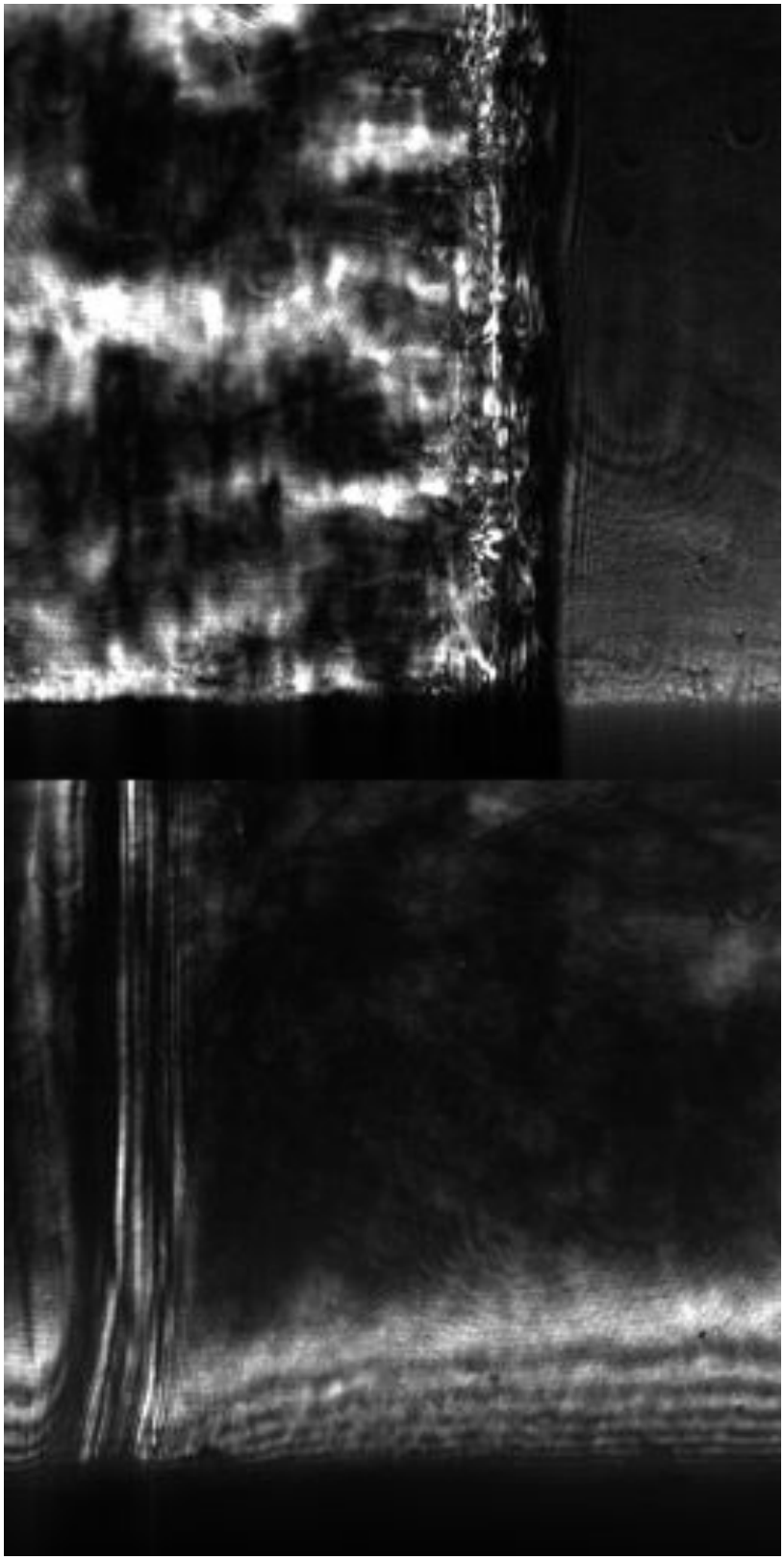

Figure E.83: Focused schlieren image of shot 2103. The field of view is approximately 14 mm wide.

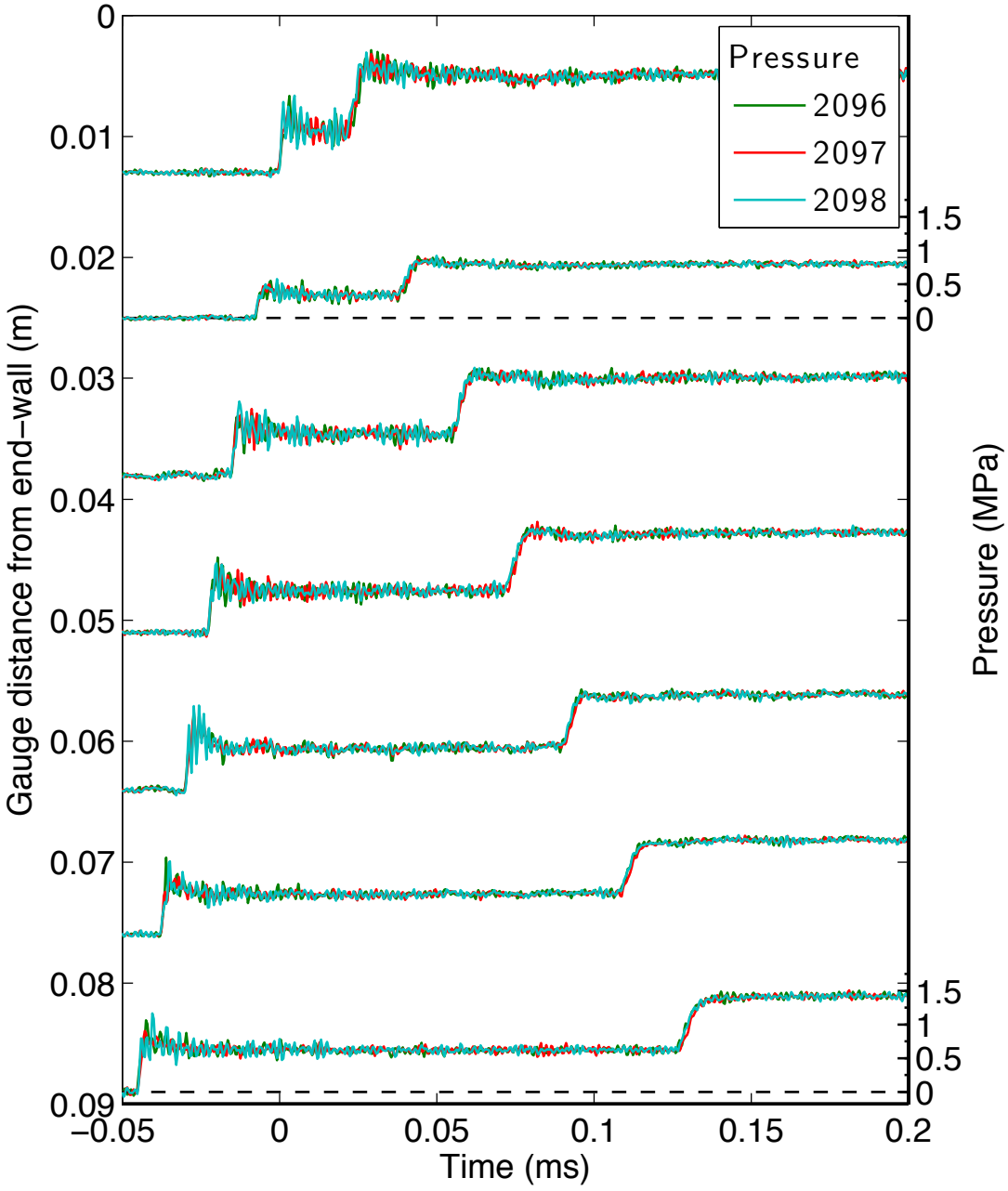

Figure E.84: Pressure traces for a detonation in stoichiometric hydrogen-oxygen with 67% argon dilution at fill pressure 40 kPa, part 1.

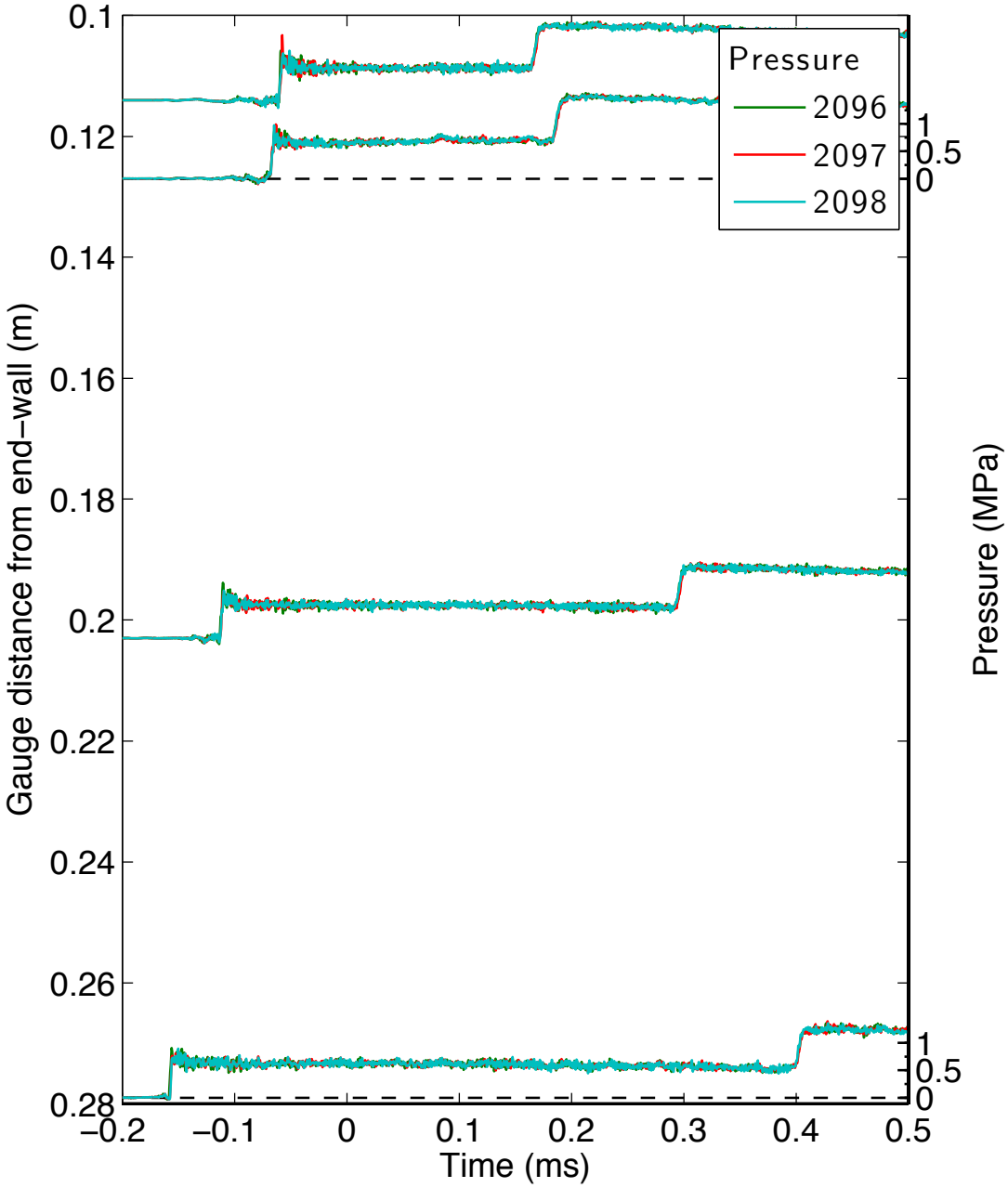

Figure E.85: Pressure traces for a detonation in stoichiometric hydrogen-oxygen with 67% argon dilution at fill pressure 40 kPa, part 2.

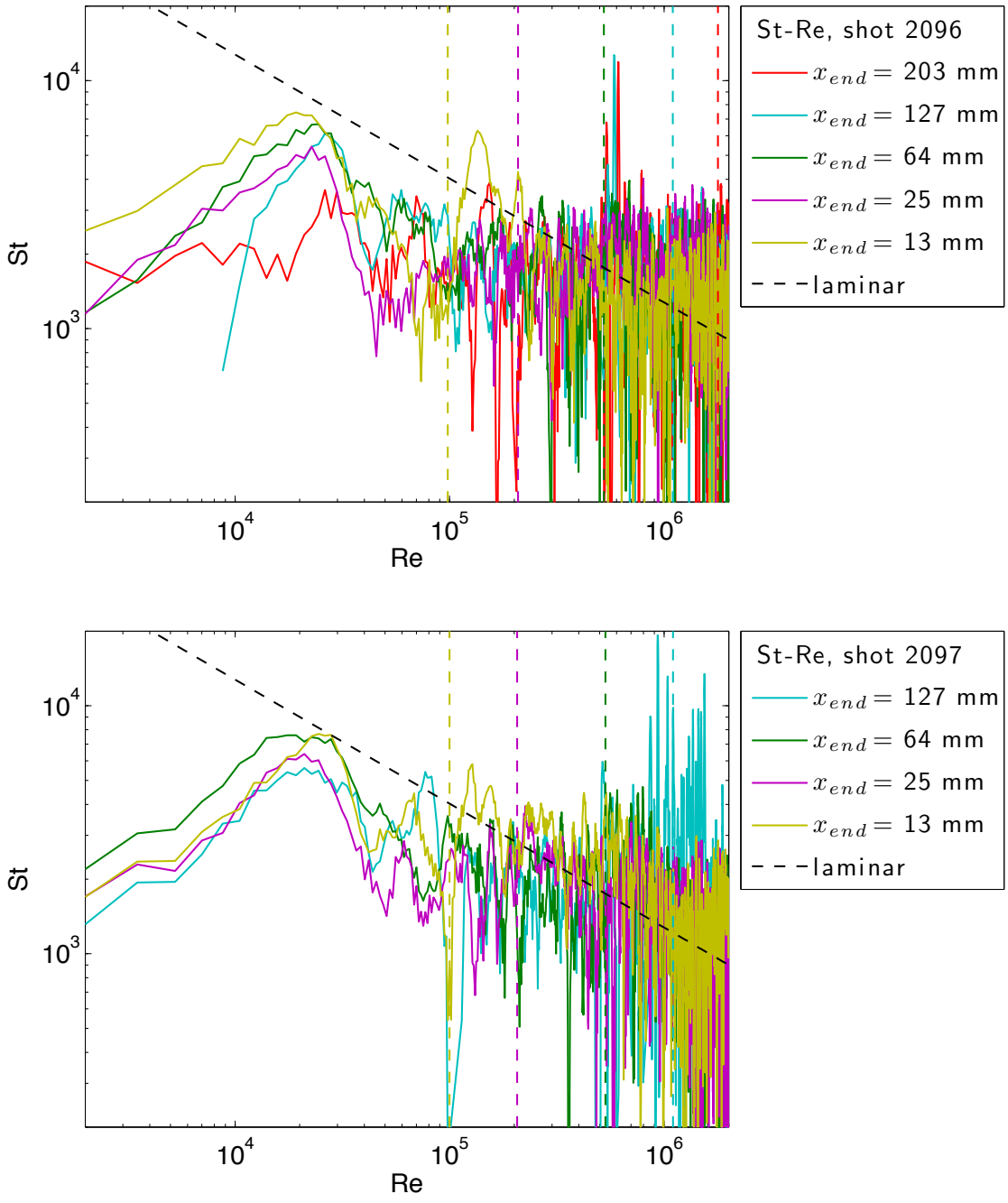

Figure E.86: Stanton-Reynolds number traces from shot 2097, a detonation in stoichiometric hydrogen-oxygen with 67% argon dilution at fill pressure 40 kPa. The dashed vertical lines represent the arrival of the reflected shock wave.

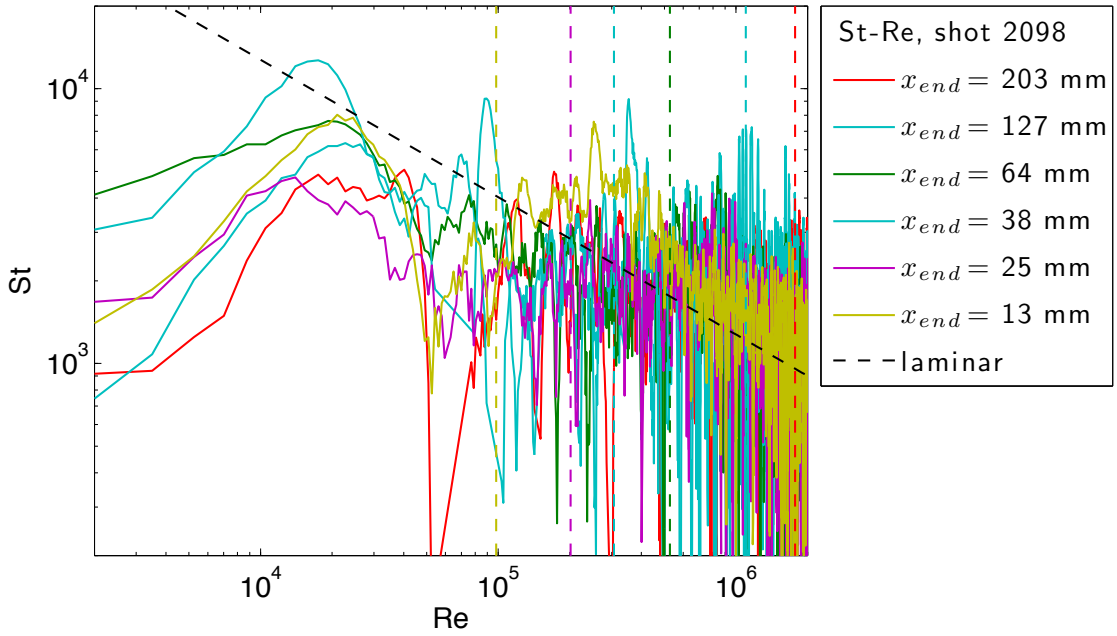

Figure E.87: Stanton-Reynolds number traces from shot 2098, a detonation in stoichiometric hydrogen-oxygen with 67% argon dilution at fill pressure 40 kPa. The dashed vertical lines represent the arrival of the reflected shock wave.

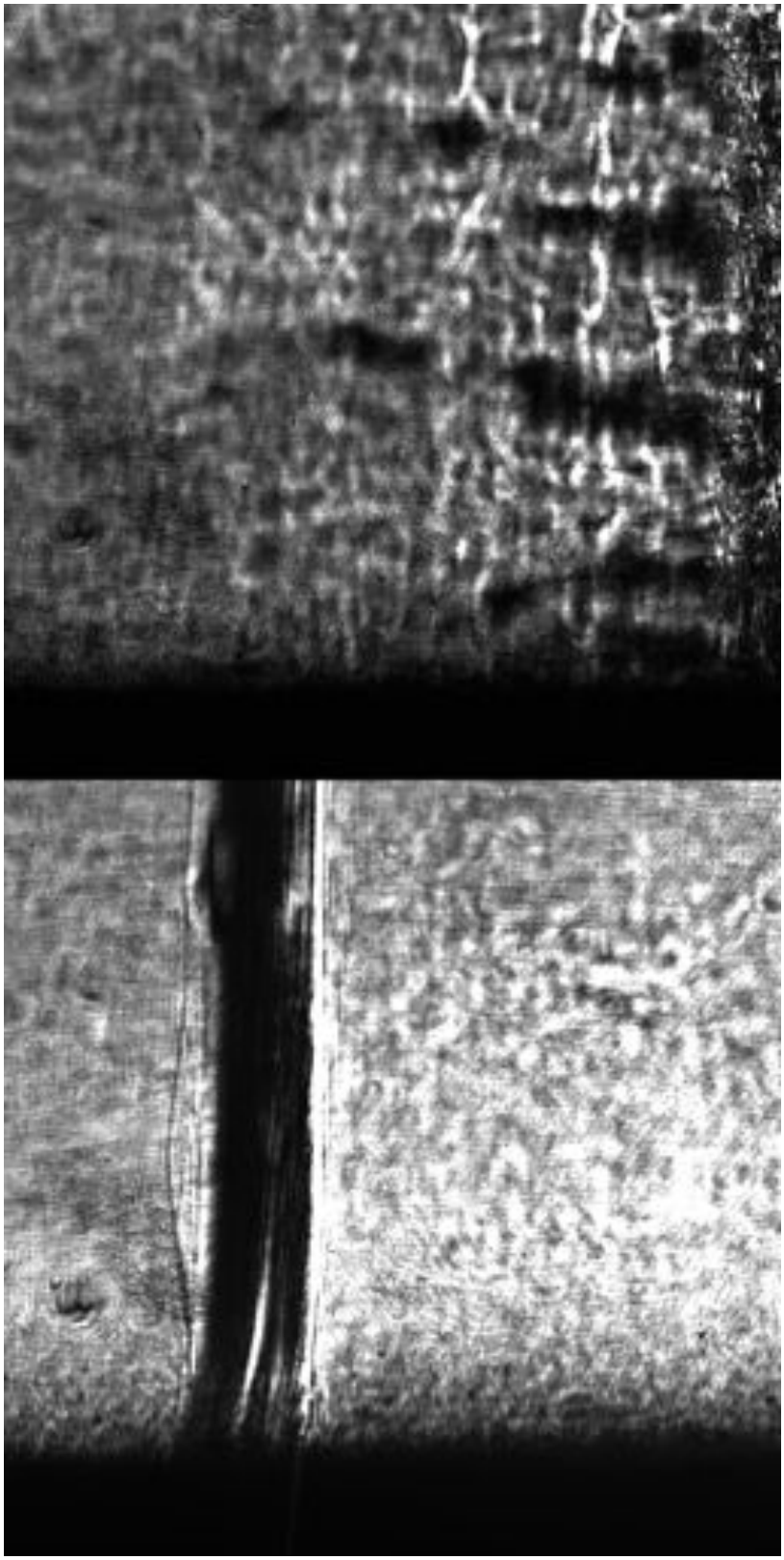

Figure E.88: Focused schlieren image of shot 2097. The field of view is approximately 14 mm wide.

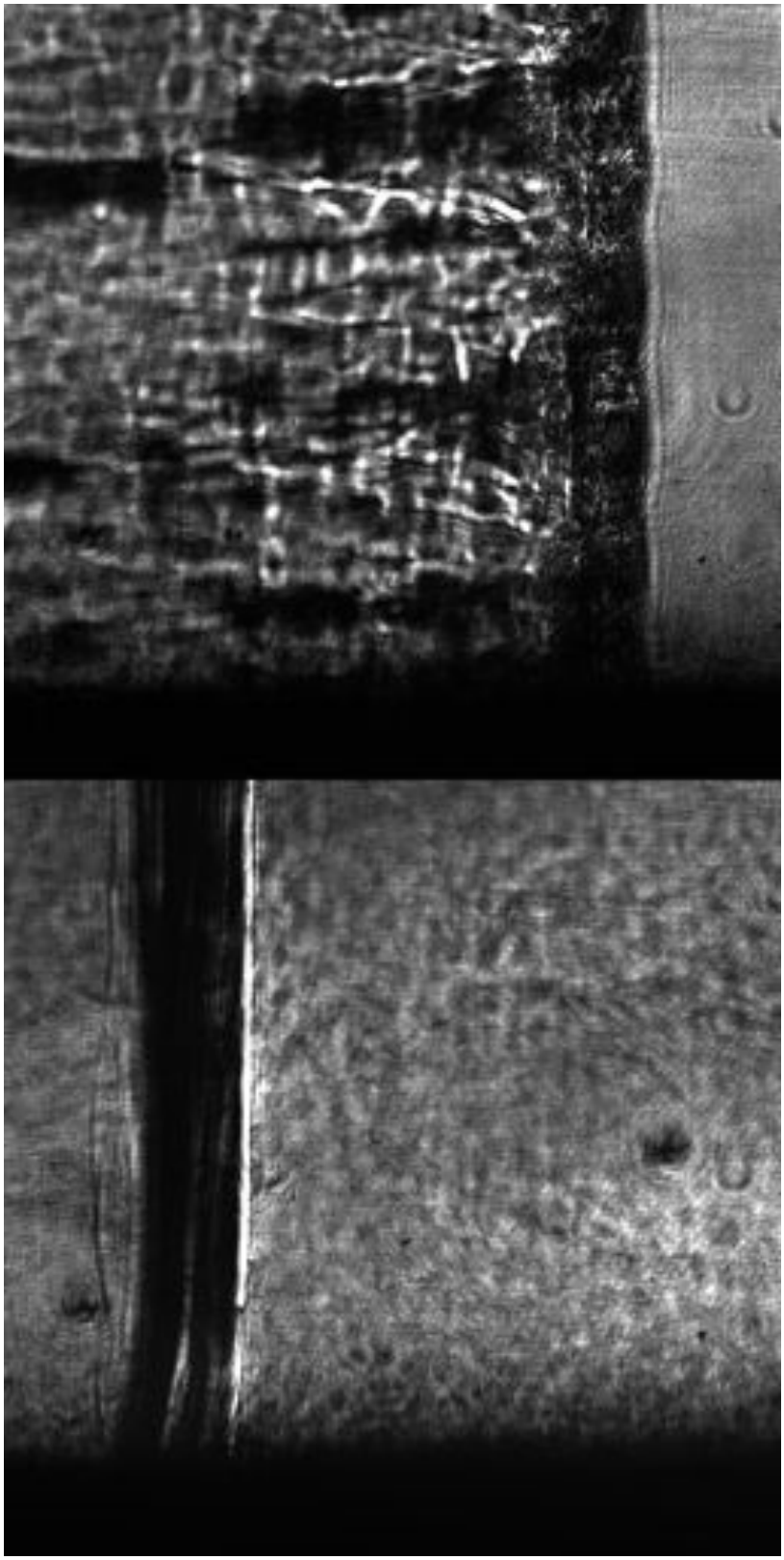

Figure E.89: Focused schlieren image of shot 2098. The field of view is approximately 14 mm wide.

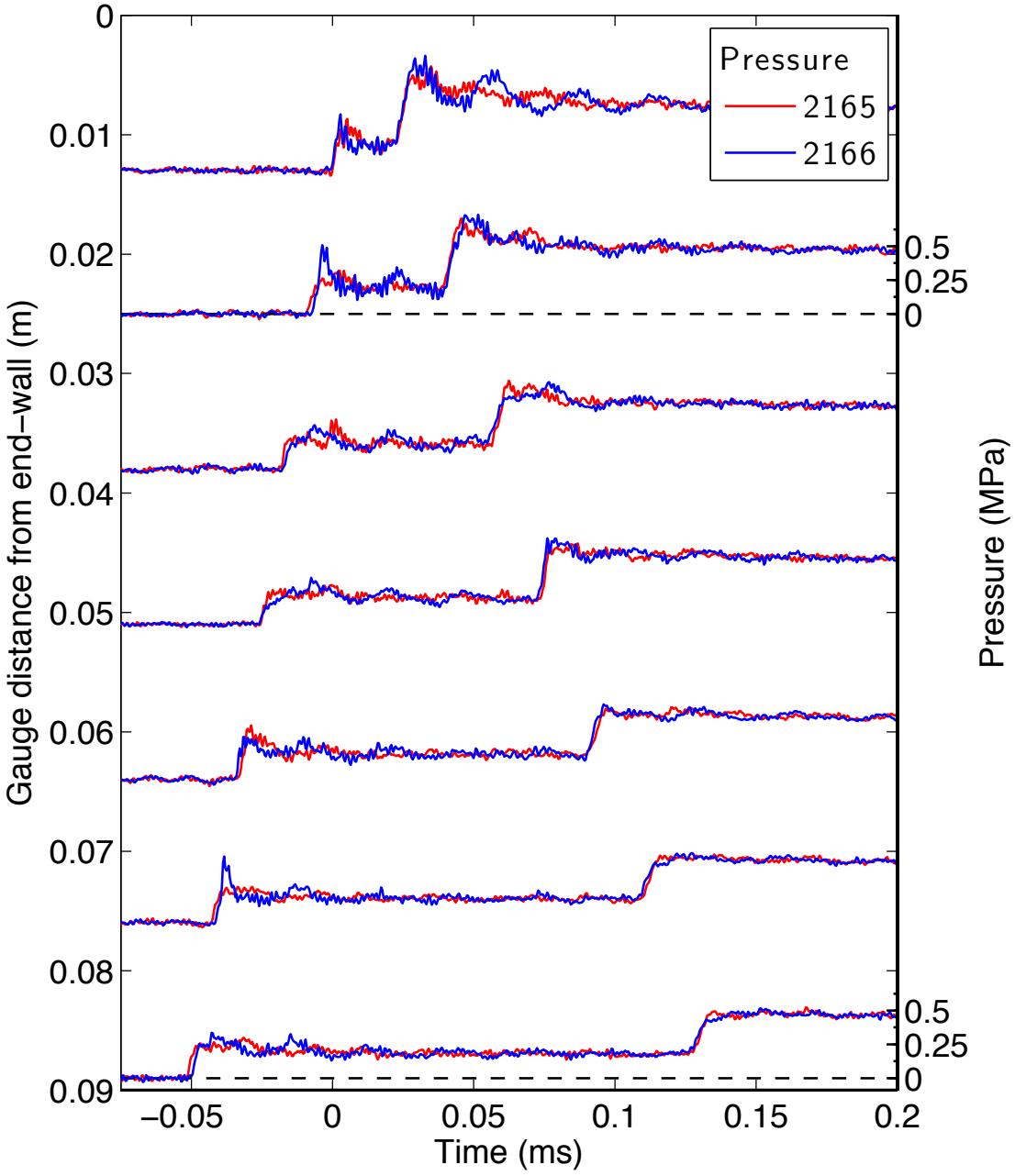

Figure E.90: Pressure traces for a detonation in stoichiometric hydrogen-oxygen with 80% argon dilution at fill pressure 10 kPa, part 1.

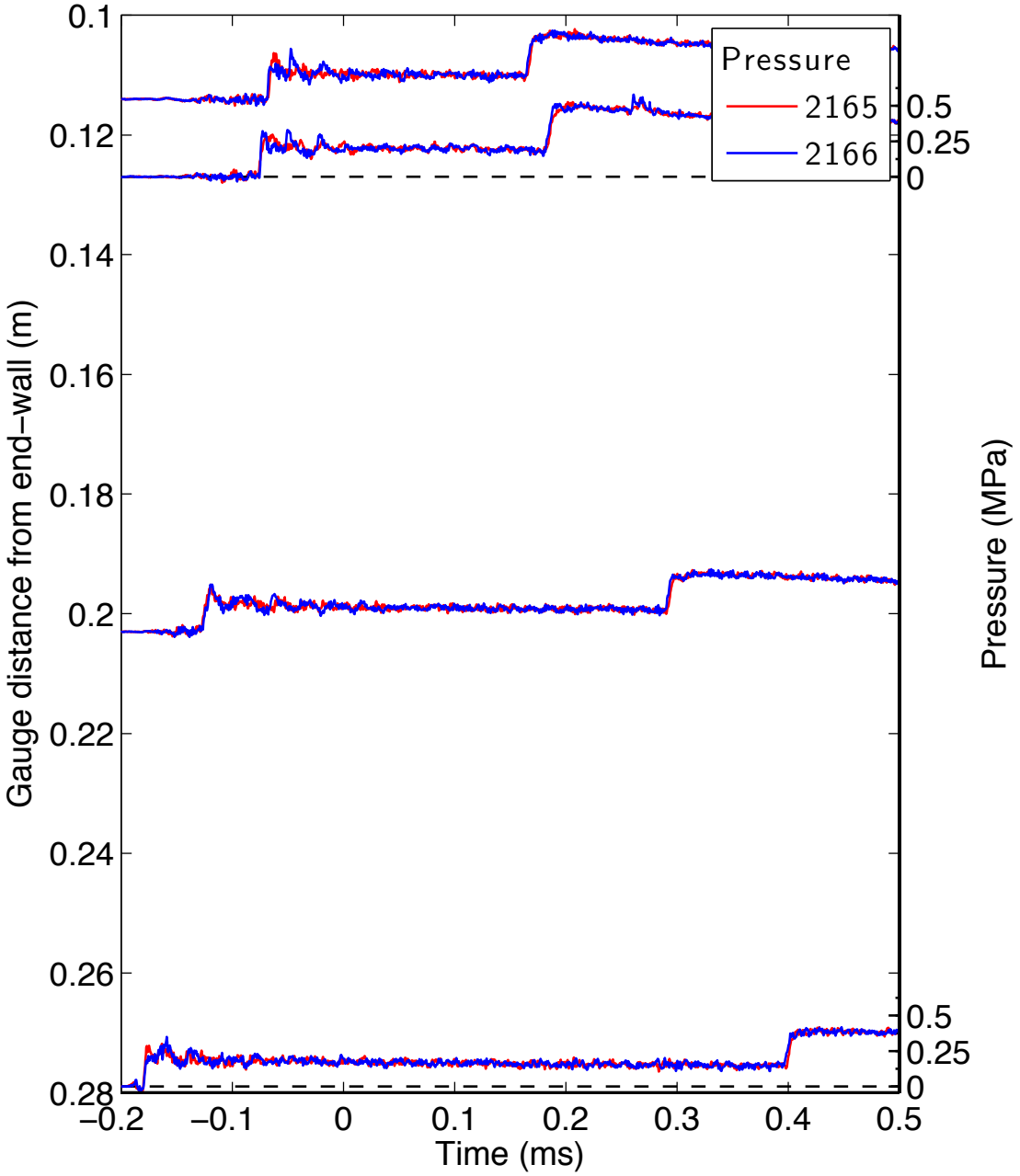

Figure E.91: Pressure traces for a detonation in stoichiometric hydrogen-oxygen with 80% argon dilution at fill pressure 10 kPa, part 2.

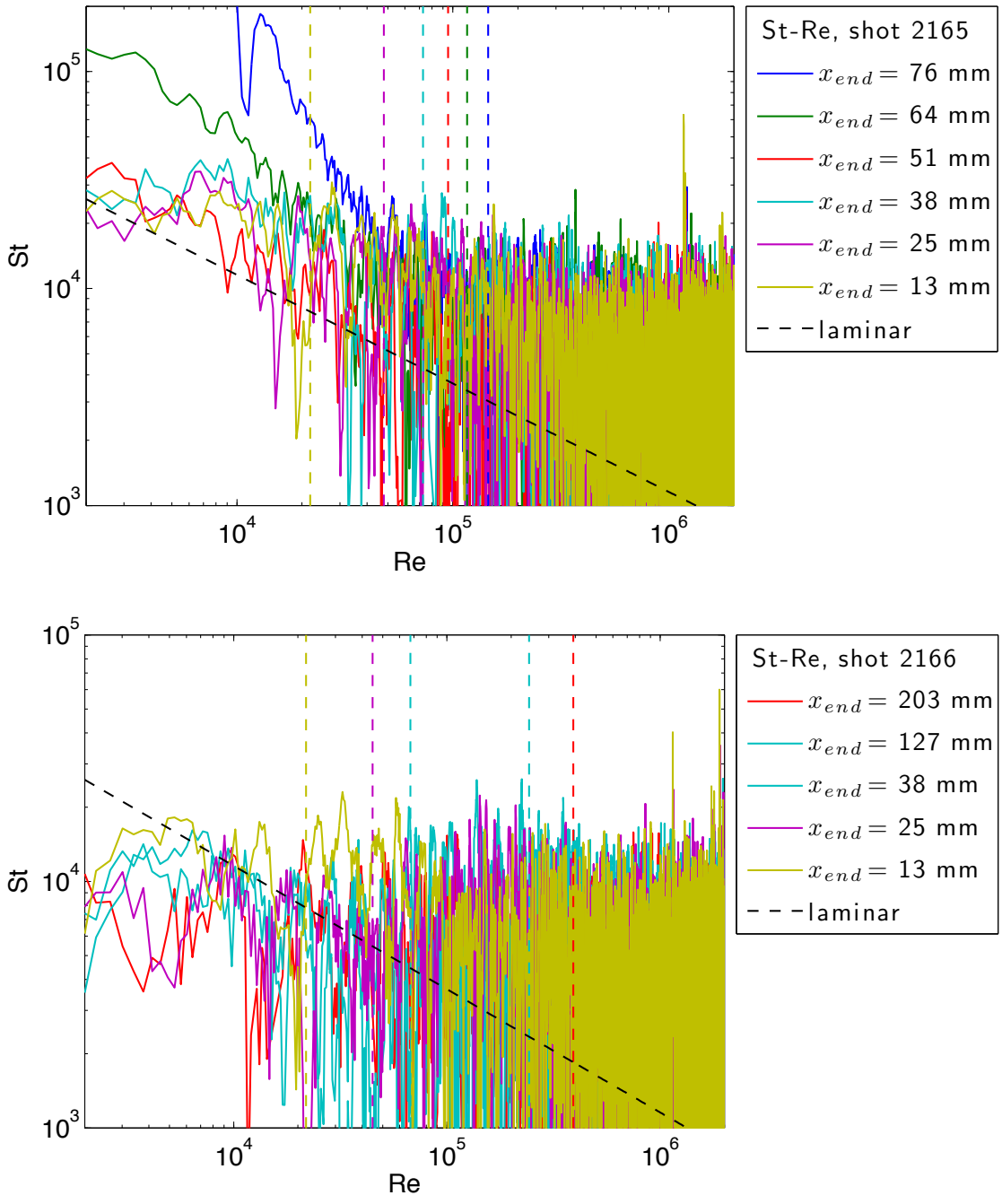

Figure E.92: Stanton-Reynolds number traces from shot 2166, a detonation in stoichiometric hydrogen-oxygen with 80% argon dilution at fill pressure 10 kPa. The dashed vertical lines represent the arrival of the reflected shock wave.

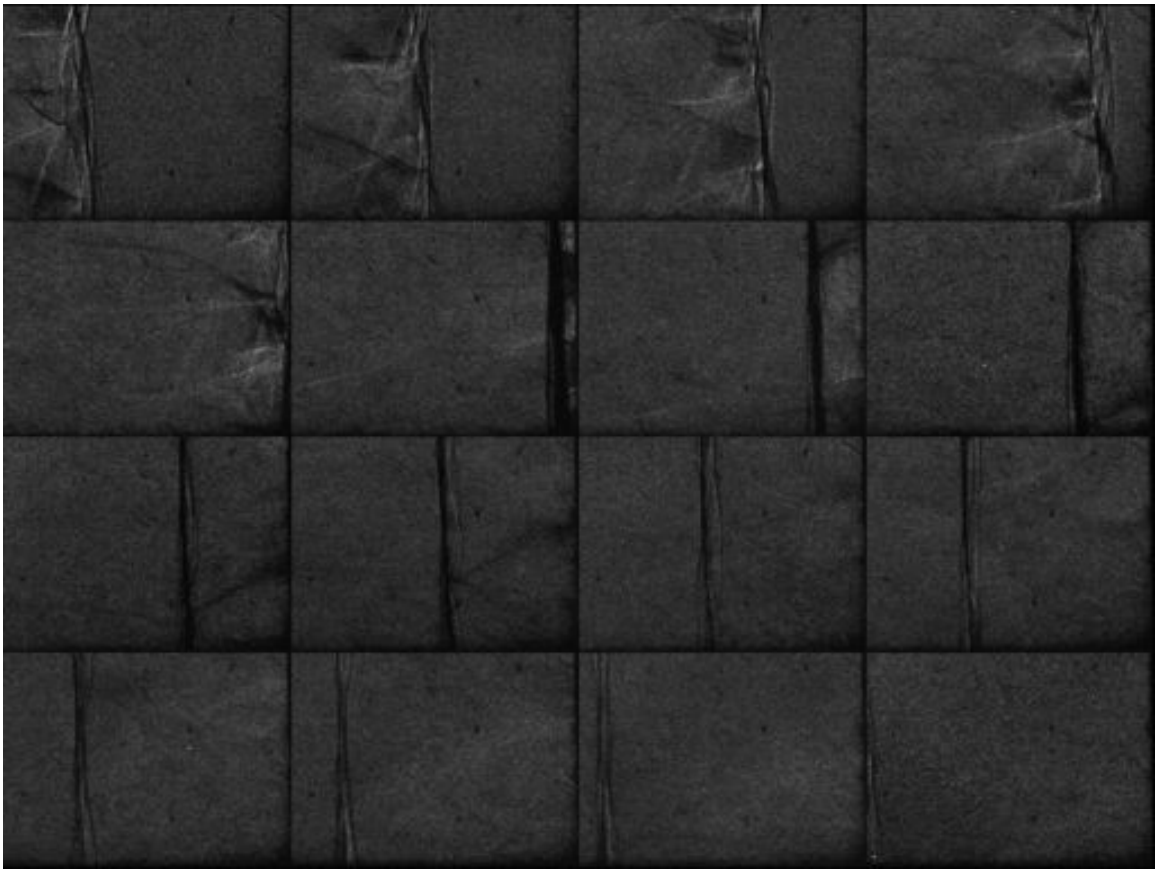

Figure E.93: Unfocused schlieren image of shot 2166. The field of view is approximately 30 mm wide.

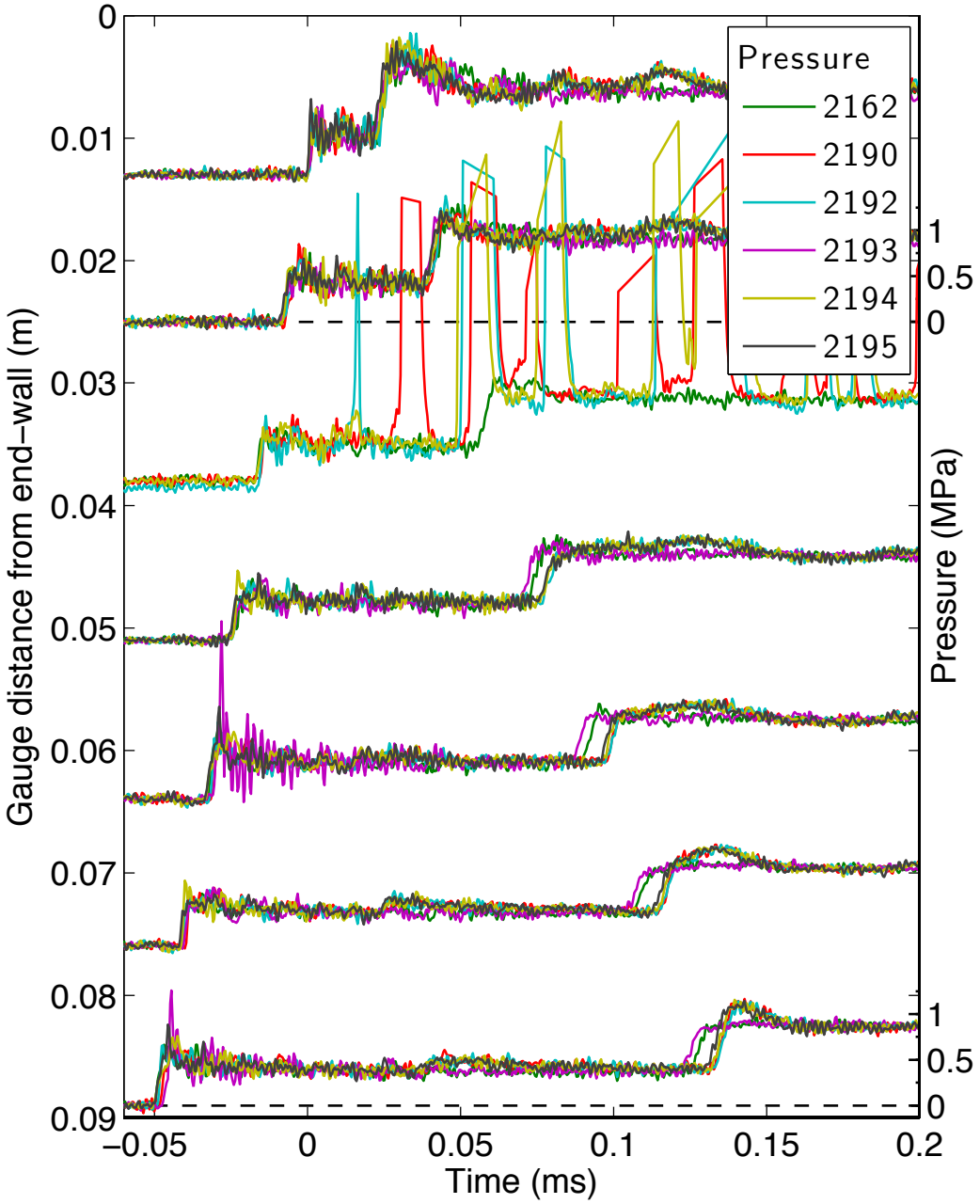

Figure E.94: Pressure traces for a detonation in stoichiometric hydrogen-oxygen with 80% argon dilution at fill pressure 25 kPa, part 1.

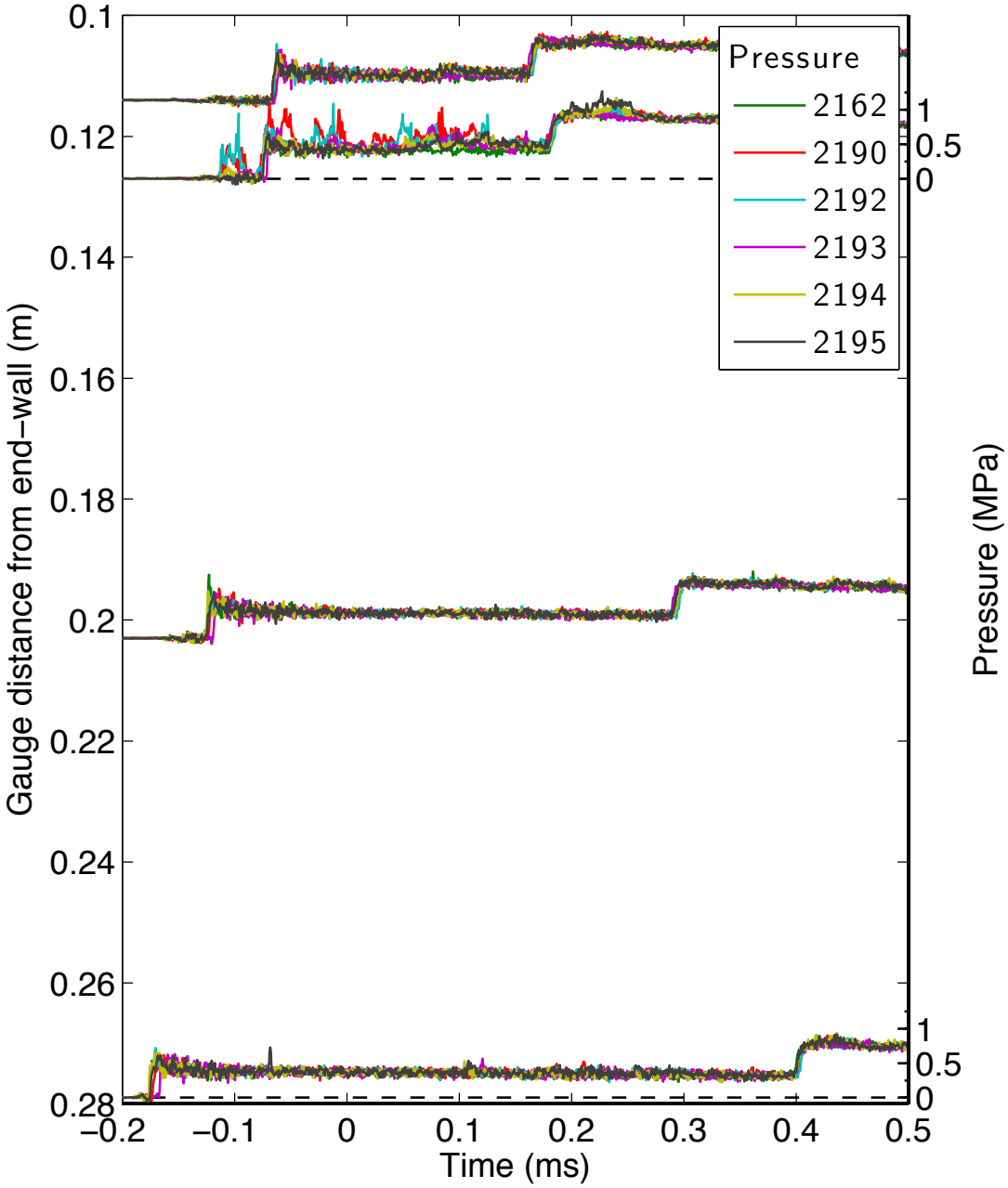

Figure E.95: Pressure traces for a detonation in stoichiometric hydrogen-oxygen with 80% argon dilution at fill pressure 25 kPa, part 2.

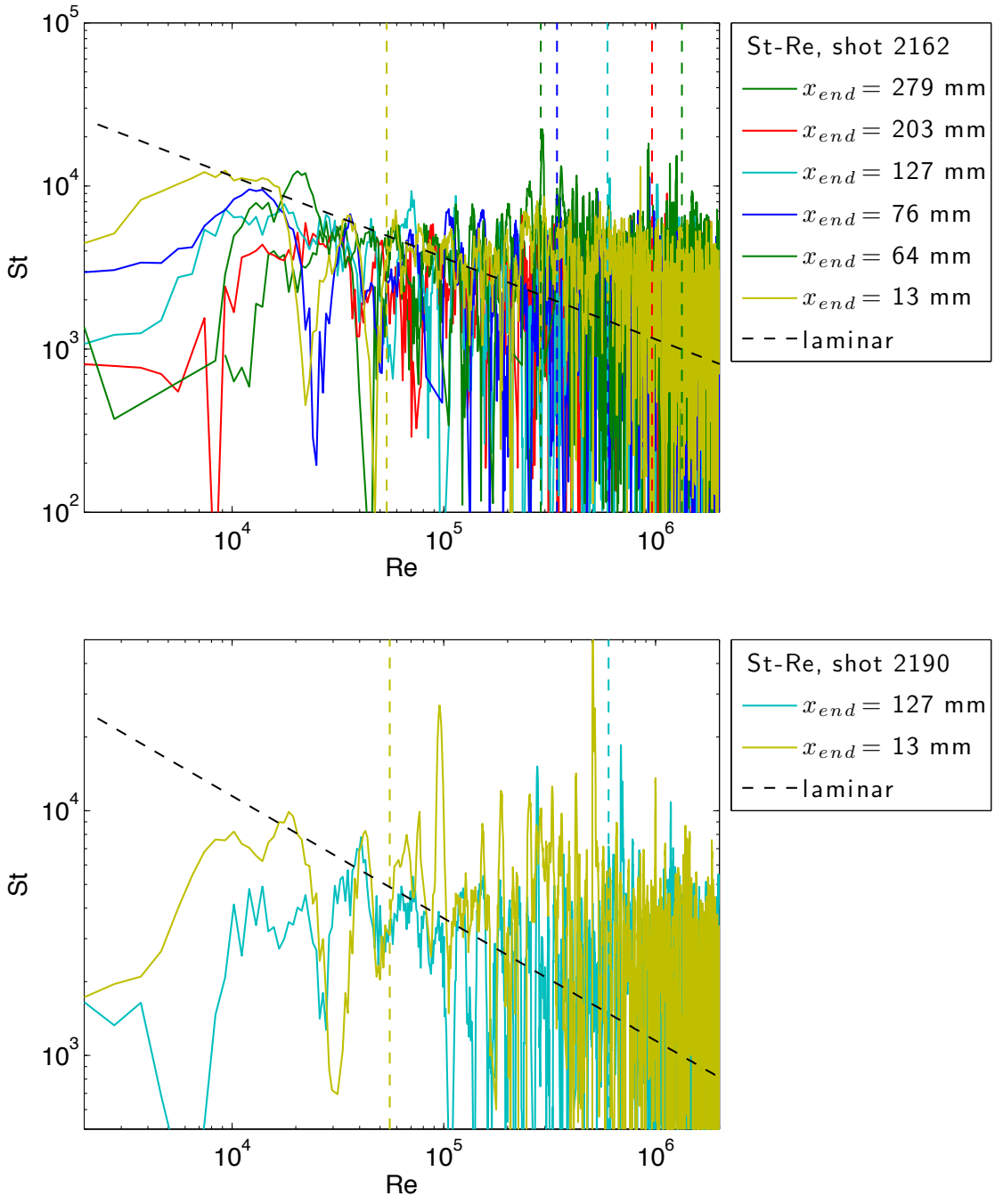

Figure E.96: Stanton-Reynolds number traces from shot 2190, a detonation in stoichiometric hydrogen-oxygen with 80% argon dilution at fill pressure 25 kPa. The dashed vertical lines represent the arrival of the reflected shock wave.

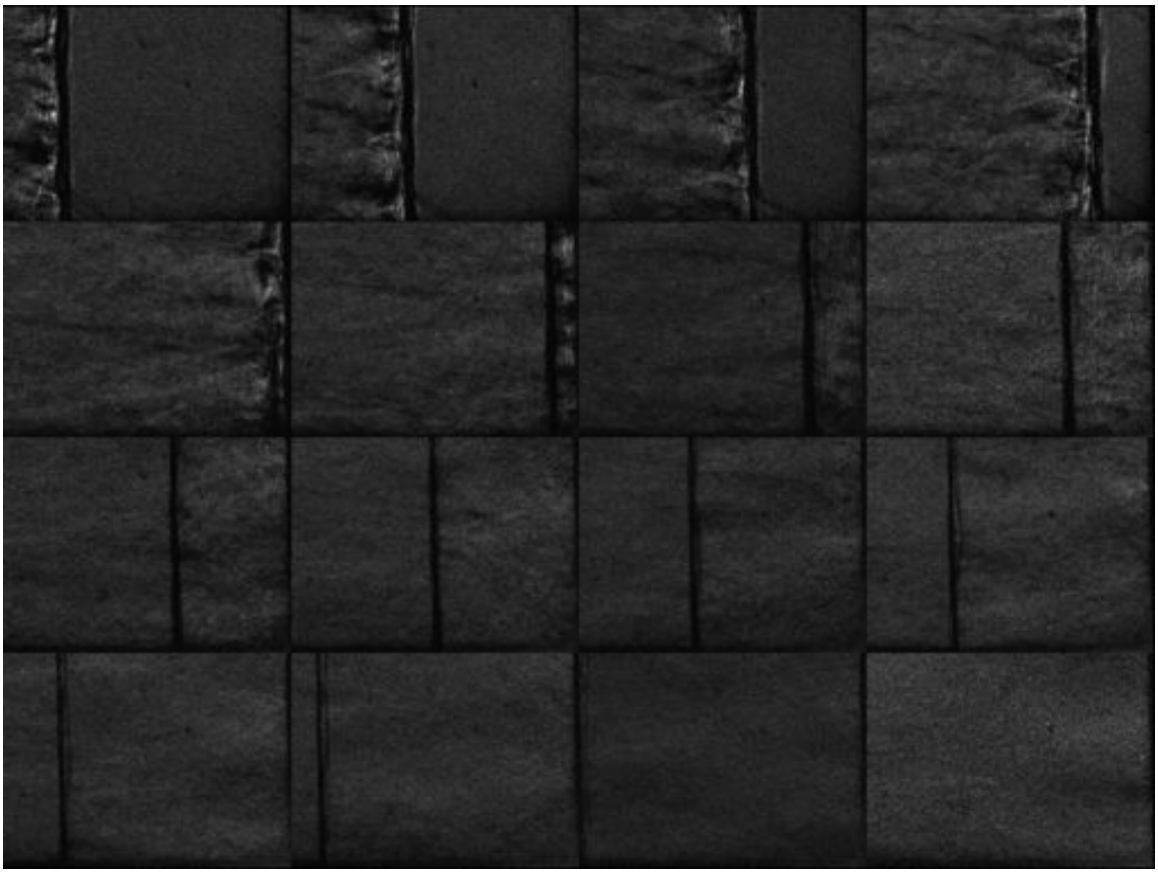

Figure E.97: Unfocused schlieren image of shot 2162. The field of view is approximately 30 mm wide.

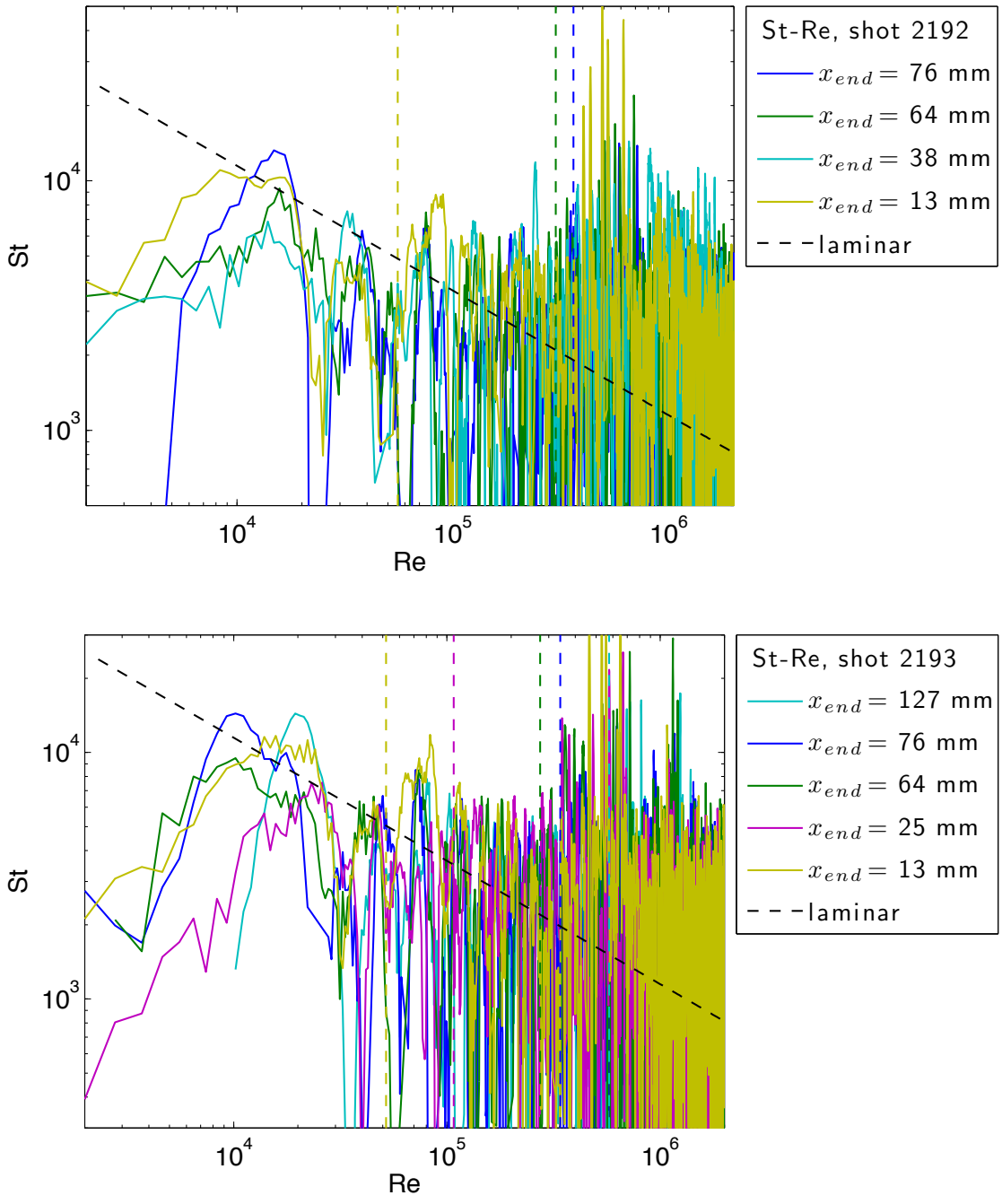

Figure E.98: Stanton-Reynolds number traces from shot 2193, a detonation in stoichiometric hydrogen-oxygen with 80% argon dilution at fill pressure 25 kPa. The dashed vertical lines represent the arrival of the reflected shock wave.

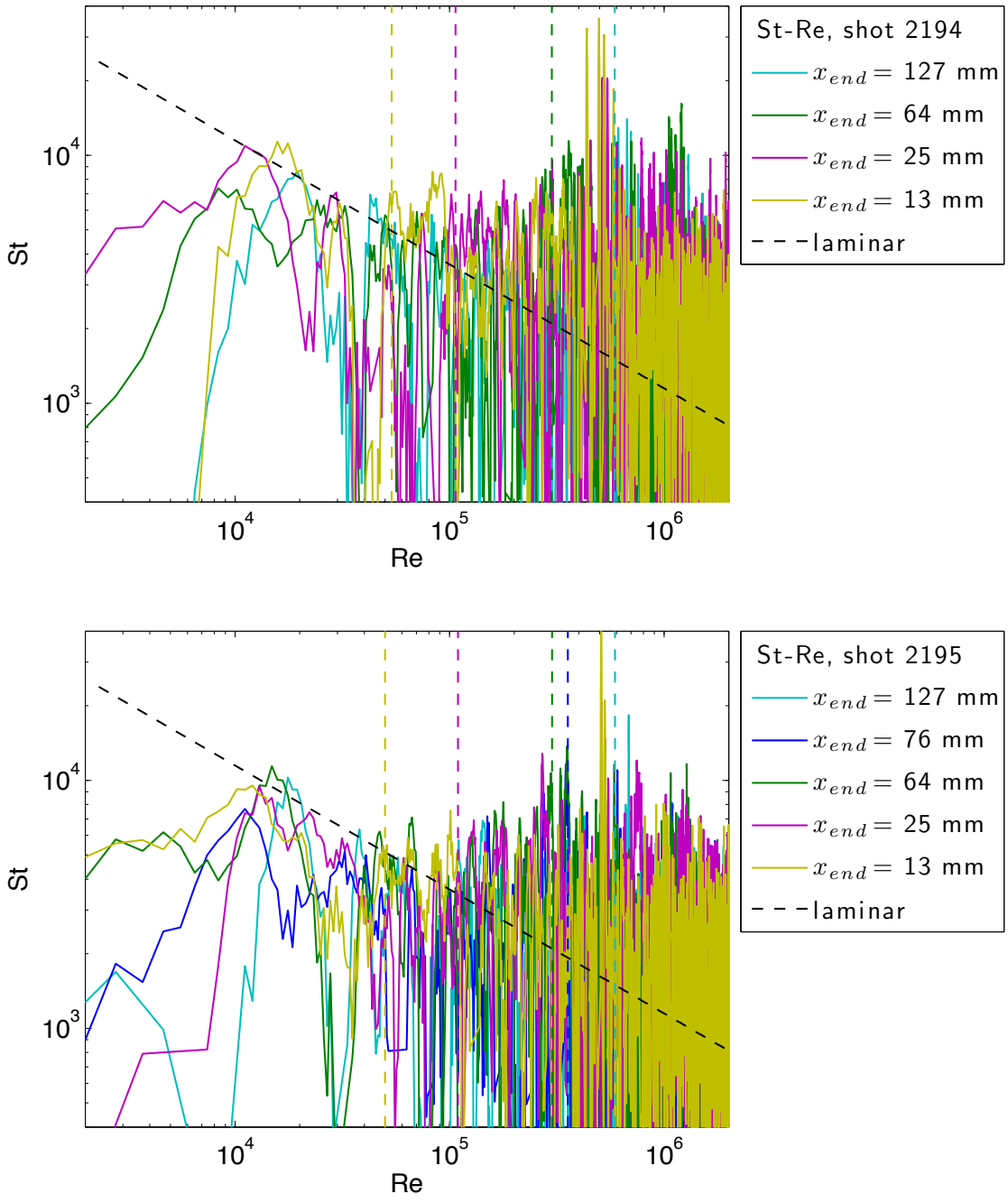

Figure E.99: Stanton-Reynolds number traces from shot 2195, a detonation in stoichiometric hydrogen-oxygen with 80% argon dilution at fill pressure 25 kPa. The dashed vertical lines represent the arrival of the reflected shock wave.

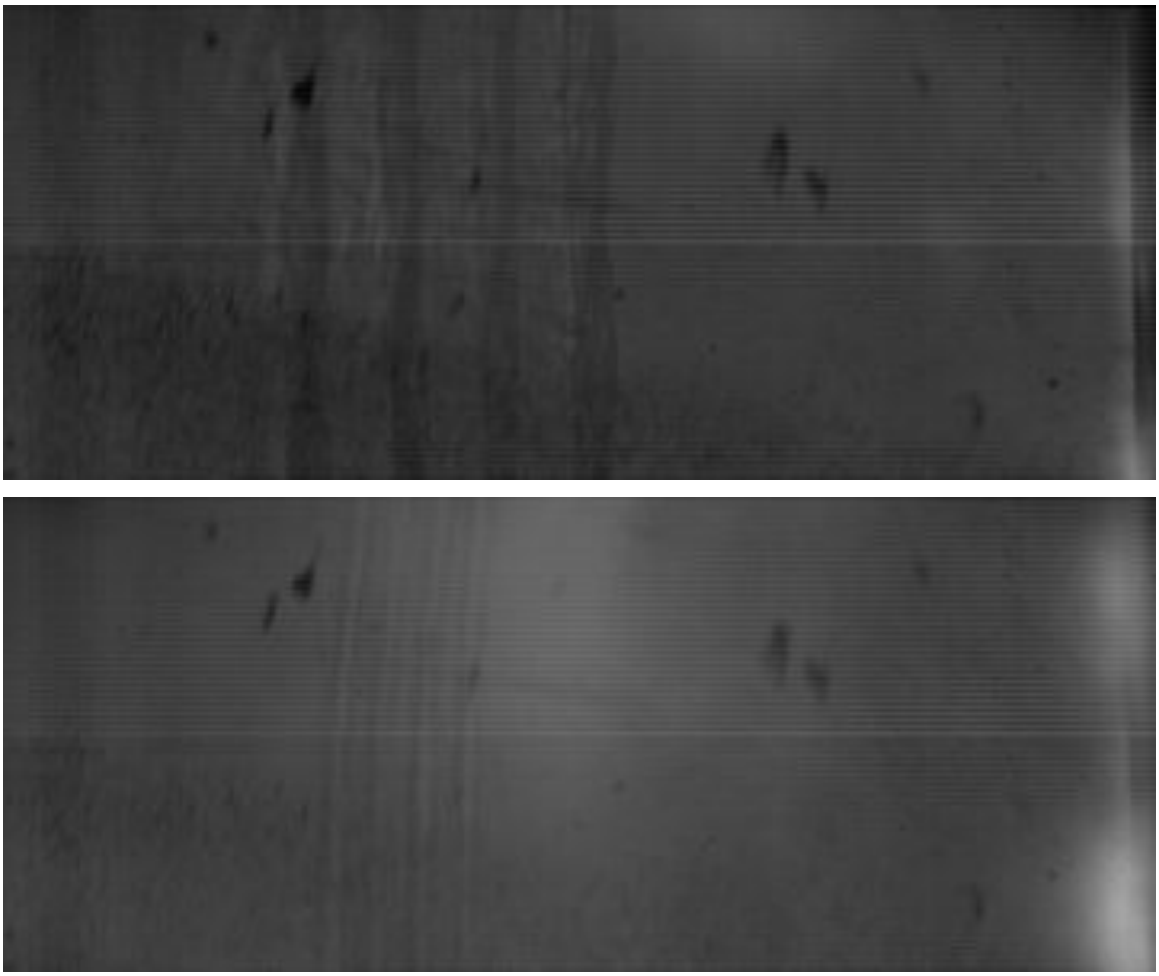

Figure E.100: Unfocused schlieren images of shot 2195. The field of view is approximately 66 mm wide.

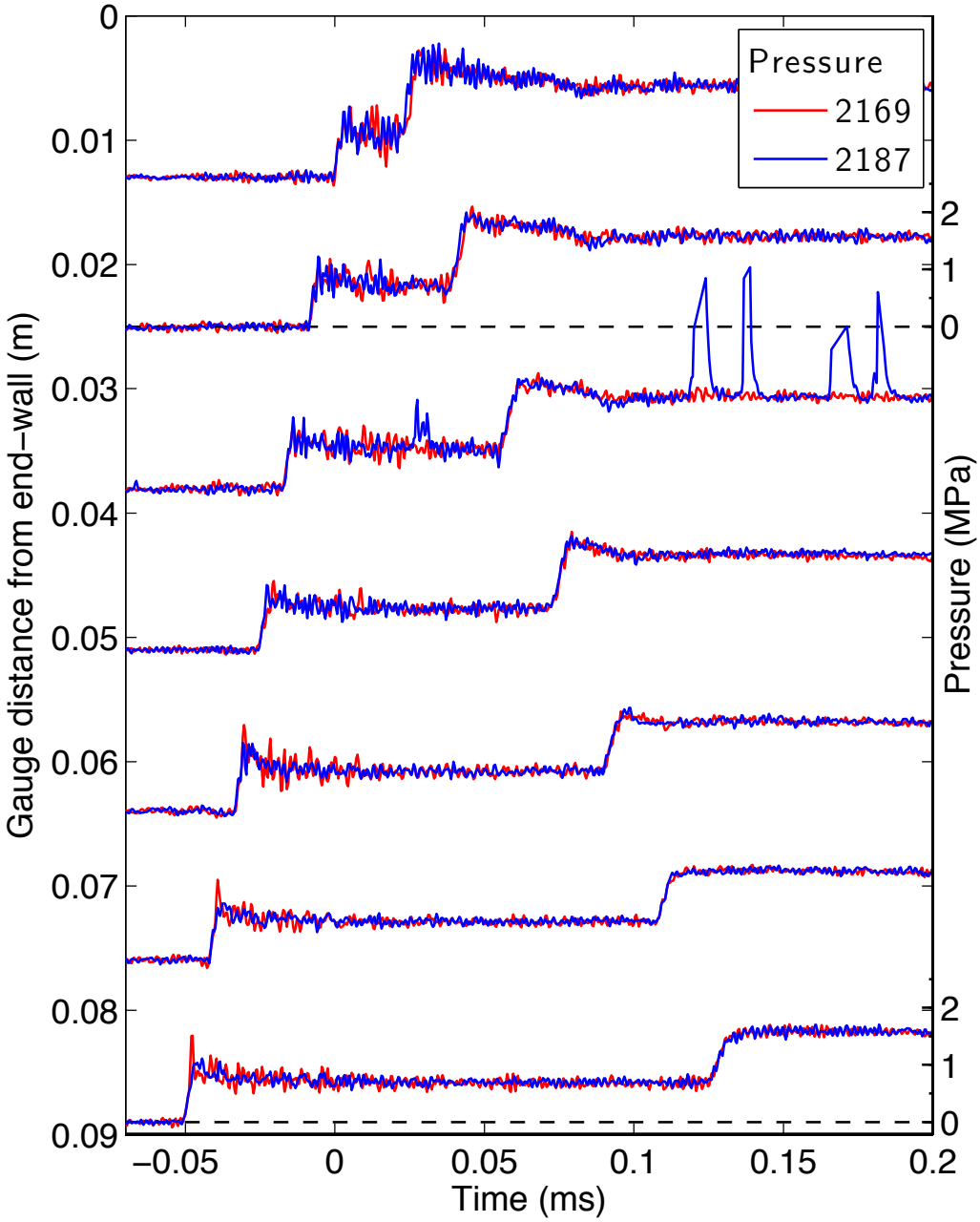

Figure E.101: Pressure traces for a detonation in stoichiometric hydrogen-oxygen with 80% argon dilution at fill pressure 50 kPa, part 1.

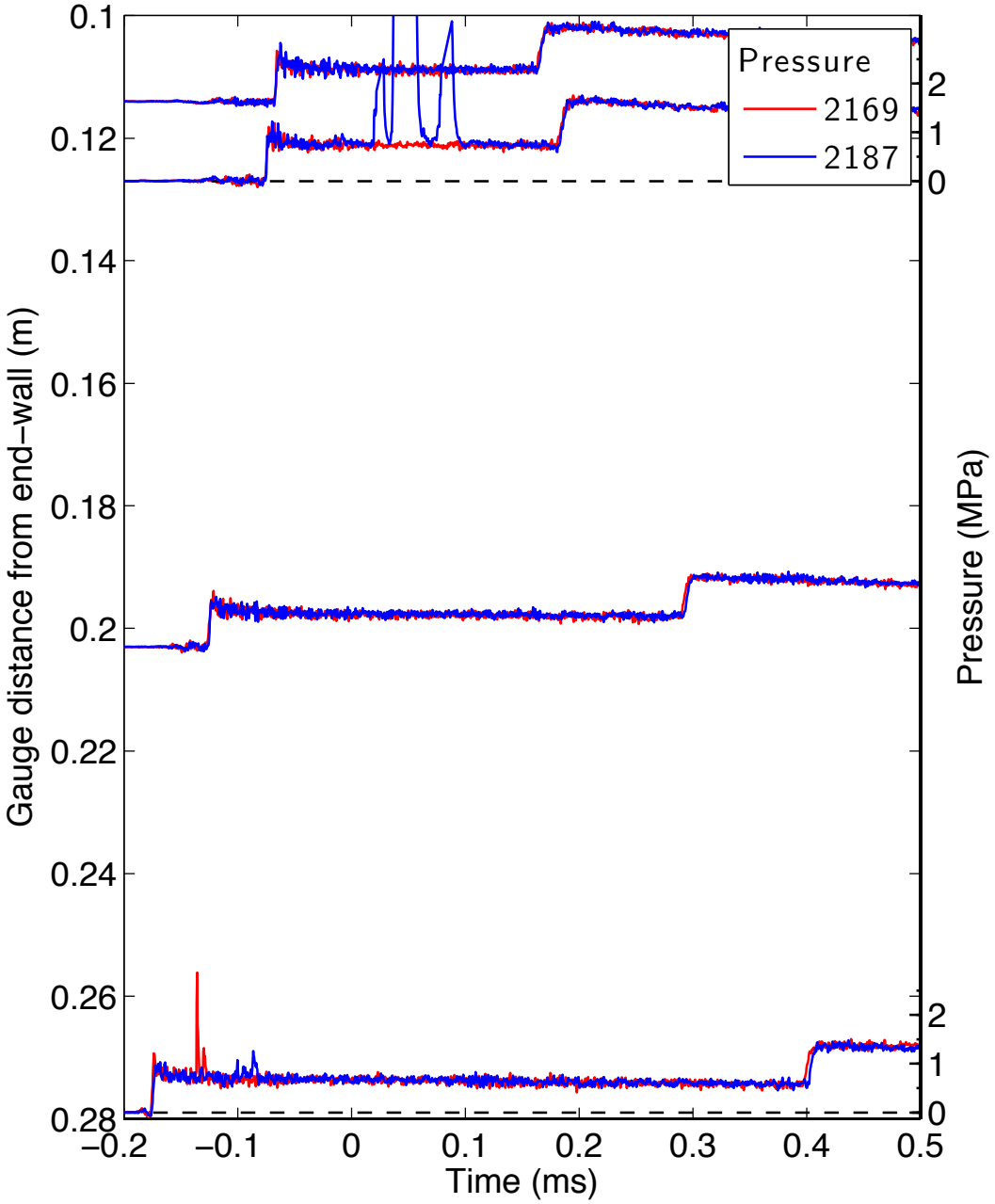

Figure E.102: Pressure traces for a detonation in stoichiometric hydrogen-oxygen with 80% argon dilution at fill pressure 50 kPa, part 2.

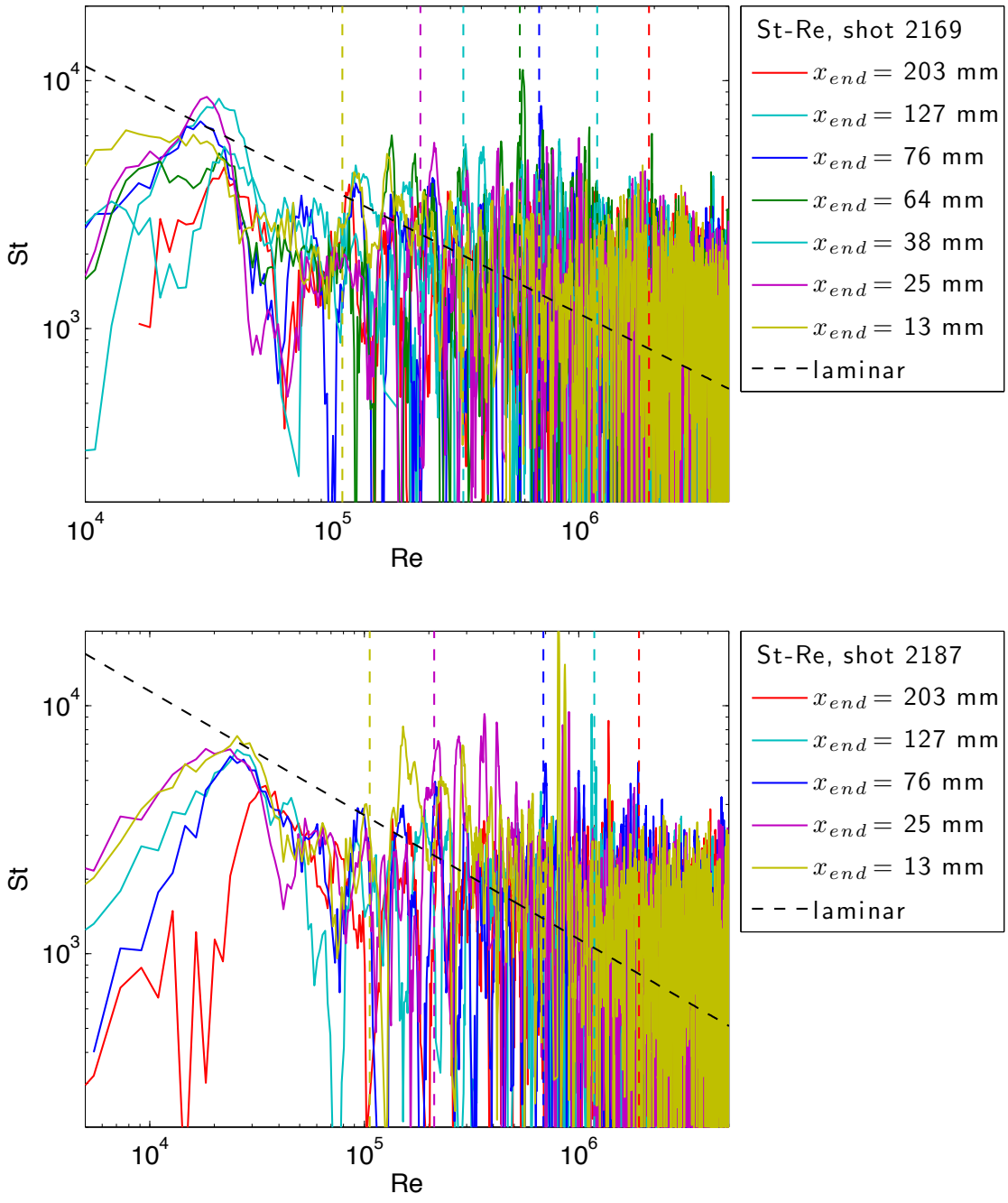

Figure E.103: Stanton-Reynolds number traces from shot 2187, a detonation in stoichiometric hydrogen-oxygen with 80% argon dilution at fill pressure 50 kPa. The dashed vertical lines represent the arrival of the reflected shock wave.

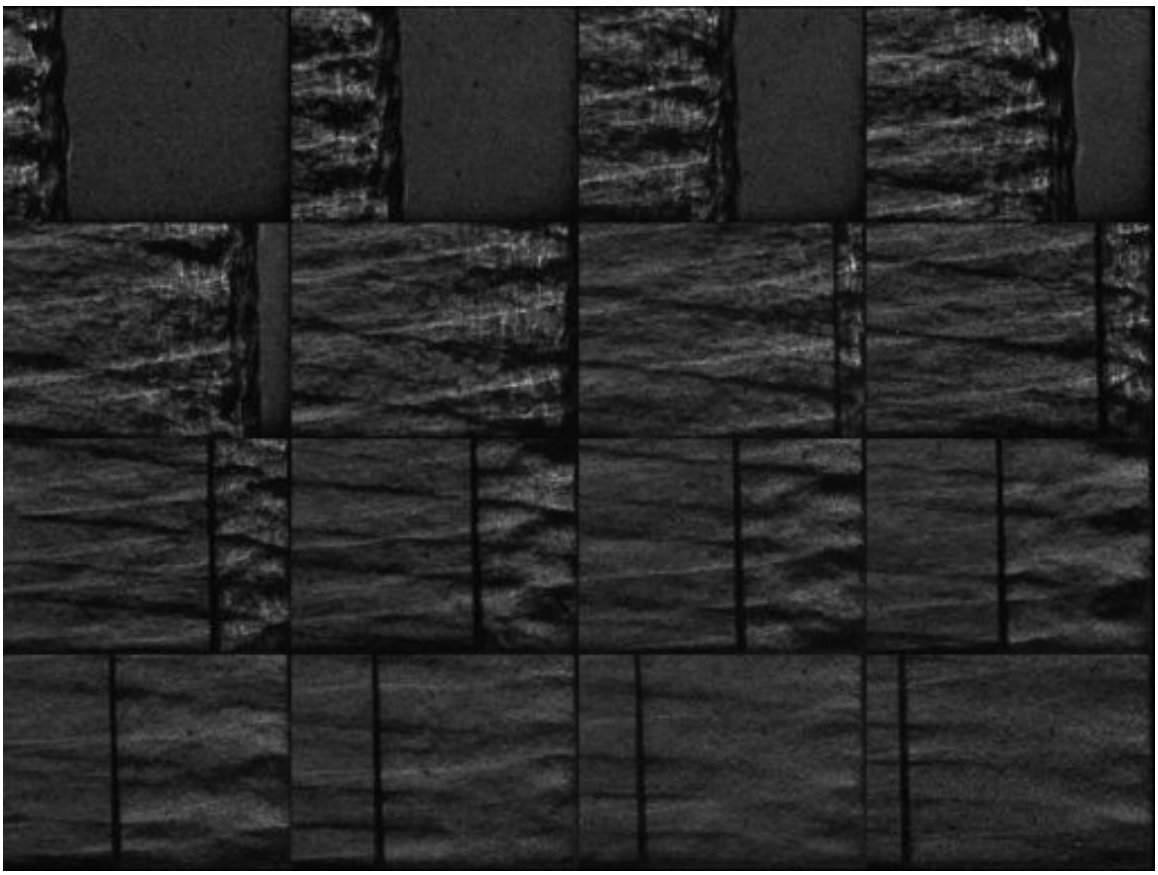

Figure E.104: Unfocused schlieren image of shot 2169. The field of view is approximately 30 mm wide.

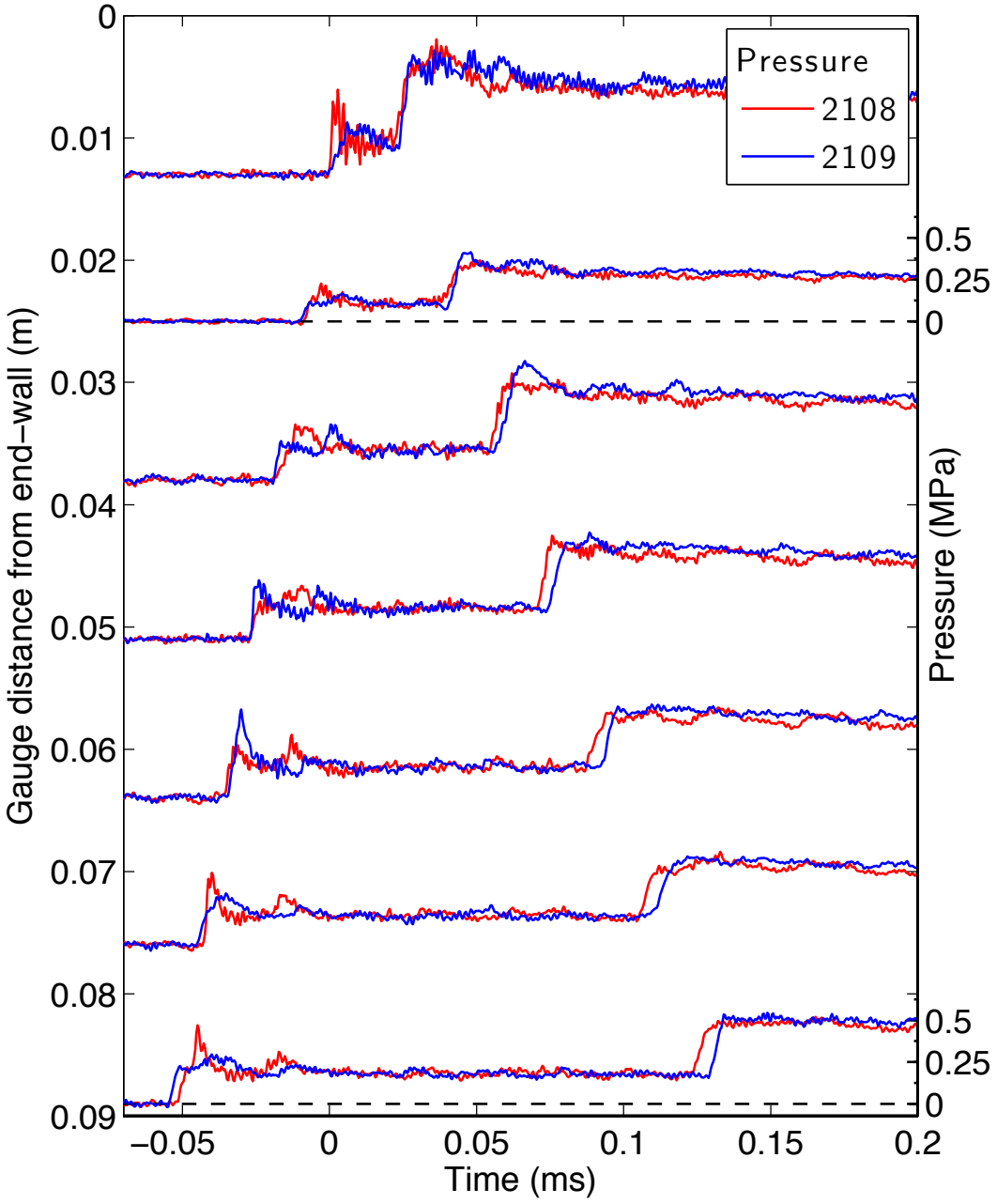

Figure E.105: Pressure traces for a detonation in stoichiometric hydrogen-oxygen with 83% argon dilution at fill pressure 10 kPa, part 1.

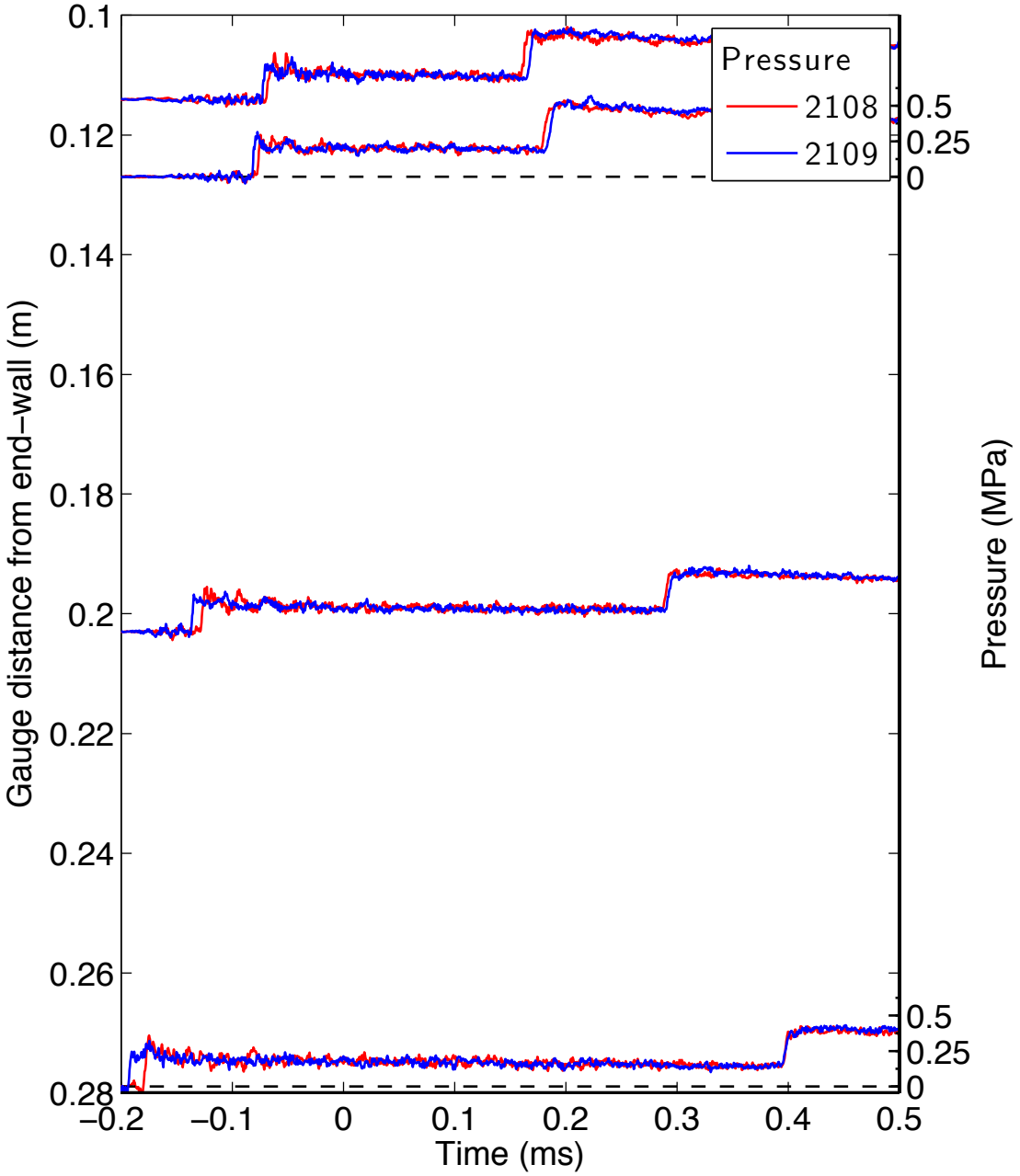

Figure E.106: Pressure traces for a detonation in stoichiometric hydrogen-oxygen with 83% argon dilution at fill pressure 10 kPa, part 2.

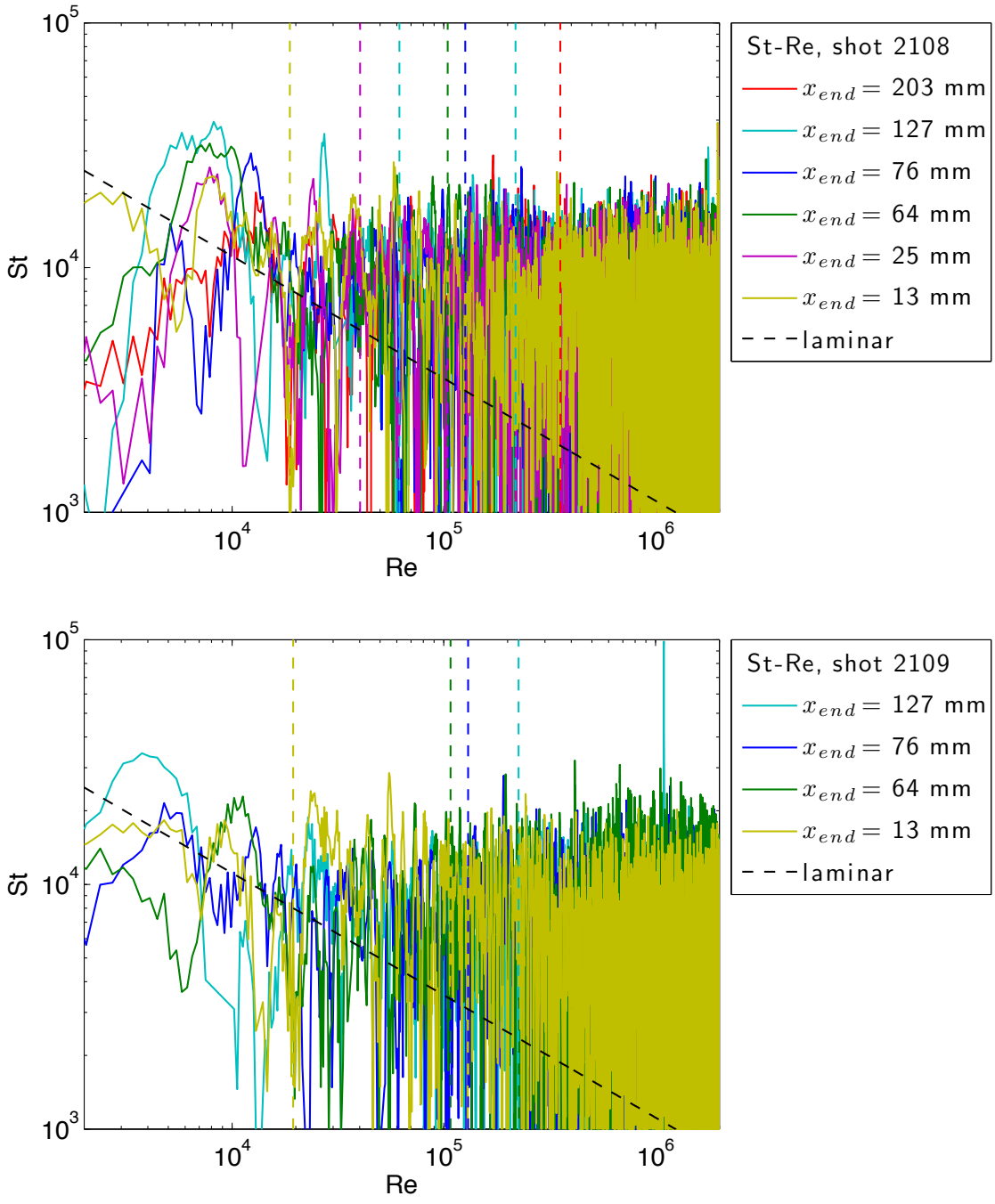

Figure E.107: Stanton-Reynolds number traces from shot 2109, a detonation in stoichiometric hydrogen-oxygen with 83% argon dilution at fill pressure 10 kPa. The dashed vertical lines represent the arrival of the reflected shock wave.

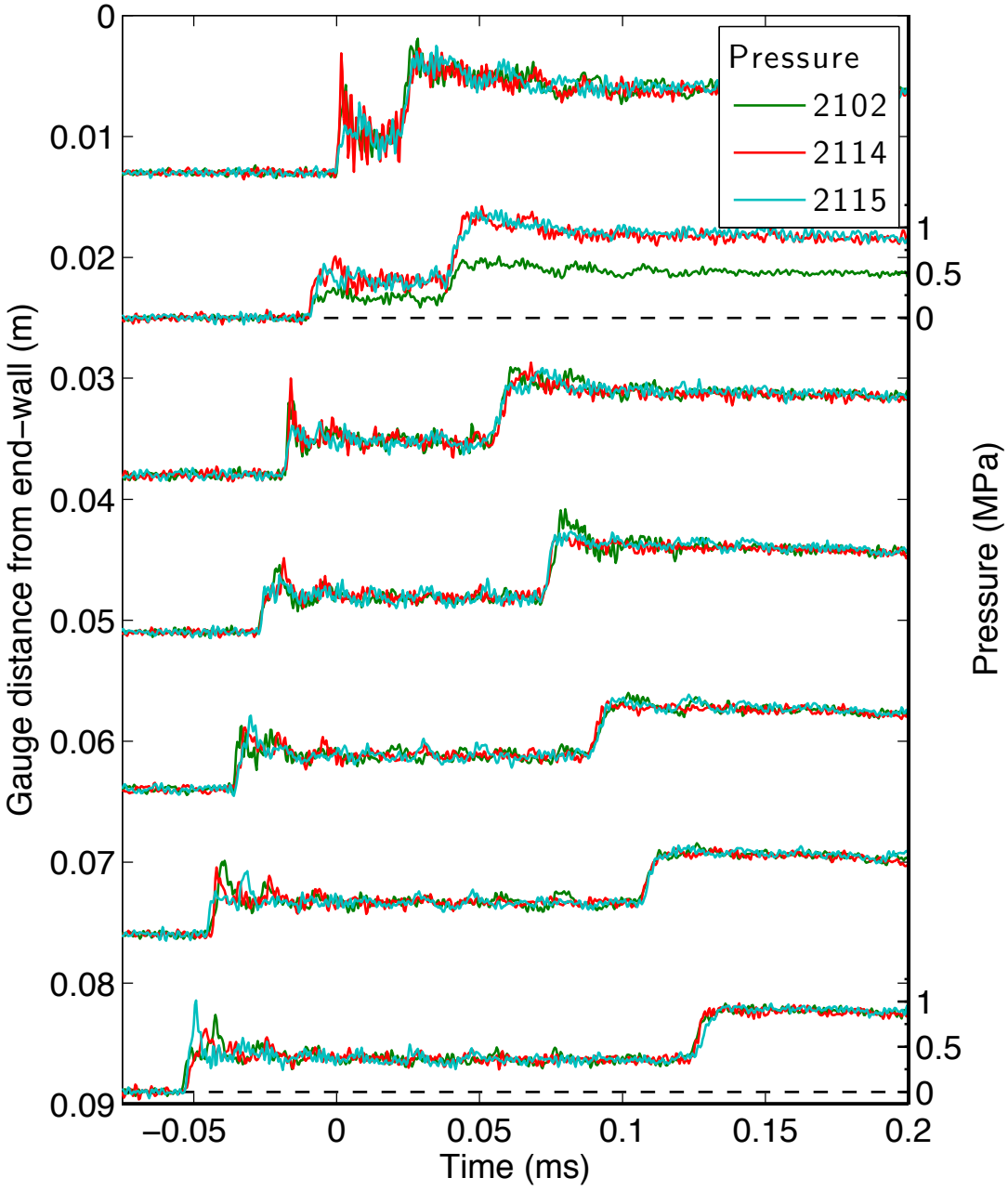

Figure E.108: Pressure traces for a detonation in stoichiometric hydrogen-oxygen with 83% argon dilution at fill pressure 25 kPa, part 1.

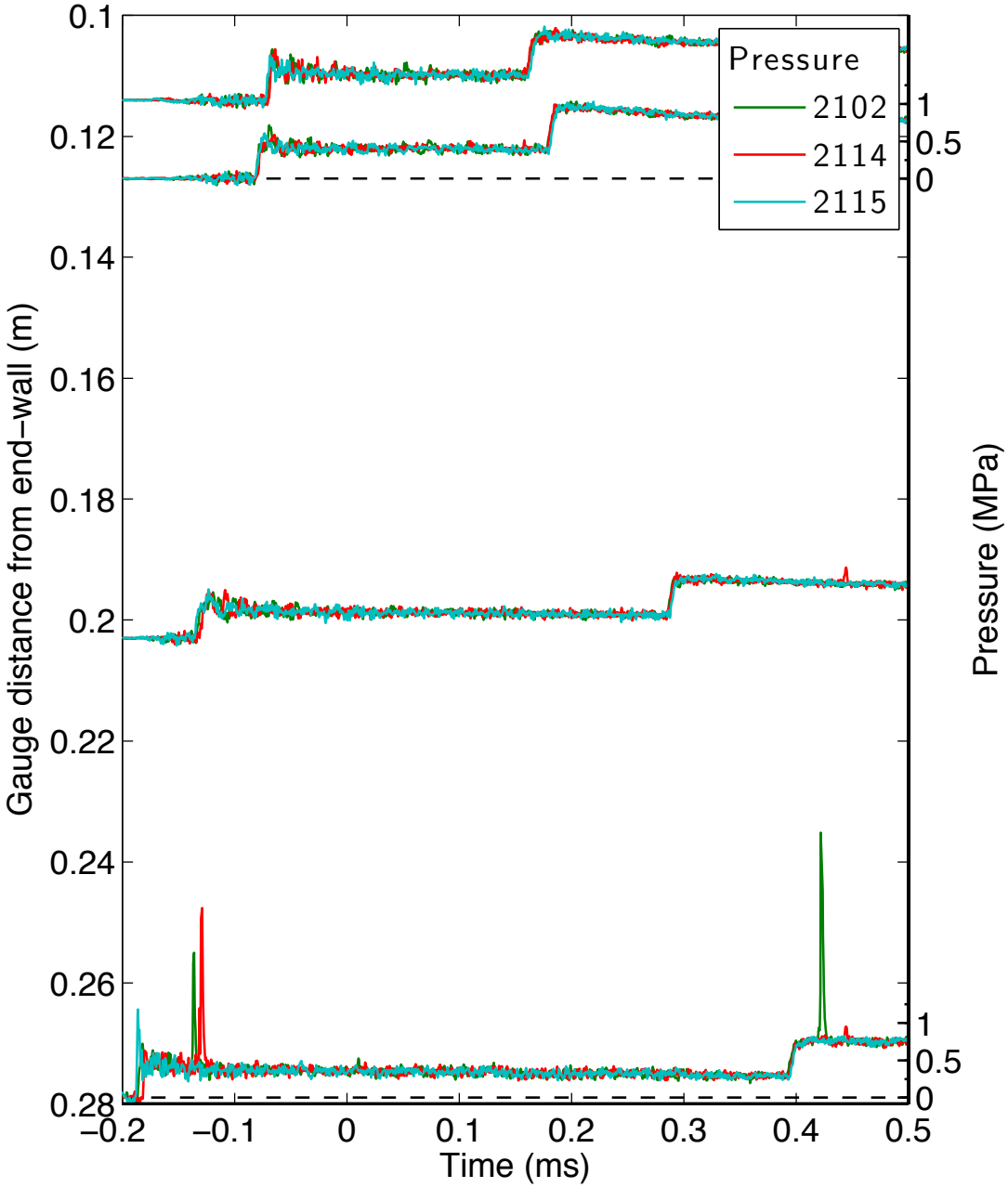

Figure E.109: Pressure traces for a detonation in stoichiometric hydrogen-oxygen with 83% argon dilution at fill pressure 25 kPa, part 2.

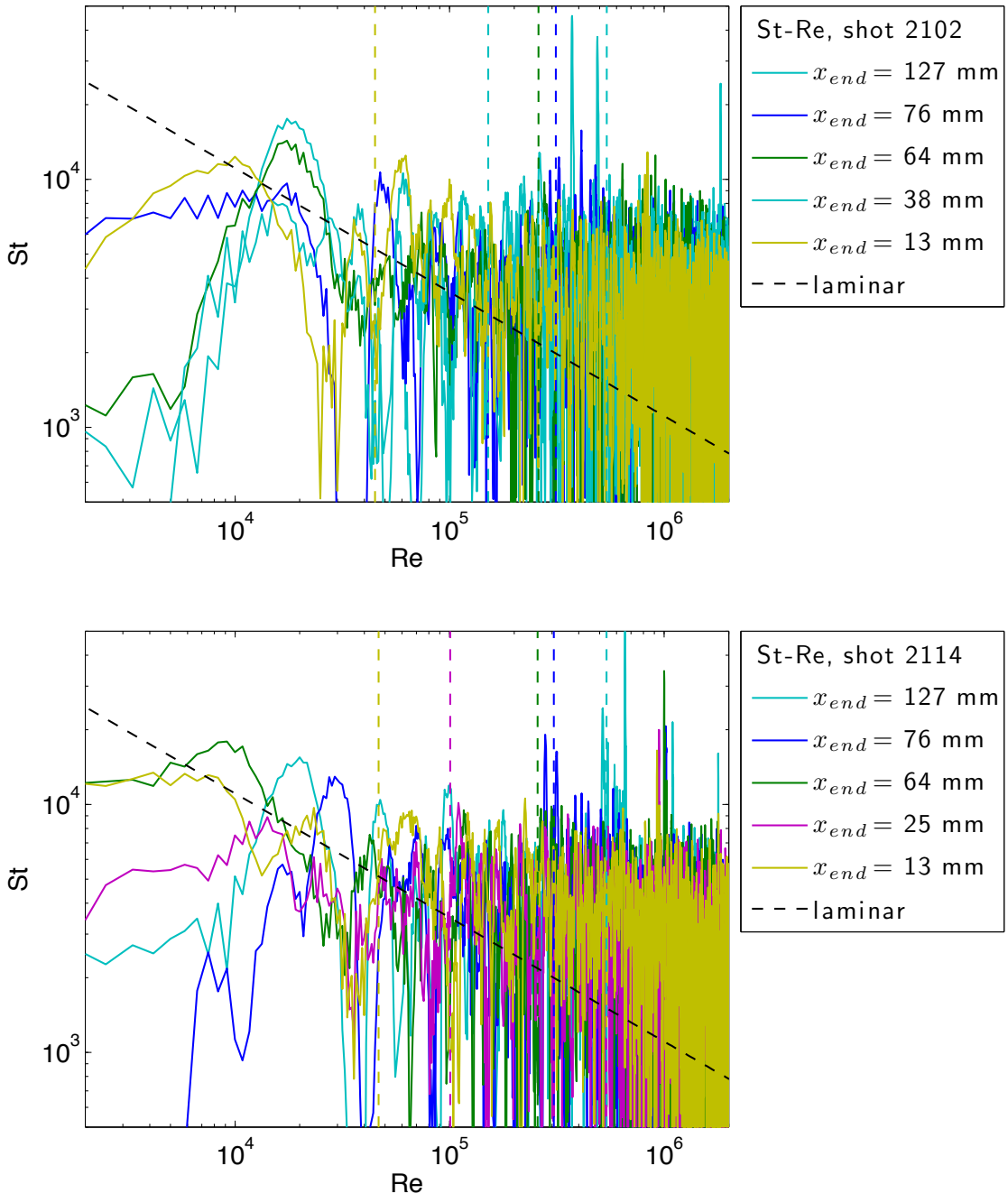

Figure E.110: Stanton-Reynolds number traces from shot 2114, a detonation in stoichiometric hydrogen-oxygen with 83% argon dilution at fill pressure 25 kPa. The dashed vertical lines represent the arrival of the reflected shock wave.

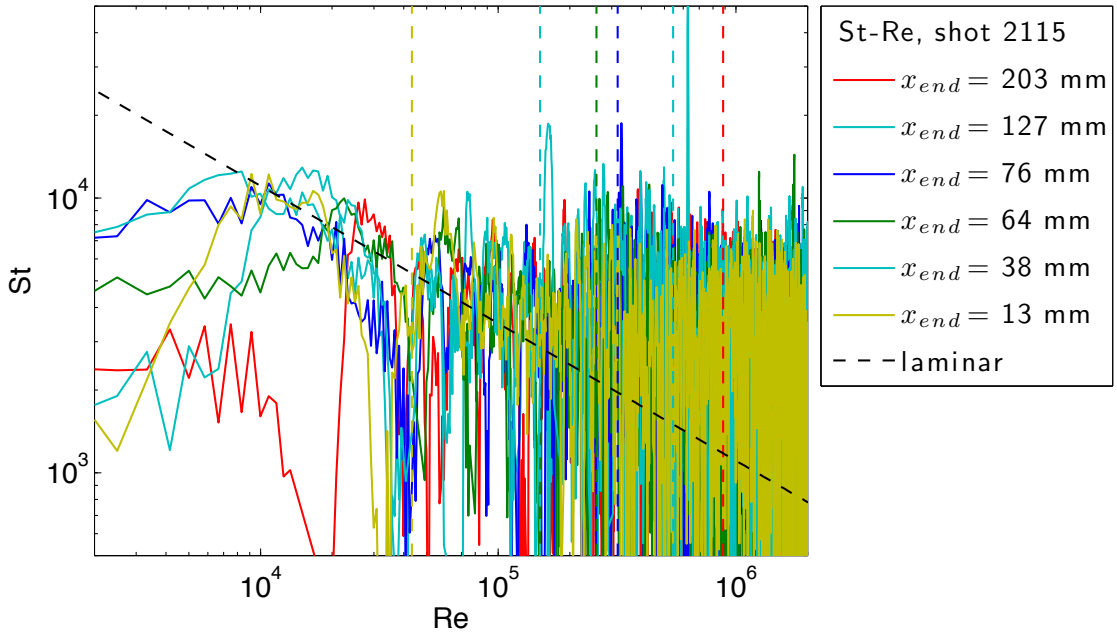

Figure E.111: Stanton-Reynolds number traces from shot 2115, a detonation in stoichiometric hydrogen-oxygen with 83% argon dilution at fill pressure 25 kPa. The dashed vertical lines represent the arrival of the reflected shock wave.

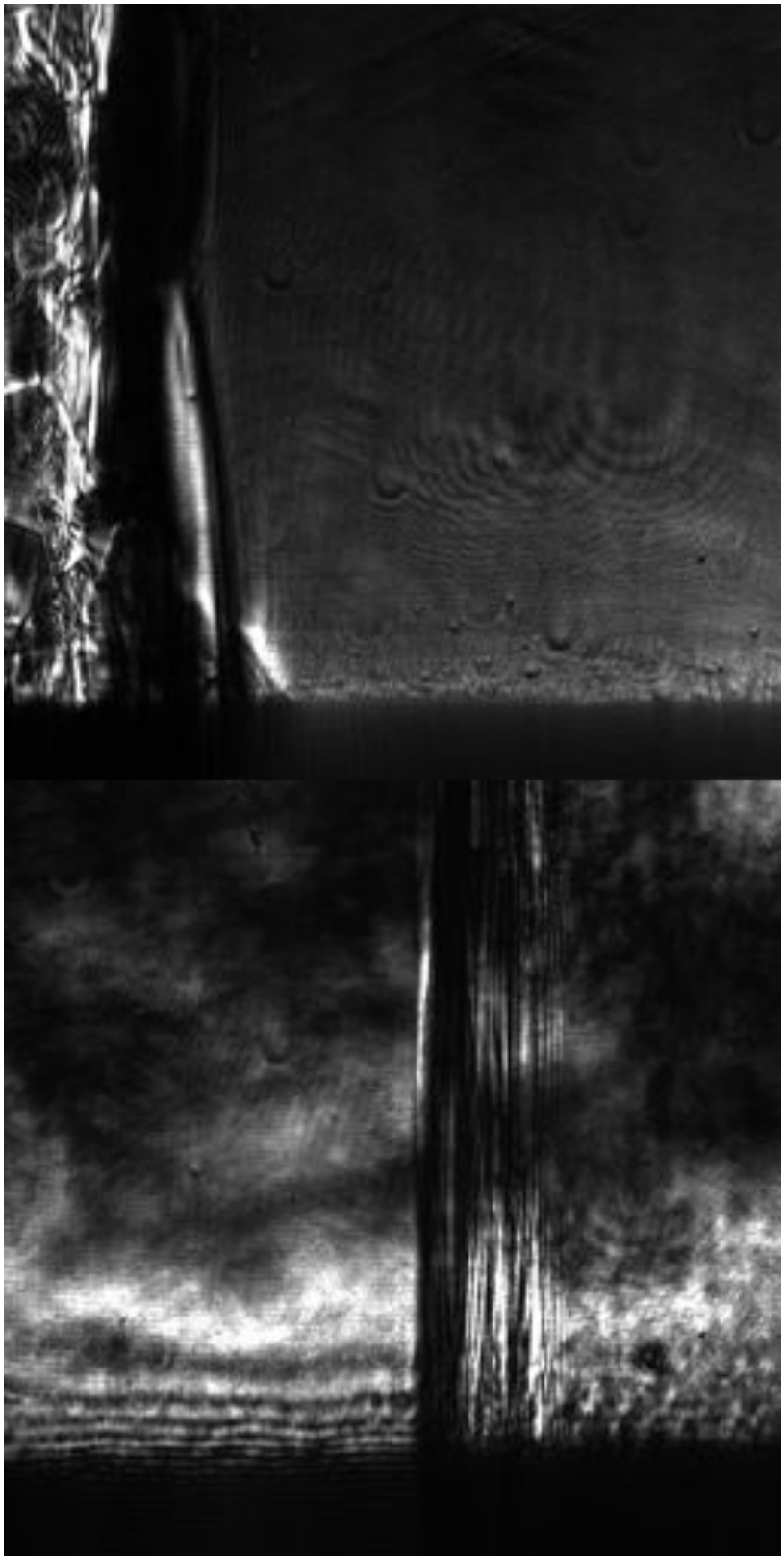

Figure E.112: Focused schlieren image of shot 2102. The field of view is approximately 14 mm wide.

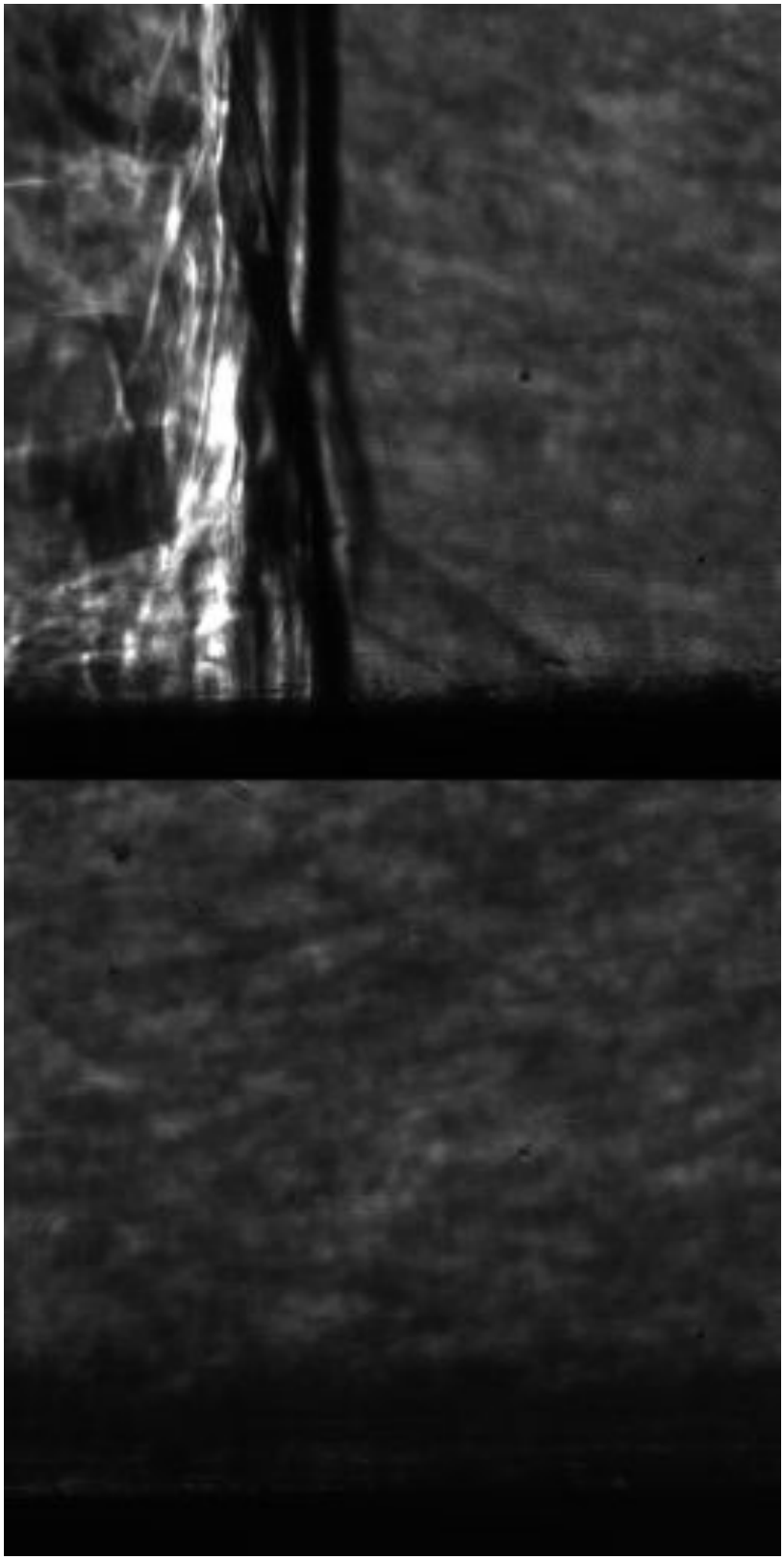

Figure E.113: Focused schlieren image of shot 2115. The field of view is approximately 14 mm wide.

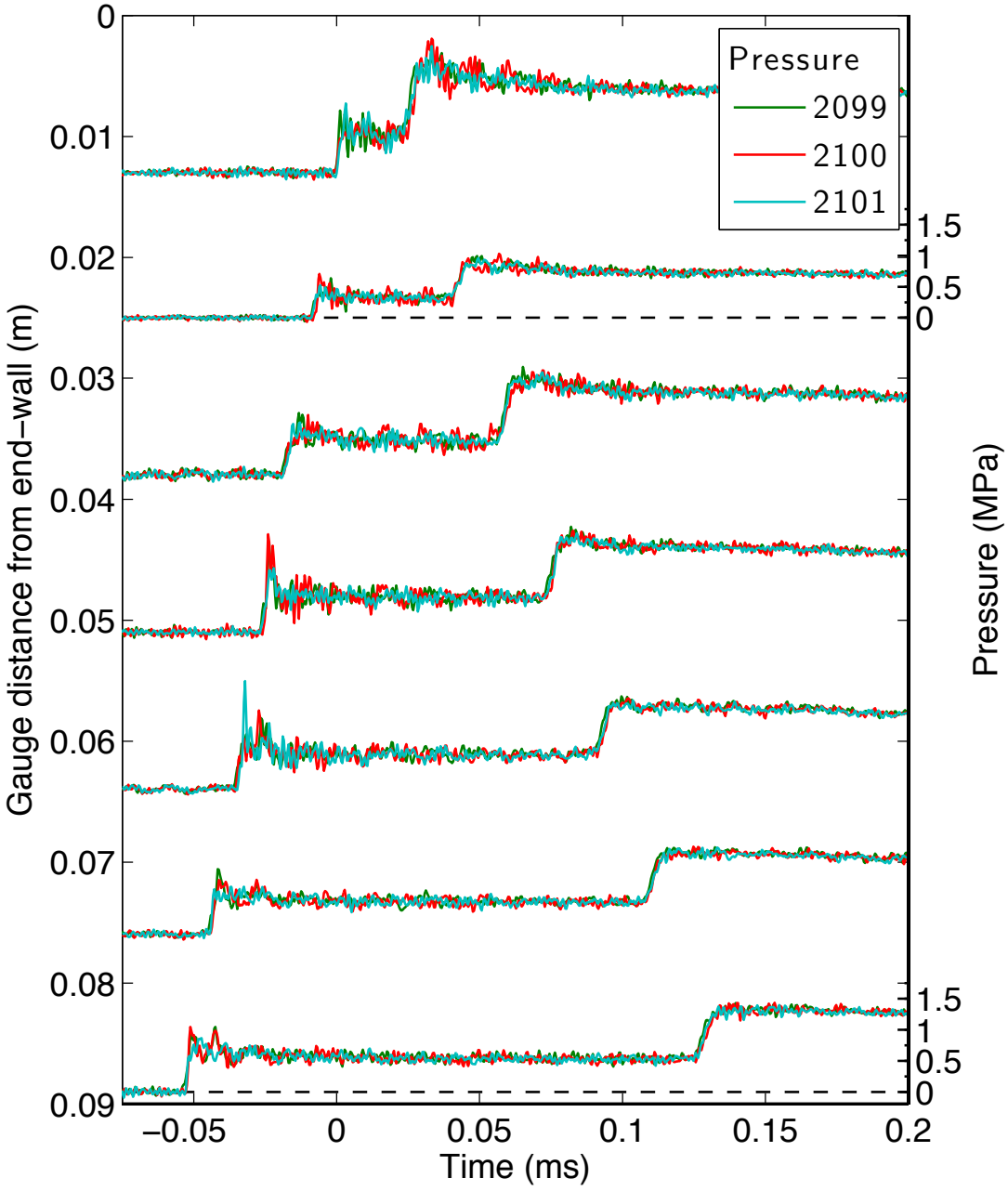

Figure E.114: Pressure traces for a detonation in stoichiometric hydrogen-oxygen with 83% argon dilution at fill pressure 40 kPa, part 1.

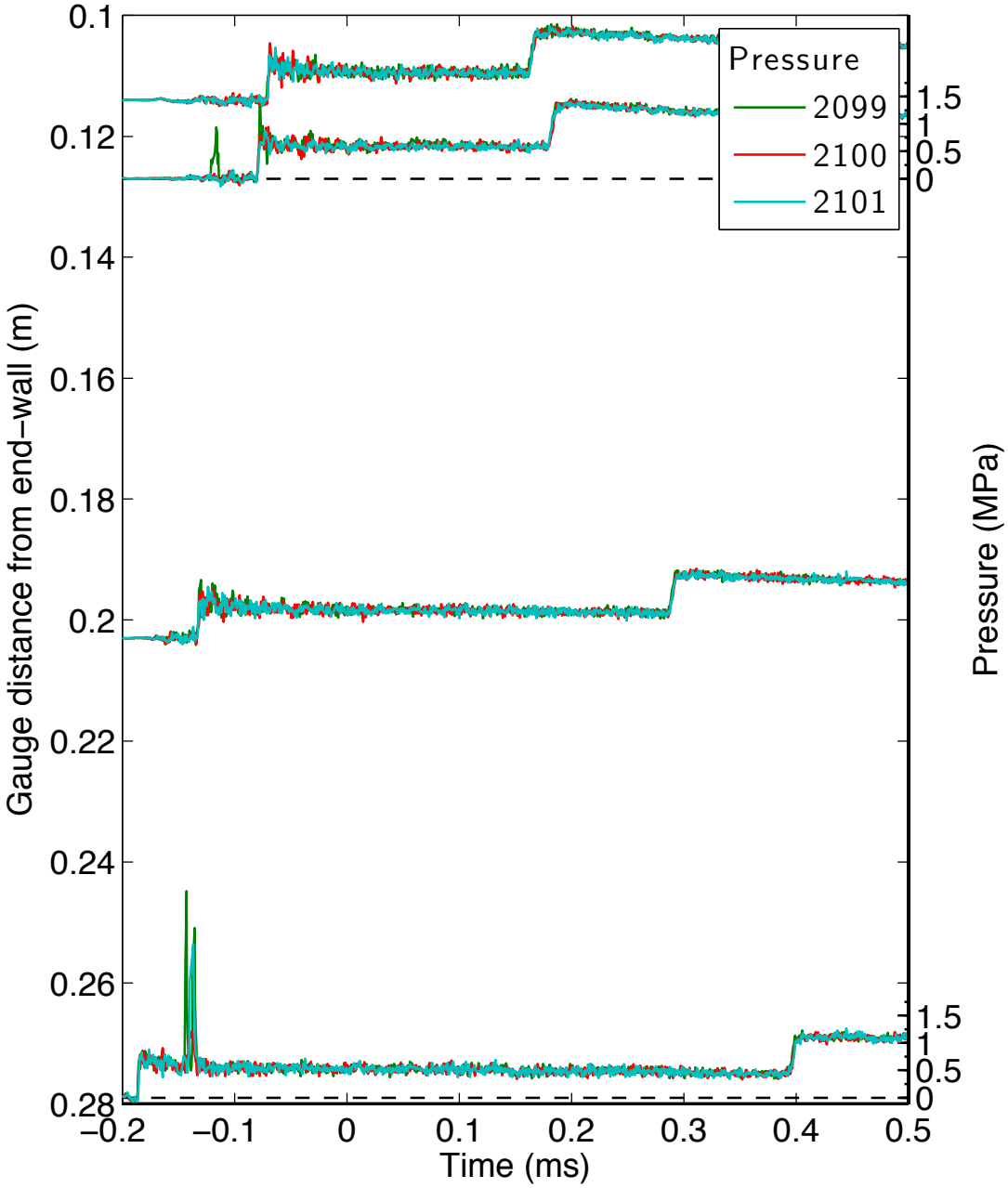

Figure E.115: Pressure traces for a detonation in stoichiometric hydrogen-oxygen with 83% argon dilution at fill pressure 40 kPa, part 2.

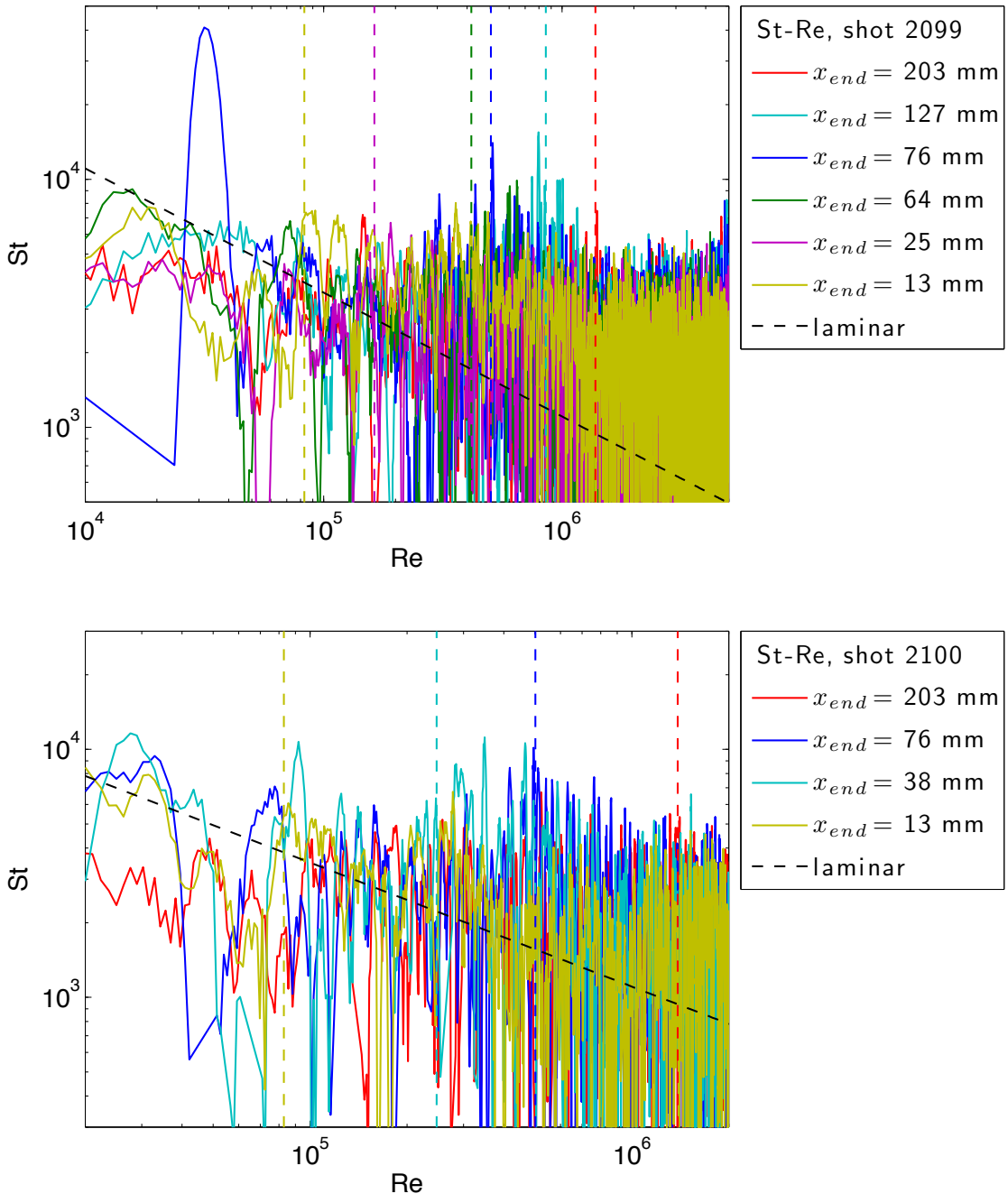

Figure E.116: Stanton-Reynolds number traces from shot 2100, a detonation in stoichiometric hydrogen-oxygen with 83% argon dilution at fill pressure 40 kPa. The dashed vertical lines represent the arrival of the reflected shock wave.

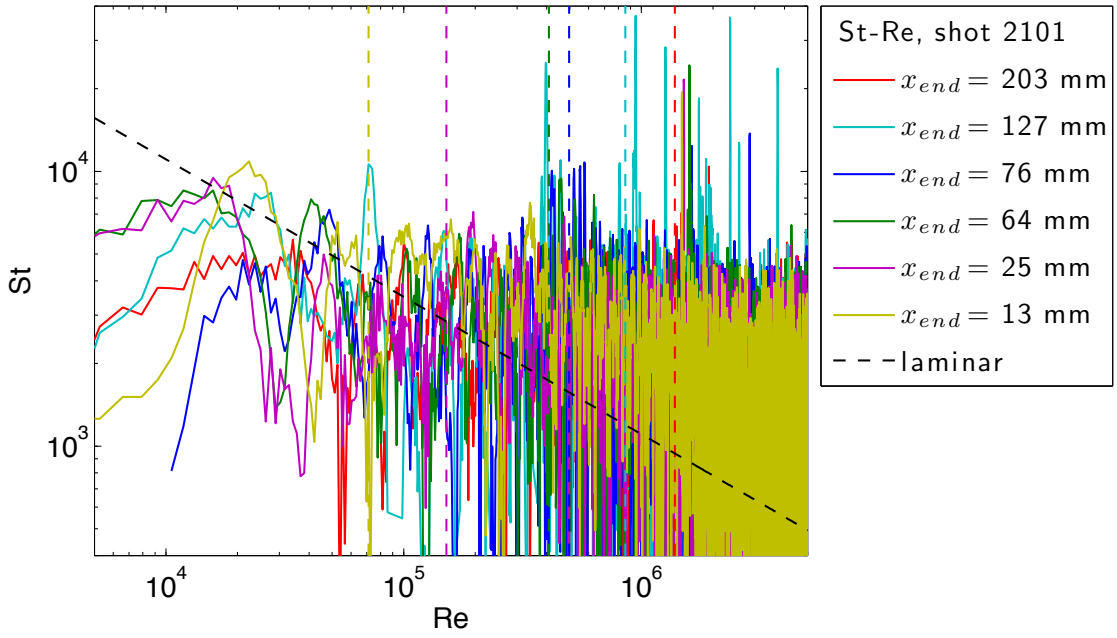

Figure E.117: Stanton-Reynolds number traces from shot 2101, a detonation in stoichiometric hydrogen-oxygen with 83% argon dilution at fill pressure 40 kPa. The dashed vertical lines represent the arrival of the reflected shock wave.

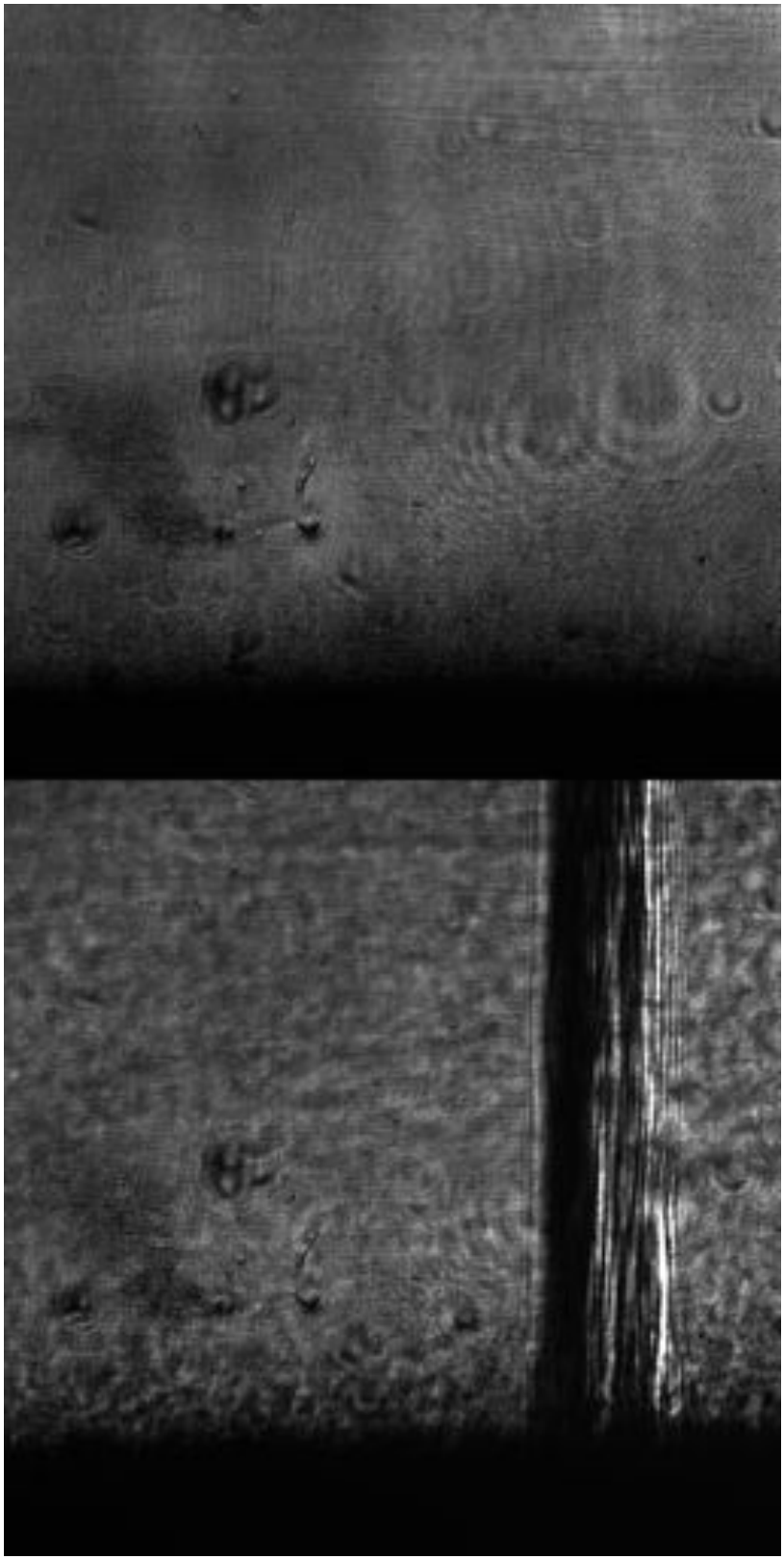

Figure E.118: Focused schlieren image of shot 2099. The field of view is approximately 14 mm wide.

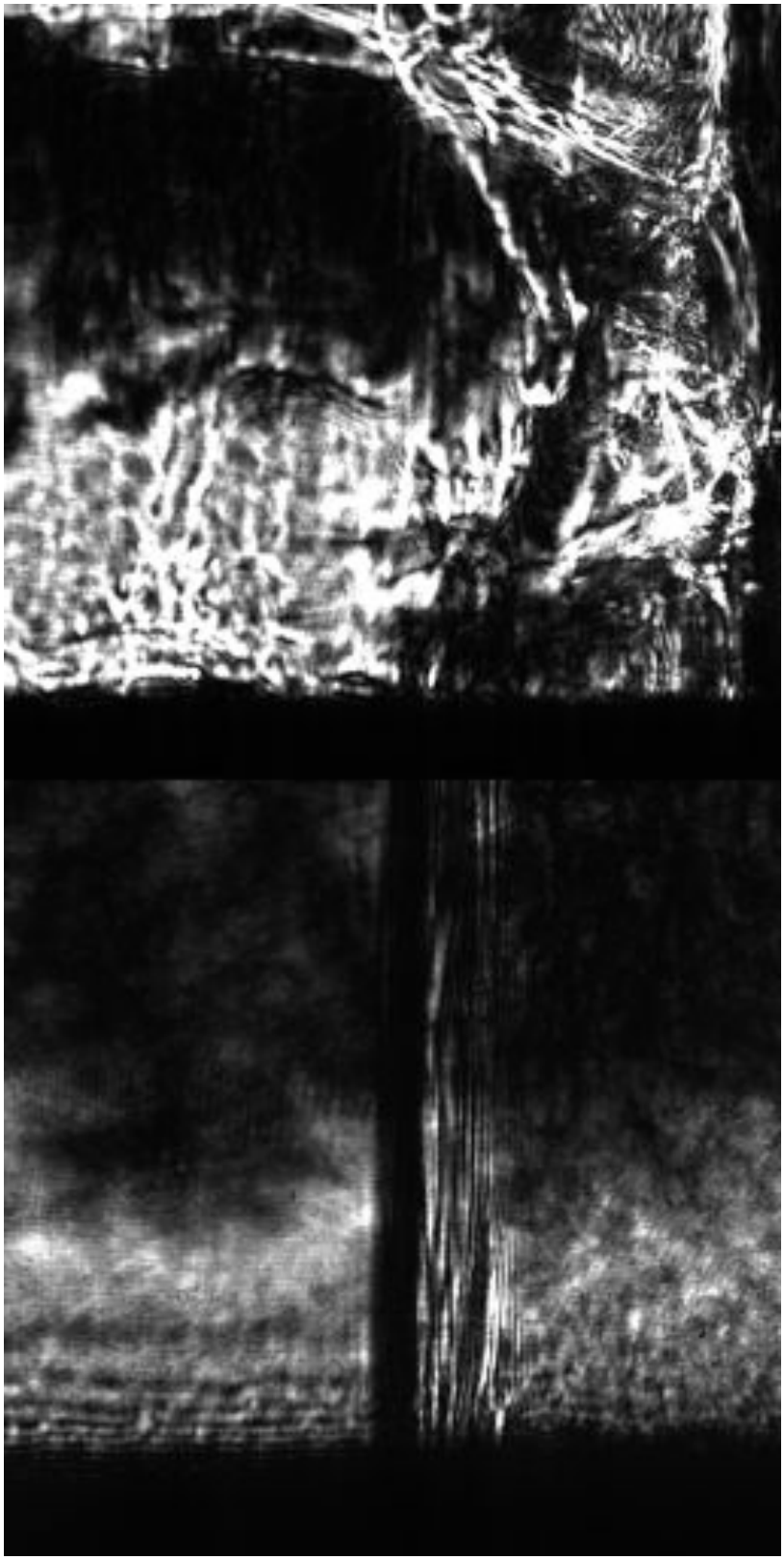

Figure E.119: Focused schlieren image of shot 2100. The field of view is approximately 14 mm wide.

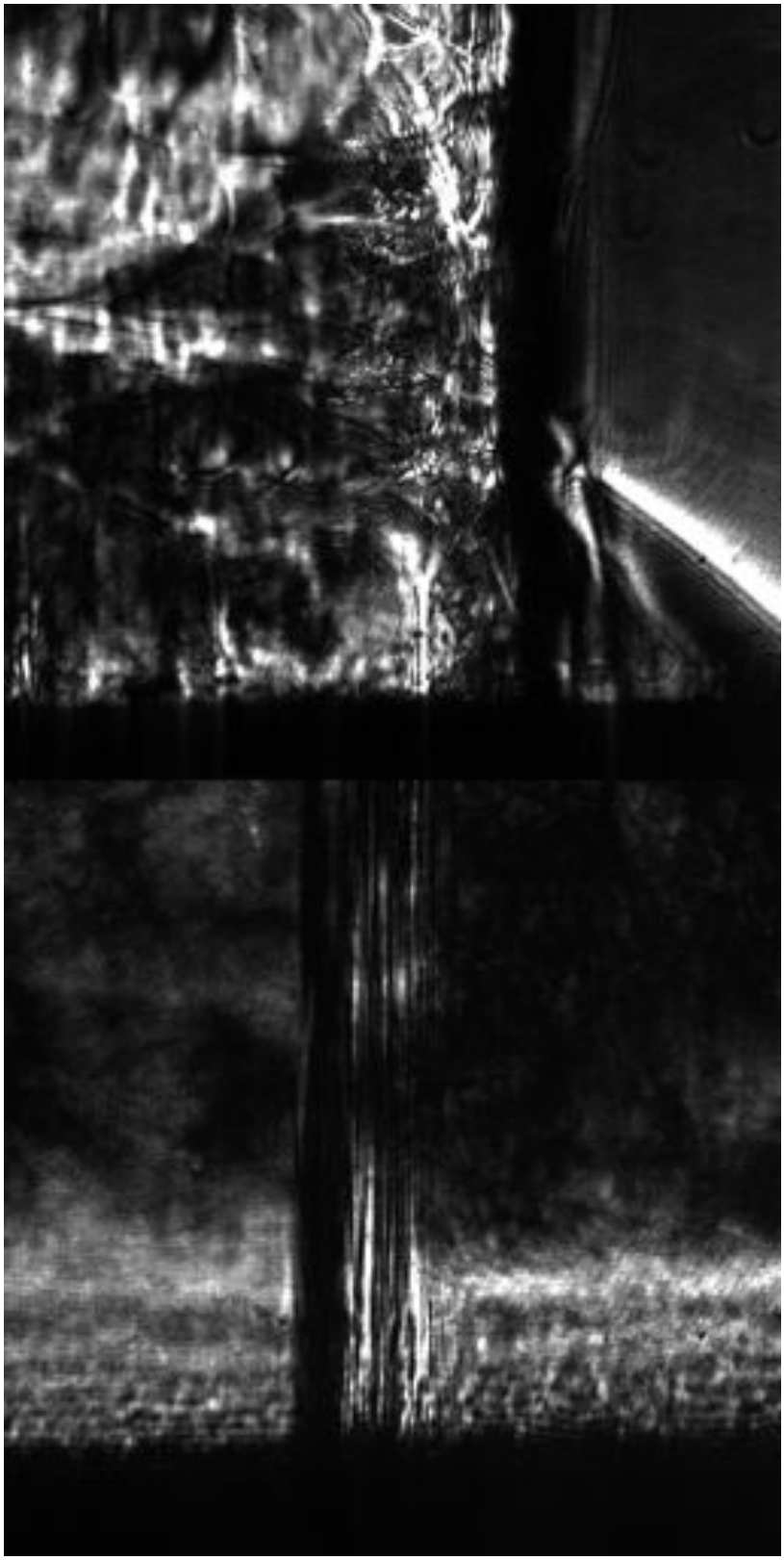

Figure E.120: Focused schlieren image of shot 2101. The field of view is approximately 14 mm wide.

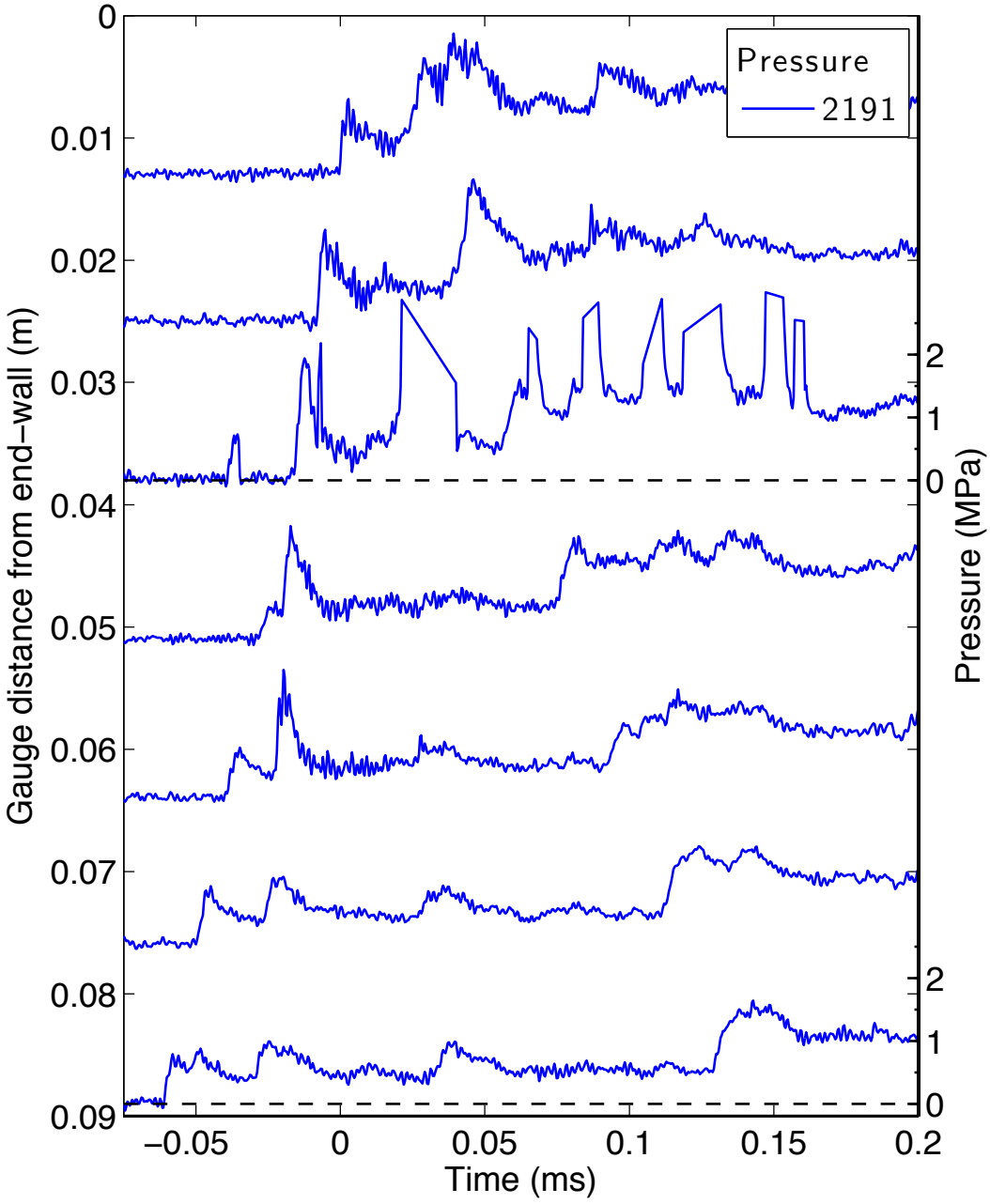

Figure E.121: Pressure traces for a detonation in stoichiometric hydrogen-oxygen with 90% argon dilution at fill pressure 50 kPa, part 1.

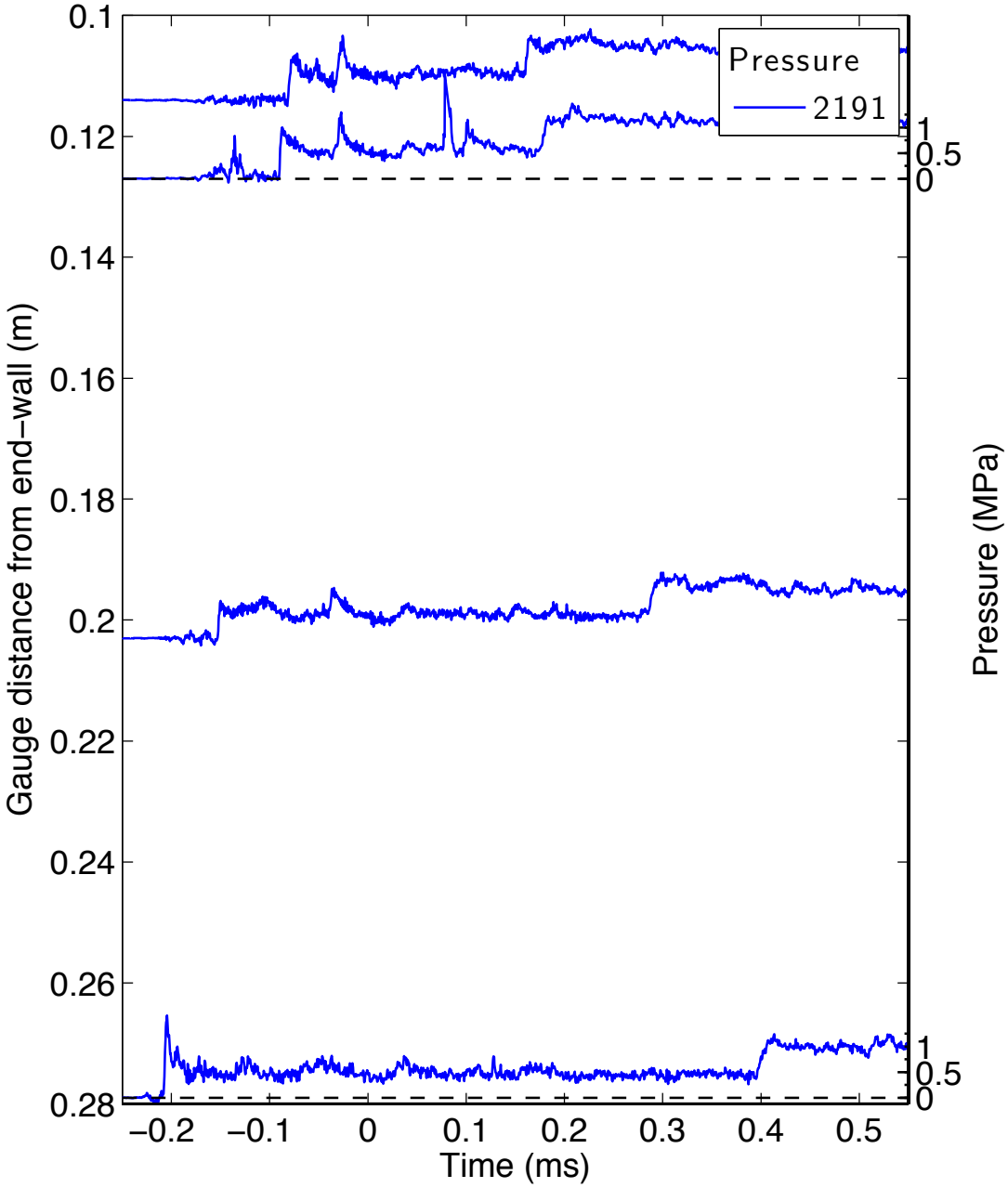

Figure E.122: Pressure traces for a detonation in stoichiometric hydrogen-oxygen with 90% argon dilution at fill pressure 50 kPa, part 2.

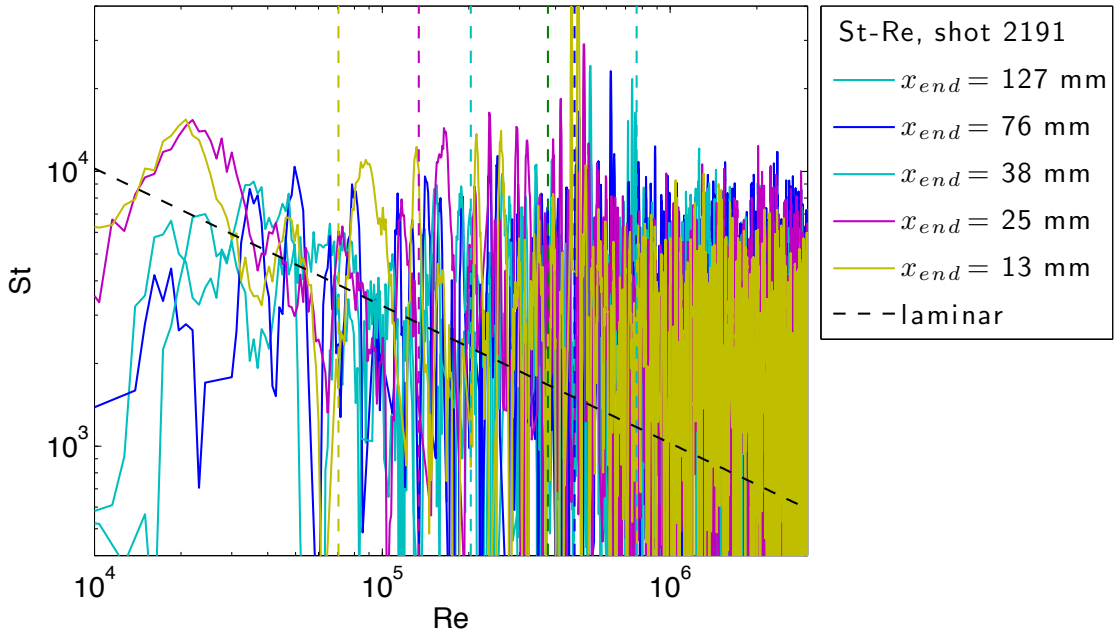

Figure E.123: Stanton-Reynolds number traces from shot 2191, a detonation in stoichiometric hydrogen-oxygen with 90% argon dilution at fill pressure 50 kPa. The dashed vertical lines represent the arrival of the reflected shock wave.

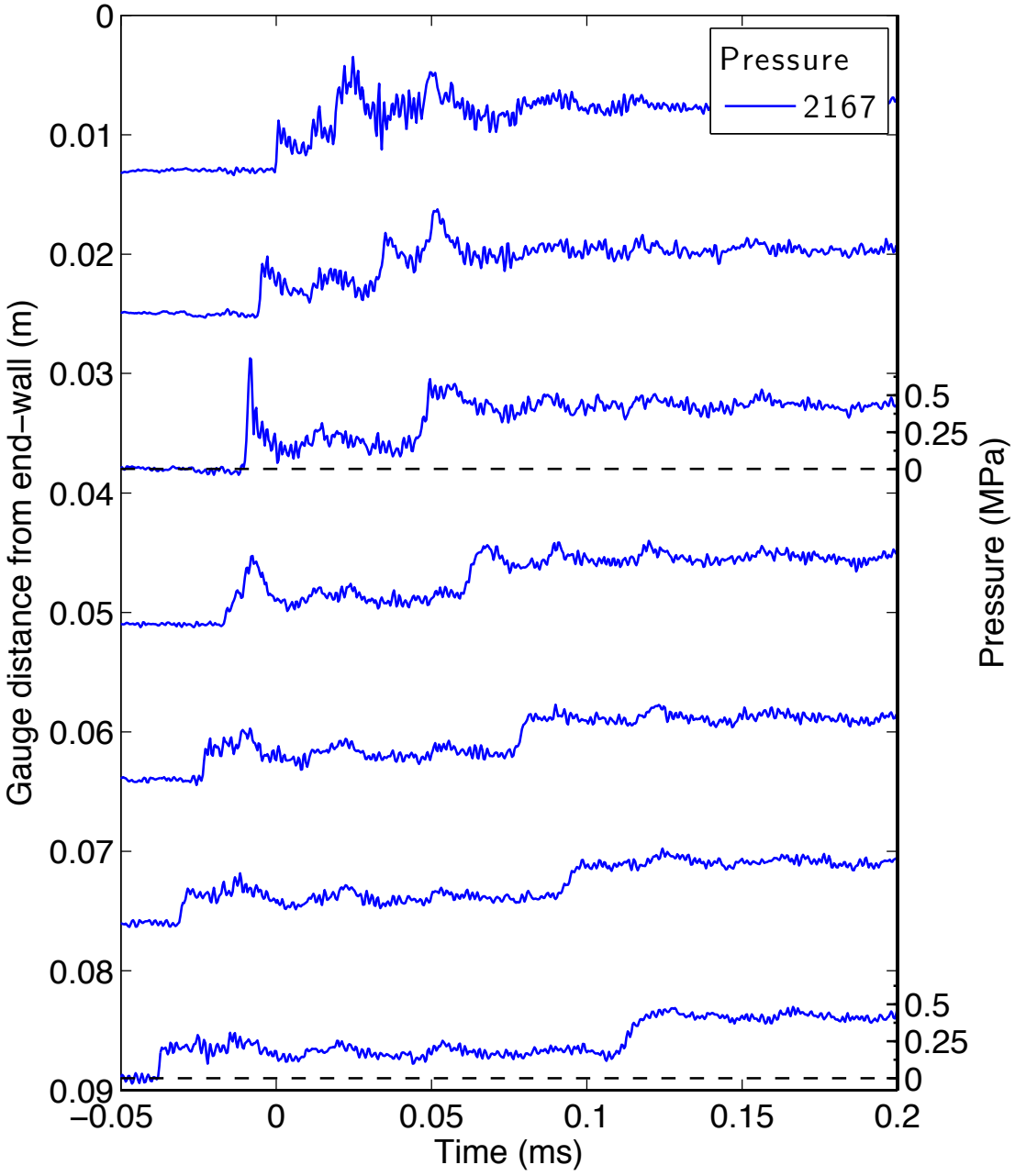

Figure E.124: Pressure traces for a detonation in stoichiometric hydrogen-oxygen with 50% nitrogen dilution at fill pressure 10 kPa, part 1.

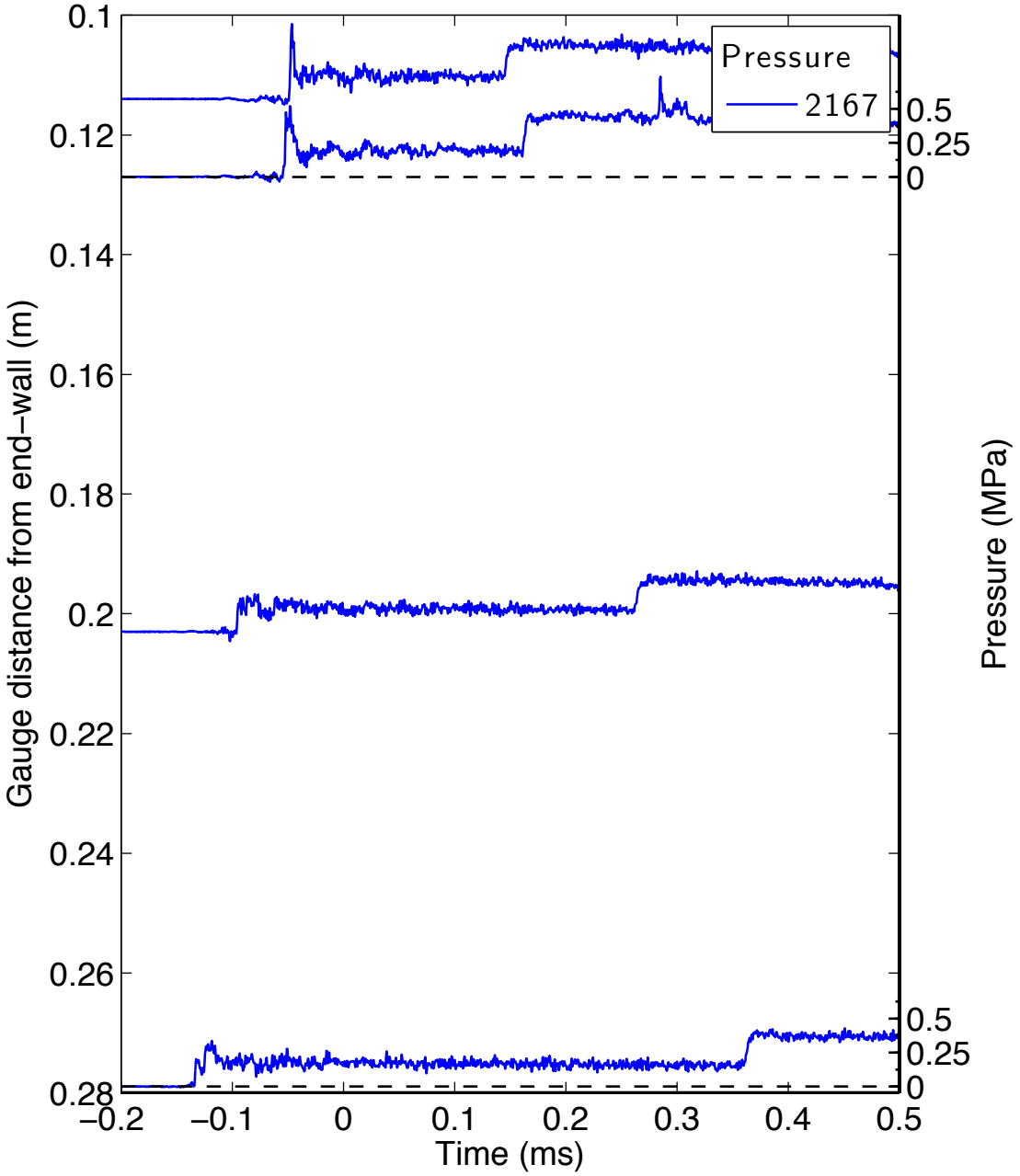

Figure E.125: Pressure traces for a detonation in stoichiometric hydrogen-oxygen with 50% nitrogen dilution at fill pressure 10 kPa, part 2.

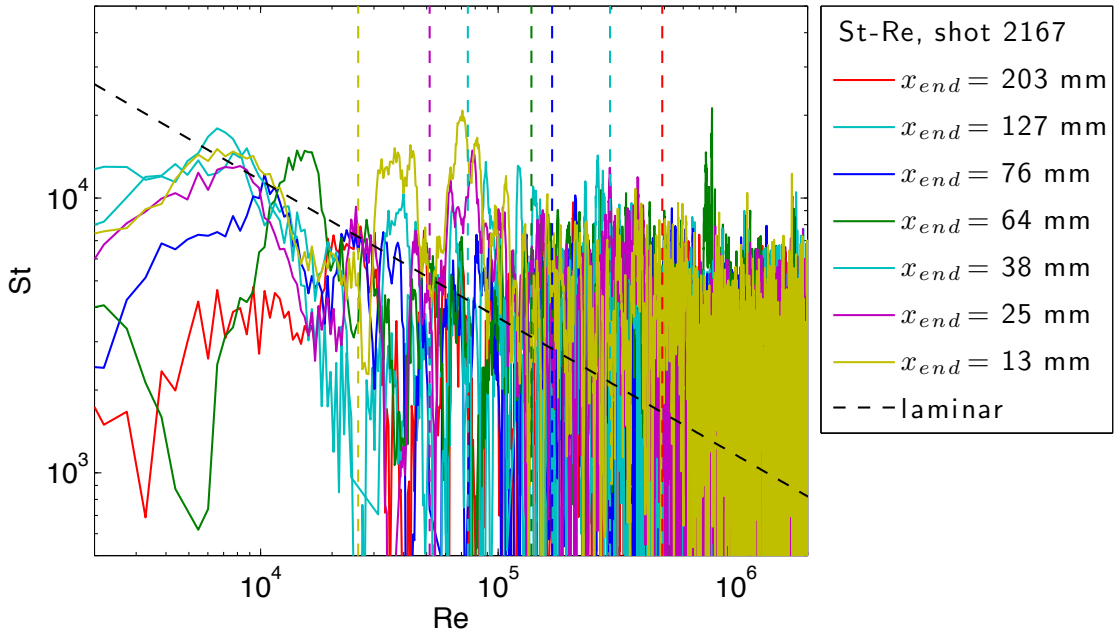

Figure E.126: Stanton-Reynolds number traces from shot 2167, a detonation in stoichiometric hydrogen-oxygen with 50% nitrogen dilution at fill pressure 10 kPa. The dashed vertical lines represent the arrival of the reflected shock wave.

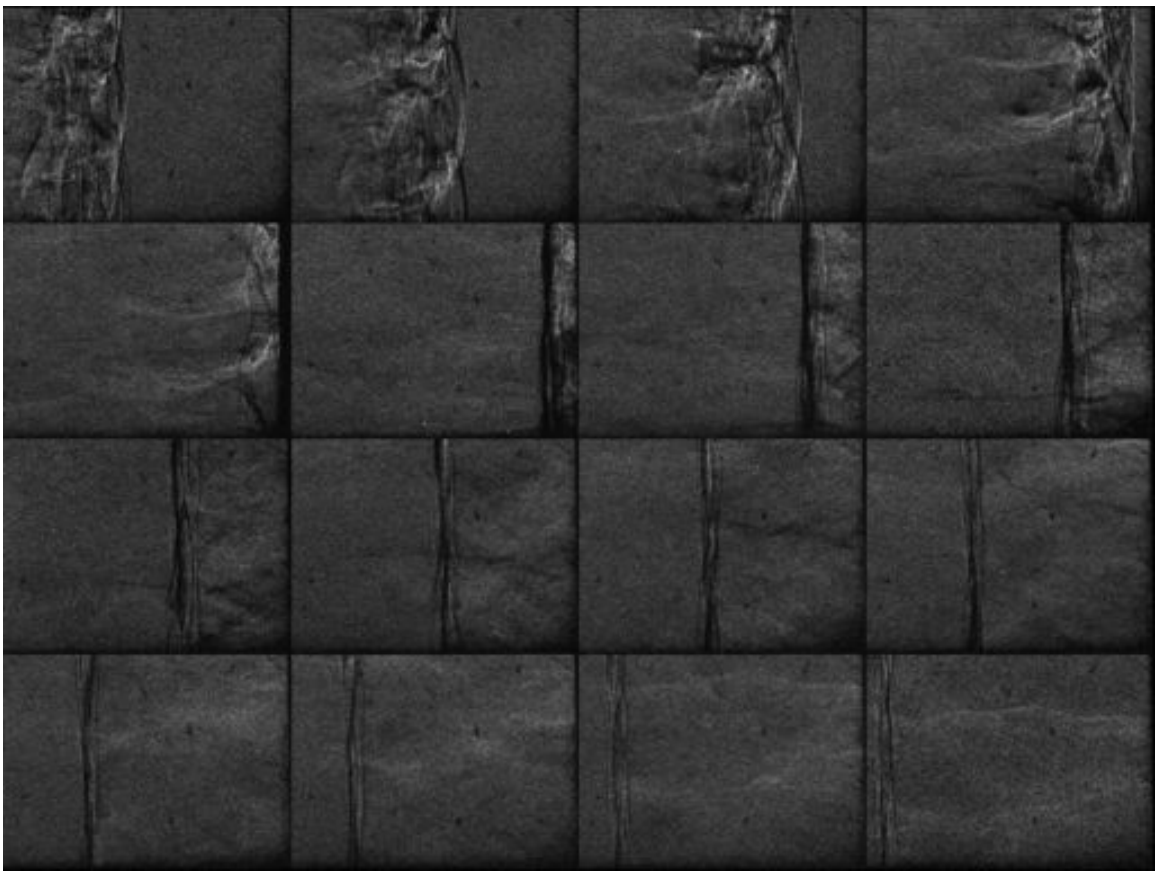

Figure E.127: Unfocused schlieren image of shot 2167. The field of view is approximately 30 mm wide.

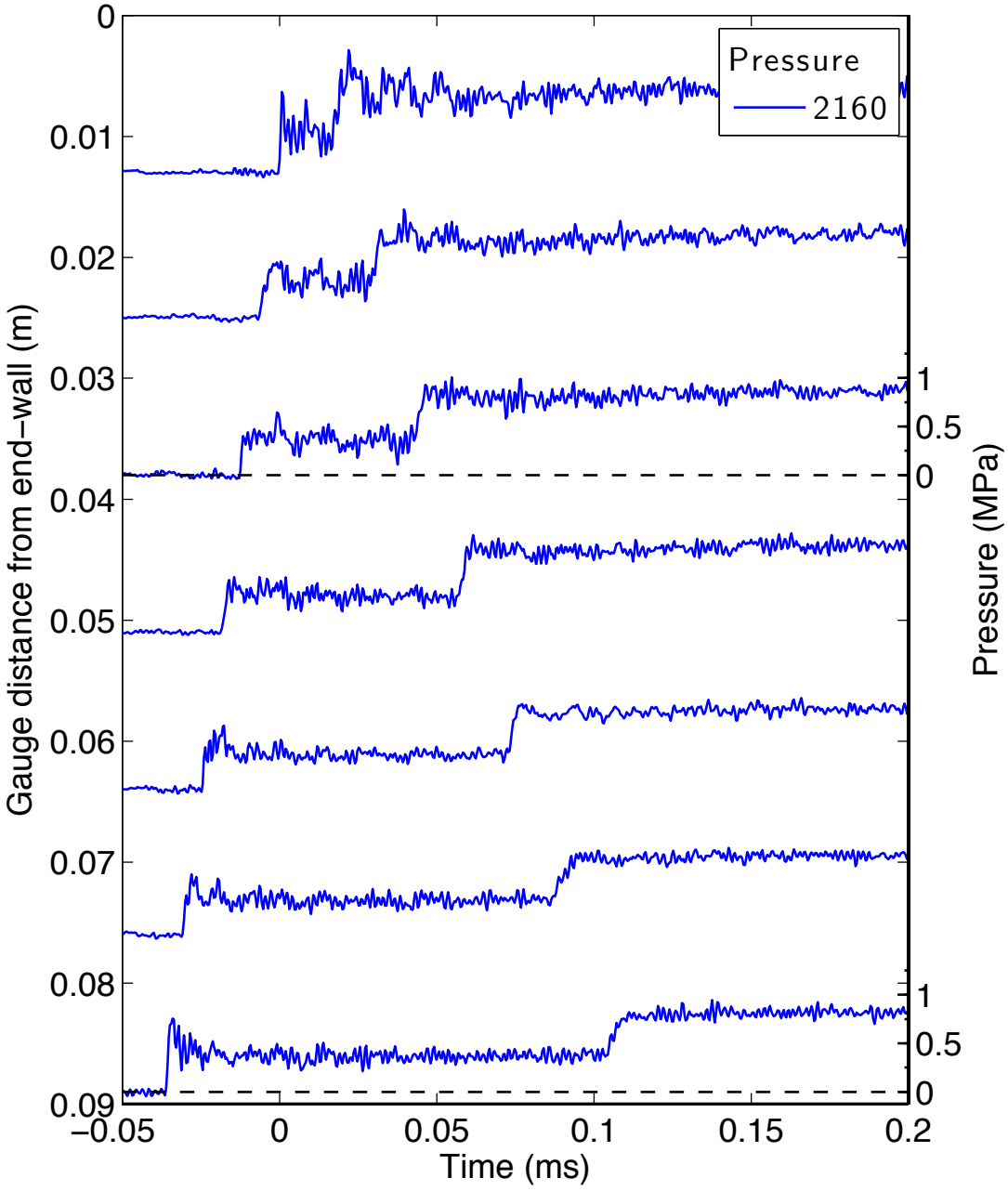

Figure E.128: Pressure traces for a detonation in stoichiometric hydrogen-oxygen with 50% nitrogen dilution at fill pressure 25 kPa, part 1.

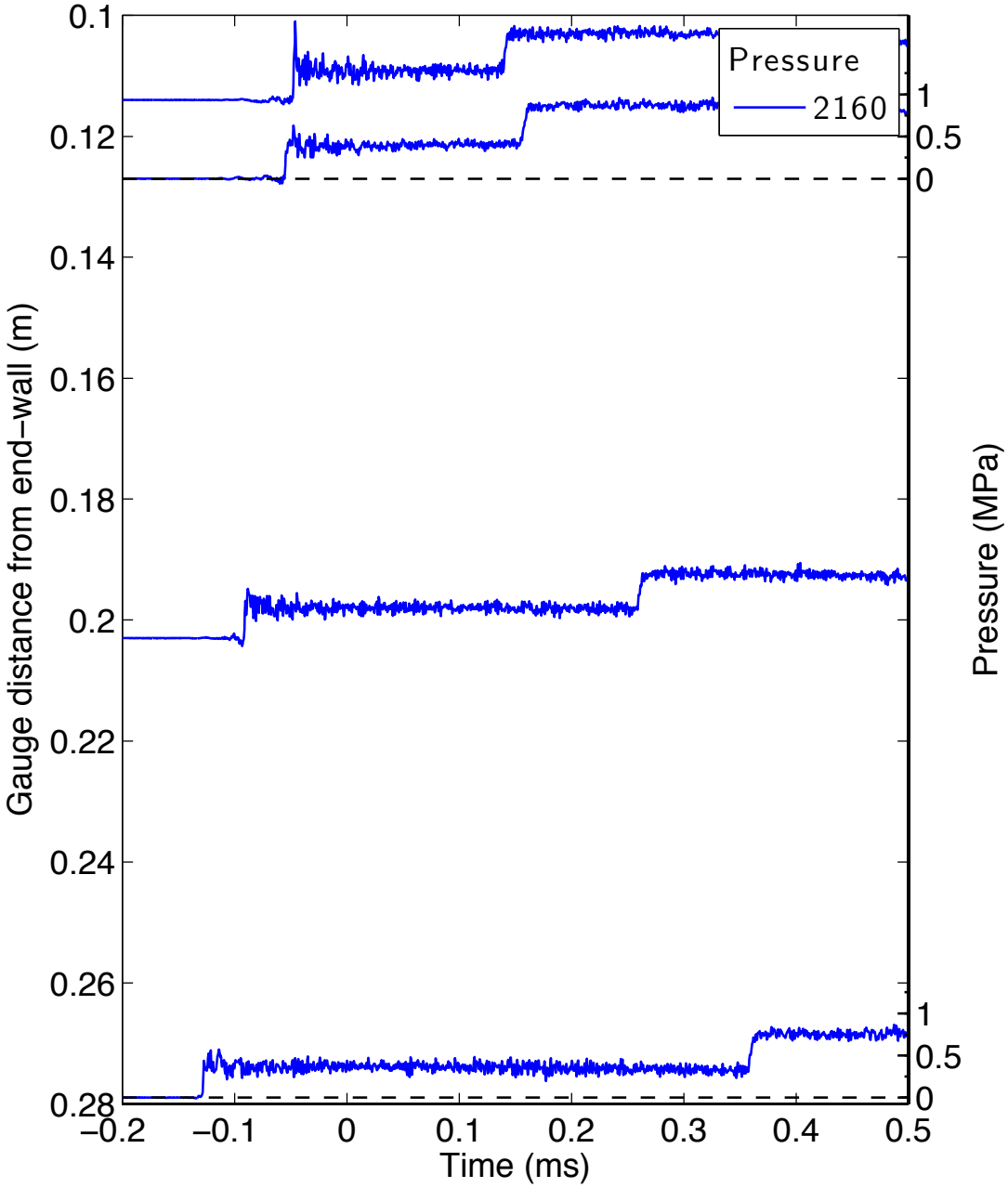

Figure E.129: Pressure traces for a detonation in stoichiometric hydrogen-oxygen with 50% nitrogen dilution at fill pressure 25 kPa, part 2.

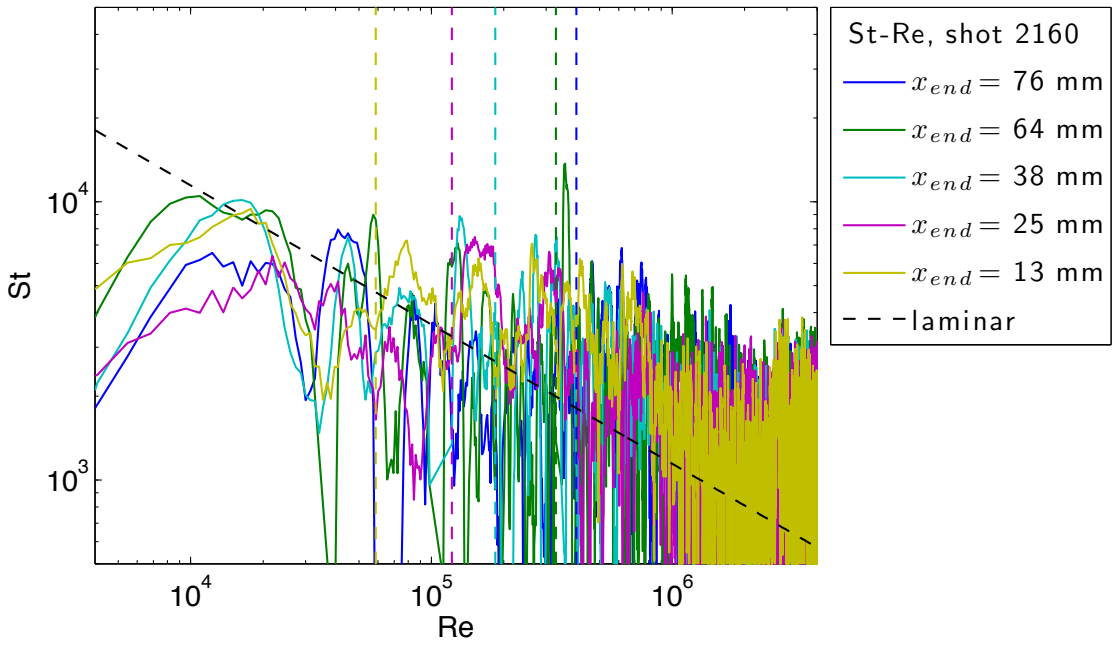

Figure E.130: Stanton-Reynolds number traces from shot 2160, a detonation in stoichiometric hydrogen-oxygen with 50% nitrogen dilution at fill pressure 25 kPa. The dashed vertical lines represent the arrival of the reflected shock wave.

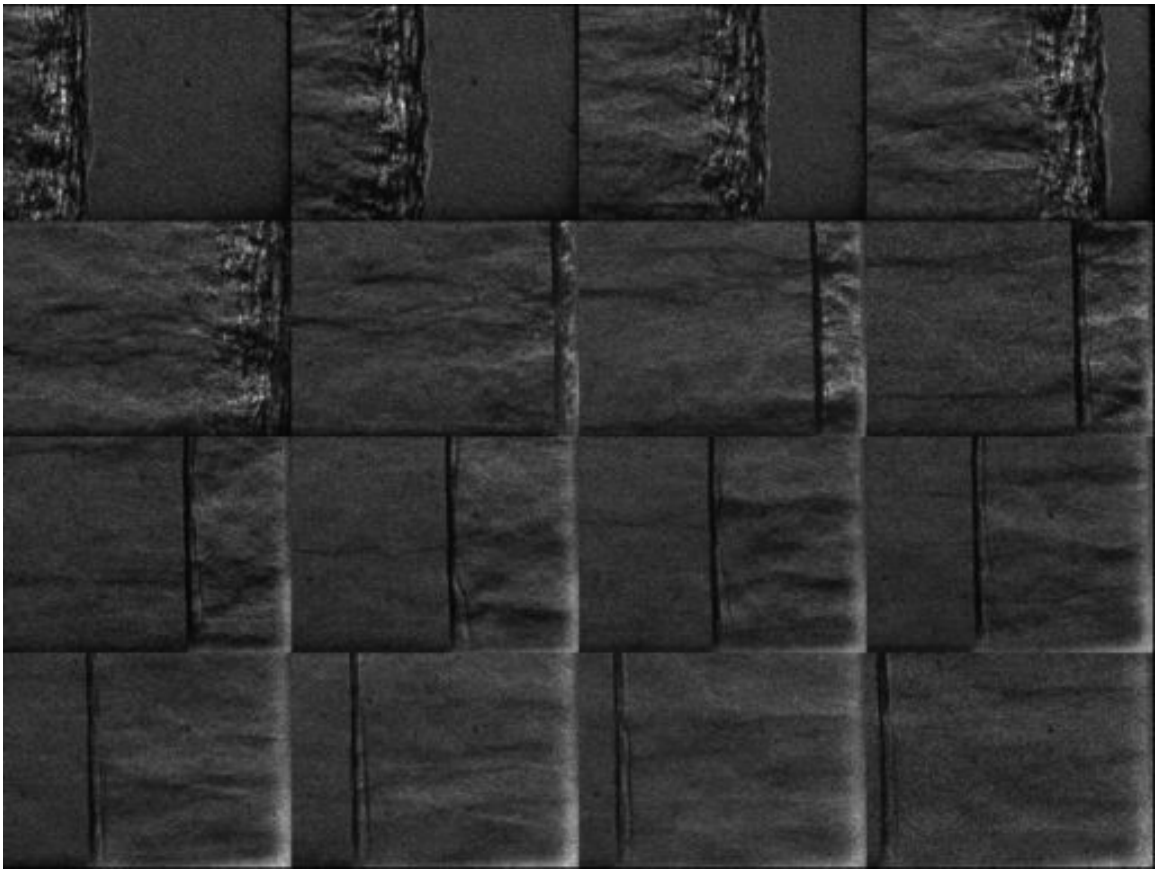

Figure E.131: Unfocused schlieren image of shot 2160. The field of view is approximately 30 mm wide.

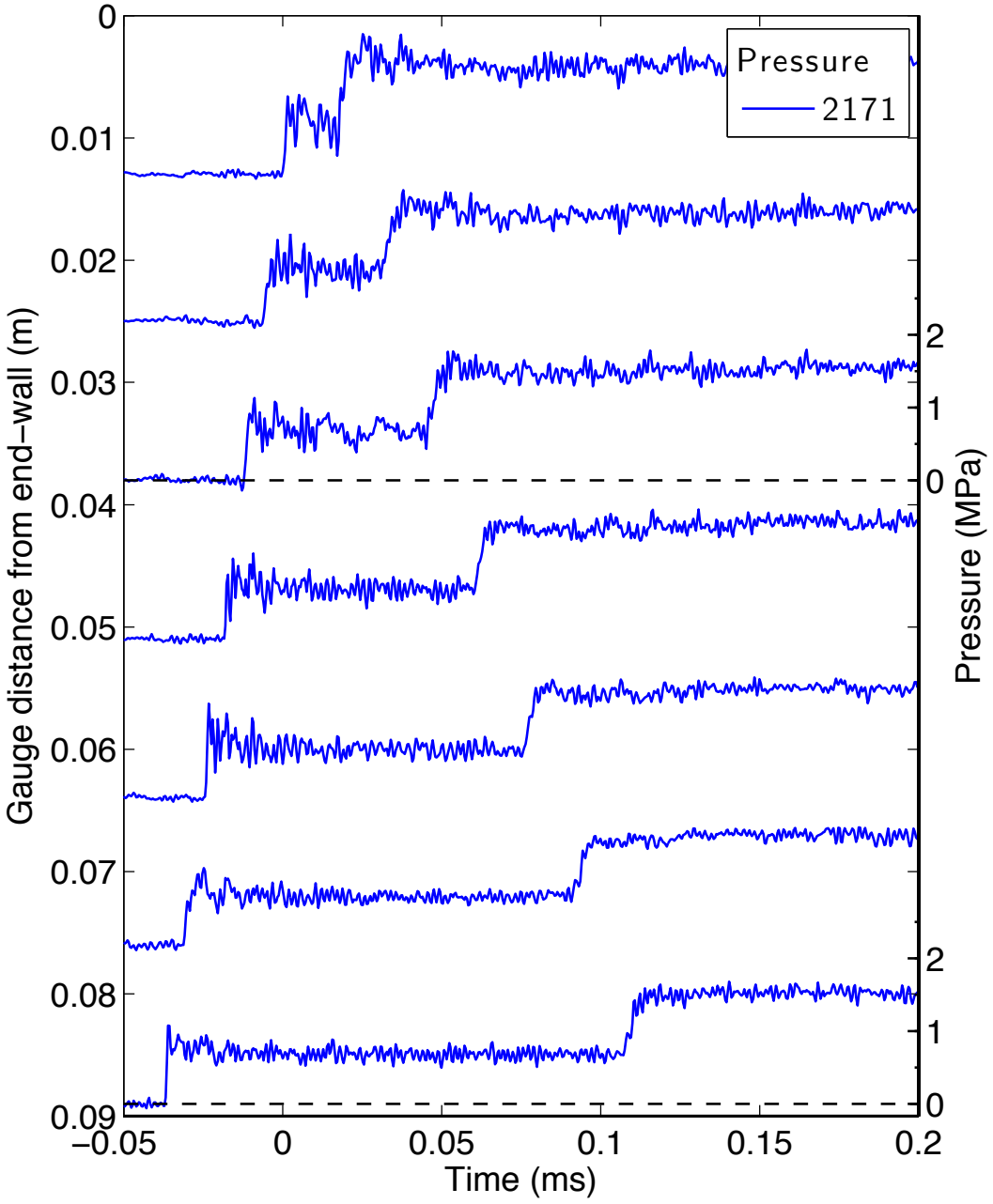

Figure E.132: Pressure traces for a detonation in stoichiometric hydrogen-oxygen with 50% nitrogen dilution at fill pressure 50 kPa, part 1.

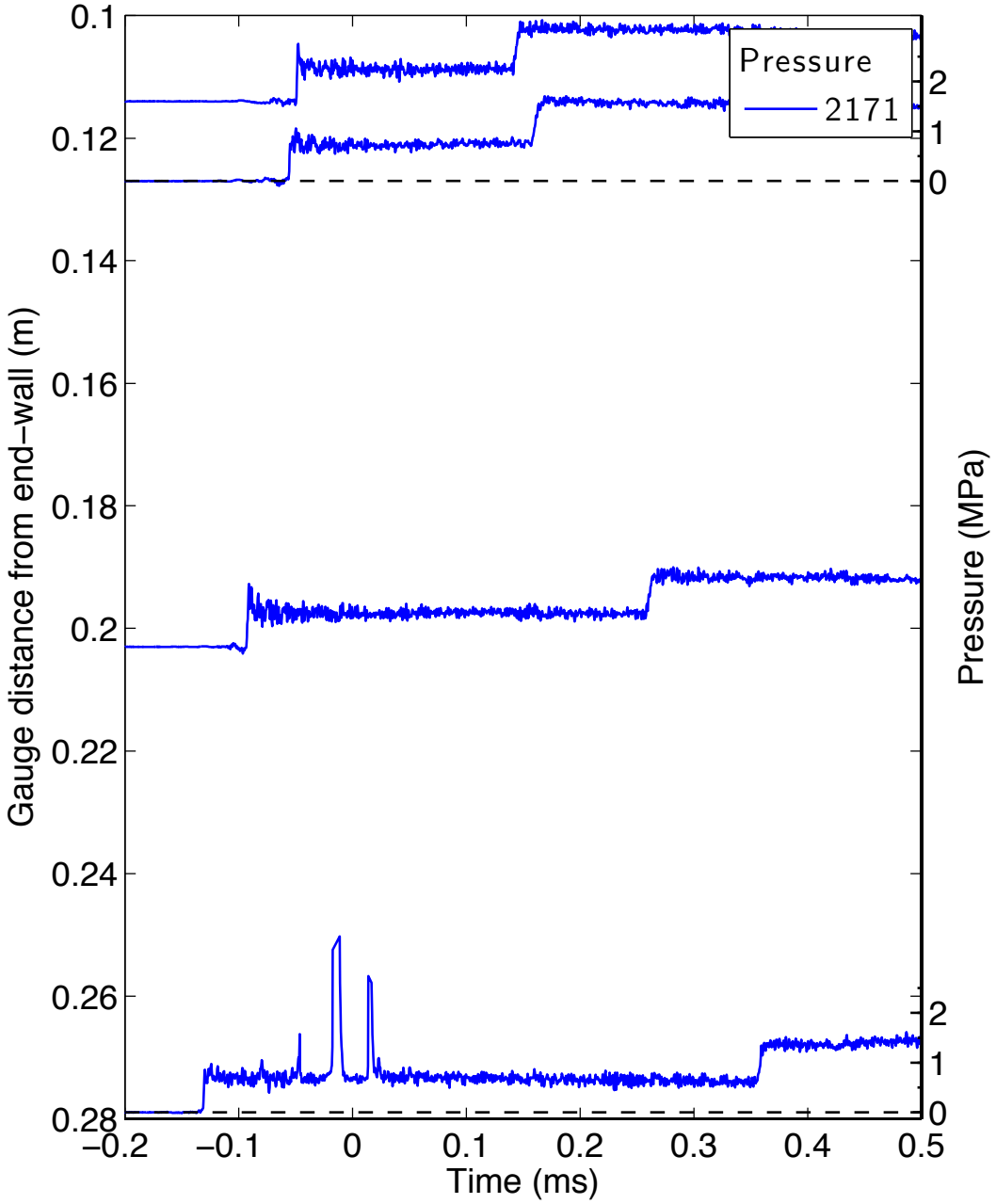

Figure E.133: Pressure traces for a detonation in stoichiometric hydrogen-oxygen with 50% nitrogen dilution at fill pressure 50 kPa, part 2.

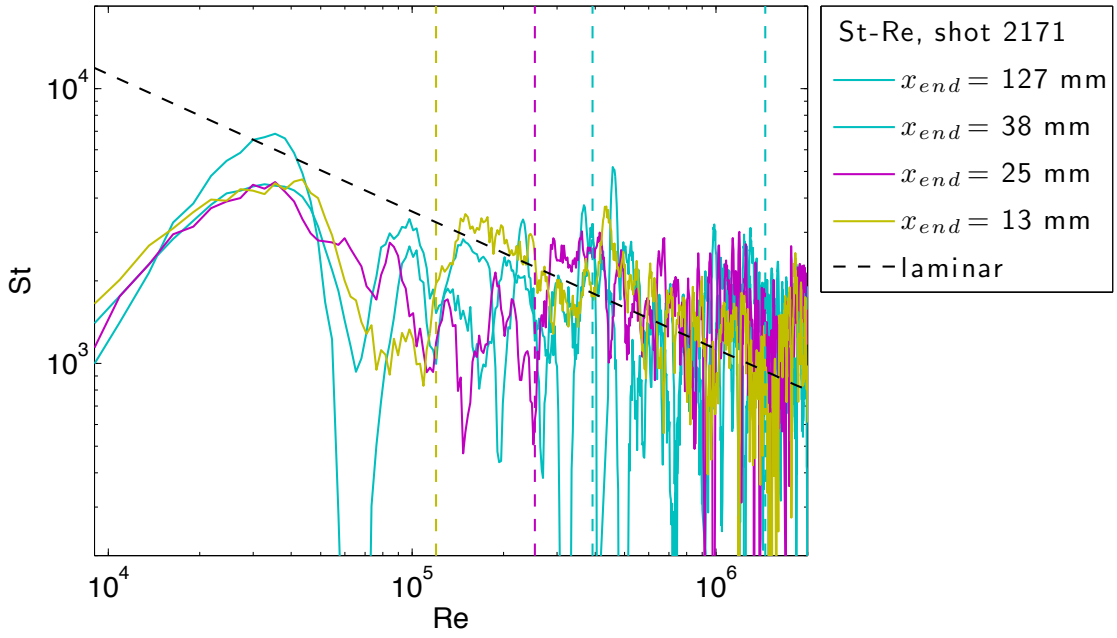

Figure E.134: Stanton-Reynolds number traces from shot 2171, a detonation in stoichiometric hydrogen-oxygen with 50% nitrogen dilution at fill pressure 50 kPa. The dashed vertical lines represent the arrival of the reflected shock wave.

Figure E.135: Unfocused schlieren image of shot 2171. The field of view is approximately 30 mm wide.

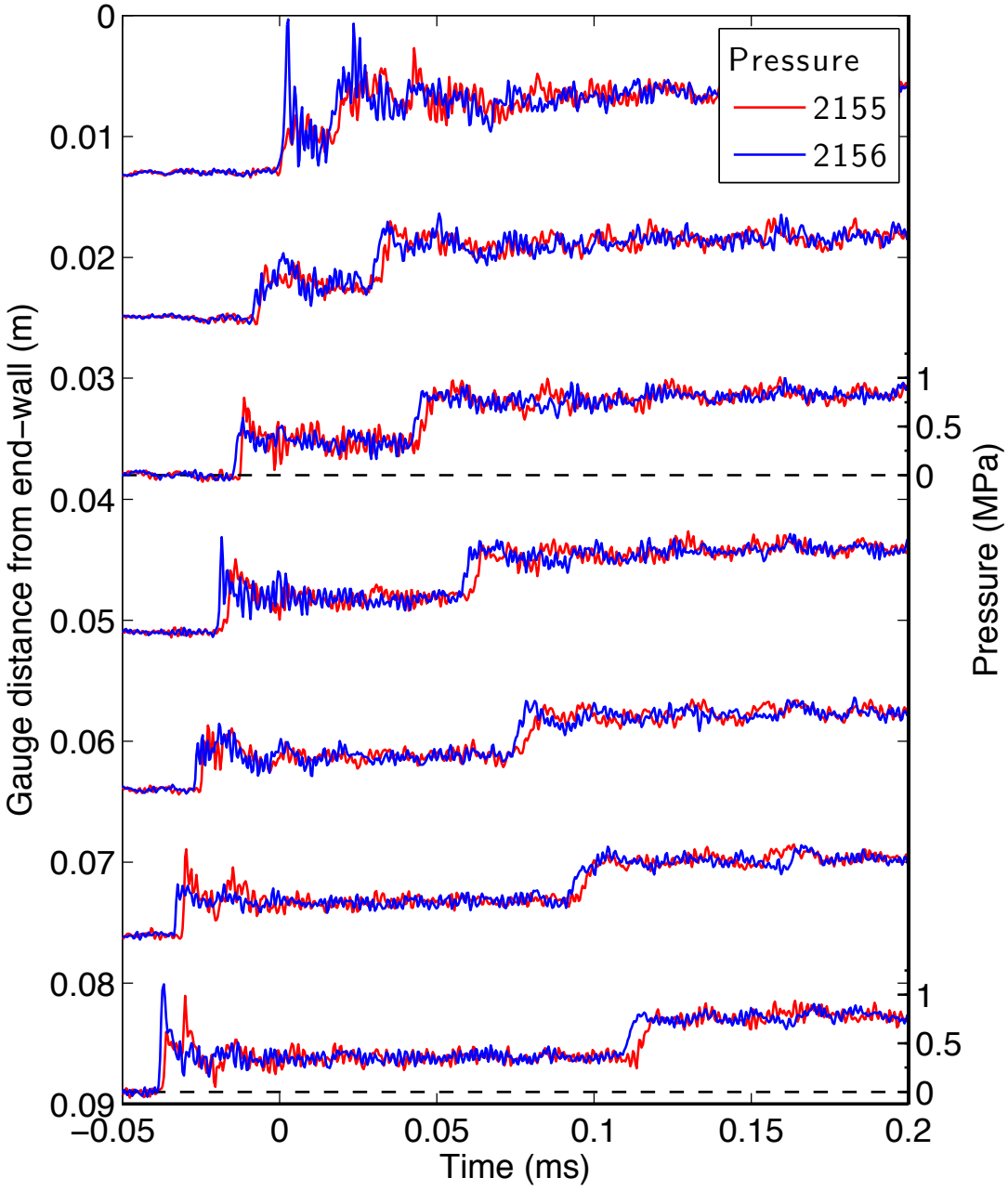

Figure E.136: Pressure traces for a detonation in stoichiometric hydrogen-oxygen with 25% carbon dioxide dilution at fill pressure 25 kPa, part 1.

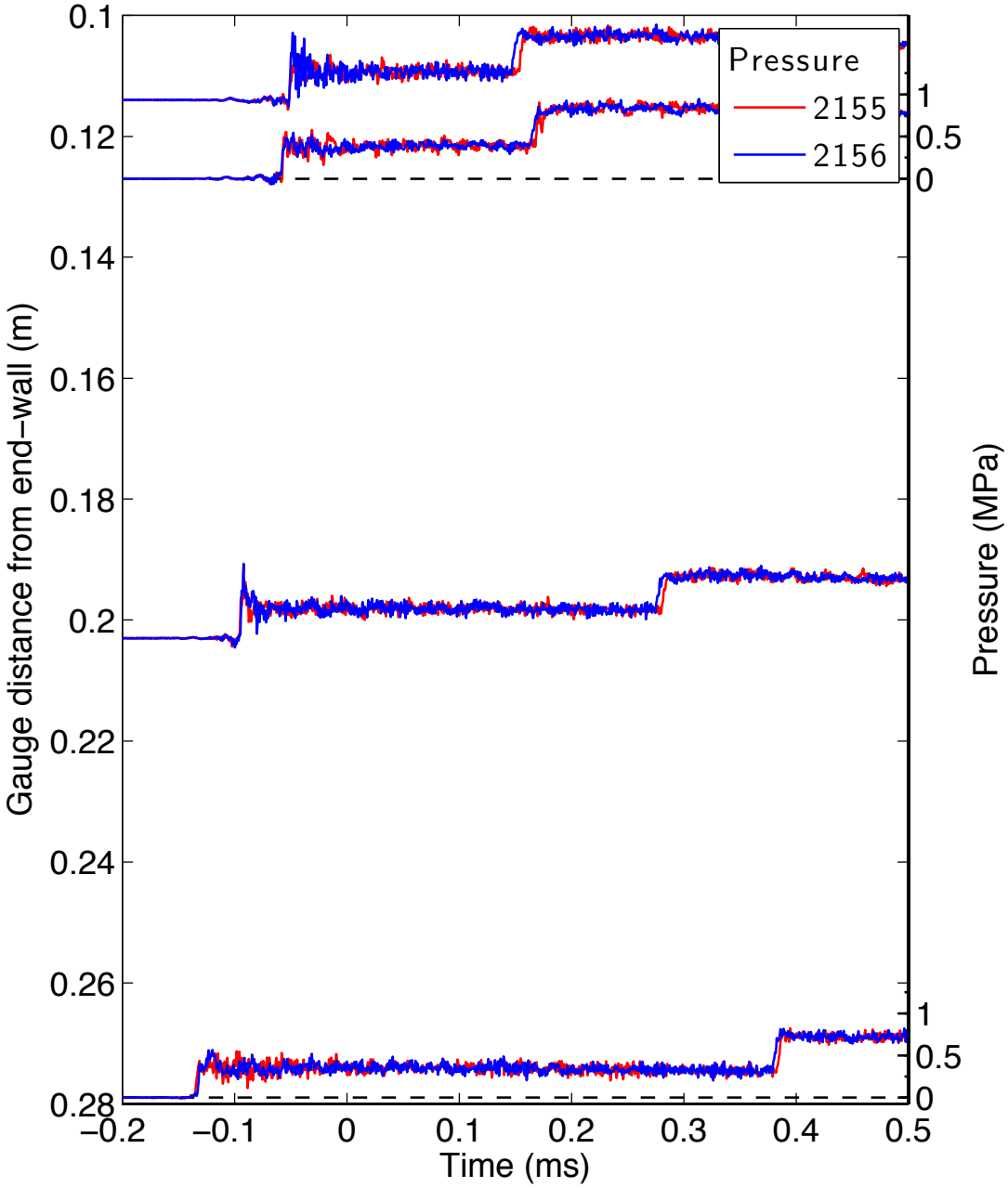

Figure E.137: Pressure traces for a detonation in stoichiometric hydrogen-oxygen with 25% carbon dioxide dilution at fill pressure 25 kPa, part 2.

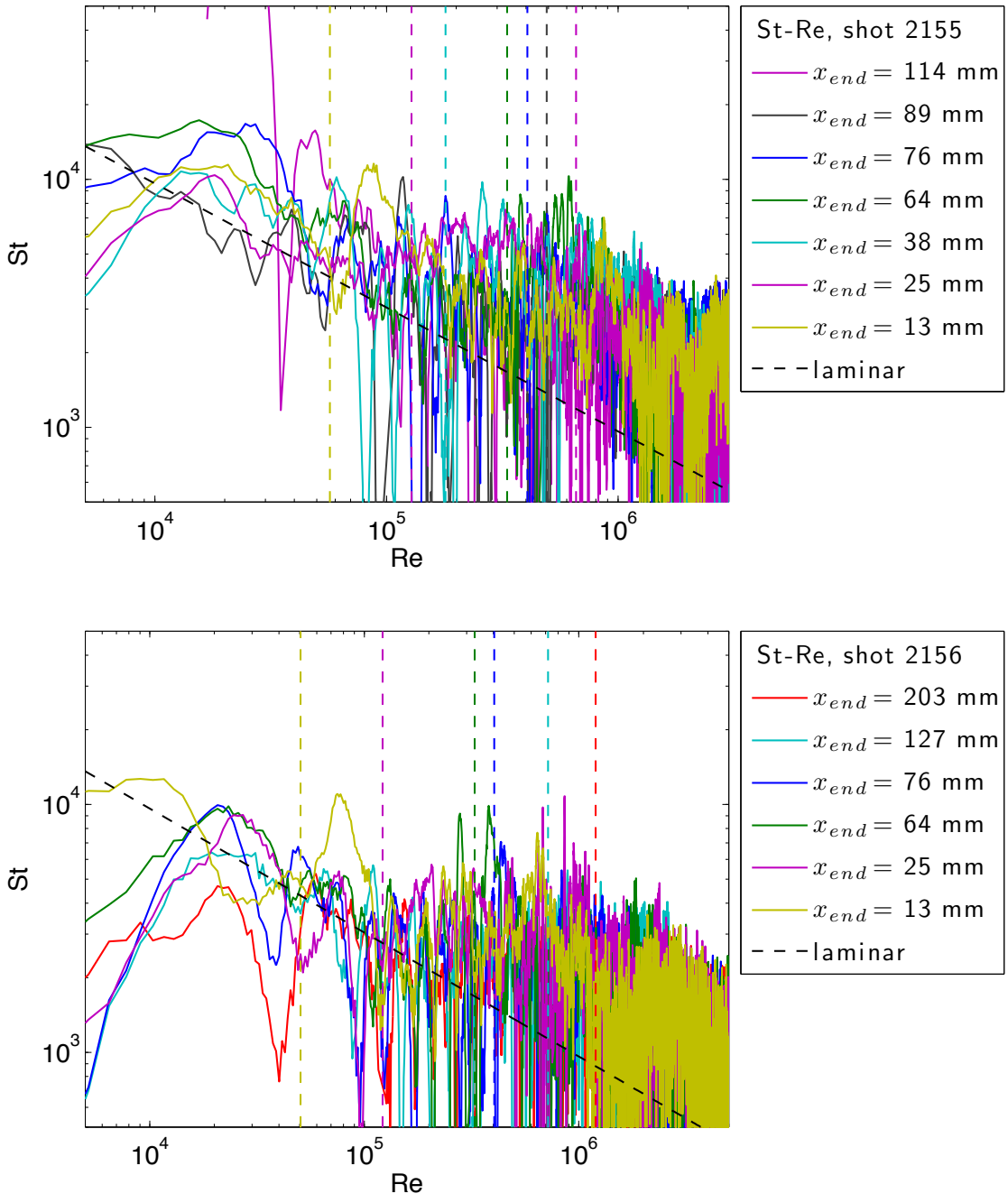

Figure E.138: Stanton-Reynolds number traces from shot 2156, a detonation in stoichiometric hydrogen-oxygen with 25% carbon dioxide dilution at fill pressure 25 kPa. The dashed vertical lines represent the arrival of the reflected shock wave.

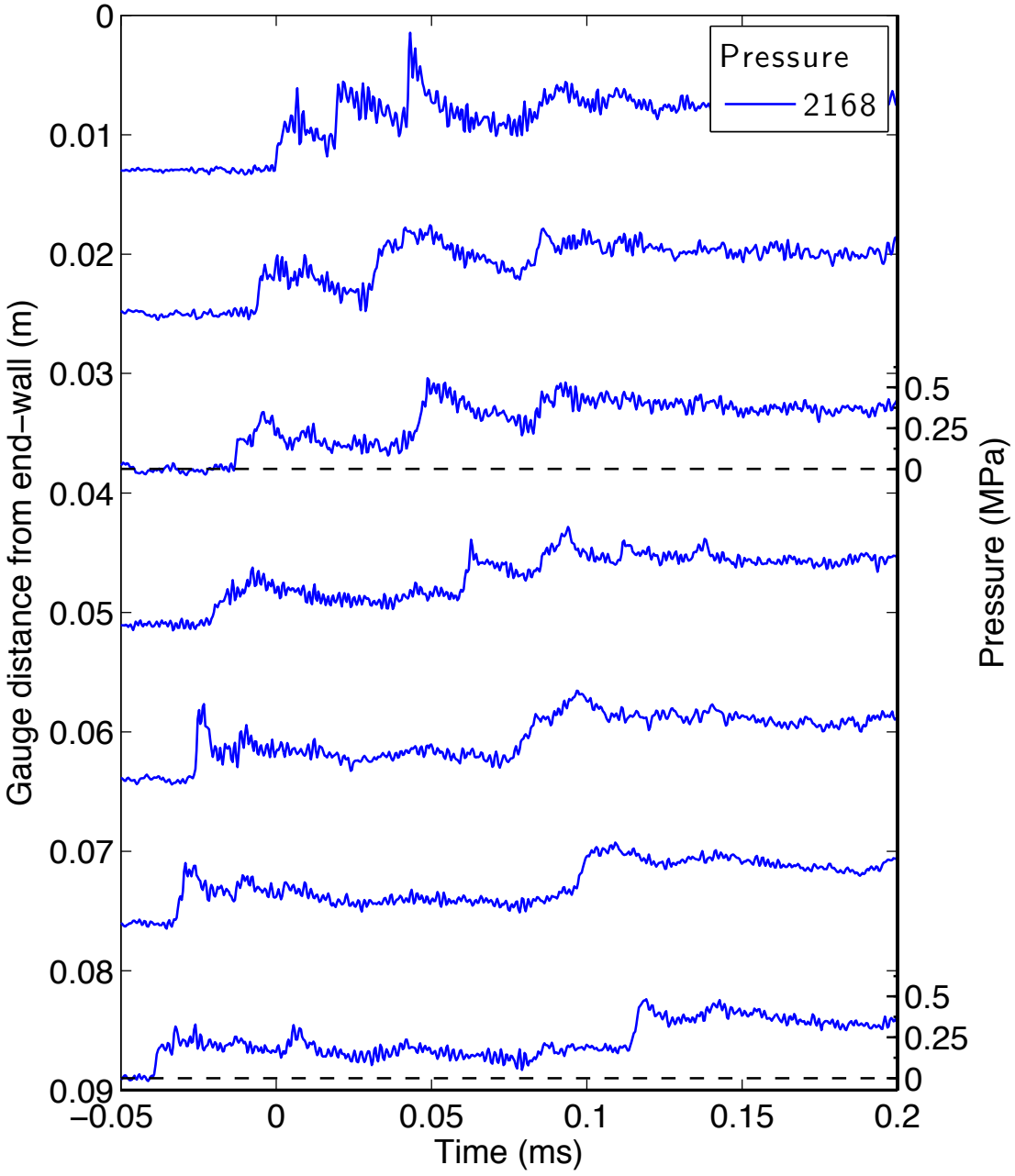

Figure E.139: Pressure traces for a detonation in stoichiometric hydrogen-oxygen with 33% carbon dioxide dilution at fill pressure 10 kPa, part 1.

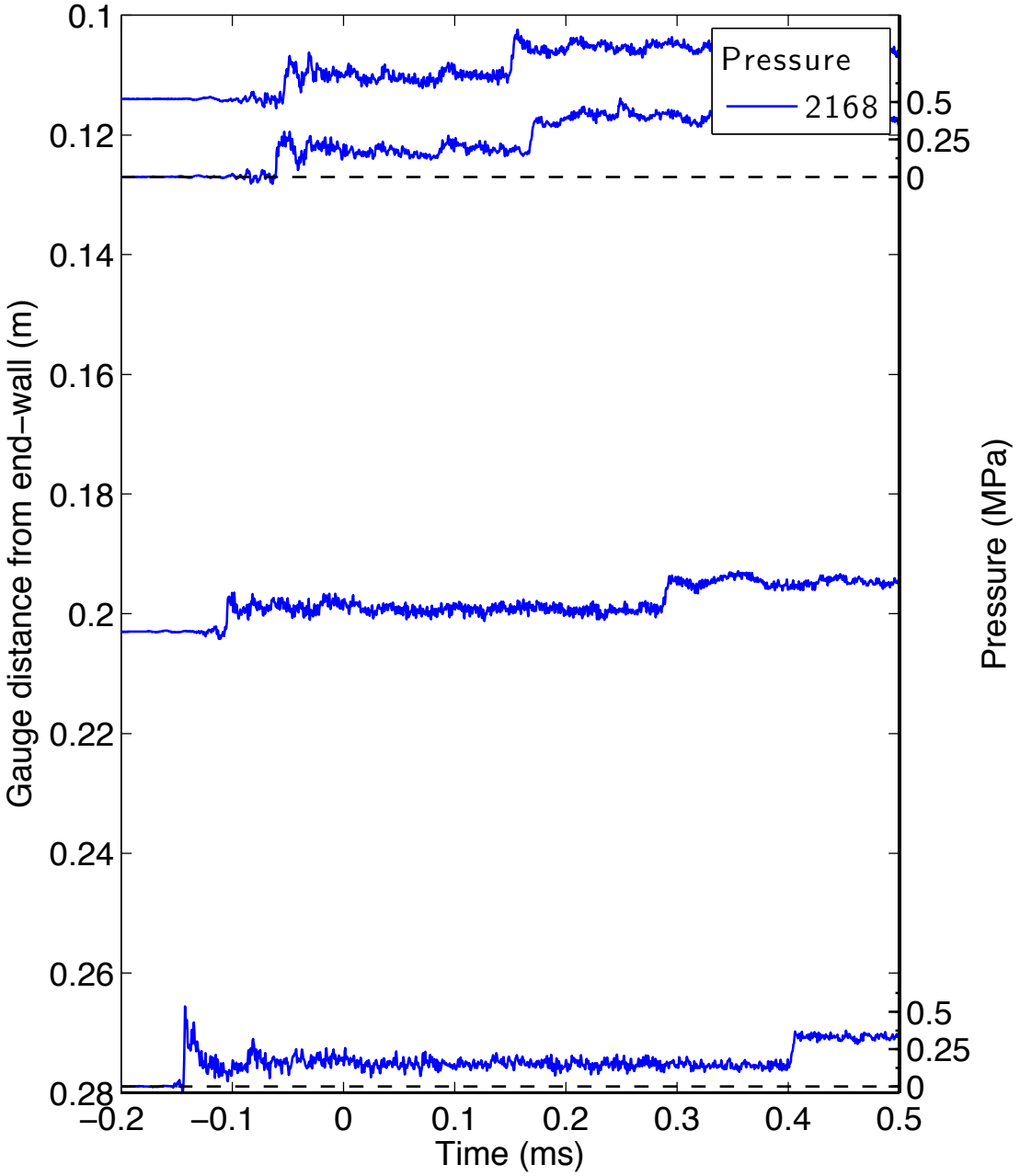

Figure E.140: Pressure traces for a detonation in stoichiometric hydrogen-oxygen with 33% carbon dioxide dilution at fill pressure 10 kPa, part 2.

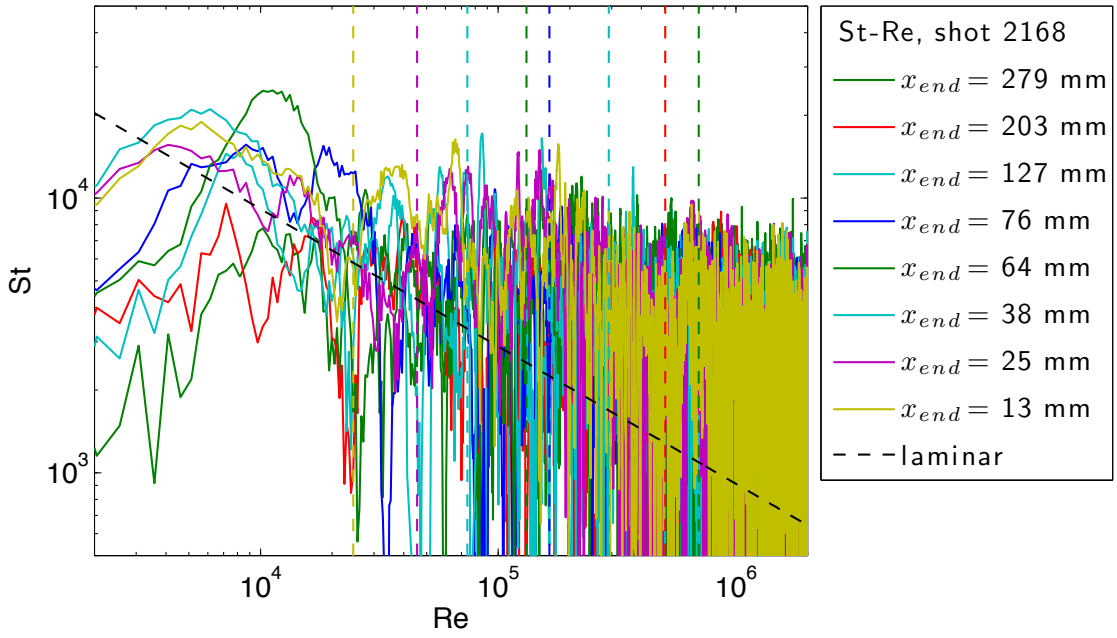

Figure E.141: Stanton-Reynolds number traces from shot 2168, a detonation in stoichiometric hydrogen-oxygen with 33% carbon dioxide dilution at fill pressure 10 kPa. The dashed vertical lines represent the arrival of the reflected shock wave.

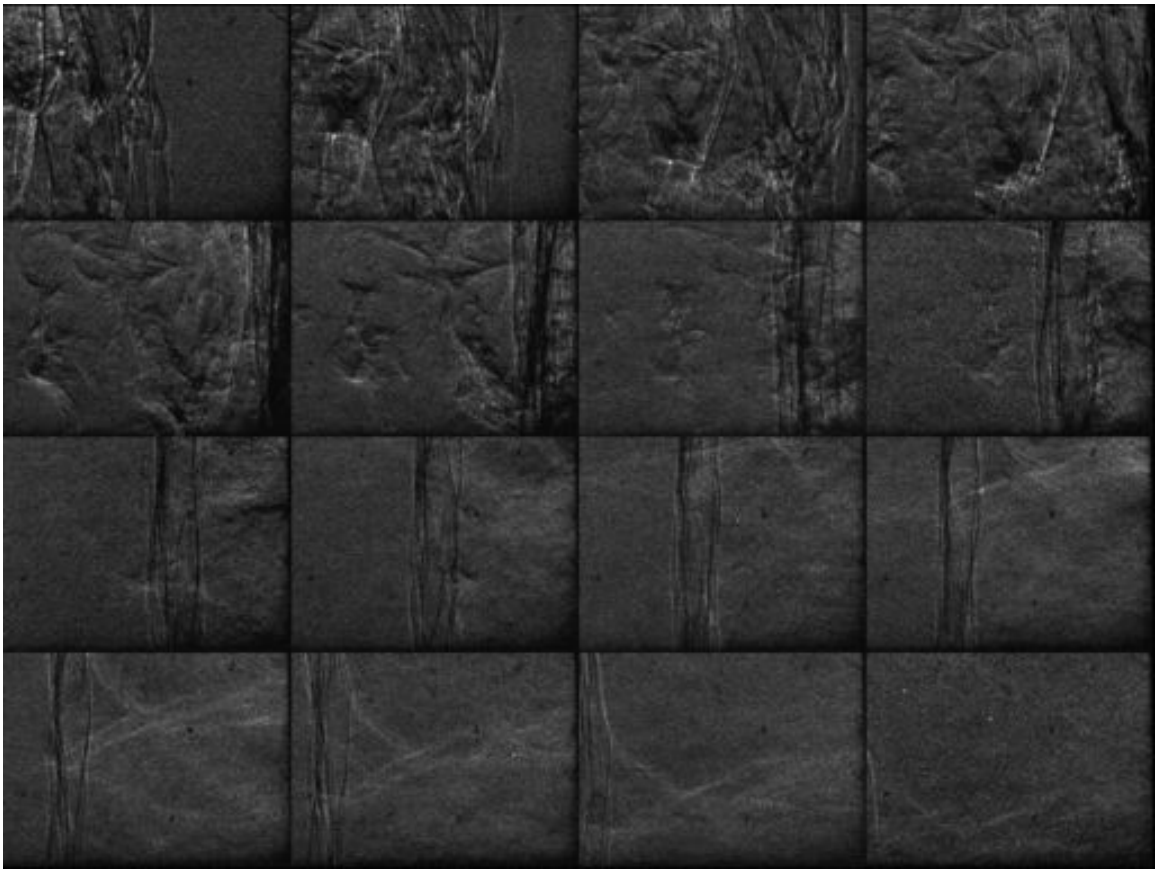

Figure E.142: Unfocused schlieren image of shot 2168. The field of view is approximately 30 mm wide.

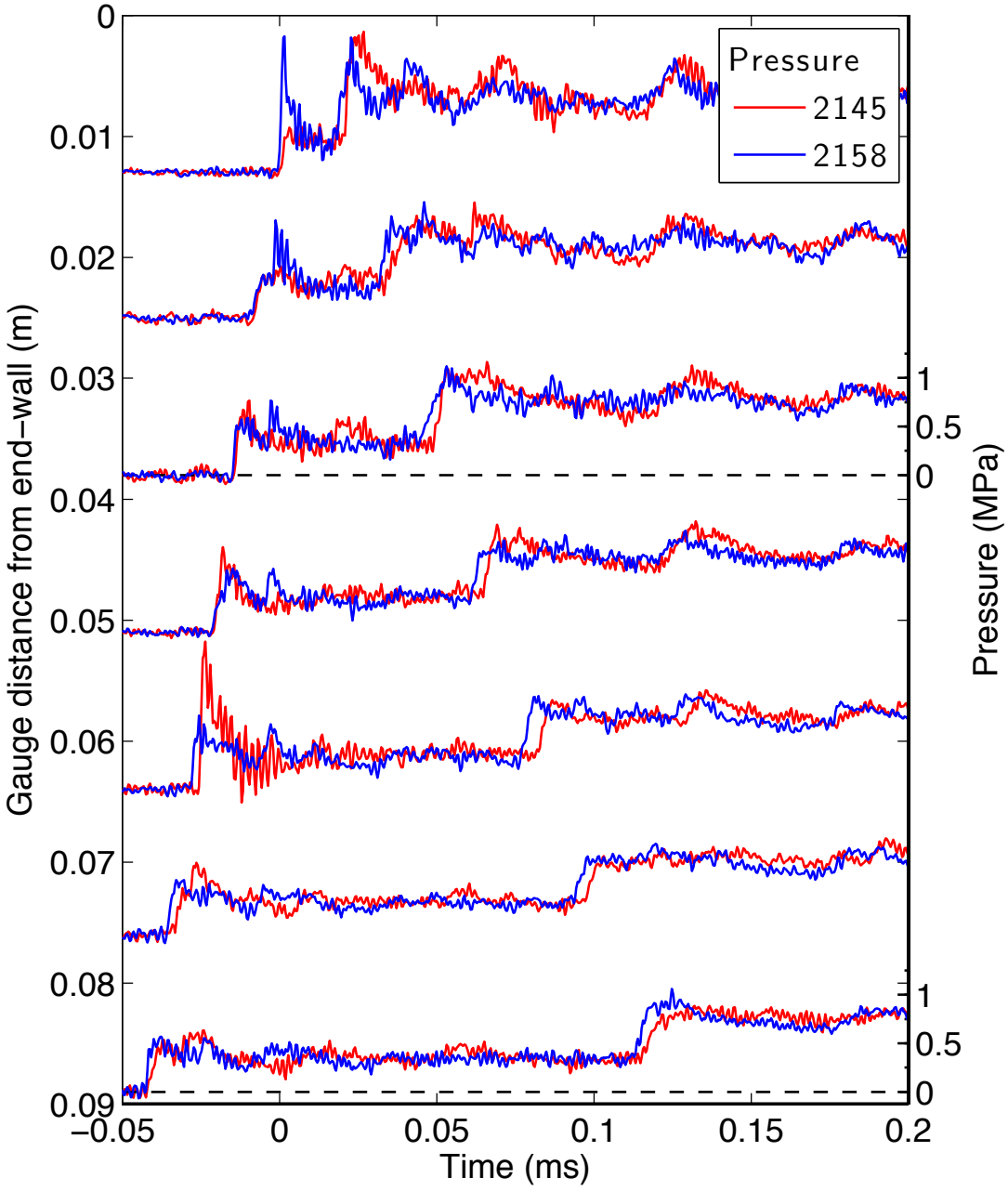

Figure E.143: Pressure traces for a detonation in stoichiometric hydrogen-oxygen with 33% carbon dioxide dilution at fill pressure 25 kPa, part 1.

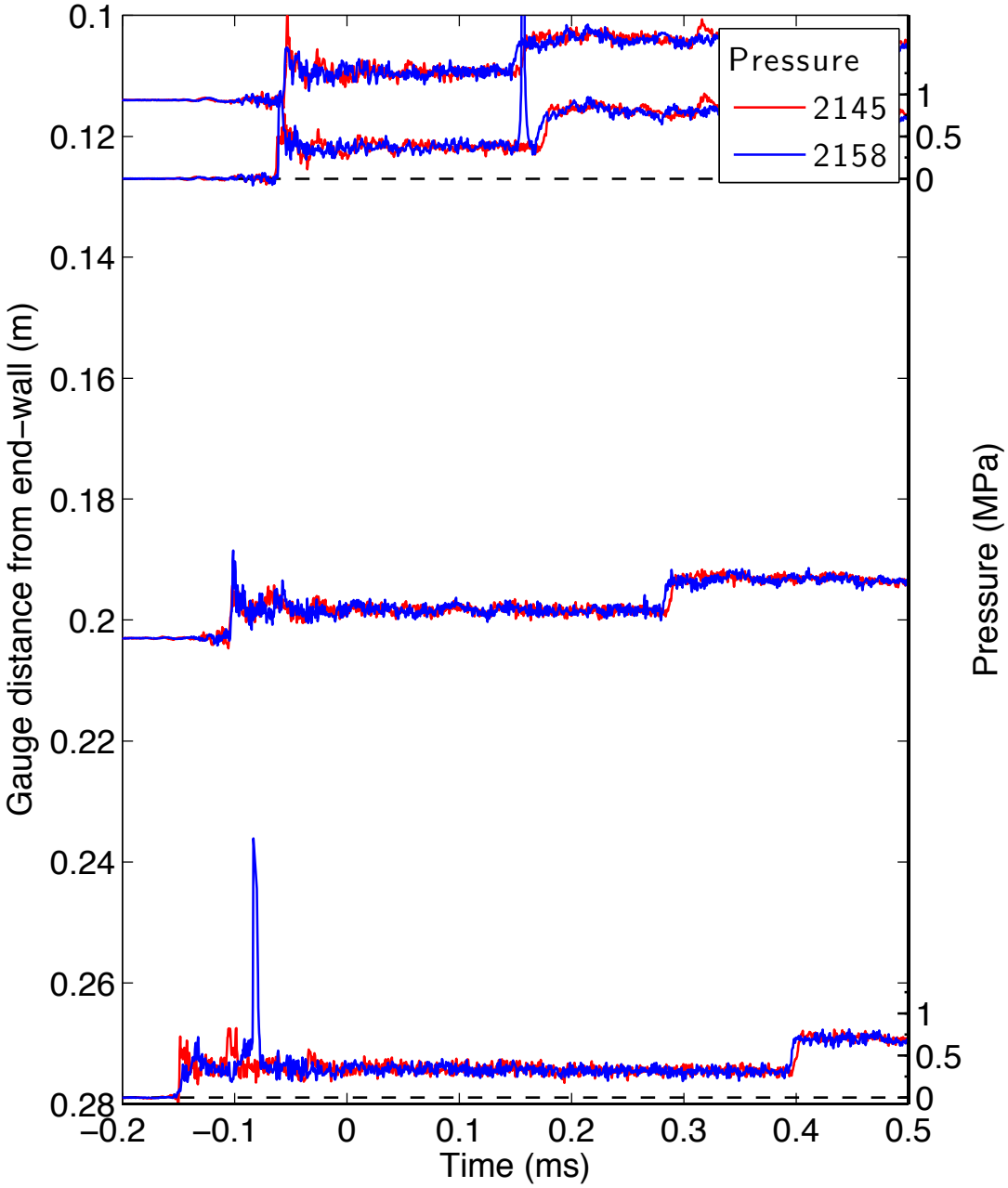

Figure E.144: Pressure traces for a detonation in stoichiometric hydrogen-oxygen with 33% carbon dioxide dilution at fill pressure 25 kPa, part 2.

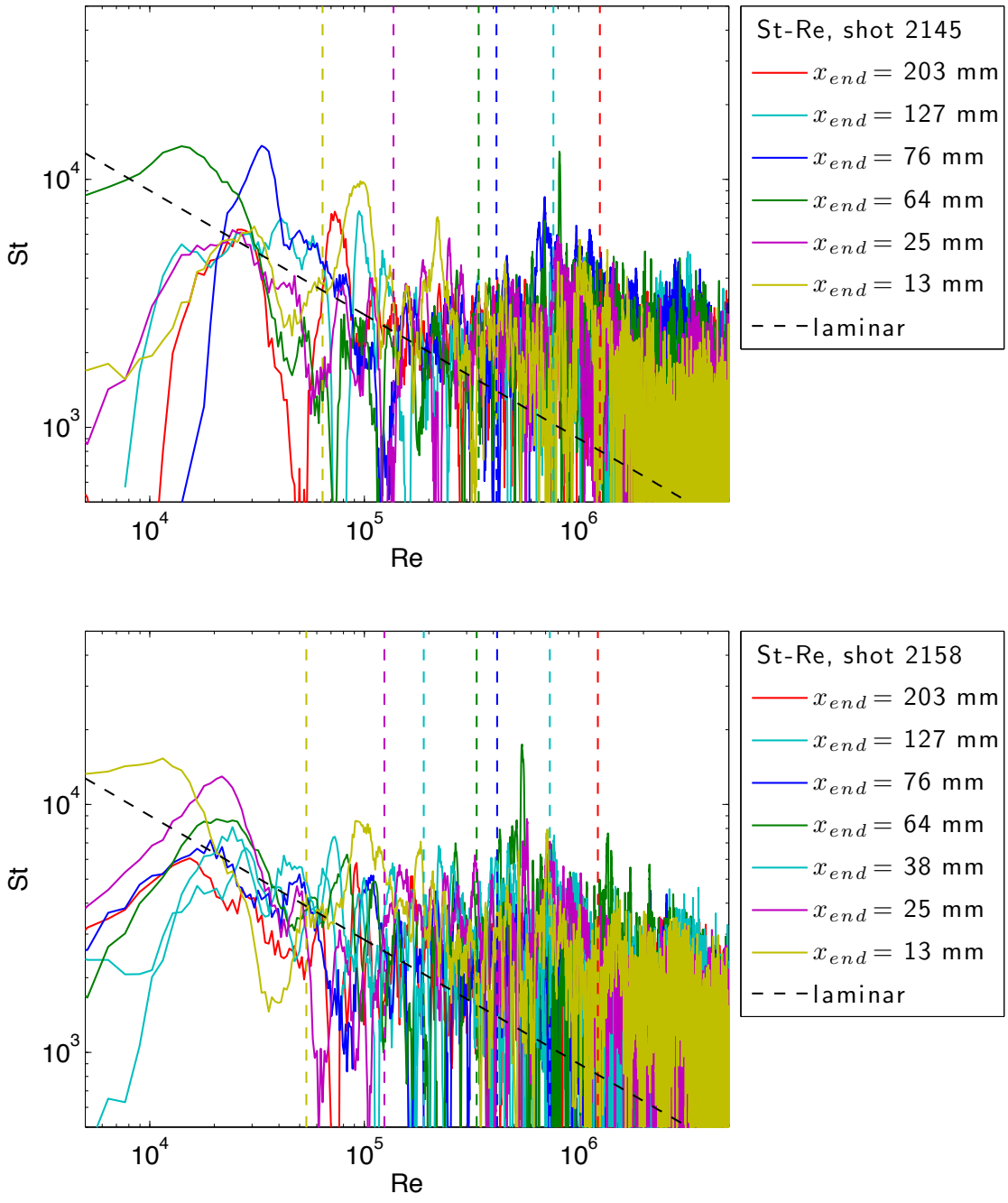

Figure E.145: Stanton-Reynolds number traces from shot 2158, a detonation in stoichiometric hydrogen-oxygen with 33% carbon dioxide dilution at fill pressure 25 kPa. The dashed vertical lines represent the arrival of the reflected shock wave.

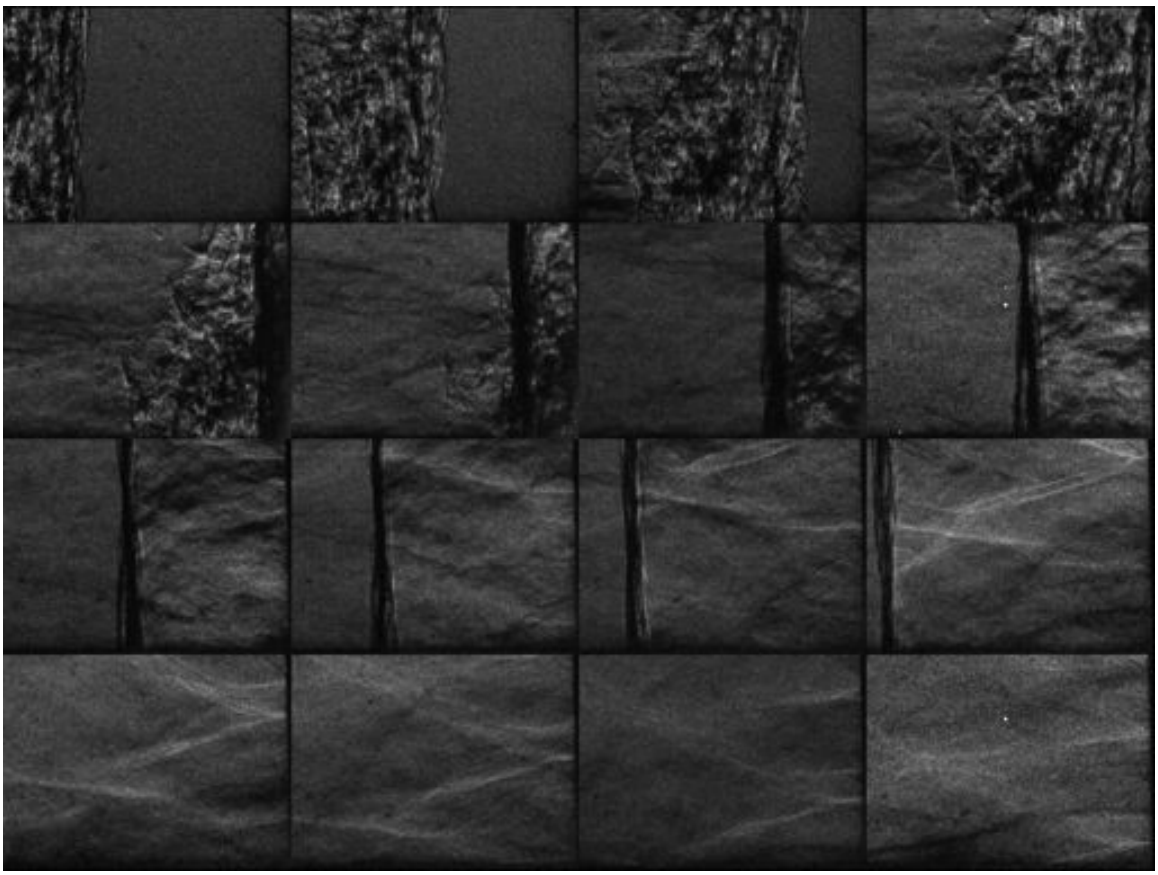

Figure E.146: Unfocused schlieren image of shot 2158. The field of view is approximately 30 mm wide.

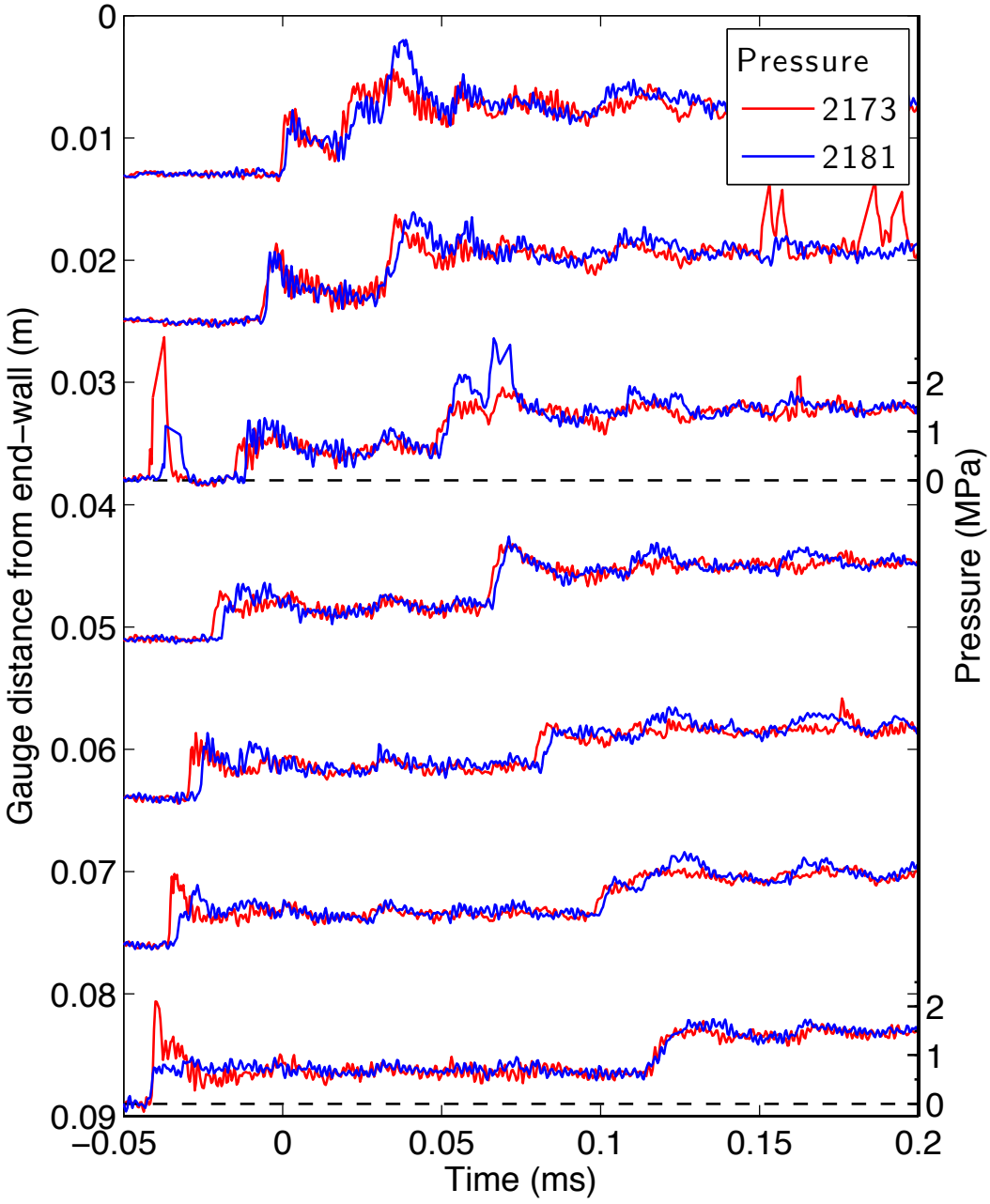

Figure E.147: Pressure traces for a detonation in stoichiometric hydrogen-oxygen with 33% carbon dioxide dilution at fill pressure 50 kPa, part 1.

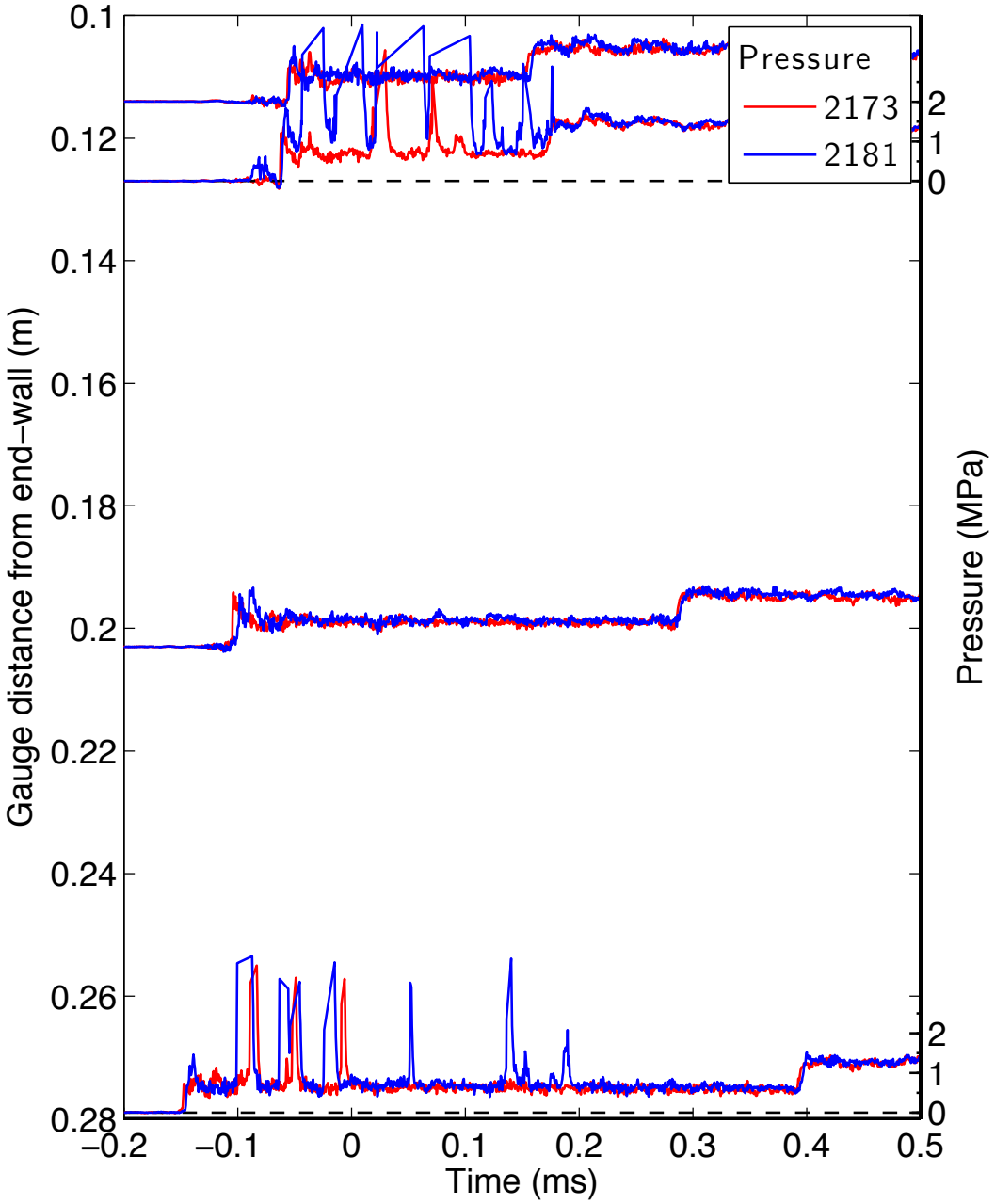

Figure E.148: Pressure traces for a detonation in stoichiometric hydrogen-oxygen with 33% carbon dioxide dilution at fill pressure 50 kPa, part 2.

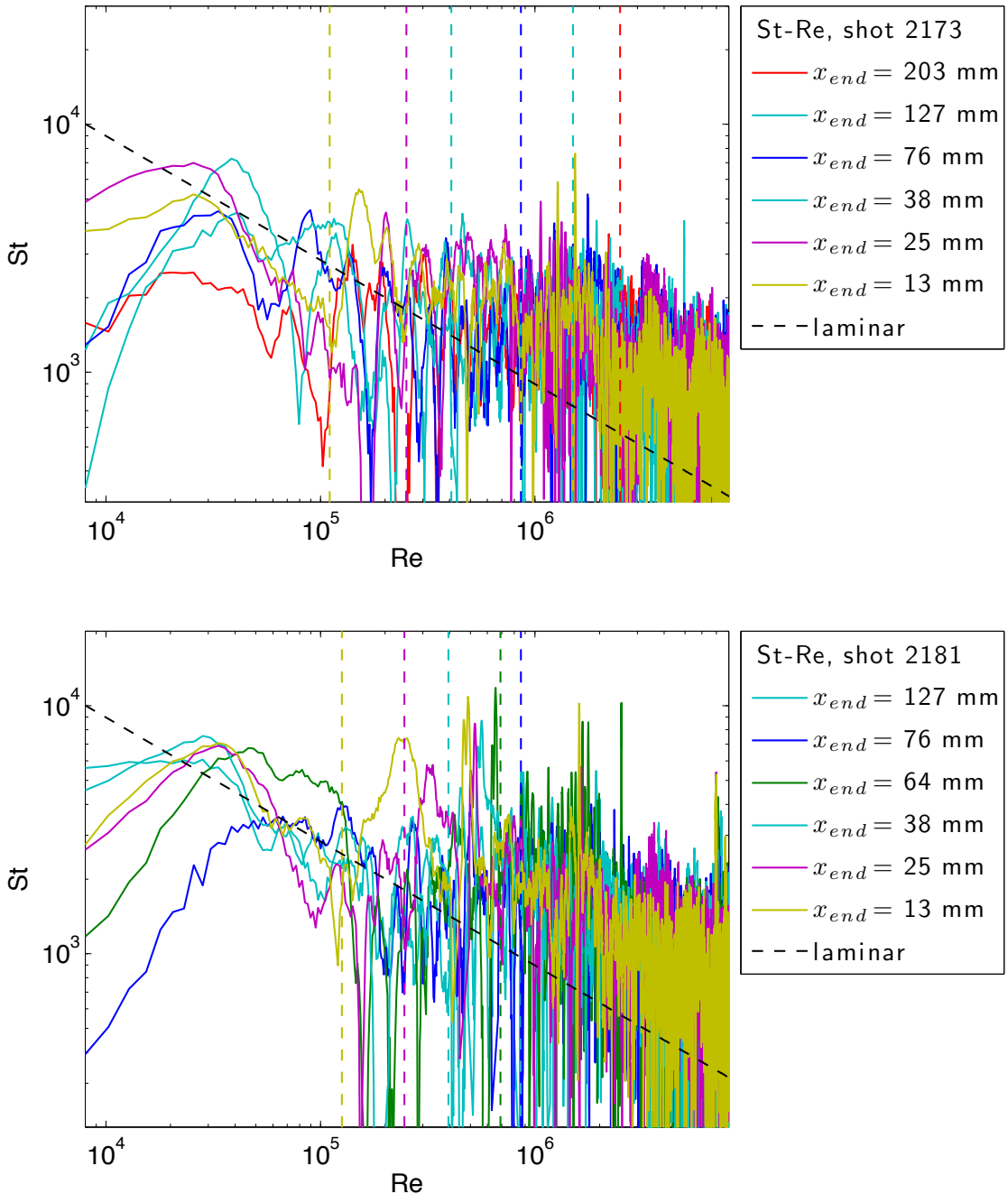

Figure E.149: Stanton-Reynolds number traces from shot 2181, a detonation in stoichiometric hydrogen-oxygen with 33% carbon dioxide dilution at fill pressure 50 kPa. The dashed vertical lines represent the arrival of the reflected shock wave.

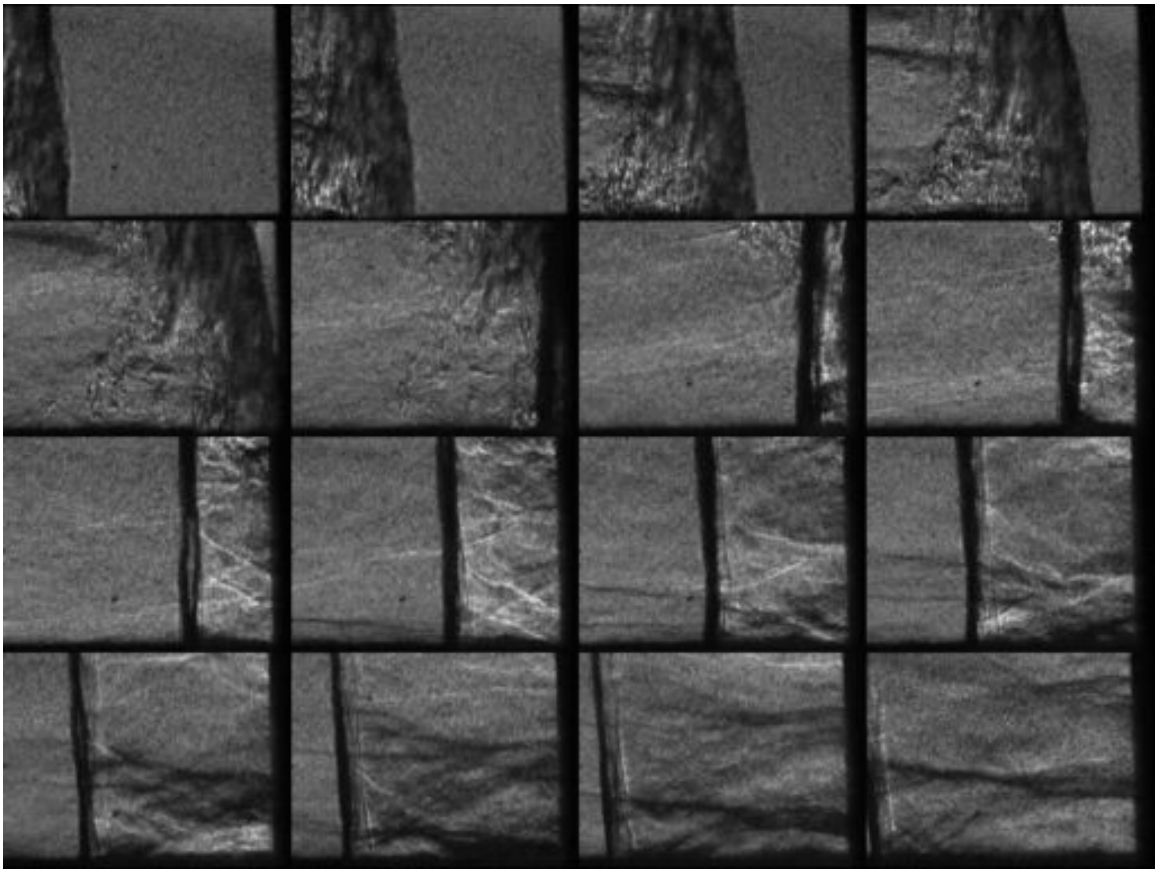

Figure E.150: Unfocused schlieren image of shot 2181. The field of view is approximately 30 mm wide.

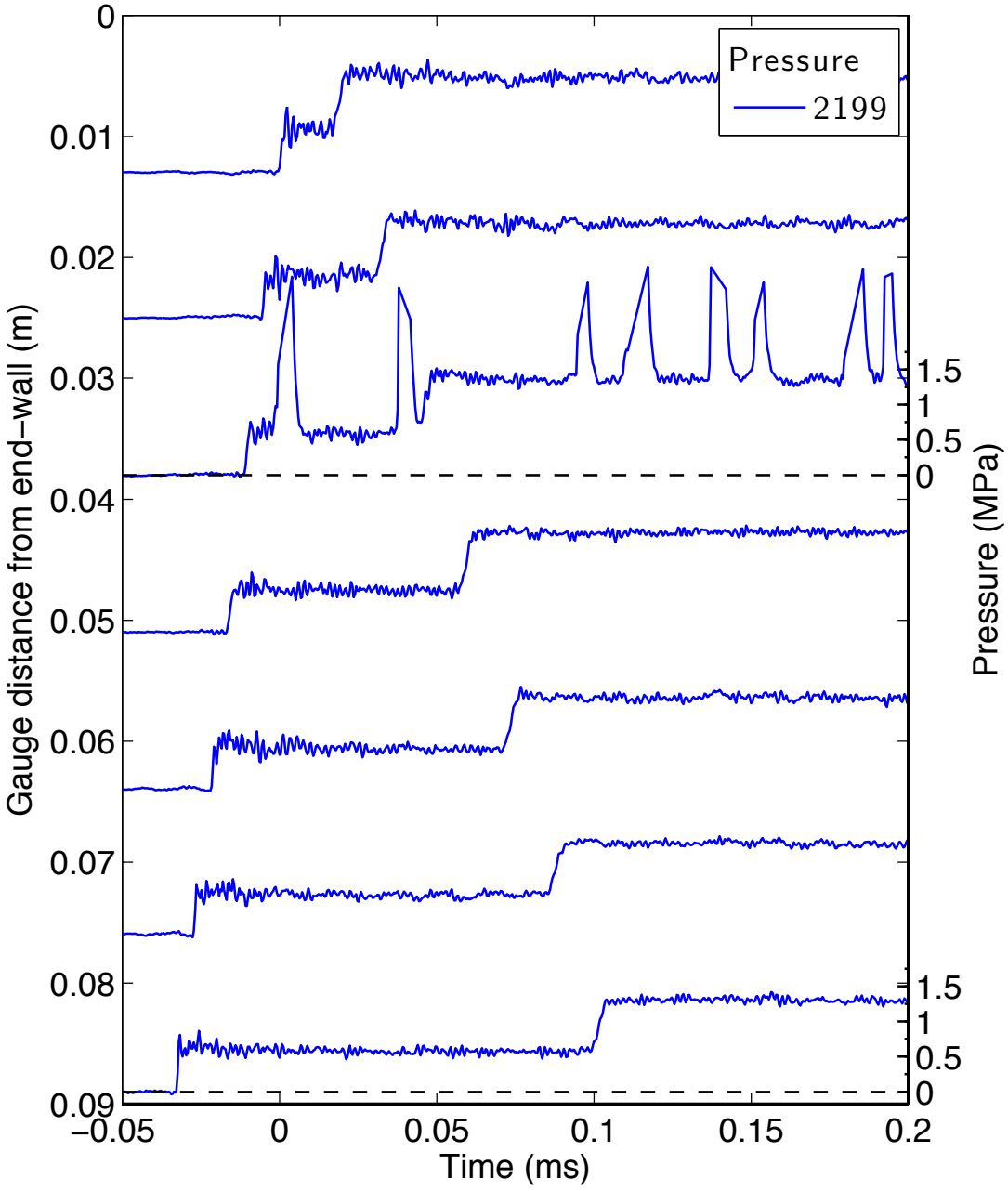

Figure E.151: Pressure traces for a detonation in stoichiometric hydrogen-nitrous oxide at fill pressure 25 kPa, part 1.

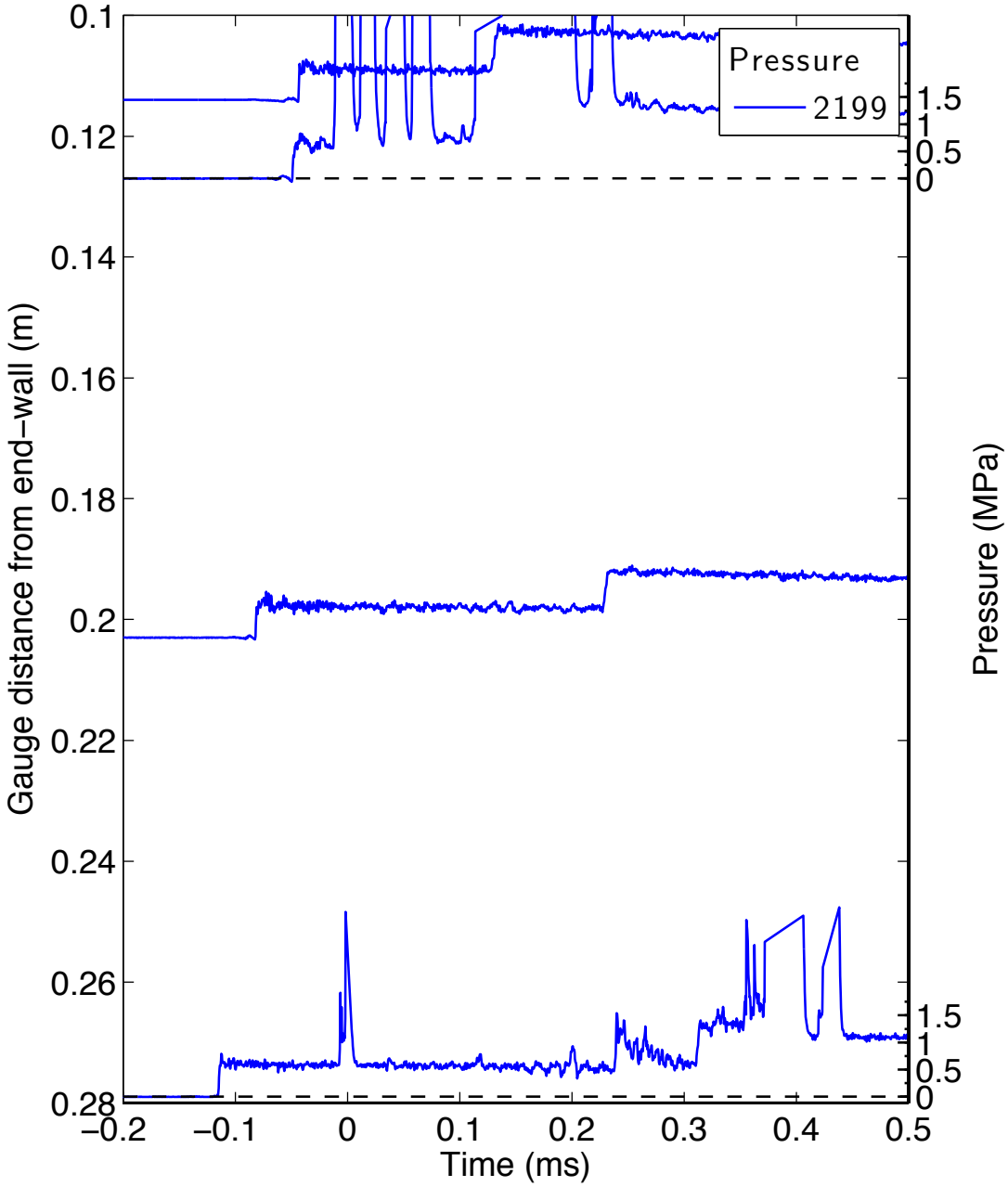

Figure E.152: Pressure traces for a detonation in stoichiometric hydrogen-nitrous oxide at fill pressure 25 kPa, part 2.

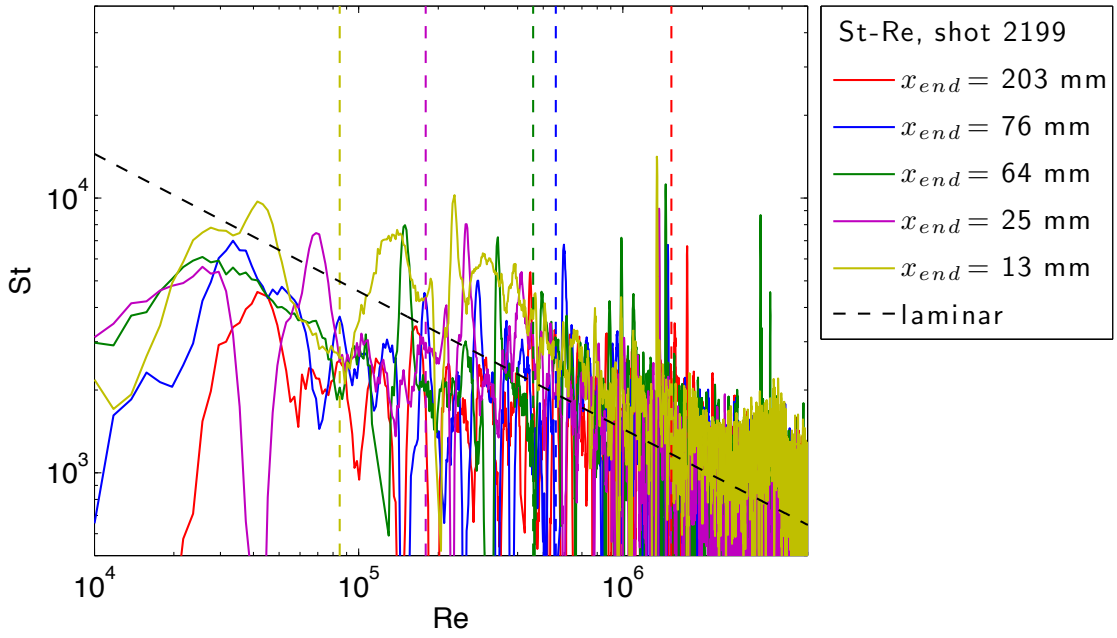

Figure E.153: Stanton-Reynolds number traces from shot 2199, a detonation in stoichiometric hydrogen-nitrous oxide at fill pressure 25 kPa. The dashed vertical lines represent the arrival of the reflected shock wave.

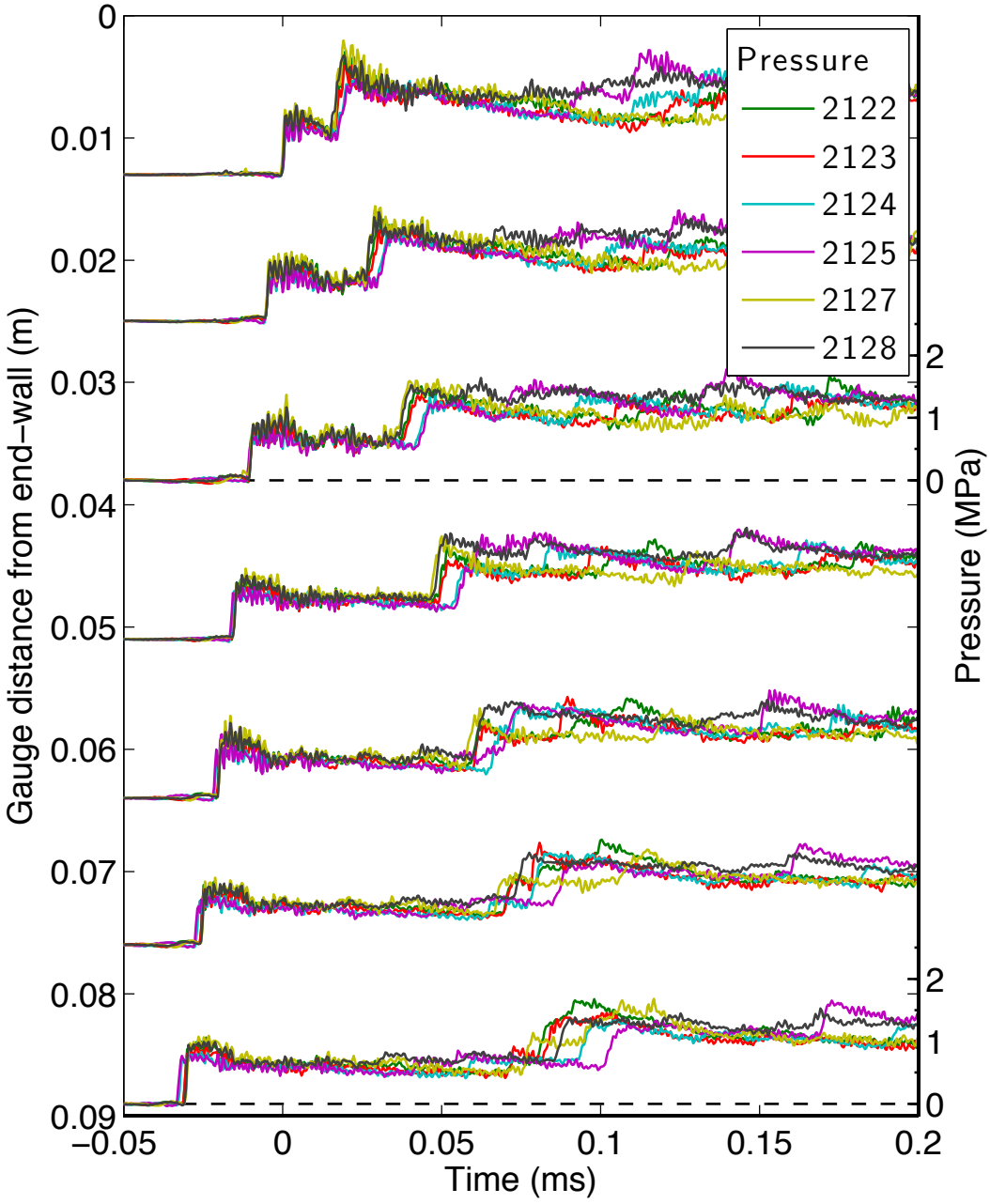

Figure E.154: Pressure traces for a detonation in stoichiometric ethylene-oxygen at fill pressure 25 kPa, part 1.

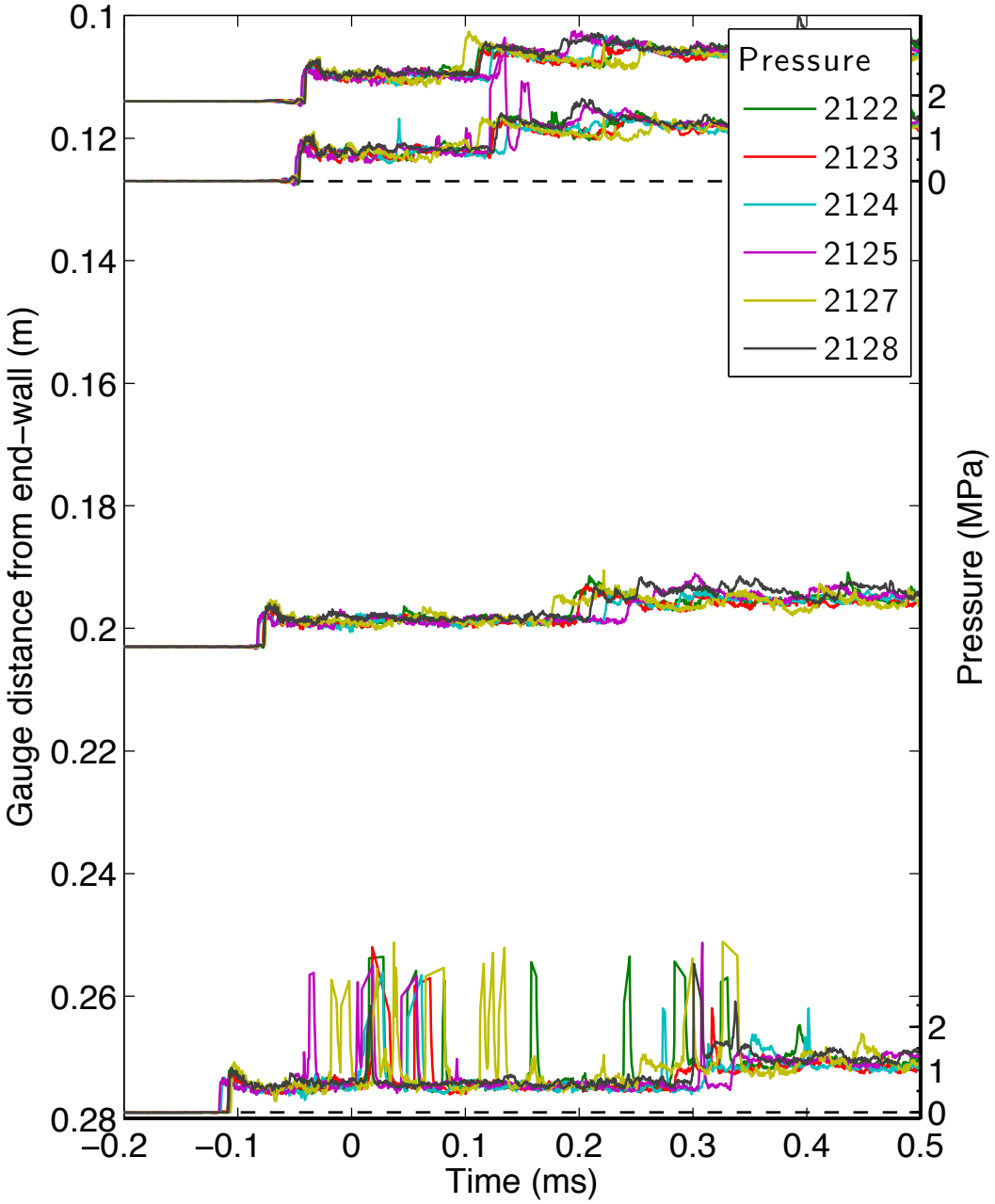

Figure E.155: Pressure traces for a detonation in stoichiometric ethylene-oxygen at fill pressure 25 kPa, part 2.

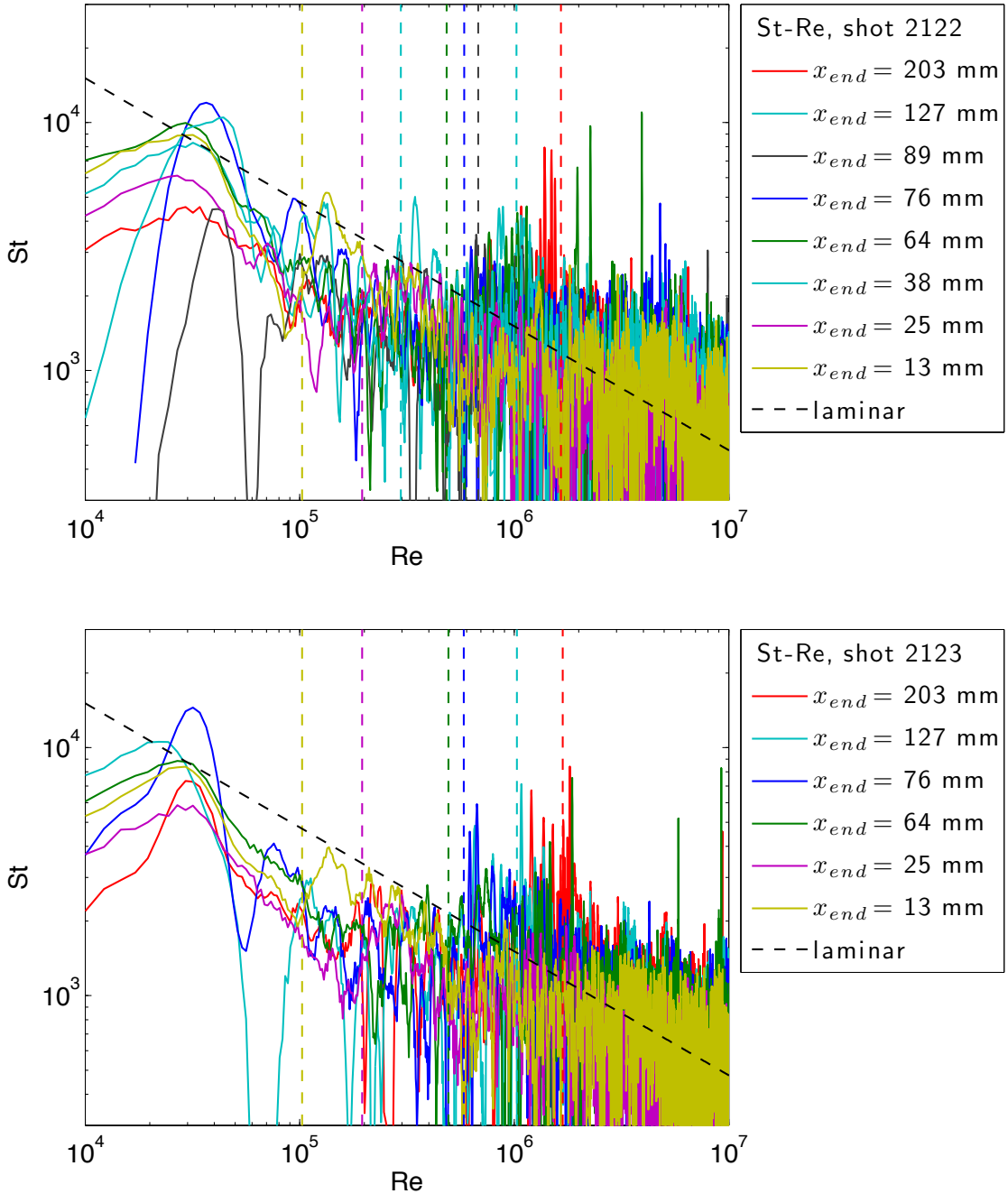

Figure E.156: Stanton-Reynolds number traces from shot 2123, a detonation in stoichiometric ethylene-oxygen at fill pressure 25 kPa. The dashed vertical lines represent the arrival of the reflected shock wave.

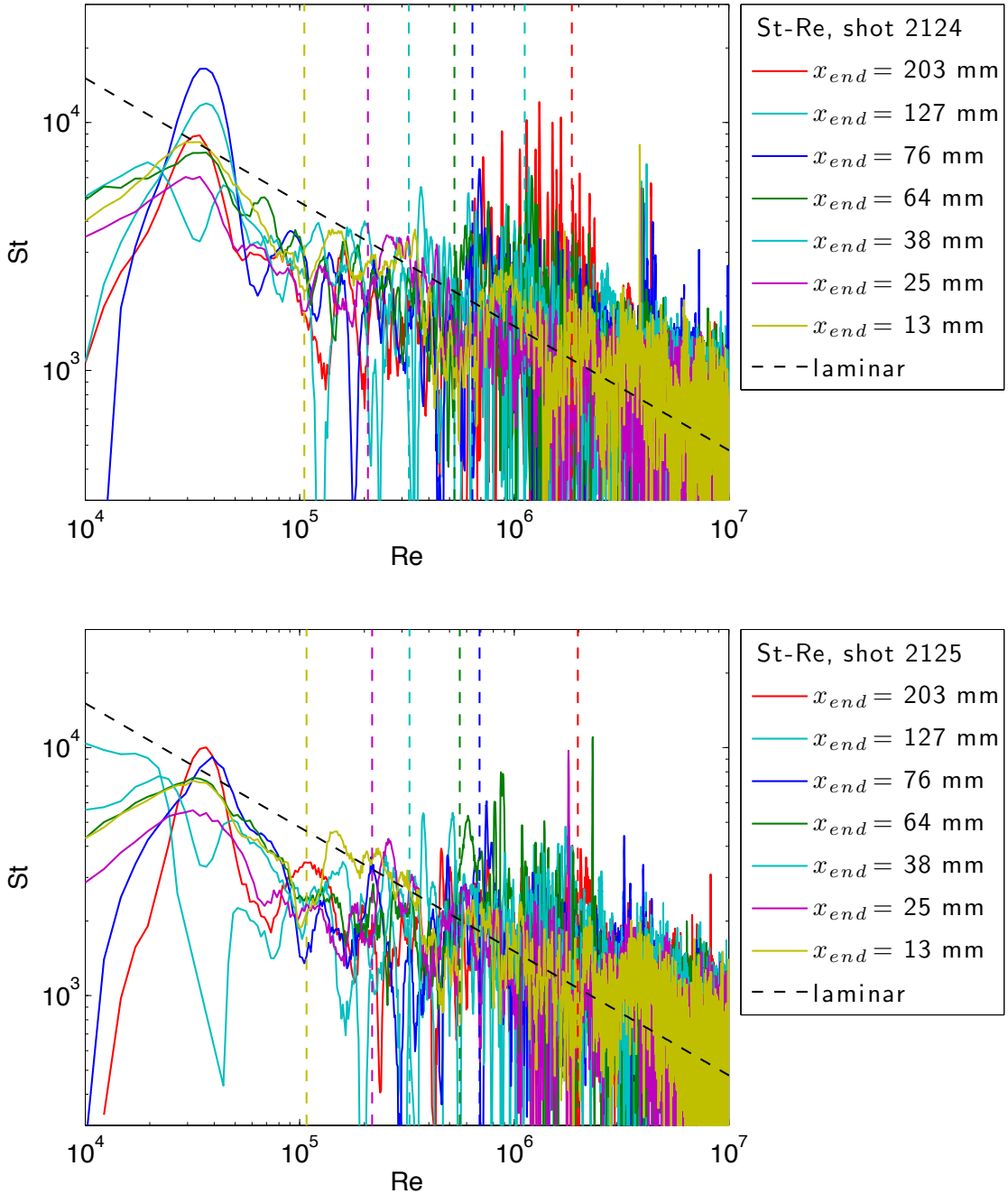

Figure E.157: Stanton-Reynolds number traces from shot 2125, a detonation in stoichiometric ethylene-oxygen at fill pressure 25 kPa. The dashed vertical lines represent the arrival of the reflected shock wave.

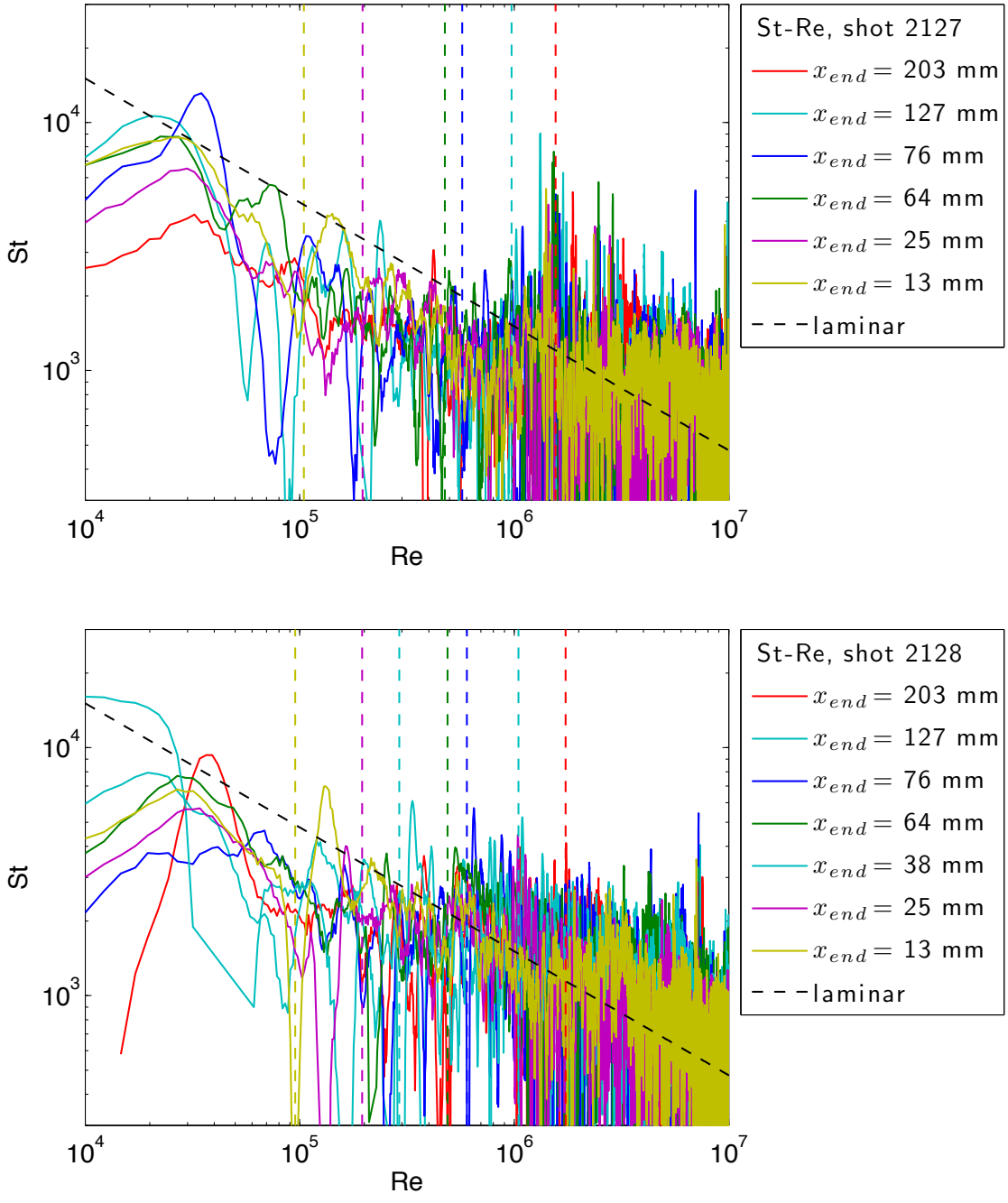

Figure E.158: Stanton-Reynolds number traces from shot 2128, a detonation in stoichiometric ethylene-oxygen at fill pressure 25 kPa. The dashed vertical lines represent the arrival of the reflected shock wave.

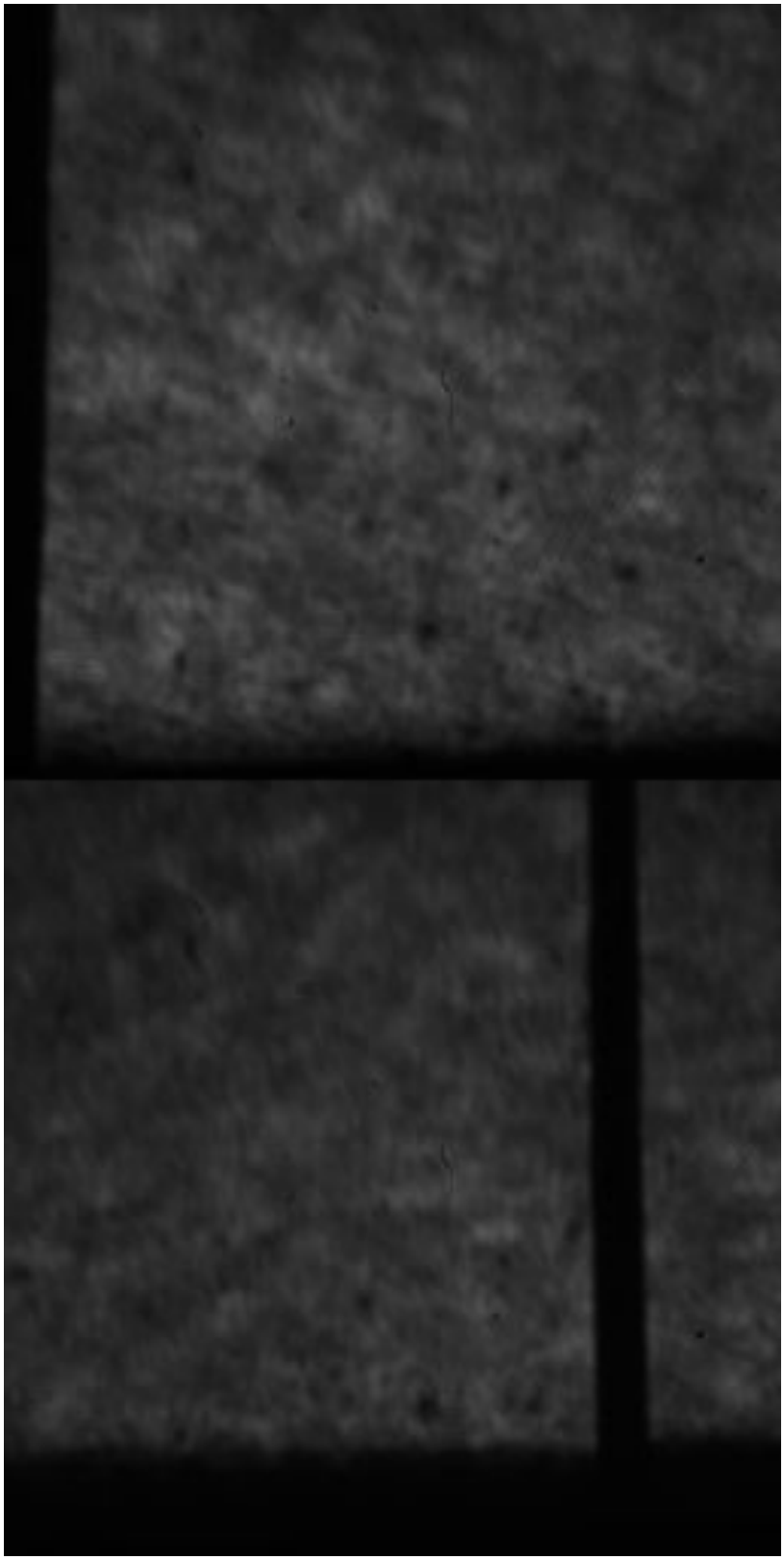

Figure E.159: Focused schlieren image of shot 2125. The field of view is approximately 14 mm wide.

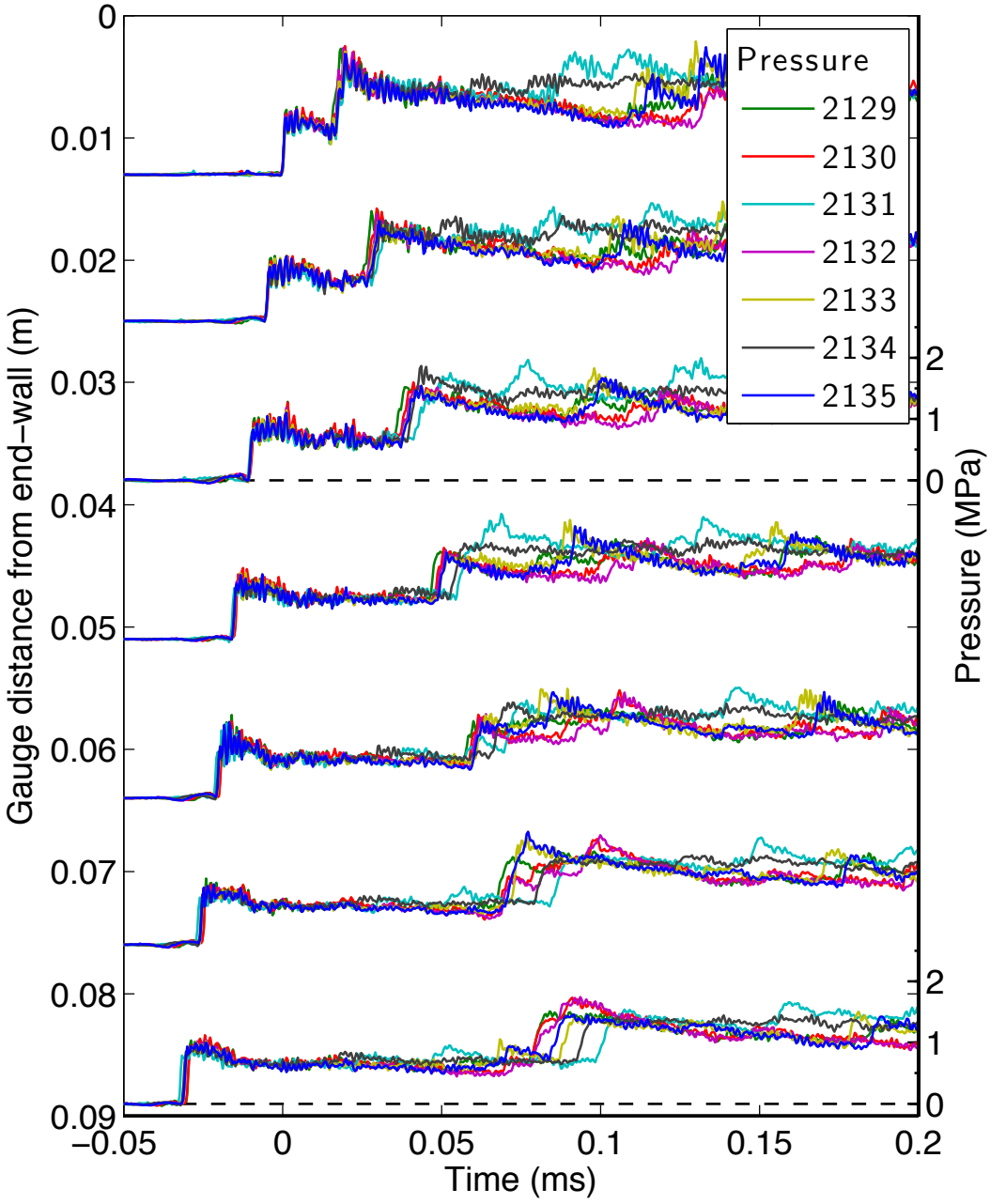

Figure E.160: Pressure traces for a detonation in stoichiometric ethylene-oxygen at fill pressure 25 kPa, part 3.

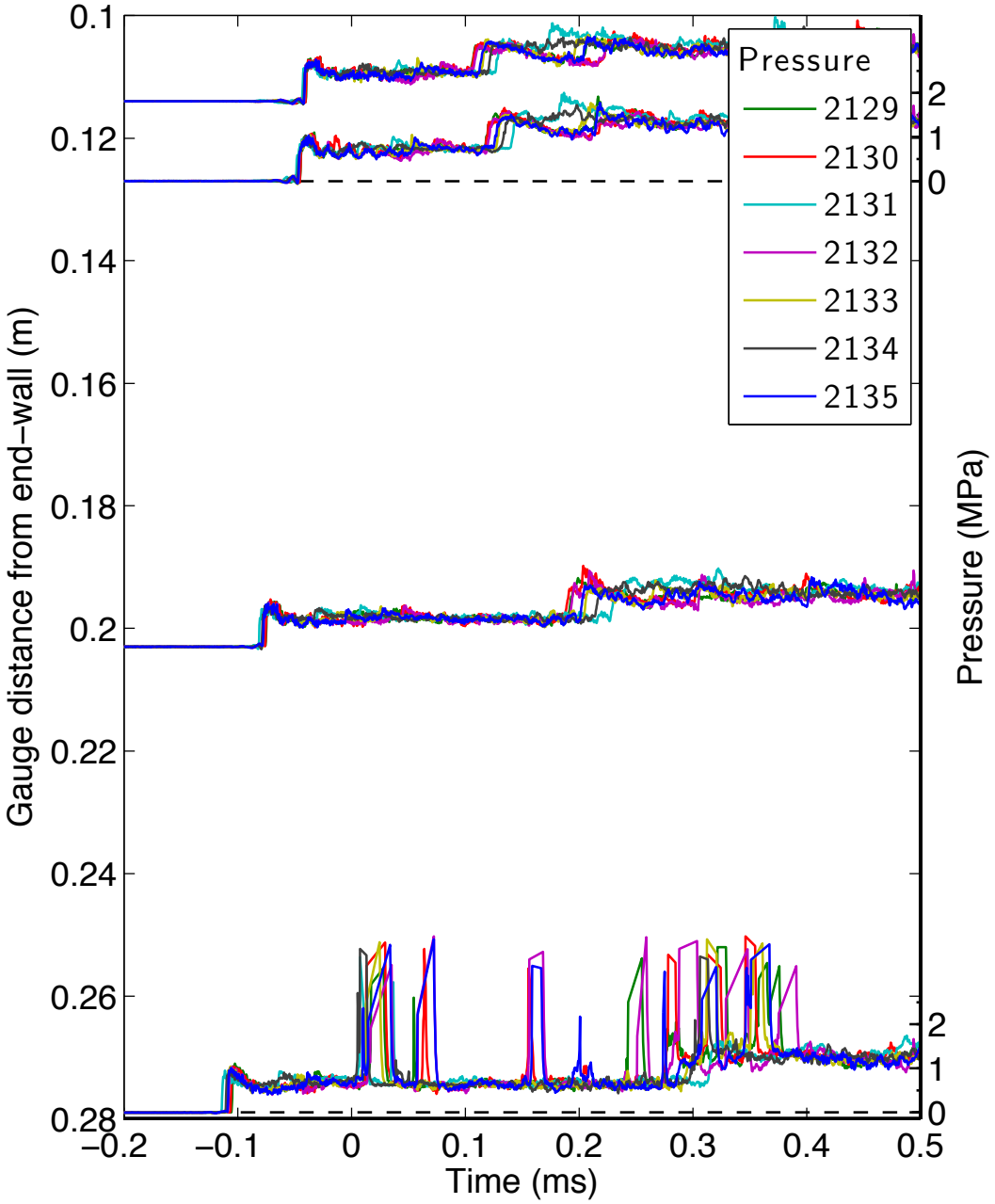

Figure E.161: Pressure traces for a detonation in stoichiometric ethylene-oxygen at fill pressure 25 kPa, part 4.

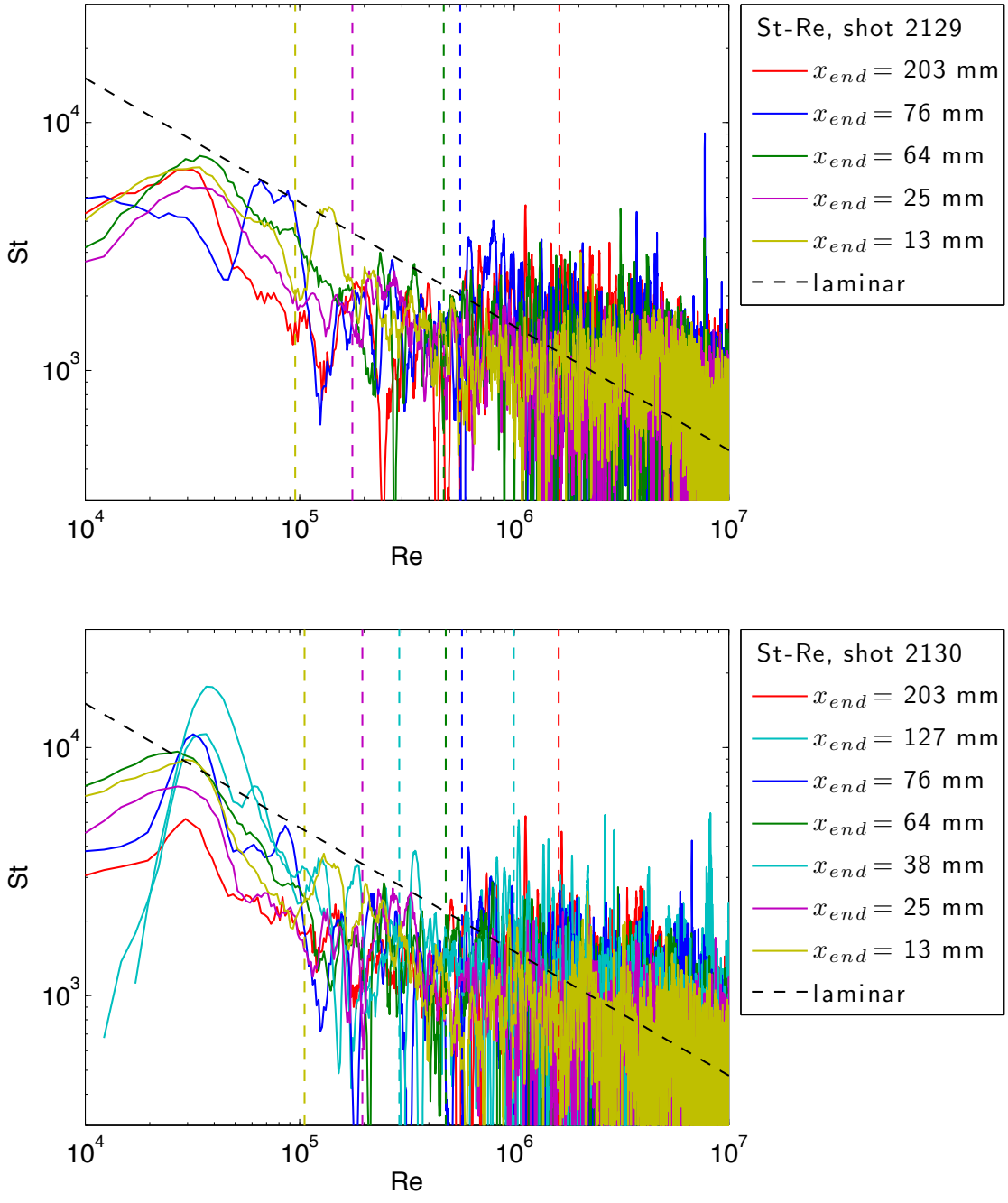

Figure E.162: Stanton-Reynolds number traces from shot 2130, a detonation in stoichiometric ethylene-oxygen at fill pressure 25 kPa. The dashed vertical lines represent the arrival of the reflected shock wave.

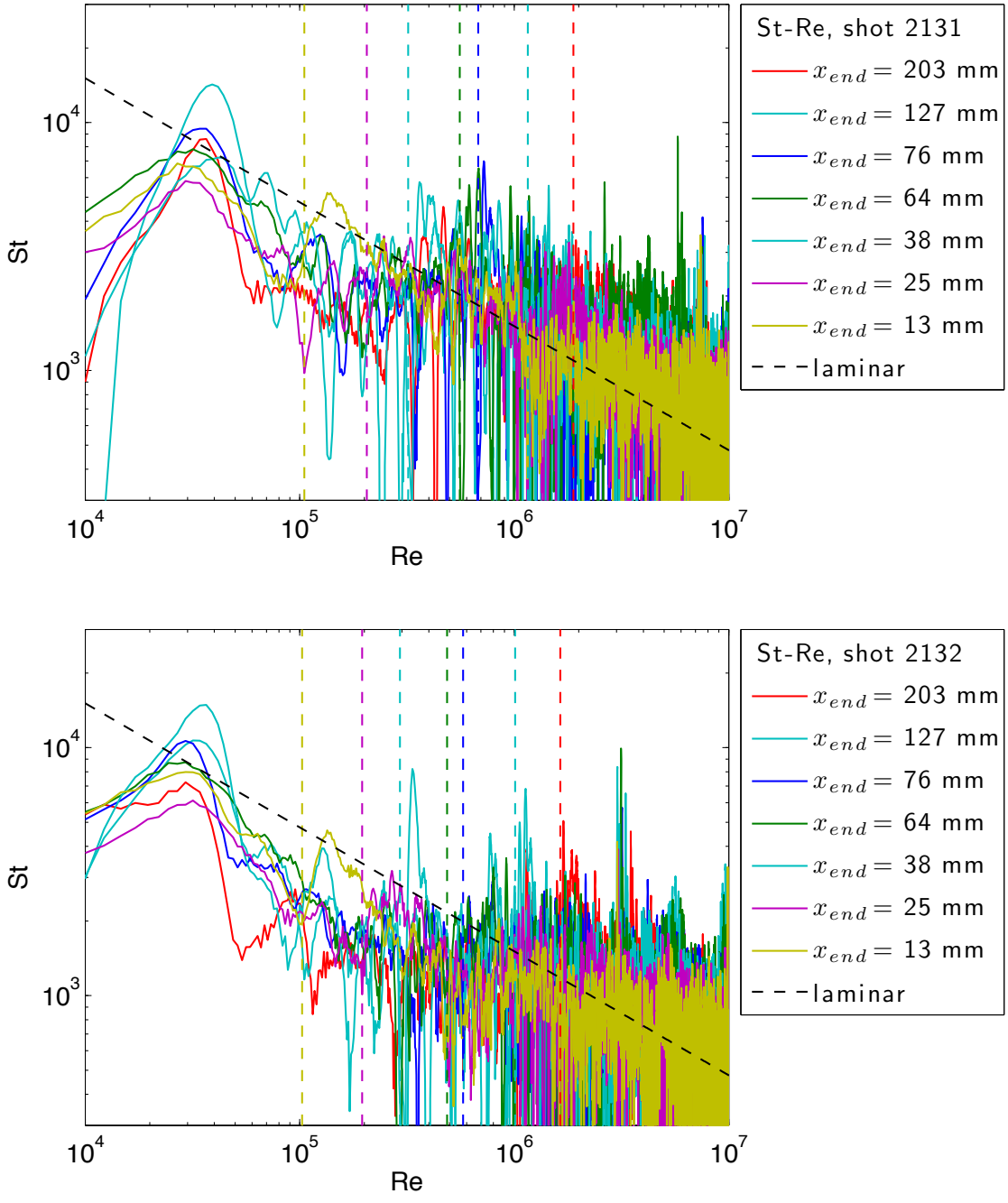

Figure E.163: Stanton-Reynolds number traces from shot 2132, a detonation in stoichiometric ethylene-oxygen at fill pressure 25 kPa. The dashed vertical lines represent the arrival of the reflected shock wave.

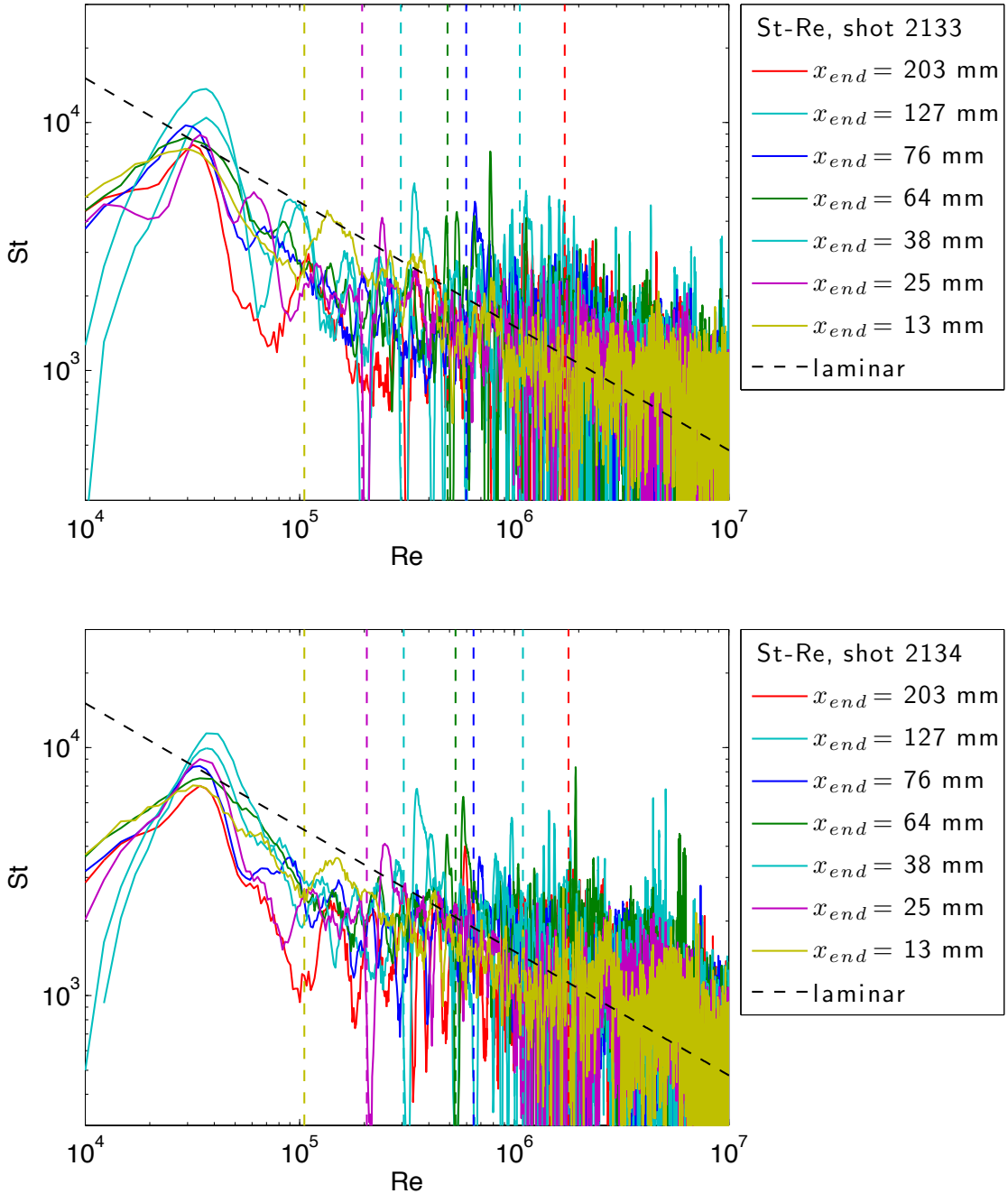

Figure E.164: Stanton-Reynolds number traces from shot 2134, a detonation in stoichiometric ethylene-oxygen at fill pressure 25 kPa. The dashed vertical lines represent the arrival of the reflected shock wave.

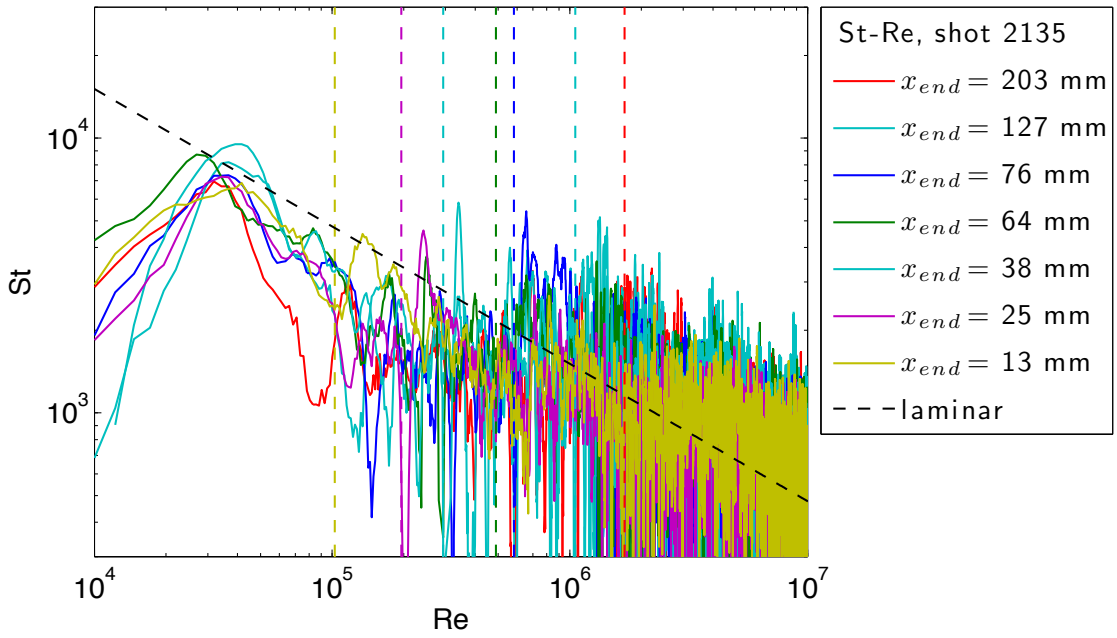

Figure E.165: Stanton-Reynolds number traces from shot 2135, a detonation in stoichiometric ethylene-oxygen at fill pressure 25 kPa. The dashed vertical lines represent the arrival of the reflected shock wave.

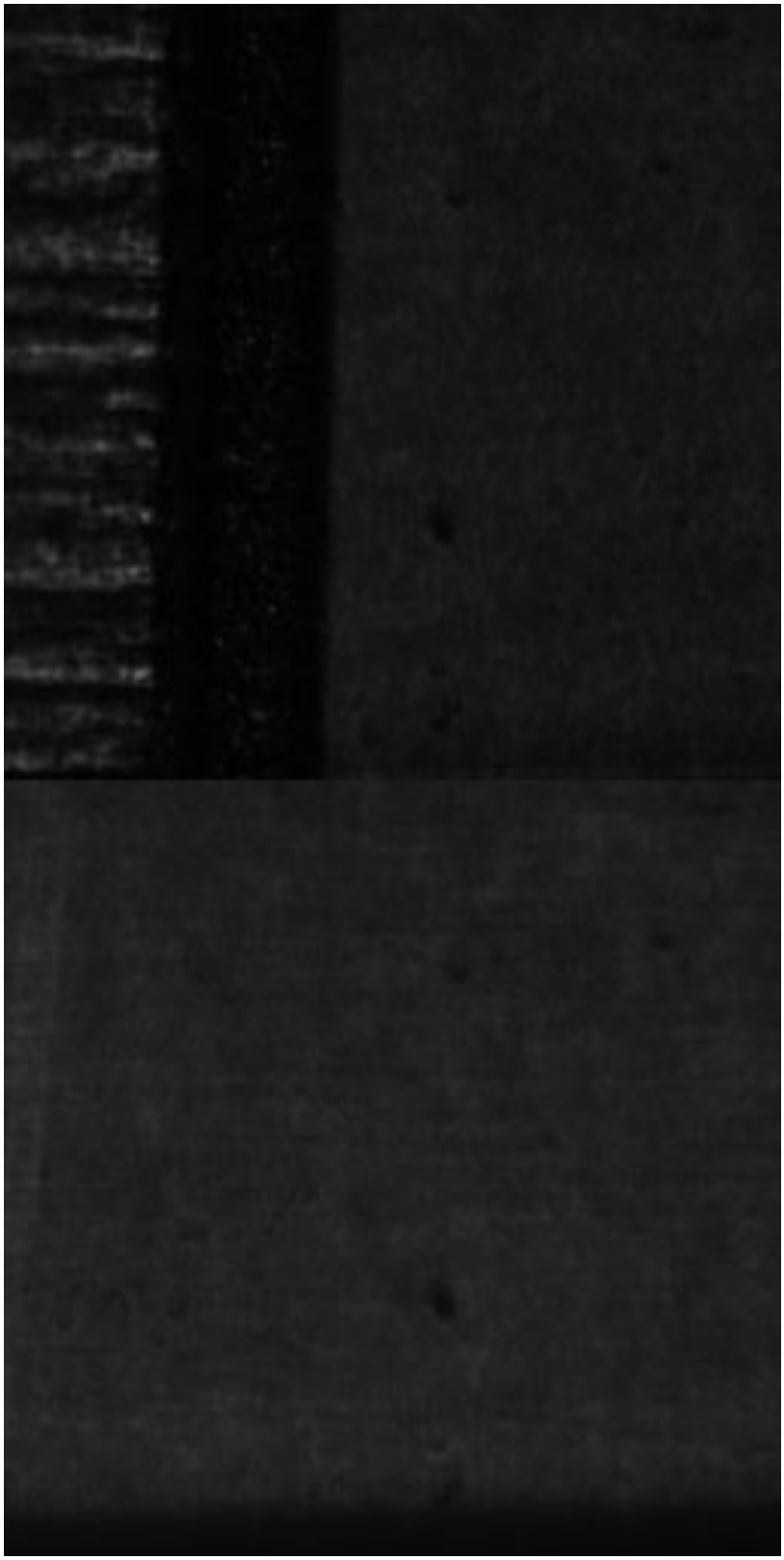

Figure E.166: Focused schlieren image of shot 2134. The field of view is approximately 14 mm wide.

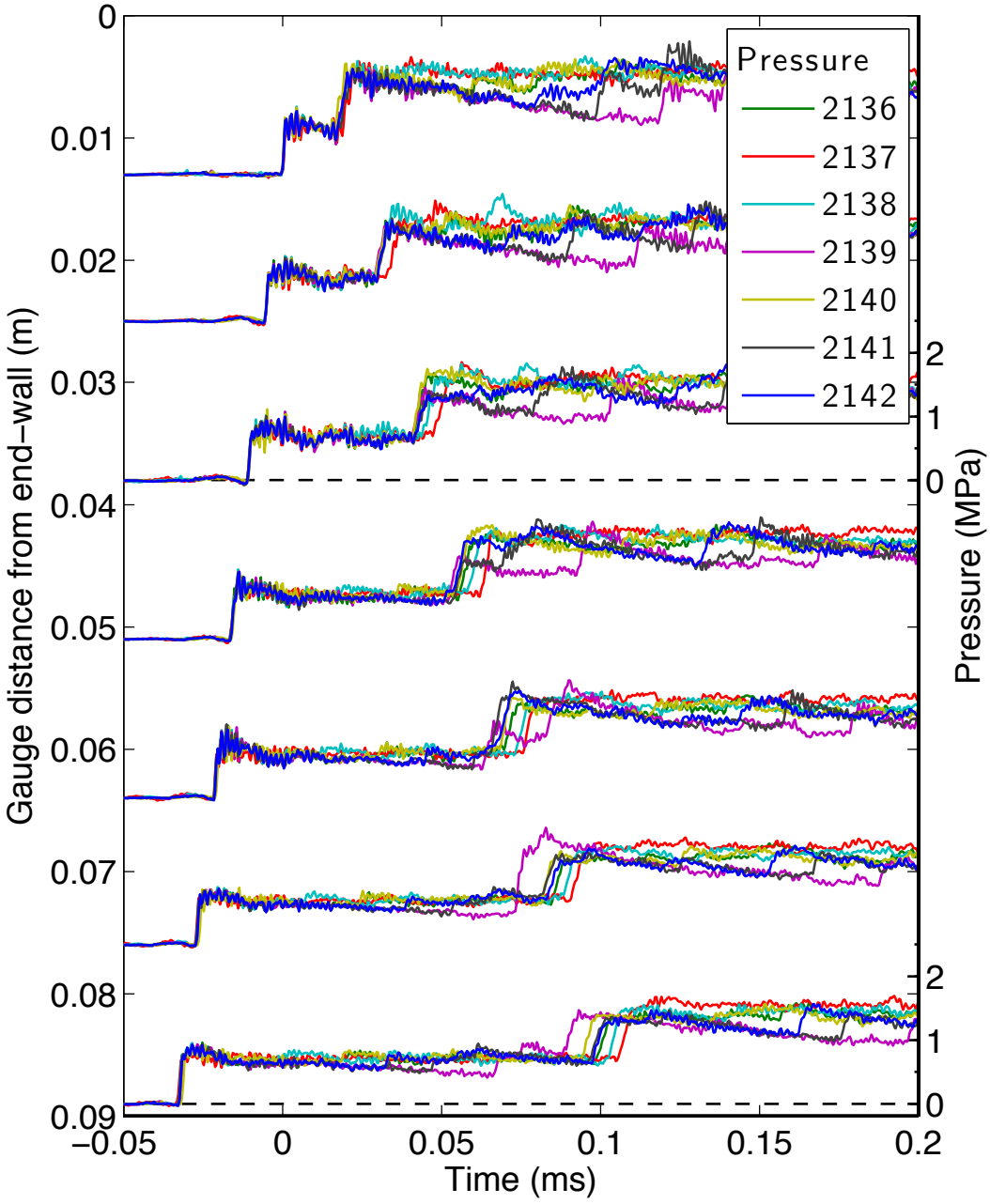

Figure E.167: Pressure traces for a detonation in stoichiometric ethylene-oxygen at fill pressure 25 kPa, part 5.

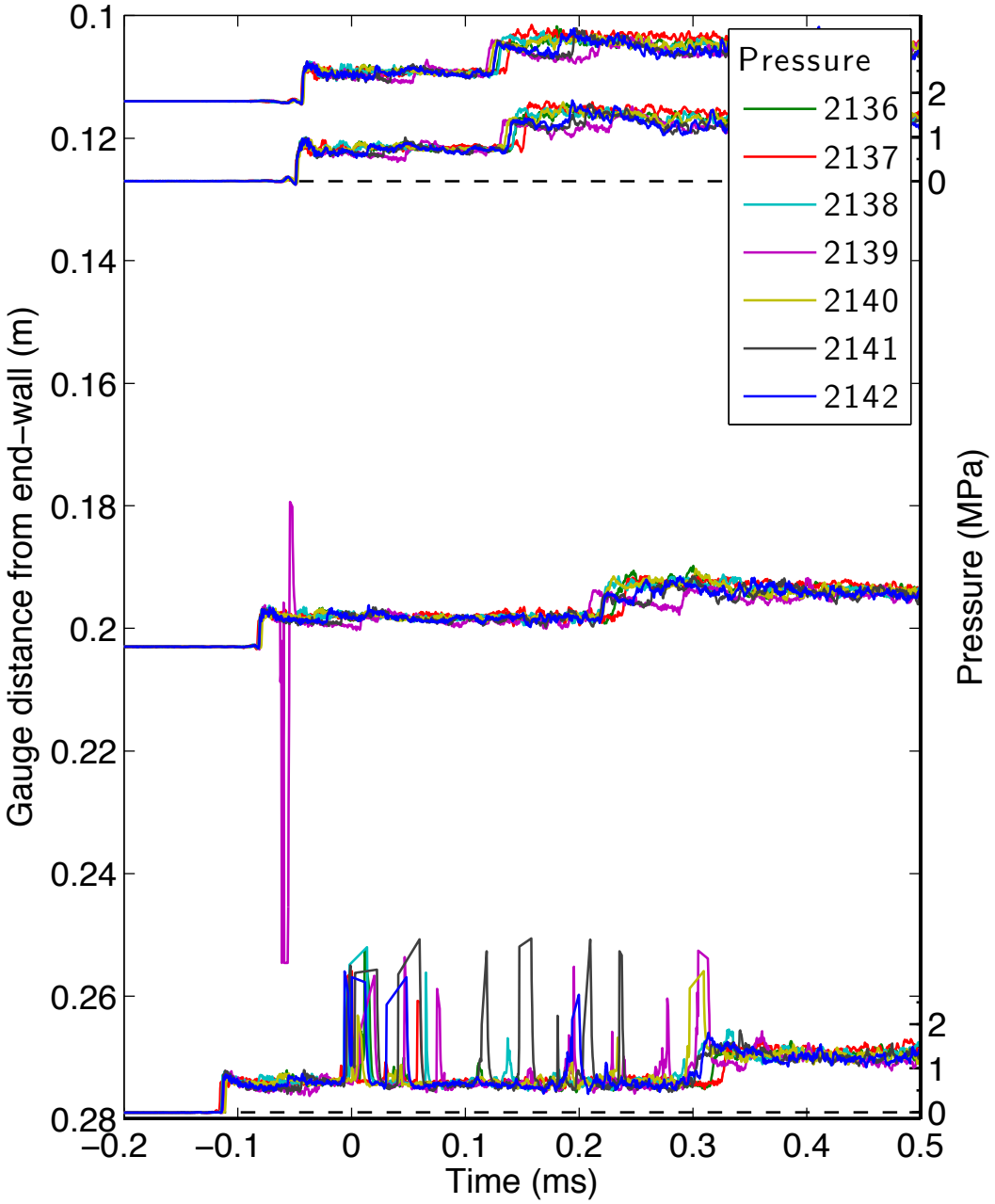

Figure E.168: Pressure traces for a detonation in stoichiometric ethylene-oxygen at fill pressure 25 kPa, part 6.

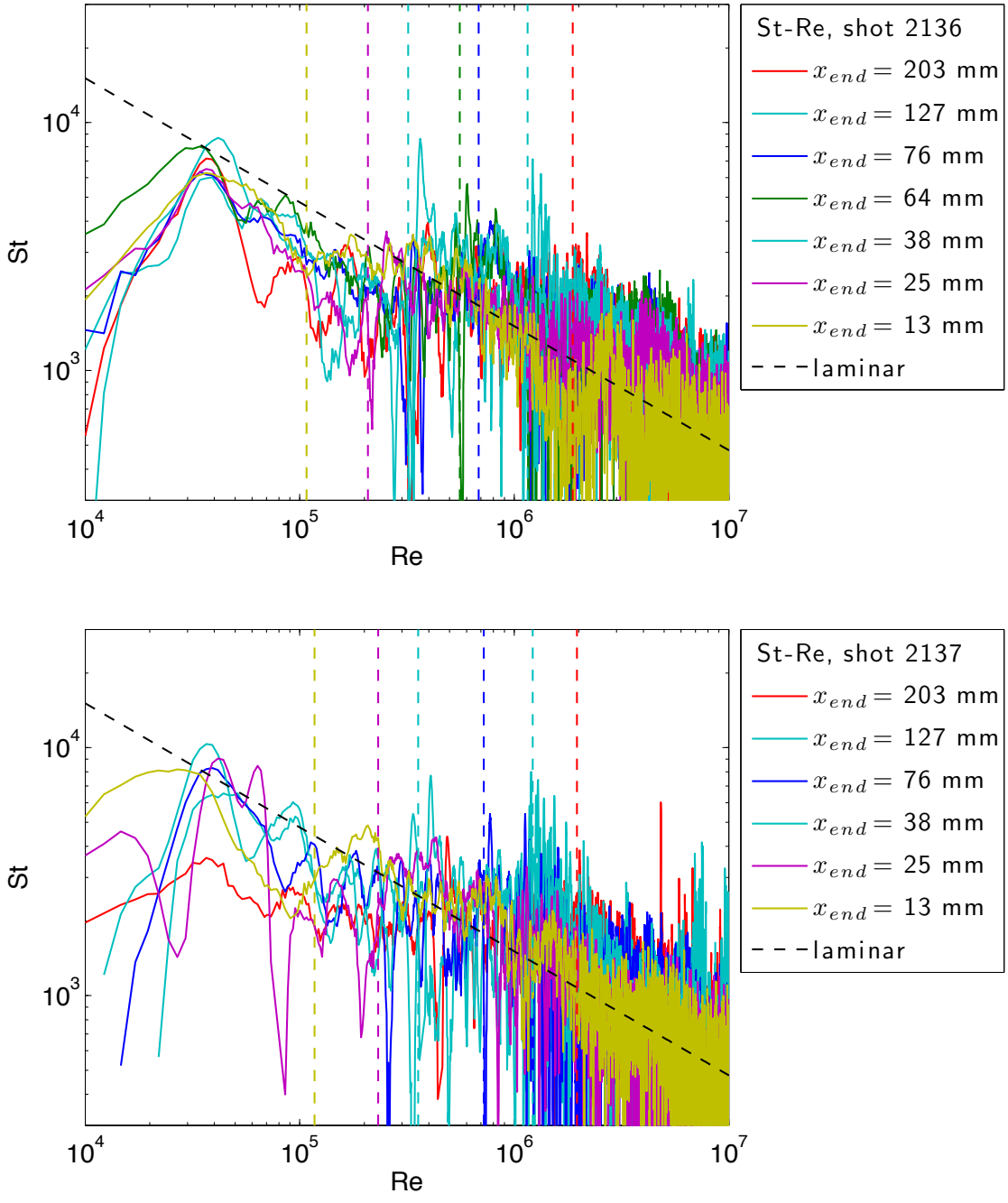

Figure E.169: Stanton-Reynolds number traces from shot 2137, a detonation in stoichiometric ethylene-oxygen at fill pressure 25 kPa. The dashed vertical lines represent the arrival of the reflected shock wave.

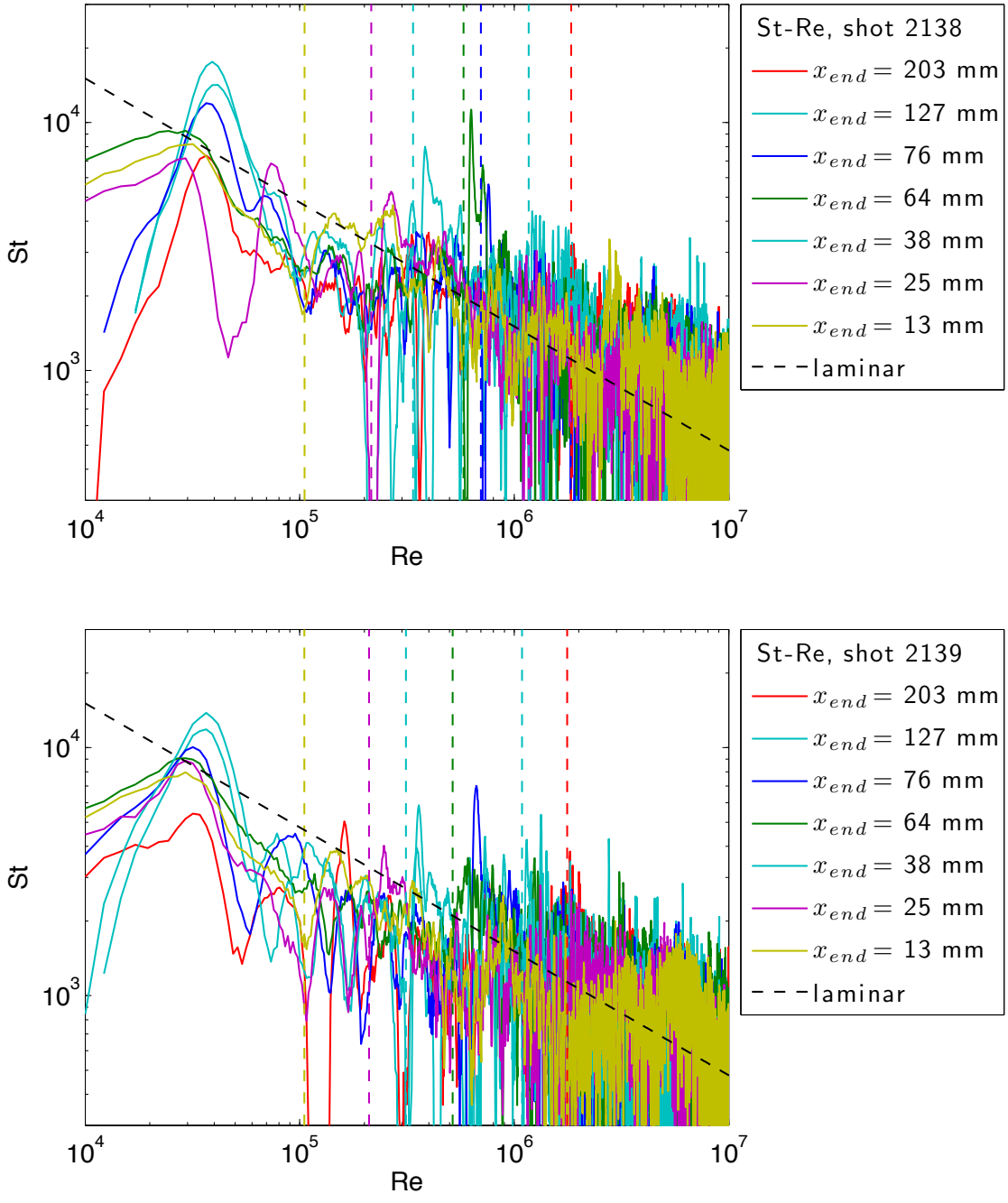

Figure E.170: Stanton-Reynolds number traces from shot 2139, a detonation in stoichiometric ethylene-oxygen at fill pressure 25 kPa. The dashed vertical lines represent the arrival of the reflected shock wave.

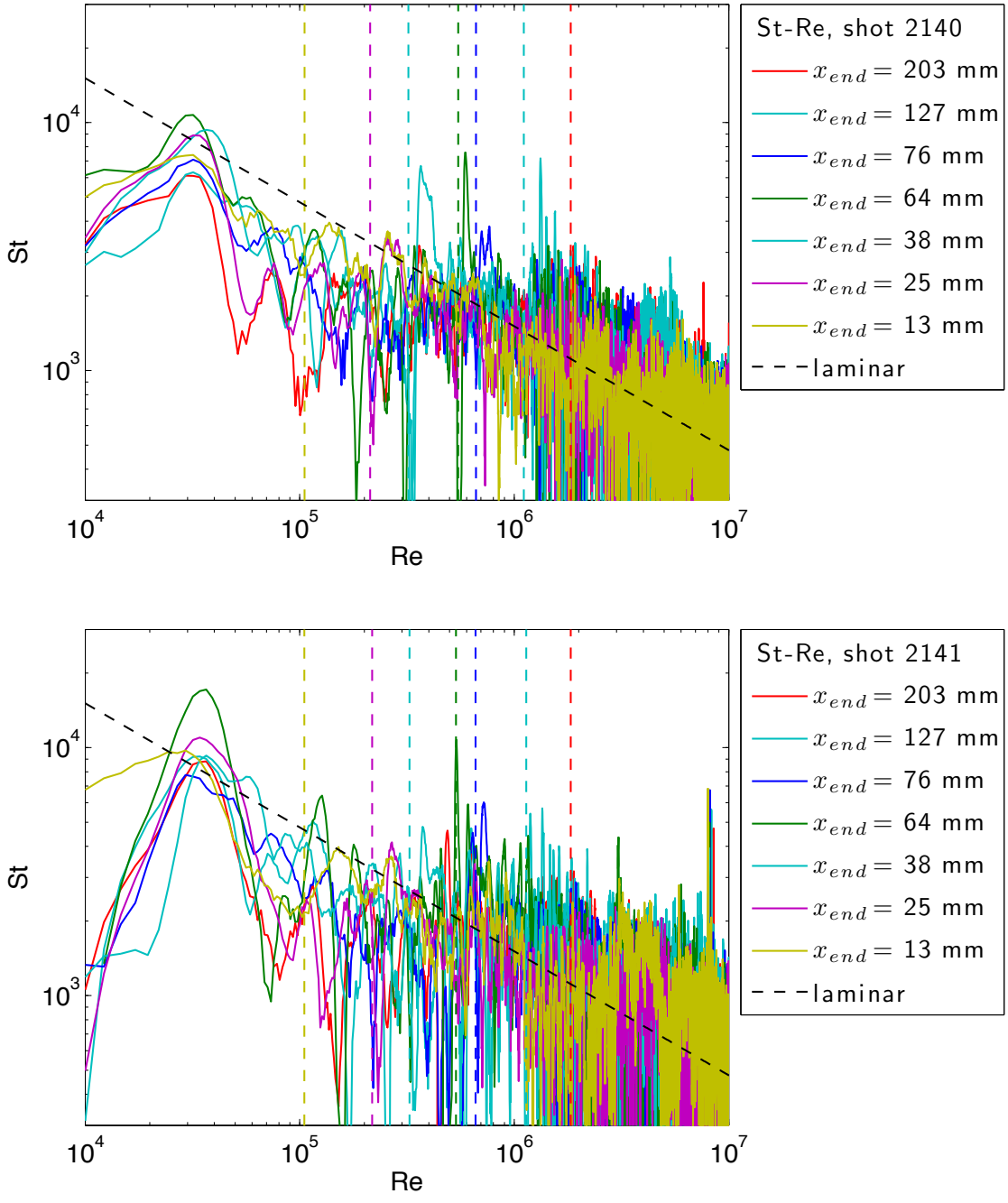

Figure E.171: Stanton-Reynolds number traces from shot 2141, a detonation in stoichiometric ethylene-oxygen at fill pressure 25 kPa. The dashed vertical lines represent the arrival of the reflected shock wave.

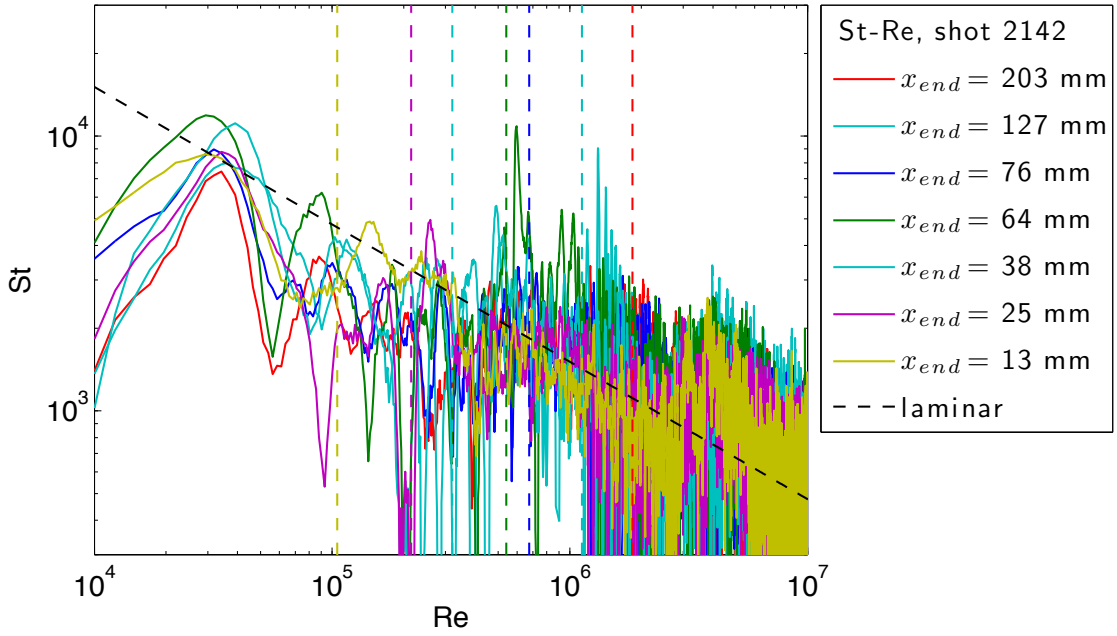

Figure E.172: Stanton-Reynolds number traces from shot 2142, a detonation in stoichiometric ethylene-oxygen at fill pressure 25 kPa. The dashed vertical lines represent the arrival of the reflected shock wave.

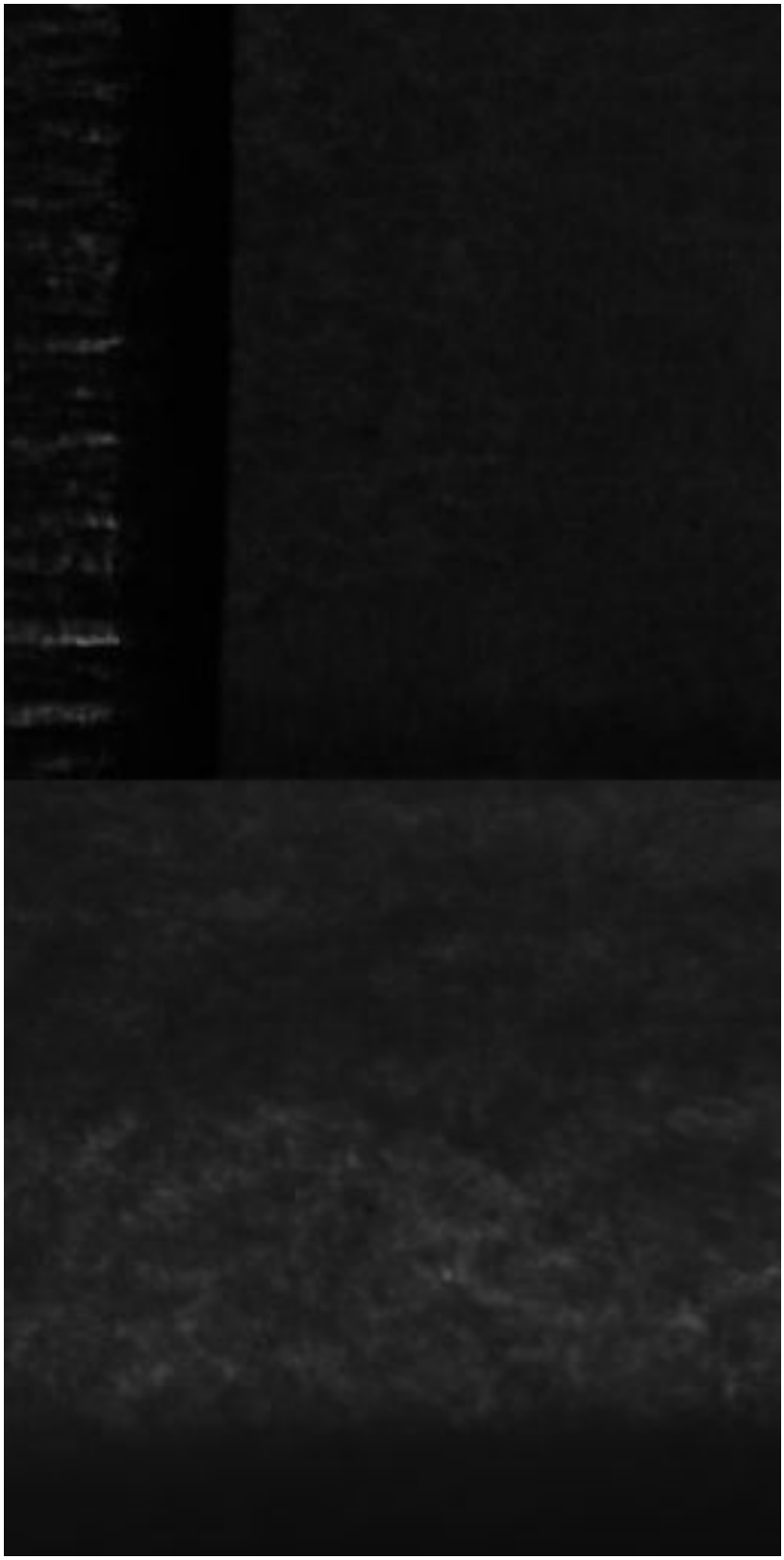

Figure E.173: Focused schlieren image of shot 2140. The field of view is approximately 14 mm wide.

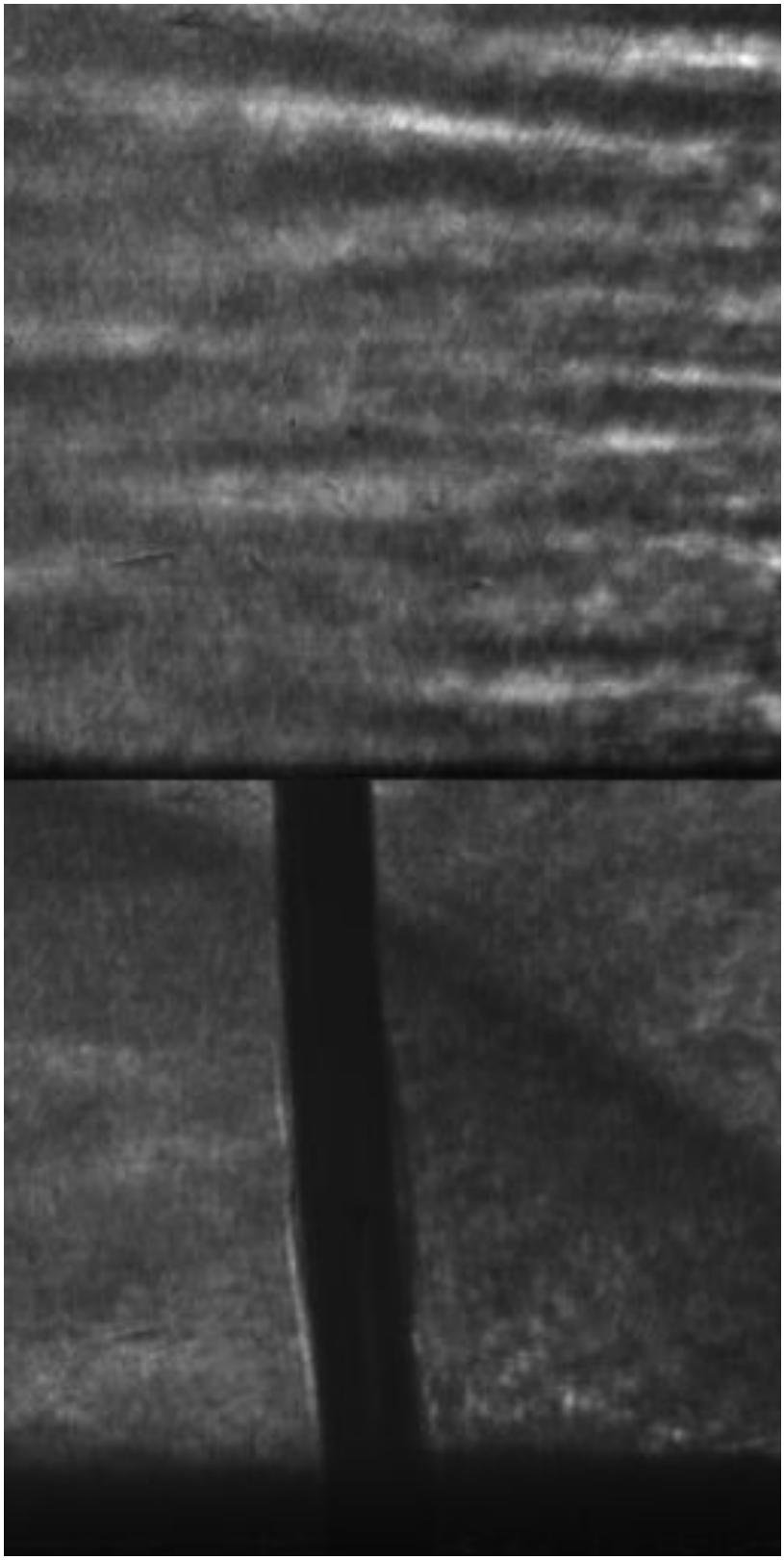

Figure E.174: Focused schlieren image of shot 2141. The field of view is approximately 14 mm wide.

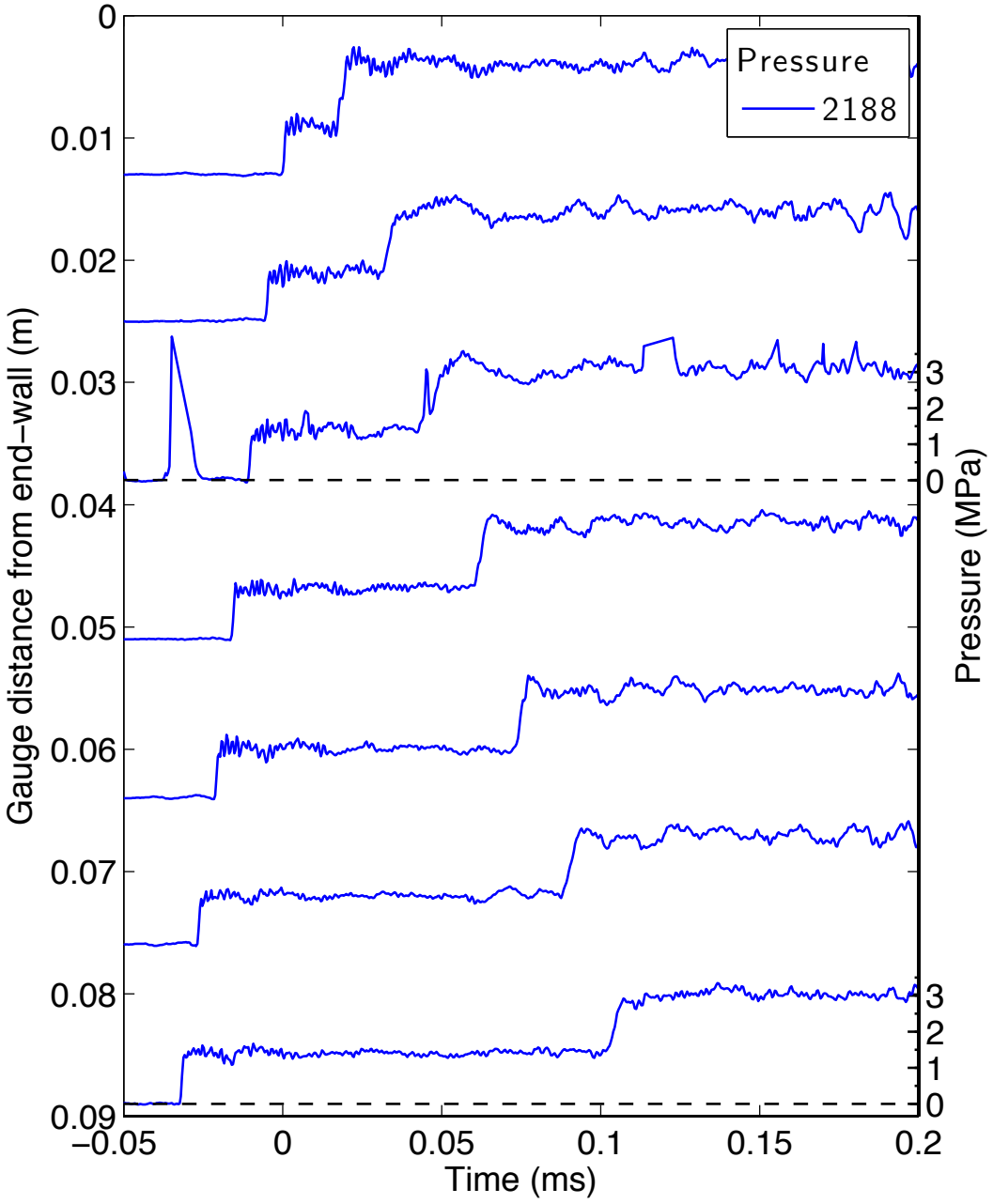

Figure E.175: Pressure traces for a detonation in stoichiometric ethylene-oxygen at fill pressure 50 kPa, part 1.

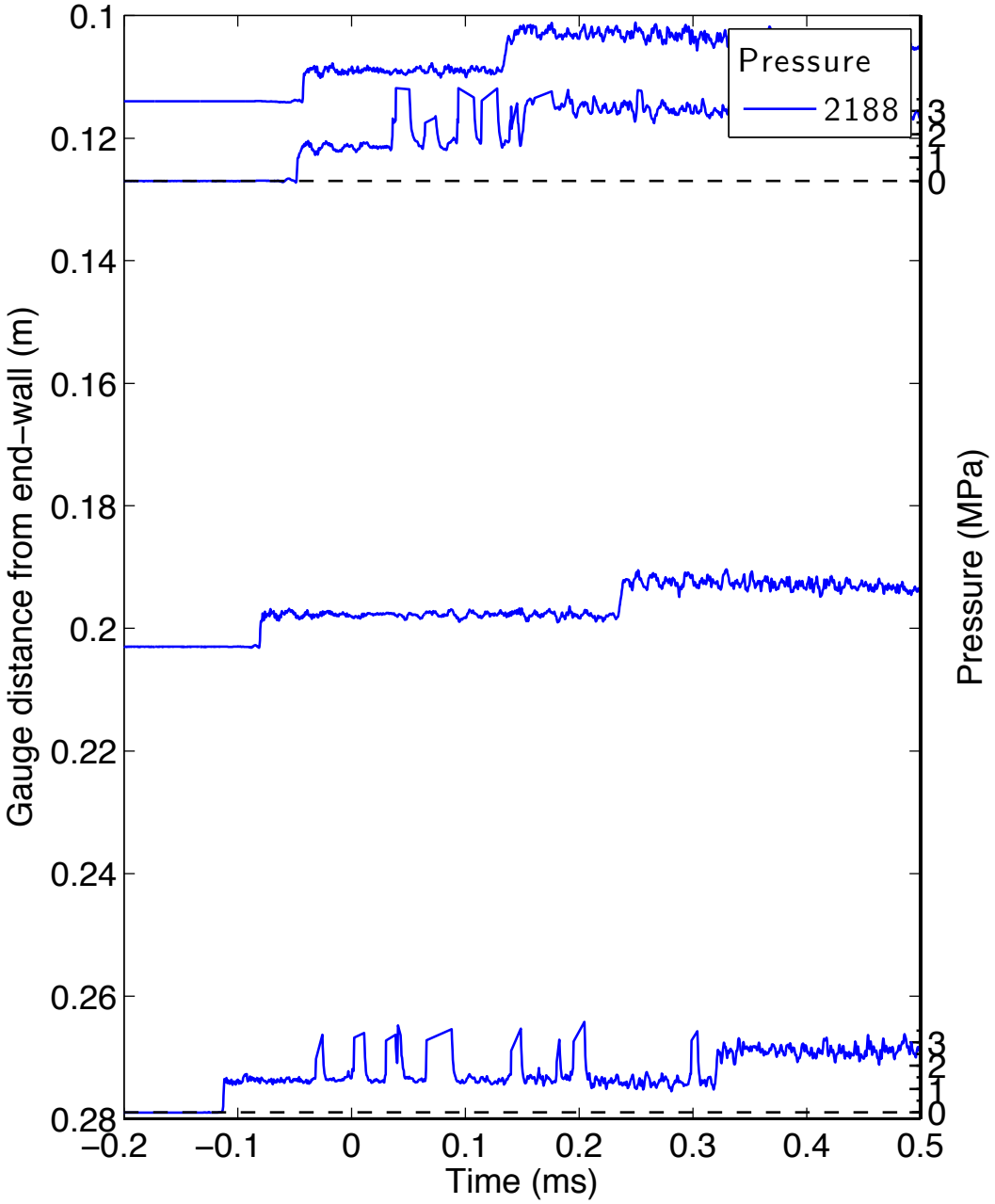

Figure E.176: Pressure traces for a detonation in stoichiometric ethylene-oxygen at fill pressure 50 kPa, part 2.

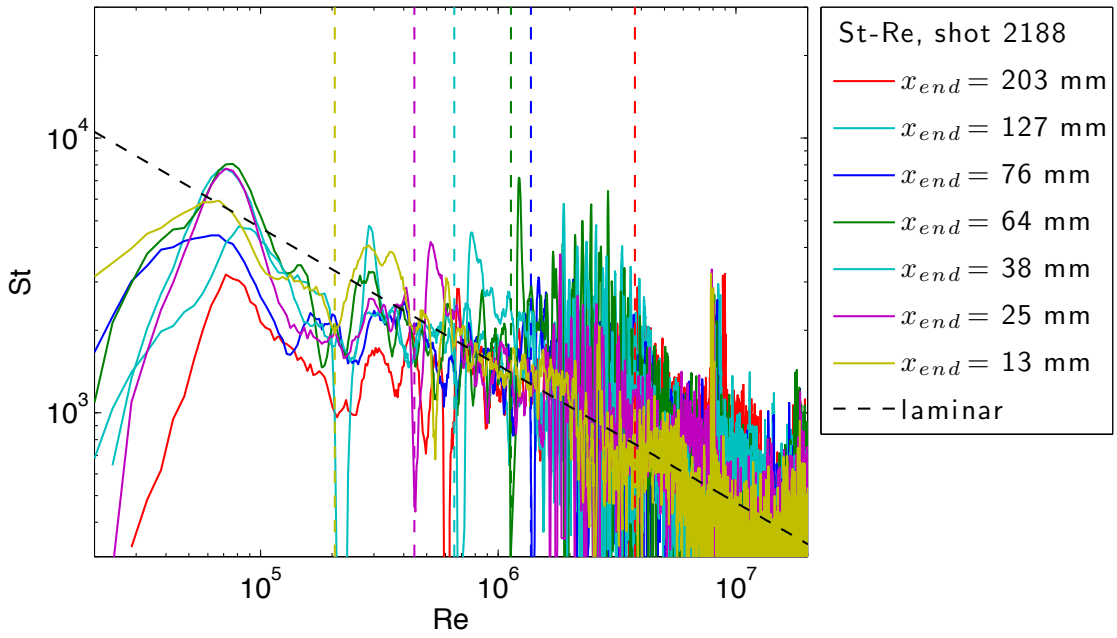

Figure E.177: Stanton-Reynolds number traces from shot 2188, a detonation in stoichiometric ethylene-oxygen at fill pressure 50 kPa. The dashed vertical lines represent the arrival of the reflected shock wave.

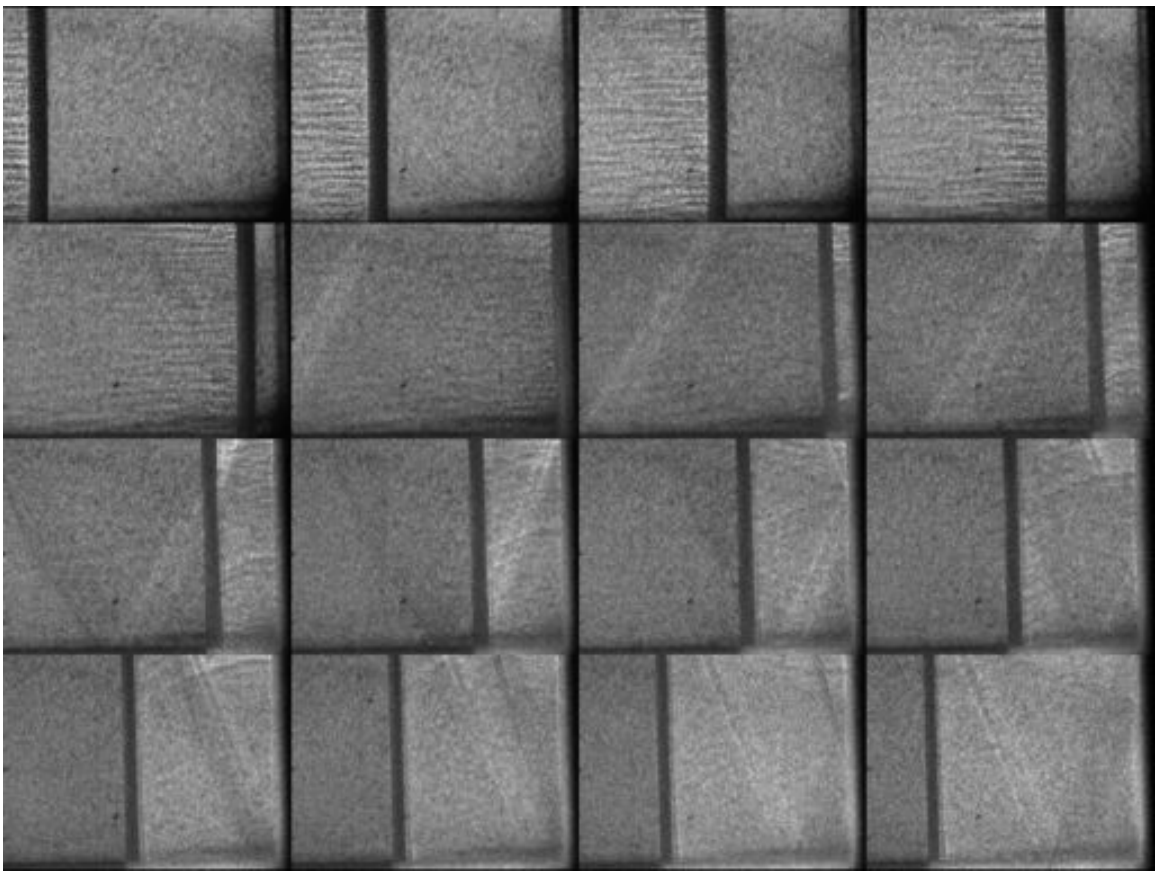

Figure E.178: Unfocused schlieren image of shot 2188. The field of view is approximately 30 mm wide.

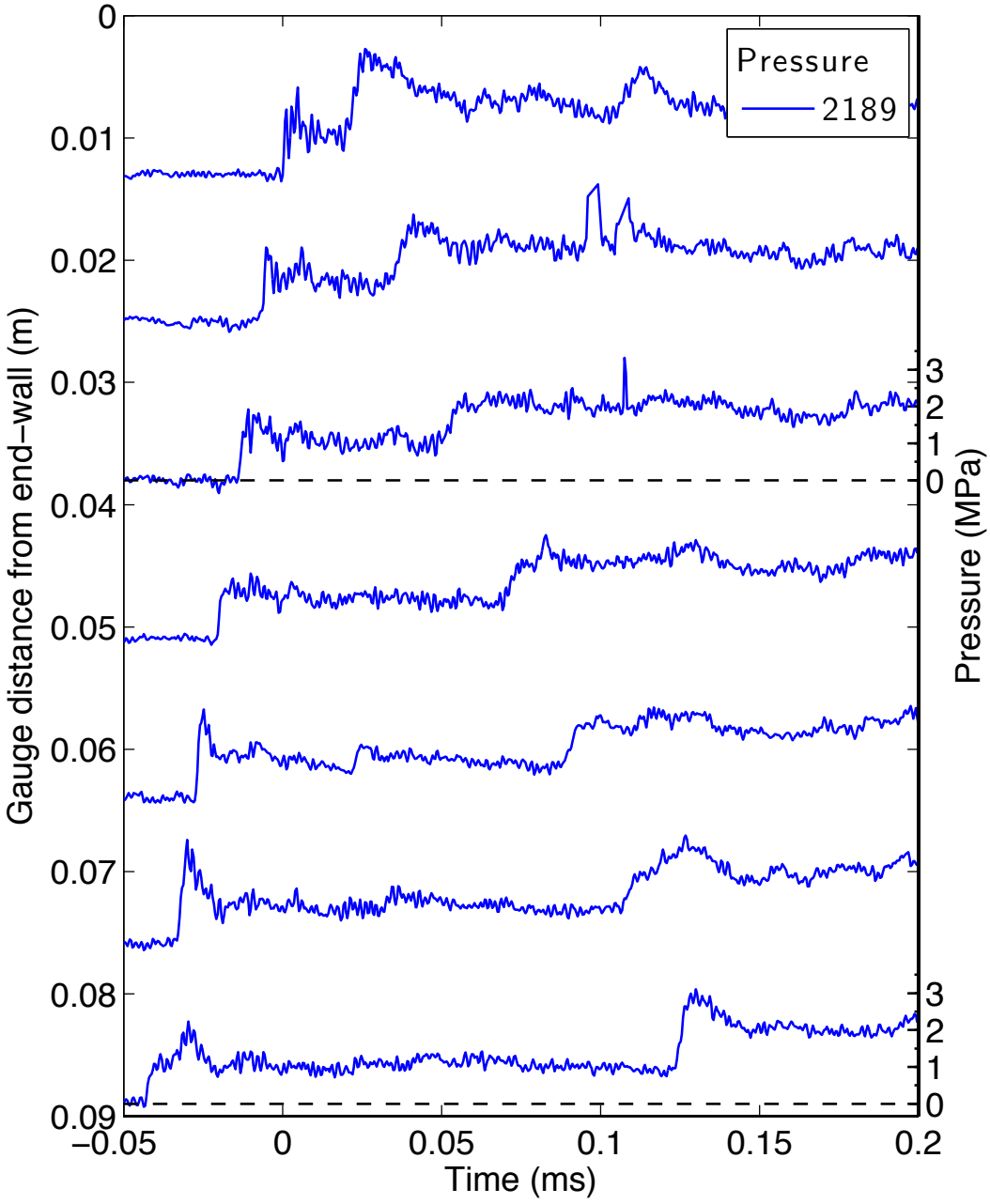

Figure E.179: Pressure traces for a detonation in stoichiometric ethylene-oxygen with 50% carbon dioxide dilution at fill pressure 50 kPa, part 1.

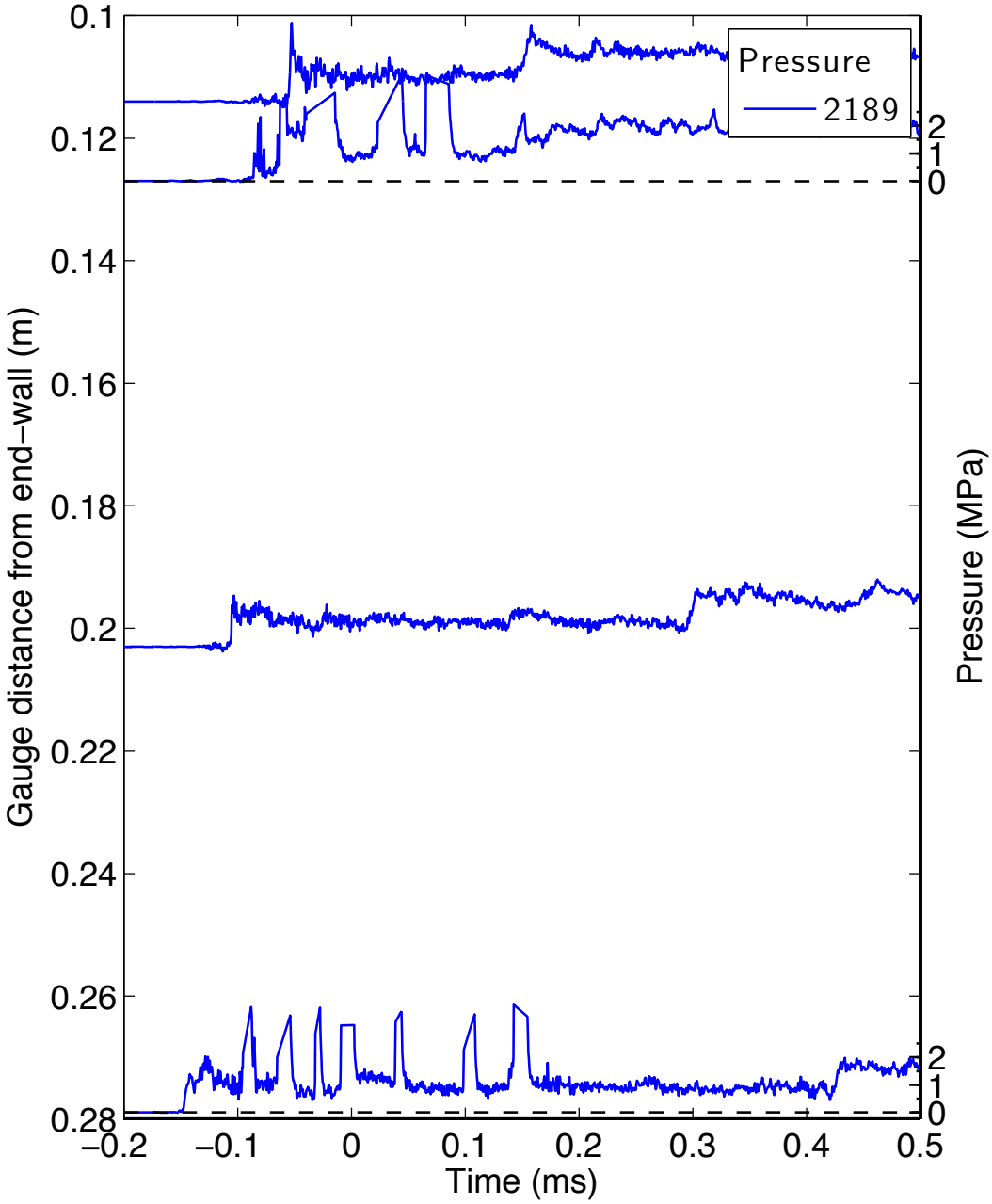

Figure E.180: Pressure traces for a detonation in stoichiometric ethylene-oxygen with 50% carbon dioxide dilution at fill pressure 50 kPa, part 2.

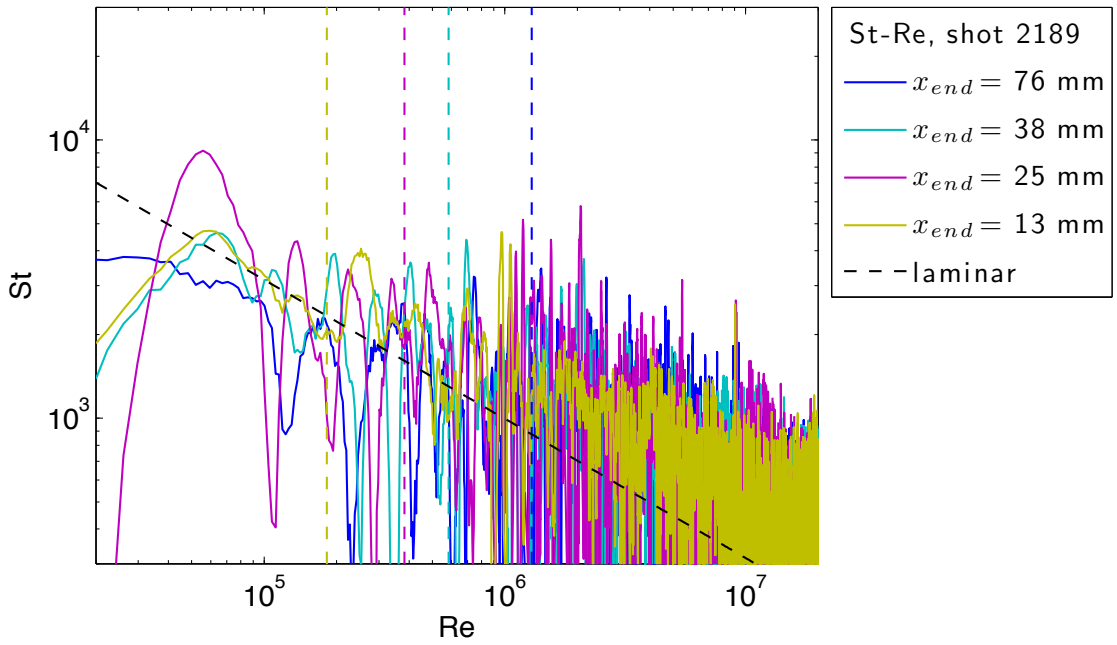

Figure E.181: Stanton-Reynolds number traces from shot 2189, a detonation in stoichiometric ethylene-oxygen with 50% carbon dioxide dilution at fill pressure 50 kPa. The dashed vertical lines represent the arrival of the reflected shock wave.

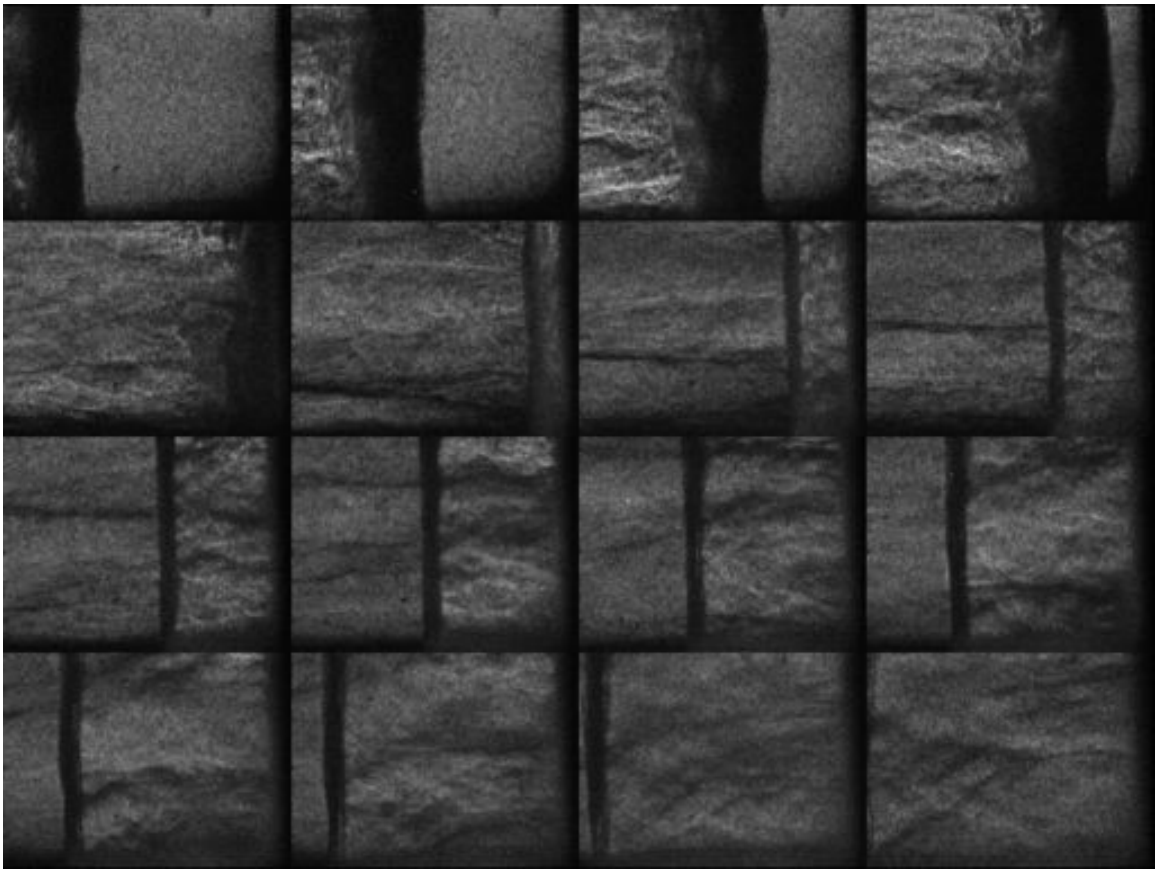

Figure E.182: Unfocused schlieren image of shot 2189. The field of view is approximately 30 mm wide.

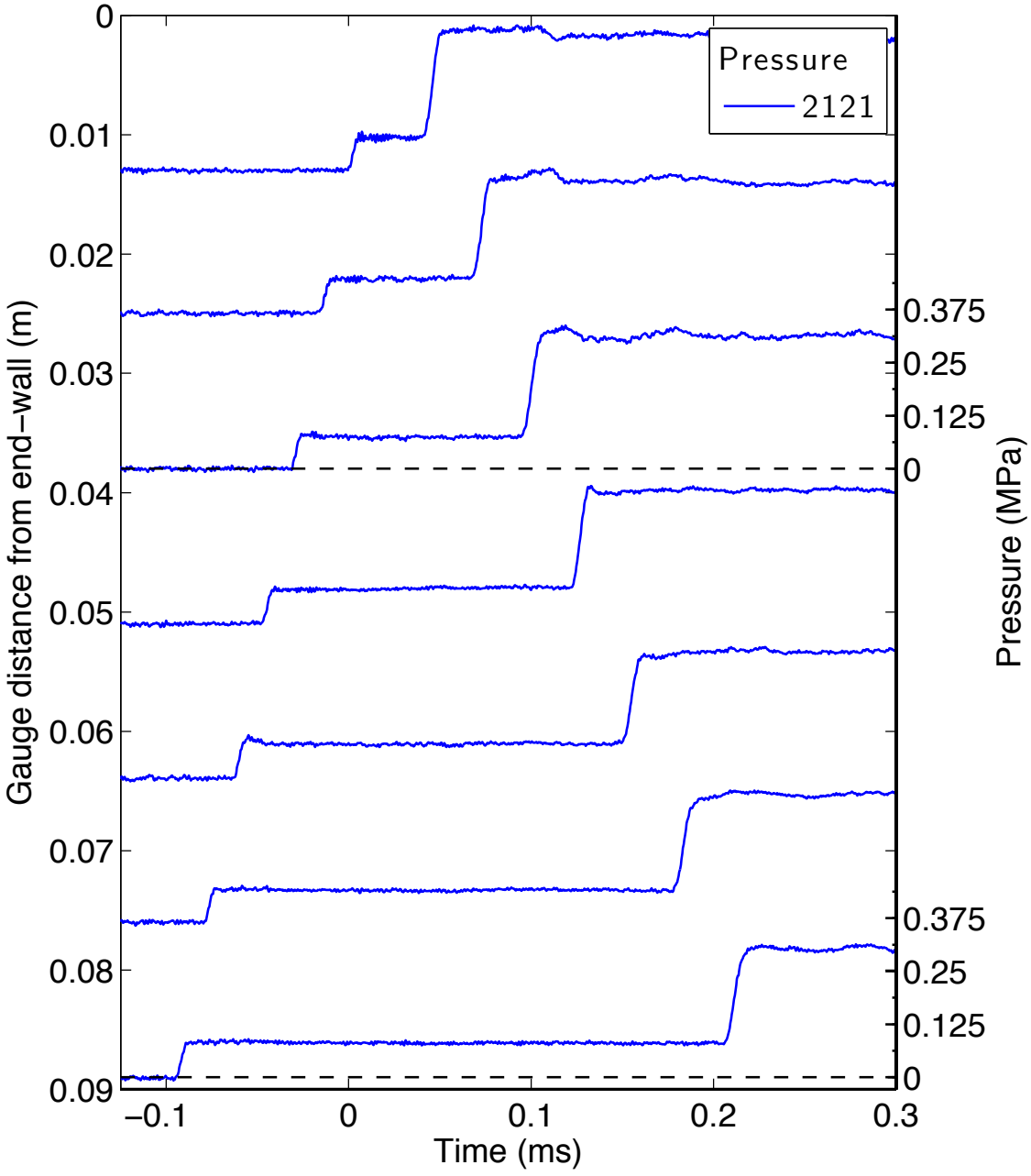

Figure E.183: Pressure traces for a shock wave in argon at fill pressure 10 kPa, part 1.

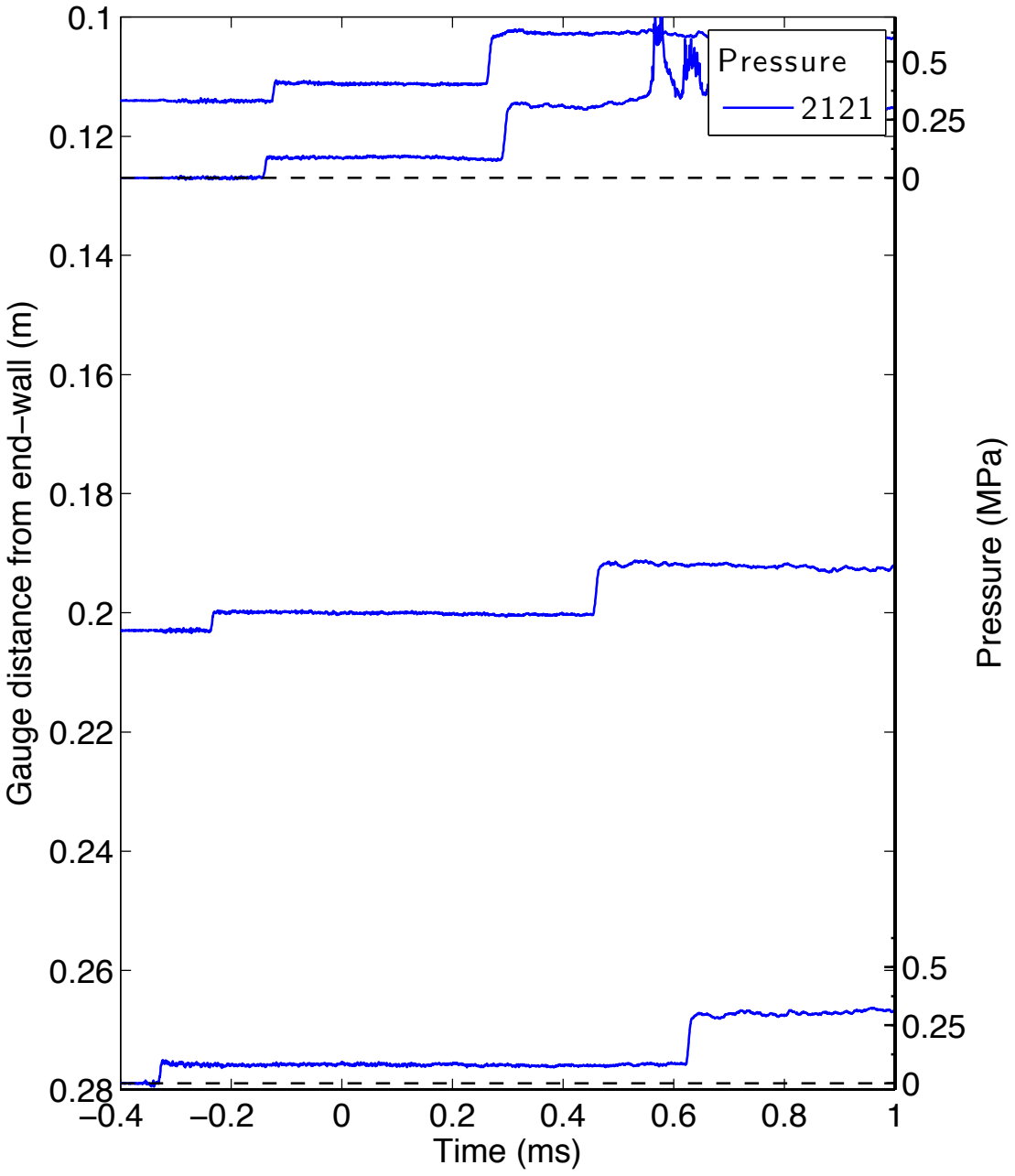

Figure E.184: Pressure traces for a shock wave in argon at fill pressure 10 kPa, part 2.

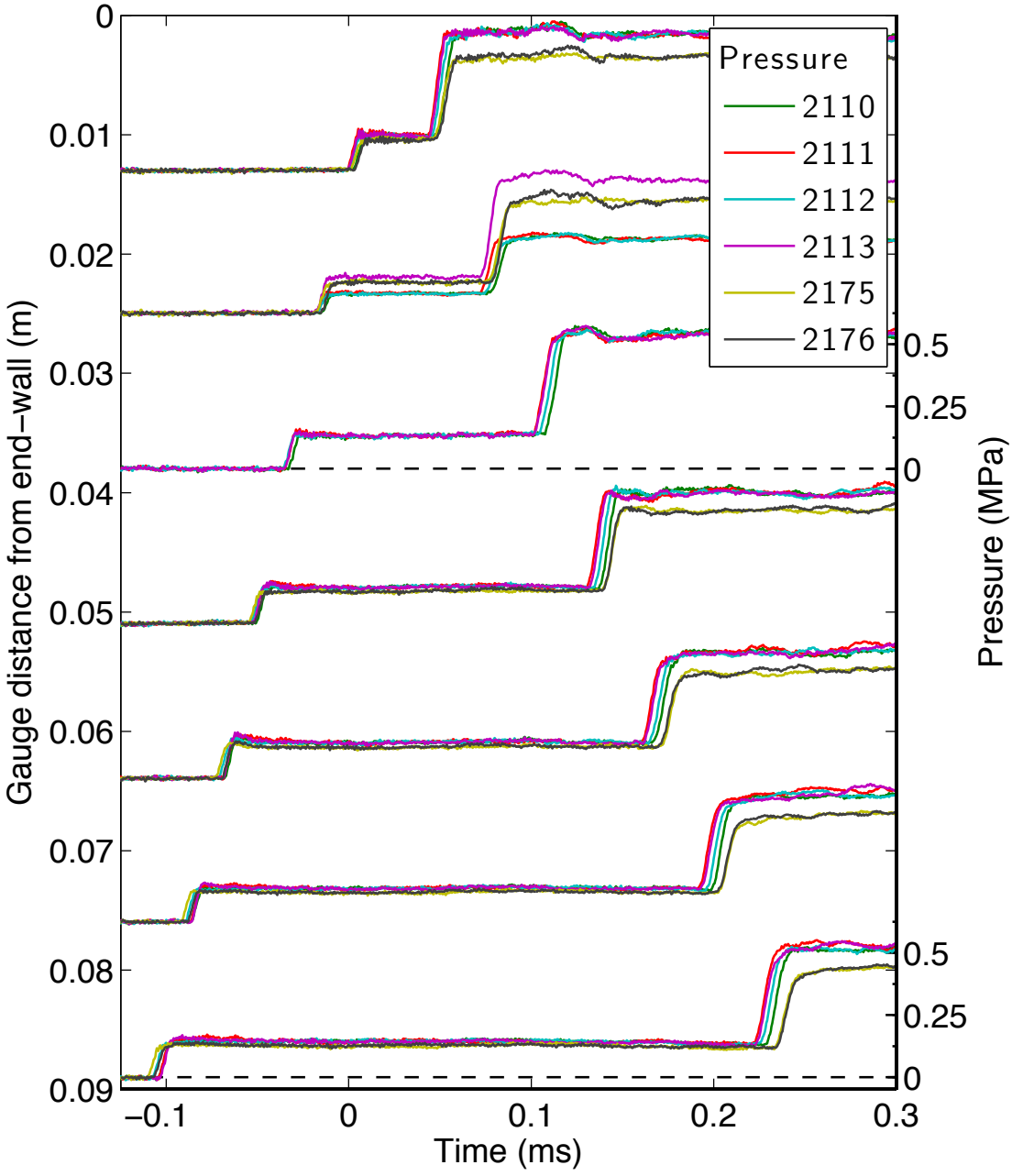

Figure E.185: Pressure traces for a shock wave in argon at fill pressure 25 kPa, part 1.

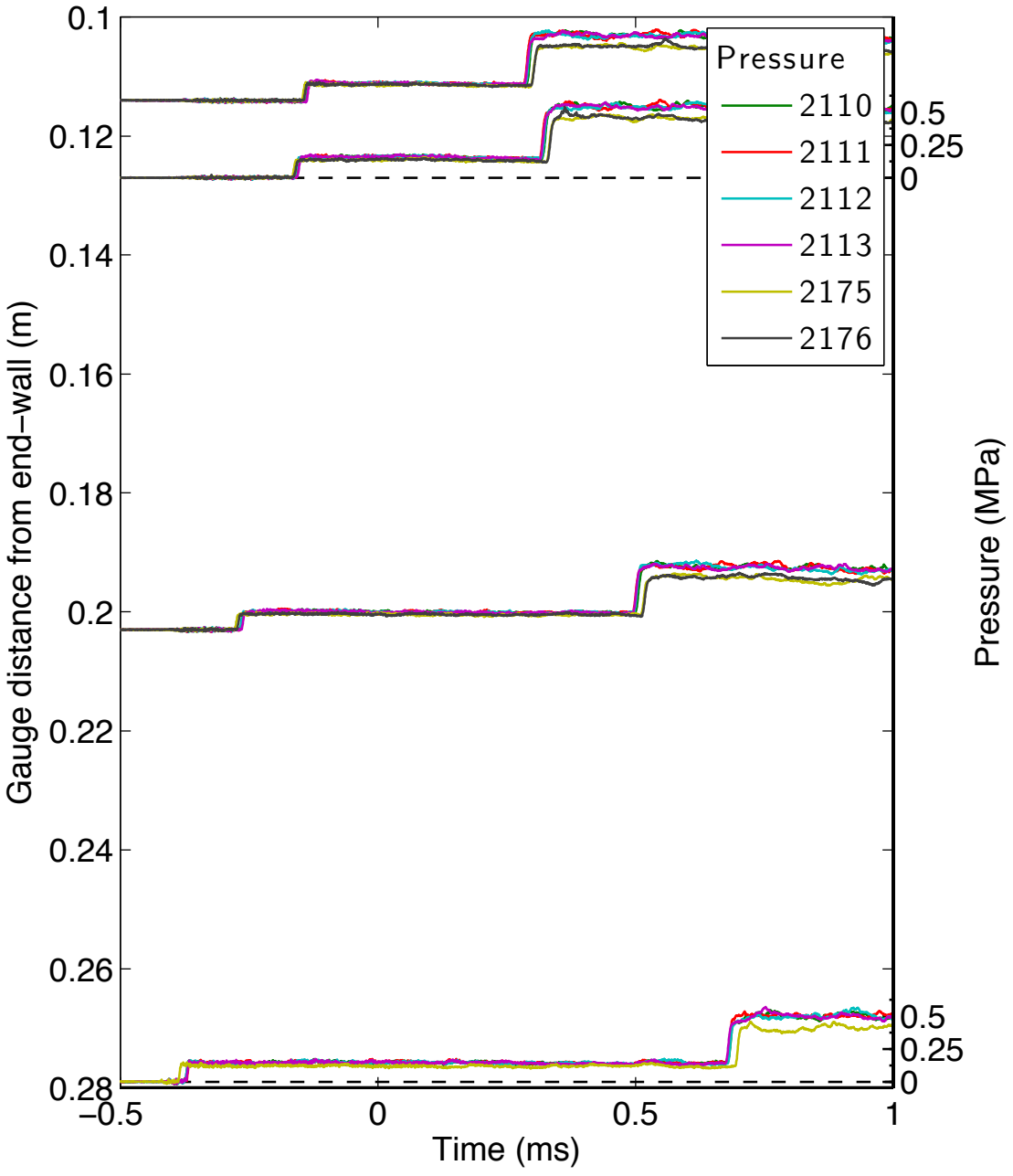

Figure E.186: Pressure traces for a shock wave in argon at fill pressure 25 kPa, part 2.

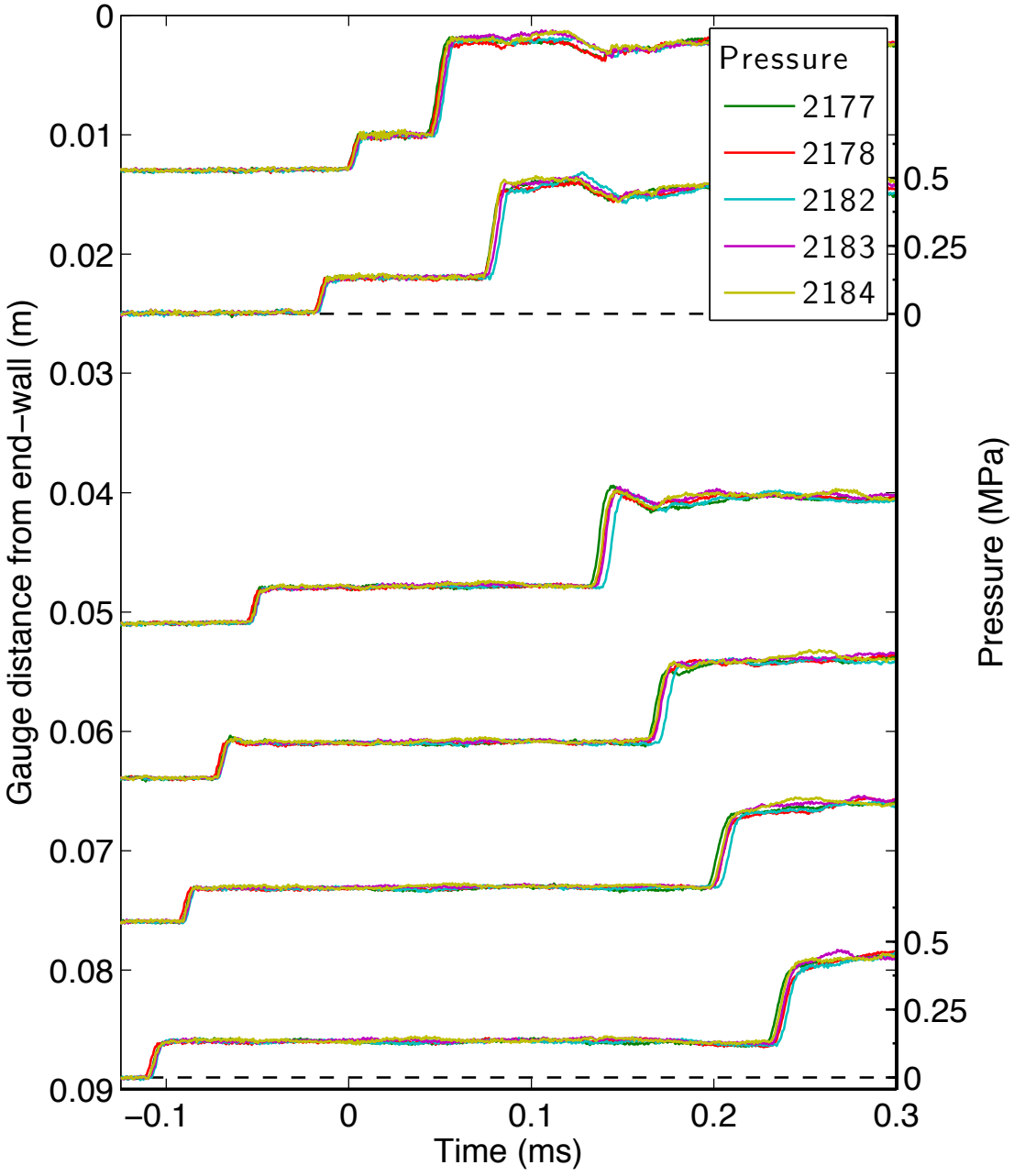

Figure E.187: Pressure traces for a shock wave in argon at fill pressure 25 kPa, part 3.

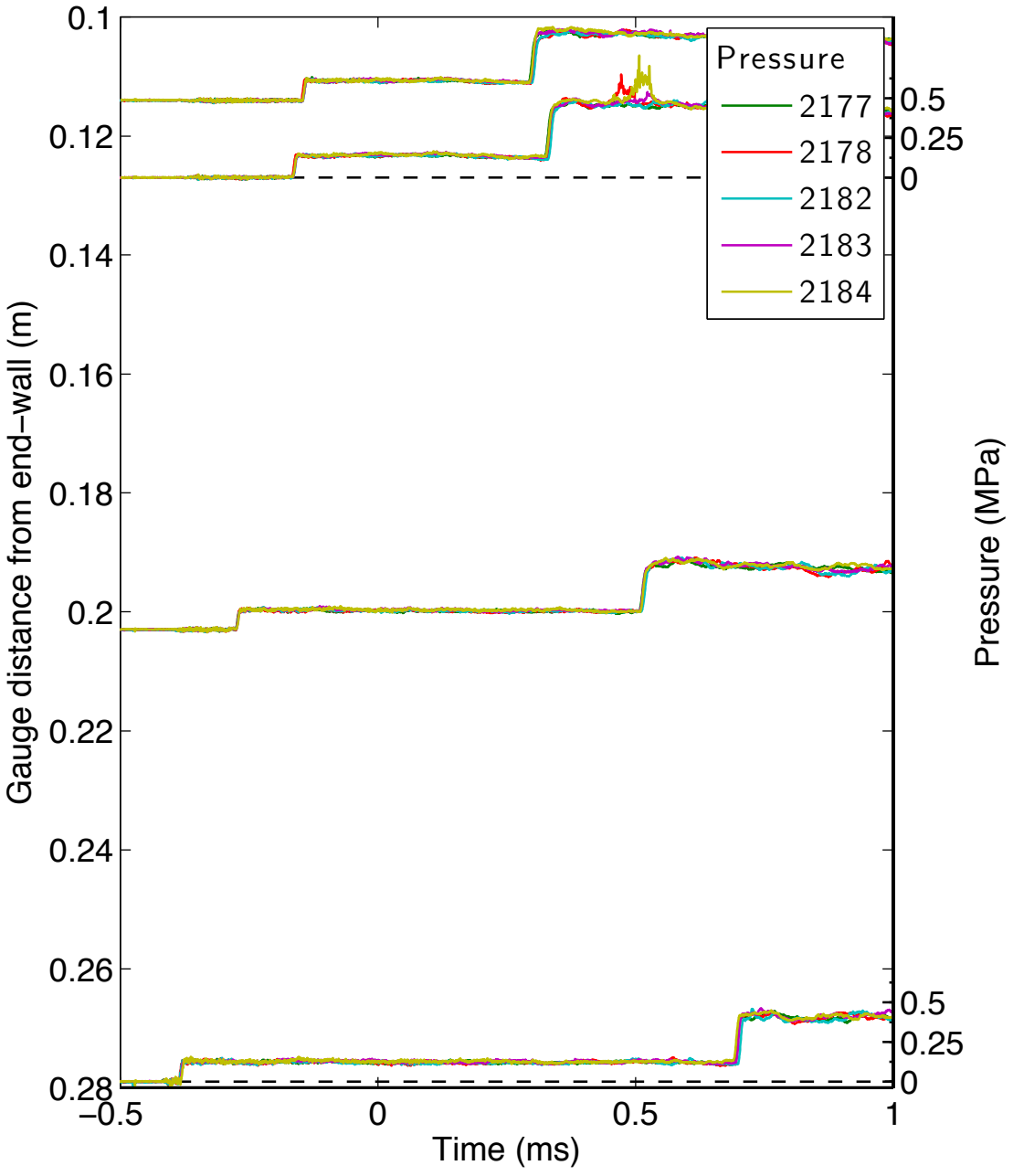

Figure E.188: Pressure traces for a shock wave in argon at fill pressure 25 kPa, part 4.

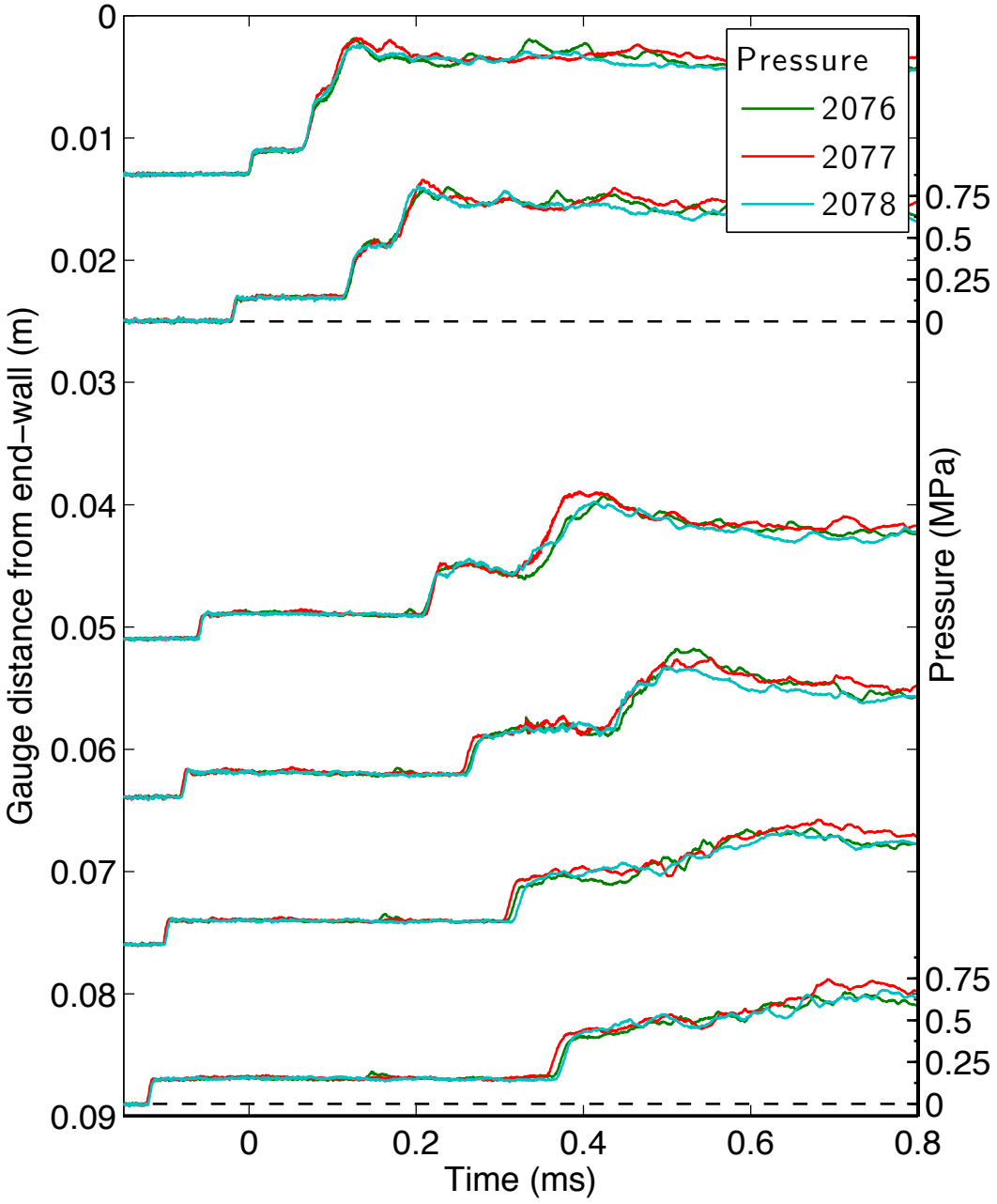

Figure E.189: Pressure traces for a shock wave in nitrous oxide at fill pressure 25 kPa, part 1.

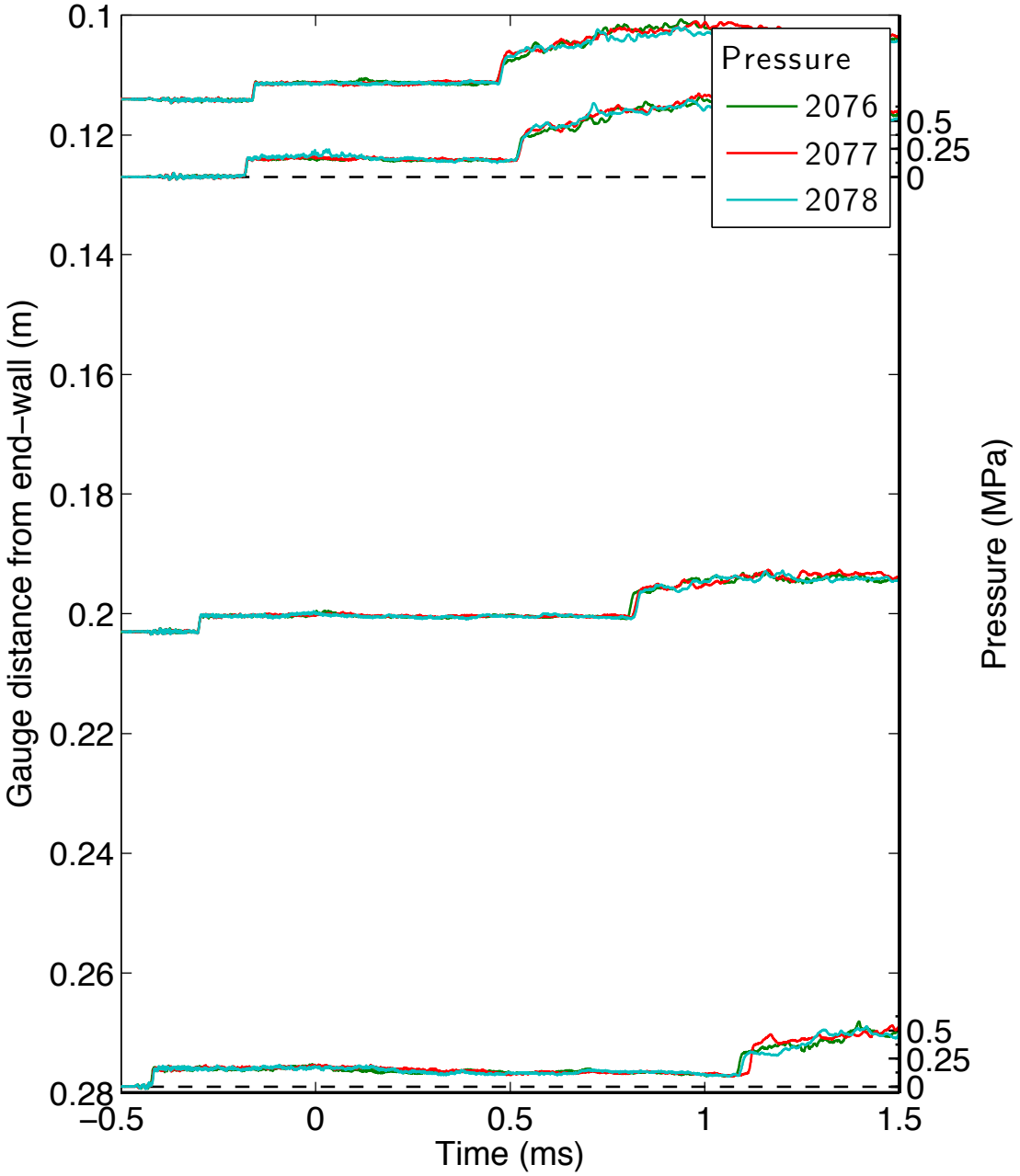

Figure E.190: Pressure traces for a shock wave in nitrous oxide at fill pressure 25 kPa, part 2.

Appendix F

Derivation of Laminar Boundary Layer Equations

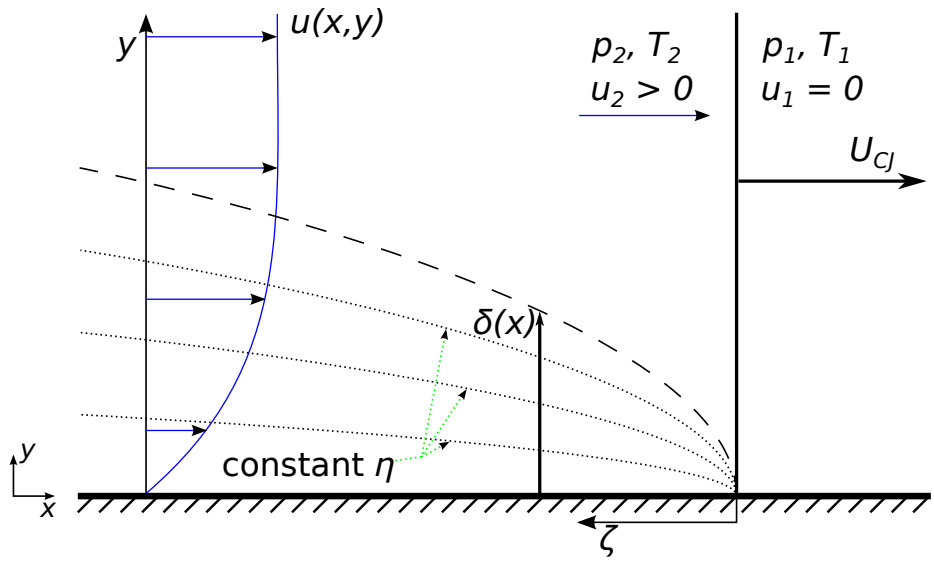

Figure F.1: Frame of reference used for boundary layer calculations.

F.1 Boundary Layer Governing Equations

The governing equations for a two-dimensional compressible laminar boundary layer in a lab-fixed frame are the conservation of mass, momentum, and energy with the boundary layer assumption that gradients with respect to the transverse direction, y,

are much larger than gradients with respect to the axial direction, x:

$$\frac{\partial \rho}{\partial t} + \frac{\partial \rho u}{\partial x} + \frac{\partial \rho v}{\partial y} = 0 \tag{F.1}$$

$$\rho \frac{\partial u}{\partial t} + \rho u \frac{\partial u}{\partial x} + \rho v \frac{\partial u}{\partial y} = -\frac{\partial p}{\partial x} + \frac{\partial}{\partial y}\left(\mu \frac{\partial u}{\partial y}\right) \tag{F.2}$$

$$\rho \frac{\partial h}{\partial t} + \rho u \frac{\partial h}{\partial x} + \rho v \frac{\partial h}{\partial y} = \frac{\partial p}{\partial t} + u \frac{\partial p}{\partial x} + \frac{\partial}{\partial y}\left(\frac{\mu}{Pr} \frac{\partial h}{\partial y}\right) + \mu \left(\frac{\partial u}{\partial y}\right)^2. \tag{F.3}$$

F.2 Definition of the Coordinate System

Variables are given in a lab fixed frame where the detonation originates at $x = 0$, $t = 0$ and proceeds in the $+\hat{x}$-direction. The position of the detonation as a function of time is $X_{det}(t)$ and the detonation velocity is given by $U_{det}(t) = U_{CJ}$. We will be applying the Levy-Lees transformation to switch to the (ζ, η, τ) coordinate system.

ζ: Axial position, x, scaled with the location of the detonation

$$\zeta(x,t) = 1 - \frac{x}{X_{det}(t)}. \tag{F.4}$$

η: Distance from the side-wall, y, scaled with compressibility ($\star_0$ represents $\star$ evaluated at a constant reference state) and boundary layer thickness δ

$$\eta(x,y,t) = \frac{\displaystyle\int_0^y \frac{\rho(x,y',t)}{\rho_0} dy'}{\delta(x,t)}. \tag{F.5}$$

τ: Time, t, scaled with the speed of the detonation and length of the detonation tube

$$\tau(t) = \frac{t U_{CJ}}{L} \tag{F.6}$$

where L is the axial length of the system in the $\hat{x}$-direction. With this list, we can apply the chain rule to note:

$$\left.\frac{\partial}{\partial x}\right|_{y,t} = \left.\frac{\partial \zeta}{\partial x}\right|_{y,t} \left.\frac{\partial}{\partial \zeta}\right|_{\eta,\tau} + \left.\frac{\partial \eta}{\partial x}\right|_{y,t} \left.\frac{\partial}{\partial \eta}\right|_{\zeta,\tau} + \cancelto{0}{\left.\frac{\partial \tau}{\partial x}\right|_{y,t}} \left.\frac{\partial}{\partial \tau}\right|_{\zeta,\eta} \tag{F.7}$$

$$= -\frac{1}{L\tau} \left.\frac{\partial}{\partial \zeta}\right|_{\eta,\tau} + \eta_x \left.\frac{\partial}{\partial \eta}\right|_{\zeta,\tau} \tag{F.8}$$

where, for the moment, we have left η_x as the derivative of η with respect to x at constant y and t. Similarly,

$$\left.\frac{\partial}{\partial y}\right|_{x,t} = \cancelto{0}{\left.\frac{\partial \zeta}{\partial y}\right|_{x,t}} \left.\frac{\partial}{\partial \zeta}\right|_{\eta,\tau} + \left.\frac{\partial \eta}{\partial y}\right|_{x,t} \left.\frac{\partial}{\partial \eta}\right|_{\zeta,\tau} + \cancelto{0}{\left.\frac{\partial \tau}{\partial y}\right|_{x,t}} \left.\frac{\partial}{\partial \tau}\right|_{\zeta,\eta} \tag{F.9}$$

$$= \frac{\rho}{\rho_0 \delta} \left.\frac{\partial}{\partial \eta}\right|_{\zeta,\tau} \tag{F.10}$$

$$\left.\frac{\partial}{\partial t}\right|_{x,y} = \left.\frac{\partial \zeta}{\partial t}\right|_{x,y} \left.\frac{\partial}{\partial \zeta}\right|_{\eta,\tau} + \left.\frac{\partial \eta}{\partial t}\right|_{x,y} \left.\frac{\partial}{\partial \eta}\right|_{\zeta,\tau} + \left.\frac{\partial \tau}{\partial t}\right|_{x,y} \left.\frac{\partial}{\partial \tau}\right|_{\zeta,\eta} \tag{F.11}$$

$$= \frac{x U_{CJ}}{X_{det}^2} \left.\frac{\partial}{\partial \zeta}\right|_{\eta,\tau} + \eta_t \left.\frac{\partial}{\partial \eta}\right|_{\zeta,\tau} + \frac{U_{CJ}}{L} \left.\frac{\partial}{\partial \tau}\right|_{\zeta,\eta} \tag{F.12}$$

$$= \frac{U_{CJ}}{L\tau} (1-\zeta) \left.\frac{\partial}{\partial \zeta}\right|_{\eta,\tau} + \eta_t \left.\frac{\partial}{\partial \eta}\right|_{\zeta,\tau} + \frac{U_{CJ}}{L} \left.\frac{\partial}{\partial \tau}\right|_{\zeta,\eta}. \tag{F.13}$$

F.2.1 Transformation Inversion

Note that we can inverse the above Levy-Lees variable transformation through

$$x(\zeta,\tau) = X_{det}(\tau)(1-\zeta) \tag{F.14}$$

$$\eta(x,y,t) = \frac{\int_0^y \frac{\rho}{\rho_0} dy'}{\delta} \tag{F.15}$$

$$\Rightarrow \quad \frac{d\eta}{dy} = \frac{\rho}{\rho_0 \delta} \tag{F.16}$$

$$\frac{dy}{d\eta} = \frac{\rho_0 \delta}{\rho} \tag{F.17}$$

$$y = \int_0^\eta \frac{\rho_0 \delta(\zeta,\tau)}{\rho} d\eta \tag{F.18}$$

$$= \rho_0 \delta \int_0^\eta \frac{RT}{p} d\eta \tag{F.19}$$

$$= \frac{\rho_0 \delta R}{p} \int_0^\eta T d\eta \tag{F.20}$$

$$= \frac{\rho_0 \delta}{\rho_0 T_0} \int_0^\eta \frac{h}{c_p} d\eta \tag{F.21}$$

$$= \frac{\delta}{T_0 c_p} \int_0^\eta h \; d\eta \tag{F.22}$$

where we've used the ideal gas law and assumed $h = c_p T$ with constant c_p.

$$t = \frac{\tau L}{U_{CJ}} \tag{F.23}$$

F.2.2 Stream Function Formulation

The compressible stream function Ψ may be defined such that

$$\rho u = \rho_0 \frac{\partial \Psi}{\partial y} \tag{F.24}$$

$$\rho v = -\rho_0 \left(\frac{\partial \Psi}{\partial x} + \frac{\partial}{\partial t}(\eta \delta) \right) \tag{F.25}$$

so that the continuity equation is satisfied automatically. Further, let us assume

$$\Psi = u_e(\zeta)\delta(\zeta,\tau)f(\zeta,\eta) \tag{F.26}$$

where $\star_e$ represents $\star$ evaluated in the free stream

$$\Rightarrow\ \Psi_\zeta = u_e'\delta f + u_e\delta_\zeta f + u_e\delta f_\zeta \tag{F.27}$$

$$\Psi_\eta = u_e\delta f_\eta \tag{F.28}$$

$$\Psi_{\zeta\eta} = u_e'\delta f_\eta + u_e\delta_\zeta f_\eta + u_e\delta f_{\zeta\eta} \tag{F.29}$$

$$\Psi_{\eta\eta} = u_e\delta f_{\eta\eta} \tag{F.30}$$

$$\Psi_\tau = u_e\delta_\tau f \tag{F.31}$$

$$\Psi_{\eta\tau} = u_e\delta_\tau f_\eta. \tag{F.32}$$

The velocities are thus given by

$$u = \frac{\rho_0}{\rho}\Psi_y = \frac{\rho_0}{\rho}\frac{\rho}{\rho_0\delta}\Psi_\eta = \frac{u_e}{\delta}\delta f_\eta \tag{F.33}$$

$$= u_e f_\eta \tag{F.34}$$

$$v = -\frac{\rho_0}{\rho}\left(\Psi_x + \frac{\partial}{\partial t}(\eta\delta)\right) \tag{F.35}$$

$$= -\frac{\rho_0}{\rho}\left(-\frac{1}{L\tau}\Psi_\zeta + \eta_x\Psi_\eta + \frac{U_{CJ}}{L\tau}(1-\zeta)\eta\delta_\zeta + \eta_t\delta + \frac{U_{CJ}}{L}\eta\delta_\tau\right) \tag{F.36}$$

$$= \frac{\rho_0}{\rho}\frac{u_e\delta f}{L\tau}\left[\frac{u_e'}{u_e} + \frac{\delta_\zeta}{\delta} + \frac{f_\zeta}{f} - \eta_x L\tau\frac{f_\eta}{f} - \frac{U_{CJ}}{u_e f}(1-\zeta)\eta\frac{\delta_\zeta}{\delta}\right.$$
$$\left. \ldots - L\tau\frac{\eta_t}{u_e f} - \frac{U_{CJ}}{u_e f}\tau\eta\frac{\delta_\tau}{\delta}\right] \tag{F.37}$$

$$= \frac{\rho_0}{\rho}\frac{u_e\delta f}{L\tau}\left[\frac{u_e'}{u_e} + \frac{\delta_\zeta}{\delta} + \frac{f_\zeta}{f} - \eta_x L\tau\frac{f_\eta}{f} - \frac{U_{CJ}}{u_e f}\eta\frac{\delta_\zeta}{\delta}\right.$$
$$\left. \ldots + \frac{U_{CJ}}{u_e f}\eta\zeta\frac{\delta_\zeta}{\delta} - L\tau\frac{\eta_t}{u_e f} - \frac{U_{CJ}}{u_e f}\tau\eta\frac{\delta_\tau}{\delta}\right] \tag{F.38}$$

using

$$\delta = \sqrt{\frac{\nu_0 L\tau\zeta}{U_{CJ}}} \tag{F.39}$$

we have

$$v = \frac{\rho_0}{\rho}\frac{u_e\delta f}{L\tau}\left[\frac{u_e'}{u_e} + \frac{1}{2\zeta} + \frac{f_\zeta}{f} - \eta_x L\tau\frac{f_\eta}{f} - \frac{U_{CJ}}{u_e f}\frac{\eta}{2\zeta} + \cancel{\frac{U_{CJ}}{u_e}\frac{\eta}{2f}}\right.$$
$$\left. \ldots - L\tau\frac{\eta_t}{u_e f} - \cancel{\frac{U_{CJ}}{u_e}\frac{\eta}{2f}}\right] \tag{F.40}$$
$$= \frac{\rho_0}{\rho}\frac{u_e\delta f}{L\tau}\left[\frac{u_e'}{u_e} + \frac{1}{2\zeta} + \frac{f_\zeta}{f} - \eta_x L\tau\frac{f_\eta}{f} - \frac{U_{CJ}}{u_e f}\frac{\eta}{2\zeta} - L\tau\frac{\eta_t}{u_e f}\right]. \tag{F.41}$$

In the case of a boundary layer behind a steady shock

$$u_e' = f_\zeta = 0 \tag{F.42}$$
$$\Rightarrow\ v = \frac{\rho_0}{\rho}\frac{u_e\delta f}{L\tau}\left[\frac{1}{2\zeta} - \eta_x L\tau\frac{f_\eta}{f} - \frac{U_{CJ}}{u_e f}\frac{\eta}{2\zeta} - L\tau\frac{\eta_t}{u_e f}\right]. \tag{F.43}$$

F.3 Momentum Equation

We next consider each term in the momentum equation separately.

$$\rho u_t = \rho\frac{\partial}{\partial t}\left(\frac{\rho_0}{\rho}\Psi_y\right) \tag{F.44}$$
$$= \rho\frac{\partial}{\partial t}\left(\frac{\rho_0}{\rho}\frac{\rho}{\rho_0\delta}\Psi_\eta\right) \tag{F.45}$$
$$= \rho\frac{\partial}{\partial t}\left(\frac{1}{\delta}u_e\delta f_\eta\right) \tag{F.46}$$
$$= \rho\left[\frac{U_{CJ}}{L\tau}(1-\zeta)\left(u_e' f_\eta + u_e f_{\eta\zeta}\right) + u_e\eta_t f_{\eta\eta}\right] \tag{F.47}$$
$$= \frac{\rho u_e^2}{L\tau}\left[\frac{U_{CJ}}{u_e}(1-\zeta)\left(\frac{u_e'}{u_e}f_\eta + f_{\zeta\eta}\right) + \cancel{\frac{L\tau}{u_e}\eta_t f_{\eta\eta}}\right]. \tag{F.48}$$

$$\rho u u_x = \rho_0 \Psi_y \frac{\partial}{\partial x}\left(\frac{\rho_0}{\rho}\Psi_y\right) \tag{F.49}$$

$$= \frac{\rho}{\delta}\Psi_\eta \frac{\partial}{\partial x}\left(\frac{1}{\delta}\Psi_\eta\right) \tag{F.50}$$

$$= \rho u_e f_\eta \frac{\partial}{\partial x}\left(u_e f_\eta\right) \tag{F.51}$$

$$= \rho u_e f_\eta \left[-\frac{1}{L\tau}u_e' f_\eta - \frac{u_e}{L\tau} f_{\zeta\eta} + u_e \eta_x f_{\eta\eta}\right] \tag{F.52}$$

$$= \frac{\rho u_e^2}{L\tau}\left[-\frac{u_e'}{u_e} f_\eta^2 - f_\eta f_{\zeta\eta} + \cancel{L\tau \eta_x f_\eta f_{\eta\eta}}\right]. \tag{F.53}$$

$$\rho v u_y = -\rho_0 \left(\Psi_x + \frac{\partial}{\partial t}(\eta\delta)\right)\frac{\partial}{\partial y}\left(\frac{\rho_0}{\rho}\Psi_y\right) \tag{F.54}$$

$$= -\rho_0 \left(\Psi_x + \frac{\partial}{\partial t}(\eta\delta)\right)\frac{\partial}{\partial y}\left(\frac{\rho_0}{\rho}\frac{\rho}{\rho_0\delta}\Psi_\eta\right) \tag{F.55}$$

$$= -\rho_0 \left(\Psi_x + \frac{\partial}{\partial t}(\eta\delta)\right)\frac{\partial}{\partial y}\left(\frac{1}{\delta}u_e \delta f_\eta\right) \tag{F.56}$$

$$= -\rho_0 \left(\Psi_x + \frac{\partial}{\partial t}(\eta\delta)\right)\frac{\rho}{\rho_0\delta}\frac{\partial}{\partial \eta}\left(u_e f_\eta\right) \tag{F.57}$$

$$= -\frac{\rho u_e}{\delta} f_{\eta\eta}\left(\Psi_x + \frac{\partial}{\partial t}(\eta\delta)\right) \tag{F.58}$$

$$= -\frac{\rho u_e}{\delta} f_{\eta\eta}\left(-\frac{1}{L\tau}\Psi_\zeta + \eta_x \Psi_\eta + \frac{U_{CJ}}{L\tau}(1-\zeta)\frac{\partial}{\partial\zeta}(\eta\delta) + \right.$$
$$\left. \ldots\ \eta_t \frac{\partial}{\partial\eta}(\eta\delta) + \frac{U_{CJ}}{L}\frac{\partial}{\partial\tau}(\eta\delta)\right) \tag{F.59}$$

$$= -\frac{\rho u_e}{\delta} f_{\eta\eta}\left(-\frac{1}{L\tau}\left(u_e'\delta f + u_e \delta_\zeta f + u_e \delta f_\zeta\right) + \eta_x u_e \delta f_\eta \right.$$
$$\left. \ldots\ + \frac{U_{CJ}}{L\tau}(1-\zeta)\eta\delta_\zeta + \eta_t \delta + \frac{U_{CJ}}{L}\eta\delta_\tau\right) \tag{F.60}$$

$$= \frac{\rho u_e^2}{L\tau}\left(\frac{u_e'}{u_e} f f_{\eta\eta} + \frac{\delta_\zeta}{\delta} f f_{\eta\eta} + f_\zeta f_{\eta\eta} - \cancel{L\tau \eta_x f_\eta f_{\eta\eta}} - \frac{U_{CJ}}{u_e}(1-\zeta)\eta\frac{\delta_\zeta}{\delta} f_{\eta\eta}\right.$$
$$\left. \ldots\ - \cancel{\frac{L\tau}{u_e}\eta_t f_{\eta\eta}} - \frac{U_{CJ}}{u_e}\tau\eta\frac{\delta_\tau}{\delta} f_{\eta\eta}\right) \tag{F.61}$$

The pressure term is given by

$$\frac{\partial p}{\partial x} = -\frac{1}{L\tau}p_\zeta + \eta_x \cancel{p_\eta}^{0} \tag{F.62}$$

$$= -\frac{p_\zeta}{L\tau} \tag{F.63}$$

also, since $p_y = 0$, we know $p = p_e(\zeta)$ implying

$$-\frac{\partial p}{\partial x} = -\frac{p_e'}{L\tau}. \tag{F.64}$$

Lastly

$$\frac{\partial}{\partial y}\left(\mu\frac{\partial u}{\partial y}\right) = \frac{\partial}{\partial y}\left(\mu\frac{\rho}{\rho_0\delta}\frac{\partial}{\partial \eta}\left(\frac{\rho_0}{\rho}\frac{\partial \Psi}{\partial y}\right)\right) \tag{F.65}$$

$$= \frac{\partial}{\partial y}\left(\mu\frac{\rho}{\rho_0\delta}\frac{\partial}{\partial \eta}\left(\frac{\rho_0}{\rho}\frac{\rho}{\rho_0\delta}\frac{\partial \Psi}{\partial \eta}\right)\right) \tag{F.66}$$

$$= \frac{\rho}{\rho_0\delta}\frac{\partial}{\partial \eta}\left(\mu\frac{\rho}{\rho_0\delta}\frac{\partial}{\partial \eta}\left(\frac{1}{\delta}u_e\delta f_\eta\right)\right) \tag{F.67}$$

$$= \frac{\rho u_e}{\rho_0\delta}\frac{\partial}{\partial \eta}\left(\mu\frac{\rho}{\rho_0\delta}f_{\eta\eta}\right) \tag{F.68}$$

$$= \frac{\rho\nu_0 u_e}{\delta^2}\frac{\partial}{\partial \eta}\left(Cf_{\eta\eta}\right) \tag{F.69}$$

where

$$C = \frac{\rho\mu}{\rho_0\mu_0} \tag{F.70}$$

is the Chapman-Rubesin parameter.

Thus we see after cancellation

$$0 = -\frac{\partial p}{\partial x} + \frac{\partial}{\partial y}\left(\mu\frac{\partial u}{\partial y}\right) - \rho\frac{\partial u}{\partial t} - \rho u\frac{\partial u}{\partial x} - \rho v\frac{\partial u}{\partial y} \tag{F.71}$$

$$\begin{aligned} =&\frac{p_e'}{L\tau} + \frac{\rho\nu_0 u_e}{\delta^2}\left(Cf_{\eta\eta}\right)_\eta - \frac{\rho u_e^2}{L\tau}\left[\frac{U_{CJ}}{u_e}(1-\zeta)\left(\frac{u_e'}{u_e}f_\eta + f_{\zeta\eta}\right)\right] \\ &\ldots - \frac{\rho u_e^2}{L\tau}\left[-\frac{u_e'}{u_e}f_\eta^2 - f_\eta f_{\zeta\eta}\right] - \frac{\rho u_e^2}{L\tau}\left[\frac{u_e'}{u_e}ff_{\eta\eta} + \frac{\delta_\zeta}{\delta}ff_{\eta\eta}\right. \\ &\left.\ldots + f_\zeta f_{\eta\eta} - \frac{U_{CJ}}{u_e}(1-\zeta)\,\eta\frac{\delta_\zeta}{\delta}f_{\eta\eta} - \frac{U_{CJ}}{u_e}\tau\eta\frac{\delta_\tau}{\delta}f_{\eta\eta}\right] \end{aligned} \tag{F.72}$$

$$\begin{aligned} =&\frac{\nu_0 L\tau}{\delta^2 u_e}\left(Cf_{\eta\eta}\right)_\eta + \frac{p_e'}{\rho u_e^2} - \left(\frac{\delta_\zeta}{\delta}f - \frac{U_{CJ}}{u_e}(1-\zeta)\,\eta\frac{\delta_\zeta}{\delta} - \frac{U_{CJ}}{u_e}\tau\eta\frac{\delta_\tau}{\delta}\right)f_{\eta\eta} \\ &\ldots - \left(\frac{u_e'}{u_e}f + f_\zeta\right)f_{\eta\eta} - \frac{U_{CJ}}{u_e}\left((1-\zeta)\left(\frac{u_e'}{u_e}f_\eta + f_{\zeta\eta}\right)\right) + \frac{u_e'}{u_e}f_\eta^2 + f_\eta f_{\zeta\eta} \end{aligned} \tag{F.73}$$

$$\begin{aligned} =&\frac{\nu_0 L\tau}{\delta^2 u_e}\left(Cf_{\eta\eta}\right)_\eta + \frac{p_e'}{\rho u_e^2} + \left(\frac{U_{CJ}}{u_e}(1-\zeta)\,\eta\frac{\delta_\zeta}{\delta} + \frac{U_{CJ}}{u_e}\tau\eta\frac{\delta_\tau}{\delta} - \frac{\delta_\zeta}{\delta}f\right)f_{\eta\eta} \\ &\ldots - \left(\frac{u_e'}{u_e}f + f_\zeta\right)f_{\eta\eta} - \frac{U_{CJ}}{u_e}\left[\left(1-\zeta-\frac{u_e}{U_{CJ}}f_\eta\right)\left(\frac{u_e'}{u_e} + \frac{f_{\zeta\eta}}{f_\eta}\right)f_\eta\right]. \end{aligned} \tag{F.74}$$

Or after rearranging and multiplying by $\zeta u_e/U_{CJ}$

$$\begin{aligned} &\frac{1}{\delta^2}\frac{\nu_0 L\tau\zeta}{U_{CJ}}\left(Cf_{\eta\eta}\right)_\eta + \left((1-\zeta)\,\eta\frac{\delta_\zeta}{\delta} + \tau\eta\frac{\delta_\tau}{\delta} - \frac{u_e}{U_{CJ}}\frac{\delta_\zeta}{\delta}f\right)\zeta f_{\eta\eta} \\ &\qquad = \zeta\left\{\left(\frac{u_e'}{U_{CJ}}f + \frac{u_e}{U_{CJ}}f_\zeta\right)f_{\eta\eta} - \frac{p_e'}{\rho u_e U_{CJ}}\right. \\ &\qquad\qquad \left.\ldots + \left(1-\zeta-\frac{u_e}{U_{CJ}}f_\eta\right)\left(\frac{u_e'}{u_e} + \frac{f_{\zeta\eta}}{f_\eta}\right)f_\eta\right\}. \end{aligned} \tag{F.75}$$

From equation (F.75), we can see that if $p_e(\zeta) = p_e \;\Rightarrow\; p_e' = 0$, $u_e(\zeta) = u_e \;\Rightarrow\; u_e' = 0$, and $f = f(\eta)$ implying $f_\zeta = f_\tau = 0$ as would be the case for a boundary layer behind a shock with uniform post-shock conditions, then the entire right-hand of

equation (F.75) side equals zero. Using

$$\delta = \sqrt{\frac{\nu_0 L \tau \zeta}{U_{CJ}}} \tag{F.76}$$

$$\Rightarrow \quad \frac{\delta_\zeta}{\delta} = \frac{1}{2\zeta} \tag{F.77}$$

$$\frac{\delta_\tau}{\delta} = \frac{1}{2\tau} \tag{F.78}$$

gives

$$\begin{aligned}(C f_{\eta\eta})_\eta + \left(\frac{\eta}{2\zeta} - \frac{\eta}{2} + \frac{\eta}{2} - \frac{u_e}{U_{CJ}}\frac{f}{2\zeta}\right)\zeta f_{\eta\eta} = \zeta\Bigg\{&\left(\frac{u_e'}{U_{CJ}} f + \frac{u_e}{U_{CJ}} f_\zeta\right) f_{\eta\eta} - \frac{p_e'}{\rho u_e U_{CJ}} \\ &... + \left(1 - \zeta - \frac{u_e}{U_{CJ}} f_\eta\right)\left(\frac{u_e'}{u_e} + \frac{f_{\zeta\eta}}{f_\eta}\right) f_\eta\Bigg\}\end{aligned} \tag{F.79}$$

$$\begin{aligned}(C f_{\eta\eta})_\eta + \frac{1}{2}\left(\eta - \frac{u_e}{U_{CJ}} f\right) f_{\eta\eta} = \zeta\Bigg\{&\left(\frac{u_e'}{U_{CJ}} f + \frac{u_e}{U_{CJ}} f_\zeta\right) f_{\eta\eta} \\ &... + \left(1 - \zeta - \frac{u_e}{U_{CJ}} f_\eta\right)\left(\frac{u_e'}{u_e} + \frac{f_{\zeta\eta}}{f_\eta}\right) f_\eta - \frac{p_e'}{\rho u_e U_{CJ}}\Bigg\}.\end{aligned} \tag{F.80}$$

If the right-hand side is zero and $C = 1$ we return the results given in Schlichting (1979):

$$f_{\eta\eta\eta} + \frac{1}{2}\left(\eta - \frac{u_e}{U_{CJ}} f\right) f_{\eta\eta} = 0. \tag{F.81}$$

We also return the results of Liu et al. (1983) if $\sigma = 0$, $\alpha = 1$. To show this is true, we need to return to equation (F.75) and instead use

$$\delta_{Liu} = \delta\sqrt{\frac{1}{2}\left(\frac{p_0}{U_{CJ}^2 b \rho_0 F_0}\right)^\omega} \tag{F.82}$$

where

$$b = \frac{\gamma(\gamma_0 - 1)}{\gamma_0(\gamma - 1)}\frac{c_{p,0}}{c_p} \tag{F.83}$$

using the terminology of Liu et al. (1983):

$$\mu = \mu_0 \left(\frac{T}{T_0}\right)^{\omega} \tag{F.84}$$

$$F = \frac{p_e}{\rho_0 U_{CJ}^2} \tag{F.85}$$

$$R = \frac{\rho_e}{\rho_0} \tag{F.86}$$

$$\phi = \frac{u_e}{U_{CJ}} \tag{F.87}$$

$$\beta = \frac{\rho\mu}{\rho_e\mu_e} = C\frac{\rho_0\mu_0}{\rho_e\mu_e} \tag{F.88}$$

we get

$$\begin{aligned}\frac{p_0^{\omega}}{U_{CJ}^{2\omega} b^{\omega} \rho_0^{\omega} F_0^{\omega}} \frac{\rho_e\mu_e}{\rho_0\mu_0} \left(\beta f_{\eta\eta}\right)_{\eta} + \left(\eta - \phi f\right) f_{\eta\eta} \\ = 2\zeta \left\{ \left(\phi' f + \phi f_{\zeta}\right) f_{\eta\eta} + \left(1 - \zeta - \phi f_{\eta}\right) \left(\frac{\phi'}{\phi} + \frac{f_{\zeta\eta}}{f_{\eta}}\right) f_{\eta} - \frac{F_{\zeta} g}{R\phi} \right\}\end{aligned} \tag{F.89}$$

this is precisely what Liu et al. observes except the first term is organized differently. To show these are equivalent observe:

$$\frac{\rho_e\mu_e}{\rho_0\mu_0} \left(\frac{p_0}{U_{CJ}^2 b \rho_0 F_0}\right)^{\omega} = \frac{\rho_e}{\rho_0} \left(\frac{T_e}{T_0}\right)^{\omega} \left(\frac{\gamma_0(\gamma-1)}{\gamma(\gamma_0-1)} \frac{c_p}{c_{p,0}}\right)^{\omega} \left(\frac{p_0}{p_e}\right)^{\omega} \left(\frac{p_e}{\rho_0 U_{CJ}^2 F_0}\right)^{\omega} \tag{F.90}$$

$$= R \left(\frac{T_e}{T_0}\right)^{\omega} \left(\frac{\gamma_0(\gamma-1)}{\gamma(\gamma_0-1)} \frac{c_p T_e}{c_{p,0} T_0}\right)^{\omega} \left(\frac{T_0}{T_e}\right)^{\omega} \left(\frac{p_0}{p_e}\right)^{\omega} \left(\frac{F}{F_0}\right)^{\omega} \tag{F.91}$$

$$= R \left(\frac{\gamma_0(\gamma-1)}{\gamma(\gamma_0-1)} \frac{h_e}{h_0}\right)^{\omega} \left(\frac{p_0}{p_e}\right)^{\omega} \left(\frac{F}{F_0}\right)^{\omega} \tag{F.92}$$

$$= R \left(\frac{p_e}{\rho_e} \frac{\rho_0}{p_0}\right)^{\omega} \left(\frac{p_0}{p_e}\right)^{\omega} \left(\frac{F}{F_0}\right)^{\omega} \tag{F.93}$$

$$= R^{1-\omega} \left(\frac{F}{F_0}\right)^{\omega} \qquad \checkmark \tag{F.94}$$

where we've used

$$h = \frac{\gamma}{\gamma - 1}\frac{p}{\rho}. \tag{F.95}$$

Note that we've shown

$$\frac{\nu_0 L \tau \zeta}{\delta_{Liu}^2 U_{CJ}} C^* = \frac{1}{2} R^{1-\omega} \left(\frac{F}{F_0}\right)^{\omega} \tag{F.96}$$

where C^* is either C or a derivative of C.

So our final equation is

$$\begin{aligned}(C f_{\eta\eta})_\eta + \frac{1}{2}\left(\eta - \frac{u_e}{U_{CJ}} f\right) f_{\eta\eta} = \zeta \Bigg\{ &\left(\frac{u_e'}{U_{CJ}} f + \frac{u_e}{U_{CJ}} f_\zeta\right) f_{\eta\eta} \\ &... + \left(1 - \zeta - \frac{u_e}{U_{CJ}} f_\eta\right)\left(\frac{u_e'}{u_e} + \frac{f_{\zeta\eta}}{f_\eta}\right) f_\eta - \frac{p_e'}{\rho u_e U_{CJ}} \Bigg\}\end{aligned} \tag{F.97}$$

with initial conditions

$$f(\zeta, 0) = f_\eta(\zeta, 0) = 0 \tag{F.98}$$

$$f_\eta(\zeta, \infty) = 1 \tag{F.99}$$

$$u(\zeta, \eta) = u_e(\zeta) f_\eta(\zeta, \eta) \tag{F.100}$$

and

$$\zeta(x, t) = 1 - \frac{x}{U_{CJ} t} \tag{F.101}$$

$$\eta(x, y, t) = \frac{\int_0^y \frac{\rho(x, y', t)}{\rho_0} dy'}{\sqrt{\nu_0 \left(t - \frac{x}{U_{CJ}}\right)}}. \tag{F.102}$$

F.3.1 Ideal Free-Stream Conditions

Assuming the conditions behind the detonation are constant at the Chapman-Jouguet values, we have $p_e = p_2$, $u_e = u_2$, and $h_e = h_2$. This leads to f only being a function

of η. Further, assuming $C = 1$, equation (F.80) becomes

$$f''' + \frac{1}{2}\left(\eta - \frac{f}{\Lambda}\right) f'' = 0 \tag{F.103}$$

where

$$\Lambda \equiv \frac{U_{CJ}}{u_2}. \tag{F.104}$$

The boundary conditions are

$$f(0) = 0 \tag{F.105}$$

$$f(\infty) = 1 \tag{F.106}$$

and u can be found from

$$u(\eta) = u_2 f'. \tag{F.107}$$

The boundary layer thickness, δ, at a given distance behind the shock x' can be calculated from:

$$\delta(x) = \sqrt{\frac{\nu_2 L \tau \zeta}{U_{CJ}}} \tag{F.108}$$

$$= \sqrt{\frac{\nu_2 L}{U_{CJ}}\left(1 - \frac{x}{X_s}\right)\frac{t U_{CJ}}{L}} \tag{F.109}$$

$$= \sqrt{\nu_2\left(t - \frac{x}{U_{CJ}}\right)} \tag{F.110}$$

using

$$t = \frac{X_s}{U_{CJ}} \tag{F.111}$$

gives

$$\delta(x) = \sqrt{\nu_2 \frac{X_s - x}{U_{CJ}}} \tag{F.112}$$

and evaluating at $x = X_s - x'$ yields

$$\delta(X_s - x') = \sqrt{\frac{\nu_2 x'}{U_{CJ}}}. \tag{F.113}$$

F.4 Energy Equation

We define g to be the non-dimensionalized enthalpy

$$g(\zeta, \eta, \tau) = \frac{h(\zeta, \eta)}{h_e(\zeta)} \tag{F.114}$$

and thus we have

$$h_\zeta = (h_e g)_\zeta = h_e' g + h_e g_\zeta \tag{F.115}$$

$$h_\eta = h_e g_\eta \tag{F.116}$$

$$h_\tau = 0. \tag{F.117}$$

We can substitute this into the conservation of energy relationship to produce

$$\rho h_t = \frac{\rho U_{CJ}}{L\tau}(1-\zeta)h_\zeta + \rho\eta_t h_\eta + \frac{\rho U_{CJ}}{L} h_\tau \tag{F.118}$$

$$= \frac{\rho U_{CJ}}{L\tau}(1-\zeta)\left(h_e' g + h_e g_\zeta\right) + \rho\eta_t h_e g_\eta \tag{F.119}$$

$$= \frac{\rho u_e}{L\tau} h_e \left[\frac{U_{CJ}}{u_e}(1-\zeta)\left(\frac{h_e'}{h_e} g + g_\zeta\right) + \cancel{\frac{L\tau}{u_e}\eta_t g_\eta}\right]. \tag{F.120}$$

$$\rho u h_x = \rho_0 \Psi_y h_x \tag{F.121}$$
$$= \rho_0 \frac{\rho}{\rho_0 \delta} \Psi_\eta \left(-\frac{1}{L\tau} h_\zeta + \eta_x h_\eta \right) \tag{F.122}$$
$$= \rho u_e f_\eta \left(-\frac{1}{L\tau} \left(h'_e g + h_e g_\zeta \right) + \eta_x h_e g_\eta \right) \tag{F.123}$$
$$= \frac{\rho u_e}{L\tau} h_e \left[-\frac{h'_e}{h_e} g f_\eta - g_\zeta f_\eta + \cancel{L\tau \eta_x g_\eta f_\eta} \right]. \tag{F.124}$$

$$\rho v h_y = -\rho_0 \left(\Psi_x + (\eta\delta)_t \right) h_y \tag{F.125}$$
$$= -\rho_0 \left(-\frac{1}{L\tau} \Psi_\zeta + \eta_x \Psi_\eta + \frac{U_{CJ}}{L\tau} (1-\zeta) (\eta\delta)_\zeta + \eta_t (\eta\delta)_\eta \right.$$
$$\left. \ldots + \frac{U_{CJ}}{L} (\eta\delta)_\tau \right) \frac{\rho}{\rho_0 \delta} h_\eta \tag{F.126}$$
$$= -\frac{\rho}{\delta} h_e g_\eta \left(-\frac{1}{L\tau} u'_e \delta f - \frac{1}{L\tau} u_e \delta_\zeta f - \frac{1}{L\tau} u_e \delta f_\zeta + \eta_x u_e \delta f_\eta \right.$$
$$\left. \ldots + \frac{U_{CJ}}{L\tau} (1-\zeta) \eta \delta_\zeta + \eta_t \delta + \frac{U_{CJ}}{L} \eta \delta_\tau \right) \tag{F.127}$$
$$= \frac{\rho u_e}{L\tau} h_e \left[\frac{u'_e}{u_e} f g_\eta + \frac{\delta_\zeta}{\delta} f g_\eta + f_\zeta g_\eta - \cancel{L\tau \eta_x f_\eta g_\eta} - \frac{U_{CJ}}{u_e} (1-\zeta) \eta \frac{\delta_\zeta}{\delta} g_\eta \right.$$
$$\left. \ldots - \cancel{\frac{L\tau}{u_e} \eta_t g_\eta} - \frac{U_{CJ}}{u_e} \tau \eta \frac{\delta_\tau}{\delta} g_\eta \right]. \tag{F.128}$$

$$p_t = \frac{U_{CJ}}{L\tau} (1-\zeta) p_\zeta + \eta_t \cancel{p_\eta}^{\,0} + \frac{U_{CJ}}{L} \cancel{p_\tau}^{\,0} \tag{F.129}$$
$$= \frac{U_{CJ}}{L\tau} (1-\zeta) p'_e \tag{F.130}$$
$$= \frac{\rho u_e}{L\tau} (1-\zeta) \frac{U_{CJ}}{u_e} \frac{p'_e}{\rho} \tag{F.131}$$
$$u p_x = \frac{\rho_0}{\rho} \Psi_y \left(-\frac{1}{L\tau} p_\zeta + \eta_x \cancel{p_\eta}^{\,0} \right) \tag{F.132}$$
$$= \frac{\rho_0}{\rho} \frac{\rho}{\rho_0 \delta} \Psi_\eta \left(-\frac{1}{L\tau} p'_e \right) \tag{F.133}$$
$$= -\frac{1}{L\tau\delta} u_e \delta f_\eta p'_e \tag{F.134}$$
$$= -\frac{\rho u_e}{L\tau} f_\eta \frac{p'_e}{\rho}. \tag{F.135}$$

$$\left(\frac{\mu}{Pr}h_y\right)_y = \frac{\rho}{\rho_0\delta}\left(\frac{\mu\rho}{Pr\rho_0\delta}h_\eta\right)_\eta \tag{F.136}$$

$$= \frac{\rho\mu_0}{\delta\rho_0}\left(\frac{\mu\rho}{\mu_0\rho_0}\frac{1}{Pr\delta}h_e g_\eta\right)_\eta \tag{F.137}$$

$$= \frac{\rho\nu_0}{\delta^2}h_e\left(\frac{C}{Pr}g_\eta\right)_\eta. \tag{F.138}$$

$$(\mu u_y)^2 = \mu\left[\left(\frac{\rho_0}{\rho}\Psi_y\right)_y\right]^2 \tag{F.139}$$

$$= \mu\left[\frac{\rho}{\rho_0\delta}\left(\frac{\rho_0}{\rho}\frac{\rho}{\rho_0\delta}\Psi_\eta\right)_\eta\right]^2 \tag{F.140}$$

$$= \mu\left[\frac{\rho}{\rho_0\delta}\left(\frac{1}{\delta}u_e\delta f_\eta\right)_\eta\right]^2 \tag{F.141}$$

$$= \frac{\mu\rho^2u_e^2}{\rho_0^2\delta^2}f_{\eta\eta}^2 \tag{F.142}$$

$$= \frac{\rho\mu_0u_e^2}{\rho_0\delta^2}Cf_{\eta\eta}^2 \tag{F.143}$$

$$= \frac{\rho\nu_0u_e^2}{\delta^2}Cf_{\eta\eta}^2. \tag{F.144}$$

After cancellation, we have

$$\rho h_t + \rho u h_x + \rho v h_y = p_t + u p_x + \left(\frac{\mu}{Pr}h_y\right)_y + \mu\left(u_y\right)^2 \tag{F.145}$$

$$\frac{\rho u_e}{L\tau}h_e\left[\frac{U_{CJ}}{u_e}(1-\zeta)\left(\frac{h'_e}{h_e}g+g_\zeta\right)-\frac{h'_e}{h_e}gf_\eta-g_\zeta f_\eta-\frac{U_{CJ}}{u_e}(1-\zeta)\eta\frac{\delta_\zeta}{\delta}g_\eta\right.$$
$$\left.\ldots+\frac{u'_e}{u_e}fg_\eta+f_\zeta g_\eta+\frac{\delta_\zeta}{\delta}fg_\eta-\frac{U_{CJ}}{u_e}\tau\eta\frac{\delta_\tau}{\delta}g_\eta\right]=\frac{\rho u_e}{L\tau}(1-\zeta)\frac{U_{CJ}}{u_e}\frac{p'_e}{\rho}$$
$$\ldots-\frac{\rho u_e}{L\tau}f_\eta\frac{p'_e}{\rho}+\frac{\rho\nu_0}{\delta^2}h_e\left(\frac{C}{Pr}g_\eta\right)_\eta+\frac{\rho\nu_0u_e^2}{\delta^2}Cf_{\eta\eta}^2 \tag{F.146}$$

$$\frac{U_{CJ}}{u_e}(1-\zeta)\left(\frac{h'_e}{h_e}g+g_\zeta\right)-\frac{h'_e}{h_e}gf_\eta-g_\zeta f_\eta-\frac{U_{CJ}}{u_e}(1-\zeta)\eta\frac{\delta_\zeta}{\delta}g_\eta+\frac{u'_e}{u_e}fg_\eta$$
$$\ldots+f_\zeta g_\eta+\frac{\delta_\zeta}{\delta}fg_\eta-\frac{U_{CJ}}{u_e}\tau\eta\frac{\delta_\tau}{\delta}g_\eta=(1-\zeta)\frac{U_{CJ}}{u_e}\frac{p'_e}{h_e\rho}-f_\eta\frac{p'_e}{h_e\rho}$$
$$\ldots+\frac{L\tau\nu_0}{u_e\delta^2}\left(\frac{C}{Pr}g_\eta\right)_\eta+\frac{\nu_0u_eL\tau}{h_e\delta^2}Cf_{\eta\eta}^2 \tag{F.147}$$

$$\frac{L\tau\nu_0}{u_e\delta^2}\left(\frac{C}{Pr}g_\eta\right)_\eta+\frac{\nu_0u_eL\tau}{h_e\delta^2}Cf_{\eta\eta}^2+\frac{U_{CJ}}{u_e}(1-\zeta)\eta\frac{\delta_\zeta}{\delta}g_\eta-\frac{\delta_\zeta}{\delta}fg_\eta+\frac{U_{CJ}}{u_e}\tau\eta\frac{\delta_\tau}{\delta}g_\eta$$
$$=\frac{u'_e}{u_e}fg_\eta+f_\zeta g_\eta+\frac{U_{CJ}}{u_e}(1-\zeta)\left(\frac{h'_e}{h_e}g+g_\zeta\right)-\frac{h'_e}{h_e}gf_\eta-g_\zeta f_\eta$$
$$\ldots-(1-\zeta)\frac{U_{CJ}}{u_e}\frac{p'_e}{h_e\rho}+f_\eta\frac{p'_e}{h_e\rho} \tag{F.148}$$

$$\frac{1}{\delta^2}\frac{\nu_0L\tau\zeta}{U_{CJ}}\left(\frac{C}{Pr}g_\eta\right)_\eta+\frac{u_e^2}{\delta^2}\frac{\nu_0L\tau\zeta}{h_eU_{CJ}}Cf_{\eta\eta}^2+(1-\zeta)\zeta\eta\frac{\delta_\zeta}{\delta}g_\eta-\frac{u_e}{U_{CJ}}\zeta\frac{\delta_\zeta}{\delta}fg_\eta+\zeta\tau\eta\frac{\delta_\tau}{\delta}g_\eta$$
$$=\zeta\left\{\left(\frac{u'_e}{U_{CJ}}f+\frac{u_e}{U_{CJ}}f_\zeta\right)g_\eta+\left(1-\zeta-\frac{u_e}{U_{CJ}}f_\eta\right)\left(\frac{h'_e}{h_e}+\frac{g_\zeta}{g}-\frac{p'_e}{\rho h_eg}\right)g\right\}. \tag{F.149}$$

Note that the right-hand side is zero in the case of steady flow behind the shock. At this point, let us use

$$\delta=\sqrt{\frac{\nu_0L\tau\zeta}{U_{CJ}}} \tag{F.150}$$

to yield

$$\left(\frac{C}{Pr}g_\eta\right)_\eta + \frac{u_e^2}{h_e}Cf_{\eta\eta}^2 + (1-\zeta)\frac{\eta}{2}g_\eta - \frac{1}{2}\frac{u_e}{U_{CJ}}fg_\eta + \frac{\zeta\eta}{2}g_\eta$$
$$= \zeta\left\{\left(\frac{u_e'}{U_{CJ}}f + \frac{u_e}{U_{CJ}}f_\zeta\right)g_\eta + \left(1-\zeta-\frac{u_e}{U_{CJ}}f_\eta\right)\left(\frac{h_e'}{h_e} + \frac{g_\zeta}{g} - \frac{p_e'}{\rho h_e g}\right)g\right\} \tag{F.151}$$

$$\left(\frac{C}{Pr}g_\eta\right)_\eta + \frac{u_e^2}{h_e}Cf_{\eta\eta}^2 + \left[(1-\zeta)\frac{\eta}{2} - \frac{1}{2}\frac{u_e}{U_{CJ}}f + \frac{\zeta\eta}{2}\right]g_\eta$$
$$= \zeta\left\{\left(\frac{u_e'}{U_{CJ}}f + \frac{u_e}{U_{CJ}}f_\zeta\right)g_\eta + \left(1-\zeta-\frac{u_e}{U_{CJ}}f_\eta\right)\left(\frac{h_e'}{h_e} + \frac{g_\zeta}{g} - \frac{p_e'}{\rho h_e g}\right)g\right\} \tag{F.152}$$

$$\left(\frac{C}{Pr}g_\eta\right)_\eta + \frac{u_e^2}{h_e}Cf_{\eta\eta}^2 + \frac{1}{2}\left[\eta - \frac{u_e}{U_{CJ}}f\right]g_\eta$$
$$= \zeta\left\{\left(\frac{u_e'}{U_{CJ}}f + \frac{u_e}{U_{CJ}}f_\zeta\right)g_\eta + \left(1-\zeta-\frac{u_e}{U_{CJ}}f_\eta\right)\left(\frac{h_e'}{h_e} + \frac{g_\zeta}{g} - \frac{p_e'}{\rho h_e g}\right)g\right\}. \tag{F.153}$$

If we now assume that $C = 1$, the Prandtl number is constant, flow properties behind the shock are constant (implying $u_e' = f_\zeta = h_e' = g_\zeta = p_e' = 0$), and $h = c_pT$, we return the solution presented in Schlichting (1979):

$$\frac{1}{Pr}g_{\eta\eta} + \frac{u_e^2}{c_pT_e}f_{\eta\eta}^2 + \frac{1}{2}\left[\eta - \frac{u_e}{U_{CJ}}f\right]g_\eta = 0. \tag{F.154}$$

The solution of Liu et al. (1983) is returned if we take the same assumptions and choice of δ as described above. This is proven by noting

$$\frac{\gamma-1}{\gamma}\frac{R\phi^2}{F} = \frac{\gamma-1}{\gamma}\frac{\rho_e}{\rho_0}\frac{\rho_0 U_{CJ}^2}{p_e}\frac{u_e^2}{U_{CJ}^2} \tag{F.155}$$
$$= \frac{\gamma-1}{\gamma}\frac{\rho_e}{p_e}u_e^2 \tag{F.156}$$
$$= \frac{u_e^2}{h_e}. \tag{F.157}$$

F.4.1 Idealized Conditions

Assuming the conditions behind the detonation are constant at the Chapman-Jouguet values, we have $p_e = p_2$, $u_e = u_2$, and $h_e = h_2$. This leads to g only being a function of η. Further assuming $C = 1$ and the Pr number is constant equation (F.153) becomes

$$g'' + PrEcf''^2 + \frac{Pr}{2}\left[\eta - \frac{f}{\Lambda}\right]g' = 0 \tag{F.158}$$

where

$$\Lambda \equiv \frac{U_{CJ}}{u_2} \tag{F.159}$$

$$Ec \equiv \frac{u_2^2}{h_2} \tag{F.160}$$

the boundary conditions are

$$g(0) = \frac{h_w}{h_2} \tag{F.161}$$

$$g(\infty) = 1 \tag{F.162}$$

and h can be found from

$$h(\eta) = h_2 g. \tag{F.163}$$